Structure and Bonding 174
Series Editor: D.M.P. Mingos

Stefanie Dehnen *Editor*

Clusters – Contemporary Insight in Structure and Bonding

Springer

174
Structure and Bonding

Aims and Scope

Structure and Bonding is a publication which uniquely bridges the journal and book format. Organized into topical volumes, the series publishes in depth and critical reviews on all topics concerning structure and bonding. With over 50 years of history, the series has developed from covering theoretical methods for simple molecules to more complex systems.

Topics addressed in the series now include the design and engineering of molecular solids such as molecular machines, surfaces, two dimensional materials, metal clusters and supramolecular species based either on complementary hydrogen bonding networks or metal coordination centers in metal-organic framework materials (MOFs). Also of interest is the study of reaction coordinates of organometallic transformations and catalytic processes, and the electronic properties of metal ions involved in important biochemical enzymatic reactions.

Volumes on physical and spectroscopic techniques used to provide insights into structural and bonding problems, as well as experimental studies associated with the development of bonding models, reactivity pathways and rates of chemical processes are also relevant for the series.

Structure and Bonding is able to contribute to the challenges of communicating the enormous amount of data now produced in contemporary research by producing volumes which summarize important developments in selected areas of current interest and provide the conceptual framework necessary to use and interpret mega-databases.

We welcome proposals for volumes in the series within the scope mentioned above. Structure and Bonding offers our authors and readers:

- OnlineFirst publication. Each chapter is published online as it is finished, ahead of the print volume
- Wide dissemination. The chapters and the volume will be available on our platform SpringerLink, one of the largest collections of scholarly content in the world. SpringerLink attracts more than 50 million users at 15.000 institutions worldwide.
- Easy manuscript preparation. Authors do not have to spend their valuable time on the layout of their contribution. Springer will take care of all the layout related issues and will provide support throughout the complete process.

More information about this series at http://www.springer.com/series/430

Stefanie Dehnen
Editor

Clusters – Contemporary Insight in Structure and Bonding

With contributions by

J.F. Corrigan · S. Dehnen · J.M. Goicoechea · C. Heindl · Y. Huang · T.I. Levchenko · M. Mehring · G. Niedner-Schatteburg · E. Peresypkina · M. Scheer · A. Schnepf · A. Virovets · F. Weigend · B. Weinert

Springer

Editor
Stefanie Dehnen
Fachbereich Chemie
Philipps-Universität Marburg and Wissenschaftliches
Zentrum für Materialwissenschaften
Marburg, Germany

ISSN 0081-5993 ISSN 1616-8550 (electronic)
Structure and Bonding
ISBN 978-3-319-52294-4 ISBN 978-3-319-52296-8 (eBook)
DOI 10.1007/978-3-319-52296-8

Library of Congress Control Number: 2017935850

Printed on acid-free paper

This Springer imprint is published by Springer Nature
The registered company is Springer International Publishing AG
The registered company address is: Gewerbestrasse 11, 6330 Cham, Switzerland

Preface

What is a cluster? This question has been a topic of discussion over the years since the famous first definition by F. A. Cotton in the early 1970s, when he introduced the term to describe complexes that comprise at least three metal atoms that are connected by direct metal–metal bonds. The historic definition was rather narrow and restrictive regarding the choice of respective compounds, but at the same time was very clear. Later on, it became obvious, however, that it is also reasonable to call other molecules a cluster if they possess a certain size, even if the metal atoms in them were connected in part or exclusively via bridging non-metal ligands. Furthermore, the term was also used for large non-metal aggregates, including non-covalently bonded assemblies, like water clusters. During the last two decades, the increasing search for buzz words unfortunately led to application of the term also to small molecular assemblies, such as binuclear coordination compounds. The latter do apparently not fulfil any prerequisite of a cluster regarding the encyclopedic definition of the word as "a group of similar things or people positioned or occurring closely together". This rather general definition is reflected by the use of the term not only in chemistry but also in other fields like Music, Arts, Linguistics, Urbanism, Astrophysics, Biology, Health Science, Engineering and Computer Sciences.

So, where are we actually today? The IUPAC provides the chemical community with the following current recommendation: "A number of metal centres grouped close together which can have direct metal bonding interactions or interactions through a bridging ligand, but are not necessarily held together by these interactions", which summarizes the aforesaid and excludes aggregates of uncountable units such as found in nanoparticles. Within this volume of *Structure and Bonding*, we try to provide the community with a collection of articles on different cluster compounds, all of which comply with the contemporary definition that relies on the literal meaning of the word. Hence, all of the examples called "clusters" within this volume exhibit a certain molecular size, with a critical minimum number of involved atoms or units equal to three. As outlined above, we do not recommend restricting the term on metal–metal bonded systems, as this would exclude a

tremendous number of beautiful molecules that cannot be named other than a cluster in a reasonable way. It remains questionable whether or not to call polyatomic non-metal main group molecules a cluster, as there are usually specific alternative terminologies for such systems, like fullerenes/-ides or boranes/-ides. However, we do not see a principal contradiction for it.

The rather semantic question on the terminology is closely related to the nature of cluster molecules regarding their structures and bonding. With this book, we aim at providing a contemporary overview and insight into different families of clusters, their synthetic approaches and their specific properties, albeit representing a selection of examples, with no claim to completeness. Our selection includes the description of physical analysis methods and theoretical descriptions of the topologies and the electronic situation. The synthetic approaches are as diverse as the products themselves; hence the book deals with compounds that were obtained by various techniques, which range from solid-state methods through solution chemistry to gas phase techniques, and also includes theoretical treatment. However, as the chapters are reviews in nature, they do not provide too many details, which are subject to the more specified descriptions in the original and comprehensively cited literature. In all of the more experimental-based chapters, typical analytical techniques will be named and briefly described in the context of their application on the specific scientific questions. According to the great diversity of the cluster molecules, ranging from electron-deficient to electron-precise molecules, the bonding spectrum also covers a variety of different systems. Some cluster families feature electron-precise covalent bonds, while others exhibit semi-localized bonding or even possess highly delocalized electronic situations that are best described by the superatom concept for clusters in the jellium model of electron shells. A diversity of different bonding concepts have been developed during the past decades that serve – to some extent – to classify different families of clusters. Such concepts and their application to the discussed species are to be found within the different chapters of this book.

The chapters are assigned to two major groups, ligand-free and ligand-decorated clusters, respectively, each being divided into four sub-chapters. *Cooperative Effects in Clusters and Oligonuclear Complexes of Transition Metals in Isolation* are presented by Gereon Niedner-Schatteburg, who introduces contemporary methods of transition metal cluster generation and oligonuclear transition metal complex isolation, along with their analysis. The chapter also describes the kinetics of small molecule adsorption and CH activation by transition metal clusters and elaborates on vibrational as well as magnetic properties. Another, theoretical, view onto ligand-free clusters is provided by Florian Weigend in his chapter *Quantum Chemical Investigations of Clusters of Heavy Metal Atoms*, which surveys the quantum chemical treatment of heavy metal atom clusters with contemporary methods. The main focus of the chapter is the impact of spin-orbit coupling on electronic and geometric structures on the one hand and how to find global minimum structures in case of binary or ternary systems on the other hand, which has been treated by application of density functional theory methods and is discussed in the

light of recent developments. The latter are exemplified on medium-sized gold clusters, and clusters of heavy p-block elements with or without interstitial transition metal atoms. In the two following chapters, ligand-free clusters are reviewed from a preparative point of view, but also including their specific properties. Jose M. Goicoechea describes *Homoatomic Polyanions of the Early p-Block Elements* based on the example of compounds with Zintl anions of group 13-15 elements. The chapter focuses on species that have been isolated in the solid state or from solution, and which were structurally determined by X-ray crystallography. Besides the structures, the author details bonding, electronic properties and formation pathways of such homoatomic clusters. An extension of the field towards *Binary and Ternary Intermetalloid Clusters* is provided in the chapter by Bastian Weinert and Stefanie Dehnen, who present intermetalloid clusters as another part of contemporary Zintl anion chemistry. These clusters combine anionic, homo- or heteroatomic main group (semi-)metal units with transition metal atoms that can be included in cages of the other elements and/or be part of a heterometallic cluster framework. This chapter gives a comprehensive overview of structures, bonding situations, electronic properties, and it comments on the still widely unknown formation pathways of these nanoscale heterometallic clusters, thereby also referring to recent DFT calculations, complementary to the chapter by Florian Weigend.

The second group of clusters are those that are decorated and hence protected by ligands. *Metalloid Clusters* are reviewed in the chapter by Andreas Schnepf. Both the dimension of these clusters and the charge of the metal atoms within them are situated between that of small molecules and the bulk metals in the solid state, which allows for some insight into dissolution and formation processes of the latter. The chapter reports on synthetic routes as well as structure and bonding of metalloid clusters of group 13 and group 14 elements, highlighting structural analogies of the clusters with structure motives found in the corresponding metals. The following two chapters are closely related. In the chapter on *Metal Oxido Clusters of Group 13-15 Elements*, Michael Mehring reports on approaches to metal oxides that are based on hydrolysis and condensation processes from precursor solutions. Metal oxido clusters represent important intermediates on the way towards metal oxides. Thus, like metalloid clusters along the formation of metals, they help to understand these processes and the structural chemistry of the metal oxide family, and how to control structure, particle size and morphology of the final hydrolysis products. The present review focuses on metal oxido clusters that are composed of more than ten atoms of group 13-15 elements and contain at least one oxido ligand, complemented by some examples comprising Ce, U, or Pu atoms. Heavier congeners of oxygen are the bridging ligands in the chapter on *Large Metal Chalcogenide Clusters and Their Ordered Superstructures via Solvothermal and Ionothermal Syntheses* by Tetyana I. Levchenko, Yining Huang and John F. Corrigan. As a complement to the previous section, this review will concentrate on nanometer-scale metal chalcogenide clusters and materials derived from those, both of which are of specific interest owing to their intricate structures and unique size-related electronic and physical properties. In this chapter, structures and bonding principles in these systems are summarized, with a focus on discrete

metal chalcogenide clusters of high nuclearity, thereby reviewing the recent progress in their preparation using solvothermal and ionothermal methods. The subject matter of the final chapter is *Inorganic Superspheres* as an outstanding class of contemporary clusters, which are reviewed by Eugenia Peresypkina, Claudia Heindl, Alexander Virovets and Manfred Scheer. The giant clusters are 2.1–4.6 nm in diameter that adopt fullerene-related or non-fullerene topologies dependent on their size. This chapter elaborates on how to control size and solubility of the superspheres as well as their interconversion in solution. Further, the reader is informed about the host-guest chemistry within the quasi-spherical voids inside such clusters and their unusual and low-dense packing motifs in the solid state.

Marburg, Germany Stefanie Dehnen

Contents

Struct Bond (2017) 174: 1–40
DOI: 10.1007/430_2016_11

Published online: 10 October 2016

Cooperative Effects in Clusters and Oligonuclear Complexes of Transition Metals in Isolation

Gereon Niedner-Schatteburg

Abstract This short review presents concepts of Transition Metal (TM) clusters and oligonuclear TM complexes and recent work on these when isolated. It focuses on experimental studies of such TM clusters and complexes in isolation and on quantum chemical calculations wherever needed. It introduces contemporary methods of TM cluster generation and of oligonuclear TM complex isolation, as well as options for their analysis. Exemplified by recent studies, the review elucidates shortly the kinetics of small molecule adsorption and of CH activation by TM clusters, the vibrations of adsorbates on TM cluster surfaces, the magnetism of TM clusters and of Single Molecule Magnets (SMMs) when isolated, and the vibrational fingerprints of oligonuclear TM complexes.

Keywords CH activation kinetics • Cooperative effects • DFT theory • IR-MPD spectroscopy • Magnetic moments • Oligonuclear transition metal complexes • Scaling laws • Single molecule magnets • Transition metal clusters

Contents

The original version of this chapter was revised. An erratum to this chapter can be found at DOI 10.1007/430_2016_14.

Dedicated to Professor Hansgeorg Schnöckel on the occasion of his 75th birthday, and to Professor Michael A. Duncan and Professor Peter B. Armentrout in recognition of their seminal contributions to the field of transition metal cluster research.

G. Niedner-Schatteburg (✉)
Fachbereich Chemie and State Research Center OPTIMAS, TU Kaiserslautern,
67663 Kaiserslautern, Germany
e-mail: gns@chemie.uni-kl.de

1 Introduction

Structure and bonding govern functionality at the molecular level. The mere sizes of the involved atoms and ions do not suffice to explain. Pairwise covalent bonding implies strong angular constraints and steric ordering. Ionic or metallic bonding does much less so. This flexibility reduces when casting salts and metals into bulk matter of crystalline periodic structures. Therefore, it is a fascinating field of research to investigate samples of Transition Metals (TM)[1] at finite size: These samples are (1) largely naked TM clusters and (2) ligand stabilized oligonuclear TM complexes. The former provide for direct TM–TM bonds, while the latter allow for TM–TM proximity, most often through bridges of Lewis basic atoms (μ-oxo and alike). Multidentate ligands may bring together TMs into proximity without necessitating such bridges.

The electronic structure of finite metal samples typically evolves in a non-scalable size dependence. This shows by their optical and mass spectra [1], in their chemical reactivity [2], and in their permanent and induced magnetic moments [3–7]. Free clusters as compared to deposited clusters have been nicely reviewed recently [8, 9].

The advent of research on TM clusters in isolation arose through the invention of pulsed laser vaporization cluster ion sources, which took place twice and in coincidence at two labs in Texas and New Jersey. Their first studies were published

[1]Transition Metals (TM) in the sense of this review are the d-block non-main group metals of groups 3–11, excluding closed shell group 12 metals (Zn, Cd, and Hg), all of which possess open shell 3d4s or 4d5s or 5d6s configurations. This TM terminology includes the noble 4d and 5d metals of groups 9, 10, and 11.

in the same issue of J. Chem. Phys [10, 11]. The Texas group detected aluminum cluster cations Al_n^+, $n < 15$, and their products of reactions with acetone [10]. They continued with fastflow reactor studies of reactions on the surfaces of TM clusters [12], hydrogen chemisorption on TM clusters [13], and an early reactivity survey of some TM clusters with D_2, N_2, and CO [14]. The New Jersey group utilized laser induced fluorescence (LIF) detection for the identification of the lead dimer Pb_2 [11] and continued with the electronic characterization of Be_2 and Cr_2 [15, 16]. A recent review nicely documents the advent of pulsed laser vaporization sources and their subsequent application to many fields of research [17]. TM clusters were utilized to undergo single and multiple cycles of catalytic activity when isolated within the ion trap of a Fourier-Transform Mass Spectrometer (FT-MS) [18, 19]. These and subsequent studies opened the route towards more systematic investigations of elementary steps in catalysis by isolated TM clusters and under single collision conditions – augmented today by sophisticated infrared studies [20]. Largely in parallel it arose a focus on the organometallic chemistry of isolated MT atomic ions [21, 22] in nice complement to their crystallographic and solution phase properties. Michael A. Duncan edited a five-volume row of books on "Metal and Semiconductor Clusters" which nicely collect much of the work done with metal clusters up to 2001 [23]. Equally important Peter Armentrout anchored activated bimolecular reactions with TM clusters and the sophisticated analysis of breakdown and appearance curves as valid tools in conceptually important gas phase ion thermochemistry [24–27]. Only recently TM clusters were once more emphasized for their role as valid model systems for gas phase catalysis [28] and much beyond.

There is an undisputable value in ligand stabilization of TM clusters in condensed phases as recognized early on [29]. A recent and exhaustive three-volume edition of books on "Metal Clusters in Chemistry" devoted itself to "Molecular Clusters," "Catalysis and Dynamics and Physical Properties," and "Nanomaterials and Solid State Chemistry," one volume each [30]. The breadth of TM cluster applications in catalysis was recently collected even more exhaustively [31]. TM clusters, in particular silver clusters and their redox potentials in solution, were recognized for their relevance in photographic development [32]. Other TM clusters, in particular those of gold, are recognized for their optical properties, which are widely tunable by their size [33]. Early, repetitively, and most recently it was emphasized that an analogy prevails amongst TM bulk surfaces and TM clusters – as surfaces in their own [34–39].

The electronic structures of TM clusters and of oligonuclear TM complexes are complicated. Due to their open shell nature a high electronic state density prevails. With growing cluster sizes there will be a nonmetal to metal transition which strongly depends on the very TM, and this transition is still largely unexplored. Many researchers drew the conclusion either to abandon TM studies at all or to restrict themselves to studying dimers – valuable in their own right. Others adventured towards medium sized systems thereby sacrificing quantum state resolution and sacrificing the chance for an unambiguous quantum chemical modeling. In any case, choices of meaningful studies are manifold: TM clusters may manifest naked

in the void, or adsorbate covered or ligand stabilized in dense media. They come charged or neutral; isolated, in solution or deposited on surfaces; and even embedded in matrices. With increasing sizes isolated TM clusters accumulate sufficient cohesive energy to withstand coulomb fission by multiple cationic charges [40]. Multi-anionic clusters withstand electron detachment the better the larger [41, 42].

In parallel to the smooth evolution of properties from atom to bulk – or vice versa – there are most often anomalous effects in particularly few TM clusters, often of single sizes, sometimes labeled "magic." Frequently, such size effects manifest in bimolecular reactions of TM clusters with single molecules (e.g., H_2, D_2, CO, NH_3, H_2O, and C_6H_6), as recognized in early studies of V, Fe, Ni, and Nb clusters [43–48]. Variation of the charge state may or may not alter the "magic" size effects of these TM clusters [49–52].

Amongst many others there were systematic studies of molecular association to and activation by isolated palladium clusters of H_2, D_2, N_2, CH_4, CD_4, C_2H_4, and C_2H_6 [53], and D_2 saturation studies [54]. Isolated iron clusters were subjected to water reactions [55]. It also became possible to investigate the structure and reactivity of bimetallic Co-V clusters for possible correlations [56].

General considerations on conceivable cluster structures, largely in terms of symmetry and in terms of fundamental interactions, are comprehended in an online data base and in an according review [58]. Despite all effort, however, there are only a limited number of cases where it became possible to identify the ground state structures of TM clusters with a significant degree of certainty, mainly from Free Electron Laser (FEL)-based far-infrared spectroscopy [59–71]. Medium sized TM cluster shape variations (2D versus 3D as, e.g., in the case of Au clusters) are accessible to Ion Mobility Spectroscopy (IMS). Today, most notable TM cluster structures stem from the Trapped Ion Electron Diffraction (TIED) technique as invented at Harvard and brought to perfection in Karlsruhe. A long-term systematic study of $n = 55$ TM anions revealed fundamental insights [57] (Fig. 1), in particular through comparison to bulk metal structures. Interestingly, the structures of all 3d and 4d TM clusters M_{55}^- fall into just four families: they are either icosahedral (M = Sc, Co, Ni, Cu, Pd, or Ag), polytetrahedral (M = V, Cr, Mn, Fe, Nb, or Mo), irregular icosahedral (M = Ti or Zr), or close packed fcc like (M = Ru or Rh). The influence of charge state is not fully elucidated, and it will become more important in smaller clusters.

The adsorption of CO onto well-defined TM surfaces under UHV conditions was often utilized to elucidate nicely the activation capabilities of such surfaces. Far-IR FEL spectroscopy proved capable to augment these findings from the TM cluster point of view [72]. The close correspondence is obvious (cf. Fig. 2), interestingly with Fe partly exempt.

A couple of recent reviews have collected the achieved insights on TM dimers by matrix isolation [74], on phase transitions in clusters [75], on chemical reactions of small gas phase metal clusters [75, 76], on H_2 saturation studies of TM clusters [77], on reactions with TM clusters [2], on gas phase ion chemistry of TM clusters, their production, reactivity, and catalysis [78], on gas phase TM clusters as model

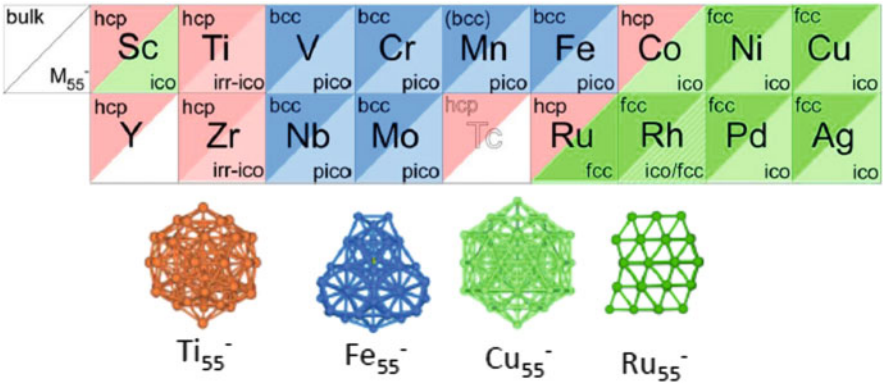

Fig. 1 Correlation of M_{55}^- cluster structure and bulk structure. Size reduction, from molar bulk to $n = 55$ samples, enhances the influence of less coordinated surface atoms, that need to minimize their surface energy by maximizing their coordination. This induces a shift of bulk structures (bcc, hcp, and fcc in cases of Fe, Co, and Ni) towards icosahedral cluster structure motifs (poly-icosahedral, pico, and icosahedral, ico). (Reprinted with permission from [57])

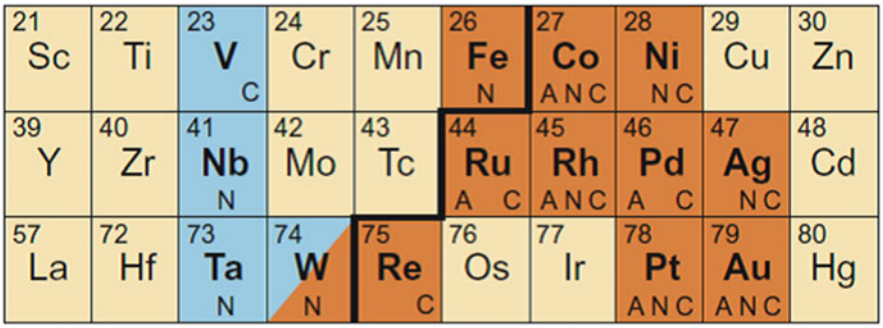

Fig. 2 Chemisorption behavior of CO on transition metal clusters as identified by the presence or absence of $\nu_s^{(CO)}$ absorption bands in the cluster complex (complexes formed at 300 K). *Dark* (*orange*) shading denotes verification of molecular chemisorptions through the presence of $\nu_s^{(CO)}$ bands, while *lighter shading* (*blue*) designates the absence of any $\nu_s^{(CO)}$ bands indicating a dissociation of CO on the cluster surface. The remaining metals have yet to be studied. The *bold line* gives the borderline between molecular and dissociative adsorption on extended surfaces at ~300 K as suggested before [73]. The lettering specifies experiments with anionic (A), neutral (N), or cationic (C) clusters. (Reprinted with permission from [72].)

systems for heterogeneous catalysis [79], on the methane activation by gaseous TM ions [80], on fundamental concepts in TM chemistry with methane [81], and on doping effects in TM cluster-mediated bond activation [82]. It is 11 years ago that someone took time to review the gas phase ion chemistry of transition metal clusters [78], in parallel to a review that focused on single site catalysis with the emphasis on atomic and cluster TM ions [83]. What has happened since then? What is the progress achieved?

The current review aims to provide an overview over some recent and most recent work on pure and ligand stabilized Transition Metal (TM) clusters and oligonuclear TM complexes. The focus of the review is on experimental studies of TM clusters while theory is cited wherever needed. Note that the quantum chemical treatment of main group metal clusters and of some selected noble metal complexes is covered by the article of F. Weigend in this volume. This short review will cut short on the photoelectron spectroscopy and electronic spectroscopy of TM clusters and complexes, and on recent X-ray diffraction studies. Instead, the review's coverage is organized as follows.

The review starts with an overview over contemporary methods of TM cluster generation and of oligonuclear TM complex isolation, followed by methods for their analysis. A short chapter devotes to the unconditionally necessary close interplay between experiment and electronic structure calculations by quantum chemistry. Seven consecutive chapters elucidate various aspects of contemporary research on TM clusters and oligonuclear TM complexes. A final short chapter concludes and provides for an outlook.

2 Additivity, Cooperativity, Synergism, and Scaling Laws

Clusters – molecular and atomic alike – are assumed to bridge between isolated monomers, namely atoms or molecules, and according bulk matter, namely metals, salts, liquids, and molecular solids such as ice. Oligonuclear TM complexes are less prone to do so. Nevertheless, they may exhibit characteristic variations of properties by their size/nuclearity.

2.1 Additivity

Many body expansion schemes [84–89] help to sort energetic contributions in large molecules, TM clusters, and in molecular clusters by their order. Let the system compose of N monomers – linked covalently, or metallically, or non-covalently. Then the total energy to first order is a mere sum of the total energies of the N monomers, each of them relaxed in the presence of $N-1$ nonrelaxed monomers. Such approximation to first order may be termed energetic or **enthalpic additivity**. Obviously, this approach is crude and it shows that it is most often an inappropriate approximation.

2.2 Cooperativity

Accordingly improved results arise from inclusion of higher-order contributions by two-body and three-body energies of dimer and trimer combinations in permutation [85–87]. Such corrections account for polarization and induction effects by adjacent monomers that may be viewed as oligomers that interact with their neighboring environment. One may be tempted to label these effects as enthalpic cooperativity. Note, however, that such a label could be possibly misleading at this stage. The achieved stabilization may occur in a cooperative way. A thereby arising new or enhanced functionally is not warranted, however. In any case, these effects are intrinsically non-additive. In large systems of many entities $N >> 3$ these three-body contributions add up to significant corrections (in liquid Argon likely more than 50 % of the viscosity [90], and in liquid water more than 20 % of the total energy [85]). Higher-order interactions beyond three-body terms are in general much smaller. Upon high interaction strengths (covalent/metallic binding) it may not be possible to sort out all particular contributions, however. Instead a lump sum scaling towards bulk properties may become appropriate (cf. below).

2.3 Differential Many Body Expansions

Non-additive/cooperative effects manifest also when invoking a differential many body expansion. This is an approach that warrants further insights in particular when dealing with heteronuclear TM species, either clusters or complexes. Implementing a many body expansion as above, such a scheme equates the differential influence of single, double, and triple substitutions of different TM atoms against each other. A recent investigation [91] labels one-body terms as energies or further properties of the subsystems, two-body terms as non-additive but pairwise contributions, and three-body as well as higher-order terms as a measure for cooperativity. This concept was applied to differences between (computed) energies, UV/Vis spectra, and electronic transition densities of similar trinuclear complexes. It must be emphasized that this nomenclature aims to exclude two-body effects from the concept of cooperativity. We will see in the following cases where such a delineation would not be constructive.

2.4 Synergism

Synergism and synergistic effects seem handy to classify many body effects in TM clusters and oligonuclear TM complexes. Despite new language there would be no gain in insight. We take these terms as synonyms for cooperativity and cooperative effects.

2.5 Cluster Size Scaling Laws

The above delineated point of view onto cluster size effects is largely derived from a perspective of increasing cluster sizes – scaling from the minor to the large. It may be put into contrast with the reverse point of view – starting with bulk matter of molar size and subtracting monomeric units (atoms or molecules) one by one. The self-evident and dominant effect in doing so is called size scaling.

Such scaling implies a change of cluster properties by their size, as represented by their number N of constituents/atoms. Scaling laws are traditional means to interpolate analytically by approximation between bulk properties and atomic properties and they should follow predictable trends when scaling from bulk to clusters [92]. Reducing sizes further towards small clusters and oligomers, one anticipates strongly size dependent and non-monotonous jumps in cluster features (as predicted and observed often before), which has led to the coinage of the term of a "non-scalable" size regime [93, 94]. Note, however, that the scalability of properties is not obsolete. Instead, "magic cluster size" related variations superimpose onto the prevailing scaling laws (see Table 1 for various common scaling laws).

In the case of some cluster size dependent property $p(N)$ a conceivable scaling law would read as follows:

$$p(N) = c + b\,N^x$$

Note that such property $p(N)$ most often refers to an intensive value [95], i.e., the property is normalized "per atom." The parameters to determine are: the reference values c, the scaling factor b, and the scaling power x. Experimental data – once available over a sufficiently extent size range – would allow for a fit of these parameters, in principle. In parallel, it is mandatory to consider the asymptotic limits and to evaluate possible physical models (Table 1).

Table 1 Various cluster properties and scaling laws – N refers to the number of particles or atoms per molecule or cluster (adopted from [96])

Cluster property		Proportional to		
Surface tension of a spherical droplet	γ	$1/R^2$	=	$N^{-1/2}$
Ratio of surface to bulk atoms in a spherical particle	N_s/N_V	$1/R$	=	$N^{-1/3}$
Binding energy/atom (cohesive energy) [97–99]	ε_{coh}			$N^{-1/3}$
Ionization potential [100–104]	I_P			$N^{-1/3}$
Electron affinity [102, 103]	E_a			$N^{-1/3}$
Resonance frequency of a spherical metal cluster [3, 105, 106]	ω_r	$1/R^3$	=	N^{-1}
Autoionization resonance energy of Hg clusters [107–109]	δ_n			N^{-1}
Average energy level spacing [110]	ΔE			N^{-1}
Magnetic dipolar interaction [111]	E_{mag}			N^{-1}
Cluster polarizabilities [3]	α_N	R^3	=	N

Let us assume a cluster of N spherical atoms in dense packing and with total diameter D. The cluster volume V_c then scales to a good approximation as $V_c \sim N \sim D^3$. It might seem confusing at first sight to define continuously varying cluster entities (diameter and volume) by relating them to a discrete number of building blocks (atoms). Nevertheless, this is straightforward and valid to a very good approximation as long as dense packing dominates. Such approximation is sometimes called a "liquid drop model." Accordingly, the number of surface atoms N_s goes by the surface area, $N_s \sim D^2$. The fraction of surface atoms N_s/Nscales as $N_s/N \sim D^{-1} \sim N^{-1/3}$. This fraction of surface atoms may be taken as a quantitative measure for the mixing in of atomic like properties, justified by the lower coordination of the surface atoms. Accordingly, $x = -1/3$, and an interpolation from the atomic case (all surface) to the bulk case (all volume) may read as:

$$p(N) = c + b\,N^{-\frac{1}{3}}$$

Subsequently, it is most often assumed that $c = p(\infty)$ and $b = p(\infty) - p(1)$ would serve as valid and appropriate choices for the reference values c and scaling factors b. Thereby we get:

$$p(N) = p(\infty) + \frac{p(1) - p(\infty)}{N^{1/3}}$$

Such a choice may look obvious at first sight. It is not forcing, however, and it takes verification. For a recently worked out example in cluster magnetism, see [96].

2.6 Cooperative Effects Beyond Mere Energetics

The above discussion of additivity, of energetic cooperativity, and of cluster size scaling laws clearly reveals the need to take into account changes in properties beyond mere energetics when studying size dependencies. This holds in particular for small TM clusters and complexes. It helps to define cooperative effects explicitly, and to sort these into three categories:

A **cooperative effect** in TM clusters or TM complexes exists if a new magnetic, optical, or reactive effect or function emerges by combining two or more TM centers. Neither of the participating TM centers show this effect or function when located sufficiently far apart from the other TM centers. The three operational categories of cooperative effects may be chosen as follows:

Functional cooperativity: TM atom A and metal atom B comprise individual functionalities. The complex AB combines these and enables a novel functionality. Examples are: (I) the combination of high spin and high magnetic anisotropy, (II) the activation of a substrate 1 by TM atom A and of a substrate 2 by TM

atom B with concerted coupling of 1 + 2 to a product, conceivably in a catalytic way, or (III) coupling of optical functionalities localized at individual TM centers to enable, e.g., luminescence, quantum cutting, energy transfer, or optical switching.

Enthalpic cooperativity: Two or three TM centers may together reduce a catalytic activation barrier significantly. This constitutes enthalpic cooperativity if the joint reduction is larger than that due to the separate metal centers. More generally, three-body enthalpic cooperativity is present if the total enthalpy of the three-body system is determined by more than pairwise contributions of its components. Note that this definition of enthalpic cooperativity is beyond a mere stabilization effect.

Entropic cooperativity: An enhanced catalytic coupling may arise though proximity of a substrate 1 and another substrate 2 when held appropriately in place by adjacent TM centers. In biochemistry a closely related effect is known as allosteric interaction: Pre-orientation of a substrate (by active centers A and B) facilitates its activation (by center C). Such effects are also of relevance, e.g., on surfaces in the case of deposited TM clusters and TM complexes.

Specific examples of cooperative effects in TM complexes encompass: (1) multiple open shell TM centers which experience exchange coupling such that they act as one effective spin manifesting properties which differ from those of the individual spin centers. (2) Two TM centers which together take part in a chemical transformation. They reduce the activation energy of a specific elementary step by an amount larger than the reduction due to a single center. In the course of this process both TM centers coordinate substrates at well-defined relative distances and orientations. (3) Two or more weakly interacting TM centers which become more strongly coupled in an excited state upon single photon absorption. This excited state is delocalized beyond a single center. Subsequent luminescence releases photons at defined wavelengths not seen without coupling of the TM centers.

Numerous further examples could be mentioned here. Note that in practice it is sometimes difficult to define a unique demarcation amongst the three chosen types of cooperativity. Mixed cases and complications due to superposition of other phenomena may occur. In any case a meaningful working definition of cooperativity implies a well-defined entity of function to optimize – in statistic known as fitness function. Choice and definition of this function governs the definition of cooperativity in each individual case.

3 Methods of TM Cluster Generation and of Their Isolation

It is not possible to compile all methods of generation and isolation of TM clusters and TM complexes. It warrants to provide an overview of those methods which are of relevance in the present context.

3.1 Ions and Neutrals: The Reasoning Why

Through contemporary methods it is possible to generate charged and neutral clusters alike. Polarity of charge may vary (cationic or anionic) as well as the charge state – often single charge, occasionally double, seldom higher [41, 42].

In most cluster ion sources, neutral clusters form in conjunction with ionic ones. For detection they need to acquire a net charge, effectively achieved by photoionization. Appropriate choice of photon energy limits or even avoids fragmentation of the TM clusters, and it is possible to suppress detachment of adsorbates. Less carefully designed experiments with neutral TM clusters would suffer from likely artifacts by inadvertent fragmentation.

In many technological applications as well as in natural and biological environments ubiquitous charges prevail and redox processes readily proceed (as, e.g., in the course of oxidative corrosion). Thus, TM clusters of relevance likely bear charges. It is thus mandatory to investigate such clusters much beyond mere neutral states and to systematically study the influence of charging and of redox states.

3.2 TM Cluster Generation and Isolation

It is well established to produce TM clusters by molecular beam methods [112, 113] and to obtain nanostructured material by deposition from such cluster beams [114]. Note that such production is an in situ synthesis within the ion source, most often according to a general protocol as follows: (1) Generation of a partly ionized hot atomic plasma by appropriate energizing of solid targets. This may arise by short pulse lasers (laser vaporization) [10, 11, 17] or by gas discharges. The latter is often applied in cw (magnetron sputter sources) [115] and less frequently in pulses [116]. Alternatively the atomization may occur through heavy particle sputtering [117–119]; (2) Well-timed mixing of plasma with cold carrier gas pulses. This ensures spatial confinement, rapid cooling, and ready nucleation; (3) Subsequent expansion into vacuum. This invokes supersonic adiabatic cooling and directional focusing. Here, it is possible to utilize a considerable choice of alternate geometries of waiting rooms, expansion channels, and supersonic nozzles. A considerable variety of combinations are in use, and their features are often not yet fully explored beyond mere try-and-error schemes; (3) Skimming and differential pumping. This is mandatory in order to handle the high gas load of the supersonic expansion and to bring the TM cluster ions into vacuum where they experience large mean free paths; (4) Electrostatic acceleration. This is mandatory in order to form an ion beam that proliferates TM clusters towards the actual experiment and towards detection. It is increasingly more often that RF ion guiding is applied. Yet this is not mandatory. The same holds for ion trapping; and (5) Once TM clusters are isolated they are ready for selection and interrogation. Mass to charge selection by means of Mass Spectrometry (MS) serves to isolate single

cluster sizes before and/or after interrogation, MS or MS–MS, cf., e.g., by ref. [120]. MS-technique is a broad topic in itself and much beyond the scope of this article.

3.3 Generation and Isolation of Multinuclear Complexes

Multinuclear TM complexes stem from ex situ synthesis in solution [29–31]. TM centers are stabilized to the outside either through multiple monodentate ligands or through fewer multidentate ligands or through a combination of both. Adjacent TM centers stabilize next to each other through bridging atoms (most often oxygen), bridging molecular ligands (most often O_2, CO, N_3^-, or others in η_2 coordination), or through some functional groups of larger multidentate ligands which also coordinate against the outside environment. A recently synthesized complex of $Mn^{II}Dy^{II}Mn^{II}$ is a good example of virtuous stabilization of three metal centers in proximity by just two multidentate ligands [121]. Bridging ligands may constitute of closed shell species or of radical species, the latter enabling strong electronic couplings. Appropriate choice and functionalization of coordinating ligands enables to obtain multinuclear TM complexes of low net charges of either polarity. Such complexes are suitable for isolation, most often by electrospray ionization (ESI) [122–127], and for interrogation much in line with what is feasible with TM clusters (cf. below). In the course of the ESI process, redox processes may occur, and there may be a ligand to solvent exchange when operating harsh ion source conditions. Even a ligand loss is possible yielding coordinatively unsaturated species. All three processes may modulate by source parameters. Additional solvation/hydration beyond first shell coordination may occur when applying humid or solvent enriched entraining gases to the ESI source [128–131].

4 Methods of Gas Phase Analysis

4.1 Analysis of TM Clusters

Interrogation of the TM clusters takes place by either of eight methods: (1) Collisional encounters with molecules, recording kinetics and product yields [2, 24, 78, 81, 132–134]; (2) Activating high energy encounters with unreactive buffer gases, recording Collision Induced Dissociation (CID) parent breakdown and fragment appearance curves [135–137]; (3) Photon absorption and indirect detection through fragmentation, photon energies ranging from the IR through all energies up to the X-rays, recording optical spectra of fundamental excitations of rotational, vibrational, or electronic degrees of freedoms in clusters and/or adsorbates (see references in the following chapters); (4) Time resolved IMS by energized drift through

buffer gas, recording isomer populations by their shape dependent drift time delays [138–143]; (5) Electron diffraction of trapped TM cluster ions (TIED) as highlighted in the introduction. This is a dedicated high level technique and currently available worldwide in just two laboratories (Harvard and KIT) [57, 144, 145]; (6) Temperature control becomes feasible by virtue of the now well established Radio Frequency (RF) and Ion Cyclotron Resonance (ICR) ion trapping techniques [120, 146, 147] in conjunction with reliable cryogenic cooling devices [148] and messenger tagging techniques [149]. While temperatures of devices and of stored ions certainly deviate, vibrational state populations of 20 K and below are achieved routinely in numerous labs; (7) Even lower temperatures of down to 0.38 K are achieved by embedding molecules and small TM clusters into superfluid Helium nanodroplets [150–154]; and (8) Time resolved studies of isolated TM clusters on the femtosecond scale, which are beyond the scope of this review.

4.2 Analysis of Multinuclear Complexes

Examples for the analysis in isolation of multinuclear TM complexes are sparse and often focus on analytical MS identification. Somewhat more fundamental studies often involve mass spectrometric screening in conjunction with infrared vibrational characterization. Electronic excitations of oligonuclear TM complexes may be probed by UV/visible laser photons, and there is no conceptual problem in doing so. To the best of our knowledge there is no study published on such experiments. There are also no studies published where isolated multinuclear TM complexes would have been characterized for inner shell excitations by X-ray photons. The chemical aspects of oligonuclear TM complexes come nicely into play when aiming at their catalytic activities by undertaking kinetic studies [155–157].

4.3 The Interplay of Experiments and Quantum Chemical Calculations

Approximate theoretical models serve for the description of the electronics in simple metal clusters [158]. Such simple models largely fail in the cases of TM clusters, however. Much more advanced electronic structure theories of TM clusters are either wave function based or they utilize Density Functional Theory (DFT) in order to enable the handling of larger systems [159]. Either cases reach limits in their accuracy and in the size of systems that may be covered. The small HOMO-LUMO gap in TM clusters leads to a multi-reference character for the electronic wave function. Thus, single-reference Hartree–Fock calculations tend to fail, and

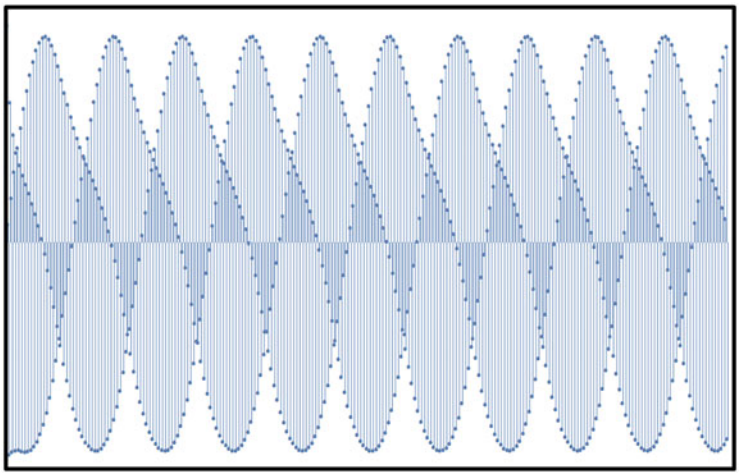

Fig. 3 Total energy in a PBE0/cc-pVTZ(N,H);ECP(Fe) calculation of an $Fe_{13}(N_2)_6(H)_2^+$ cluster in 36tet configuration (35 unpaired e^-) throughout more than 700 SCF cycles. The calculated energy oscillates by more than 10^{-6} around a mean value of −2,268.00755 a.u. without converging to a self-consistent solution. Despite all effort such oscillations happen often and in a largely unpredictable way when simulating high spin TM clusters – due to the high density of near degenerate states of varying d-orbital occupancies

this cannot be compensated by a post-Hartree–Fock treatment of the dynamic electron correlation. Instead, DFT based methods account for the multi-reference character of TM clusters, albeit in a non-systematic manner. Wave function-based multi-reference methods would allow for a systematic treatment of TM clusters. At present, such an endeavor is doomed to fail by the exceeding computational costs.

In practice, DFT based methods allow for the modeling of larger TM clusters and TM complexes, at the expense of employing semiempirical choices of exchange-correlation functionals [160–165]. We refrain from reviewing the published literature on DFT calculations of small open d-shell TM clusters. A good overview may be obtained elsewhere [166, 167]. Most notably, a DFT case study on structures and IR spectra of small niobium cluster cations managed to achieve predictions that found swift confirmation by unpublished IR spectra, despite some ongoing debate on details [168–170]. The application of DFT to TM clusters occasionally reaches practical limits due to intrinsic instabilities (Fig. 3). It is sometimes possible to overcome those, which is not guaranteed, however. Conceptual problems in the treatment of antiferromagnetic couplings may be overcome these days by the broken symmetry DFT method [171–178].

5 Selected Examples

5.1 Some Examples of Recent TM Cluster Studies

By this chapter we aim to provide some overview on the recent studies (2005 and beyond, thus not covered by either of two recent reviews [78, 83]) of size selected gas phase TM clusters and oligonuclear TM complexes with respect to their production, likely structure and functional properties. It is in no way possible to cover all aspects of TM cluster and studies on TM clusters as published since 2005. Rather than aiming at full coverage – which is almost impossible – the following chapters shall encompass a bunch of studies that elucidate fascinating aspects of choice – in an objective manner as far as possible.

Many studies of the gas phase reactivity of oxide clusters of early TM metals (V, Ce, and Nb) are largely motivated by their relevance for large-scale industrial oxidation catalysis [79, 121, 134, 179–249]. Such studies have revealed valuable insight into the actual mechanisms at work. Activating guided ion beam studies have revealed a rich ion thermochemistry of TM clusters (lately of Fe and Co), their oxides, and their adsorbate complexes (with D_2, N_2, CO, and O_2) and at benchmark quality of significant importance [25–27, 250–256]. FEL-based IR-MPD spectroscopy enabled further valuable insight into structure and reactivity of TM oxide clusters [257–262], in part driven by the relevance of NO oxidation in the context of car exhaust fume oxidation catalysis [263–266].

In contrast to largely inert bulk gold, its nanoparticles and clusters provide for a range of unexpected properties in the areas of photonics and catalysis [267–271]. Studies of the gas phase and solution phase chemistry of small and nanosized gold clusters revealed size dependent catalytic activities [272–281]. IMS in conjunction with DFT calculations verified a transition from planar to 3D structures in small anionic gold clusters [282, 283]. Independent confirmation arose by far-IR FEL spectroscopy, revealing evidence for a planar Au_7 and a pyramidal Au_{20} structure [284] and further fascinating insights [285–290]. Interestingly, a recent study of small silver clusters $Ag_{3,5,7}^+$ revealed that they seemingly allow for replacement of an Ag atom for an H-atom while preserving much of their properties, in particular their reactivity with small alcohols and amines [291].

5.2 Kinetics of H_2, CO, and N_2 Adsorption by TM Clusters in Isolation

Early studies of H_2 adsorption on TM clusters [13, 43–45, 48, 76, 77] revealed a subtle interplay of electronic odd–even effects and conceivable cluster geometries. The conceptional insight may be summarized as "every atom counts," and the fundamentals of H_2 binding and reactivity on transition metals have been reviewed before [292].

It is obviously of high relevance to understand in detail the adsorption and desorption of further molecules such as N_2 which are reluctant to react and may hardly activate on their own. Niobium cluster anions were amongst the first ones that were studied for their absorption of N_2 and CO molecules [293], the issue of possibly competing electron detachment remaining open. Issendorff et al. subsequently determined PES spectra of Nb_n^- [103], and the obtained vertical electron affinity values suggest that strongly exothermic CO chemisorption may induce electron detachment. Recently, it became possible to identify the CO binding sites on the surfaces of Fe, Ru, Re, and W clusters [294] and on Ni, Pd, and Pt clusters [295], and to elucidate charge effects on the red shift of stretching vibrations in adsorbed CO on TM clusters by a so-called charge dilution model [72]. Earlier it had become possible to deduce likely structures of cobalt and nickel clusters through the titration of their surface binding sites by N_2 absorption at ~150 K [296–299], assuming an unconditional one-to-one correspondence between N_2 binding site and TM surface atom.

In our own laboratory it became recently possible to investigate N_2 adsorption to size selected TM clusters under isothermal cryo-conditions, namely when stored within a cryo-cooled RF ion trap and in the presence of a helium buffer gas of hundredfold excess, first spectroscopic studies being published [300]. The prior adsorption limits of Ni and Co clusters were well reproduced at 26 K. However, it showed that absorption readily continued beyond these limits, and new saturation stoichiometries were found. Rate constants from fits by genetic algorithms confirmed consecutive steady adsorption up to the first saturation limit where kinetics slowed down. Beyond this limit kinetics speed up slightly until the second saturation limit is reached, which by size is much below the closure of a second layer of N_2 adsorbates. The found two-step kinetics revealed a remarkably strong cluster size dependence which points towards strong cooperative effects. By the found stoichiometric ratios a second layer adsorption seems unlikely. In the cases of cobalt and nickel the recorded kinetics reveal no evidence for N_2 activation and nitride formation – further work pending [301].

5.3 Kinetics of Aliphatic and Aromatic CH Activation by TM Clusters in Isolation

5.3.1 Methane Activation

The activation of small alkanes – when void of functional groups – has been coined a “holy grail” of chemistry [81]. Indeed, such activation is a demanding task that many sole 3d and 4d TM atoms fail to achieve, whereas clusters of some 4d TMs succeed (see below). Activation of methane through TM complexes or TM clusters was achieved and characterized as follows: by platinum atomic ions [302–305], by platinum complexes [306, 307] and clusters [308, 309], by vanadium oxides and other TM doped oligonuclear oxides [121, 181], by other ligated/oxidized

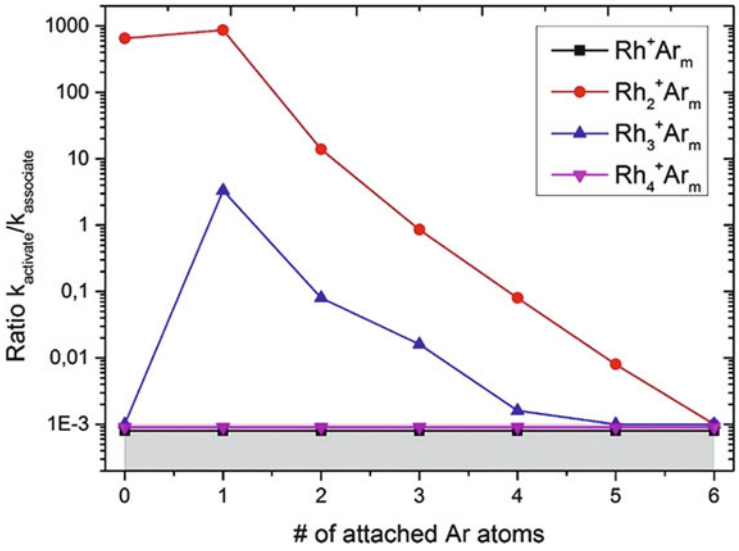

Fig. 4 Ratio of room temperature methane activation $k_{activate}$ and association $k_{associate}$ by Rh^+Ar_m clusters as a function of m. Depicted ratios of the cases Rh^+Ar_m and $Rh_4^+Ar_m$ are upper limits. Other data stem from [319] and [320] with some estimates included

mononuclear TM complexes [222–224, 310, 311], even by iron carbides [312], and in one case even the direct conversion of methane to formaldehyde through $Al_2O_3^+$, namely without involvement of any TM center [235]. Recently, the activation of methane was achieved even by small gold, palladium, and binary gold palladium clusters [226, 313–316]. There is published in other reviews a systematic coverage of gas phase metal ion chemistry with methane, putting mononuclear and oligonuclear TM ions and their oxides into the focus of these reviews [81, 317, 318]. There is currently – to the best of our knowledge – a single published report on the vibrational spectroscopy of methane when adsorbed or activated by TM clusters [69], and there is another study on the vibrational characterization of a CH_4-FeO^+ complex that resembles an intermediate of methane to methanol conversion [213] (Fig. 4).

Some time ago we took chance to utilize TM clusters of rhodium in conjunction with argon coating [319] for some kinetic investigations under single collision conditions. These quite elusive complexes bear promises to learn about activation kinetics by the loss of argon chaperons that act as a boiling heat bath. No accurate binding energies at hand, the insight is of a merely qualitative nature, however. Bimolecular collisions with methane revealed the following processes in competition:

$$Rh_n^+Ar_m + CH_4 - k_{activate} \rightarrow Rh_n^+CH_2 + H_2 + m\,Ar\ (activation)$$

$$Rh_n^+Ar_m + CH_4 - k_{associate} \rightarrow Rh_n^+CH_4 + m\,Ar\ (association)$$

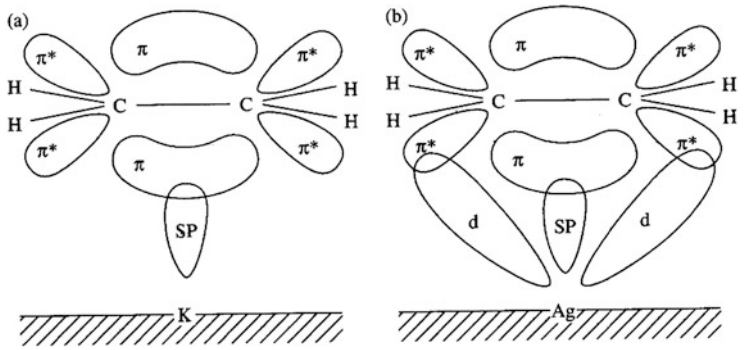

Fig. 5 Sketch of orbitals involved in olefine bonding with: (**a**) main group and (**b**) transition metal cations (reproduced with permission from [325]). Sizes are not to scale, symmetries hold. Filled d-orbitals of TMs may donate into empty π* orbitals at the olefin and enable C–C or C–H activation. Main group metals largely fail to do so. Empty or partially filled d-orbitals of early TMs may accept electron density from occupied π orbitals, likewise assisting in C–C activation

Most notably, the (n,m) stoichiometry modulates the observable reactivity ratio $k_{\text{activate}}/k_{\text{associate}}$. Monomeric and tetrameric rhodium cations fail to activate methane under any circumstances – irrespective of the heat bath of chaperons. A single argon chaperon enhances methane activation by rhodium dimers and enables it by rhodium trimmers – otherwise absent. It looks as if in these cases the encounter complex lifetime benefits from stabilization through evaporative cooling. Likely sterically demanding C–H activation thereby becomes more likely – it gets more time to proceed. Such a behavior is indicative of a tight transition state that comes with a large negative transition entropy. Additional chaperons likely hamper the C–H activation either cooling too effectively or by simply blocking direct contact to the activating TM center(s). While this branch of study was not continued at that time, it now seems fertile to utilize the newly available cryo- and laser-technologies for a resumption of such studies. This shall take place in the near future aiming to unveil details of the TMs cooperative actions.

5.3.2 Olefines and Aromatic Compounds

The early "Dewar-Chatt-Duncanson model" [321, 322] extended the H_2 to TM binding concept towards olefin binding [323], in general known today as π-backbonding. The later "Blyholder model" re-emphasized the acceptor donor synergism in adsorption of alkenes and CO on TM centers [324] and explains why this is not possible with main group metals (cf. Fig. 5).

We have studied the activation of olefins and of benzene by TM cluster cations and anions repeatedly [326–331]. Strong size effects on activation point to likely icosahedral structures of niobium clusters and to high and even coordination of surface atoms ("smooth surface") in the cases of $Nb_{19}^{+/-}$. Simple aromatic

heterocycles undergo most likely carbidization through complete dehydrogenation [39]. Some clusters of particular sizes (most notably $n = 19$) fail to activate homocyclic benzene and naphthalene molecules. Instead seemingly intact adsorption is observed which proves that activation is kinetically hindered at some point. These findings were taken as strong evidence for initial coordination to the metal clusters of the heterocycles through their lone pair orbitals. An inverse H/D isotope effects showed by the activation under single collision conditions of C_6H_6 and of benzene-d_6 C_6D_6 by size selected cationic cobalt clusters Co_n^+ and by anionic cobalt clusters Co_n^- in the cluster size range $n = 3 - 28$ [332]. The dehydrogenation by cationic clusters is sparse, while it is ubiquitous in reactions by anionic clusters. Kinetic Isotope Effects (KIEs) in total reaction rates are inverse and – in part – large. Dehydrogenation Isotope Effects (DIEs) are normal. A multistep model of adsorption and stepwise dehydrogenation from the precursor adsorbate unravels a possible origin of the inverse KIE: Single step C–H bond activation is swift (no KIE in forward direction) and largely reversible (normal KIE backwards) while H/D tunneling is likely to contribute (backwards). DFT calculations of the structures and energetics along the reaction path in $[Co_{13}C_6H_6]^+$ lend support to the proposed multistep model. The many size dependent variations of total reaction rates, KIEs and DIEs, impressively manifest prevailing cooperative effects.

Benzene activation and H/D isotope effects in reactions of mixed cobalt platinum clusters, $Co_nPt_m^{\pm}$ in the size range $n + m \leq 8$, reveal the influence of charge and of composition [333]. Dehydrogenation by cationic cobalt clusters Co_n^+ is sparse, it is effective in small bimetallic clusters $Co_nPt_m^+$, $n + m \leq 3$. Single platinum atoms promote benzene dehydrogenation while further cobalt atoms quench it. Mixed triatomic clusters $Co_2Pt_1^-$ and $Co_1Pt_2^-$ are special in causing effective reactions in a cooperative way. KIE(n) in total reaction rates are inverse and large, DIE(n) are normal – allowing to follow the interpretation scheme of pure cobalt clusters as devised before.

Despite all of this effort it did not become possible to deduce explicit electronic or geometrical information of the studied clusters. Glimpses were within reach, conclusions beyond. It became mandatory to switch gears and head for conceptually simpler systems in conjunction with complementary methods of analysis.

5.4 *Vibrations of Adsorbates on the Surfaces of TM Clusters*

Spectroscopy of molecular adsorbate on TM surfaces is manifold and has become a topic of each textbook on surface science. Spectroscopic studies of molecular adsorbates on the surfaces of TM clusters are sparse. Early studies elucidated the spectroscopy of methanol on gold oligomers and found the $\nu_s^{(CO)}$ vibration of methanol to change discontinuously with cluster size [334]. IR spectroscopy of CO on late transition metal clusters (Co, Ni, and Rh) revealed that the $\nu_s^{(CO)}$ vibration approaches asymptotes that are not the same as found for $\nu_s^{(CO)}$ when

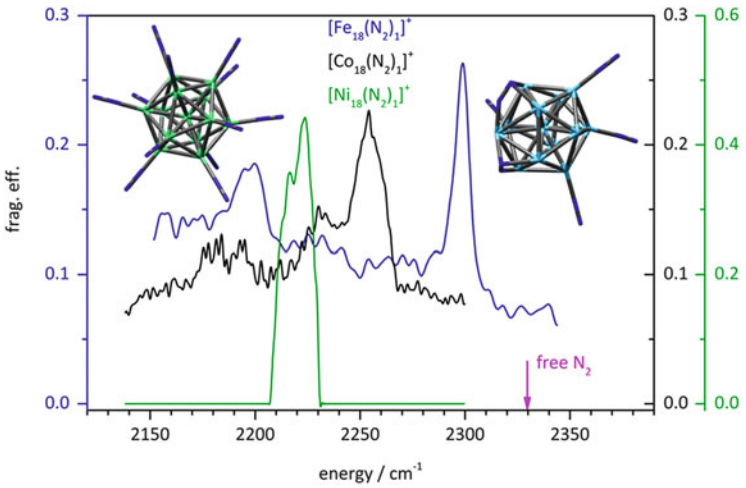

Fig. 6 IR-MPD spectra of $[Fe_{18}(N_2)_1]^+$, $[Co_{18}(N_2)_1]^+$, and of $[Ni_{18}(N_2)_1]^+$ when trapped within 26 K buffer gas. Other than naively expected the red shifts of N_2 adsorbate vibrations, $\Delta\nu_{Ni} > \Delta\nu_{Co} > \Delta\nu_{Fe}$, do not coincide with predicted bond strengths, $\Delta_{ads}H(Fe_n\text{-}N_2) > \Delta_{ads}H(Co_n\text{-}N_2) > \Delta_{ads}H(Ni_n\text{-}N_2)$. Note the large difference in broadband background fragmentation. *Insets* depict possible motifs of multiple N_2 adsorptions on Ni_{13}^+ (10tet, 9 unpaired e^-, *left*) and Fe_{13}^+ (30tet, 29 unpaired e^-, *right*). (unpublished data of work in progress [301])

bound to a single crystal metal surface [335]. This was taken as strong evidence for low coordination of binding sites on medium sized clusters as compared to highly coordinated metal surface sites [335]. Further studies elucidated the very aspects of CO adsorption on TM clusters in much more detail [72, 258, 294, 295, 335–342]. In particular the influence of cluster charge became well understood in terms of a so-called charge dilution model [72]. Subsequent to the structural elucidation of small ruthenium clusters [343], their potential for N_2 activation was nicely investigated by FEL-based far-IR spectroscopy [344]. By the same methodology, polarizable rare gas atoms were found to bound strongly to cobalt, gold, and gold alloy clusters [345–348], and H_2 adsorption was investigated for reconstruction in vanadium, cobalt, and other TM clusters, and H_2 co-adsorption with CO for the mutual influences on binding and activation [349–353].

Our recent study of IR active N_2 stretching frequencies in isolated and size selected cobalt cluster nitrogen adsorbate complexes, $[Co_n(N_2)_1]^+$ ($n = 8$–17), revealed significantly red shifted frequencies with respect to the IR inactive vibrations of free N_2. These bands were assigned to a μ_1 head-on type of coordination of the N_2 to the cobalt cluster surface, revealing remarkable cluster size dependent features much beyond swift interpretation [301]. Current work in progress extends this work onto other TM metal clusters, revealing unexpected features (cf. Fig. 6). DFT modeling of such clusters and adsorbates is at its limits. Optimized structures are of help. Predictions on spin states and vibrational frequencies need to be taken with a grain of salt. The more it is of help to extend the current spectroscopic studies

from single adsorbates to TM clusters with varying degrees of adsorbate coverage up to full monolayers – speaking in terms of surface science language. Such work is currently underway and shows first promising results that may eventually lead into the unraveling of coordination patterns and of their change with coverage, eventually unraveling cluster surface morphologies that manifest cooperative effects.

5.5 Magnetism of TM Clusters

Ferro-, ferri-, antiferromagnetism, and alike are collective magnetic phenomena that arise from electronic couplings of multiple spin bearing atomic centers – most often TMs or rare earth elements. These are cooperative effects by definition.

5.5.1 Bulk Phase Experiments on Cluster Magnetization

Through application of ultrasensitive Squid-Magnetometer technology [354] it became feasible to study nanoparticles in liquid suspensions. Recent examples are studies on colloidal suspension of electrochemically generated cobalt particles [355, 356] and nanometer sized Co clusters (25–7,000 atoms) [357] as reviewed before [6]. It became possible to investigate a magnetization reversal in nanometer sized particles [358]. NMR investigations of polynuclear coordination compounds reveal indirect evidence for electronic coupling motifs as of relevance to magnetic moments and are thus limited to rather special cases [359].

5.5.2 Stern–Gerlach Investigations of Neutral TM Clusters in Isolation

Stern–Gerlach experiments have managed to determine magnetic moments in isolated neutral clusters by application of inhomogeneous magnetic fields [360] revealing a surprising left right asymmetry [361–363], that is understood by now as relaxation of the TM clusters through spin–rotation-coupling [364–369].

Small magnetic clusters are typically single domain particles. Since the total magnetic anisotropy energy of the clusters scales with the number of atoms these clusters usually show superparamagnetic behavior above the so-called blocking temperature. The blocking temperature depends on the particle size and on the anisotropy energy per atom which may be significantly higher than for bulk samples.

Through resolving the old controversy on the interpretation of the Stern–Gerlach findings the way towards meaningful investigations was paved. It could be concluded that small clusters of iron, cobalt, and nickel reveal magnetic moments per atom which are significantly enhanced compared to the bulk values and which are sometimes close to the atomic moments. Larger clusters with about 30–700 atoms exhibit surface induced spin density waves that modulate the total magnetic

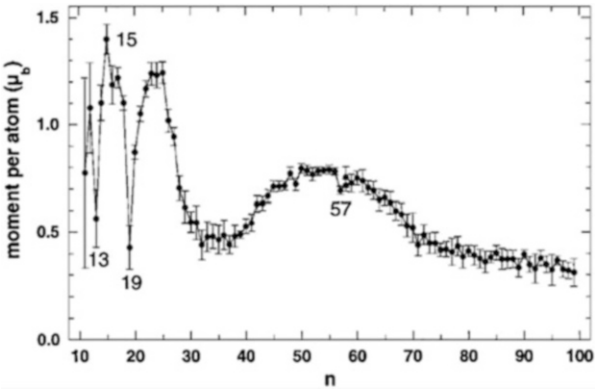

Fig. 7 Magnetic moments per atom of Mn_n clusters by Stern–Gerlach experiments (adopted with permission from [371]). Note the single low moments at $n = 13$, 19, and 57 (indicative of icosahedral structure and partial antiferromagnetic coupling), superimposed to the systematic shell like variation of moments, likely Friedel oscillations

moments which gradually approach towards the bulk limit [7]. Investigations on $Ni_{5\text{-}740}$ independently confirmed the non-monotonic approach to the bulk limit through shell effects and, in addition, revealed a considerable temperature dependence of determined values [370]. Manganese clusters $Mn_{11\text{-}99}$ revealed superparamagnetism when subjected to Stern–Gerlach experiments [371] and act as molecular ferrimagnets ($n = 5$–22) [372, 373].

Chemistry comes into play when $Fe_{10\text{-}25}H_m$ clusters undergo adsorbate induced enhancement of their magnetic moments [104]. In quite remarkable contrast hydrogen and CO adsorption onto Ni_n (up to $n = 25$) decreases the total magnetic moments [104, 371]. A transition from nonmagnetic to magnetic behavior upon reduction of sample size was first observed through Stern–Gerlach experiments in the case of rhodium clusters [374, 375]. Notably, ruthenium and palladium clusters were found to remain nonmagnetic. In niobium clusters Nb_n with $n < 100$ both ferroelectricity and evidence for superconductivity through spin uncoupling were found [376]. Subsequently this spin uncoupling was related to low temperature magnetization as observed in Stern–Gerlach experiments [377]. Further interpretation of Stern–Gerlach experiments in terms of spin relaxation [372] and by invocation of magnetic anisotropy energies [378] helped to clarify uncertainties in previous experiments.

Despite the generally good interpretation of findings from Stern–Gerlach experiments it is still not possible to strictly separate the spin and orbit contributions to the total moments in free clusters by such experiments alone. Combination with negative ion photoelectron spectroscopy was suggested some time ago [379] but no such combined experiments took place up to now (Fig. 7).

The Stern–Gerlach type of molecular beam experiments have enabled the tentative determination of total magnetic moments in 3d TM clusters [106, 361, 369, 370, 380–384], while the seemingly limited control of cluster temperatures remains an issue, unless evaluated carefully [369]. DFT based modeling has tried to mimic such clusters [385–388] while the predictive power of these calculations stays uncertain. Recently multi-sandwich type TM complexes were studied by

Stern–Gerlach experiments revealing ferromagnetic couplings by benzene mediated superexchange [389–392].

5.5.3 XMCD Investigations of Isolated TM Cluster Cations

Beyond the application of inhomogeneous magnetic fields to neutral TM cluster beams or the application of SQUID magnetometry to bulk samples there is another method of choice available in order to elucidate magnetic moments of TM clusters and complexes: Resonant Inner shell ionization by circularly polarized monochromatic X-rays may exhibit dichroism, provided that the magnetic moments of the sample are oriented, e.g., by sufficiently high magnetic field (7 Tesla) at sufficiently low sample temperature (<20 K). The effect and the technique are known as X-ray induced Magnetic Circular Dichroism (XMCD) [393–395], and it is routinely applied to $2p->3d$ transitions in TM metal containing bulk samples. It shows that this effect suffices for an approximate evaluation by the so-called sum rule analysis [394, 395] in order to obtain the numerical values of the z components of spin and orbital moments, $m_S{}^{(z)}$ and $m_L{}^{(z)}$ in units of μ_B:

$$m_L{}^{(z)} = \left[-\frac{4(A+B)}{3C} n_h\right] / \eta_{pol}$$

$$m_S{}^{(z)} = \left[-\frac{2(A-2B)}{C} n_h - 7T_z\right] / \eta_{pol}$$

The parameters A and B represent the integrated dichroic effects ($\sigma^+ - \sigma^-$) at the L_2 and L_3 absorption edges of the experimental X-ray spectra, and C is the corresponding value of the isotropic spectrum which is approximated by the sum of spectra of both polarizations ($\sigma^+ + \sigma^-$), corrected for non-resonant background absorption. $\langle T_z \rangle$ is the anisotropic dipole term, and n_h is the number of unoccupied 3d valence states ("3d holes"). The finite degree of circular polarization η_{pol} as available by synchrotron sources these days (about 90 %) necessitates the application of an according linear correction. Conversion to total moments m_S and m_L arises by the Brillouin formula.

Application of XMCD to deposited TM clusters on surfaces occurred lately [396]. While X-ray absorption spectroscopy of isolated TM clusters arose subsequently, it took a separate approach to develop an XMCD application for such samples. First results arose on isolated Co clusters [397] revealing spin and orbital moments of clusters in between of those of bulk and atoms. Subsequent studies confirmed, extended, and refined the previous approach obtaining independent data of Fe, Co, and Ni clusters [398, 399]. A recent XANES study of $Nb_{13}{}^+$ confirmed its icosahedral structure [400], and a study of single Au and Rh on size selected Co cluster revealed a lack of heteroatom effect onto the magnetic moments [401]. Other XMCD experiments did reveal high spin electronic ground states of Cr, Mn, Fe, and Co dimer cations in isolation [402, 403].

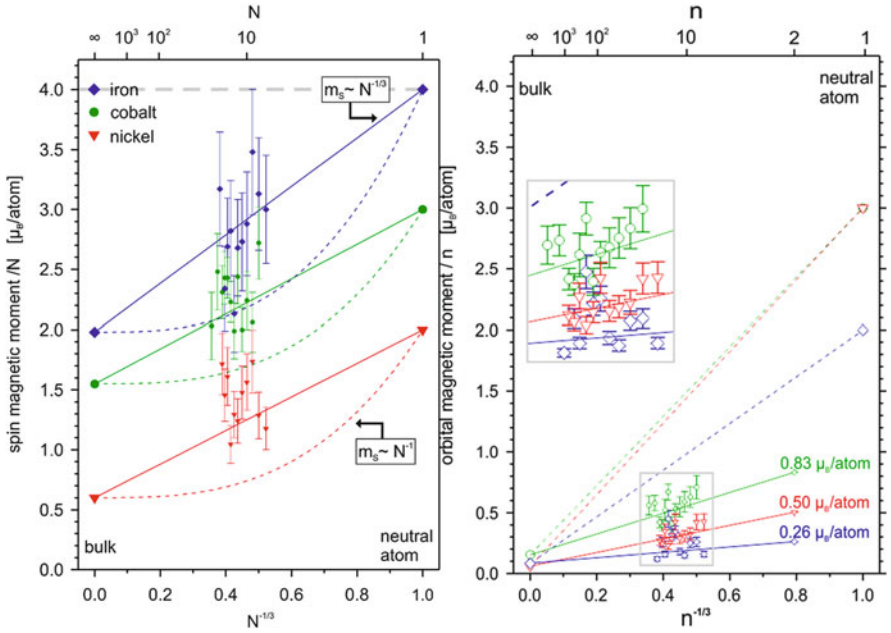

Fig. 8 Spin (*left*) and orbital (*right*) magnetic moments of size selected clusters in comparison to conceivable trends that would interpolate between bulk metals and neutral atoms. Note that the recorded spin moments seem to follow an $n^{-1/3}$ scaling. Orbital moments of $n = 2$ clusters ($n^{-1/3} = 0.794$, *solid symbols*) are tentative predictions from the $n^{-1/3}$ fits of experimental bulk and cluster data as displayed, with atomic values exempt from the fit (see text for discussion, adapted from [96])

Most recently, our re-investigation by XMCD of the spin and orbit contributions to Fe, Ni, and Co clusters revealed different scaling laws for spin and orbit [404]. We find a spin scaling law "per cluster diameter," that interpolates between known atomic and bulk values. In remarkable contrast, the orbital moments do likewise only if the atomic asymptotes are exempt. This explains through a concept of primary orbital moments, which persist in atoms on their own through degeneracy of partially filled d-orbitals, and secondary orbital moments, which are induced through relativistic spin–orbit coupling – coupling to total moments by cooperative effects (Fig. 8).

5.6 *Magnetism of Single Molecule Magnets and TM Complexes in Isolation*

When applying the aforementioned approximate sum rule analysis one usually neglects contributions from the magnetic dipole operator term (then regarded as $<10\,\%$). This is a good approximation in cases of clusters and compounds where

magnetic anisotropy is small and minor. Homogeneous TM clusters and even their alloys are amongst these cases. When, however, direct TM–TM proximity seizes and, e.g., μ-oxo bridging (and other types of bridges) prevail, the so-called superexchange comes into play. Such directional bonding and coordination is a herald of anisotropy. Current research aims to utilize and maximize the anisotropy in order to induce the so-called Single Molecule Magnet (SMM) behavior [405].

The synthesis and characterization of such SMMs is a fertile field of research. The SMMs are most often based on appropriate combinations of 3d TMs (Mn and Fe) and/or 4f lanthanoids (e.g., Dy) [121, 406–457]. This field is well covered by appropriate reviews [458–463].

However, there has been no attempt published on a magnetic characterization of SMMs in isolation, e.g., by mass spectrometric methods. The newly devised GAMBIT technique [397] and its most recent adaption by the NanoclusterTrap [398] at BESSY II came handy to try for XMCD experiments on SMMs in isolation. The archetypal $[Mn^{III}{}_8Mn^{IV}{}_4O_{12}(CH_3COO)_{16}]$ [405] has a high spin ground state by cooperative, ferrimagnetic (spin antiparallel) coupling between the 8 ferromagnetically (spin up) coupled Mn^{III} ions ($S = 16$) and 4 ferromagnetically (spin down) arranged Mn^{IV} ($S = 6$). This results in a spin ground state of $S = 16 - 6 = 10$. This molecular spin, in conjunction with a uniaxial molecular magnetic anisotropy induced by the Jahn-Teller distorted Mn^{III}, leads to a molecule-based barrier to the spin reversal between the ground state orientations $m_S = \pm 10$ and to hysteresis. Such properties are most often associated with 3D length scale ordering and are not regarded as intrinsic molecular properties. Bulk samples seem to reveal SMM properties, surface deposition seemingly alters those, an illuminating benchmark of the isolated molecule amiss, up to now (Fig. 9).

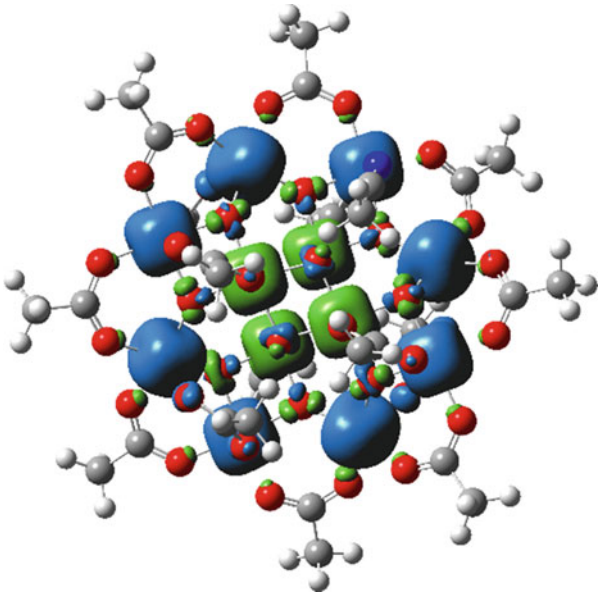

Fig. 9 Densities of α (*blue*) and β (*green*) spins in $[Mn_{12}O_{12}(CH_3COO)_{16}]$ by broken symmetry DFT calculations (PBE0-D3/def2-TZVP). Negligible differences arise by variation of the exchange-correlation functional or by swapping a sole peripheral CH3COO$^-$ ligand for a neutral CH_3CN ligand as in experiment. The revealed spin coupling pattern is robust. (unpublished work in progress [464])

Our very recent, yet unpublished, study reports the molecular magnetic signature of a truly isolated cationic species $[Mn_{12}ac]^+$ using X-ray XMCD spectroscopy as well as broken symmetry DFT calculations [24–27, 177, 178]. These allow us to substantiate the intrinsic molecule-based magnetic properties of this compound void of bulk or surface effects and confirm the molecular origin of the magnetic behavior [464]. These studies are currently in extension towards further complexes that comprise of 3d TM – 4f Rare Earth (RE) metal combinations in varying stoichiometries and coordinations [465].

5.7 IR Spectroscopic Characterization of Multinuclear Complexes

Still, it is most often uncertain, how the electronic coupling looks like in an isolated oligonuclear TM complex. The more it is of value to look for cases where auxiliary information is available. Such information may arise through the response of particular ligand vibrations to the spin states of the coordinated TM center(s). Early IR spectra of niobium–acetonitrile complexes revealed such spectral shifts by spin states, fostered by according DFT studies [466]. More recently unsaturated vanadium carbonyl complexes revealed relative IR intensities and IR frequencies by experiments and DFT calculations that sufficed to deduce a spin state reduction by increasing ligand coordination number [467]. It is most worthwhile to further elucidate such spin state reporting vibrations – this the more so – as the subsequent interpretation will help to elucidate further cooperative effects in the investigated complexes.

We conducted an IR-MPD study by ESI-MS of a cationic $[(Ag^I)_2(1MT\text{-}H)^-(DDA)]^+$complex, which self-assembled from two Ag^I ions, a deprotonated 1-methyl-thymine $(1MT\text{-}H)^-$, and a 1,3-dideaza-adenine (DDA) in methanolic solution [468]. Assignment of vibrational bands and identification of the silver coordination pattern arose from comparison of one- and two-color IR-MPD spectra (1,000–4,000 cm^{-1}) thereby identifying two structurally and energetically close isomers that resemble a metalated Hoogsteen-like binding motif. The two-color IR/IR double resonance scheme proved in particular useful to observe weakly absorbing or weakly fragmenting vibrational modes. By another study the two-color IR/IR double resonance with pulse delayed tuning revealed a torsional isomerization within a "ligand–metal–chelate" complex $[AgL_1L_2]^+$ [469]. The concomitant ab initio calculations revealed the torsional barrier height as well as the change in vibrational frequencies and IR intensities along the isomerization pathway. We further conducted a study of metal base pairs of Ag^I cations and 1-methylthymine, (1MT) or $(1MT\text{-}H)^-$ [470], and we recorded IR-MPD spectra of mass-selected complexes of type $[Ag^I{}_2(1MT)(1MT\text{-}H)^-]^+$ and $[Ag^I{}_3(1MT\text{-}H)^-{}_2]^+$ to assign isomeric structures, and to elucidate probable formation pathways in

aqueous solution. These findings paved the way for subsequent UV investigations of the multi-metal mediated base pairs, which are in the making.

We most recently found that a novel bifunctional iron–palladium complex exhibits in CID the competing fragmentation channels of HCl and $FeCl_2$ elimination, where the relative yields are modulated by the solvent [471]. The identified *syn* and *anti* isomers favor and disfavor the much involved $FeCl_2$ elimination, which proceeds by chlorido and Cp ligand exchange amongst the metallic centers in a cooperative, ballet like manner – reminiscent of a concerted salt metathesis. A multitude of stationary points were identified along the computed multistep reaction coordinates of the three conceivable spin states, a direct singlet to quintet transition driving the process with the triplet state left aside as a spectator without involvement. The observation of $FeCl_2$ elimination is of relevance to conceivable technical applications.

There is a potentially large impact of cationization on the molecular structures and catalytic activities of oligonuclear TM complexes. We cationized a bimetallic complex $[AuZnCl_3]$ with alkali metal ions (M^+) and investigated the charged adducts $[AuZnCl_3M]^+$ via ESI-MS [472]. The combination of IR-MPD experiments and DFT calculations revealed a μ^3-binding motif of all alkali ions to the three chlorido ligands. The cationization induces a reorientation of the organic backbone. CID studies revealed switches of fragmentation channels by the alkali ion and by the CID amplitude. The Li^+ and Na^+ adducts prefer the sole loss of $ZnCl_2$, whereas the K^+, Rb^+, and Cs^+ adducts most preferably split off MCl_2ZnCl. Calculated free Gibbs energies and fragmentation coordinate profiles showed that the Zn^{2+} cation wins against K^+, Rb^+, and Cs^+, the competition for the nitrogen coordination sites, and it looses against Li^+ and Na^+ – in remarkable deviation from a naive HSAB concept. The computations indicated expulsion of MCl_2ZnCl rather than of MCl and $ZnCl_2$. The variation of the Au–Zn–alkali cooperation was elucidated in detail.

6 Summary and Concluding Remarks

It is not possible to survey the field of TM clusters and TM complexes in total, and even the current survey of restricted coverage (2005–2016) is doomed to suffer from a biased view and from incompleteness. Nevertheless, we feel confident to provide glimpses onto current work of relevance and to put these studies into perspective with respect to the larger field of research and to the current status of knowledge. When this survey will help the reader to find interest and orientation in TM cluster research, then it has served its purpose.

We see a bunch of current, largely open questions and challenges for future generations of young and devoted researchers: (1) In the chemistry community TM clusters are often regarded primarily as those oligomeric TM complexes that occur in the form of ligand stabilized, coordinatively stabilized oligomers in bulk solution and solids. In the physics community TM clusters are most often regarded primarily as naked clusters, isolated in the gas phase or deposited on surfaces. The delineation

is obvious, the area in between is largely unexplored. Both communities may want to learn to talk to each other and to find a common language for improved interchange of ideas and concepts. (2) Isolated TM clusters in the gas phase do serve well for the study of *cluster size selected reactions* up to catalytic cycles. It is probably even more demanding – and accordingly much less often achieved – to study such processes with TM clusters when deposited on various surfaces, as, e.g., done in the groups of U. Heiz at TU Munich and of K.H. Meiwes-Broer at U Rostock, and others. (3) The high level DFT based description of coupled TM cluster surface systems is a challenge. Early studies were done by N. Rösch at TU Munich. Recent systematic studies were spear headed by J. Sauer at HU Berlin, in particular of TM clusters on metal oxide surfaces. (4) It is well within reach to fabricate materials made of clusters [473–476]. Self-assembly is a topic [477]. There are examples of Metal Organic Frameworks (MOF) with trimetallic cores [478]. (5) Another topic of current and future interest are TM clusters in liquids and in bio environments [277–279, 479, 480]. (6) Last but not least we like to point out a study of our own that asks for continuation: Micrometer sized nanoparticles act vividly as nucleation seeds for the crystallization of organic polymer melts which visualizes through polarization microscopy [481]. What about smaller clusters and complexes (of TMs)? The field of research in TM clusters and oligomeric TM complexes is wide open. Go for it!

Acknowledgments The author thanks his many prior and current co-workers, all of whom have enabled him to gain insight beyond his own imagination into the fascinating realms of TM clusters and TM complexes. Particular thanks go to Matthias Tombers and Manfred Kappes for critical reading and valuable comments. Sebastian Dillinger helped to prepare Fig. 6. The author acknowledges financial support by the state research center OPTIMAS, by the DFG funded collaborative research center "Cooperative effects in homo and heteronuclear transition metal complexes" **3MET.de**, and by the *Carl Zeiss Stiftung*. The stated definitions of cooperative effects are in line with the 3MET working definitions as defined by its consortium of principal investigators.

References

1. Castleman AW, Bowen KH (1996) J Phys Chem 100:12911
2. Knickelbein MB (1999) Annu Rev Phys Chem 50:79
3. de Heer WA (2000) In: Meiwes-Broer K-H (ed) Metal clusters at surfaces. Springer, Berlin, p 1
4. Majetich S (1998) Cluster materials. JAI Inc. Press, Stamford
5. Pastor GM, Bennemann K (1999) In: Ekardt W (ed) Metal clusters. Wiley, Chichester, p 211
6. Wernsdorfer W (1999) Metal clusters at surfaces. Springer, Berlin
7. Billas IML, Chatelain A, Deheer WA (1994) Science 265:1682
8. Bansmann J, Baker SH, Binns C, Blackman JA, Bucher JP, Dorantes-Davila J, Dupuis V, Favre L, Kechrakos D, Kleibert A, Meiwes-Broer KH, Pastor GM, Perez A, Toulemonde O, Trohidou KN, Tuaillon J, Xie Y (2005) Surf Sci Rep 56:189
9. Terasaki A (2003) In: Kondow T, Mafune F (eds) Progress in experimental and theoretical studies of clusters. World Scientific Inc., Singapor, p 55
10. Dietz TG, Duncan MA, Powers DE, Smalley RE (1981) J Chem Phys 74:6511
11. Bondybey VE, English JH (1981) J Chem Phys 74:6978

12. Geusic ME, Morse MD, Obrien SC, Smalley RE (1985) Rev Sci Instrum 56:2123
13. Geusic ME, Morse MD, Smalley RE (1985) J Chem Phys 82:590
14. Morse MD, Geusic ME, Heath JR, Smalley RE (1985) J Chem Phys 83:2293
15. Bondybey VE, English JH (1983) Chem Phys Lett 94:443
16. Bondybey VE (1984) Chem Phys Lett 109:436
17. Duncan MA (2012) Rev Sci Instrum 83:041101
18. Schnabel P, Irion MP, Weil KG (1991) J Phys Chem 95:9688
19. Schnabel P, Weil KG, Irion MP (1992) Angew Chem Int Ed 31:636
20. Harding DJ, Fielicke A (2014) Chem Eur J 20:3258
21. Eller K, Schwarz H (1991) Chem Rev 91:1121
22. Freiser BS (1992) Organometallic ion chemistry. Kluwer, Dordrecht, p IX + 335
23. Duncan MA (1993–2001) JAI Press and Elsevier, Hampton Hill and Amsterdam, vol 1–5
24. Armentrout PB (2001) Annu Rev Phys Chem 52:423
25. Armentrout PB (2013) J Am Soc Mass Spectrom 24:173
26. Armentrout PB (2014) Catal Sci Technol 4:2741
27. Armentrout PB (2015) Int J Mass Spectrom 377:54
28. Lang SM, Bernhardt TM (2014) Bunsen-Magazin 15:283
29. Adams RD, Cotton FA (1998) Catalysis by di- and polynuclear metal cluster complexes. Wiley, Chichester
30. Braunstein P, Oro LA, Raithby PR (1999) Metal clusters in chemistry, vol I–III. Wiley-VCH, Weinheim
31. Buchwalter P, Rose J, Braunstein P (2015) Chem Rev 115:28
32. Belloni J, Amblard J, Marignier JL, Mostafavi M (1994) In: Haberland H (ed) Clusters of atoms and molecules. Springer, Berlin, p 290
33. Kreibig U, Vollmer M (1995) Optical properties of metal clusters. Springer, Berlin
34. Muetterties EL (1975) Bull Soc Chim Belg 84:959
35. Muetterties EL (1977) Science 196:839
36. Muetterties EL, Rhodin TN, Band E, Brucker CF, Pretzer WR (1979) Chem Rev 79:91
37. Ertl G (2008) Angew Chem Int Ed 47:3524
38. Shustorovich E (1986) In: Veillard A (ed) Quantum chemistry: the challenge of transition metals and coordination chemistry. Springer Netherlands, p 445
39. Pfeffer B, Jaberg S, Niedner-Schatteburg G (2009) J Chem Phys 131:194305
40. Saito N, Koyama K, Tanimoto M (2002) In: Kawazoe Y, Ohno K, Kondow T (eds) Clusters and nanomaterials – theory and experiment. Springer, Berlin, p 89
41. Herlert A, Kruckeberg S, Schweikhard L, Vogel M, Walther C (1999) Phys Scr T80B:200
42. Martinez F, Bandelow S, Marx G, Schweikhard L, Vass A (2015) J Phys Chem C119:10949
43. Elkind JL, Weiss FD, Alford JM, Laaksonen RT, Smalley RE (1988) J Chem Phys 88:5215
44. Hoffman WF, Parks EK, Nieman GC, Pobo LG, Riley SJ (1987) Z Phys D7:83
45. Parks EK, Nieman GC, Pobo LG, Riley SJ (1987) J Phys Chem 91:2671
46. Parks EK, Nieman GC, Pobo LG, Riley SJ (1987) J Chem Phys 86:1066
47. Parks EK, Nieman GC, Pobo LG, Riley SJ (1988) J Chem Phys 88:6260
48. Parks EK, Weiller BH, Bechthold PS, Hoffman WF, Nieman GC, Pobo LG, Riley SJ (1988) J Chem Phys 88:1622
49. Zakin MR, Brickman RO, Cox DM, Kaldor A (1988) J Chem Phys 88:6605
50. Zakin MR, Brickman RO, Cox DM, Kaldor A (1988) J Chem Phys 88:5943
51. Zakin MR, Brickman RO, Cox DM, Kaldor A (1988) J Chem Phys 88:3555
52. Zakin MR, Cox DM, Brickman RO, Kaldor A (1989) J Phys Chem 93:6823
53. Fayet P, Kaldor A, Cox DM (1990) J Chem Phys 92:254
54. Cox DM, Fayet P, Brickman R, Hahn MY, Kaldor A (1990) Catal Lett 4:271
55. Weiller BH, Bechthold PS, Parks EK, Pobo LG, Riley SJ (1989) J Chem Phys 91:4714
56. Nonose S, Sone Y, Onodera K, Sudo S, Kaya K (1990) J Phys Chem 94:2744
57. Rapps T, Ahlrichs R, Waldt E, Kappes MM, Schooss D (2013) Angew Chem Int Ed 52:6102
58. Wales DJ, Scheraga HA (1999) Science 285:1368

59. Fielicke A, Kirilyuk A, Ratsch C, Behler J, Scheffler M, von Helden G, Meijer G (2004) Phys Rev Lett 93:023401
60. Fielicke A, Ratsch C, von Helden G, Meijer G (2005) J Chem Phys 122:091105
61. Fielicke A, von Helden G, Meijer G (2005) Eur Phys J D34:83
62. Ratsch C, Fielicke A, Kirilyuk A, Behler J, von Helden G, Meijer G, Scheffler M (2005) J Chem Phys 122:124302
63. Fielicke A, Rabin I, Meijer G (2006) J Phys Chem A110:8060
64. Fielicke A, Ratsch C, von Helden G, Meijer G (2007) J Chem Phys 127:234306
65. Gruene P, Fielicke A, Meijer G (2007) J Chem Phys 127:234307
66. Harding DJ, Gruene P, Haertelt M, Meijer G, Fielicke A, Hamilton SM, Hopkins WS, Mackenzie SR, Neville SP, Walsh TR (2010) J Chem Phys 133:214304
67. Harding DJ, Walsh TR, Hamilton SM, Hopkins WS, Mackenzie SR, Gruene P, Haertelt M, Meijer G, Fielicke A (2010) J Chem Phys 132:011101
68. Haertelt M, Lapoutre VJF, Bakker JM, Redlich B, Harding DJ, Fielicke A, Meijer G (2011) J Phys Chem Lett 2:1720
69. Harding DJ, Kerpal C, Meijer G, Fielicke A (2012) Angew Chem Int Ed 51:817
70. Bowlan J, Harding DJ, Jalink J, Kirilyuk A, Meijer G, Fielicke A (2013) J Chem Phys 138:031102
71. Lapoutre VJF, Haertelt M, Meijer G, Fielicke A, Bakker JM (2013) J Chem Phys 139:121101
72. Fielicke A, Gruene P, Meijer G, Rayner DM (2009) Surf Sci 603:1427
73. Broden G, Rhodin TN, Brucker C, Benbow R, Hurych Z (1976) Surf Sci 59:593
74. Moskovits M (1991) Annu Rev Phys Chem 42:465
75. Bechthold PS, Parks EK, Weiller BH, Pobo LG, Riley SJ (1990) Z Phys Chem 169:101
76. Riley SJ (1994) In: Haberland H (ed) Clusters of atoms and molecules. Springer, Berlin, p 221
77. Parks EK, Riley SJ (1990) In: Scoles G (ed) The chemical physics of atomic and molecular clusters. North-Holland, Amsterdam, p 761
78. O'Hair RAJ, Khairallah GN (2004) J Cluster Sci 15:331
79. Lang SM, Bernhardt TM (2012) Phys Chem Chem Phys 14:9255
80. Schroeder D (2010) Angew Chem Int Ed 49:850
81. Schwarz H (2011) Angew Chem Int Ed 50:10096
82. Schwarz H (2015) Angew Chem Int Ed 54:10090
83. Bohme DK, Schwarz H (2005) Angew Chem Int Ed 44:2336
84. Hankins D, Moskowit J, Stilling F (1970) J Chem Phys 53:4544
85. Xantheas SS (2000) Chem Phys 258:225
86. Fedorov DG, Kitaura K (2004) J Chem Phys 120:6832
87. Dahlke EE, Truhlar DG (2007) J Chem Theor Comput 3:46
88. Shavitt I, Bartlett RJ (2009) Many-body methods in chemistry and physics: MBPT and coupled-cluster theory. Cambridge University Press, Cambridge
89. Chmela J, Harding ME, Matioszek D, Anson CE, Breher F, Klopper W (2016) ChemPhysChem 17:37
90. Lishchuk SV (2012) J Chem Phys 136:164501
91. Klopper W, Chmela J, Harding ME, Matioszek D, Anson CE, Breher F (2015) ChemPhysChem
92. Moskovits M (1990) In: Scoles G (ed) The chemical physics of atomic and molecular clusters. North-Holland, Amsterdam, p 397
93. Rips I, Jortner J (1992) J Chem Phys 97:536
94. Haberland H, Kleinermanns K, Träger F (2006) In Lehrbuch der Experimentalphysik Band 5 - Gase, Nanosysteme, Flüssigkeiten, 2nd edn. Walter de Gruyter, p 819
95. Atkins P, de Paula J (2005) Elements of physical chemistry, 4th edn. W. H. Freeman and Company, Oxford
96. Meyer J, Tombers M, van Wuellen C, Niedner-Schatteburg G, Peredkov S, Eberhardt W, Neeb M, Palutke S, Martins M, Wurth W (2015) J Chem Phys 143:104302

97. Bachels T, Schäfer R (2000) Chem Phys Lett 324:365
98. Baletto F, Ferrando R (2005) Rev Mod Phys 77:371
99. Kohn A, Weigend F, Ahlrichs R (2001) Phys Chem Chem Phys 3:711
100. Herrmann A, Schumacher E, Woste L (1978) J Chem Phys 68:2327
101. Kappes MM, Schar M, Radi P, Schumacher E (1986) J Chem Phys 84:1863
102. Wrigge G, Hoffmann MA, Issendorff B (2002) Phys Rev A65:063201
103. Wrigge G, Astruc Hoffmann M, Issendorff B, Haberland H (2003) Eur Phys J D24:23
104. Knickelbein MB (2002) Chem Phys Lett 353:221
105. Alvarez MM, Khoury JT, Schaaff TG, Shafigullin MN, Vezmar I, Whetten RL (1997) J Phys Chem B101:3706
106. Billas IML, Becker JA, Chatelain A, Deheer WA (1993) Phys Rev Lett 71:4067
107. Bréchignac C, Broyer M, Cahuzac P, Delacretaz G, Labastie P, Wolf JP, Wöste L (1988) Phys Rev Lett 60:275
108. Brechignac C, Broyer M, Cahuzac P, Delacretaz G, Labastie P, Wöste L (1985) Chem Phys Lett 120:559
109. Pastor GM, Bennemann KH (1994) In: Haberland H (ed) Clusters of atoms and molecules. Springer, p 96
110. Harrison MR, Edwards PP (1985) In: Edwards PP, Rao CNR (eds) The metallic and non-metallic states of matter. Francis & Taylor, London, p 389
111. Getzlaff M (2008) Fundamentals of magnetism. Springer, Berlin
112. Kappes M, Leutwyler S (1988) In: Scoles G (ed) Atomic and molecular beam methods. Oxford University Press, Oxford, p 380
113. Pauly H (2000) Atom, molecules, and cluster beams. Springer, Berlin, p 71
114. Milani P, Iannotta S (1999) Cluster beam synthesis of nano-structured materials. Springer, Berlin
115. Haberland H, Karrais M, Mall M (1991) Z Phys D20:413
116. Lu Y-J, Lehman JH, Lineberger WC (2015) J Chem Phys 142:044201
117. Fayet P, Patthey F, Roy HV, Detzel T, Schneider WD (1992) Surf Sci 269:1101
118. Keller R, Nohmayer F, Spadtke P, Schonenberg MH (1984) Vacuum 34:31
119. Schaffner MH, Jeanneret JF, Patthey F, Schneider WD (1998) J Phys D31:3177
120. Marshall AG, Hendrickson CL, Jackson GS (1998) Mass Spectrom Rev 17:1
121. Bhunia A, Gamer MT, Ungur L, Chibotaru LF, Powell AK, Lan Y, Roesky PW, Menges F, Riehn C, Niedner-Schatteburg G (2012) Inorg Chem 51:9589
122. Fenn JB, Mann M, Meng CK, Wong SF, Whitehouse CM (1989) Science 246:64
123. Fenn JB, Mann M, Meng CK, Wong SF, Whitehouse CM (1990) Mass Spectrom Rev 9:37
124. Mann M, Hendrickson RC, Pandey A (2001) Annu Rev Biochem 70:437
125. Fenn JB (2003) Angew Chem Int Ed 42:3871
126. Cooks RG, Ouyang Z, Takats Z, Wiseman JM (2006) Science 311:1566
127. Nguyen S, Fenn JB (2007) Proc Natl Acad Sci U S A 104:1111
128. Blades AT, Jayaweera P, Ikonomou MG, Kebarle P (1990) Int J Mass Spectrom Ion Processes 102:251
129. Peschke M, Blades AT, Kebarle P (1998) J Phys Chem A102:9978
130. Wang LS, Ding CF, Wang XB, Barlow SE (1999) Rev Sci Instrum 70:1957
131. Kamariotis A, Boyarkin OV, Mercier SR, Beck RD, Bush MF, Williams ER, Rizzo TR (2006) J Am Chem Soc 128:905
132. Armentrout PB, Baer T (1996) J Phys Chem 100:12866
133. Bernhardt TM (2005) Int J Mass Spectrom 243:1
134. Xue W, Wang Z-C, He S-G, Xie Y, Bernstein ER (2008) J Am Chem Soc 130:15879
135. Rodgers MT, Ervin KM, Armentrout PB (1997) J Chem Phys 106:4499
136. Rodgers MT, Armentrout PB (2000) Mass Spectrom Rev 19:215
137. Muntean F, Armentrout PB (2001) J Chem Phys 115:1213
138. Hill HH, Siems WF, Stlouis RH, McMinn DG (1990) Anal Chem 62:A1201
139. Clemmer DE, Jarrold MF (1997) J Mass Spectrom 32:577

140. Steinfeld JI, Wormhoudt J (1998) Annu Rev Phys Chem 49:203
141. Wyttenbach T, Bowers MT (2003) Mod Mass Spectrom 225:207
142. Moore DS (2004) Rev Sci Instrum 75:2499
143. Kanu AB, Dwivedi P, Tam M, Matz L, Hill HH Jr (2008) J Mass Spectrom 43:1
144. Maier-Borst M, Cameron DB, Rokni M, Parks JH (1999) Phys Rev A59:R3162
145. Kruckeberg S, Schooss D, Maier-Borst M, Parks JH (2000) Phys Rev Lett 85:4494
146. Douglas DJ, Frank AJ, Mao DM (2005) Mass Spectrom Rev 24:1
147. Hu QZ, Noll RJ, Li HY, Makarov A, Hardman M, Cooks RG (2005) J Mass Spectrom 40:430
148. Rizzo TR, Stearns JA, Boyarkin OV (2009) Int Rev Phys Chem 28:481
149. Kamrath MZ, Garand E, Jordan PA, Leavitt CM, Wolk AB, Van Stipdonk MJ, Miller SJ, Johnson MA (2011) J Am Chem Soc 133:6440
150. Auboeck G, Nagl J, Callegari C, Ernst WE (2007) J Phys Chem A111:7404
151. Nagl J, Auboeck G, Hauser AW, Allard O, Callegari C, Ernst WE (2008) Phys Rev Lett 100:063001
152. Bunermann O, Mudrich M, Weidemuller M, Stienkemeier F (2004) J Chem Phys 121:8880
153. Mudrich M, Bunermann O, Stienkemeier F, Dulieu O, Weidemuller M (2004) Eur Phys J D31:291
154. Mueller S, Krapf S, Koslowski T, Mudrich M, Stienkemeier F (2009) Phys Rev Lett 102:183401
155. Moret M-E, Serra D, Bach A, Chen P (2010) Angew Chem Int Ed 49:2873
156. Oeschger RJ, Ringger DH, Chen P (2015) Organometallics 34:3888
157. Serra D, Moret M-E, Chen P (2011) J Am Chem Soc 133:8914
158. Eckardt W (1999) Metal clusters. Wiley, Chichester, p XIII + 286
159. Cramer CJ, Truhlar DG (2009) Phys Chem Chem Phys 11:10757
160. Perdew JP, Chevary JA, Vosko SH, Jackson KA, Pederson MR, Singh DJ, Fiolhais C (1992) Phys Rev B46:6671
161. Adamo C, Barone V (1999) J Chem Phys 110:6158
162. Boese AD, Martin JML (2004) J Chem Phys 121:3405
163. Zhao Y, Truhlar DG (2005) J Chem Theor Comp 1:415
164. Zhao Y, Schultz NE, Truhlar DG (2006) J Chem Theor Comp 2:364
165. Zhao Y, Truhlar DG (2006) J Chem Phys 125:194101
166. Jena P, Khanna SN, Rao BK (1996) In: Sattler K (ed) Cluster assembled materials. CRC Press, p 1
167. Jena P, Khanna SN, Rao BK (1999) In: Jellinek J (ed) Theory of atomic and molecular clusters: with a glimpse at experiments. Springer, Heidelberg, p 27
168. Pham Vu N, Vu Thi N, Truong Ba T, Minh Tho N (2011) J Phys Chem A115:14127
169. Fielicke A, Meijer G (2011) J Phys Chem A115:7869
170. Pham Vu N, Vu Thi N, Truong Ba T, Minh Tho N (2011) J Phys Chem A115:3523
171. Caballol R, Castell O, Illas F, Moreira PR, Malrieu JP (1997) J Phys Chem A101:7860
172. Cabrero J, Ben Amor N, de Graaf C, Illas F, Caballol R (2000) J Phys Chem A104:9983
173. Soda T, Kitagawa Y, Onishi T, Takano Y, Shigeta Y, Nagao H, Yoshioka Y, Yamaguchi K (2000) Chem Phys Lett 319:223
174. Lovell T, Li J, Liu TQ, Case DA, Noodleman L (2001) J Am Chem Soc 123:12392
175. Ciofini I, Daul CA (2003) Coord Chem Rev 238:187
176. Neese F (2004) J Phys Chem Solids 65:781
177. van Wuellen C (2009) J Phys Chem A113:11535
178. Kessler EMV, Schmitt S, van Wuellen C (2013) J Chem Phys 139:184110
179. Dietl N, Schlangen M, Schwarz H (2012) Angew Chem Int Ed 51:5544
180. Feyel S, Scharfenberg L, Daniel C, Hartl H, Schroeder D, Schwarz H (2007) J Phys Chem A111:3278
181. Feyel S, Doebler J, Schroeder D, Sauer J, Schwarz H (2006) Angew Chem Int Ed 45:4681
182. Feyel S, Schroder D, Schwarz H (2006) J Phys Chem A110:2647
183. Feyel S, Schroeder D, Schwarz H (2008) Eur J Inorg Chem 4961

184. Feyel S, Schroeder D, Schwarz H (2009) J Phys Chem A113:5625
185. Feyel S, Schwarz H, Schroeder D, Daniel C, Hartl H, Doebler J, Sauer J, Santambrogio G, Woeste L, Asmis KR (2007) Chemphyschem 8:1640
186. Nagata T, Miyajima K, Hardy RA, Metha GF, Mafune F (2015) J Phys Chem A119:5545
187. Nagata T, Miyajima K, Mafune F (2015) J Phys Chem A119:10255
188. Nagata T, Miyajima K, Mafune F (2015) J Phys Chem A119:1813
189. Schlangen M, Schwarz H (2012) Catal Lett 142:1265
190. Takeda Y, Mafune F (2014) Chem Phys Lett 599:110
191. Wu X-N, Tang S-Y, Zhao H-T, Weiske T, Schlangen M, Schwarz H (2014) Chem Eur J 20:6672
192. Wang B, Chen W-J, Zhao B-C, Zhang Y-F, Huang X (2010) J Phys Chem A114:1964
193. Feyel S, Schroeder D, Rozanska X, Sauer J, Schwarz H (2006) Angew Chem Int Ed 45:4677
194. Koszinowski K, Schlangen M, Schroder D, Schwarz H (2005) Eur J Inorg Chem 2464
195. Zhai HJ, Huang X, Waters T, Wang XB, O'Hair RAJ, Wedd AG, Wang LS (2005) J Phys Chem A109:10512
196. Huang X, Zhai HJ, Li J, Wang LS (2006) J Phys Chem A110:85
197. Huang X, Zhai HJ, Waters T, Li J, Wang LS (2006) Angew Chem Int Ed 45:657
198. Janssens E, Santambrogio G, Brummer M, Woste L, Lievens P, Sauer J, Meijer G, Asmis KR (2006) Phys Rev Lett 96:233401
199. Schroeder D, Roithova J, Schwarz H (2006) Int J Mass Spectrom 254:197
200. Xu Y, Shelton WA, Schneider WF (2006) J Phys Chem B110:16591
201. Asmis KR, Sauer J (2007) Mass Spectrom Rev 26:542
202. Zhai H-J, Doebler J, Sauer J, Wang L-S (2007) J Am Chem Soc 129:13270
203. Johnson GE, Reilly NM, Tyo EC, Castleman AW Jr (2008) J Phys Chem C112:9730
204. Johnson GE, Reveles JU, Reilly NM, Tyo EC, Khanna SN, Castleman AW Jr (2008) J Phys Chem A112:11330
205. Johnson GE, Tyo EC, Castleman AW Jr (2008) Proc Natl Acad Sci U S A 105:18108
206. Santambrogio G, Bruemmer M, Woeste L, Doebler J, Sierka M, Sauer J, Meijer G, Asmis KR (2008) Phys Chem Chem Phys 10:3992
207. Dong F, Heinbuch S, Xie Y, Rocca JJ, Bernstein ER (2009) J Phys Chem A113:3029
208. Johnson GE, Reilly NM, Castleman AW Jr (2009) Int J Mass Spectrom 280:93
209. Johnson GE, Mitric R, Bonacic-Koutecky V, Castleman AW Jr (2009) Chem Phys Lett 475:1
210. Rozanska X, Sauer J (2009) J Phys Chem A113:11586
211. Xie Y, Dong F, Heinbuch S, Rocca JJ, Bernstein ER (2009) J Chem Phys 130:114306
212. Zhai H-J, Wang B, Huang X, Wang L-S (2009) J Phys Chem A113:3866
213. Altinay G, Citir M, Metz RB (2010) J Phys Chem A114:5104
214. Chen W-J, Zhai H-J, Zhang Y-F, Huang X, Wang L-S (2010) J Phys Chem A114:5958
215. Hirabayashi S, Ichihashi M, Kondow T (2010) J Phys Chem A114:13040
216. Ma J-B, Wu X-N, Zhao Y-X, Ding X-L, He S-G (2010) J Phys Chem A114:10024
217. Ma Y-P, Ding X-L, Zhao Y-X, He S-G (2010) Chemphyschem 11:1718
218. Reveles JU, Johnson GE, Khanna SN, Castleman AW Jr (2010) J Phys Chem C114:5438
219. Sierka M (2010) Prog Surf Sci 85:398
220. Wende T, Doebler J, Jiang L, Claes P, Janssens E, Lievens P, Meijer G, Asmis KR, Sauer J (2010) Int J Mass Spectrom 297:102
221. Zhai H-J, Wang L-S (2010) Chem Phys Lett 500:185
222. Zhang X, Schwarz H (2010) ChemCatChem 2:1391
223. Altinay G, Kocak A, Daluz JS, Metz RB (2011) J Chem Phys 135:084311
224. Dietl N, van der Linde C, Schlangen M, Beyer MK, Schwarz H (2011) Angew Chem Int Ed 50:4966
225. Huebner O, Himmel H-J (2011) Phys Chem Chem Phys 13:2963
226. Lang SM, Bernhardt TM (2011) Faraday Discuss 152:337
227. Lv L, Wang Y, Jin Y (2011) Theor Chem Acc 130:15
228. Qiao B, Wang A, Yang X, Allard LF, Jiang Z, Cui Y, Liu J, Li J, Zhang T (2011) Nat Chem 3:634

229. Tyo EC, Nossler M, Mitric R, Bonacic-Koutecky V, Castleman AW Jr (2011) Phys Chem Chem Phys 13:4243
230. Xu B, Zhao Y-X, Li X-N, Ding X-L, He S-G (2011) J Phys Chem A115:10245
231. Zhao Y-X, Wu X-N, Ma J-B, He S-G, Ding X-L (2011) Phys Chem Chem Phys 13:1925
232. Asmis KR (2012) Phys Chem Chem Phys 14:9270
233. Asmis KR, Wende T, Bruemmer M, Gause O, Santambrogio G, Stanca-Kaposta EC, Doebler J, Niedziela A, Sauer J (2012) Phys Chem Chem Phys 14:9377
234. Wang Z-C, Yin S, Bernstein ER (2012) J Phys Chem Lett 3:2415
235. Wang Z-C, Dietl N, Kretschmer R, Ma J-B, Weiske T, Schlangen M, Schwarz H (2012) Angew Chem Int Ed 51:3703
236. Wu L, Zhang C, Krasnokutski SA, Yang D-S (2012) J Chem Phys 137:084312
237. Lang SM, Frank A, Fleischer I, Bernhardt TM (2013) Eur Phys J D67:19
238. Lin S-J, Zhang X-H, Xu L, Wang B, Zhang Y-F, Huang X (2013) J Phys Chem A117:3093
239. Wang Z-C, Yin S, Bernstein ER (2013) J Phys Chem A117:2294
240. Wang Z-C, Liu J-W, Schlangen M, Weiske T, Schroeder D, Sauer J, Schwarz H (2013) Chem Eur J 19:11496
241. Hirabayashi S, Ichihashi M (2014) Phys Chem Chem Phys 16:26500
242. Yamazoe S, Koyasu K, Tsukuda T (2014) Acc Chem Res 47:816
243. Reber AC, Khanna SN (2014) J Phys Chem C118:20306
244. Wang L-F, Xie L, Fang H-L, Li Y-F, Zhang X-B, Wang B, Zhang Y-F, Huang X (2014) Spectrochim Acta A131:446
245. Xu B, Meng J-H, Hei S-G (2014) J Phys Chem C118:18488
246. Bhattacharya S, Sonin BH, Jumonville CJ, Ghiringhelli LM, Marom N (2015) Phys Rev B91:241115
247. Hirabayashi S, Ichihashi M (2015) J Phys Chem C119:10850
248. Lin S-J, Cheng J, Zhang C-F, Wang B, Zhang Y-F, Huang X (2015) Phys Chem Chem Phys 17:11499
249. Ma J-B, Meng J-H, He S-G (2015) Dalton Trans 44:3128
250. Citir M, Liu F, Armentrout PB (2009) J Chem Phys 130:054309
251. Li M, Liu S-R, Armentrout PB (2009) J Chem Phys 131:144310
252. Liu F, Li M, Tan L, Armentrout PB (2008) J Chem Phys 128:194313
253. Liu FY, Armentrout PB (2005) J Chem Phys 122:194320
254. Liu FY, Li FX, Armentrout PB (2005) J Chem Phys 123:064304
255. McNary CP, Armentrout PB (2014) Phys Chem Chem Phys 16:26467
256. Tan L, Liu FY, Armentrout PB (2006) J Chem Phys 124:084302
257. Fielicke A, Meijer G, von Helden G (2003) J Am Chem Soc 125:3659
258. Fielicke A, von Helden G, Meijer G, Simard B, Denommee S, Rayner DM (2003) J Am Chem Soc 125:11184
259. Fielicke A, Gruene P, Haertelt M, Harding DJ, Meijer G (2010) J Phys Chem A114:9755
260. Kirilyuk A, Fielicke A, Demyk K, von Helden G, Meijer G, Rasing T (2010) Phys Rev B82:020405
261. Kerpal C, Harding DJ, Hermes AC, Meijer G, Mackenzie SR, Fielicke A (2013) J Phys Chem A117:1233
262. van Dijk CN, Roy DR, Fielicke A, Rasing T, Reber AC, Khanna SN, Kirilyuk A (2014) Eur Phys J D68:357
263. Fielicke A, von Helden G, Meijer G, Simard B, Rayner DM (2005) Phys Chem Chem Phys 7:3906
264. Hamilton SM, Hopkins WS, Harding DJ, Walsh TR, Gruene P, Haertelt M, Fielicke A, Meijer G, Mackenzie SR (2010) J Am Chem Soc 132:1448
265. Hamilton SM, Hopkins WS, Harding DJ, Walsh TR, Haertelt M, Kerpal C, Gruene P, Meijer G, Fielicke A, Mackenzie SR (2011) J Phys Chem A115:2489
266. Hermes AC, Hamilton SM, Hopkins WS, Harding DJ, Kerpal C, Meijer G, Fielicke A, Mackenzie SR (2011) J Phys Chem Lett 2:3053

267. Jin RC (2010) Nanoscale 2:343
268. Pyykko P (2004) Angew Chem Int Ed 43:4412
269. Daniel MC, Astruc D (2004) Chem Rev 104:293
270. Bond GC, Thompson DT (1999) Catal Rev 41:319
271. Hostetler MJ, Wingate JE, Zhong CJ, Harris JE, Vachet RW, Clark MR, Londono JD, Green SJ, Stokes JJ, Wignall GD, Glish GL, Porter MD, Evans ND, Murray RW (1998) Langmuir 14:17
272. Cao Y, Hoeckendorf RF, Beyer MK (2008) ChemPhysChem 9:1383
273. Cao Y, van der Linde C, Hoeckendorf RF, Beyer MK (2010) J Chem Phys 132:224307
274. Himeno H, Miyajima K, Yasuike T, Mafune F (2011) J Phys Chem A115:11479
275. Hoeckendorf RF, Cao Y, Beyer MK (2010) Organometallics 29:3001
276. Matsuo N, Muto H, Miyajima K, Mafune F (2007) Phys Chem Chem Phys 9:6027
277. Shoji M, Miyajima K, Mafune F (2008) J Phys Chem C112:1929
278. Takeda Y, Kondow T, Mafune F (2006) J Phys Chem B110:2393
279. Takeda Y, Mafune F, Kondow T (2009) J Phys Chem C113:5027
280. Yamada K, Miyajima K, Mafune F (2007) J Phys Chem C111:11246
281. Yamada K, Tokumoto Y, Nagata T, Mafune F (2006) J Phys Chem B110:11751
282. Furche F, Ahlrichs R, Weis P, Jacob C, Gilb S, Bierweiler T, Kappes MM (2002) J Chem Phys 117:6982
283. Johansson MP, Lechtken A, Schooss D, Kappes MM, Furche F (2008) Phys Rev A77:053202
284. Gruene P, Rayner DM, Redlich B, van der Meer AFG, Lyon JT, Meijer G, Fielicke A (2008) Science 321:674
285. Ling L, Claes P, Gruene P, Meijer G, Fielicke A, Minh Tho N, Lievens P (2010) ChemPhysChem 11:1932
286. Woodham AP, Meijer G, Fielicke A (2012) Angew Chem Int Ed 51:4444
287. Woodham AP, Meijer G, Fielicke A (2013) J Am Chem Soc 135:1727
288. Gruene P, Butschke B, Lyon JT, Rayner DM, Fielicke A (2014) Zeitschrift Fur Physikalische Chemie Int J Res Phys Chem Chem Phys 228:337
289. Woodham AP, Fielicke A (2014) Angew Chem Int Ed 53:6554
290. Woodham AP, Fielicke A (2014) In: Mingos DMP (ed) Gold clusters, colloids and nanoparticles I. Springer, p 243
291. Khairallah GN, O'Hair RAJ (2005) Dalton Trans 2702
292. Kubas GJ (2007) Chem Rev 107:4152
293. Mwakapumba J, Ervin KN (1997) Int J Mass Spectrom 161:161
294. Lyon JT, Gruene P, Fielicke A, Meijer G, Rayner DM (2009) J Chem Phys 131:184706
295. Gruene P, Fielicke A, Meijer G, Rayner DM (2008) Phys Chem Chem Phys 10:6144
296. Parks EK, Zhu L, Ho J, Riley SJ (1995) J Chem Phys 102:7377
297. Parks EK, Riley SJ (1995) Z Phys D33:59
298. Ho J, Parks EK, Zhu L, Riley SJ (1995) Chem Phys 201:245
299. Parks EK, Zhu L, Ho J, Riley SJ (1994) J Chem Phys 100:7206
300. Dillinger S, Mohrbach J, Hewer J, Gaffga M, Niedner-Schatteburg G (2015) Phys Chem Chem Phys 17:10358
301. Dillinger S, Mohrbach J, Niedner-Schatteburg G (2016) unpublished, work in progress
302. Wesendrup R, Schroder D, Schwarz H (1994) Angew Chem Int Ed 33:1174
303. Pavlov M, Blomberg MRA, Siegbahn PEM, Wesendrup R, Heinemann C, Schwarz H (1997) J Phys Chem A101:1567
304. Aschi M, Bronstrup M, Diefenbach M, Harvey JN, Schroder D, Schwarz H (1998) Angew Chem Int Ed 37:829
305. Diefenbach M, Bronstrup M, Aschi M, Schroder D, Schwarz H (1999) J Am Chem Soc 121:10614
306. Schröder D, Schwarz H (2005) Can J Chem 83:1936
307. Achatz U, Beyer M, Joos S, Fox BS, Niedner-Schatteburg G, Bondybey VE (1999) J Phys Chem A103:8200

308. Achatz U, Berg C, Joos S, Fox BS, Beyer MK, Niedner-Schatteburg G, Bondybey VE (2000) Chem Phys Lett 320:53
309. Kummerloewe G, Balteanu I, Sun Z, Balaj OP, Bondybey VE, Beyer MK (2006) Int J Mass Spectrom 254:183
310. Schroeder D, Schwarz H (2008) Proc Natl Acad Sci U S A 105:18114
311. Schlangen M, Schwarz H (2009) Dalton Trans 10155
312. Li H-F, Li Z-Y, Liu Q-Y, Li X-N, Zhao Y-X, He S-G (2015) J Phys Chem Lett 6:2287
313. Lang SM, Bernhardt TM, Barnett RN, Landman U (2010) Chemphyschem 11:1570
314. Lang SM, Bernhardt TM, Barnett RN, Landman U (2010) Angew Chem Int Ed 49:980
315. Lang SM, Frank A, Bernhardt TM (2013) Int J Mass Spectrom 354:365
316. Lang SM, Frank A, Bernhardt TM (2013) Catal Sci Technol 3:2926
317. Schwarz H (2014) Isr J Chem 54:1413
318. Schwarz H (2015) Chem Phys Lett 629:91
319. Albert G, Berg C, Beyer M, Achatz U, Joos S, NiednerSchatteburg G, Bondybey VE (1997) Chem Phys Lett 268:235
320. Bondybey VE, Beyer M, Achatz U, Fox B, Niedner-Schatteburg G (2001) Solvated metal ions and ion clusters, and the effect of ligands upon their reactivity. In: Duncan MA (ed) Metal ion solvation and metal-ligand interactions, vol 5. JAI Press Inc., Stamford, p 295
321. Dewar JS (1951) Bull Soc Chim Fr 18:C71
322. Chatt J, Duncanson LA (1953) J Chem Soc 2939
323. Kubas GJ (2001) J Organomet Chem 635:37
324. Blyholder G (1964) J Phys Chem 68:2772
325. Davydov A (2003) Molecular spectroscopy of oxide catalyst surfaces. Wiley, Chichester
326. Berg C, Schindler T, Niednerschatteburg G, Bondybey VE (1995) J Chem Phys 102:4870
327. Berg C, Schindler T, Lammers A, Niednerschatteburg G, Bondybey VE (1995) J Phys Chem 99:15497
328. Berg C, Niedner Schatteburg G, Bondybey VE (1996) In: Durig JR, Klabunde KJ (eds) Second international conference on low temperature chemistry, BkMk Press, Kansas City, p 189
329. Berg C, Beyer M, Schindler T, NiednerSchatteburg G, Bondybey VE (1996) J Chem Phys 104:7940
330. Berg C, Beyer M, Achatz U, Joos S, Niedner-Schatteburg G, Bondybey VE (1998) J Chem Phys 108:5398
331. Berg C, Schindler T, Kantlehner M, Niedner-Schatteburg G, Bondybey VE (2000) Chem Phys 262:143
332. Barzen L, Tombers M, Merkert C, Hewer J, Niedner-Schatteburg G (2012) Int J Mass Spectrom 330:271
333. Tombers M, Barzen L, Niedner-Schatteburg G (2013) J Phys Chem A117:1197
334. Dietrich G, Kruckeberg S, Lutzenkirchen K, Schweikhard L, Walther C (2000) J Chem Phys 112:752
335. Fielicke A, von Helden G, Meijer G, Pedersen DB, Simard B, Rayner DM (2006) J Chem Phys 124:194305
336. Fielicke A, von Helden G, Meijer G, Pedersen DB, Simard B, Rayner DM (2004) J Phys Chem B108:14591
337. Pedersen DB, Rayner DM, Simard B, Addicoat MA, Buntine MA, Metha GF, Fielicke A (2004) J Phys Chem A108:964
338. Fielicke A, von Helden G, Meijer G, Pedersen DB, Simard B, Rayner DM (2005) J Am Chem Soc 127:8416
339. Fielicke A, von Helden G, Meijer G, Simard B, Rayner DM (2005) J Phys Chem B109:23935
340. Swart I, de Groot FMF, Weckhuysen BM, Rayner DM, Meijer G, Fielicke A (2008) J Am Chem Soc 130:2126
341. Kerpal C, Harding DJ, Meijer G, Fielicke A (2011) Eur Phys J D63:231
342. Hermes AC, Hamilton SM, Cooper GA, Kerpal C, Harding DJ, Meijer G, Fielicke A, Mackenzie SR (2012) Faraday Discuss 157:213

343. Kerpal C, Harding DJ, Rayner DM, Lyon JT, Fielicke A (2015) J Phys Chem C119:10869
344. Kerpal C, Harding DJ, Lyon JT, Meijer G, Fielicke A (2013) J Phys Chem C117:12153
345. Gehrke R, Gruene P, Fielicke A, Meijer G, Reuter K (2009) J Chem Phys 130:034306
346. Ghiringhelli LM, Gruene P, Lyon JT, Rayner DM, Meijer G, Fielicke A, Scheffler M (2013) New J Phys 15
347. Shayeghi A, Johnston RL, Rayner DM, Schaefer R, Fielicke A (2015) Angew Chem Int Ed 54:10675
348. Shayeghi A, Schaefer R, Rayner DM, Johnston RL, Fielicke A (2015) J Chem Phys 143:024310
349. Swart I, Fielicke A, Rayner DM, Meijer G, Weckhuysen BM, de Groot FMF (2007) Angew Chem Int Ed 46:5317
350. Swart I, Fielicke A, Redlich B, Meijer G, Weckhuysen BM, de Groot FMF (2007) J Am Chem Soc 129:2516
351. Swart I, de Groot FMF, Weckhuysen BM, Gruene P, Meijer G, Fielicke A (2008) J Phys Chem A112:1139
352. Swart I, Gruene P, Fielicke A, Meijer G, Weckhuysen BM, de Groot FMF (2008) Phys Chem Chem Phys 10:5743
353. Kerpal C, Harding DJ, Rayner DM, Fielicke A (2013) J Phys Chem A117:8230
354. Clarke J, Braginski AI (2006) The SQUID handbook, vol 2: Applications. Wiley-VCH, Weinheim
355. Becker JA, Schafer R, Festag R, Ruland W, Wendorff JH, Pebler J, Quaiser SA, Helbig W, Reetz MT (1995) J Chem Phys 103:2520
356. Becker JA, Schafer R, Festag JR, Wendorff JH, Hensel F, Pebler J, Quaiser SA, Helbig W, Reetz MT (1996) Surf Rev Lett 3:1121
357. Luis F, Torres JM, Garcia LM, Bartolome J, Stankiewicz J, Petroff F, Fettar F, Maurice JL, Vaures A (2002) Phys Rev B65:094409
358. Wernsdorfer W (2001) Adv Chem Phys 118:99
359. Jung JK, Procissi D, Jang ZH, Suh BJ, Borsa F, Luban M, Kogerler P, Muller A (2002) J Appl Phys 91:7391
360. Knight WD, Monot R, Dietz ER, George AR (1978) Phys Rev Lett 40:1324
361. Deheer WA, Milani P, Chatelain A (1990) Z Phys Chem 169:63
362. Deheer WA, Milani P, Chatelain A (1990) Phys Rev Lett 65:488
363. Bucher JP, Douglass DC, Xia P, Haynes B, Bloomfield LA (1991) Z Phys D19:251
364. Bucher JP, Douglass DC, Bloomfield LA (1991) Phys Rev Lett 66:3052
365. Khanna SN, Linderoth S (1991) Phys Rev Lett 67:742
366. Linderoth S, Khanna SN (1992) J Magn Magn Mater 104:1574
367. Jensen PJ, Mukherjee S, Bennemann KH (1991) Z Phys D21:349
368. Jensen PJ, Bennemann KH (1994) Z Phys D29:67
369. Billas IML, Chatelain A, deHeer WA (1997) J Magn Magn Mater 168:64
370. Apsel SE, Emmert JW, Deng J, Bloomfield LA (1996) Phys Rev Lett 76:1441
371. Knickelbein MB (2001) Phys Rev Lett 86:5255
372. Knickelbein MB (2004) J Chem Phys 121:5281
373. Khanna SN, Rao BK, Jena P, Knickelbein M (2003) Chem Phys Lett 378:374
374. Cox AJ, Louderback JG, Bloomfield LA (1993) Phys Rev Lett 71:923
375. Cox AJ, Louderback JG, Apsel SE, Bloomfield LA (1994) Phys Rev B49:12295
376. Moro R, Xu XS, Yin SY, de Heer WA (2003) Science 300:1265
377. Moro R, Yin SY, Xu XS, de Heer WA (2004) Phys Rev Lett 93:086803
378. Xie YN, Blackman JA (2003) J Phys Condens Matter 15:L615
379. Jones NO, Khanna SN, Baruah T, Pederson MR (2004) Phys Rev B70:045416
380. Cox DM, Trevor DJ, Whetten RL, Rohlfing EA, Kaldor A (1985) Phys Rev B32:7290
381. Douglass DC, Bucher JP, Bloomfield LA (1992) Phys Rev B45:6341
382. Douglass DC, Cox AJ, Bucher JP, Bloomfield LA (1993) Phys Rev B47:12874
383. Knickelbein MB (2005) Phys Rev B71:184442

384. Xu XS, Yin SY, Moro R, de Heer WA (2005) Phys Rev Lett 95:237209
385. Kohl C, Bertsch GF (1999) Phys Rev B60:4205
386. Briere TM, Sluiter MHF, Kumar V, Kawazoe Y (2002) Phys Rev B66:064412
387. Kabir M, Mookerjee A, Kanhere DG (2006) Phys Rev B73:224439
388. Datta S, Kabir M, Ganguly S, Sanyal B, Saha-Dasgupta T, Mookerjee A (2007) Phys Rev B76:014429
389. Miyajima K, Nakajima A, Yabushita S, Knickelbein MB, Kaya K (2004) J Am Chem Soc 126:13202
390. Miyajima K, Yabushita S, Knickelbein MB, Nakajima A (2007) J Am Chem Soc 129:8473
391. Hosoya N, Takegami R, Suzumura J-i, Yada K, Miyajima K, Mitsui M, Knickelbein MB, Yabushita S, Nakajima A (2014) J Phys Chem A118:8298
392. Miyajima K, Knickelbein MB, Nakajima A (2008) J Phys Chem A112:366
393. Thole BT, Carra P, Sette F, Vanderlaan G (1992) Phys Rev Lett 68:1943
394. Chen CT, Idzerda YU, Lin HJ, Smith NV, Meigs G, Chaban E, Ho GH, Pellegrin E, Sette F (1995) Phys Rev Lett 75:152
395. Schütz G, Goering E, Hermann S (2007) In: Kronmüller H, Parkin S (eds) Handbook of magnetism and advanced magnetic materials. Wiley, Chichester, p 1311
396. Lau JT, Fohlisch A, Nietubyc R, Reif M, Wurth W (2002) Phys Rev Lett 89:057201
397. Peredkov S, Neeb M, Eberhardt W, Meyer J, Tombers M, Kampschulte H, Niedner-Schatteburg G (2011) Phys Rev Lett 107:233401
398. Niemeyer M, Hirsch K, Zamudio-Bayer V, Langenberg A, Vogel M, Kossick M, Ebrecht C, Egashira K, Terasaki A, Moeller T, Issendorff BV, Lau JT (2012) Phys Rev Lett 108:057201
399. Langenberg A, Hirsch K, Lawicki A, Zamudio-Bayer V, Niemeyer M, Chmiela P, Langbehn B, Terasaki A, Issendorff BV, Lau JT (2014) Phys Rev B90:184420
400. Kravtsova AN, Lomachenko KA, Soldatov AV, Meyer J, Niedner-Schatteburg G, Peredkov S, Eberhardt W, Neeb M (2014) J Electron Spectrosc Relat Phenomena 195:189
401. Dieleman D, Tombers M, Peters L, Meyer J, Peredkov S, Jalink J, Neeb M, Eberhardt W, Rasing T, Niedner-Schatteburg G, Kirilyuk A (2015) Phys Chem Chem Phys 17:28372
402. Zamudio-Bayer V, Hirsch K, Langenberg A, Niemeyer M, Vogel M, Lawicki A, Terasaki A, Lau JT, von Issendorff B (2015) Angew Chem Int Ed 54:4498
403. Zamudio-Bayer V, Hirsch K, Langenberg A, Lawicki A, Terasaki A, V Issendorff B, Lau JT (2015) J Chem Phys 143:244318
404. Meyer J, Tombers M, van Wuellen C, Niedner-Schatteburg G, Peredkov S, Eberhardt W, Neeb M, Palutke S, Martins M, Wurth W (2015) J Chem Phys 143:104302
405. Gatteschi D, Sessoli R, Villain J (2006) Molecular nanomagnets. Oxford University Press, Oxford
406. Artus P, Boskovic C, Yoo J, Streib WE, Brunel LC, Hendrickson DN, Christou G (2001) Inorg Chem 40:4199
407. Yoo J, Yamaguchi A, Nakano M, Krzystek J, Streib WE, Brunel LC, Ishimoto H, Christou G, Hendrickson DN (2001) Inorg Chem 40:4604
408. Brechin EK, Boskovic C, Wernsdorfer W, Yoo J, Yamaguchi A, Sanudo EC, Concolino TR, Rheingold AL, Ishimoto H, Hendrickson DN, Christou G (2002) J Am Chem Soc 124:9710
409. Wernsdorfer W, Aliaga-Alcalde N, Hendrickson DN, Christou G (2002) Nature 416:406
410. Mishra A, Wernsdorfer W, Abboud KA, Christou G (2004) J Am Chem Soc 126:15648
411. Osa S, Kido T, Matsumoto N, Re N, Pochaba A, Mrozinski J (2004) J Am Chem Soc 126:420
412. Soler M, Wernsdorfer W, Folting K, Pink M, Christou G (2004) J Am Chem Soc 126:2156
413. Bircher R, Chaboussant G, Dobe C, Gudel HU, Ochsenbein ST, Sieber A, Waldmann O (2006) Adv Funct Mater 16:209
414. Chakov NE, Lee S-C, Harter AG, Kuhns PL, Reyes AP, Hill SO, Dalal NS, Wernsdorfer W, Abboud KA, Christou G (2006) J Am Chem Soc 128:6975
415. Ferbinteanu M, Kajiwara T, Choi K-Y, Nojiri H, Nakamoto A, Kojima N, Cimpoesu F, Fujimura Y, Takaishi S, Yamashita M (2006) J Am Chem Soc 128:9008
416. Lu ZL, Yuan M, Pan F, Gao S, Zhang DQ, Zhu DB (2006) Inorg Chem 45:3538

417. Miyasaka H, Nakata K, Lecren L, Coulon C, Nakazawa Y, Fujisaki T, Sugiura K, Yamashita M, Clerac R (2006) J Am Chem Soc 128:3770
418. Mori F, Nyui T, Ishida T, Nogami T, Choi KY, Nojiri H (2006) J Am Chem Soc 128:1440
419. Yang EC, Wernsdorfer W, Zakharov LN, Karaki Y, Yamaguchi A, Isidro RM, Lu GD, Wilson SA, Rheingold AL, Ishimoto H, Hendrickson DN (2006) Inorg Chem 45:529
420. Lecren L, Wernsdorfer W, Li Y-G, Vindigni A, Miyasaka H, Clerac R (2007) J Am Chem Soc 129:5045
421. Milios CJ, Inglis R, Vinslava A, Bagai R, Wernsdorfer W, Parsons S, Perlepes SP, Christou G, Brechin EK (2007) J Am Chem Soc 129:12505
422. Stamatatos TC, Foguet-Albiol D, Lee S-C, Stoumpos CC, Raptopoulou CP, Terzis A, Wernsdorfer W, Hill SO, Perlepes SP, Christou G (2007) J Am Chem Soc 129:9484
423. Takamatsu S, Ishikawa T, Koshihara S-y, Ishikawa N (2007) Inorg Chem 46:7250
424. AlDamen MA, Clemente-Juan JM, Coronado E, Marti-Gastaldo C, Gaita-Arino A (2008) J Am Chem Soc 130:8874
425. Chibotaru LF, Ungur L, Soncini A (2008) Angew Chem Int Ed 47:4126
426. Mereacre V, Ako AM, Clerac R, Wernsdorfer W, Hewitt IJ, Anson CE, Powell AK (2008) Chem Eur J 14:3577
427. Milios CJ, Piligkos S, Brechin EK (2008) Dalton Trans 1809
428. Ritchie C, Ferguson A, Nojiri H, Miras HN, Song Y-F, Long D-L, Burkholder E, Murrie M, Koegerler P, Brechin EK, Cronin L (2008) Angew Chem Int Ed 47:5609
429. Roubeau O, Clerac R (2008) Eur J Inorg Chem 4325
430. Ako AM, Mereacre V, Clerac R, Wernsdorfer W, Hewitt IJ, Anson CE, Powell AK (2009) Chem Commun 544
431. AlDamen MA, Cardona-Serra S, Clemente-Juan JM, Coronado E, Gaita-Arino A, Marti-Gastaldo C, Luis F, Montero O (2009) Inorg Chem 48:3467
432. Stamatatos TC, Teat SJ, Wernsdorfer W, Christou G (2009) Angew Chem Int Ed 48:521
433. Mannini M, Pineider F, Danieli C, Totti F, Sorace L, Sainctavit P, Arrio MA, Otero E, Joly L, Cezar JC, Cornia A, Sessoli R (2010) Nature 468:417
434. Murrie M (2010) Chem Soc Rev 39:1986
435. Rinck J, Novitchi G, Van den Heuvel W, Ungur L, Lan Y, Wernsdorfer W, Anson CE, Chibotaru LF, Powell AK (2010) Angew Chem Int Ed 49:7583
436. Xu G-F, Wang Q-L, Gamez P, Ma Y, Clerac R, Tang J, Yan S-P, Cheng P, Liao D-Z (2010) Chem Commun 46:1506
437. Blagg RJ, Muryn CA, McInnes EJL, Tuna F, Winpenny REP (2011) Angew Chem Int Ed 50:6530
438. Habib F, Lin P-H, Long J, Korobkov I, Wernsdorfer W, Murugesu M (2011) J Am Chem Soc 133:8830
439. Long J, Habib F, Lin P-H, Korobkov I, Enright G, Ungur L, Wernsdorfer W, Chibotaru LF, Murugesu M (2011) J Am Chem Soc 133:5319
440. Mills DP, Moro F, McMaster J, van Slageren J, Lewis W, Blake AJ, Liddle ST (2011) Nat Chem 3:454
441. Anwar MU, Thompson LK, Dawe LN, Habib F, Murugesu M (2012) Chem Commun 48:4576
442. Baldovi JJ, Cardona-Serra S, Clemente-Juan JM, Coronado E, Gaita-Arino A, Palii A (2012) Inorg Chem 51:12565
443. Coutinho JT, Antunes MA, Pereira LCJ, Bolvin H, Marcalo J, Mazzanti M, Almeida M (2012) Dalton Trans 41:13568
444. Jeon I-R, Clerac R (2012) Dalton Trans 41:9569
445. Langley SK, Chilton NF, Ungur L, Moubaraki B, Chibotaru LF, Murray KS (2012) Inorg Chem 51:11873
446. Mondal KC, Sundt A, Lan Y, Kostakis GE, Waldmann O, Ungur L, Chibotaru LF, Anson CE, Powell AK (2012) Angew Chem Int Ed 51:7550
447. Novitchi G, Pilet G, Ungur L, Moshchalkov VV, Wernsdorfer W, Chibotaru LF, Luneau D, Powell AK (2012) Chem Sci 3:1169

448. Song Y-m, Luo F, Luo M-b, Liao Z-w, Sun G-m, Tian X-z, Zhu Y, Yuan Z-J, Liu S-j, Xu W-y, Feng X-f (2012) Chem Commun 48:1006
449. Tuna F, Smith CA, Bodensteiner M, Ungur L, Chibotaru LF, McInnes EJL, Winpenny REP, Collison D, Layfield RA (2012) Angew Chem Int Ed 51:6976
450. Wang Y-X, Shi W, Li H, Song Y, Fang L, Lan Y, Powell AK, Wernsdorfer W, Ungur L, Chibotaru LF, Shen M, Cheng P (2012) Chem Sci 3:3366
451. Chilton NF, Langley SK, Moubaraki B, Soncini A, Batten SR, Murray KS (2013) Chem Sci 4:1719
452. Habib F, Brunet G, Vieru V, Korobkov I, Chibotaru LF, Murugesu M (2013) J Am Chem Soc 135:13242
453. Le Roy JJ, Jeletic M, Gorelsky SI, Korobkov I, Ungur L, Chibotaru LF, Murugesu M (2013) J Am Chem Soc 135:3502
454. Suzuki K, Sato R, Mizuno N (2013) Chem Sci 4:596
455. Zhu Y-Y, Cui C, Zhang Y-Q, Jia J-H, Guo X, Gao C, Qian K, Jiang S-D, Wang B-W, Wang Z-M, Gao S (2013) Chem Sci 4:1802
456. Pedersen KS, Bendix J, Clerac R (2014) Chem Commun 50:4396
457. Zhang P, Zhang L, Wang C, Xue S, Lin S-Y, Tang J (2014) J Am Chem Soc 136:4484
458. Gatteschi D, Sessoli R (2003) Angew Chem Int Ed 42:268
459. Beltran LMC, Long JR (2005) Acc Chem Res 38:325
460. Aromi G, Brechin EK (2006) In: Winpenny R (ed) Single-molecule magnets and related phenomena. Springer, Berlin, p 1
461. Wang X-Y, Wang Z-M, Gao S (2008) Chem Commun 281
462. Bagai R, Christou G (2009) Chem Soc Rev 38:1011
463. Sessoli R, Powell AK (2009) Coord Chem Rev 253:2328
464. Tombers M, Meyer J, Meyer J, Lawicki A, Zamudio-Bayer V, Hirsch K, Lau T, von Issendorff B, Terasaki A, Schlathölter T, Hoekstra R, Schmidt S, Powell AK, Kessler E, Prosenc M, van Wüllen C, Niedner-Schatteburg G (2016) (manuscript in preparation)
465. Tombers M, Meyer J, Hewer J, Meyer J, Lawicki A, Zamudio-Bayer V, Lau T, Niedner-Schatteburg G (2016) draft manuscript
466. Reinhard BM, Lagutschenkov A, Lemaire J, Maitre P, Boissel P, Niedner-Schatteburg G (2004) J Phys Chem A108:3350
467. Ricks AM, Brathwaite AD, Duncan MA (2013) J Phys Chem A117:1001
468. Nosenko Y, Menges F, Riehn C, Niedner-Schatteburg G (2013) Phys Chem Chem Phys 15:8171
469. Lang J, Gaffga M, Menges F, Niedner-Schatteburg G (2014) Phys Chem Chem Phys 16:17417
470. Nosenko Y, Riehn C, Niedner-Schatteburg G (2016) Phys Chem Chem Phys
471. Gaffga M, Munstein I, Mueller P, Lang J, Thiel WR, Niedner-Schatteburg G (2015) J Phys Chem A119:12587
472. Lang J, Cayir M, Walg SP, Di Martino-Fumo P, Thiel WR, Niedner-Schatteburg G (2016) Chem Eur J 22:2345
473. Dagotto E, Hotta T, Moreo A (2001) Phys Rep 344:1
474. Templeton AC, Wuelfing MP, Murray RW (2000) Acc Chem Res 33:27
475. Jensen P (1999) Rev Mod Phys 71:1695
476. Gates BC (1995) Chem Rev 95:511
477. Swiegers GF, Malefetse TJ (2000) Chem Rev 100:3483
478. Wang XL, Qin C, Wang EB, Su ZM (2006) Chem Eur J 12:2680
479. Barcikowski S, Mafune F (2011) J Phys Chem C115:4985
480. Muto H, Yamada K, Miyajima K, Mafune F (2007) J Phys Chem C111:17221
481. Schlarb AK, Suwitaningsih DN, Kopnarski M, Niedner-Schatteburg G (2014) J Appl Polym Sci 131:39655

Struct Bond (2017) 174: 41–62
DOI: 10.1007/430_2016_1

Published online: 9 July 2016

Quantum Chemical Investigations of Clusters of Heavy Metal Atoms

Florian Weigend

Abstract This contribution reports quantum chemical treatments of clusters of heavy metal atoms with contemporary methods and focuses on two aspects: the impact of spin–orbit coupling on electronic and geometric structure as well as the problem of finding global minimum structures in case of binary or ternary systems. At present, the only suited quantum chemical tools for metal clusters are methods of density functional theory. For the first aspect, the impact of spin–orbit coupling, so-called two-component methods are required; for the second aspect, it is advisable to extend usual global optimization procedures like genetic algorithms by tools for the aimed search of most favorable atom-type-to-atom-position assignments. Respective recent developments for these two purposes are discussed, and applications to midsized clusters of gold and heavy p-elements, mixtures of heavy p-elements, and mixtures of heavy p-elements encapsulating transition metal atoms are presented.

Keywords Binary clusters • Density functional theory • Genetic algorithms • Heavy elements • Perturbation theory • Relativistic effects

Contents

F. Weigend (✉)
Karlsruher Institut für Technologie, Institut für Physikalische Chemie, Abteilung für Theoretische Chemie, Karlsruher Institut für Technologie, Fritz-Haber-Weg 2, 76131 Karlsruhe, Germany

Institut für Nanotechnologie, Karlsruher Institut fürTechnologie, Hermann-von-Helmholtz-Platz 1, 76344 Eggenstein-Leopoldshafen, Germany
e-mail: florian.weigend@kit.edu

1 Introduction

Metal clusters are of interest for physical and chemical experimental and theoretical basic research, as they are intermediates between single atoms and the bulk phase. They are not stable under ambient conditions, not any metal cluster can be kept in a test tube. Nevertheless, for low particle densities and at moderate temperature clusters of (nearly) any size are known to exist for (nearly) any metal, which indicates that they are stable with respect to atom loss or fission. Vice versa, the most stable form is the bulk phase. Apart from low densities other strategies to prevent clusters to react to the bulk phase are the protection with an organic ligand shell or – for polyionic cluster species like Zintl anions – the crystallization together with suited counterions like complexed alkaline metal ions.

Within the last decades several review articles about the theory of (metal) clusters in general [1, 2], about quantum chemical calculations [3], and in particular about density functional theory (DFT) treatments [4, 5] were published. The present review focuses on two aspects: heavy elements, which require consideration of relativistic effects including spin–orbit coupling, as well as binary and ternary systems, which implicate the problem of assigning elements to atom positions.

The latter systems are of special interest, as here a second parameter apart from size comes into play: the composition, which allows for tunable properties. This is a challenge for experiment, as similar elements cannot be distinguished by common tools of experimental analysis, as well as for theory, as the number of possibilities to distribute element types on atomic positions is huge: 2^N for a binary system with N atoms. For arbitrary element combinations, it is a common strategy to select promising distributions by economic Lennard–Jones methods and recalculate them at DFT level [6]. For elements with similar nuclear charges Z, the aimed search directly at DFT level is possible by first calculating the energy and wave function of a homo-atomic system and subsequently the energy change $\partial E/\partial Z$ for each atomic position [7]. This technique may be used as complement to X-ray structure analysis

[8], like in Sect. 4.4, and also to find the global energy minimum structures for binary and ternary systems [9] like in Sects. 3.3 and 4.3.

Finding global minimum structures is a hard task already for homo-atomic systems. For systems with very few atoms, one might be able to guess most of the promising structures, but for more than ca. 8 atoms, this is not a reliable procedure. Several techniques have been applied for this purpose, for instance, simulated annealing [10], basin hopping [11], and genetic algorithms (GA, [12–14]). All these techniques require a large number of energy calculations, and thus, if these calculations are done at level of DFT or even higher, their application is limited to systems with several ten atoms.

Concerning methods for electronic structure calculations of metal clusters, presently DFT is the technique of choice. Metal clusters usually have a small energy gap between highest occupied (HO) and lowest unoccupied (LU) molecular orbital (MO). This leads to multi-reference character for the electronic wave function; single-reference methods like Hartree–Fock thus are unsuited in most cases, also when followed by post-Hartree–Fock treatments for the dynamic electron correlation. DFT, which bases on the electron density instead of the wave function, accounts for this feature at least in a nonsystematic manner. Wave-function-based multi-reference methods would be a desirable alternative but are by far too expensive.

For heavy elements, which are the focus of this contribution, relativistic effects [15] must be considered; for some cases also spin–orbit coupling plays an important role, for instance, for the rationalization of a double peak in the UV–Vis spectrum of a highly symmetric gold cluster (Sect. 4.1) and for the energetic sequence of isomers of bismuth clusters (Sect. 4.2). Main aspects concerning relativity are summarized in Sect. 2.2. Technical aspects like choice of suited density functionals, basis sets, and ways to account for relativity are discussed in Sect. 2.3.

2 Electronic Structure

Quantum chemical calculations yield molecular orbitals (MOs), which are necessarily delocalized, at least in case of symmetric molecules, as any symmetry operation maps a (nondegenerate) orbital on itself or on its negative. Inspection of MOs is helpful for characterizing the electronic structure and also for estimating the stability of the cluster as a whole. The latter often is explained by the number of valence electrons, in particular by the so-called “magic” electron numbers (2, 8, 20, 40, 70…) of valence electrons, which result from cluster orbitals for a very simple model. In Sect. 2.1 the origin of these numbers is briefly reviewed, and their limitations are discussed. Origin of relativistic effects and the consequences for the treatment of heavy-element clusters are briefly summarized in Sect. 2.2. Technical aspects like suited density functionals, basis sets, and ways to account for relativity are discussed in Sect. 2.3.

2.1 Cluster Orbitals and Magic Electron Numbers

Magic electron numbers correspond to electronic shell closings in the spherical jellium or superatom model [2]. In this model, clusters are assumed to be spheres, and the positive charges of atomic cores (nuclei plus inner electrons) are replaced by a uniformly positive charged background. For a single electron or for noninteracting (valence) electrons, the potential is that of a spherical harmonic oscillator. The Schrödinger equation can be solved analytically yielding spherical harmonic (S, P, D,...) eigenfunctions with the following energetic sequence of shells: (1S),(1P),(1D2S),(1F2P),.... Each shell is separated from the next one by the same energy difference. Adding the respective occupations (2, 6, 10 + 2, 14 + 6,...) yields the "magic" electron numbers 2, 8, 20, 40,... as electronic shell closings for noninteracting electrons in a uniformly charged sphere. Consequently, in such cases the HOMO–LUMO gap is particularly large, which indicates high stability of the respective system. Electron–electron interaction leads to splitting of levels with different angular quantum numbers and thus to additional gaps after subshell closings at 18, 34,... electrons. This model very well agrees with calculated electronic structures for alkaline (earth) metal clusters, for which (a) icosahedral structures are preferred and (b) valence electrons come from the atomic valence s-orbitals (s-AOs) only, which are furthermore well separated from the inner orbitals. The situation for main-group element systems is different in both respects. This has consequences on the electronic structure. For nonspherical systems angular momentum degeneracy is lifted; thus, for instance, the D shells split to $T_{2g} + E_g$ in case of O_h symmetry or to $A_1' + E' + E''$ for D_{3h} symmetry. The size of the splitting depends on the degree of distortion (or vice versa). Further, the valence shell consists of s- and p-AOs. This has significant consequences, as might become evident by the inspection of the MOs of Pb_9^{4-} [16] and Pb_5^{2-} [17] (see Fig. 1). For methods of calculation, see Sect. 2.3. Pb_9^{4-} has $9 \cdot (2+2) + 4 = 40$ valence electrons, which is a magic electron number. Consequently, the shells 1S1P1D2S1F2P are fully occupied, and the HOMO–LUMO gap is quite large, ca. 2 eV. Contrary to the jellium model, a very large gap of ca. 5 eV is observed between the 1D and the 2S shell, which separates MOs that dominantly consist of s-AOs from those consisting of p-AOs. This is not surprising, as the s-AOs are lower in energy than the respective p-AOs by ca. 8 eV. Differences to the jellium model become even more evident for Pb_5^{2-} with 22 valence electrons or 11 occupied cluster MOs, respectively. Again, a large gap between s-AO and p-AO-dominated cluster MOs is evident between the fifth and the sixth cluster MO. The fifth MO is the $1D_z^2$, consisting of the s-AOs of the two apical atoms and of the three equatorial atoms with opposite phase. For the other members of the D shell, the p-AOs are required; consequently these MOs are higher in energy by ca. 5 eV. Of similar energy are the 2S MO and the $1F_z^3$ MO, which is occupied by the remaining two electrons. It is separated from the other (unoccupied) 1 F MOs by ca. 2 eV. The enhanced stability of the $1F_z^3$ MO is expected, as it is the binding combination of all p_z AOs, whereas the other members of the F shell are (partially)

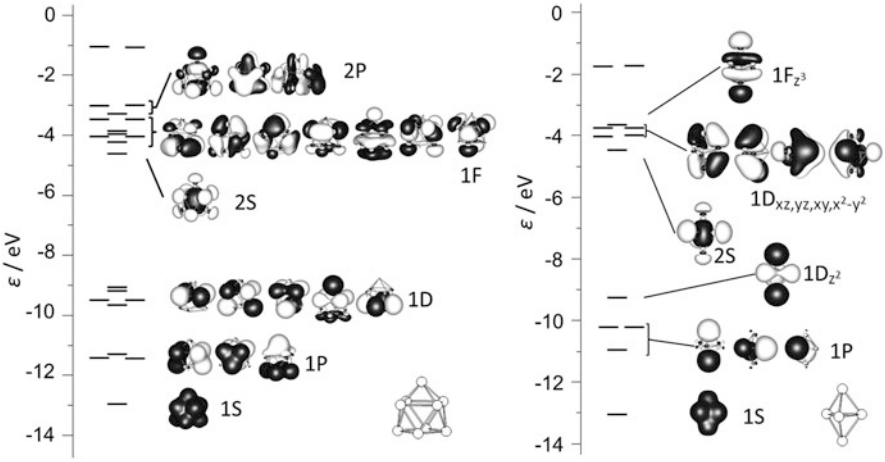

Fig. 1 Cluster orbitals and respective energies of Pb_9^{4-} (*left*) and Pb_5^{2-} (*right*)

antibonding. So, the HOMO–LUMO gap is large, and the stability is comparably high but not due to a shell closing but to a shell splitting because of suited AOs for one of the MOs.

2.2 Heavy Elements: Relativistic Effects

For heavy elements relativistic effects play an important role. The meaning of "heavy" depends on the properties that one is interested in and on the desired/required accuracy. For the present purpose, structure, and bonding of clusters, relativistic effects should be considered for the elements beyond Kr. Incorporation of relativity in quantum chemical methods is an intensively studied field; further several excellent review articles are available describing the impact or relativity on chemistry, e.g., by Pyykkö [15, 18]. A very brief summary, as far as relevant for the present purpose, is given now.

Starting point of the relativistic treatment of electrons is the Dirac equation. It fulfills the postulates of both quantum mechanics and special relativity. It is a four-component equation; consequently the eigenfunctions are no longer scalar orbitals $\Psi(\mathbf{r},t)$, like in Schrödinger's theory, but so-called four-component spinors $(\Psi_1(\mathbf{r},t),\Psi_2(\mathbf{r},t),\Psi_3(\mathbf{r},t),\Psi_4(\mathbf{r},t))$. The spectrum of eigenvalues contains a positive (>0) and a negative ($<-2c^2$) region; the latter are positronic states, which are not of interest for chemistry. It is possible to project out these positronic states by decoupling this four-component equation; one ends in leading order ($1/c^2$) at the two-component electronic problem

$$\left[\left(\hat{t}+\hat{v}^{\mathrm{Ne}}+\hat{h}^{\mathrm{SR}}\right)\mathbf{1}+\vec{\boldsymbol{\sigma}}\hat{\vec{h}}^{\mathrm{SO}}\right]\Psi_n(\vec{r})=E_n\Psi_n(\vec{r}). \tag{1}$$

1 is a 2×2 unity matrix, $\hat{t}$ and $\hat{v}^{\mathrm{Ne}}$ are the kinetic and the potential energy operators, just like in the nonrelativistic case, $\hat{h}^{\mathrm{SR}}$ contains scalar relativistic corrections, namely, the mass velocity term and the Darwin term, and $\vec{\boldsymbol{\sigma}}\hat{\vec{h}}^{\mathrm{SO}}$ is the spin–orbit coupling (SOC), where the spin operator is given by the vector $\vec{\boldsymbol{\sigma}}=(\boldsymbol{\sigma}_x,\boldsymbol{\sigma}_y,\boldsymbol{\sigma}_z)$ of the complex 2×2 Pauli matrices:

$$\boldsymbol{\sigma}_x=\begin{pmatrix}0&1\\1&0\end{pmatrix},\quad \boldsymbol{\sigma}_y=\begin{pmatrix}0&-i\\i&0\end{pmatrix},\quad \boldsymbol{\sigma}_z=\begin{pmatrix}1&0\\0&-1\end{pmatrix}. \tag{2}$$

For this, the solutions of the equation, the one-electron wave functions Ψ_n, are also two-component complex objects, so-called spinors. In the treatment of clusters in the past, usually only scalar relativistic effects (third term) were included, whereas SOC (fourth term) was neglected, possibly for good reasons: its influence was expected to be small, and its consideration would require a two-component structure in the program code, which also comes along with greater computational effort (see below). Nevertheless, SOC leads to splitting of atomic orbital (or spinor) shells with angular quantum number l into $l+1/2$ and $l-1/2$. This splitting amounts to ca. 3 eV for the 6p AOs, which can be expected to influence the electronic structure and possibly also the geometric structure of molecules. Several examples are shown in Sects. 4.1–4.3.

2.3 *Technical Requirements for the Calculation of the Electronic Structure*

In quantum chemical treatments, one has to specify the method of calculation, the basis set, and, at least for heavy elements, the way how to treat relativistic effects. Concerning the method, the obvious choice for clusters of metal atoms are methods of density functional theory, as they are relatively stable across the periodic table compared to (single-determinant) Hartree–Fock (plus post-Hartree–Fock methods for dynamic electron correlation). Multi-reference methods usually are not feasible due to the system size. Among the DFT methods, gradient-corrected functionals like BP86 [19, 20] or PBE [21] turned out to work reasonably; meta-GGA functionals like TPSS [22] are sometimes slightly better but also more expensive. The reliability of hybrid functionals (mixtures of pure DFT and Hartree–Fock exchange) decreases with increasing metallic character of the systems. While their usage may be reasonable for main-group element clusters, at least as long as they are not too large and thus not too "metallic," it is not for transition metals, where the admixture of Hartree–Fock exchange usually makes results worse.

Similar holds for the methods that base on Hartree–Fock: for small main-group clusters, coupled cluster methods including single and double excitations and a perturbative correction for triple excitations, CCSD(T), may be used as reference; for other clusters it is less reasonable. A good agreement for dissociation energies obtained with CCSD(T) and DFT(TPSS) within ca. 0.2 eV found, which was documented for instance for small clusters of gallium [23].

For the inclusion of relativistic effects, the most pragmatic choice is the employment of effective core potentials [24]. The inner shells are modeled by an effective potential, which covers also relativistic effects when fitted for instance to the result of fully relativistic four-component Dirac–Fock calculations. The energies of the explicitly treated valence shells then show excellent agreement to fully relativistic calculations. Proven ECPs for the 4d/5p or 5d/6p elements are those by Dolg et al. [25, 26], which cover the inner 28 or 60 electrons, respectively; they are available in two variants, either covering only scalar relativistic effects or also including SOC. Scalar relativistic contributions are only an additional term in the one-electron part, whose evaluation does not change the program structure. Like in nonrelativistic treatments, the algorithm calculates the $n \times n$ matrix of the expansion coefficients for the n MOs, each of them being a linear combination of n AOs. In case of open-shell calculations, one has $2n$ MOs (n of alpha-spin and n of beta-spin); thus, two $n \times n$ matrices have to be determined: one for the alpha-spin MOs and one for the beta-spin MOs. When including SOC, MOs no longer are of pure alpha or beta-spin character but are mixtures, so one has to deal with $2n$ MOs, each of them being a linear combination of $2n$ AOs. The matrix of expansion coefficients is of dimension $(2n) \times (2n)$ and complex, as the Hamiltonian (see above) is also complex, which leads to much higher costs than for one-component treatments. Efficient two-component algorithms for the ground state [27] and excited state [28] used in the applications given below have been developed within the last years. An alternative to ECPs are quasi-relativistic all-electron calculations, like the exact two-component decoupling (X2C) method, by which also the electronic core levels are accessible. These methods require the setup of the one-electron four-component Dirac–Fock matrix, which is then decoupled to the two-component (or one-component) form. This step itself is much more consuming than the evaluation of ECP contributions, and same is true for the subsequent self-consistent field (SCF) procedure, as also all inner orbitals are involved now. Further, two-electron relativistic effects are neglected in the X2C approach. Results for clusters are similar to those obtained with ECPs, as demonstrated for Ag clusters [29].

Recommendable basis sets for DFT are sets of polarized triple-zeta valence quality, TZVP, for which the errors of the basis are much smaller than that of the method itself. This usually is also true for the smaller double-zeta ("split valence") valence bases, SV(P), which in particular for pre-optimization of structure parameters are very well suited. Usage of larger quadruple-zeta valence bases at DFT level usually is not necessary, at least for the calculations discussed here. For elements beyond Kr, segmented contracted basis sets optimized for the use in combination with one- and two-component Dirac–Fock ECPs are available within

the Karlsruhe system of error-balanced basis sets (prefix "dhf" [30]), which for two-component treatments have increased flexibility (suffix "2c") for non-valence shells in order to describe the two different levels $l+1/2$ and $l-1/2$ [31].

Many of the clusters in Sect. 4 are highly charged ions, which crystallize together with suited counterions. In calculations the counterions usually are not regarded explicitly but are modeled. For this purpose the conductor-like screening model, COSMO [32], turned out to be a valuable tool, where the cluster forms a cavity within a dielectric continuum of permittivity ε, which for modeling counterions is set to infinity. The DFT equations are then solved for the boundary condition that the electrostatic potential vanishes at the cavity surface. The counterions are represented by the resulting screening charges.

Finally, for atomic arrangements far from the equilibrium, e.g., such generated by a genetic algorithm, convergence of SCF procedures is sometimes problematic. Here the employment of fractional occupation numbers [33] is helpful. Orbital occupations n_i are calculated according to

$$n_i = \frac{1}{2}\operatorname{erfc}\frac{\varepsilon_i - \varepsilon_F}{4kT/\sqrt{\pi}}, \tag{3}$$

where i labels orbitals, ε_i their energy, and ε_F the Fermi energy. With an initial (pseudo-) temperature $T = 500$ K, which is gradually reduced during the SCF procedure, one usually achieves convergence to integer occupation numbers, that is, a state-specific solution of the Kohn–Sham equations.

3 Geometric Structure

The geometric structure is the foremost property of a cluster. If it is unknown, like for the applications presented in Sect. 4.3, it has to be determined first. For this purpose, genetic algorithms are a very powerful tool, which is briefly reviewed in Sect. 3.1. For mixed metallic systems, a further difficulty arises: the different elements have to be assigned to atomic positions in the energetically most favorable way. For an N-atomic binary cluster, this means 2^N possibilities, which of course are reduced if the composition is known and/or the cluster exhibits symmetry. Nevertheless, usually a huge number of possible arrangements remain in particular for 1:1 mixtures. For mixtures of elements with similar nuclear charge, a comparably simple first-order approach can be applied, which is presented in Sect. 3.2. This may be used for the aimed search of the best distribution of elements to places when the geometric structure is known but not the element distribution, which is a frequently occurring situation for experimentalists, but also in combination with genetic algorithms, as illustrated in Sect. 3.2

3.1 Exploring the Energy Surface: Genetic Algorithms

Quantum chemical calculations usually are carried out for fixed nuclei. The parametric dependence of the energy on the positions of nuclei is termed energy surface, experimentally observed isomers that correspond to local minima on this surface, the most stable one to the global minimum. Several techniques to efficiently find these minima and in particular the global minimum have been proposed and tested for this purpose, for example, simulated annealing [10], basin hopping [11], and genetic algorithms (GAs, [12–14]). These techniques can be used basing on empirical potentials or on DFT. The latter has the advantage of not involving system-specific parameters and thus allowing for an unbiased search, but requires by far higher computational costs. Genetic algorithms as well as the other abovementioned techniques require a large number of single-point calculations or geometry optimizations, which limit their application to relatively small clusters with several ten atoms at most.

The basic idea of a GA is briefly outlined. One starts with P randomly generated structures, whose structure parameters are optimized, in case of metal clusters usually with methods of DFT (generation 0). In the next step, isomers are cut into parts; the resulting fragments are merged to give p new structures ("child structures"), fragments of clusters with low energy which are preferred in this step. These new structures are also optimized. From the resulting $P+p$ structures, the P lowest-energy isomers with distinct geometric structures are kept (generation 1). Again, isomers are cut and merged forming the next generation. For clusters of ca. 10 atoms, a population size of $P = 20$ structures and the creation of $p = 10$ new structures per generation turned out to be reasonable. Typically several ten to hundred generations are sufficient to locate the global minimum for such species.

3.2 Binary Systems: Atom-Type Assignment via Perturbation Theory

For a system A_nB_{N-n}, for which the distribution of atom types A and B to the N positions is unclear, preference of sites preferred by either A or B can be estimated by first-order perturbation theory, if the difference in nuclear charges of A and B is not too large. This procedure requires only the calculation of the electrostatic potential at the N nuclear positions, $V_i = V(\mathbf{R}_i)$, without the contribution of the nucleus located at $\mathbf{R}_i$. This also holds for a system of type $A_nB_{N-n}C_m$, C_m being, e.g., a ligand or a third atom type, for which the assignment to the positions is clear; also C = A or C = B is not excluded. Details are given in [7]. For the simplest case it is done as follows. At first, an SCF calculation of the "homogenized" system is done, then the electrostatic potential for all sites is calculated, and finally, if $Z_A > Z_B$, type A is assigned to the n sites with the lowest electrostatic potential and B to the remaining sites. The best choice for the nuclear charge of the (pseudo-)

atoms in the homogenized system M turned out [8] to be the weighted average of the nuclear charges of A and B,

$$Z_{\mathrm{M}} = \frac{n}{N} Z_{\mathrm{A}} + \frac{N-n}{N} Z_{\mathrm{B}}. \tag{4}$$

In this case the number of electrons in the homogenized and the mixed atomic system are the same, and thus the reference wave function (that of the homogenized system) and that of the mixed atomic system have the greatest possible similarity.

A weakness of this first-order approximation becomes evident for highly symmetric systems. If one considers, e.g., a square of composition A_2B_2, the electrostatic potential resulting from the calculation of the homogenized system M_4 will be the same for all positions. Here obviously the simple approach fails, as the effect, that introducing the first A (or B) atom will change the potential for the other sites, is not included. This problem can be solved by successively replacing atoms and repeatedly calculating the wave function and the electrostatic potential. In detail, for determining the preferred sites for A and B in A_nB_{N-n}, $Z_{\mathrm{A}} > Z_{\mathrm{B}}$, the first calculation is done for M_N, with Z_{M} given in Eq. (4). The first atom of type A is assigned to the position with the lowest potential. The subsequent calculations $k = 1,2,\ldots n$ are done for $M_{N-k}A_k$ with the average nuclear charge being changed accordingly. In each step one A atom is assigned to the site with the lowest potential. In this way, higher orders of perturbation are included. Of course, this needs n calculations instead of a single one, but this is still much less than the explicit calculation of all distributions. As usual for perturbative treatments, reliability decreases for increasing size of the perturbation, here the difference in the nuclear charges of A and B. The method thus is restricted to atoms with similar atomic number. In particular, mixing of elements from different periods is not possible.

3.3 *Combining Genetic Algorithms with Atom-Type Assignment by Perturbation Theory*

For the search of minimum structures of binary clusters, GAs can be extended by the reassignment (R) of atoms to positions by perturbation theory (P), GA-RP [9]. For this purpose, the optimization of structure parameters is extended by the above procedure that reassigns the atoms to the sites one or more times during the structure optimization. For balancing costs and benefit, the number of reassignment steps is kept small. It turned out that it is best to start with a rough pre-optimization of structure parameters consisting of ca. 10 cycles, then insert the RP step, and to continue the optimization of structure parameters for the assignment found in the RP step.

For the performance of GA-RP compared to usual GA, the tri-metallic Zintl ion $[LaPb_7Bi_7]^{4-}$ may serve as an illustrating example, which was first predicted [9]

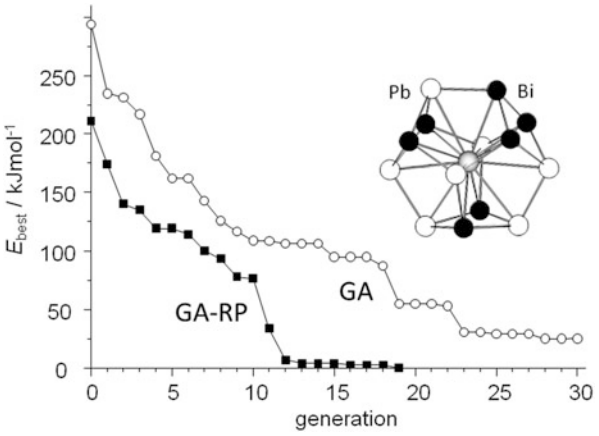

Fig. 2 Performance of a conventional genetic algorithm (GA) and the extended genetic algorithm (GA-RP) for the search of the global minimum of $(La@Pb_7Bi_7)^{4-}$. The graph shows the energy of the best isomer within the respective generation relative to the global minimum; results are averaged over five independent runs for each variant

and later on observed [34]. The choice of this system was motivated by the previously found homologue system $[LaSn_7Bi_7]^{4-}$, for which in a combined experimental and computational study, the structure (via X-ray diffraction) and the atom-type assignment (via explicit calculation of isomers) were determined [35]. The GA was carried out both in its usual form and with atom-type reassignment. In both cases the population size was $P = 20$, the number of child structures $p = 10$, and the number of generations $G = 30$. The COSMO model was applied to simulate the counterions. For statistical purposes, both types of runs were carried out five times.

For both procedures the energy of the best isomer of each generation is shown in Fig. 2, displayed is the average over the respective five runs. With the GA + RP technique, the best structure found is identical to $[LaSn_7Bi_7]^{4-}$. This isomer was found in all five runs, latest in generation 19, earliest in generation 11. Also with the pure GA, the correct topology was found in all five runs, typically after ca. 20 generations, but never the best occupation. The best isomers after 30 generations are disfavored by ca. 30 kJ/mol with respect to the GA + RP minimum. Thus, both concerning the energy of best structure and the number of trials to find this structure, the additional RP step significantly improves the efficiency of the pure GA for these mixed metallic systems.

4 Selected Applications

As noted in the beginning, we restrict ourselves to treatments where either the SOC turned out to be important and/or to treatments of binary or ternary clusters. In the next two subsections, it is shown that SOC leads to splitting of cluster MOs which has consequences for the UV–Vis spectrum and even for the geometric structure in case of interplaying with Jahn–Teller distortion. Section 4.3 compares the structures of Pb and Bi cluster mono-cations, which were obtained by combining DFT-based GA results and experimental cross-sectional data. Further, for the

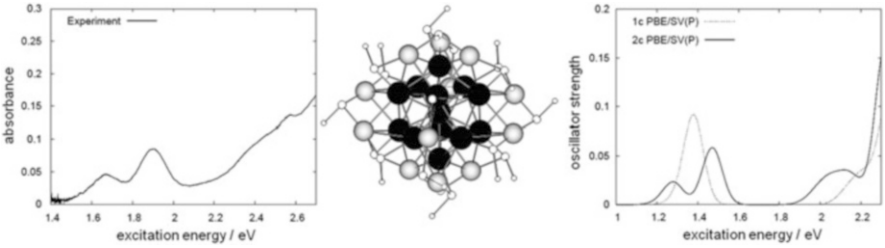

Fig. 3 *Middle*: Molecular structure of $Au_{25}(SMe)_{18}^-$. The 13-gold atoms of the central icosahedron are drawn in *black*, the remaining 12 in *gray*; hydrogen atoms are omitted for clarity. *Left*: Measured UV–Vis spectrum. *Right*: Calculated UV–Vis spectrum at one-component level (1c PBE/SV(P)) and at two-component level (2c PBE/SV(P))

mixed system $(Pb_nBi_{N-n})^+$, the structure change from the pure Pb to the pure Bi cluster is studied with a DFT-based GA extended by the atom-type (re-) assignment via perturbation theory. In Sect. 4.4 ternary core–shell clusters of type $[MA_nB_{N-n}]^{q-}$ are considered, M being a transition metal or lanthanide, A and B being different main-group elements, and q being the charge. The focus is set on the influence of the type of the M atom on structure and bonding of the A_nB_{N-n} shell.

4.1 Cluster Orbitals Under Spin–Orbit Coupling: UV–Vis Spectrum of $Au_{25}(SR)_{18}^-$

A prototype example for superatom-type cluster orbitals is $Au_{25}(SR)_{18}^-$ [36], R=Me, Ph, CH_2CH_2Ph, etc., which is one of the most studied ligand-protected metal clusters. It consists of an icosahedral Au_{13} core plus 12 face-capping gold atoms. Each of the 18 SR units, R=Me in the simplest case, bridges two gold atoms (see Fig. 3). Scalar relativistic DFT calculations yielded a threefold (near) degenerate HOMO and a fivefold (near) degenerate LUMO, which were identified as 1P and 1D superatom orbitals [37]. Time-dependent (TD) DFT calculations of excitation energies consequently yielded a single peak [38], which was characterized as 1P-1D (HOMO–LUMO) transition. The optical absorption spectrum in contrast shows two maxima, at 1.67 and at 1.90 eV. It was suspected that SOC leads to energetic splitting of cluster orbitals and consequently to splitting of the peak.

This was proven recently by a two-component TDDFT calculation [39] of $Au_{25}(SMe)_{18}^-$. Figure 3 shows the experimental electronic excitation spectrum and the TDDFT-calculated one-component (scalar relativistic, without SOC) spectrum as well as the two-component (with SOC) spectrum obtained from calculation of the ~200 lowest excitations. Whereas the one-component calculation yields a single peak (like in [38]), the two-component calculation reproduces the observed double-peak structure even quantitatively with a splitting of 0.2 eV between the two peaks (experiment, 0.23 eV). This splitting is also reflected by the splitting of the

HOMO, which decomposes to a nondegenerate and two (near-) degenerate levels, which are higher in energy by 0.2 eV. The systematic underestimation of excitation energies by ca. 0.4 eV is well known for TDDFT. It is noted in passing that this is by far the largest system calculated at two-component TDDFT level so far.

4.2 *Jahn–Teller Distortion Versus Spin–Orbit Coupling: Au_{20}^-*

In the preceding section, it was illustrated that SOC leads to splitting of degenerate cluster orbitals. This may have consequences also for the geometric structure, if the frontier orbitals for an idealized highly symmetric structure are degenerate and partially filled, e.g., 1, 2, 4, or 5 electrons in a threefold-degenerate cluster orbital. Such a situation leads to a Jahn–Teller distortion lowering the symmetry and thus lifting degeneracy. We have just seen the threefold degeneracy may be lifted by SOC, or, more precisely, the degeneracy is a consequence of neglecting SOC; so, when including it, there might be no longer a reason for a Jahn–Teller distortion. Known cases are Tl_6^-, Re_6^+ and Re_6 [40], Tl_8^{6-} in $Cs_{18}Tl_8O_6$, [41], as well as Au_{20}^- [42], which is discussed in detail now.

Neutral Au_{20} is a perfectly tetrahedral cluster (T_d symmetry) of unusual high stability [43], both with respect to cohesive energy and with respect to electronic structure, with a HOMO–LUMO gap amounting to 1.9 eV (TPSS functional/dhf-TZVP-2c basis). At one-component level (i.e., without accounting for SOC), the HOMO is a twofold-degenerate e-representation, the LUMO a threefold-degenerate t_2 representation (see left part of Fig. 4, label "1c(T_d)"). Both removing and adding one electron yields a partially filled degenerate shell; thus, the symmetry of ionic species is lowered due to Jahn–Teller distortion. For the anion the lowest energy is obtained by distortion to D_{2d} symmetry and occupation of the b_2 representation (t_2 in T_d symmetry splits into b_2 and e in D_{2d}). All vibrational frequencies are real (see below); this structure is a minimum. The distortion may be characterized by the splitting of lengths of edges of the cluster: For the neutral system all edges have the same length (808.0 pm), and for the distorted anionic species, four longer (817.8 pm) and two shorter edges (803.8 pm) are obtained.

Two-component calculations (i.e., accounting for SOC) reveal a very different picture. The LUMO of the neutral species is nondegenerate; LUMO+1 is twofold degenerate (see left part of Fig. 4, label "2c(T_d)"). This is a result of SOC. In this case, adding one electron does no longer lead to a partially filled shell, and thus there is no reason for a Jahn–Teller distortion. So, at this higher level of theory, also the ionic systems are expected to be of T_d symmetry. Indeed, optimization of structure parameters at two-component level starting from the D_{2d} structure obtained without SOC ends in T_d symmetry. Numerical calculation of vibration frequencies from the gradients for this structure yields real frequencies throughout, ranging from ca. 30 to 170 cm^{-1}; the high-symmetric T_d structure thus is a

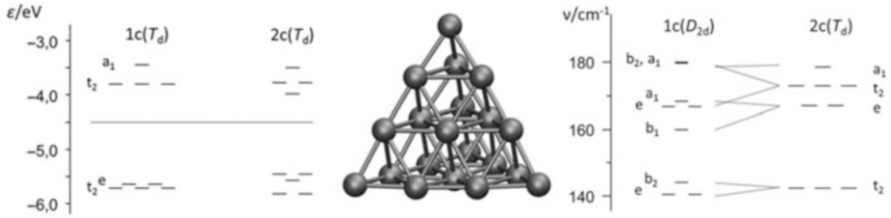

Fig. 4 *Middle*: Molecular structure of Au_{20}. *Left*: MO scheme of (neutral) T_d-symmetric Au_{20} calculated at one-component level (1c, neglecting SOC) and at two-component level (2c, including SOC). *Right*: Lowest vibrational frequencies of Au_{20}^- for the D_{2h}-symmetric structure obtained at 1c level and for the T_d-symmetric structure obtained at 2c level

minimum at two-component level. The influence of SOC is also reflected by differences in the vibrational spectrum of the T_d-symmetric species obtained at two-component level, 2c(T_d), and that of the D_{2d}-symmetric species obtained at one-component level, 1c(D_{2d}). The highest vibrational levels for both cases are shown in the right hand part of Fig. 4. For instance, the second-highest level in the 2c(T_d) case, a threefold-degenerate t_2 vibration (172.9 cm^{-1}), is split into a twofold-degenerate level (166.7 cm^{-1}) and a nondegenerate one (179.8 cm^{-1}) for 1c(D_{2d}). SOC thus lifts degeneracy of electronic levels and in this way causes degeneracy of vibronic levels

4.3 Cluster Cations of Pb and Bi and Mixtures

In the preceding chapters, the calculations were carried out for known structures or at least known topologies. This is not the case for the present chapter, which is dedicated to the determination of the structures of bare clusters in the gas phase. It is a typical feature of metal clusters that there are various isomers with an energetic separation of about 0.1 eV, which is in the same range as the errors of DFT. Also structure information from experimental studies alone is not fully conclusive. For a reliable determination of the ground-state structure of bare clusters, thus a combination of both calculations and experiments is a proven tool, which was applied several times in the past, e.g., for cluster ions of gold [44], boron [45], or tin [46]. Types of experiments carried out for the measurement of cluster properties were ion-mobility spectroscopy (IMS [47]) for cross sections, trapped ion electron diffraction (TIED [48]) for reduced molecular scattering intensities, and collision-induced dissociation (CID [47]) for relative intensities of different fragmentation channels. IMS measurements were done for up to 15 atoms; TIED is possible for systems of larger than ca. 10 atoms, as intensities are too low otherwise. Structure proposals from DFT-based GA treatments served as input for the computation of cross sections from IMS and reduced scattering intensities from TIED, which then were compared with experimental results. Here we focus on studies involving

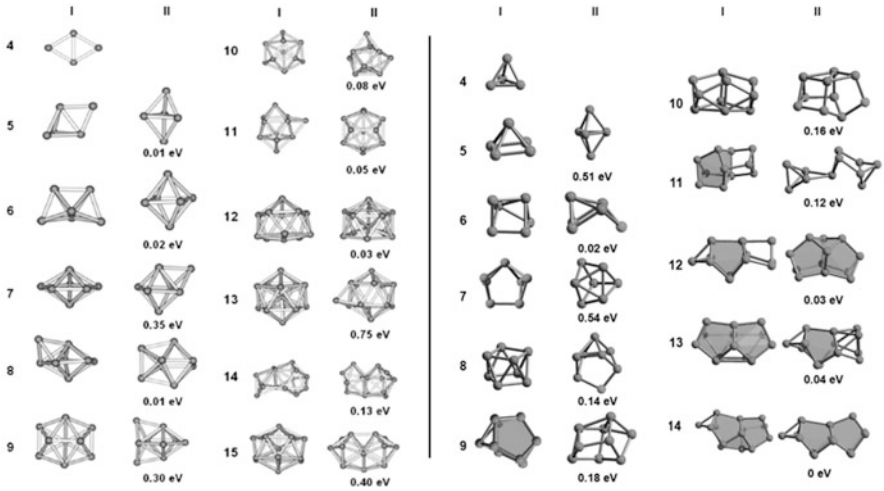

Fig. 5 Lowest (I) and second-lowest (II) energy structures of Pb_n^+ (*left*) and Bi_n^+ (*right*). Stabilities of II with respect to I are given in eV. The frequent eight-atom structure motif of Bi clusters is highlighted

heavy elements, namely, the systems Pb_N^+ ($N = 4$–15) and Bi_N^+, which were investigated in the manner just described. The structure motifs turned out to be quite different for these two elements; thus, in the second part of this chapter, very recent results of clusters consisting of both elements are discussed; here the nine-atomic systems are of particular interest because of their relationship to the Zintl ions Pb_9^{4-} and Bi_9^{5+}.

The clusters cations of Pb [49] and Bi [50] were investigated in the same manner. A GA was utilized; every single structure was optimized with the functional BP86, large-core ECPs [51], which cover the inner 78 electrons and account for scalar relativistic effects only, and double-zeta valence basis sets, def-SV(P) [52]. The finally obtained best structures were recalculated with the TPSS functional at two-component level (including SOC) using small-core two-component Dirac–Fock ECPs [26] covering the inner 60 electrons and triple-zeta valence basis sets dhf-TZVP-2c. The results displayed in Fig. 5 reveal the following picture. In all cases except for Pb_5^+, the lowest-energy structure gives the best fit to IMS; for Pb_5^+ the best-fitting isomer, a trigonal bipyramid, is only 0.01 eV higher in energy than the structure with the lowest energy, an edge-capped tetrahedron. Overall, structures of lead clusters are significantly more compact, which is evident, e.g., for the 13- and 12-atomic species: In case of Pb-filled icosahedral structures are found (with a missing outer atom in case of Pb_{12}^+), for the respective Bi clusters, a frequently occurring eight-atomic building unit is two pentagons that share one edge; Bi_{12}^+ consists of one such unit added by a capping triangle and a capping single atom; Bi_{13}^+ consists of two of these units fused together. This unit is observed first for Bi_9^+ (plus one additional capping atom); Pb_9^+ in contrast may

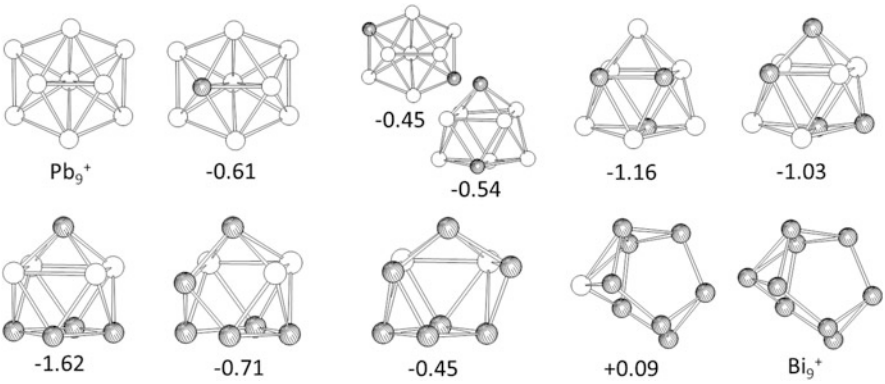

Fig. 6 Lowest-energy structures of $(Pb_nBi_{9-n})^+$. Stabilities with respect to the homo-atomic species (see text) are given in eV. For all compositions except of $(Pb_7Bi_2)^+$ (first row, third and fourth from the *left*), isomers with qualitatively different topologies are higher in energy by more than 0.1 eV

be described as two fused trigonal bipyramids forming a much more compact structure. We note that in particular for Bi, SOC has a significant impact on the results (one-component data were also presented by Yan et al. [53]) and that results accounting for SOC generally are better in line with the experimental data.

Recognizing the very different shapes of clusters consisting of Bi and Pb, one might ask how mixed metallic clusters consisting of these two elements will look like, in particular, how the structure depends on the mixing ratio. This was investigated in a very recent study [54]. Like for the pure Pb/Bi systems, a GA was used but now extended by the atom-to-place reassignment step (see Sect. 3.3). Further, now the TPSS functional, the more flexible basis and the effect of SOC were used within in the GA. Here we confine ourselves to the nine-atomic systems; the results are displayed in Fig. 6 and may be summarized as follows. For species with only one heteroatom, the topology of the pure clusters is maintained. In Pb_8Bi, Bi replaces Pb on one of the fused pentagonal bipyramids of Pb_9^+; in $PbBi_8$, Pb replaces Bi as the capping atom; the eight-atomic Bi unit described above remains unchanged. All other mixtures are more or less distorted variants of the (C_{4v}-symmetric) structure of Pb_9^{4-}. $Pb_4Bi_5^+$, which is isoelectronic to Pb_9^{4-}, shows C_{4v} symmetry, the degree of distortion increases with increasing compositional difference to this case. The distribution of Pb and Bi in $Pb_4Bi_5^+$ as well as in the other cases largely follows the principle of maximizing the number of hetero-atomic bonds. This is in line with the well-known fact that slightly different energies of the atomic levels of two bond partners lead to lowering of the binding combination of them [55] and thus to increased stability of a hetero-atomic system compared to the isoelectric homo-atomic system. The preference of hetero-atomic bonds can also be explained by the perturbation theory discussed above. For this purpose consider two Bi and two Pb atoms occupying the four equivalent positions on a square. In the procedure described above and used for the assignment of Pb/Bi

for the nine-atom clusters, one starts with calculation of the wave function and the electrostatic potential for a system with four atoms of nuclear charge $Z = 82.5$. The potential is the same for all positions, and the first Bi atom is placed arbitrarily. In the second step, for this position the nuclear charge is $Z = 83$, and for the three remaining positions $Z = 82.333$. As a result, electrons will accumulate at the atom with the higher nuclear charge, yielding an electron deficit, which is highest for the neighbors of Bi. In this way, the two (equivalent) positions neighbored to the Bi atom show a higher (less negative) electrostatic potential than the more distant opposite position. This makes these two positions less attractive for Bi, and thus the second Bi atom is placed on the opposite position.

4.4 Ternary Cluster Anions

Ternary cluster ions of type $[M_mA_nB_{N-n}]^{q-}$, M being a transition metal or lanthanide, A and B being different main-group elements, are widely discussed in the contribution by Weinert and Dehnen in the present volume. In this chapter we consider only cases with $m = 1$ and $N = 12$, 13, 14 and focus on the influence of the type of the M atom on structure and bonding of the A_nB_{N-n} shell.

The 12-, 14-, and 13-atom shells are shown in Fig. 7. For both the 12- and the 14-atom shells, each atom has three neighbors within the shell; thus, (hypothetical) shells of type Bi_{12} or Bi_{14} are electron precise. Also the shells of the clusters $[La@Pb_7Bi_7]^{4-}$, $[V@Ge_8As_4]^{3-}$ [56], $[Nb@Ge_8As_6]^{3-}$, as well as $[Rh@Ge_{12}]^{3-}$, the diamagnetic hypothetic analog to experimentally observed $[Ru@Ge_{12}]^{3-}$ [57], can be considered being formally electron precise, if all q electrons from the negative charge and all valence electrons of the central atom are assigned to the cluster shell. In the following, the limits of this ionic description are explored. For this, a helpful tool is a localization procedure, where linear combinations of (delocalized) orbitals are formed by a unitary transformation yielding orbitals that are localized at as few as possible atoms, e.g., by minimizing the spatial extent of each LMO (Boys [58]). For electron-precise systems, like the (hypothetical) shells

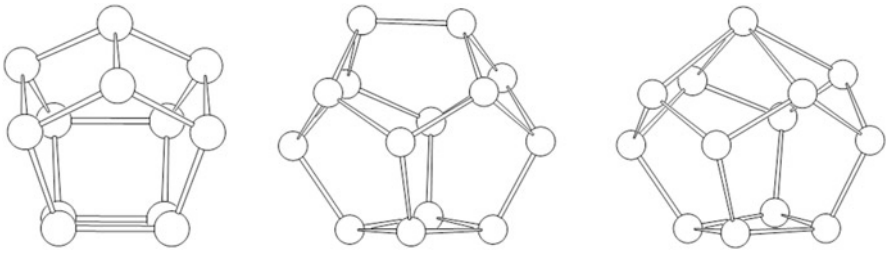

Fig. 7 12-, 14- and 13-atom shells of the ternary clusters $[MA_nB_{N-n}]^{q-}$ (M is omitted). For details see text

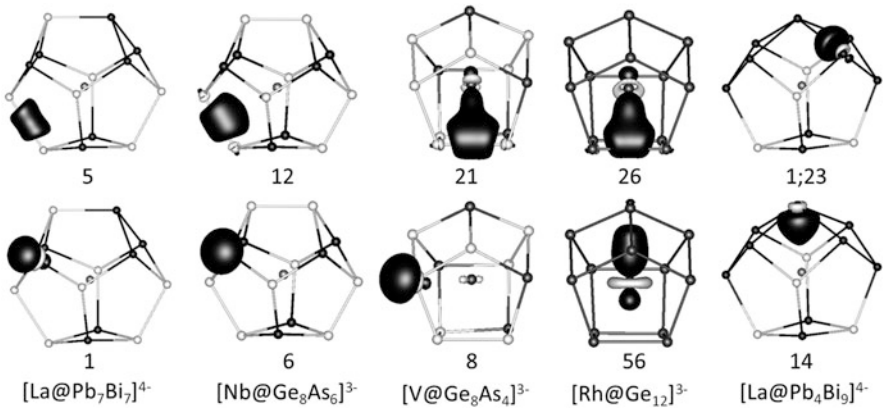

Fig. 8 Localized molecular orbitals representing bonds (*upper row*) and lone pairs (*lower row*) for calculated 12-, 14- and 13-shell atom clusters. For each type of LMOs, those with the highest contribution of the central atom are shown, given in percent below the respective images. For the bond in $[La@Pb_4Bi_9]^{4-}$ (*top*, *right*), the second number (23%) is the contribution of the top Bi atom that binds to four atoms within the shell

Bi_{12} or Bi_{14}, this results in only two-electron-two-center bonds and lone electron pairs.

Atom-type assignment was done as described in Sect. 3.2. The validity of the ionic description of the present systems is estimated by inspecting the differences of the character of the LMOs of the clusters from the ideal cases lone-pair or two-center bond. A suited measure for this is the (Mulliken [59]) contribution of the central atom to the LMOs. In Fig. 8, for each of the 12- and 14-atomic clusters, two LMOs are shown. One of them represents a bond within the shell, the other one a lone pair at a shell atom; for both classes the LMO with the largest contribution of the central atom is shown. It is evident that the validity of the idealized ionic description decreases with increasing number of valence electrons of the transition metal atom and additionally from the 14- to the 12-atom shell. For $[La@Pb_7Bi_7]^{4-}$ (three valence electrons at the central atom), the largest contribution from the central atom amounts to only 5 %; this system is quite well described as Ln^{3+} in an electron-perfect $[Pb_7Bi_7]^{7-}$ shell. For $[Nb@Ge_8As_6]^{3-}$ this is still a good and for $[V@Ge_8As_4]^{3-}$ at least a rough approximation. The bonds within the shell are supported by the central atom, but still the contributions from the shell atoms are the largest; lone pairs are dominantly located at the shell atoms. In contrast, $[Rh@Ge_{12}]^{3}$ with nine valence electrons at the central atom obviously is not reasonably described in this way. Most evident is the change of four lone-pair-type LMOs in $[V@Ge_8As_4]^{3-}$ to V–Ge bonds. Also the three-center character of the shell bonds is further enhanced.

The 13-atom shell cluster is not electron precise, as the top Bi atom is bonded to four atoms within the shell. According to the LMOs, the situation is best described by four strongly polarized bonds to the neighbor atoms and a compensating

contribution of the central atom to the lone-pair LMO that points to the cluster center, in contrast to the usual way.

$[LaPb_7Bi_7]^{4-}$ and $[LaPb_4Bi_9]^{4-}$ are members of a family of similar clusters, which may be summarized as $[Ln@Pb_nBi_{14-n}]^{q-}$ and $[Ln@Pb_mBi_{13-m}]^{q-}$, Ln being a lanthanide, $n/q = 7/4$, 6/3, and $m/q = 4/4$, 3/3. According to ESI mass spectra, one finds both 13- and 14-atom cages for all of the investigated lanthanides La, Ce, Nd, Sm, Gd, and Tb, but there is a preference of the 14-atom cage for La and of the 13-atom cage for Nd and the heavier (smaller) lanthanides; for Ce no preference is evident. The energies of the hypothetical exchange reactions

$$[Ln@Pb_3Bi_{10}]^{3-} + [Pb_6Bi_8]^{6-} \rightarrow [Pb_3Bi_{10}]^{6-} + [Ln@Pb_6Bi_8]^{3-}, \quad (5)$$

and

$$[Ln@Pb_4Bi_9]^{4-} + [Pb_7Bi_7]^{7-} \rightarrow [Pb_4Bi_9]^{7-} + [Ln@Pb_7Bi_7]^{4-}, \quad (6)$$

thus are expected to be comparably small energies and to change from negative to positive numbers when going from La to Tb. Quantum chemical calculations of these reactions for all lanthanides with Pb/Bi positions for all species assigned via perturbation theory exactly confirm this (see Fig. 9).

For La the 14-atom cage is preferred by ca. 20 kJ/mol, this preference continuously decreases with increasing nuclear charge (and thus decreasing atom size) and changes to a preference for the 13-atom cage. While trends are very well

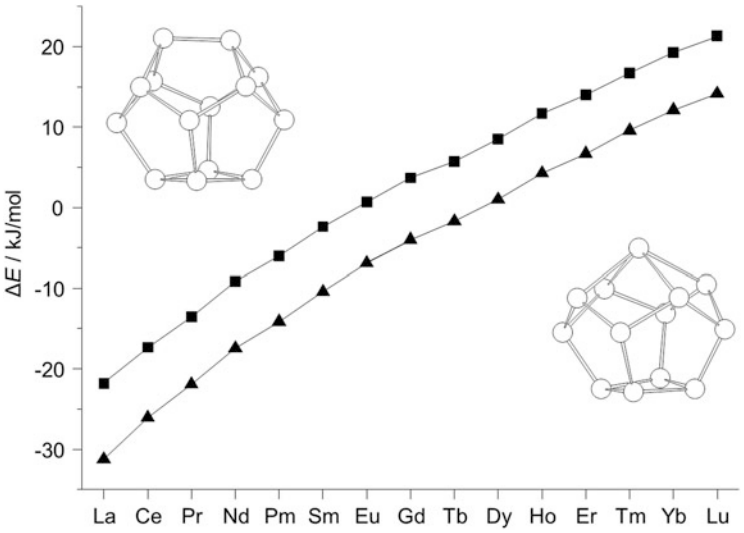

Fig. 9 Calculated energies for the two exchange reactions given in the text. Positive reaction energies indicate the preference of the 13-atom cage. *Squares* refer to the reaction given in Eq. (6), *triangles* to that given in Eq. (5)

reproduced, the change of preference according to calculations occurs at slightly higher nuclear charges than experimentally observed. Nevertheless, it is evident that the shape of the cage can be tuned by the choice of the lanthanide. It is noteworthy that "empty" cages like $[Pb_6Bi_8]^{6-}$ or isoelectric $[Pb_7Bi_7]^{7-}$ or also isoelectric Bi_{14} are not the global minima of the respective energy hypersurface. For $Bi_{14,}$ for instance, the respective neutral species of the Bi_{14} cation shown in Fig. 5 (bottom, right) is significantly (ca. 70 kJ/mol) preferred over the 14-atom cage in Fig. 7. This indicates that the lanthanide comes into play already during the cluster shell formation.

5 Summary and Concluding Remarks

Considerable progress has been made concerning the development of tools for binary systems as well as concerning the reliability and stability of methods including spin–orbit effects. Genetic algorithms basing on density functional methods accounting for these two aspects allow for reliably predicting low-lying isomers of heavy-element clusters. The prediction of the respective energetically lowest isomer is and remains a challenge for quantum chemistry, as in particular for binary clusters there are typically several isomers separated by less than 0.1 eV, which presently is the limit of accuracy for density functional theory applied to clusters of main-group or noble metal elements.

Further, still very little is known about the formation of clusters. A possible step to be done might be the connection of local minimum structures by reaction pathways, for instance, by applying a parameter-free generalization of a quasi-Newton method [60] for their exploration. Like for the determination of global-minima (Sect. 4.3) experimental results, the preparation of (putable) intermediates would be of great help for this purpose. Very recent results for ternary Ta/Ge/As clusters [61] are a first step toward this goal.

References

1. Mingos DMP, Johnston RL (1987) Struct Bond 68:29–87
2. De Heer W (1993) Rev Mod Phys 65:611–676
3. Fernando A, Dimuthu KL, Weerawardene M, Karimova NV, Aikens CM (2015) Chem Rev 115:6112–6216
4. Cramer CJ, Truhlar DG (2009) Phys Chem Chem Phys 11:10757–10816
5. Weigend F, Ahlrichs R (2010) Philos Trans A 368:1245–1263
6. Ferrando R, Jellinek J, Johnston R (2006) Chem Rev 108:846–904
7. Weigend F, Schrodt C, Ahlrichs R (2004) J Chem Phys 121:10380–10384
8. Weigend F, Schrodt C (2005) Chem Eur J 11:3559–3564
9. Weigend F (2014) J Chem Phys 141:134103
10. Kirkpatrick S, Gelatt CD Jr, Vecchi MP (1983) Science 220:671–680
11. Wales DJ, Doyle JPK (1997) J Phys Chem A 101:5111–5116

12. Hartke B (1993) J Phys Chem 97:9973–9976
13. Deaven D, Ho KM (1995) Phys Rev Lett 75:288–291
14. Sierka M, Döbler J, Sauer J, Santambrogio G, Brümmer M et al (2007) Angew Chem Int Ed 46:3372–3375
15. Pyykkö P (1988) Chem Rev 88:563–594
16. Zintl E, Harder A (1931) Z Phys Chem Abt A 154:1–5
17. Edwards PA, Corbett JD (1977) Inorg Chem 16:903–907
18. Pyykkö P (2012) Ann Rev Phys Chem 63:45–64
19. Becke AD (1988) Phys Rev A 38:3098–3100
20. Perdew JP (1986) Phys Rev B 33:8822–8824
21. Perdew JP, Burke K, Ernzerhof M (1996) Phys Rev Lett 77:3865–3868
22. Tao J, Perdew JP, Staroverov VN, Scuseria G (2003) Phys Rev Lett 91:12129–12137
23. Drebov N, Weigend F, Ahlrichs R (2011) J Chem Phys 135:044314
24. Cao XY, Dolg M (2012) Chem Rev 112:403–480
25. Figgen D, Rauhut G, Dolg M, Stoll H (2005) Chem Phys 311:227–244
26. Metz B, Stoll H, Dolg M (2000) J Chem Phys 113:2563–2569
27. Armbruster MK, Weigend F, van Wüllen C, Klopper W (2008) Phys Chem Chem Phys 10:1748–1756
28. Kühn M, Weigend F (2013) J Chem Theory Comput 9:5341–5348
29. Peng D, Middendorf N, Weigend F, Reiher M (2013) J Chem Phys 138:184105
30. Weigend F, Baldes A (2010) J Chem Phys 133:174102
31. Armbruster K, Klopper W, Weigend F (2006) Phys Chem Chem Phys 8:4862–4865
32. Klamt A, Schüürmann G (1993) J Chem Soc Perkin Trans 2:799–805
33. Warren RW, Dunlap BI (1996) Chem Phys Lett 262:384–392
34. Ababei R, Massa W, Weinert B, Pollak P, Xie X et al (2015) Chem Eur J 21:386–394
35. Lips F, Holynska M, Clerac R, Linne U, Schellenberg I (2012) J Am Chem Soc 134:1181–1191
36. Heaven MW, Dass A, White PS, Holt KM, Murray RW (2008) J Am Chem Soc 130:3754–3755
37. Walter M, Akola J, Lopez-Acevedo O, Jadzinsky PD, Calero G et al (2008) Proc Natl Acad Sci U S A 105:9157–9162
38. Zhu M, Aikens CM, Hollander FJ, Schatz GC, Jin R (2008) J Am Chem Soc 130:5883–5885
39. Jiang D, Kühn M, Tang Q, Weigend F (2014) J Phys Chem Lett 5:3286–3289
40. Baldes A, Gulde R, Weigend F (2011) J Clust Sci 22:355–363
41. Wedig U, Saltykow V, Nuss J, Jansen M (2010) J Am Chem Soc 132:12458–12463
42. Baldes A, Weigend F (2013) Mol Phys 111:2617–2624
43. Li J, Li X, Zhai HJ, Wang LS (2003) Science 299:864–867
44. Furche F, Ahlrichs R, Weis P, Jacob C, Gilb S et al (2002) J Chem Phys 117:6982–6990
45. Oger E, Crawfdord NRM, Kelting R, Weis P, Kappes MM et al (2007) Angew Chem Int Ed 46:8503–8506
46. Oger E, Kelting R, Weis P, Lechtken A, Schooss D et al (2009) J Chem Phys 130:124305
47. Weis P, Gilb S, Gerhardt P, Kappes MM (2002) Int J Mass Spectrom 216:59–73
48. Schooss D, Blom M, Parks JH, v Issendorf B, Haberland H et al (2005) Nano Lett 5:1972–1977
49. Kelting R, Otterstätter R, Weis P, Drebov N, Ahlrichs R et al (2011) J Chem Phys 136:211103
50. Kelting R, Baldes A, Schwarz U, Rapps T, Schooss D et al (2012) J Chem Phys 136:154309
51. Küchle W, Dolg M, Stoll H, Preuss H (1991) Mol Phys 74:1245–1263
52. Eichkorn K, Weigend F, Treutler O, Ahlrichs R (1997) Theor Chem Acc 97:119–124
53. Yuan HK, Chen H, Shi DN, Wang BL (2008) Eur Phys J D 47:359–366
54. Longo L, Seifried C, Weigend F, unpublished results
55. Kutzelnigg W (2002) Einführung in die Theoretische Chemie, vol 2. Wiley, Weinheim, p 117f
56. Mitzinger S, Broeckaert L, Massa W, Weigend F, Dehnen S (2015) Chem Commun 51:3866–3869

57. Espinoza-Quintero G, Duckworth JCA, Myers WK, McGrady JE, Goicoechea JM (2014) J Am Chem Soc 136:1210–1213
58. Foster JM, Boys SF (1960) Rev Mod Phys 32:300–302
59. Mulliken RS (1955) J Chem Phys 23:1833–1840
60. Plessow P (2013) J Chem Theory Comput 9:2305–2310
61. Mitzinger S, Broeckaert L, Massa W, Weigend F, Dehnen S (2016) Nat Commun 7:10480. doi:10.1038/natcomms10480)

Struct Bond (2017) 174: 63–98
DOI: 10.1007/430_2015_5003

Published online: 9 July 2016

Homoatomic Polyanions of the Early p-Block Elements

Jose M. Goicoechea

Abstract This article reviews the chemistry of homoatomic polyanions of the early p-block elements (groups 13–15). The focus is on species that have been structurally authenticated in solid-state compounds and/or isolated from solution. The structures, bonding, electronic properties, and formation pathways of these homoatomic species are described in detail.

Keywords Clusters • Pnictogens • Polyanions • Tetrels • Triels • Zintl ions

Contents

Dedicated to Professor Hansgeorg Schnöckel on the occasion of his 75th birthday.

J.M. Goicoechea (✉)
Department of Chemistry, University of Oxford, Chemistry Research Laboratory, 12 Mansfield Road, Oxford OX1 3TA, UK
e-mail: jose.goicoechea@chem.ox.ac.uk

1 Introduction

The preference for catenation or cluster formation of the heavier main elements is classically exemplified by referring to the prevalent allotropes of the elements. Thus while dinitrogen (N_2) exists as a diatomic species under ambient conditions, the most common allotrope of phosphorus (although, paradoxically, the least thermodynamically stable) is white phosphorus, P_4, (P_2 can only be isolated under extreme conditions, at temperatures over 800°C and low pressures) [1, 2]. The same comparison can be drawn between O_2 and S_8. This empirical observation is rationalized in the context of the so-called double bond rule [3–5], which is largely a thermodynamic phenomenon; bond dissociation energies for π-bonds weaken at a greater rate than for σ-bonds on going down a given group, making the formation of σ-bonds more favorable. In other words, for nitrogen, the triple bond is preferred since it has more than three times the energy of a single bond, whereas for phosphorus the reverse is true (Table 1). These historical arguments have recently been disputed by an energy decomposition analysis conducted by Jerabek and Frenking [6]. In their study, the authors report that the contribution of P–P π-bonding to the chemical bond in P_2 is even higher than the contribution of N–N π-bonding to the chemical bond of N_2 and that consequently N_4 is unstable relative to N_2 due to a significant weakening of the N–N σ-bonds in this hypothetical species.

In many ways, the discrete tetrahedral units found in white phosphorus (P_4) can be thought of as the archetypal main-group cluster. This species can be rationalized as an electron-precise molecule where each P–P bond represents a two-center, two-electron bond. At the same time, the P_4 cluster also conforms to the rules developed by Wade and Mingos for bonding in electron-deficient species such as boranes [8–11]. A phosphorus atom is isolobal with a C–H unit and thus has three

Table 1 Comparison of bond energies for multiple and single bonds for selected main-group elements [7]. Thermodynamic values rounded to nearest integer. The values in curved brackets are alternative bond dissociation energies derived from different compounds containing E–E bonds

Bond energies (kJ mol^{-1})	Nitrogen	Phosphorus
E ≡ E	942 in N_2	481 in P_2
E–E	167 (or 247)[a]	201 (or 239)[b]
Ratio E ≡ E/E–E	5.64 (or 3.81)	2.39 (or 2.01)
	Oxygen	**Sulfur**
E = E	494 in O_2	425 in S_2
E–E	142 (or 207)[c]	226 (or 268)[d]
Ratio E = E/E–E	3.48 (or 2.39)	1.88 (or 1.59)

Bond energies reported for [a]N_2H_4: the first value is for the estimated N–N bond taking into account the total energy of atomization of hydrazine and the estimated N–H bond energies of ammonia, whereas the value in brackets represents the dissociation into two amino radicals
[b]P_4 (P_2Cl_4)
[c]As for [a] using H_2O_2
[d]S_8 (H_2S_2)

orbitals and three electrons available for cluster bonding. This would give the cluster a total of six skeletal electron pairs (SEP), or $n+2$, where n represents the total number of vertices. It can therefore be rationalized as a *nido*-cluster, derived from a trigonal bipyramid that is missing a vertex (i.e., a tetrahedron).

A similar preference for catenation and cluster formation is also commonplace for polyatomic cations and anions of the heavier p-block elements. This area of research is enormously vast and includes a number of what have now become classical textbook examples of main-group compounds. The scope of this review will be limited to substituent-free (or "naked") homoatomic polyanions. That is to say, species which contain a single type of atom and that are not stabilized by any functional groups and/or ligands. It is worth noting, however, that "free" ions only exist as such in the gas phase and that in reality the majority of the species discussed herein are stabilized by significant electrostatic interactions with other counterions and/or solvent. In this review, we will aim to provide an overview of the species that have been experimentally isolated in one form or another. While the scope of this review is on cluster anions, for completeness, other smaller chains and cyclic species are also discussed in an effort to offer a comprehensive interpretation of the bonding and structural variety of the polyanions of the early p-block elements.

2 Homoatomic Polyanions of Group 13

The chemistry of substituent-free homoatomic polyanionic species of the group 13 elements is limited to species generated in the gas phase and to solid-state compounds (such as Zintl phases). To our knowledge, no such clusters have been isolated from solution. This review will largely focus on clusters that have been structurally authenticated in isolable compounds and will overlook the vast number of cluster anions that have been proposed and computed by theoretical chemists and/or characterized in matrix-isolation studies.

Zintl phases are formed by reaction of the main-group elements with alkali (A), alkaline-earth (Ae), or other electropositive elements, typically under melt conditions. Such species represent equilibrium phases, or thermodynamic minima, at a given point of the phase diagram (as opposed to metastable solids). For the group 13 elements (or triel elements), the overwhelming majority of such compounds are comprised of formally anionic extended three-dimensional networks which are stabilized by cationic elements. Such solid-state compounds have been extensively explored by Kauzlarich, Benin, Corbett, Sevov, Fässler, and others, and numerous reviews are available in the literature [12–20]. For our purposes, we will limit ourselves to discussing the discrete polyanions that have been structurally authenticated in such phases and will discuss the structure and bonding of relevant examples.

Zintl phases of the group 13 elements containing more or less discrete clusters are much rarer than for the elements of groups 14 and 15, in large part due to the large negative charges associated with the corresponding cluster anions. The group

Table 2 Isolated anionic structural motifs found in group 13 element-containing phases synthesized through solid-state methods

Anion	Element	Compound	References
$[E^{III}]^{5-}$	Ga	Mg_5Ga_2	[21]
		Ln_5Ga_3 (Ln = Y, La, Gd, Ho, Er)	[22]
	Tl	$LiMg_2Tl$	[23]
		$Na_{23}K_9Tl_{15.3}$	[24]
$[E^{III}_2]^{8-}$	Ga	Mg_2Ga	[25]
$[E^{III}_3]^{7-}$	Tl	$Na_{23}K_9Tl_{15.3}$	[24]
$[E^{III}_4]^{8-}$	In	Na_2In	[26]
	Tl	$Na_{23}K_9Tl_{15.3}$	[24]
$[E^{III}_5]^{7-}$	Tl	$Na_{23}K_9Tl_{15.3}$	[24]
		$Na_2K_{21}Tl_{19}$	[27]
$[E^{III}_5]^{9-}$	In	La_3In_5	[28]
$[E^{III}_6]^{6-}$	Tl	ATl (A = K, Cs)	[29, 30]
$[E^{III}_6]^{8-}$	Ga	$Ba_5Ga_6H_2$	[31, 32]
	Tl	$Na_{14}K_6MTl_{18}$ (M = Mg, Zn–Hg)	[33]
$[E^{III}_7]^{7-}$	Tl	$Na_{12}K_{38}Tl_{48}Au_2$	[34]
		$K_{10}Tl_7$	[35]
$[E^{III}_9]^{9-}$	Tl	$Na_2K_{21}Tl_{19}$	[27]
		$Na_{12}K_{38}Tl_{48}Au_2$	[34]
$[E^{III}_{11}]^{7-}$	Ga	Cs_8Ga_{11}	[36]
	In	A_8In_{11} (A = K, Rb)	[37, 38]
	Tl	A_8Tl_{11} (A = K–Cs)	[39, 40]
		$As_{15}Tl_{27}$ (A = Rb, Cs)	[41]
		$K_{18}Tl_{20}Au_3$	[42]
$[E^{III}_{13}]^{10-}$	Tl	$Na_4A_6Tl_{13}$ (A = K–Cs)	[43, 44]
$[E^{III}_{13}]^{11-}$	Tl	$Na_3K_8Tl_{13}$	[44]

13 elements only possess three valence electrons, and, consequently, if they are to afford clusters such as those available to boranes $[B_xH_y]^{z-}$, the resulting substituent-free clusters must carry large negative charges (i.e., a B–H fragment is isolobal with a naked group 13 element anion). Consequently, the number of isolated homoatomic species is relatively small, and such species are more predominant for the heavier group 13 elements, particularly thallium. These are presented in Table 2. For completion purposes, we also highlight phases with discrete isolated monoatomic, chain-like, and cyclic anions.

2.1 Linear Polyanions of the Group 13 Elements

Phases that are rich in electropositive elements, such as Mg_5Ga_2 and Mg_2Ga, are known to contain isolated anions, Ga^{5-}, and dimers, Ga_2^{8-} [21–25]. The linear Tl_3^{7-} trimer has also been observed in $Na_{23}K_9Tl_{15.3}$ and is the first homoatomic

example of such a species for the group 13 elements [24]. It is important to note, however, that the assignment of charges for such anions is largely a formalism in the context of the Zintl–Klemm–Busmann concept and, consequently, that such charges do not represent true elemental oxidation states. It is unlikely that any of these highly charged species can exist in systems where the negative charges are not stabilized by strong coulombic interactions with charge-balancing cations. Moreover, the importance of electron polarization, or covalent interactions, between cations and anions cannot be overlooked. It is no coincidence that the greatest number of these highly anionic species have been isolated in thallium-containing phases, as this is one of the least electronegative of the group 13 elements and highly polarizable and, therefore, the most likely to be involved in some degree of covalent interaction with the other elements in the lattice.

2.2 *Electron-Deficient Clusters of the Group 13 Elements*

The chemistry of homoatomic polyanions of the group 13 elements is dominated by hypoelectronic clusters, i.e., anions with electron counts that fall short of those that would be expected on the grounds of classical rules for bonding in electron-deficient clusters. This is perhaps unsurprising as "conventional" cluster anions would be required to carry prohibitively high negative charges. Closed deltahedral *closo*-type clusters of the group 13 elements would be expected to conform to the following formulae $[E^{III}_n]^{(n+2)-}$. Thus, Tl_5^{7-} and $[E^{III}_6]^{8-}$ (E = Ga, Tl) both obey this rule and exhibit the classical *closo*-topologies expected for such species, i.e., trigonal bipyramidal and octahedral, respectively [24, 27, 31–33]. Similarly, $[E^{III}_4]^{8-}$ (E^{III} = In, Tl) and In_5^{9-} also conform to Wade–Mingos rules and exhibit *nido*-geometries consistent with clusters with $n+2$ skeletal electron pairs available for bonding (see Fig. 1 for selected examples of these clusters) [24, 26, 28]. Accordingly, the X-ray structures of the phases in which they occur reveal a tetrahedral cluster for $[E^{III}_4]^{8-}$ and a square pyramidal geometry for In_5^{9-}.

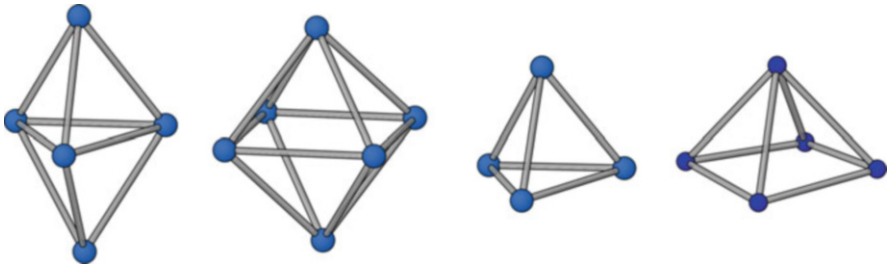

Fig. 1 Electron-deficient cluster anions (and selected solid-state phases in which they occur) of the group 13 elements. From *left* to *right*: *closo*-Tl_5^{7-} ($Na_{23}K_9Tl_{15.3}$), *closo*-Tl_6^{8-} ($Na_{14}K_6Tl_{18}Zn$), *nido*-Tl_4^{8-} ($Na_{23}K_9Tl_{15.3}$), and *nido*-In_5^{9-} (La_3In_5). *Differently sized* and *colored spheres* are used to distinguish between indium and thallium

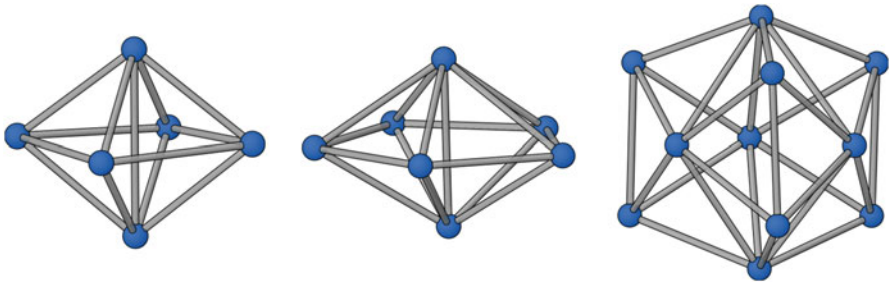

Fig. 2 Hypoelectronic clusters of the group 13 elements (and selected solid-state phases in which they occur). From *left* to *right*: Tl_6^{6-} (CsTl), Tl_7^{7-} ($K_{10}Tl_7$), and Tl_{11}^{7-} (K_8Tl_{11})

2.3 Hypoelectronic Clusters of the Group 13 Elements

The prevalence of hypoelectronic clusters increases with increasing nuclearity (selected examples of such clusters are pictured in Fig. 2). Thus, for systems where $n > 6$, the electron counts fall short of what would be expected for *closo*-type geometries ($[E^{III}_n]^{(n+2)-}$). Species such as Tl_6^{6-} and Tl_7^{7-} achieve this by means of a Jahn–Teller-type distortion which results in an axial compression of the parent clusters *closo*-Tl_6^{8-} and the hypothetical *closo*-Tl_7^{9-} (which have octahedral and pentagonal bipyramidal structures, respectively) [29, 30, 34, 35]. In the case of Tl_7^{7-}, the distortion is significant enough to allow for the formation of a transannular Tl–Tl bond (0.1–0.2 Å shorter than comparable distances in the cluster). In the case of Tl_6^{6-}, the tetragonal compression forces one of the degenerate t_{1u} molecular orbitals of the octahedral Tl_6^{8-} cluster to rise in energy (giving the resulting a_{2u} orbital antibonding character). This leaves the cluster with $2n$ electrons (or n skeletal electron pairs) for cluster bonding as opposed to $2n+2$.

A similar rationale can be applied to the $[E^{III}_{11}]^{7-}$ clusters which readily occur in this family of solid-state compounds [36–42]. In fact, the first "isolated" homoatomic cluster of the group 13 elements was the eleven-atom cluster In_{11}^{7-} found in K_8In_{11} [37]. This phase, paradoxically, is not a true Zintl phase as there has not been a complete transfer of electrons from potassium to indium and, thus, is best formulated as $[K^+]_8[In_{11}^{7-}][e^-]$. It fits into a group of phases which can be called "metallic Zintl phases" or "metallic salts" (and are effectively Zintl analogues of salts such as CeS and LaI_2). The compound is Pauli paramagnetic and metallic. Nevertheless, the cluster is deltahedral and exhibits delocalized bonding. Yet, its geometry and electron count differ from that expected for a borane cage of eleven atoms. The cluster geometry can be generated by capping the two basal faces of a D_{3h} symmetric trigonal prism and compressing along the threefold rotation axis (with concomitant radial expansion). This geometric change implies that instead of carrying the enormous charge of 13– corresponding to $(n+2)$ for *closo*-species of group 13, its charge is the more reasonable 7–.

Another family of clusters that warrants discussion are the thallium-centered clusters Tl_{13}^{x-} ($x = 10$, 11) [43, 44]. The Tl_{13}^{11-} cluster can be considered as a standard *closo*-Tl_{12}^{14-} icosahedron that is centered by an interstitial Tl^{3+} cation. A related structural motif has also been identified in the $[Na@Tl_{12}]^{13-}$-type cluster observed in $Na_{15}K_6Tl_{18}H$ [45]. The Tl_{13}^{10-} anion is one electron short of the overall count needed to satisfy traditional electron counting rules, and consequently the phases in which it has been identified, $Na_4A_6Tl_{13}$ (A = K–Cs), exhibit Curie–Weiss magnetic behavior.

It is worth noting that a number of other heteroatomic cluster anions are also available for the elements of group 13; however, these do not form the focus of this review and will not be discussed in detail. Suffice to say that in the presence of other elements that occur later in the p-block, the overall negative charges of the resulting cluster anions can be dramatically reduced and a wealth of novel cluster geometries and endohedral clusters become available.

3 Homoatomic Polyanions of Group 14

On moving from group 13 to group 14 elements, the availability of an additional valence electron has a dramatic effect of the overall charges associated with polyanionic chains, rings, and clusters. The isolobal relationship between a B–H fragment and a group 14 element (each having three orbitals and two electrons available for cluster bonding) implies that clusters of general formulae $[E^{IV}_n]^{2-}$ should exhibit *closo*-geometries according to the established rules for bonding in electron-deficient clusters. On account of the reduced charges associated with such anions, it is possible not only to isolate such clusters in extended lattices but also from solution, a development which has led to a very rich and varied chemistry. For clarity, we will discuss such homoatomic polyanionic clusters as two separate groups, those isolated in solid-state structures and those isolated in solution, and finally highlight the relationship that exists between these two families of compounds.

3.1 Historical Perspective

The existence of polyanions of the group 14 elements (or tetrels) has been known since early experiments by Joannis who demonstrated that solutions of elemental sodium and lead give rise to intensely colored green solutions [46]. Soon afterward, Kraus demonstrated that tin is also soluble in ammonia in the presence of a sodium, giving rise to a deep-red solution [47]. The colors of these solutions are attributable to the presence of the homoatomic polyanions $[E^{IV}_9]^{4-}$, although the exact composition of these anions was not determined until much later in experiments conducted by Eduard Zintl [48, 49]. Consequently these anions, and the solid-

state compounds in which they are also known to occur, bear his name. Zintl was able to identify a number of anions of the main-group elements using potentiometric titration methods. These solution-based methods allow for the generation of a number of anionic compounds; however, in order to stabilize more electron-rich species, solid-state reactions are required. In the first instance, this review will focus on the polyanionic species available via such solid-state methods. As with the compounds discussed for the group 13 elements (*vide supra*), the combination of an electropositive alkali, alkaline-earth, or rare-earth element with a more electronegative element of the p-block gives rise to ionic solids, many of which consist of two- and three-dimensional networks of the main-group elements which are accompanied by charge-balancing cations. In certain phases where the stoichiometric loading of the elements is appropriate, discrete polyanions are also available (see Table 3 for a full list) [50–97], many of which are also found in solution (*vide infra*). Such polyanions contain homopolar element–element bonds and are stabilized in the lattice by electrostatic interactions with the cations. They are effectively ionic salts containing covalently bonded polyanions and as such exhibit many of the properties that one might expect from a salt. They are brittle, insulating, and soluble in polar media. Non-protic solvents with a high dielectric constant are optimal for such a purpose, with ammonia and ethylenediamine being the most commonly used.

3.2 Linear Polyanions of the Group 14 Elements

As with the group 13 elements, alkali-metal-rich phases of the group 14 elements have been shown to contain isolated $[E^{IV}]^{4-}$ tetraanions and dimers $[E^{IV}{}_2]^{6-}$ with electronic configurations analogous to the noble gases and diatomic halogens, respectively [50–60]. The homoatomic polyanions isolated thus far can largely be divided into three separate categories, depending on the geometries of the anions and the overall negative charge associated with each atom. Thus, highly electron-rich species give rise to extended chains of the elements of general formulae $[E^{IV}{}_n]^{x-}$ (where $n = 3$, 4, 6 and 8). According to the Zintl–Klemm–Busmann concept, such species are expected to carry specific integer negative charges in order to satisfy valency requirements ($[E^{IV}{}_n]^{(2n+2)-}$). Thus, a dimer is expected to carry a 6– charge, a trimer an 8– charge, and so on: $[E^{IV}{}_4]^{10-}$, $[E^{IV}{}_6]^{14-}$, and $[E^{IV}{}_8]^{18-}$. Examples of electron-precise chains have been observed in a number of phases, and thus $Si_6{}^{14-}$ and $Si_8{}^{18-}$ are both known [53, 58]. Empirically, however, many of the anions isolated carry smaller negative charges than what would be expected based on valency arguments. This is perhaps unsurprising as very large negative charges are required for the stabilization of such electron-precise anions. Thus, for the vast majority of Zintl phases that contain discreet zigzag chains, the overall negative charge associated with such chains is less than expected. Consequently, such species are considered to have a greater degree of multiple-bond character. Shorter interatomic distances would be expected for such systems, and this is indeed observed

Table 3 Isolated anionic structural motifs found in group 14 element-containing phases synthesized through solid-state methods

Anion	Element	Compound	References
$[E^{IV}]^{4-}$	Si	Li_8MgSi_6	[50]
		$Li_{2.2}Mg_{17.8}Sr_{12}Si_{20}$	[51]
		$Li_{0.969}Mg_{2.031}Ca_8Si_8$	[52]
		$Mg_2Sr_{11}Si_{10}$	[53]
		$Mg_{7.5+/-8}Ca_7Si_{14}$	[54]
	Ge	$Li_{11}Ge_6$	[55]
		$Li_{1.18}Mg_{1.82}Ca_8Ge_8$	[52]
	Sn	Na_8BaSn_6	[56]
		$Li_{8.84}CaSn_{6.16}$	[56]
	Pb	Na_8BaPb_6	[57]
$[E^{IV}{}_2]^{6-}$	Si	Mg_3BaSi_4	[58]
	Ge	Ca_7Ge_6	[59]
	Sn	Ca_7Sn_6	[60]
$[E^{IV}{}_3]^{7-}$	Sn	Li_7Sn_3	[61]
$[E^{IV}{}_3]^{7.45-}$	Si	$Li_{2.2}Mg_{17.8}Sr_{12}Si_{20}$	[51]
$[E^{IV}{}_4]^{4-}$	Si	A_4Si_4 (A = Na–Cs)	[62–65]
		$A_{12}Si_{17}$ (A = K, Rb)	[66, 67]
		LiK_7Si_8	[68]
		LiK_3Si_4	[68]
		$BaSi_2$	[69]
		$Sr_{1-x}Ba_xSi_2$ ($x = 0.2$–1.0)	[70]
	Ge	A_4Ge_4 (A = Na–Cs)	[62, 64, 71]
		$A_{12}Ge_{17}$ (A = Na, K)	[72, 73]
		$NaRb_7Ge_8$	[74]
		$Na_2Cs_2Ge_4$	[75]
		NaK_7Ge_8	[74]
		$AeGe_2$ (Ae = Sr, Ba)	[76]
	Sn	A_4Sn_4 (A = Na–Cs)	[77–80]
		$A_{12}Sn_{17}$ (A = K, Rb)	[66]
		$A_{52}Sn_{82}$ (A = K, Cs)	[81]
	Pb	A_4Pb_4 (A = Na–CS)	[82–84]
		LiA_3Pb_4 (A = K–Cs)	[85]
		$NaCs_3Pb_4$	[85]
$[E^{IV}{}_4]^{8-}$	Ge	Ca_7Ge_6	[59]
	Sn	Ca_7Sn_6	[60]
$[E^{IV}{}_4]^{12-}$	Si	$Li_{12}Si_7$	[86, 87]
Cyclo-$[E^{IV}{}_5]^{x-}$ ($x = 6$–10)	Si	$Li_{12}Si_7$	[86, 87]
		Li_8MgSi_6	[50]
	Ge	$Li_{11}Ge_6$	[55]
	Sn	Na_8BaSn_6	[56]
		$Li_5Ca_7Sn_{11}$	[57]
		$Li_{8.84}CaSn_{6.16}$	[56]
	Pb	Na_8BaPb_6	[57]

(continued)

Table 3 (continued)

Anion	Element	Compound	References
Cyclo-$[E^{IV}_6]^{10-}$	Si	$Li_2Ae_4Si_6$ (Ae = Ba, Sr)	[88, 89]
	Ge	$Li_2Ba_4Ge_6$	[88]
$[E^{IV}_6]^{12.45-}$	Ge	$Li_{3.1}Mg_{4.9}Ba_6Ge_{12}$	[90]
$[E^{IV}_6]^{12.65-}$	Si	$Li_{2.7}Mg_{5.3}Ba_6Si_{12}$	[91]
$[E^{IV}_6]^{12.82-}$	Ge	$Li_{1.18}Mg_{1.82}Ca_8Ge_8$	[52]
$[E^{IV}_6]^{13-}$	Sn	$LiCa_7Sn_{11}$	[57]
$[E^{IV}_6]^{13.03-}$	Si	$Li_{0.969}Mg_{2.031}Ca_8Si_8$	[52]
$[E^{IV}_6]^{14-}$	Si	$Mg_3Ba_2Si_4$	[58]
$[E^{IV}_8]^{18-}$	Si	$Mg_2Sr_{11}Si_{10}$	[53]
$[E^{IV}_9]^{4-}$	Si	$A_{12}Si_{17}$ (A = K, Rb)	[66, 67]
	Ge	A_4Ge_9 (A = K, Cs)	[92, 93]
		$A_{12}Ge_{17}$ (A = Na, K)	[72, 73]
	Sn	K_4Sn_9	[94]
		$A_{12}Sn_{17}$ (A = K, Rb)	[66]
		$A_{52}Sn_{82}$ (A = K, Cs)	[81]
	Pb	A_4Pb_9 (A = K–Cs)	[65, 95, 96]
		$K_6Cs_{10}Pb_{36}$	[95]
Cyclo-$[E^{IV}_{10}]^{20-}$	Si	SrSi	[97]
Cyclo-$[E^{IV}_{12}]^{21-}$	Si	$Mg_{7.25}Ca_7Si_{14}$	[54]

in the solid-state structures of such anions. A greater degree of multiple-bond character also requires the presence of orbitals capable of interacting with one another, and as a result for $[E^{IV}_n]^{x-}$ anions where $x < 2n + 2$, the geometries of the chains have E–E–E bond angles that are closer to 120° consistent with greater sp^2 character for the atoms involved in bonding.

3.3 *Cyclic Polyanions of the Group 14 Elements*

Another way of reducing the high negative charges required for the formation of homoatomic polyanionic chains is to increase the number of σ-bonding interactions between the tetrel elements. This can be achieved by the formation of cyclic polyanions (selected examples are pictured in Fig. 3). These cyclic systems have been studied in depth by the groups of von Schnering, Nesper, and Sevov. A recurring structural motif of such phases is that the rings are often separated by charge-balancing cations in infinite one-dimensional arrays. By far the most common structural motifs in this family of compounds are five- and six-membered ring systems [50, 55–57, 86–89], although larger, branched rings are also known for silicon (Si_{10}^{20-} and Si_{12}^{21-}) [54, 97]. Quasi-aromatic five-membered ring systems

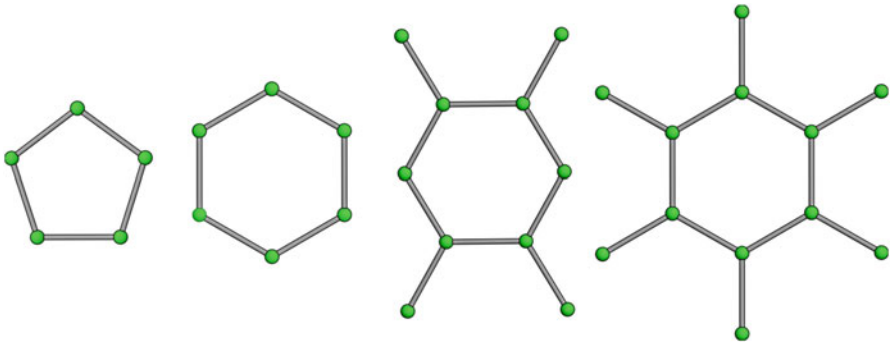

Fig. 3 Cyclic polyanions of the group 14 elements (and selected solid-state phases in which they occur). From *left* to *right*: Si_5^{6-} (Li_8MgSi_6), Si_6^{10-} ($Li_2Ba_4Si_6$), Si_{10}^{20-} (SrSi), and Si_{12}^{21-} ($Mg_{7.25}Ca_7Si_{14}$)

would be expected to carry a 6– charge, making them isoelectronic with the cyclopentadienyl anion. However, in reality, all of the phases containing such five-membered rings are accompanied by additional, more highly reduced, anions such as $[E^{IV}]^{4-}$. Korber has argued that this is motivated by the fact that the valence electron number per anion atom (N_E) for *cyclo*-$[E^{IV}_5]^{6-}$ is very close to values obtained for cluster-like species such as $[E^{IV}_4]^{4-}$ and $[E^{IV}_9]^{4-}$ and that, for such values, ring formation is not favored due to the remarkable stability of the clusters (*vide infra*). Consequently, such systems can only be stabilized in the presence of other, more reduced anions, which has the effect of increasing N_E.

3.4 Electron-Deficient Clusters of the Group 14 Elements

The final family of homoatomic polyanions observed in Zintl phases is the $[E^{IV}_4]^{4-}$ and $[E^{IV}_9]^{4-}$ cluster anions (Fig. 4). These species occur in binary phases of general formulae $A_4E^{IV}_4$, $A_4E^{IV}_9$, and $A_{12}E^{IV}_{17}$ (the latter containing both $[E^{IV}_4]^{4-}$ and $[E^{IV}_9]^{4-}$ in a 2:1 ratio) [62–85, 92–96], as well as in more complex ternary systems. These phases contain discrete isolated anions which can be rationalized in the context of rules for electron-deficient clusters. Thus, the $[E^{IV}_4]^{4-}$ cluster is a *nido*-system with $n+2$ skeletal electron pairs and the expected tetrahedral geometry. Similarly, the $[E^{IV}_9]^{4-}$ cluster anions also have the electron count expected for a *nido*-cluster and exhibit a monocapped square antiprismatic geometry (with C_{4v} symmetry and derived from a bicapped square antiprism).

Closely related to the $[E^{IV}_4]^{4-}$ tetrahedra described above are the more reduced anions $[E^{IV}_4]^{6-}$ (E = Si, Ge) which have been isolated in $Ba_3E^{IV}_4$ phases [98–100]. These butterfly-shaped anions can be thought of as reduced forms of $[E^{IV}_4]^{4-}$ tetrahedra where an E^{IV}–E^{IV} bond has been cleaved, and two of the atoms carry a formal 2– charge (Fig. 4). This is the result of populating a σ*-orbital which

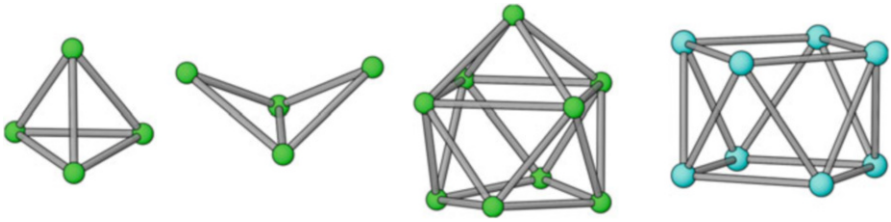

Fig. 4 Electron-deficient clusters of the group 14 elements (and selected solid-state phases in which they occur). From *left* to *right*: Si_4^{4-} (Na_4Si_4), Si_4^{6-} (Ba_3Si_4), Si_9^{4-} ($K_{12}Si_{17}$), and Sn_8^{6-} (KLi_2Sn_8)

effectively results in reductive cleavage of one of the bonds of the tetrahedron. Alternatively, such species can also be considered as *arachno*-clusters with $n+3$ skeletal electron pairs. Consequently, the anions exhibit structures derived from an octahedron that is missing two adjacent vertices.

The final family of clusters worth mentioning in this section is the $[Sn_8]^{6-}$ anions discovered by Sevov and coworkers in the ternary compound Li_2ASn_8 (A = K, Rb) (Fig. 4) [101]. These phases contain square antiprismatic cluster anions consistent with the $n+3$ skeletal electron pairs available for cluster bonding. As with $[E_4^{IV}]^{6-}$, that makes the Sn_8^{6-} anion an *arachno*-species, and the geometry is derived from a bicapped square antiprism that is missing the two capping vertices. (It is interesting to note at this stage that, unlike boranes, where *arachno*-species are typically generated by removal of adjacent vertices, the same does not seem to hold true for Zintl anions.) That being said, this geometry is clearly stabilized in the solid state by close interactions between the square faces of the Sn_8^{6-} anion and the Li^+ cations. If such interactions are considered as covalent, i.e., there has not been completed electron transfer from the lithium metal to the cluster anion, the cluster can also be considered as a *closo*-$(Li_2Sn_8)^{4-}$ system with $n+1$ skeletal electron pairs. The same cluster geometry (albeit with a different overall negative charge) is also observed in $Ba_{16}Na_{204}Sn_{310}$ [102]. This phase also contains Sn_{56}^{44-} cluster anions and $[Na@Sn_{12}]^{12-}$ anions. This type of endohedral clusters, $[A@E^{IV}{}_{12}]^{12-}$ (where A = Na and Li), is also known to occur in $AeNa_{10}Sn_{12}$ and Li_7RbGe_8 (the latter of which also contains $[Ge_4]^{4-}$ tetrahedra) [103, 104].

3.5 Solution-Phase Behavior

It is interesting to note that on account of the relatively small overall negative charges associated with some of these anions, phases such as $A_4E^{IV}{}_4$, $A_4E^{IV}{}_9$, and $A_{12}E^{IV}{}_{17}$ are soluble in polar non-protic solvents such as liquid ammonia. Dissolution of these phases gives rise to solutions containing the homoatomic polyanions discussed earlier. These polyanions can subsequently be recrystallized from solution or used as precursors to a number of additional homo- and heteroatomic cluster anions (see Table 4) [105–156].The solution-phase reactivity of group 14 Zintl ions

Table 4 Isolated anionic structural motifs of the group 14 elements isolated from solution

Anion	Element	Compound	References
$[E^{IV}_4]^{4-}$	Sn	$Rb_4Sn_4{\cdot}2NH_3$	[105]
		$Cs_4Sn_4{\cdot}2NH_3$	[105]
	Pb	$Rb_4Pb_4{\cdot}2NH_3$	[105]
$[E^{IV}_5]^{2-}$	Si	$[K(2,2,2\text{-crypt})]_2Si_5{\cdot}4NH_3$	[106]
		$[Rb(2,2,2\text{-crypt})]_2Si_5{\cdot}4NH_3$	[107]
	Ge	$[K(2,2,2\text{-crypt})]_2Ge_5{\cdot}THF$	[108]
		$[A(2,2,2\text{-crypt})]_2Ge_5{\cdot}4NH_3$ (A = K, Rb)	[109]
	Sn	$[Na(2,2,2\text{-crypt})]_2Sn_5$	[110]
		$[K(2,2,2\text{-crypt})]_2Sn_5$	[111]
	Pb	$[Na(2,2,2\text{-crypt})]_2Pb_5$	[110, 112]
$[E^{IV}_9]^{4-}$	Si	$Rb_4Si_9{\cdot}4.75NH_3$	[113]
		$Rb_4Si_9{\cdot}5NH_3$	[106]
		$Rb_3[Rb(18\text{-crown-}6)]Si_9{\cdot}4NH_3$	[113]
	Ge	$K_4Ge_9{\cdot}9NH_3$	[114]
		$Rb_4Ge_9{\cdot}5NH_3$	[114]
		$A_4Ge_9{\cdot}en$ (A = Rb, Cs)	[115, 116]
		$[K(18\text{-crown-}6)]_6(Ge_9)_2{\cdot}2.5en$	[117]
		$K_3[K(2,2,2\text{-crypt})]Ge_9{\cdot}2en$	[118]
	Sn	$Na_4Sn_9{\cdot}7en$	[119, 120]
		$[Li(NH_3)_4]_4Sn_9{\cdot}NH_3$	[121]
		$[Na(2,2,2\text{-crypt})]_4Sn_9$	[112, 122]
		$K_2[K(18\text{-crown-}6)]_2Sn_9{\cdot}1.5en$	[123]
		$K[K(2,2,2\text{-crypt})]_3Sn_9$	[124, 125]
		$K[K(2,2,2\text{-crypt})]_3Sn_9{\cdot}18NH_3$	[126]
		$[K(2,2,2\text{-crypt})]_4Sn_9$	[125]
		$Rb_2[Rb(18\text{-crown-}6)]_2Sn_9{\cdot}1.5en$	[127]
		$Cs_2[K(diaza\text{-}18\text{-crown-}6)]_2Sn_9{\cdot}2en$	[128]
		$Cs_7[K(2,2,2\text{-crypt})](Sn_9)_2{\cdot}3en$	[129]
	Pb	$[Li(NH_3)_4]_4Sn_9{\cdot}NH_3$	[120]
		$K_2[K(18\text{-crown-}6)]_2Pb_9{\cdot}1.5en$	[130]
		$[K(18\text{-crown-}6)]_4Pb_9{\cdot}en{\cdot}tol$	[131]
		$K[K(2,2,2\text{-crypt})]_3Pb_9$	[132]
$[E^{IV}_9]^{3-}$	Si	$[K(2,2,2\text{-crypt})]_3Si_9{\cdot}8NH_3$	[107]
		$[K(2,2,2\text{-crypt})]_3Si_9{\cdot}2.5py$	[107]
		$[Rb(2,2,2\text{-crypt})]_6(Si_9)_2{\cdot}6.3NH_3$	[107]
	Ge	$[K(2,2,2\text{-crypt})]_3Ge_9{\cdot}x\text{en}$ ($x = 0.25, 0.5, 0.75$)	[133, 134]
		$K_4[K(2,2,2\text{-crypt})]_2(Ge_9)_2{\cdot}6en$	[135]
		$[K(2,2,2\text{-crypt})]_3Ge_9{\cdot}PPh_3$	[136]
		$[K(18\text{-crown-}6)][Rb(18\text{-crown-}6)]_2Ge_9{\cdot}6NH_3$	[137]
		$[Rb(18\text{-crown-}6)]_3Ge_9{\cdot}9NH_3$	[137]
		$[Cs(18\text{-crown-}6)]_3Ge_9{\cdot}6NH_3$	[137]

(continued)

Table 4 (continued)

Anion	Element	Compound	References
	Sn	$[K(2,2,2\text{-crypt})]_3Sn_9 \cdot 1.5en$	[138]
		$[K(2,2,2\text{-crypt})]_6(Sn_9)_2 \cdot 1.5en \cdot 0.5tol$	[133, 139]
		$[K(2,2,2\text{-crypt})]_3Sn_9 \cdot 0.5tol$	[140, 141]
	Pb	$[K(2,2,2\text{-crypt})]_3Pb_9$	[132]
		$[K(2,2,2\text{-crypt})]_3Pb_9 \cdot 0.5en$	[133]
		$[K(2,2,2\text{-crypt})]_6(Pb_9)_2 \cdot 1.5en \cdot 0.5tol$	[133, 139]
$[E^{IV}_9]^{2-}$	Si	$[K(2,2,2\text{-crypt})]_2Si_9 \cdot py$	[142]
	Ge	$[K(2,2,2\text{-crypt})]_2Ge_9$	[143]
		$[K(18\text{-crown-}6)]_6(Ge_9)_2 \cdot 2.5en$	[117]
$[E^{IV}_{10}]^{2-}$	Ge	$[K(2,2,2\text{-crypt})]_2Ge_{10}$	[144]
	Pb	$[K(2,2,2\text{-crypt})]_2Pb_{10}$	[145]
$[(E^{IV}_9)_2]^{6-}$	Ge	$K_{12}[(Ge_9)_2]_2 \cdot 25DMF$	[146]
		$Rb_6(Ge_9)_2 \cdot 12DMF$	[146]
		$K_4[K(2,2,2\text{-crypt})]_2(Ge_9)_2 \cdot 14NH_3$	[147]
		$K_3[K(2,2,2\text{-crypt})]_3(Ge_9)_2 \cdot 18NH_3$	[147]
		$K_2[K(2,2,2\text{-crypt})]_4(Ge_9)_2 \cdot 17.3NH_3$	[147]
		$K_4[K(2,2,2\text{-crypt})]_2(Ge_9)_2 \cdot 4en$	[148]
		$Rb_4[Rb(2,2,2\text{-crypt})]_2(Ge_9)_2$	[148]
		$Rb_4[Rb(2,2,2\text{-crypt})]_2(Ge_9)_2 \cdot 4en$	[148]
		$Cs_3[K(2,2,2\text{-crypt})]_3(Ge_9)_2$	[148]
		$Cs_4[K(2,2,2\text{-crypt})]_2(Ge_9)_2 \cdot 6en$	[149]
$[(E^{IV}_9)_3]^{6-}$	Ge	$[K(18\text{-crown-}6)]_6(Ge_9)_3 \cdot 3en \cdot tol$	[150]
		$[Rb(2,2,2\text{-crypt})]_6(Ge_9)_3 \cdot 3en$	[151]
$[(E^{IV}_9)_4]^{8-}$	Ge	$[K(18\text{-crown-}6)]_8(Ge_9)_4 \cdot 8en$	[152]
		$[Rb(18\text{-crown-}6)]_8(Ge_9)_4 \cdot 2en$	[153]
		$[Rb(18\text{-crown-}6)]_8(Ge_9)_4 \cdot 6en$	[153]
$[(E^{IV}_9)_\infty]^{2-}$	Ge	$\{[K(18\text{-crown-}6)]_2Ge_9 \cdot en\}_\infty$	[154]
		$\{K[K(2,2\text{-diaza-}18\text{-crown-}6)]Ge_9 \cdot 3en\}_\infty$	[155]
		$\{[Rb_2(4,2,1,1\text{-crypt})]Ge_9 \cdot en\}_\infty$	[156]

2,2,2-crypt 4,7,13,16,21,24-hexaoxa-1,10-diazabicyclo[8.8.8]hexacosane, *THF* tetrahydrofuran, *18-crown-6* 1,4,7,10,13,16-hexaoxacyclooctadecane, *en* ethylenediamine, *tol* toluene, *py* pyridine, *DMF* dimethylformamide, *2,2-diaza-18-crown-6* 1,4,10,13-tetraoxa-7,16-diazacyclooctadecane, *4,2,1,1-crypt* a dimeric crypt and obtained from radical coupling of two molecules of 2,2,2-crypt

has been extensively reviewed in the recent literature, and the reader is referred to these excellent articles for information outside of the remit of this review, namely, on the synthesis or heteroatomic cluster anions [157–160].

The first group 14 homoatomic polyanions to be isolated from solution and structurally authenticated, $[E^{IV}_9]^{4-}$ (E = Ge, Sn), were reported by Diehl in 1976 [119, 120]. These were obtained by dissolution of A/E^{IV} phases in ethylenediamine. The following year, Corbett showed that the addition of a cation-sequestering agent such as 2,2,2-crypt facilitated the dissolution of such phases and aided crystallization as the sequestered counter-cations had a greater radius and packed more

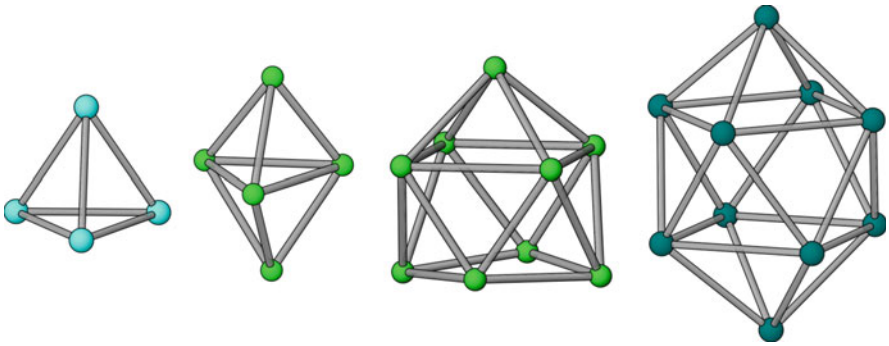

Fig. 5 Electron-deficient clusters of the group 14 elements available from solution. From *left* to *right*: Sn_4^{4-}, Si_5^{2-}, Si_9^{2-}, and Pb_{10}^{2-}

efficiently with the anions [122]. These sequestering agents also prevented the transfer of electrons from the homoatomic polyanion back to the cation. This strategy of dissolving a preformed binary phase in the presence of a cation-sequestering agent allowed for the isolation of a wide library of cluster anions from solution in subsequent years $[E^{IV}_9]^{x-}$ and $[E^{IV}_5]^{2-}$ ($x = 3$, 4; E^{IV} = Ge, Sn, Pb). These anions are pictured in Fig. 5.

Perhaps the most notable observation that can be made from these early solution-phase studies is that the $[E^{IV}_9]^{4-}$ cluster anions that are present in $A_4E^{IV}_9$ phases are readily oxidized in solution, affording species where there is a reduced net negative change per atom. An example of this is the solution-phase isolation of $[E^{IV}_5]^{2-}$ (E^{IV} = Ge, Sn, Pb), a family of *closo*-trigonal pyramidal clusters that can be obtained from solutions of $A_4E^{IV}_9$-type precursors (Fig. 5) [108–112]. In these clusters, the net negative charge per group 14 element (0.40–) is reduced from that of the $[E^{IV}_9]^{4-}$ precursor (0.44–), indicating the potential for complex solution-phase dynamics. It is interesting to note that to date, $[E^{IV}_5]^{2-}$-type clusters have not been isolated in the solid state. Similar considerations can be made for the isolation of higher-nuclearity cluster anions such as $[E^{IV}_{10}]^{2-}$ (E = Ge, Pb) (see Fig. 5) [144, 145]. It is worth noting at this point that while Pb_{10}^{2-} has been clearly identified in solution, the structural corroboration of Ge_{10}^{2-} is still disputed and believed to be a Ge_9^{2-} cluster which exhibits extensive crystallographic disorder. In these formally *closo*-bicapped square antiprismatic clusters, the overall negative charge associated with the anions (0.22–) is significantly reduced from that of the $[E^{IV}_9]^{4-}$ precursors. The mechanism for the formation of both $[E^{IV}_5]^{2-}$ and $[E^{IV}_{10}]^{2-}$ cluster anions from solutions of binary phases that exclusively contain $[E^{IV}_9]^{4-}$ clusters is one of the great unsolved mysteries in this area of chemistry. Clearly, these are electrochemical processes which result in a net cluster oxidation, yet the solution dynamics which permit a variation of cluster nuclearity are entirely ignored. There must be a significant degree of cluster aggregation and dissociation in solution which, in turn, is accompanied by complex redox equilibria.

Another example of this redox activity is the solution-phase behavior of $[E^{IV}_9]^{4-}$ which can be oxidized to the radical trianion, $[E^{IV}_9]^{3-}$, and diamagnetic dianion, $[E^{IV}_9]^{2-}$ [107, 117, 133–143]. The first indications for this came from early literature reports of the seemingly arbitrary synthesis of $[E^{IV}_9]^{3-}$ and $[E^{IV}_9]^{4-}$. Apparently similar conditions would result in the crystallization of clusters with differing net charges. It was later observed that the syntheses often differed in the amount of sequestering agent added to the reaction mixture. This seemingly insignificant factor plays an important role in the crystallization of these species, as one of the roles of the sequestering agent is to provide cations of a size comparable to that of the anionic clusters. The effective size of the complex cation of 2,2,2-crypt with a captured alkali-metal cation is nearly 56 times larger than that of a naked alkali-metal cation. Sevov has proposed that four of such cations are too large to effectively pack with $[E^{IV}_9]^{4-}$ and the crystalline product is typically $[E^{IV}_9]^{3-}$. This is not to say that a $[E^{IV}_9]^{4-}$ cation cannot be isolated with four encapsulated cations but rather that other phases crystallize more readily. Conversely, a deficiency of sequestering agent (by approximately 25%) results in the availability of smaller naked alkali-metal cations, and a combination of three large cations and one small one packs well with $[E^{IV}_9]^{4-}$ in a crystal lattice, as found in compounds such as $K[K(2,2,2\text{-crypt})]_3[E^{IV}_9]$. These observations suggest that $[E^{IV}_9]^{3-}$ and $[E^{IV}_9]^{4-}$ coexist in solution and that the crystalline product depends on the sizes of the available cations. The Sevov group has shown that in the case of germanium (and in all likelihood tin and lead), the three differently charged clusters coexist in solution in complex equilibria with solvated electrons.

Also worth highlighting at this stage is a recent seminal study by Eichhorn and coworkers showing that protonation of the Sn_9^{4-} cluster anion to afford $(HSn_9)^{3-}$ in solution is also a possibility [161]. The authors unequivocally demonstrated the existence of the protonated anion by means of ^{119}Sn and $^{119}Sn\{^1H\}$ nuclear magnetic resonance (NMR) experiments and were able to structurally identify the protonated anion in $[K(2,2,2\text{-crypt})]_3(HSn_9)\cdot 1.5en$. The ^{119}Sn NMR spectrum of $(HSn_9)^{3-}$ shows a single time-averaged resonance which appears with satellites due to ^{117}Sn containing isotopomers, however crucially, and, in contrast to the spectrum of Sn_9^{4-} (*vide infra*), exhibits a weak $^{119}Sn–^1H$ coupling constant of 21 Hz. These studies show that in addition to redox equilibria allowing for the interconversion of nonatetralide anions with 2–, 3–, and 4– charges, additional Brønsted acid–base equilibria may also be at play, further complicating the solution-phase behavior of these anions. This recent study suggests that several of the known structures for $[E^{IV}_9]^{3-}$ anions may in fact contain the $[HE^{IV}_9]^{3-}$ anion, although the paramagnetic character of a number of $[E^{IV}_9]^{3-}$ anions (E = Ge, Sn, Pb) has been established by means of EPR spectroscopy [162]. In all cases, the spectra exhibit broad resonances and display no resolvable hyperfine coupling.

One of the advantages of solution-phase methods is that they allow for the spectroscopic characterization of such cluster anions. The first studies in the area were reported by Rudolph and coworkers who recorded the ^{119}Sn and ^{207}Pb NMR spectra for Sn_9^{4-} and Pb_9^{4-} [163, 164]. The most notable observation was that

despite having C_{4v} monocapped square antiprismatic topology in the solid state, these cluster anions are highly fluxional, exhibiting a single resonance in solution (even at −40°C in liquid ammonia). This fluxionality is believed to proceed via a "diamond–square–diamond"-type mechanism. It is worth noting that the energy barrier between the monocapped square antiprismatic (C_{4v}) and tricapped trigonal prismatic (D_{3h}) geometries is relatively small and that often both cluster topologies are observed in the same lattice [95]. The chemical shifts for these resonances are found to be highly cation dependent, indicating the electrostatic interaction of cations and anions in solution. Thus while solutions of Li_4Sn_9 exhibit a resonance at −1,241 ppm, solutions of Cs_4Sn_9 resonate at −1,115 ppm. Logically these chemical shifts are strongly dependent on the presence of cation-sequestering agents and solvent which disrupt such interactions. The same is true for solutions of Pb_9^{4-}. The presence of two NMR active tin isotopes ^{117}Sn and ^{119}Sn gives rise to multiplet structures due to coupling between the different isotopomers. Thus, the ^{119}Sn NMR spectrum of Sn_9^{4-} exhibits a multiplet pattern with a distribution of line intensities in a 0.05:0.23:0.65:1:0.65:0.23:0.05 ratio. It is interesting to note that while this fluxionality is observed by NMR spectroscopy (which has a relatively slow timescale), ^{119}Sn Mössbauer spectra of $[Na(2,2,2\text{-crypt})]_4Sn_9$ crystals at 77K reveal three environments in roughly a 4:4:1 ratio [165]. At higher temperature, Mössbauer and EXAFS studies suggest fluxional behavior [166].

Binary phases containing more reduced anions, such as $A_4E^{IV}{}_4$ and $A_{12}E^{IV}{}_{17}$, are less soluble in solvents such as ethylenediamine. The high negative charges associated with the anions are believed to reduce the solvent to dihydrogen and an amide, resulting in oxidized clusters with reduced negative charges. Consequently, highly reduced cluster anions are only isolable using liquid ammonia as a solvent. This has been elegantly demonstrated by Korber and coworkers who have shown that dissolution of $A_4E^{IV}{}_4$ phases in liquid ammonia can be used for the isolation of Sn_4^{4-} and Pb_4^{4-} clusters [105]. A similar strategy involving the dissolution of $K_{12}Si_{17}$ and $Rb_{12}Si_{17}$ allowed for the isolation of the first silicon-containing Zintl ions from solution: Si_9^{3-} and Si_5^{2-} [107]. The Si_9^{2-} dianion was reported soon afterward, as were electrochemical studies which demonstrated a quasi-reversible interconversion between Si_9^{3-} and Si_9^{2-} [142].

$[E^{IV}{}_4]^{4-}$ (E = Si, Sn) cluster anions have also recently been spectroscopically identified in solution. The tetrahedral silicon species Si_4^{4-} was observed as a singlet resonance at −323 ppm [167]. This value is close to the chemical shifts observed in the MAS spectra of K_4Si_4 and Rb_4Si_4 [168, 169]. The analogous Sn_4^{4-} cluster exhibits a ^{119}Sn resonance at −1,727 ppm with a coupling constant of 1,466 Hz and a satellite pattern arising due to coupling with ^{117}Sn nuclei in a 0.12:1:0.12 ratio. Interestingly, a similar coupling pattern and a comparable chemical shift of −1,895 ppm have previously been attributed to the more oxidized Sn_4^{2-} anion [170], a species which has been observed in the solid state [171]. Neither Pb_4^{4-}nor Pb_4^{2-} has been observed in solution.

A final redox phenomenon which is characteristic of nonatetralide clusters, $[E^{IV}{}_9]^{4-}$, is their ability to oxidatively couple to afford oligomeric and polymeric species (Fig. 6) [146–156]. This phenomenon thus far appears to be the exclusive domain of germanium-containing cluster anions. Two Ge_9^{4-} cluster

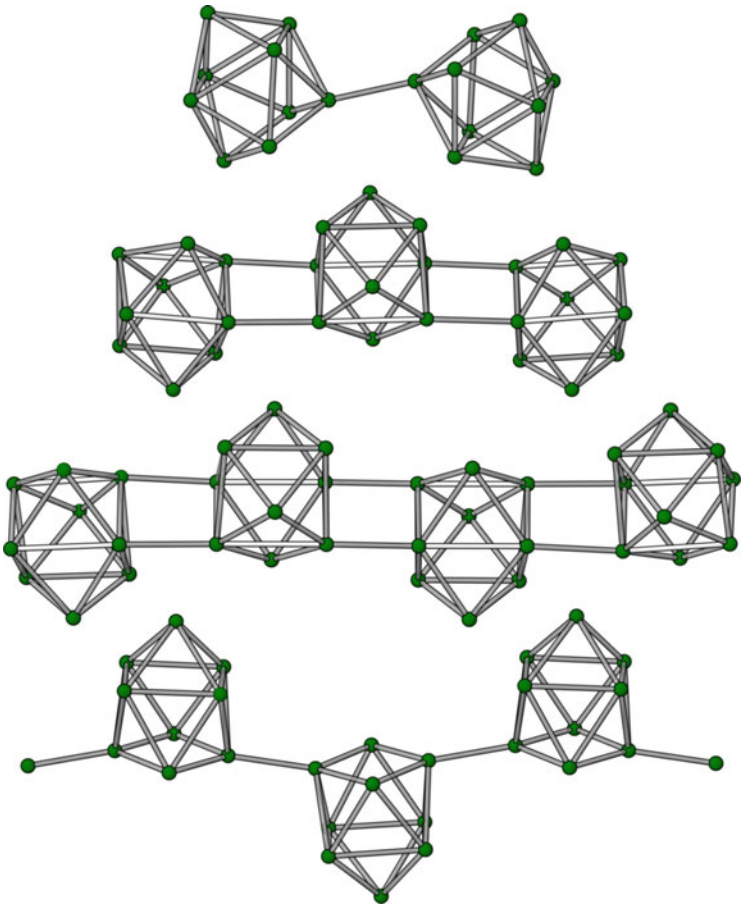

Fig. 6 Oligomeric and polymeric clusters resulting from oxidative coupling of $[Ge_9]^{4-}$. From *top* to *bottom*: $(Ge_9)_2^{6-}$, $(Ge_9)_3^{6-}$, $(Ge_9)_4^{8-}$, and $(Ge_9)_\infty^{2-}$. *White bonds* indicate long Ge–Ge interactions

anions can couple to form a dimeric $(Ge_9–Ge_9)^{6-}$ species in which the clusters are connected by a single two-center, two-electron bond [146–149]. The formation of such a compound is the net result of a two-electron oxidation. In related transformations, the cluster anions can couple to give rise to extended one-dimensional polymer chains $(Ge_9)_\infty^{2-}$ [154–156]. As with the dimeric analogue, the intercluster bonds in such polymeric structures are consistent with conventional Ge–Ge single bonds. Perhaps more interestingly, such clusters can also give rise to oligomeric species which exhibit delocalized bonding. Thus trimeric and tetrameric clusters are also known $(Ge_9)_3^{6-}$and $(Ge_9)_4^{8-}$ [150–153]. In these oligomeric species, intercluster separation is typically much greater and consistent with electron delocalization along the oligomer backbone (in other words, the intercluster bonds are not two-center, two-electron bonds).

4 Homoatomic Polyanions of Group 15

On moving from the elements of group 14 to those of group 15, the availability of an additional valence electron per element permits a greater degree of structural variations for the formation of polyanionic species. Critically, the greater number of electrons allows for the formation of electron-precise structures. That is to say, species in which all of the bonds represent two-center, two-electron bonds.

In contrast to the known polyanions of the earlier p-block groups, many of the known polyanions of the group 15 elements (pnictogens) were first identified via solution-phase methods, via the reduction of the elements in the presence of an alkali metal. This is particularly true in the case of phosphorus-containing systems, where ^{31}P NMR spectroscopy allowed for the identification of polyanions in solution. That being said, a vast number of species have been identified in the solid state, accessed by thermal treatment of the pnictogen elements with more electropositive elements, typically alkali metals. The solid-state chemistry of polypnictides was reviewed by von Schnering in 1988 in a remarkably thorough review article [172]. We will discuss the isolated polyanions which are known to occur in solid-state phases of the pnictogens first (Table 5) [173–202].

The simplest polyanion of the group 15 elements is the dimeric $[E^V_2]^{2-}$ anion which was first characterized in Cs_3Bi_2 [173]. This species is another example of a "metallic Zintl phase" and is best represented as $[Cs^+]_3[Bi_2{}^{2-}][e^-]$. Magnetic measurements on this phase indicated temperature-independent magnetization and positive corrected molar susceptibility, indicating Pauli-type paramagnetic behavior consistent with metallic conductivity. This suggests the presence of the $Bi_2{}^{2-}$ anion which is isoelectronic with singlet dioxygen. The short Bi–Bi distance of 2.976(2) Å is the shortest of its kind observed in neat solids and indicative of higher bond order.

Longer, electron-precise chains which satisfy the valence bond concept have also been identified in solid-state phases; thus $[E^V_3]^{5-}$, $[E^V_4]^{6-}$, $[E^V_6]^{8-}$, and $[E^V_8]^{10-}$ have all been structurally authenticated in solids (Fig. 7) [176, 179–181, 187]. As would be expected for linear systems derived from elements which possess five valence electrons, in order to satisfy the octet rule, all central atoms of the chain must carry a formal negative charge while terminal atoms are formally dianionic. Thus, electron-precise chains should generally conform to the formula $[E^V_n]^{(n+2)-}$. This is however not always the case, and there are a handful of systems which carry a reduced negative charge. These systems are believed to possess a greater degree of multiple-bond character. One such family of compounds is the $[E^V_4]^{4-}$ anions isolated in phases such as $A_5E^V_4$ (A = K, Rb, Cs) [177, 178]. As with the Cs_3Bi_2 phase discussed above, these phases are also examples of metallic salts exhibiting temperature-independent Pauli-like paramagnetism. Structurally, they exhibit alternating long–short–long bond distances which are shorter than the values expected for single E^V–E^V bonds.

Cyclic systems have also structurally authenticated in solid-state phases. The smallest of these, $As_3{}^{3-}$, was identified in CsAs [174]. An expanded electron-

Table 5 Isolated homoatomic chain, ring, and cage structural motifs found in polypnictides synthesized through solid-state methods

Anion	Element	Compound	References
$[E^{V}_{2}]^{2-}$	Bi	Cs_3Bi_2	[173]
$[E^{V}_{3}]^{3-}$	As	Cs_3As_3	[174]
$[E^{V}_{3}]^{4-}$	P	K_4P_3	[175]
$[E^{V}_{3}]^{5-}$	P	KBa_4P_5	[176]
$[E^{V}_{4}]^{4-}$	As, Sb, Bi	$A_5E^{V}_{4}$ (A = K, Rb, Cs)	[177, 178]
$[E^{V}_{4}]^{6-}$	P, As	$Ae_3E^{V}_{4}$ (Ae = Ca, Sr, Ba)	[179–181]
$[E^{V}_{5}]^{5-}$	As	ABa_2As_5 (A = K, Rb)	[182]
$[E^{V}_{6}]^{4-}$	P	K_4P_6	[183]
		Rb_4P_6	[184, 185]
		Cs_4P_6	[185]
	As	A_4As_6 (A = Rb, Cs)	[186]
$[E^{V}_{6}]^{8-}$	Sb	Ae_2Sb_3 (Ae = Ba, Sr)	[187]
$[E^{V}_{7}]^{3-}$	P	Li_3P_7	[188]
		Na_3P_7 (A = Na–Rb)	[189]
		Cs_3P_7	[189, 190]
		Sr_3P_{14}	[191]
		Ba_3P_{14}	[192]
	As	Li_3As_7	[193]
		Na_3As_7	[194]
		K_3As_7	[175]
		Rb_3As_7	[175, 195]
		Cs_3As_7	[176]
		Ba_3As_{14}	[196]
	Sb	Rb_3Sb_7	[197]
		Cs_3Sb_7	[197, 198]
$[E^{V}_{8}]^{10-}$	Sb	Ca_2As_3	[180]
$[E^{V}_{9}]^{10-}$	P	Ba_5P_9	[199]
$[E^{V}_{11}]^{3-}$	P	Na_3P_{11}	[200]
		K_3P_{11} (A = K–Cs)	[201]
	As	K_3As_{11}	[201]
		A_3As_{11} (A = Rb, Cs)	[201, 202]

precise ring has also been identified for arsenic in As_5^{5-} which exhibits a nonplanar "envelope"-type structure in which each As–As bond is formally a two-center, two-electron single bond [182]. Arguably, the most interesting species in this family of compounds are the $[E^{V}_{6}]^{4-}$ anions (E^{V} = P, As) which are aromatic according to Hückel's rules for aromaticity [183–186]. Interestingly, however, the ^{31}P MAS NMR spectra of K_4P_6 do not reveal a low-field chemical shift for the P_6^{4-} anion, in contrast to what would be expected for an aromatic compound. Moreover, quantum chemical calculations reveal that the optimized geometry of the P_6^{4-} ring is not planar but rather slightly distorted to afford a chair-like conformations. This

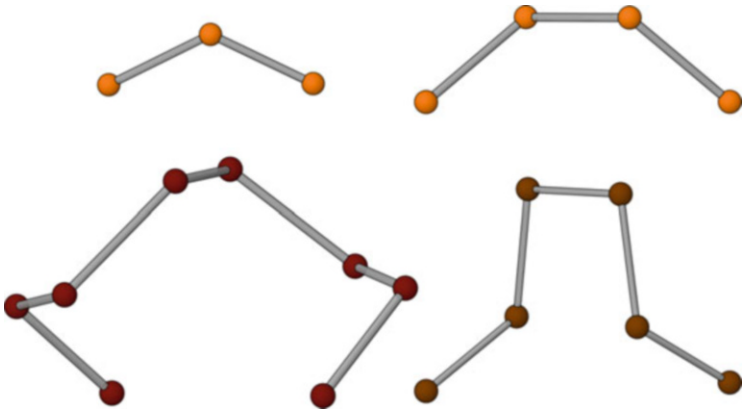

Fig. 7 Electron-precise chains of the group 15 elements isolated in the solid state (and selected solid-state phases in which they occur). Clockwise from *top left*: P_3^{5-} (KBa_4P_5), P_4^{6-} (Sr_3P_4), Sb_6^{8-} (Ba_2Sb_3), and As_8^{10-} (Ca_2As_3)

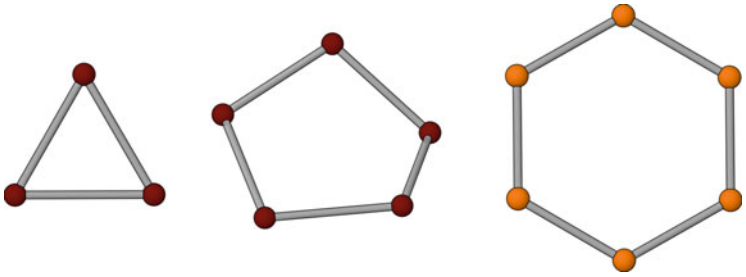

Fig. 8 Cyclic compound of the group 15 elements (and selected solid-state phases in which they occur). From *left* to *right*: As_3^{3-} (Cs_3As_3), As_5^{5-} (KBa_2As_5), and P_6^{4-} (K_4P_6)

has led to the hypothesis that the planarity observer for the P_6^{4-} anion may in fact be crystallographically imposed [203, 204]. Selected cyclic anions are pictured in Fig. 8.

The final family of polyanions isolated from Zintl ion phases is the electron-precise clusters $[E^V_7]^{3-}$ ($E^V = P$, As, Sb) and $[E^V_{11}]^{3-}$ ($E^V = P$, As) (Fig. 9) [175, 188–198, 200–202]. The first of these cluster anions, $[E^V_7]^{3-}$, exhibits a nortricyclane-type structure with C_{3v} symmetry. It can be thought of as a tetrahedron in which three pnictide vertices are inserted along adjacent E^V–E^V bonds. The P_7^{3-} anion has been shown to be fluxional in both solution and the solid state as evidenced by ^{31}P NMR spectroscopy, and the nature of this fluxional behavior will be discussed in greater detail below. The $[E^V_{11}]^{3-}$ anion exhibits a D_{3d} symmetric "ufosane" structure. The solution-phase dynamics of these anions are discussed in further detail below.

The solution-phase chemistry of the polyanions of group 15 is among the richest, and most thoroughly studied, of the p-block elements. This is particularly true for phosphorus-containing polyanions which can be studied by means of ^{31}P NMR

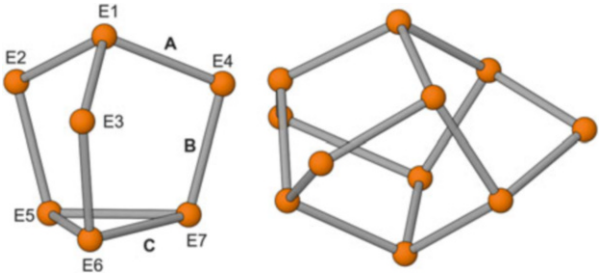

Fig. 9 Cluster compounds of the group 15 elements (and selected solid-state phases in which they occur) isolated in the solid state. From *left* to *right*: P_7^{3-} (Li_3P_7) and P_{11}^{3-} (K_3P_{11})

spectroscopy. This spectroscopic handle allowed for the discovery of many anionic polyphosphides prior to the elucidation of their structures. The chemical reduction of elemental phosphorus with alkali metals in solution affords a wide range of anionic polyphosphides, many of which can be targeted as compositionally pure compounds by careful control of stoichiometric loadings, solvents, and reaction conditions. A number of research groups have made significant contributions to this area; however, special mention must be made of the pioneering work of Baudler who identified a number of phosphorus-containing polyanions through the interpretation of what were often phenomenally complex ^{31}P NMR spectra [205–207]. Many of the polyanions they first identified have since been structurally authenticated. A table of all of the known polypnictide anions isolated from solution is presented in Table 6 [203, 208–260].

The simplest of the polyanions isolated using solution-phase methods is the $[Bi_2]^{2-}$ anion which has also been observed in solid-state phases (*vide supra*) [208]. The Bi–Bi distance in this anion is 2.8377(7) Å which is significantly shorter than that observed in Cs_3Bi_2 (2.976(2) Å) and consistent with a double bond.

Cyclic $[E^V_4]^{2-}$-type anions are known for all of the heavier group 15 elements [209–215]. The first of these anions to be isolated, Bi_4^{2-}, was reported by Corbett in 1977 [214].The discovery of the antimony analogue followed in 1984 [213]. More recently, Korber and coworkers have been able to isolate the lighter analogues from liquid ammonia solutions [209–212]. It is worth nothing that P_4^{2-} cannot be isolated by direct reduction of white phosphorus in liquid ammonia solutions but rather requires diphosphane ($H_2P–PH_2$) as a precursor. When white phosphorus is reduced under similar conditions, the reactions afford P_7^{3-}. As would be expected for cyclic systems with six electrons available in the π-manifold, all of the $[E^V_4]^{2-}$ anions are planar and exhibit D_{4h} geometries. The aromatic character of these anions is further corroborated by the ^{31}P NMR spectrum of P_4^{2-} which exhibit a downfield shift of 345.8 ppm at –60 °C in liquid ammonia. A formal reduction of Bi_4^{2-} with an additional four electrons results in a linear zigzag chain of Bi_4^{6-}, similar to the $[E^V_4]^{6-}$ (E = P, As) chains which have been isolated in binary phases.

One of the most interesting homoatomic polyanions of the group 15 elements is the pentaphospholide anion (or pentaphosphacyclopentadienide ion), P_5^-. This species was first reported by Baudler and coworkers in 1987 and is isolobal with the ubiquitous cyclopentadienide anion. The anion was first obtained by refluxing a

Table 6 Isolated homoatomic chain, ring, and cage structural motifs found in polypnictides synthesized through solution methods (and in some cases also solid-state methods). In some cases, structures are known with many different cations or solvates. We have endeavored to include all of these

Anion	Element	Compound	References	Synthetic method
$[E^{V}_2]^{2-}$	Bi	$[K(2,2,2\text{-crypt})]_2Bi_2$	[208]	Solution/solid state
$[E^{V}_4]^{2-}$	P	$Cs_2P_4{\cdot}2NH_3$	[209, 210]	Solution
		$[K(18\text{-crown-}6)]_2P_4{\cdot}8.5NH_3$	[211]	Solution
	As	$[Li(NH_3)_4]_2As_4$	[212]	Solution
		$[Na(NH_3)_5]_2As_4{\cdot}3NH_3$	[212]	Solution
		$[Cs_{0.35}Rb_{0.65}(2,2,2\text{-crypt})]_2As_4{\cdot}2NH_3$	[212]	Solution
	Sb	$[K(2,2,2\text{-crypt})]_2Sb_4$	[213]	Solution
	Bi	$[K(2,2,2\text{-crypt})]_2Bi_4$	[214]	Solution
		$[A(2,2,2\text{-crypt})]_2Bi_4(A = K, Rb)$	[215]	Solution
$[E^{V}_4]^{6-}$	Bi	$K_6Bi_4{\cdot}8NH_3$	[216]	Solution
$[E^{V}_5]^{-}$	P	NaP_5 solutions in THF	[217–219]	Solution
$[E^{V}_5]^{5-}$	Sb	$[Li(NH_3)_4]_3[Li(NH_3)]_2Sb_5{\cdot}2NH_3$	[220]	Solution
$[E^{V}_6]^{4-}$	As	$[Rb(18\text{-crown-}6)]_2Rb_2As_6{\cdot}6NH_3$	[203]	Solution/solid state
$[E^{V}_7]^{3-}$	P	$[Li(TMEDA)]_3P_7$	[221]	Solution/solid state
		$Cs_3P_7{\cdot}3NH_3$	[222]	Solution/solid state
		$Rb_3P_7{\cdot}7NH_3$	[210]	Solution/solid state
		$Ba_3(P_7)_2{\cdot}18NH_3$	[223]	Solution/solid state
		$[NEt_3Me]Cs_2P_7{\cdot}NH_3$	[224]	Solution/solid state
		$[NEt_4]Cs_2P_7{\cdot}4NH_3$	[224]	Solution/solid state
		$[NEtMe_3]Cs_2P_7{\cdot}2NH_3$	[225]	Solution/solid state
		$[NMe_4]_2RbP_7{\cdot}NH_3$	[226]	Solution/solid state
		$[Rb(18\text{-crown-}6)]_3P_7{\cdot}6NH_3$	[211]	Solution/solid state
		$K_3[K(18\text{-crown-}6)]_3P_{72}{\cdot}10NH_3$	[211]	Solution/solid state
	As	$[Li(TMEDA)]_3As_7{\cdot}1.5tol$	[227]	Solution/solid state
		$[Li(NH_3)_4]_3As_7{\cdot}NH_3$	[228]	Solution/solid state
		$Cs_3As_7{\cdot}6NH_3$	[228]	Solution/solid state
		$Cs_3As_7{\cdot}NH_3$	[229]	Solution/solid state
		$[Li(TMEDA)]_3As_7{\cdot}OEt_2$	[230]	Solution/solid state
		$[Li(DME)]_3As_7{\cdot}OEt_2$	[231]	Solution/solid state
		$[NMe_4]_2RbAs_7{\cdot}NH_3$	[232]	Solution/solid state
		$[Rb(18\text{-crown-}6)]_3As_7{\cdot}8NH_3$	[228]	Solution/solid state
		$[PPh_4]_2CsAs_7{\cdot}5NH_3$	[228]	Solution/solid state
		$[K(2,2,2\text{-crypt})]_3K_3As_{72}$	[233]	Solution/solid state
	Sb	$[Li(TMEDA)]_3Sb_7{\cdot}tol$	[234]	Solution/solid state
		$[Na(2,2,2\text{-crypt})]_3Sb_7$	[235]	Solution/solid state
		$Na_3Sb_7{\cdot}4en$	[236]	Solution/solid state
		$[Na(TMEDA)]_3Sb_7{\cdot}3THF$	[227]	Solution/solid state
		$[Li(NHMe_2)_2]_3Sb_7$	[234]	Solution/solid state
		$[Li(TMEDA)]_3Sb_7{\cdot}3tol$	[234]	Solution/solid state
		$[K(2,2,2\text{-crypt})]_3Sb_7{\cdot}2en$	[213]	Solution/solid state
		$[Na(PMDETA)]_3Sb_7{\cdot}tol$	[237]	Solution/solid state
		$[Rb(18\text{-crown-}6)]_3Sb_7{\cdot}4NH_3$	[238]	Solution/solid state
	Bi	$[K(2,2,2\text{-crypt})]_3Bi_7{\cdot}2py$	[239]	Solution

(continued)

Table 6 (continued)

Anion	Element	Compound	References	Synthetic method
$[E^{V}_{8}]^{8-}$	Sb	$K_{17}(NH_2)(Sb_8)_2{\cdot}17.5NH_3$	[240]	Solution
$[E^{V}_{11}]^{3-}$	P	$[NEtMe_3]_4P_{11}$	[241]	Solution/solid state
		$Cs_3P_{11}{\cdot}3NH_3$	[242]	Solution/solid state
		$BaCsP_{11}{\cdot}11NH_3$	[243]	Solution/solid state
		$Cs[NEt_3Me]_2P_{11}{\cdot}5NH_3$	[244]	Solution/solid state
		$[NEt_4]_3P_{11}$	[226]	Solution/solid state
		$[K(18\text{-crown-}6)]_3P_{11}{\cdot}2en$	[245]	Solution/solid state
	As	$[K(2,2,2\text{-crypt})]_3As_{11}$	[246]	Solution/solid state
		$[Cs(18\text{-crown-}6)]_2CsAs_{11}{\cdot}8NH_3$	[246]	Solution/solid state
	Sb	$[Na(2,2,2\text{-crypt})]_3Sb_{11}$	[247]	Solution
		$[K(18\text{-crown-}6)(NH_3)_2]Sb_{11}{\cdot}5.5NH_3$	[246]	Solution
		$[K(2,2,2\text{-crypt})]_3Sb_{11}$	[248]	Solution
		$[Li(12\text{-crown-}4)]_3Sb_{11}$	[249]	Solution
	Bi	$[K(2,2,2\text{-crypt})]_3Bi_{11}{\cdot}2py{\cdot}tol$	[250]	Solution
$[E^{V}_{14}]^{4-}$	P	$Na_4(DME)_{7.5}P_{14}$	[251]	Solution
		$[Na(en)_{1.5}]_4P_{14}$	[251]	Solution
		$[Li(NH_3)_4]_4P_{14}{\cdot}NH_3$	[252]	Solution
	As	$[Rb(18\text{-crown-}6)]_4As_{14}{\cdot}6NH_3$	[252]	Solution
$[E^{V}_{16}]^{2-}$	P	$[Na(18\text{-crown-}6)]_2P_{16}$	[253]	Solution
		$[PPh_4]_2P_{16}$	[254]	Solution
$[E^{V}_{19}]^{3-}$	P	Li, Na, K in DMF, THF or DME	[255]	Solution
$[E^{V}_{21}]^{3-}$	P	Li or Na solutions	[256]	Solution
		$[Li(12\text{-crown-}4)_2]_3P_{21}{\cdot}2THF$	[257]	Solution
$[E^{V}_{22}]^{4-}$	P	$[NEtMe_3]_4P_{22}{\cdot}2NH_3$	[258]	Solution
	As	$[Rb(2,2,2\text{-crypt})]_4As_{22}{\cdot}4DMF$	[259]	Solution
$[E^{V}_{26}]^{4-}$	P	$Li_4P_{26}{\cdot}16THF$	[260]	Solution

TMEDA tetramethylethylenediamine, *DME* dimethoxyethane, *PMDETA* *N,N,N′,N′,N″*-pentamethyldiethylenetriamine, *12-crown-4* 1,4,7,10-tetraoxacyclododecane

bis(2-methoxyethyl)ether (diglyme) suspension of phosphorus and sodium in a 2:1 ratio for 6 h under rigorously inert conditions [207]. The anion was obtained alongside a number of other polyphosphides including P_{16}^{2-}, P_{19}^{3-}, P_{21}^{3-}, and P_{26}^{4-}. A clean solution of the anion may also be obtained by slow addition of a hot THF solution of P_4 to a boiling solution of $Li(PH_2)(DME)$ in THF. The anion exhibits single resonance in the ^{31}P NMR spectrum at 469 ppm which is indicative of its aromatic character. The heavier group 15 element analogues of this remarkable ring system have not yet been isolated as free anions, although a more reduced Sb_5^{5-} anion has been reported by Korber [220]. As expected, this cyclic compound is not planar but rather displays a bent envelope-like structure analogous to the As_5^{5-} anion isolated in ABa_2As_5 (A = K, Rb) [182].

The six-membered ring As_6^{4-}, which was first observed in binary phases A_4As_6 (A = Rb, Cs) [186], has also been isolated from solution [203]. This anion and its phosphorus analogue have planar D_{6h} structures in the phases in which they occur

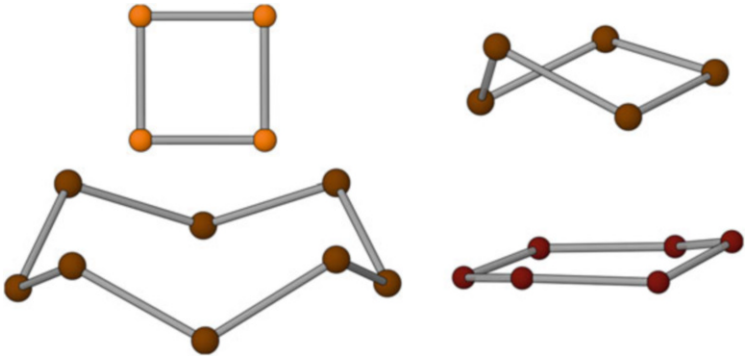

Fig. 10 Cyclic compounds of the group 15 elements isolated using solution-phase methods. Clockwise from *top left*: P_4^{2-},Sb_5^{5-}, As_6^{4-}, and Sb_8^{8-}

and formally have 10 π-electrons available for bonding. When isolated from solution, however, it was observed that the As_6^{4-} anion has a moderate chair-like conformation with As–As bonds that vary between 2.399(4) to 2.415(3) Å. Computational studies including electron localization function (ELF) calculations indicate that these anions are only planar when coordinated by charge-balancing alkali-metal counter-cations. The calculations also demonstrated that the anions are not 10 π- or lone-pair aromatics but are rather best understood as six-membered systems with a localized double bond and negative charges on all of the other pnictogen atoms that are not involved in the π-bond.

More expanded eight-membered rings are also available using solution-phase methods as evidenced by the isolation of Sb_8^{8-} by reduction of antimony with potassium metal in liquid ammonia [240]. Sb_8^{8-} is isoelectronic with the well-known S_8 ring system and exhibits a comparable zigzag structure. Selected examples of cyclic group 15 anions are presented in Fig. 10.

Of the clusters highlighted thus far, very few are available using both solid-state and solution-phase methodologies. One such family of clusters is the $[E^V_7]^{3-}$ and $[E^V_{11}]^{3-}$ (E^V = P, As, Sb) cluster anions. Of these two, P_7^{3-} has been the most extensively studied on account of its synthetic accessibility and well-understood behavior in both solution and the solid state.

As mentioned earlier, the $[E^V_7]^{3-}$ cluster anions adopt a C_{3v} symmetric nortricyclane-like structure. A basal three-membered ring (E5, E6, E7) is linked by three bridging atoms (E2, E3, E4) to a single apical atom (E1) as pictured in Fig. 9. Each of the bridging atoms can be considered as being a pseudo-group 16 atom, thus carrying a formal negative charge, in agreement with the overall three minus charge of the anion.

Analysis of the interatomic distances for P_7^{3-} shows that the longest bonds are found in the base of the clusters. The basal P–P interatomic distances of 2.255Å (on average) and P–P–P angles of approximately 60° in $[Li(TMEDA)]_3P_7$ are very similar to those observed for white phosphorus (2.21 Å; 60.0°) [261] and suggest

Table 7 Mean bond lengths in the $[E_7]^{3-}$ clusters (in Å). Labeling refers to that used in Fig. 9

Bond	$[P_7]^{3-}$	$[As_7]^{3-}$	$[Sb_7]^{3-}$	$[Bi_7]^{3-}$
A	2.20	2.43	2.78	2.94
B	2.15	2.40	2.70	2.90
C	2.26	2.50	2.86	3.07

significant ring strain. As would be expected, the arsenic and antimony congeners possess structures that are identical, albeit with substantially lengthened bonds (Table 7).

The structure and dynamics of the P_7^{3-} cluster have been extensively probed using ^{31}P NMR spectroscopy, both in solution and the solid state. At room temperature, in solution, only a very broad, non-distinct resonance is observed. On heating to 50 °C, this sharpens to a singlet at –119 ppm, implying the equivalence of all seven atoms on the NMR timescale via a fluxional process that exchanges them all. Upon cooling to −60 °C, this fluxionality is frozen out, and the spectrum reveals three multiplet resonances at −57, −103, and −162 ppm integrating in the ratio 1:3:3. These were assigned to the apical vertex, bridging vertices and basal vertices, respectively. Similar behavior is observed in variable temperature solid-state ^{31}P NMR spectroscopy on amorphous samples of $[Li(DME)]_3P_7$ [262]. This has been attributed to a reversible valence tautomerism process analogous to the degenerate Cope rearrangement in the hydrocarbon bullvalene. The process is undoubtedly driven by the strain inherent within the base of the cluster and assisted by the presence of easily movable electron pairs on the bridging phosphide vertices (and electron delocalization throughout the cluster). It seems reasonable to assume that there are analogous dynamic processes in the As_7^{3-} and Sb_7^{3-} clusters, although neither element has a suitable NMR active nucleus that would allow for this phenomenon to be investigated.

The slightly oxidized P_{11}^{3-} anion is accessible through both solid-state and solution-based methods. The eleven vertex trianion can be extracted into solution by dissolution of preformed phases such as Cs_3P_{11} and subsequently recrystallized as alkali-metal or tetraalkylammonium salts. The MAS ^{31}P NMR spectrum of this anion has been reported and features four resonances at 174.5, 167.9, −102.3, and −209.4 ppm which integrate in a 3:3:2:3 ratio (with significant overlap of the two lower-field resonances).

The remaining high-nuclearity clusters $[E^V_{14}]^{4-}$, $[E^V_{16}]^{2-}$, $[E^V_{19}]^{3-}$, $[E^V_{21}]^{3-}$, $[E^V_{22}]^{4-}$, and $[E^V_{26}]^{4-}$ have all been isolated by solution methods (structurally authenticated anions are pictured in Fig. 11). Several of these cages can be interpreted as being derived from the formal oxidation of smaller nuclearity cluster anions. Thus, $[E^V_{14}]^{4-}$ is the result of the oxidative coupling of two $[E^V_7]^{3-}$ cages with concomitant loss of two electrons (E^V = P, As). Similarly, the $[E^V_{22}]^{4-}$ cages can be thought of as the result of coupling two $[E^V_{11}]^{3-}$ cages (E^V = P, As). These processes are similar to the dimerization of Ge_9^{4-} clusters to afford $(Ge_9–Ge_9)^{6-}$ as discussed above. By analogy, the P_{21}^{3-} cage can also be thought of as the result of the coupling of three P_7^{3-} cages with the concomitant loss of six electrons. The

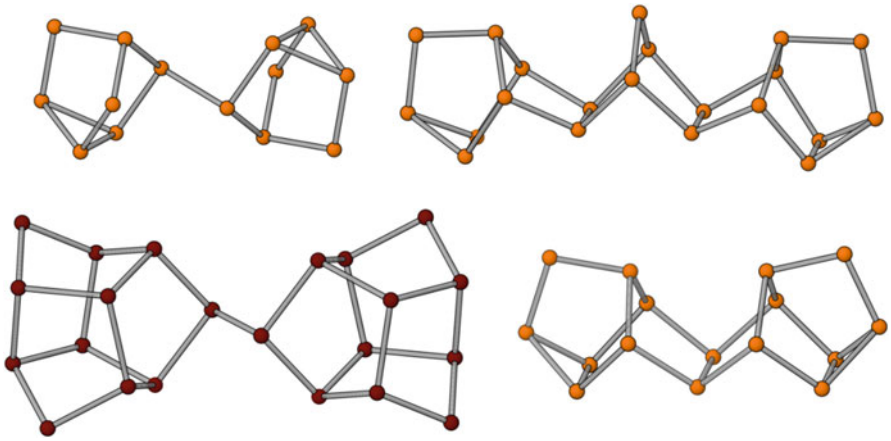

Fig. 11 High-nuclearity polyphosphide cages available through solution-phase methods

Table 8 ^{31}P NMR data for all of the known homoatomic polyanions of phosphorus. Chemical shifts given to the nearest integer

Polyanion	NMR data (ppm)	Charge per atom
P_5^-	470	−0.200
P_7^{3-}	−119 (at 20 °C)	−0.429
P_{11}^{3-}	174, 168, −102, −209	−0.273
P_{14}^{4-}	N/A	−0.286
P_{16}^{2-}	60, 38, 6, −34, −134, −180	−0.125
P_{19}^{3-}	49, 6, −55, −74, −95, −170, −192	−0.158
P_{21}^{3-}	72, 61, −15, −108, −118, −146	−0.143
P_{22}^{4-}	N/A	−0.182
P_{26}^{4-}	84, 54, 30, −15, −88, −128, −135, −169	−0.154

formation of the remaining clusters is more difficult to rationalize as there must be other species formed in solution.

Many of these cages have been characterized in solution by ^{31}P NMR spectroscopy. A table with the NMR resonance and the average oxidation state of each phosphorus atom of the cages is presented in Table 8.

The solution dynamics which allow for interconversion between polyanions is not fully understood; however, redox interconversion between P_{16}^{2-} and P_{21}^{3-} has been reported by Guérin and Richeson [263]. On dissolving a pure sample of K_2P_{16} in THF, ^{31}P NMR and X-ray fluorescence measurements showed conversion to P_{21}^{3-} and elemental phosphorus. Removing the THF from such solutions under a dynamic vacuum and redissolving the residue in ethanol restored the ^{31}P NMR spectrum of P_{16}^{2-}. This process is evidence for the shallow energy surface on which such species lie. It appears that the most stable polyphosphides available in solutions are those where the negative charges are either well separated (such as in P_{21}^{3-} and P_{16}^{2-}) or a mechanism exists for the transfer of charge over multiple

phosphorus atoms (fluxional processes in P_7^{3-} or delocalization in P_5^-). It is interesting to note that conversion between P_{21}^{3-} and P_{16}^{2-} would formally involve a P_5^- moiety, although spectroscopic studies of such mixtures are invariably more complex.

Information on the heavier analogues of these cluster anions is less readily available. All of the $[E^V_7]^{3-}$ and $[E^V_{11}]^{3-}$ (E^V = P–Bi) cluster anions are known, although it is worth noting that the bismuth-containing clusters were only isolated in the last two years. Of the remaining polyanionic species, only the oxidatively coupled dimers As_{14}^{4-} and As_{22}^{4-} have been reported. It is likely that there are heavier main-group analogues of the clusters which have thus far been reported for phosphorus; however, the lack of NMR spectroscopic handles has thus far precluded their characterization. It is only a matter of time, however, before such species are structurally authenticated.

Finally, in relation to the chemistry of group 14 clusters, it is also worth noting that protonation of P_7^{3-} and P_{11}^{3-} cluster cages has also been demonstrated. These studies show that in addition to redox equilibria in solution, the possibility of acid–base interactions makes the solution-phase behavior of such anions enormously varied and complex. The hydrogenheptaphosphide anion, $(HP_7)^{2-}$, was first described by Baudler and coworkers in solution in 1984 by the disproportionation reaction of diphosphane with ^{n}BuLi at low temperature [264]. At room temperature, the cage atoms undergo an exchange process that renders two sets of them equivalent on the NMR timescale, in a manner analogous to the parent P_7^{3-} cage. On cooling to –60 °C, the fluxional process is frozen out, with seven resonances corresponding to the seven inequivalent phosphorus environments being observed at −9.0, −67.5, −83.7, −119.4, −134.8, −145.2, and −215.9 ppm. It was not until 2004 that the anion was isolated and an X-ray structural study performed, confirming the connectivity of the anion [265, 266]. A high-yielding preparative synthesis of the anion, and its arsenic analogue, was reported recently [267–268]. There is only one report of the monoanionic $(H_2P_7)^-$ cage in the literature [269]. It was structurally characterized as the $[PPh_4]^+$ salt; however, orientational disorder within the cluster prevented the location of the hydrogen atoms and an analysis of the bond metric data. NMR data were not reported due to the compound decomposing into higher polyphosphorus species upon dissolution into dimethyl sulfoxide or acetonitrile. The presence of a P–H bond was inferred from the presence of a strong, sharp band at 2,250 cm^{-1} in the IR spectrum and the cluster charge from the X-ray crystal structure obtained. Analogous arsenic and antimony cages are currently unknown. The neutral heptaphosphane, H_3P_7, is available through the methanolysis of the tris(trimethylsilyl)-substituted cage, $(Me_3Si)_3P_7$,, in the absence of solvent [270]. ^{31}P NMR spectroscopy studies were carried out on solutions formed directly in benzene, 1-methylnaphthalene, or 1-methylnaphthalene/phenanthrene mixtures, which have to be performed rapidly before the decomposition of the compound into PH_3 and elemental phosphorus [271]. The heavier arsenic and antimony cages are currently unknown. Protonation of P_{11}^{3-} has allowed for the structural characterization of (HP_{11}^{2-}) [241, 272, 273].

5 Conclusions

The aim of this review was to provide a comprehensive overview of the chemistry of homoatomic polyanions of the p-block elements. While this area of chemistry is over a hundred years old, it has been in constant development ever since early empirical observations demonstrated that many p-block metalloids and metals can be dissolved in liquid ammonia in the presence of alkali metals. Moreover, the solution-phase dynamics of these cluster anions is still poorly understood. Interconversion processes between clusters with differing nuclearities and net negative charges are not fully understood, while the involvement of Brønsted acid–base equilibria serves to further complicate matters and may hint at proton-assisted mechanisms. Matters get increasingly more complex (and fascinating) as other metals are incorporated into the mix. This area of chemistry, which is not the remit of this review (see article by Weinert and Dehnen [274]), has allowed for the isolation of cluster architectures which are both beautiful and puzzling, forcing the community to consider new bonding paradigms. I have no doubt that many interesting discoveries will continue to be made in the field in the coming years and that, ultimately, this research will allow for the controlled use of cluster anions of the p-block in chemical synthesis and the formation of novel main-group-based materials.

Acknowledgments The author thanks the Engineering and Physical Sciences Research Council (EPSRC) and the University of Oxford for the continued financial support.

References

1. Greenwood NN, Earnshaw A (1997) Chemistry of the elements, 2nd edn. Elsevier, Oxford
2. Pitzer KS (1948) J Am Chem Soc 70:2140
3. Stevenson DP, Yost DM (1941) J Chem Phys 9:403
4. Bock H, Muller H (1984) Inorg Chem 23:4365
5. Scherer OJ (2000) Angew Chem Int Ed Engl 39:1029
6. Jerabek P, Frenking G (2014) Theor Chem Acc 133:1447
7. Huheey JE, Keiter EA, Keiter RL (1993) Inorganic chemistry: principles of structure and reactivity, 4th edn. Harper Collins, New York
8. Wade K (1971) J Chem Soc D 792
9. Wade K (1976) Adv Inorg Chem Radiochem 18:1
10. Mingos DMP (1972) Nat Phys Sci 236:99
11. Mingos DMP (1984) Acc Chem Res 17:311
12. Kauzlarich SM (ed) (1996) Chemistry, structure and bonding of zintl phases and anions. VCH, New York
13. Corbett JD (1997) Struct Bonding 87:157
14. Belin C, Tillard-Charbonnel M (1998) Coord Chem Rev 178–180:529
15. Corbett JD (2000) Angew Chem Int Ed 39:670
16. Corbett JD (2000) Inorg Chem 39:5178
17. Sevov SC (2002) In: Westbrook JH, Freisher RL (eds) Intermetallic compounds, principles and practice: progress. Wiley, Chichester

18. Fässler TF (2003) Chem Soc Rev 32:80
19. Fässler TF (2006) Z Anorg Allg Chem 632:1125
20. Corbett JD (2010) Inorg Chem 49:13
21. Schubert K, Gauzzi F, Frank K (1963) Z Metallk 54:422
22. Zhao JT, Corbett JD (1994) J Alloys Compd 210:1
23. Nesper R (1990) Prog Solid State Chem 20:1
24. Dong ZC, Corbett JD (1996) Inorg Chem 35:3107
25. Frank K, Schubert K (1970) J Less Common Met 20:215
26. Sevov SC, Corbett JD (1993) J Solid State Chem 103:114
27. Dong ZC, Corbett JD (1994) J Am Chem Soc 116:3429
28. Zhao JT, Corbett JD (1995) Inorg Chem 34:378
29. Dong ZC, Corbett JD (1993) J Am Chem Soc 115:11299
30. Dong ZC, Corbett JD (1996) Inorg Chem 35:2301
31. Liu Q, Hoffmann R, Corbett JD (1994) J Phys Chem 98:9360
32. Henning RW, Leon-Escamilla EA, Zhao JT, Corbett JD (1997) Inorg Chem 36:1282
33. Dong ZC, Corbett JD (1996) Angew Chem Int Ed 35:1006
34. Huang DP, Dong ZC, Corbett JD (1998) Inorg Chem 37:5881
35. Kaskel S, Corbett JD (2000) Inorg Chem 39:778
36. Henning RW, Corbett JD (1997) Inorg Chem 36:6045
37. Sevov SC, Corbett JD (1991) Inorg Chem 30:4875
38. Blase W, Cordier G, Müller V, Häussermann U, Nesper R (1993) Z Naturforsch B 48b:754
39. Cordier G, Müller V (1992) Z Kristallogr 198:281
40. Dong ZC, Corbett JD (1995) J Cluster Sci 6:187
41. Dong ZC, Corbett JD (1996) Inorg Chem 35:1444
42. Dong ZC, Corbett JD (1995) Inorg Chem 34:5042
43. Cordier G, Müller V (1994) Z Naturforsch B 49b:935
44. Dong ZC, Corbett JD (1995) J Am Chem Soc 117:6447
45. Dong ZC, Corbett JD (1995) Inorg Chem 34:5709
46. Joannis A (1891) C R Hebd Seances Acad Sci 113:795
47. Kraus CA (1907) J Am Chem Soc 29:1557
48. Zintl E, Dullenkopf W (1932) Z Phys Chem Abt B 16:183
49. Zintl E, Goubeau J, Dullenkopf W (1931) Z Phys Chem Abt A 154:1
50. Nesper R, Curda J, von Schnering HG (1986) J Solid State Chem 62:199
51. Nesper R, Wengert S (1999) Chem Monthly 130:197
52. Zurcher F, Nesper R (2001) Z Kristallogr NCS 216:507
53. Currao A, Curda J, Nesper R (1996) Z Anorg Allg Chem 622:85
54. Nesper R, Currao A, Wengert S (1998) Chem Eur J 4:2251
55. Frank U, Müller W (1975) Z Naturforsch B 30b:313
56. Todorov I, Sevov SC (2005) Inorg Chem 44:5361
57. Todorov I, Sevov SC (2004) Inorg Chem 43:6490
58. Wengert S, Nesper R (1998) Z Anorg Allg Chem 624:1801
59. Palenzona A, Manfrinetti P, Fornasini ML (2002) J Alloys Compd 345:144
60. Palenzona A, Manfrinetti P, Fornasini ML (2000) J Alloys Compd 312:165
61. Müller W (1974) Z Naturforsch B 29:304
62. Witte J, von Schnering HG (1964) Z Anorg Allg Chem 317:260
63. Goebel T, Prots Y, Haarman F (2008) Z Kristallogr NCS 223:187
64. Busmann E (1961) Z Anorg Allg Chem 313:90
65. von Schnering HG, Schwarz M, Chang JH, Peters K, Peters EM et al (2005) Z Kristallogr NCS 220:525
66. Hoch C, Wendorff M, Röhr C (2003) J Alloys Compd 361:206
67. Queneau V, Todorov I, Sevov SC (1998) J Am Chem Soc 120:3263
68. von Schnering HG, Schwarz M, Nesper R (1986) Angew Chem 98:558
69. Janzon KH, Schafer H, Weiss A (1970) Z Anorg Allg Chem 372:87

70. Eisenmann B, Riekel C, Schafer H, Weiss A (1970) Z Anorg Allg Chem 372:325
71. von Schnering HG, Llanos J, Chang JH, Peters K, Peters EM et al (2005) Z Kristallogr NCS 220:324
72. Carrillo-Cabrera W, Gil RC, Somer M, Persil O, von Schnering HG (2003) Z Anorg Allg Chem 629:601
73. von Schnering HG, Baitinger M, Bolle U, Carrillo-Cabrera W, Curda J et al (1997) Z Anorg Allg Chem 623:1037
74. Llanos J, Nesper R, von Schnering HG (1983) Angew Chem Int Ed 22:998
75. von Schnering HG, Llanos J, Grin Y, Carrillo-Cabrera W, Peters EM et al (1998) Z Kristallogr NCS 213:661
76. Betz A, Schafer H, Weiss A, Wulf R (1968) Z Naturforsch B 23:878
77. Müller W, Volk K (1977) Z Naturforsch B 32:709
78. Grin Y, Baitinger M, Kneip R, von Schnering HG (1999) Z Kristallogr NCS 214:453
79. Hewaidy IF, Busmann E, Klemm W (1964) Z Anorg Allg Chem 328:283
80. Baitinger M, Grin Y, von Schnering HG, Kneip R (1999) Z Kristallogr NCS 214:457
81. Hoch C, Wendorff M, Röhr C (2003) Z Anorg Allg Chem 629:2391
82. Marsh RE, Shoemaker DP (1953) Acta Crystallogr 6:197
83. Röhr C (1995) Z Naturforsch B 50:802
84. Baitinger M, Peters K, Somer M, Carrillo-Cabrera W, Grin Y et al (1999) Z Kristallogr NCS 214:455
85. Bobev S, Sevov SC (2002) Polyhedron 21:641
86. Nesper R, von Schnering HG, Curda J (1986) Chem Ber 119:3576
87. von Schnering HG, Nesper R, Curda J, Tebbe KF (1980) Angew Chem Int Ed 19:1033
88. von Schnering HG, Boelle U, Curda J, Peters K, Carrillo-Cabrera W et al (1996) Angew Chem Int Ed 35:984
89. Bolle U, Carrillo-Cabrera W, Peters K, von Schnering HG (1998) Z Kristallogr NCS 210:689
90. Zurcher F, Nesper R (2001) Z Kristallogr NCS 216:505
91. Wengert S, Nesper R (2000) Inorg Chem 39:2861
92. Ponou S, Fässler TF (2007) Z Anorg Allg Chem 633:393
93. Queneau V, Sevov SC (1997) Angew Chem Int Ed 36:1754
94. Hoch C, Wendorff M, Röhr C (2002) Acta Crystallogr C 58:I45
95. Queneuau V, Sevov SC (1998) Inorg Chem 37:1358
96. Todorov I, Sevov SC (1998) Inorg Chem 37:3889
97. Eisenmann B, Schafer H, Turban K (1974) Z Naturforsch B 29:464
98. Eisenmann B, Janzon KH, Schafer H, Weiss A (1969) Z Naturforsch B 24:457
99. Aydemir U, Ormeci A, Borrmann H, Bohme B, Zurcher F et al (2008) Z Anorg Allg Chem 634:1651
100. Zurcher F, Nesper R (1998) Angew Chem Int Ed 37:3314
101. Bobev S, Sevov SC (2000) Angew Chem Int Ed 39:4108
102. Bobev S, Sevov SC (2002) J Am Chem Soc 123:3359
103. Bobev S, Sevov SC (2001) Inorg Chem 40:5361
104. Bobev S, Sevov SC (2001) Angew Chem Int Ed 40:1507
105. Wiesler K, Brandl K, Fleischmann A, Korber N (2009) Z Anorg Allg Chem 635:508
106. Joseph S, Suchentrunk C, Korber N (2010) Z Naturforsch B 65:1059
107. Goicoechea JM, Sevov SC (2004) J Am Chem Soc 126:6860
108. Campbell J, Schrobilgen GJ (1997) Inorg Chem 36:4078
109. Suchentrunk C, Korber N (2006) New J Chem 30:1737
110. Edwards PA, Corbett JD (1977) Inorg Chem 16:903
111. Somer M, Carrillo-Cabrera W, Peters EM, Kaupp M, von Schnering HG (1999) Z Anorg Allg Chem 625:37
112. Corbett JD, Edwards PA (1975) J Chem Soc Chem Commun 984
113. Joseph S, Suchenrunk C, Kraus F, Korber N (2009) Eur J Inorg Chem 2009:4641

114. Suchentrunk C, Daniels J, Somer M, Carrillo-Cabrera W, Korber N (2005) Z Naturforsch B B60:277
115. Somer M, Carrillo-Cabrera W, Peters EM, Peters K, von Schnering HG (1998) Z Anorg Allg Chem 624:1915
116. Carrillo-Cabrera W, Aydemir U, Somer M, Kircali A, Fässler TF et al (2007) Z Anorg Allg Chem 633:1575
117. Belin CHE, Corbett JD, Cisar A (1977) J Am Chem Soc 99:7163
118. Downie C, Mao JG, Guloy AM (2001) Inorg Chem 40:4721
119. Diehl L, Khodadadeh K, Kummer D, Strähle J (1976) Z Naturforsch B 31:522
120. Diehl L, Khodadadeh K, Kummer D, Strähle J (1976) Chem Ber 109:3404
121. Korber N, Fleischmann A (2001) Dalton Trans 2001:383
122. Corbett JD, Edwards PA (1977) J Am Chem Soc 99:3313
123. Hauptmann R, Fässler TF (2003) Z Kristollogr NCS 218:455
124. Burns R, Corbett JD (1985) Inorg Chem 24:1489
125. Fässler TF, Hoffmann R (1999) Angew Chem Int Ed 38:543
126. Benda CB, Waibel M, Kochner T, Fässler TF (2014) Chem Eur J 20:16738
127. Hauptmann R, Fässler TF (2002) Z Anorg Allg Chem 628:1500
128. Hauptmann R, Fässler TF (2003) Z Kristollogr NCS 218:458
129. Hauptmann R, Hoffmann R, Fässler TF (2001) Z Anorg Allg Chem 627:2220
130. Yong L, Hoffmann SD, Fässler TF (2006) Inorg Chim Acta 359:4774
131. Fässler TF, Hoffmann R (1999) J Chem Soc Dalton Trans 1999:3339
132. Campbell J, Dixon DA, Mercier HPA, Schrobilgen GJ (1995) Inorg Chem 34:5798
133. Fässler TF, Hunziker M (1994) Inorg Chem 33:5380
134. Fässler TF, Schutz U (1999) Inorg Chem 38:1866
135. Hauptmann R, Fässler TF (2003) Z Kristallogr NCS 218:461
136. Angilella V, Belin C (1991) J Chem Soc Faraday Trans 87:203
137. Suchentrunk C, Korber N (2006) Inorganica Chim Acta 359:267
138. Critchlow SC, Corbett JD (1983) J Am Chem Soc 105:5715
139. Fässler TF, Hunziker M (1996) Z Anorg Allg Chem 622:837
140. Fässler TF, Hoffmann R (2000) Z Kristallogr NCS 215:139
141. Yong L, Hoffmann SD, Fässler TF (2005) Z Kristallogr NCS 49:220
142. Goicoechea JM, Sevov SC (2005) Inorg Chem 44:2654
143. Akerstedt J, Ponou S, Kloo L, Lidin S (2011) Eur J Inorg Chem 2011:3999
144. Belin C, Mercier H, Angilella V (1991) New J Chem 15:931
145. Spiekermann A, Hoffmann SD, Fässler TF (2006) Angew Chem Int Ed 45:3459
146. Nienhaus A, Hoffmann SD, Fässler TF (2006) Z Anorg Allg Chem 632:1752
147. Scharfe S, Fässler TF (2011) Z Anorg Allg Chem 637:901
148. Hauptmann R, Fässler TF (2003) Z Anorg Allg Chem 629:2266
149. Xu L, Sevov SC (1999) J Am Chem Soc 121:9245
150. Yong L, Hoffmann SD, Fässler TF (2005) Z Anorg Allg Chem 631:1949
151. Ugrinov A, Sevov SC (2002) J Am Chem Soc 124:10990
152. Yong L, Hoffmann SD, Fässler TF (2004) Z Anorg Allg Chem 630:1977
153. Ugrinov A, Sevov SC (2003) Inorg Chem 42:5789
154. Downie C, Tang Z, Guloy AM (2000) Angew Chem Int Ed 39:337
155. Downie C, Tang Z, Guloy AM (2004) Inorg Chem 43:1992
156. Ugrinov A, Sevov SC (2005) C R Chim 8:1878
157. Sevov SC, Goicoechea JM (2006) Organometallics 25:5678
158. Scharfe S, Fässler TF (2010) Philo Trans R Soc A 368:1265
159. Scharfe S, Kraus F, Stegmaier S, Schier A, Fässler TF (2011) Angew Chem Int Ed 50:3630
160. Fässler TF (2011) Struct Bond 140:91
161. Kocak FS, Downing DO, Zavalij P, Lam YF, Vedernikov AN et al (2012) J Am Chem Soc 134:9733
162. Fässler TF, Hunziker M, Spahr ME (2000) Z Anorg Allg Chem 626:692

163. Wilson WL, Rudolph RW, Lohr LL (1986) Inorg Chem 25:1535
164. Wilson WL (1982) Preparation and NMR characterization of tin and lead anionic clusters, Ph. D. dissertation; University of Michigan, Michigan
165. Birchall T, Burns RC, Devereux LA, Schrobilgen GJ (1985) Inorg Chem 24:890
166. Rosdahl J, Fässler TF, Kloo L (2005) Eur J Inorg Chem 2888
167. Neumeier M, Fendt F, Gärtner S, Koch C, Gärtner T et al (2013) Angew Chem Int Ed 52:4483
168. Stearns LA, Gryko J, Diefenbacher J, Ramachandran GK, McMillan PF (2003) J Solid State Chem 173:251
169. Goebel T, Ormeci A, Pecher O, Haarmann F (2012) Z Anorg Allg Chem 638:1437
170. Rudolph RW, Wilson WL, Taylor RC (1981) J Am Chem Soc 103:2480
171. Critchlow SC, Corbett JD (1981) J Chem Soc Chem Commun 5:236
172. von Schnering HG, Hönle W (1988) Chem Rev 88:243
173. Gascoin F, Sevov SC (2000) J Am Chem Soc 122:10251
174. Emmerling F, Röhr C (2002) Z Naturforsch 57b:963
175. von Schnering HG, Hartweg M, Hartweg U, Hönle W (1989) Angew Chem Int Ed 28:56
176. Derrien G, Tillard M, Manteghetti A, Belin C (2003) Z Anorg Allg Chem 629:1601
177. Gascoin F, Sevov SC (2001) Inorg Chem 40:5177
178. Somer M, Hartweg M, Peters K, von Schnering HG (1991) Z Kristallogr NCS 195:103
179. von Schnering HG, Wittmann M, Sommer D (1984) Z Anorg Allg Chem 510:61
180. Deller K, Eisenmann B (1976) Z Naturforsch B 31:1023
181. Deller K, Eisenmann B (1977) Z Naturforsch B 32:1368
182. Emmerling F, Petri D, Röhr C (2004) Z Anorg Allg Chem 630:2490
183. Abicht HP, Hönle W, von Schnering HG (1984) Z Anorg Allg Chem 519:7
184. von Schnering HG, Meyer T, Hönle W, Schmettow W, Hinze U et al (1987) Z Anorg Allg Chem 553:261
185. Schmettow W, Lipka A, von Schnering HG (1974) Angew Chem Int Ed Engl 13:345
186. Hönle W, Krogull G, Peters K, von Schnering HG (1999) Z Kristallogr NCS 214:17
187. Eisenmann B, Jordan H, Schafer H (1985) Z Naturforsch B 40:1603
188. Manriquez V, Hönle W, von Schnering HG (1986) Z Anorg Allg Chem 539:95
189. Santandrea RP, Mensing C, von Schnering HG (1986) Thermochim Acta 98:301
190. Meyer T, Hönle W, von Schnering HG (1987) Z Anorg Allg Chem 552:69
191. Dahlmann W, von Schnering HG (1972) Naturwissenschaften 59:420
192. Dahlmann W, von Schnering HG (1973) Naturwissenschaften 60:429
193. Hönle W, Buresch J, Peters K, Chang JH, von Schnering H (2002) Z Kristallogr NCS 217:485
194. Hönle W, Buresch J, Peters K, Chang JH, von Schnering H (2002) Z Kristallogr NCS 217:487
195. Hönle W, Buresch J, Wolf J, Peters K, Chang JH et al (2002) Z Kristallogr NCS 217:489
196. Schmettow W, von Schnering HG (1977) Angew Chem Int Ed Engl 16:857
197. Dorn FW, Klemm W (1961) Z Anorg Allg Chem 309:189
198. Hirschle C, Röhr C (2000) Z Anorg Allg Chem 626:1992
199. Eisenmann B, Rossler U (2003) Z Anorg Allg Chem 629:459
200. Wichelhaus W, von Schnering HG (1973) Naturwissenschaften 60:104
201. von Schnering HG, Somer M, Kliche G, Hönle W, Meyer T et al (1991) Z Anorg Allg Chem 601:13
202. Emmerling F, Röhr C (2003) Z Anorg Allg Chem 629:467
203. Kraus F, Hanauer T, Korber N (2005) Angew Chem Int Ed 44:7200
204. Kraus F, Schemedt auf der Günne J, DiSalle BF, Korber N (2006) Chem Commun 218
205. Baudler M (1982) Angew Chem Int Ed Engl 21:492
206. Baudler M, Glinka K (1993) Chem Rev 93:1623
207. Baudler M (1987) Angew Chem Int Ed Engl 26:419
208. Xu L, Bobev S, El-Bahraoui J, Sevov SC (2000) J Am Chem Soc 122:1838
209. Kraus F, Aschenbrenner JC, Korber N (2003) Angew Chem Int Ed 42:4030
210. Kraus F, Korber N (2005) Chem Eur J 11:5945
211. Kraus F, Hanauer T, Korber N (2006) Inorg Chem 45:1117

212. Hanauer T, Kraus F, Reil M, Korber N (2006) Monatsh Chem 137:147
213. Critchlow SC, Corbett JD (1984) Inorg Chem 23:770
214. Cisar A, Corbett JD (1977) Inorg Chem 16:2482
215. Kuznetsov AN, Fässler TF (2002) Z Anorg Allg Chem 628:2537
216. Benda CB, Fässler TF (2014) Z Anorg Allg Chem 640:40
217. Baudler M, Düster D, Ouzounis D (1987) Z Anorg Allg Chem 544:87
218. Baudler M, Akpapoglou S, Ouzounis D, Wasgestian F, Meinigke B et al (1988) Angew Chem Int Ed Engl 27:280
219. Milyukov VA, Kataev AV, Sinyashin OG, Hey-Hawkins E (2006) Russ Chem Bull Int Ed 55:1297
220. Korber N, Richter F (1997) Angew Chem Int Ed Engl 36:1512
221. Hönle W, von Schnering HG, Schmidpeter A, Burget G (1984) Angew Chem Int Ed Engl 23:817
222. Korber N, Daniels J (1996) Helv Chim Acta 79:2083
223. Korber N, Daniels J (1999) Z Anorg Allg Chem 625:189
224. Korber N, Daniels J (1996) J Chem SocDalton Trans: 1653
225. Korber N, Daniels J (1996) Acta Crystallogr C52:2454
226. Korber N, von Schnering HG (1996) Chem Ber 129:155
227. Bashall A, Beswick MA, Choi N, Hopkins AD, Kidd SJ et al (2000) J Chem Soc Dalton Trans 479
228. Hanauer T, Grothe M, Reil M, Korber N (2005) Helv Chim Acta 88:950
229. Somer M, Hönle W, von Schnering HG (1989) Z Naturforsch B 44:296
230. Driess M, Merz K, Pritzkow H, Janoschek R (1996) Angew Chem Int Ed Engl 35:2507
231. Hübler K, Becker G (1998) Z Anorg Allg Chem 624:483
232. Korber N, von Schnering HG (1997) Z Kristallogr NCS 212:85
233. Castleman AW, Khanna SN, Sen A, Reber AC, Qian M et al (2007) Nano Lett 7:2734
234. Beswick MA, Choi N, Harmer CN, Hopkins AD, McPartlin M et al (1998) Science 281:1500
235. Adolphson DG, Corbett JD, Merryman DJ (1976) J Am Chem Soc 98:7234
236. Diehl L, Khodadadeh K, Kummer D, Strahle J (1976) Z Naturforsch 31:522
237. Breunig HJ, Ghesner ME, Lork E (2005) Z Anorg Allg Chem 631:851
238. Mutzbauer F, Korber N (2011) Acta Crystallogr E67:m1551
239. Perla LG, Oliver AG, Sevov SC (2015) Inorg Chem 54:872
240. Reil M, Korber N (2007) Z Anorg Allg Chem 633:1599
241. Korber N, Daniels J, von Schnering HG (1996) Angew Chem Int Ed Engl 35:1107
242. Knettel D, Reil M, Korber N (2001) Z Naturforsch 56b:965
243. Korber N, Daniels J (1996) Z Anorg Allg Chem 622:1833
244. Korber N, Daniels J (1996) Polyhedron 15:2681
245. Dai FR, Xu L (2007) Chin J Struct Chem 26:45
246. Hanauer T, Korber N (2006) Z Anorg Allg Chem 632:1135
247. Bolle U, Tremel W (1992) J Chem Soc Chem Commun 91
248. Jun Z, Li XU (2011) Chin J Struct Chem 30:1091
249. García F, Less RJ, Naseri V, McPartlin M, Rawson JM et al (2008) Chem Commun 859
250. Weinert B, Eulenstein AR, Ababei R, Dehnen S (2014) Angew Chem Int Ed 53:4704
251. Miluykov V, Kataev A, Sinyashin O, Lönnecke P, Hey-Hawkins E (2006) Z Anorg Allg Chem 632:1728
252. Hanauer T, Aschenbrenner JC, Korber N (2006) Inorg Chem 45:6723
253. Baudler M, Düster D (1987) Z Naturforsch B 42:335
254. von Schnering HG, Manriquez V, Hönle W (1981) Angew Chem Int Ed Engl 20:594
255. Baudler M, Düster D, Germeshausen J (1986) Z Anorg Allg Chem 534:19
256. Baudler M, Düster D, Langerbeins K, Germeshausen J (1984) Angew Chem Int Ed Engl 23:317
257. Fritz G, Schneider HW, Hönle W, von Schnering HG (1988) Z Naturforsch B 43:561
258. Korber N (1997) Phosphorus Sulfur Silicon Relat Elem 124:339

259. Haushalter RC, Eichhorn BW, Rheingold AL, Geib SJ (1988) J Chem Soc Chem Commun 1027
260. Baudler M, Heumüller R, Düster D, Germeshausen J, Hahn J (1984) Z Anorg Allg Chem 518:7
261. Simon A, Borrmann H, Craubner H (1987) Phosphorus Sulfur Silicon Relat Elem 30:507
262. Sen T, Poupko R, Fleischer U, Zimmermann H, Luz Z (2000) J Am Chem Soc 122:889
263. Guérin F, Richeson D (1995) Inorg Chem 34:2793
264. Baudler M, Heumüller R, Langerbeins K (1984) Z Anorg Allg Chem 514:7
265. Aschenbrenner JC, Korber N (2004) Z Anorg Allg Chem 630:31
266. Dai FR, Xu L (2006) Inorg Chim Acta 359:4265
267. Turbervill RSP, Goicoechea JM (2012) Organometallics 31:2452
268. Turbervill RSP, Goicoechea JM (2014) Eur J Inorg Chem 2014:1660
269. Korber N, von Schnering HG (1995) J Chem Soc Chem Commun 1713
270. Baudler M, Ternberger H, Faber W, Hahn J (1979) Z Naturforsch 34:1690
271. Baudler M, Riekehof-Böhner R (1985) Z Naturforsch 40:1424
272. Ye YZ, Xu L (2008) Chin J Struct Chem 27:75
273. Korber N, Daniels J (1997) Inorg Chem 36:4906
274. Weinert B, Dehnen S (2016) Binary and ternary intermetalloid clusters. Struct Bond. doi:10.1007/430_2015_5002

Struct Bond (2017) 174: 99–134
DOI: 10.1007/430_2015_5002

Published online: 9 July 2016

Binary and Ternary Intermetalloid Clusters

Bastian Weinert and Stefanie Dehnen

Abstract Compounds containing molecular Zintl anions, which are homo- or heteroatomic, anionic molecules of groups 13–15, have served as starting materials for a variety of derivatives. Besides ligand attachment to these clusters or oxidative coupling, the cages were used as polyatomic ligands in transition metal complexes and as sources for intermetalloid clusters and nanostructured crystalline materials. This review article deals with the structures, bonding situations, electronic properties, and formation pathways of these nanoscale heterometallic clusters.

Keywords Binary • Heterometallic • Intermetalloid • Ternary • Zintl anions

Contents

Dedicated to Professor Hansgeorg Schnöckel on the occasion of his 75th birthday.

B. Weinert and S. Dehnen (✉)
Fachbereich Chemie, Philipps-Universität Marburg, Hans-Meerwein-Straße 4, 35043 Marburg, Germany
e-mail: dehnen@chemie.uni-marburg.de

1 Introduction and General Remarks on Heterometallic and Intermetalloid Clusters

The chemistry of the main group elements with moderate electronegativity is compellingly diverse, particularly regarding the structures of the known compounds. This holds especially for compounds based on so-called Zintl polyanions, which were investigated for the first time in detail by Eduard Zintl in the 1930s [1] and were therefore named after him *posthumously* [2]. The reported architectures range from small molecules and linked clusters to nanoscale clusters and complicated networks. Especially the investigation of the transition from clusters to bulk material is a promising research field, since the change of properties between these two regimes offers the opportunity of a better understanding of chemical bonding and insight into potential applications [3–6]. The top-down method that (formally) cuts off bulk material into nanomaterials has been well established over the last decades. In contrast, controlled bottom-up syntheses have been studied and applied to a much lesser extent, although such methods provide an even larger product spectrum on account of a virtually endless pool of accessible precursors. Consequently, the knowledge of formation pathways, large-scale synthesis, and size control is still unsatisfying to date and subject to ongoing contemporary work. In this chapter, we will focus on bottom-up approaches for compounds bearing binary or ternary heterometallic or intermetalloid clusters, which are composed of transition metal and main group metal elements of groups 13 to 15.

The term "intermetalloid" has been introduced in several different ways. Generally, the definition "molecular intermetalloid" categorizes small molecules with a direct metal–metal contact [7]. The term "intermetalloid cluster" was derived from the definition of "metalloid clusters" that contain ligand-free and ligand-coordinated metal atoms of the same element, with more metal–metal than metal–ligand bonds. The resulting formal oxidation state of the metal atoms is thus close to zero, and the clusters exhibit structures that resemble fragments of the elemental (metal) structures [8, 9]. "Intermetalloid clusters," as a first class of clusters discussed in this article, extend the homoatomic "metalloid" cluster family by related heteroatomic species. The term thus specifies nanoscale particles that are composed of at least two different (semi-)metals, which have been observed both with ligands (anionic or neutral) or as ligand-free cluster anions. In particular, such clusters are based on one or more central (endohedral, interstitial) metal atom(s) M (usually followed by an "@" symbol), surrounded by a shell of at least one other type of (semi-)metal atoms [10]. This discriminates "intermetalloid clusters" from "heterometallic clusters," as the second class of species discussed herein, which are composed of two or more different types of metal atoms, however, lacking any interstitial one(s). A third class of clusters is also heterometallic in nature, but it is based on a homoatomic (semi-)metal cluster with the second sort of (semi-)metal atoms being part of a terminal ligand attached to it.

This article focuses on ligand-free binary or ternary heterometallic and intermetalloid clusters, their bonding situations, electronic properties, and

formation pathways. Related ligand-decorated clusters as well as the named third category of cluster compounds will be mentioned only briefly. Several review articles on clusters comprising main group atoms of groups 14 or 15 are available in the literature, with three of them also elaborating on binary clusters [11–13]. For completeness, we will summarize such systems and comment on their properties but put the main emphasis on ternary systems.

The following remarks summarize a couple of circumstances that are common to all of the discussed materials. Further, some of the remarks are fundamental to the understanding of the article and introduce the terminology used throughout herein.

1. Compounds comprising intermetalloid clusters were usually synthesized by reactions of solved molecular Zintl anions with transition metal complexes. Reaction media were polar amines, amides, or nitriles. The products were crystallized by temperature control or slow diffusion of solvents. Uncommon procedures will be specified below.
2. Binary intermetalloid clusters were accessed starting from a homoatomic Zintl anion unless otherwise stated, whereas all of the known ternary intermetalloid clusters have been reaction products of binary Zintl anions or quaternary intermetallic phases to date.
3. Intermetalloid clusters that preserve the bonding situation and electronic properties of the utilized homoatomic Zintl anions can be equally described by applying the Zintl–Klemm–Busmann *pseudo*-element concept [14], if being electron precise and comprising relatively strong covalent bonds, or Wade–Mingos rules [15, 16], if being electron deficient and relying on electron delocalization and multicenter bonding. In several cases, a simple description of the electronic situation fails, usually as a function of the complexity of the system as the number of atom and/or metal types is increased. In such cases, detailed quantum chemical studies are required to shed light on bonding and electronic properties.
4. To illustrate the conformation of the clusters, the "@" symbol is used to indicate interstitial atoms in intermetalloid clusters (first class), whereas for metal atoms that are coordinated by a polyanionic ligand in the style of a coordination compound, thereby forming a heterometallic cluster, this symbol is not employed; instead, such metal atoms are linked to the ligand's formula by a "–" dash. Different atom types within one cluster shell are combined without discrimination.
5. To simplify the prose, we will not discriminate between semimetal atoms and metal atoms in the following – except for the description of electronic or material properties.

2 Binary Heterometallic and Intermetalloid Clusters

2.1 *M/Tt-Based Clusters*

A versatile synthetic route for generating compounds with intermetalloid clusters makes use of Zintl anions – either in solution starting from soluble, molecular Zintl anions or via high-temperature routes. Soluble-starting materials permit comparatively controllable reactions, as they contain small molecular Zintl anions – e.g., Tt_4^{4-}, Tt_9^{4-}, and Pn_7^{3-} (Tr=triel=group 13 element, Tt=tetrel=group 14 element, Pn=pnictogen=group 15 element) beside alkali or earth alkali metal counterions [11–13]. Focusing on simple binary Zintl compounds like NaSi, one assumes that all atoms of the electropositive elements transfer their valence electrons to the moderate electronegative partner [17]. Therefore, NaSi formally consists of Na^+ and Si^- ions. The latter form Si_4^{4-} tetrahedra in the solid state, isoelectronic to white phosphorous, which are surrounded by Na^+ cations within a saltlike Zintl phase $(Na^+)_4(Si^-)_4$. Some of the Zintl phases are soluble, usually in very basic and polar solvents such as NH_3, ethane-1,2-diamine (*en*), or dimethylformamide (DMF), which allows their use in solution syntheses of larger clusters. However, the solubility largely depends on the charge density of the anion. Compounds with small and highly charged anions, such as Tt_4^{4-}, are restricted to reactions in liquid ammonia, leading to their limited use as precursors and only a handful of compounds containing these building blocks. The larger Tt_9^{4-} anion, in contrast, is well soluble without decomposition in the named solvents and has therefore been most frequently used as the starting species. To increase both the solubility and the crystallization tendency of reactants as well as products, and to inhibit decomposition of the anions by electron transfer back to the cation, most of the starting materials in reactions toward heterometallic and intermetalloid clusters have been salts of polyanions comprising sequestrated cations. The most commonly used sequestration agents have so far been 1,4,7,10,13,16-hexaoxacyclooctadecane (18-crown-6) or 4,7,13,16,21,24-hexaoxa-1,10-diazabicyclo[8.8.8]-hexacosane ([2.2.2]crypt).

During the past two decades, a large number of compounds comprising binary intermetalloid cluster anions of the type $[M@Tt_x]^{y-}$ (M=transition metal) have been synthesized. Most of the compounds were obtained by reaction of a binary Zintl phase containing homoatomic, deltahedral Zintl anions with a transition metal complex of an electron-rich metal atom. Usually, the transition metal released the afore bound organic ligands during the reaction, to be completely encapsulated by the cage, which often retained its original, deltahedral structure. To date, it remains unclear whether the uptake of the transition metal atoms is enabled by a simple "breathing" of the cage to let the metal atom enter or whether a cascade of more or less significant deconstructions/reconstructions are necessary for the generation of the finally observed products. Most indications are in favor of the latter; however, these processes are too quick to be traceable by nuclear magnetic resonance (NMR) spectroscopy, for example.

Table 1 gives an overview of structurally characterized binary assemblies involving tetrel atoms. As outlined above, the list comprises intermetalloid clusters

Table 1 Overview of structurally characterized binary transition metal–tetrel intermetalloid or heterometallic clusters and transition metal complexes with homoatomic polytetrelide anions as ligands (with increasing number of Tt atoms for each of the categories) that were extracted as single crystals from solution as $[K([2.2.2]crypt)]^+$ salts or from a solid-state reaction. Other cations than $[K([2.2.2]crypt)]^+$ are denoted in the footnote

Formula	Tt reactant	References	Figure no.
Ge			
$[Ni@Ge_9]^{3-}$	K_4Ge_9	[18, 19]	
$[Ni@Ge_9–NiCO]^{2-}$	K_4Ge_9	[18]	Fig. 1a
$[Ni@Ge_9–NiPPh_3]^{2-}$	K_4Ge_9	[20]	
$[Ni@Ge_9–NiCCPh]^{3-}$	K_4Ge_9	[18]	
$[Ni@Ge_9–PdPPh_3]^{2-}$	K_4Ge_9	[21]	
$[Fe@Ge_{10}]^{3-}$	K_4Ge_9	[22]	Fig. 1e
$[Co@Ge_{10}]^{3-}$	K_4Ge_9	[23]	Fig. 1e
$[Ru@Ge_{12}]^{3-}$	K_4Ge_9	[24]	Fig. 1f
$[Ni_2@Ge_{13}Ni_4(CO)_5]^{4-}$	K_4Ge_9	[20]	Fig. 1h
$[Co_2@Ge_{16}]^{4-}/[Co_2@Ge_{16}]^{-}$	K_4Ge_9	[25]	
$[Ni_3@Ge_{18}]^{4-}$	K_4Ge_9	[19]	Fig. 1m
$[Pd_2@Ge_{18}]^{4-}$	K_4Ge_9	[26]	Fig. 1l
$[(\eta^3,\eta^3\text{-}\{Si_{4-x}Ge_x\})(CuMes)_2]^{4-}$ [a]	$Rb_{12}Si_{12}Ge_5$	[27, 29]	Fig. 2a
$[(\eta^2\text{-}\{Si/Ge\}_4)Zn(\eta^2\text{-}\{Si/Ge\}_4)]^{6-}$	$K_{12}Si_{12}Ge_5$	[28]	
$[(\eta^3\text{-}Ge_4)Zn(\eta^2\text{-}Ge_4)]^{6-}$	$K_{14}ZnGe_{16}$	[29]	Fig. 2b
$[Ge_8Fe(CO)_3]^{3-}$	K_4Ge_9	[30]	
$[Ge_8(Mo\{CO\}_3)_2]^{4-}$	K_4Ge_9	[31]	Fig. 2e
$[Ge_9(Si\{SiMe_3\})_3(Cr\{CO\}_3)]^{-}$ [b]	$[Li(thf)_4][Ge_9(Si\{SiMe_3\}_3)_3]$	[32]	Fig. 3d
$[(\eta^3\text{-}Ge_9\{Si(SiMe_3)_3\}_3)Pd(\eta^3\text{-}Ge_9\{Si(SiMe_3)_3\}_3)]^{2-}$	K_4Ge_9	[33]	Fig. 3e
$[(\eta^3\text{-}Ge_9\{Si(SiMe_3)_3\}_3)Cu(\eta^3\text{-}Ge_9\{Si(SiMe_3)_3\}_3)CuPPh_3]$	K_4Ge_9	[33]	Fig. 2f
$[M(Ge_9\{Si(SiMe_3)_3\}_3)_2]^{-}$; M=Cu, Ag;[b] M=Au[b]	$[Li(thf)_4][Ge_9(Si\{SiMe_3\}_3)_3]$	[34, 35]	
$[(\eta^3\text{-}Ge_9\{Si(SiMe_3)_3\}_3)M(\eta^3\text{-}Ge_9\{Si(SiMe_3)_3\}_3)]$ M=Zn, Cd, Hg	$[Li(thf)_4][Ge_9(Si\{SiMe_3\}_3)_3]$	[36]	
$[(\eta^{3,4}\text{-}Ge_9)–ML]^{3-}$; M=Cu; L=$P^iPr_3$, PCy_3[c]; M=Ni; L=CO	K_4Ge_9	[37]	Fig. 3c
M=Pd; L=PPh_3	K_4Ge_9	[18]	
M=Zn; L=Ph, ^{i}Pr, Mes	K_4Ge_9	[21, 38, 39]	Fig. 4c
$[Ge_9 - Cu(\eta^4\text{-}Ge_9)]^{7-}$ [d]	K_4Ge_9	[37]	
$[Ge_9Au_3Ge_9]^{5-}$	K_4Ge_9	[40]	Fig. 3k
$[Au_3Ge_{45}]^{9-}$ [e]	K_4Ge_9	[41]	
$[Ge_6(M\{CO\}_5)_6]^{2-}$; M=Cr, Mo, W [f]	GeI_2	[42, 43]	Fig. 2d
$[Ge_9(InPh_3)_2]^{4-}$	K_4Ge_9	[31]	
$[Ge_9(Si\{SiMe_3\})_3(Cr\{CO\}_5)]^{-}$ [b]	$[Li(thf)_4][Ge_9(Si\{SiMe_3\}_3)_3]$	[32]	
$[Ge_{10}(Mn\{CO\}_4)]^{3-}$	K_4Ge_9	[44]	Fig. 2f

(continued)

Table 1 (continued)

Formula	Tt reactant	References	Figure no.
$[Ge_{10}(Fe\{CO\}_4)_8]^{6-}$ [e]	GeBr	[45]	Fig. 2g
$^1_\infty[Hg(\eta^3\text{-}Ge_9)]^{2-}$)[c]	K_4Ge_9	[46, 47]	
$[Hg_3(\eta^2\text{-}Ge_9)_4]^{10-}$	K_4Ge_9	[48]	Fig. 3h
Sn			
$[Co@Sn_9]^{4-}$	$K_{4.79}Co_{0.79}Sn_9$	[49]	
$[Co@Sn_9]^{5-}$ [d]	$K_{12.92}Co_{0.95}Sn_{17}$, $K_{13}CoSn_{17}$, $K_{4.79}Co_{0.79}Sn_9$	[50, 51]	
$[Ni@Sn_9]^{4-}$ [g]	$Na_{11.98}Ni_{0.93}Sn_{17}$	[50, 52]	
$[Ni@Sn_9\text{–}NiCO]^{2-}$	K_4Sn_9	[53]	Fig. 1b
$[Pt@Sn_9\text{–}PtPPh_3]^{2-}$	K_4Sn_9	[53]	
$[Pt@Sn_9H]^{3-}$	K_4Sn_9	[54]	
$[Cu@Sn_9]^{3-}$ [h]	K_4Sn_9, $K_{12}Sn_{17}$	[55–57]	Fig. 1c
$[Fe@Sn_{10}]^{3-}$	K_4Sn_9	[58]	
$[Ir@Sn_{12}]^{3-}$	K_4Sn_9	[59]	
$[Ti_4@Sn_{15}Cp_5]^{z-}$ $(z = 4...5)$ [d,h]	K_4Sn_9	[60]	Fig. 1i
$[Sn_{17}\{GaCl(ddp)\}_4]$	$SnCl_2$	[61]	
$[Co_2@Sn_{17}]^{5-}$	$K_{4.79}Co_{0.79}Sn_9$	[49, 51]	
$[Ni_2@Sn_{17}]^{4-}$	K_4Sn_9	[62]	Fig. 1j
$[Pt_2@Sn_{17}]^{4-}$	K_4Sn_9	[54]	Fig. 1k
$[Pd_2@Sn_{18}]^{4-}$	K_4Sn_9	[63, 64]	
$[Sn@Cu_{12}@Sn_{20}]^{12-}$ [d,g]	$Na_{12}Cu_{12}Sn_{21}$, $K_{12}Cu_{12}Sn_{21}$	[65]	Fig. 1n
$[(\eta^2\text{-}Sn_4)Au(\eta^2\text{-}Sn_4)]^{7-}$	$K_{12}Sn_{17}$	[57]	
$[(\eta^4\text{-}Sn_8)TiCp]^{3-}$	K_4Sn_9	[60]	
$(TlSn_8)^{3-}$	KTlSn	[66]	
$(TlSn_9)^{3-}$	KTlSn	[66]	
$[(\eta^4\text{-}Sn_9)M(CO)_3]^{4-}$; M=Cr	K_4Sn_9, $KSn_{2.05}$	[67, 68]	Fig. 3b
M=Mo			
M=W		[67, 69, 70]	
$[(\eta^4\text{-}Sn_9)M\text{–}L]^{3-}$; M=Zn; L=Ph	K_4Sn_9	[38]	
M=Zn; L=C_3H_7, C_9H_{11}		[39]	
M=Cd; L=$PhSn^nBu_3$		[71]	
M=Ir; L=cod		[59, 72]	
$[(\eta^5\text{-}Sn_9)WCO_3]^{4-}$	K_4Sn_9	[67]	Fig. 3a
$[(\eta^3\text{-}Sn_9)Ag(\eta^3\text{-}Sn_9)]^{5-}$	K_4Sn_9	[73]	Fig. 3j
$[(\eta^3\text{-}Sn_9)Hg(\eta^3\text{-}Sn_9)]^{6-}$	K_4Sn_9	[74]	Fig. 3g
$[Sn_6(M\{CO\}_5)_6]^{2-}$; M=Cr[f]	$SnCl_2$	[43]	
M=Mo, W[f]		[42]	
$[TiCp_2(\eta^1\text{-}Sn_9)(NH_3)]^{3-}$	K_4Sn_9	[60]	

(continued)

Table 1 (continued)

Formula	Tt reactant	References	Figure no.
Pb			
$[Cu@Pb_9]^{3-}$	K_4Pb_9	[57]	
$[Ni@Pb_{10}]^{2-}$	K_4Pb_9	[75]	Fig. 1d
$[Mn@Pb_{12}]^{3-}$	K_4Pb_9	[76]	Fig. 1g
$[Rh@Pb_{12}]^{3-}$	K_4Pb_9	[77]	
$[Ni@Pb_{12}]^{2-}$	K_4Pb_9	[78]	
$[Pd@Pb_{12}]^{2-}$	K_4Pb_9	[78]	
$[Pt@Pb_{12}]^{2-}$	K_4Pb_9	[79]	
$[(\eta^5\text{-}Pb_5)\{MoCO_3\}_2]^{4-}$	K_4Pb_9	[80]	Fig. 2c
$[(\eta^4\text{-}Pb_9)M(CO)_3]^{4-}$; M=Cr	$KPb_{2.26}$, K_4Pb_9	[81]	
M=Mo		[69, 82]	
M=W		[69]	
$[(\eta^5\text{-}Pb_9)MoCO_3]^{4-}$	K_4Pb_9	[82]	
$[(\eta^4\text{-}Pb_9)ML]^{3-}$; M=Zn; L=Ph	K_4Pb_9	[38]	
M=Zn; L=C_3H_7, C_9H_{11}		[39]	
M=Cd; L=Ph		[71]	
M=Ir; L=cod		[72]	
$[(\eta^4\text{-}Pb_9)\text{–}Cd\text{–}Cd\text{–}(\eta^3\text{-}Pb_9)]^{6-}$	K_4Pb_9	[83]	Fig. 3i

[a] $[Rb(18\text{-crown-}6)]^+$
[b] $[Li(thf)_n]^+$ (n = 4,6)
[c] $[K([2.2]crypt)]^+$
[d] K^+
[e] Na^+/K^+
[f] $[PPh_4]^+$
[g] Na^+
[h] $[K(18\text{-crown-}6)]^+$ and/or $[K([2.2.2]crypt)]^+$ counterion
thf tetrahydrofurane, *Mes* mesityl, *Ph* phenyl, *iPr* isopropyl, *Cy* cyclohexyl, *cod* 1,4-cyclooctadiene, *nBu* *n*-butyl, *Cpr* cyclopropyl, *[2.2]crypt* 1,7,10,16-tetraoxa-4,13-diazacyclooctadecane, *ddp* $HC(CMeNC_6H_3\text{-}2,6\text{-}iPr_2)_2$

with up to three interstitial transition metal atoms within a shell comprising tetrel atoms, heterometallic clusters that are composed of two different type of atoms, and homoatomic clusters with terminal ligands that are linked to the cluster via a second type of metal atoms. The first and selected examples of the second class are outlined into more detail in the subsequent text; selected molecular structures are shown in Figs. 1, 2, and 3. Figure 4 illustrates molecular orbitals of selected clusters.

The smallest binary intermetalloid clusters $[M@Tt_9]^{x-}$ ($x = 3,\ldots, 5$, Fig. 1c) have been obtained from reactions of Tt_9^{4-} anions with d^{10} transition metal complexes [18, 19, 50, 51, 55–57]. The resulting intermetalloid clusters show the same behavior as their parent Zintl anions, which are highly fluxional in solution. Alike the empty cages, they undergo structural fluctuations from a capped square antiprism (C_{4v} symmetry) into a tricapped trigonal prism (D_{3h} symmetry) and back, with an only small energy barrier between them, and they are prone to one-electron redox reactions. Electron paramagnetic resonance (EPR) as well as ^{119}Sn, ^{207}Pb,

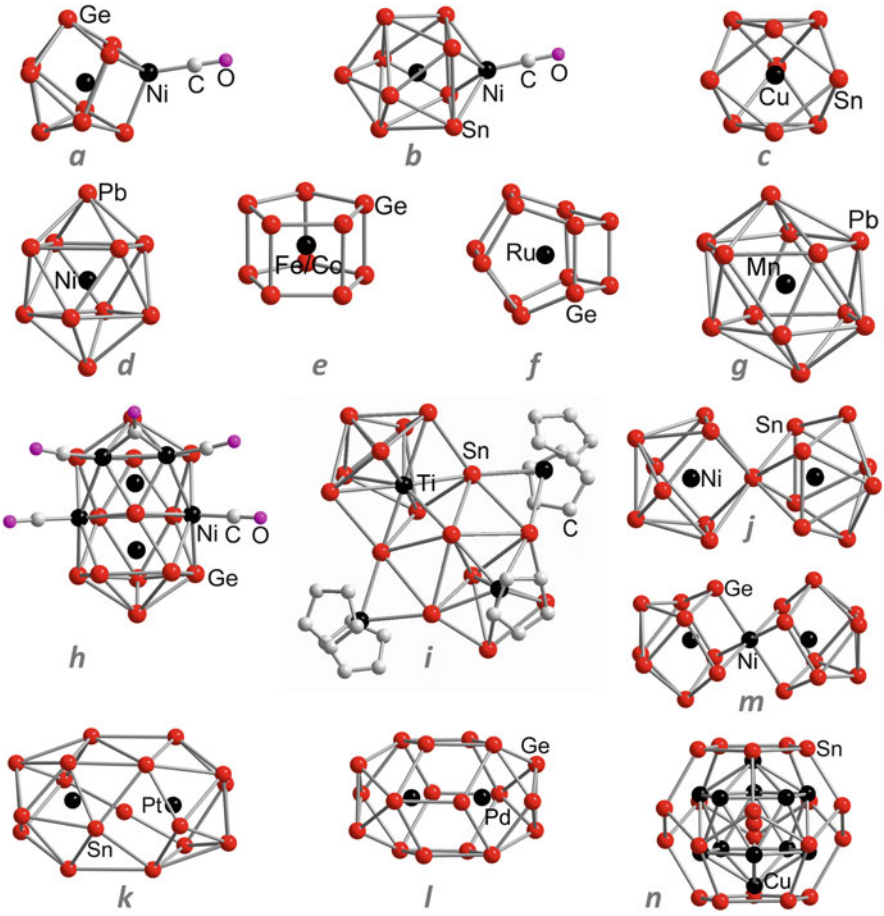

Fig. 1 Examples for molecular structures of binary transition metal–tetrel intermetalloid clusters (**a**–**n**) (For details, see the text)

and ^{63}Cu NMR studies confirmed the existence of paramagnetic $[Ni(0)@(Ge_9)^{3-}]^{3-}$ and diamagnetic $[Cu(I)(Tt_9)^{4-}]^{3-}$ species and the described fluxionality of the cages. The clusters are disordered in their crystal structures, which seems to be a general problem of nearly all known spheroidal intermetalloid clusters. Furthermore, in several cases, the two conformations according to C_{4v} or D_{3h} symmetry, respectively, coexist in the solid state [19]. The electronic structures of the C_{4v} symmetric species are in line with the description given by the Wade–Mingos rules for *nido*-type, 22 skeleton electron clusters [(9 × 4 valance electrons from Tt) + 4 charge electrons – 9 × 2 *exo*-electrons = 40 valence electrons – 18 *exo*-electrons], as the interstitial atoms with their closed d^{10} electron shells do formally not contribute to the cluster skeleton electron number. The paramagnetic cluster, however, is highly disordered, such that a direct electron number–structure

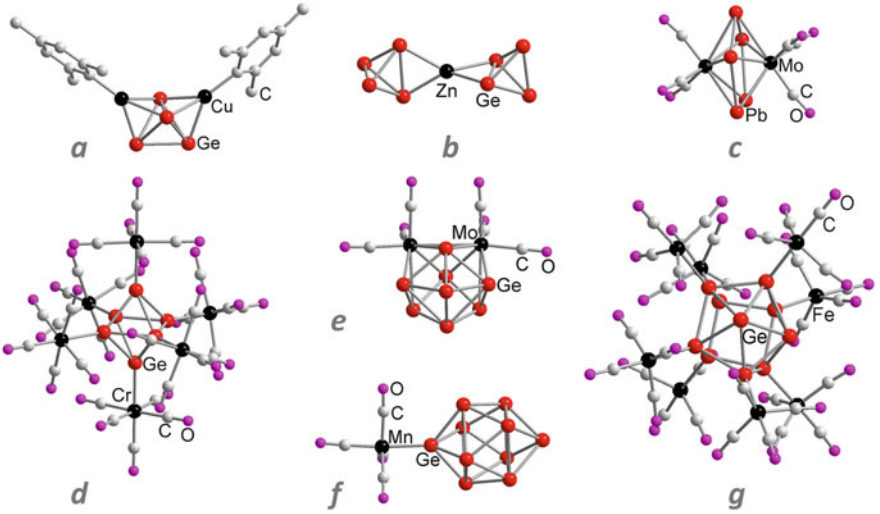

Fig. 2 Examples for molecular structures of binary transition metal–tetrel heterometallic clusters or transition metal complexes with tetrel polyanions with up to ten atoms as ligands (**a**–**g**) – except for those based on nine-atom tetrel cages, which are shown in Fig. 3 (For details, see Table 1)

correlation is impossible. As an exception regarding the synthetic approach, $[Co@Sn_9]^{5-}$ was the first intermetalloid cluster of this *nido*-type family, which was directly extracted from a ternary Zintl phase formed in a high-temperature reaction without the "detour" over the isolated homoatomic Zintl anion. The compound was furthermore used for the generation of $[K([2.2.2]crypt)]_5[Co_2@Sn_{17}]$ [49, 51] discussed below [50, 51]. As reported for the empty Tt_9^{4-} cages as ligands in complexes of the type $[Tt_9–ML_n]^{x-}$ (e.g., in $[(\eta^4\text{-}Ge_9)ML]^{3-}$, M=Cu; L=$P^iPr_3$, PCy_3 [37], $[(\eta^5\text{-}Pb_9)Mo(CO)_3]^{4-}$ [82], and $[(\eta^5–Sn_9)W(CO)_3]^{4-}$ [67], see Table 1), also the endohedrally filled clusters $[M@Tt_9]^{x-}$ can act as ligands to transition metal atoms. The resulting clusters like $[Ni@Ge_9–NiCO]^{2-}$ (Fig. 1a), $[Ni@Ge_9–NiCCPh]^{3-}$ [18], $[Ni@Ge_9–PdPPh_3]^{2-}$ [21], or $[Ni@Ge_9–NiPPh_3]^{2-}$ [20] resemble *hypo-closo*-type cages with the Ni-centered *nido* cluster acting as η^4 ligand throughout.

Upon (formal) expansion of the cage by another atom, one obtains clusters of the type $[M@Tt_{10}]^{x-}$ ($x = 2$, 3), which adopt one of the two different cage types: a deltahedral, bicapped square antiprismatic one in $[Ni@Pb_{10}]^{2-}$ (Fig. 1d) [75] or a pentagonal prismatic cage in $[M@Ge_{10}]^{3-}$ (M=Fe, Co, Fig. 1e) [22, 23]. The deltahedral cage is a *closo*-type cluster with 22 skeleton electrons, following the same formalism as given above [(10 × 4 electrons from Ge) + 2 charge electrons – 10 × 2 *exo*-electrons = 42 valence electrons – 20 *exo*-electrons], such as the known empty ones with the formula Tt_{10}^{2-} [12]. The incorporation of Fe and Co atoms – as the first interstitial metals from groups left of group 10 – led to the first examples of non-deltahedral polytetrelide cages: $[M@Ge_{10}]^{3-}$ represents M-centered pentagonal prisms of Ge atoms. Ge–Ge and Ge–M distances are hereby similar to those

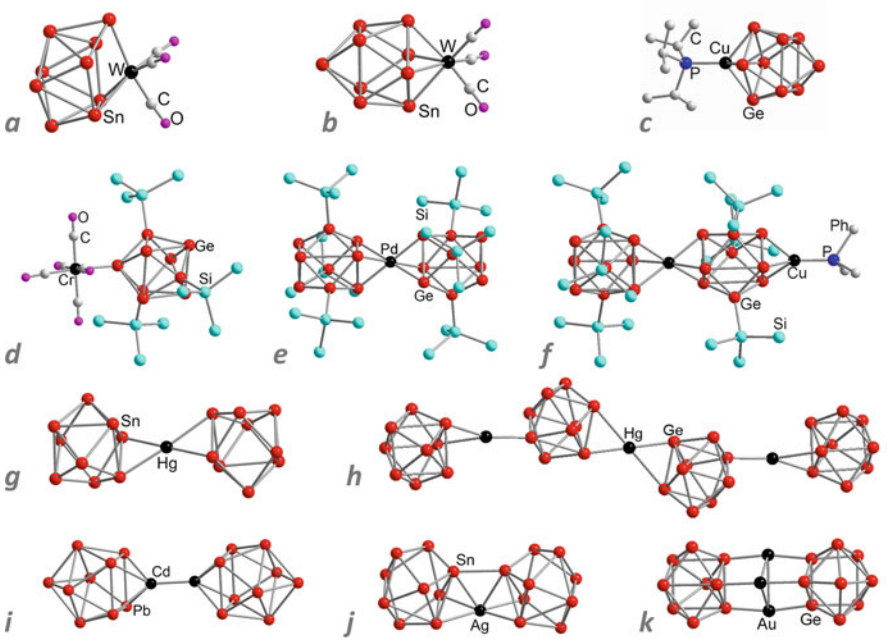

Fig. 3 Examples for molecular structures of binary transition metal–tetrel heterometallic clusters or transition metal complexes based on tetrel polyanions with nine atoms as ligands (**a**–**k**) (For details, see Table 1)

in binary intermetallic compounds, which rationalized their denomination as intermetalloid clusters. Conventional electron counting is impractical for both anions. Nevertheless, according to DFT (density functional theory) calculations, Ge–Ge bonds are only partially localized (Fig. 4c). The total energies of the isomeric D_{5h}-symmetric and D_{4d}-symmetric states differ by 55.7 kJ/mol ($[Co@Ge_{10}]^{3-}$) and 22.3 kJ/mol ($[Ni@Ge_{10}]^{2-}$), respectively, with the first being the favored structure for M=Co and the second being the slightly preferred one in the case M=Ni [23]. However, the formation pathway of these clusters out of deltahedral $(Ge_9)^{4-}$ anions remains unknown to date.

Several binary *closo*-clusters with icosahedral shape, $[M@Tt_{12}]^{x-}$ ($x = 2...3$), are accessible upon reaction of heavier tetrel nine-atom cages with electron-rich transition metal complexes bearing cod (1,4-cyclooctadiene) or phosphine ligands – either as main product or as side product, like in the case of $[Ni@Pb_{12}]^{2-}$, which is heavily distorted owing to the small atomic radius of the Ni atom (Fig. 1g) [55, 59, 78, 79]. The organic ligands seem to play the role as oxidizing agents, being reductively coupled or hydrogenated themselves. $[Ir@Sn_{12}]^{3-}$ was obtained in a stepwise reaction, which allowed some insight into the formation mechanism of the so-called stannaspherene cluster [59]. Starting out from K_4Sn_9, [2.2.2]crypt and $[IrCl(cod)]_2$ in *en*, an intermediate product containing a hetero-10-atomic cage,

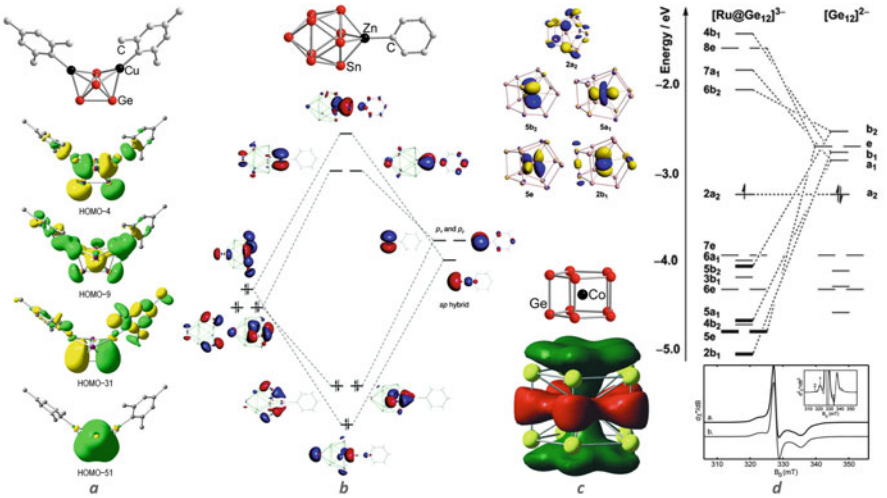

Fig. 4 Molecular structure (*top*) and illustration of s-, p-, and d-type cluster orbitals (*bottom*) of $[(\eta^3,\eta^3\text{-}\{Ge_4\})(CuMes)_2]^{4-}$ (reproduced with permission from the American Chemical Society) (**a**). Molecular structure (*top*) and frontier orbital region of the qualitative MO scheme (*bottom*) of complexes of the type *closo*-$[E_9ZnPh]^{3-}$ (E = Si, Ge, Sn, Pb) (reproduced with permission from the American Chemical Society) (**b**). Molecular structure (*center*) and one of the bonding orbitals (*bottom)* of $[Co@Ge_{10}]^{3-}$ (reproduced with permission from Wiley-VCH) (**c**). MO scheme along with the illustration of selected molecular orbitals (*top*) and measured as well as simulated EPR spectrum (*bottom*) of the intermetalloid cluster $[Ru@Ge_{12}]^{3-}$ (Reproduced with permission from the American Chemical Society) (**d**)

$[Sn_9Ir(cod)]^{3-}$, was isolated. Upon further heating to 80°C, the cod ligand was removed under oxidation and reorganization of the cluster to yield $[Ir@Sn_{12}]^{3-}$.

Two clusters with 12-atom cages break ranks. Similar to the Fe-centered 10-vertex cluster, the related Ge_{12} cage in $[Ru@Ge_{12}]^{3-}$ (Fig. 1f) features a non-deltahedral architecture [24]. All Ge atoms have three neighbors, thus acting as *pseudo*-pnictogen atom. The cage possesses idealized D_{2d} symmetry. Whereas the low-lying Fe 3d orbitals are structurally inert, the Ru 4d orbitals are strongly mixed with unoccupied cluster orbitals, resulting in an extensive delocalization of electron density from the Ru atom onto the main group atom shell. As a result, one can describe the $\{Ge_{12}\}$ cage as being electron precise – with the lack of one electron, hence, resulting in a paramagnetic cluster shell, as confirmed by EPR spectroscopy (Fig. 4d). A second uncommon 12-atom open-shell cluster is found with the $[Mn@Pb_{12}]^{3-}$ anion (Fig. 1g). It adopts near D_{2h} symmetry [76], with a relatively broad range of Pb–Pb distances (2.589–2.883 Å), which was put down to the electron richness of the transition metal atom that leads to an initial loss of electron deficiency. Assuming that electron transfer takes place from the transition metal onto the surrounding cage, also in this case, $[Mn@Pb_{12}]^{3-}$ can be viewed as a 50 electron system [$(12 \times 4$ valence electrons$) + 2$ electrons from Mn], with five additional electrons within the $3d^5$ shell of the inner Mn(II) ions, and three electrons form the negative charge as an add-on, resulting in a "magnetic superatom" with

paramagnetic center and diamagnetic cage. In a theoretical study, all possible clusters of the type $[M@Tt_{12}]^{q-}$, with Tt being Si and Ge, M being Ti...Zn or Y...Cd, and q being 0 or 3, were investigated with DFT methods in six different topologies [84]. For each of the compositions, the authors compared the energies of a perfect icosahedron (I_h), a distorted icosahedron (D_{2d}), a hexagonal antiprism (D_{6d}), a hexagonal prism (D_{6h}), a puckered hexagonal prism (D_{3d}), and a bicapped pentagonal prism (D_{2d}), which represents the topology of the $[Ru@Ge_{12}]^{3-}$ anion, respectively. From this, some general trends for the cluster structures were derived: a preference for the D_{6h}-symmetric cluster is unique to anions with Tt=silicon, thus, not only depending on the electron count only (in turn, for $[M@Si_{12}]$, the icosahedron is extremely unfavorable and is never the global minimum). For total numbers of 54–56 and 58–60 electrons, the hexagonal prismatic and the bicapped pentagonal prismatic structures with three-connected atoms are generally preferred. A hexagonal antiprism is preferred as the cluster possesses less than 54 electrons. A puckered structure (D_{3d}) is observed for electron counts above 56 in the case of $[M@Si_{12}]$ (even above 54 for $[Cr@Ge_{12}]$ and $[Mo@Ge_{12}]$). The relative stability of the icosahedral clusters is greatest for d electron-rich transition metals. Hexagonal prismatic or bicapped pentagonal prismatic clusters are favored over the icosahedral ones as the principal quantum number of the d orbitals and/or the negative charge increases.

Twelve-atom cages are special in Zintl cluster chemistry – yet, empty Tt_{12}^{2-} anions have so far been unobserved. All known intermetalloid clusters with 12 vertices require stabilization by an interstitial atom. As the cluster shell grows, one atom does not seem to sufficiently stabilize the system. Hence, larger cages that were obtained in crystalline solids from solution possess at least two interstitial atoms. Solvents or transition metal complex ligands play a crucial role in product formation, again as redox-active reagents. $[Ni_2@Ge_{13}Ni_4(CO)_5]^{4-}$ (Fig. 1h), as a related case, is composed of two Ni-centered, *nido*-type 11-atom icosahedra fragments that share a $\{Ge_3Ni_3\}$ pentagonal face [16].

$[Ni_2@Sn_{17}]^{4-}$ (Fig. 1j) can be viewed as a coupling product of two $[Ni@Sn_9]^{2-}$ units [62]. Both cluster shells share a Sn atom. As compared to the Sn_9^{4-} parent cages, the shells are significantly deformed; the entire cluster adopts crystallographic D_{2d} symmetry in the end. The electron count for these species is in accordance with Wade–Mingos rules for fused clusters. The sum of valence electrons resembles the sum of electrons for all clusters, minus the number of electrons for eliminated fragments (upon fusion) that obey the octet rule: $[Ni_2@Sn_{17}]^{4-}$ is composed of two *nido*-$[Ni@Sn_9]^{4-}$ clusters. The central Sn atom, as eliminated fragment, is formally a Sn^{4-} atom (octet rule): 2 $[Ni@Sn_9]^{4-}$ – Sn^{4-} → $[\{Ni@Sn_8(\mu\text{-}Sn)_{1/2}\}_2]^{4-}$ [(2 × 40) electrons – 8 electrons = 72 electrons]. This sum matches the number of valance electrons provided by 17 Sn atoms + 4 negative charges. A kind of a *pseudo*-ternary species, comprising two different types of (semi-)metal atoms of tetrel elements, was reported with $[\{Ni@Sn_8(\mu\text{-}Ge)_{1/2}\}_2]^{4-}$ [52]. The anion is isostructural and isoelectronic to the $[Ni_2@Sn_{17}]^{4-}$ homolog [62], and it was obtained as its $[K([2.2.2]crypt)]^+$ salt upon co-extraction of the ternary Zintl phase $K_4Ge_{4.5}Sn_{4.5}$ with [2.2.2]crypt and $[Ni(cod)_2]$. Due to the size,

the larger Pt atoms can obviously not be incorporated into a 9-vertex cage. The $[Pt_2@Sn_{17}]^{4-}$ anion (Fig. 1k) is observed instead, as a closed polyhedron of 17 Sn atoms and an interstitial Pt dumbbell [54]. In the isostructural $[Pd_2@Ge_{18}]^{4-}$ [26] and $[Pd_2@Sn_{18}]^{4-}$ clusters (Fig. 1l) [63, 64], a prolate deltahedral shell surrounds a Pd dumbbell. The d^{10} Pd atoms have no bonding interaction with each other. In $[Ni_3@Ge_{18}]^{4-}$ (Fig. 1m), a linear $\{Ni_3\}$ fragment is protected by two highly distorted $\{Ge_9\}$ clusters that include one Ni atom each and coordinate to a third, shared one via one of the triangular faces [19]. The relation to the other, closed $\{Tt_{18}\}$ deltahedra is reduced to the (near) D_{3h} symmetry of the overall cluster and the presence of six Tt_3 rings that arise in a staggered manner along the C_3 axis.

As already mentioned in the introduction, the formation pathways of the clusters that comprise more than nine cage atoms are currently an actively investigated field [63, 64]. Valuable insights into formation processes in solution were recently accessible in liquid ammonia [60]. In a reaction of K_4Sn_9 and $K_{12}Sn_{17}$ with $[TiCp_2Cl_2]$ (Cp, cyclopentadienyl anion), diverse promising intermediates were crystallized as K^+ or $[K(18\text{-crown-}6)]^+$ salts: $[Ti(\eta^4\text{-}Sn_8)Cp]^{3-}$, $[TiCp_2(\eta^1\text{-}Sn_9)(NH_3)]^{3-}$, and $[Ti_4Sn_{15}Cp_5]^{z-}$ ($z = 4...5$, Fig. 1i). The Sn_8Ti fragment resembles a cutout of an $[M@Tt_{12}]^{z-}$ icosahedron or $[Ni_2@Sn_{17}]^{4-}$, and it is proposed to be the intermediate compound in the formation of the larger clusters. The diversity in the coordination environment of the Ti atoms in $[TiCp_2(\eta^1\text{-}Sn_9)(NH_3)]^{3-}$ and $[Ti_4Sn_{15}Cp_5]^{z-}$ largely suggests the participation of the transition metal in the formation of intermetalloid clusters starting from smaller aggregates. Nevertheless, the transfer of these observations onto other reactions at room temperature could not be realized, since experiments in more common solvents like *en*, DMF, or acetonitrile failed so far [60].

In summary, two formation pathways are currently discussed for the formation of larger intermetalloid clusters. According to the first suggestion, the Zintl anion replaces a ligand at the transition metal atom, which may then by encapsulated by the first with the possibility of subsequent capping of the cluster by another transition metal complex fragment or which may be coordinated by another Zintl anion with or without further distortion or oxidative aggregation of the parent anions. The second way would be a redox-mediated fragmentation/rearrangement of the cluster shell of a given intermetalloid cluster.

One should keep in mind the differences between cluster formation in solution, in the gas phase or in the solid state, respectively: in the gas phase, shell atoms are added atom by atom around a doping atom [85], and the processes in solid state are even more difficult to explore than in solution. For this, the formation of $[Co@Sn_9]^{5-}$ [50, 51], $[Ni@Sn_9]^{4-}$ [50], and the onion-like anion $[Sn@Cu_{12}@Sn_{20}]^{12-}$ [65] (Fig. 1n) could not yet be elucidated.

A large number of complexes were reported that can be viewed as heterometallic clusters (without interstitial metal atom) or as transition metal complexes with Zintl anions of tetrel atoms as ligands. Besides some complexes that comprise Tt_4^{4-} units as ligands, including several *pseudo*-ternary examples with mixed-atomic $(Tt_{4-x}Tt'_x)^{4-}$ anions, $[(\eta^3,\eta^3\text{-}\{Tt_{4-x}Tt'_x\})(CuMes)_2]$ (Tt, Tt′=Si, Ge, Sn, see Fig. 4a) [27] and $[(\eta^{2/3}\text{-}\{Tt_{4-x}Tt'_x\})M(\eta^{2/3}\text{-}\{Tt_{4-x}Tt'_x\})]$ (Tt, Tt′=Si; Ge; M=Zn) [28, 29],

most of the known examples are based on Tt_9^{4-} that coordinate to transition metal atoms in manifold ways. In some cases, the resulting complexes form spherical shells together, hence, representing heterometallic clusters (see Fig. 4b), such that a clear discrimination between these two categories becomes difficult. Some mixed-atomic cages $(Tt_{9-x}Tt'_x)^{4-}$ are also known [86]. However, only in one reported case, an underlying ternary alloy was used as starting material in reactions with transition metal complexes [52]. There exist also further heteroatomic nine-atom cages with elemental combinations Ge/Bi, Ge/Sb, or Ge/Sn/Bi, containing formal Pn^+ cations, which have been introduced as "doped" Zintl anions and have been further modified with organic and element-organic groups [87, 88]. Figure 2 shows a selection of complexes with tetrahedral tetrel atom cages as ligands to transition metal atoms and heterometallic clusters with five, six, eight, or ten tetrel atoms. In Fig. 3, the molecular structures of representative examples of clusters or complexes involving tetrel nine-atom cages are given. The bonding interaction of Ge_9^{4-} with a {ZnPh} fragment is discussed in Sect. 3.2 along with a related complex comprising a binary tetrel/pnictogen ligand.

2.2 *M/Pn-Based Clusters*

The solution chemistry of pnictogen polyanions, in particular Pn_7^{3-} or Pn_{11}^{3-} [89–119], has been known for longer than that of the polytetrelide anions. This is due to the much more established field of polypnictide chemistry in general and polyphosphide chemistry in particular. This type of species has a long tradition also in organoelement chemistry of accordingly neutral molecules with organic or element-organic substituents. Consequently, polypnictide cages have been easily transferrable into organic solvents and thus accessible for reactions with transition metal compounds. Also, intermetalloid cluster syntheses were systematically studied already in the late 1980s and early 1990s, starting out with reactions of the relatively well-soluble salts of Pn_7^{3-} (Pn=P, As, Sb) [89–101]. The very first example were $[(\eta^4\text{-}P_7)M(CO)_3]^{3-}$ [120] and $[Sb_7(NiCO)_3]^{3-}$ [121]. Related experiments with Bi_7^{3-} [101] or Bi_{11}^{3-} [122] have been missing so far, as the respective salts have only been isolated and published for the first time in 2015 and 2014, respectively. Instead, another access toward mixed-metallic clusters comprising Bi atoms was chosen, employing the intermetallic phase K_4Bi_5 [123, 124]. It contains planar, zigzag-type anions $Bi_4^{(4+\delta)-}$, which are known to produce Bi_2^{2-} and Bi_3^{3-} anions upon dissolving the phase in *en*, which made the phase a suitable starting material for polybismutide solution chemistry.

Table 2 provides an overview of structurally characterized binary assemblies involving pnictogen atoms. As for the clusters based on polytetrelide units, the list comprises intermetalloid clusters with an interstitial transition metal atom within a shell comprising pnictogen atoms, heterometallic clusters that are composed of two different types of atoms, and homoatomic clusters with terminal ligands that are linked to the cluster via a second type of metal atoms. The first and selected

Table 2 Overview of structurally characterized binary transition metal–pnictogen intermetalloid or heterometallic clusters and transition metal complexes with homoatomic polypnictide anions as ligands (with increasing number of Tt atoms for each of the categories) that were extracted as single crystal from solution as $[K([2.2.2]crypt)]^+$ salts or from a solid-state reaction. Other cations than $[K([2.2.2]crypt)]^+$ are denoted in the footnote

Formula	Pn reactant	References	Figure no.
P			
$[(P_5)Co\{HP=P(Mes)\}]^{2-}$	K_3P_7	[125]	
$[(Cp^*Mo)(\mu,\eta^6\text{-}cyclo\text{-}P_6)(Cp^*Mo)]$	P_4	[126]	
$[P_6(Cp^*Co)_3]$	$P_7(SiMe_3)_3$	[127]	
$[P_6(Cp^*Fe)_3]$	$P_7(SiMe_3)_3$	[127]	
$[(\eta^4\text{-}P_7)M(CO)_3]^{3-}$; M = Cr, Mo, W	K_3P_7	[120]	Fig. 6c
$[(\eta^4\text{-}P_7)NiCO]^{3-}$	K_3P_7	[128]	Fig. 6b
$[(\eta^2\text{-}P_7)PtH(PPh_3)]^{2-}$	K_3P_7	[128, 129]	
$[P_8(Cp^*_2Sm)_4]$	P_4	[130]	Fig. 5p
$[P_6(Cp^*Fe)_3(\{\mu^3\text{-}P_3\}Fe)]$	$P_7(SiMe_3)_3$	[127]	
$[(\eta^4\text{-}P_7)Cu_2(\eta^4\text{-}P_7)]^{4-}$	K_3P_7	[131]	
$[M_2(HP_7)_2]^{2-}$; M = Ag, Au	K_3P_7	[132]	
$[(Ni\{PBu_3\}_2)_4(P_{14})]$	$Li_3P_7 \cdot 3$ dme	[127]	Fig. 6g
$[(\eta^2\text{-}P_7)M(\eta^2\text{-}P_7)]^{4-}$; M = Zn, Cd	K_3P_7	[131]	Fig. 6e
$[P_7(FeCp\{CO\}_2)_3]$	$Li_3P_7 \cdot 3$ dme	[127]	Fig. 6d
As			
$[Nb@As_8]^{3-}$ [a]	Rb_3As_7	[133]	Fig. 5b
$[Mo@As_8]^{2-}$	K_3As_7	[133]	Fig. 5b
$[As@Ni_{12}@As_{20}]^{3-}$ [b]	K_3As_7	[134]	Fig. 1n
$[\{As_4(Mes)_2\}Co(As_3)]^{2-}$	K_3As_7	[135]	
$[(\mu^3\text{-}As_3)Co(CO)_3]$	$(AsCH_3)_5$	[136]	
$[(CpMo)(\mu,\eta^5\text{-}cyclo\text{-}As_5)(CpMo)]$	$(AsCH_3)_5$	[137]	Fig. 5n
$[(\eta^4\text{-}As_7)M(CO)_3]^{3-}$; M = Cr, Mo, W[a]	K_3As_7, Rb_3As_7	[120, 138]	
$[(\eta^2\text{-}As_7)PtH(PPh_3)]^{2-}$	K_3As_7	[129]	Fig. 6a
$[As_6(\mu^3\text{-}As_3)_2(CoPEt_2Ph)_6]$	K_3As_7	[127]	Fig. 5d
$[(\eta^2\text{-}As_7)M_2(\eta^2\text{-}As_7)]^{4-}$; M = Pd, Cu, Au[a,c]	K_3As_7, Rb_3As_7, $CsAs_7$	[131, 139, 140]	Fig. 6f
$[(\eta^2\text{-}As_7)M(\eta^2\text{-}As_7)]^{4-}$; M = Zn, Cd	K_3As_7	[131]	
$[Pd_7As_{16}]^{4-}$	K_3As_7	[139]	Fig. 5f
Sb			
$[(\mu^3\text{-}Sb_3)(MoCp\{CO\}_2)]/[(\mu^3\text{-}Sb_3)(MoCp^*\{CO\}_2)]$	cyclo-^{t}Bu$_4$Sb$_4$	[141]	Fig. 5j
$[Sb_3Ni_4(CO)_6]^{3-}$	K_5Sb_4	[142]	
$[(MoCp')(\mu,\eta^5\text{-}Sb_5)(MoCp')]$	cyclo-^{t}Bu$_4$Sb$_4$	[143]	
$[Sb_3Au_3Sb_3]^{3-}$	K_5Sb_4	[144]	
$[Sb_7M(CO)_3]^{3-}$; M = Cr, Mo, W	K_3Sb_7	[121, 145]	
$[Sb_7(NiCO)_3]^{3-}$	K_3Sb_7	[121]	Fig. 5o
$[Ni_5Sb_{17}]^{4-}$	K_3Sb_7	[146]	Fig. 5q

(continued)

Table 2 (continued)

Formula	Pn reactant	References	Figure no.
Bi			
$[Ni@Bi_6Ni_6(CO)_8]^{4-}$	K_5Bi_4	[142]	Fig. 5a
$[Zn@Zn_8Bi_4@Bi_7]^{5-}$	K_5Bi_4	[147]	Fig. 5c
$[Ni@Bi_6(NiCO)_4(Ni\{\eta^3\text{-}Bi_3\})_2]^{4-}$	K_5Bi_4	[148]	Fig. 5e
$[Bi{-}Zn{-}Bi]^{4-b}$	K_4ZnBi_2, K_3Bi_2	[149, 150]	
$[Bi_3M_2(CO)_6]^{3-}$; M = Cr, Mo	K_5Bi_4	[151]	Fig. 5i
$[Bi_3Ni_4(CO)_6]^{3-}$	K_5Bi_4	[142]	Fig. 5h
$[Bi_3Ni_6(CO)_9]^{3-}$	K_5Bi_4	[142]	Fig. 5g
$[Bi_4Fe_4(CO)_{13}]^{2-d}$	$[NEt_4]$ $[BiFe_3(CO)_{10}]$	[152]	Fig. 5m
$[Bi_4(Fe\{CO\}_3)_3(FeCp'\{CO\}_2)_2]$	$[(Cp\{CO\}_2Fe)$ $BiCl_2]$	[153]	Fig. 5k
$[Bi_4Ni_4(CO)_6]^{2-}$	K_5Bi_4	[142]	Fig. 5l

[a] $[Rb([2.2.2]crypt)]^+$
[b] $[P^nBu_4]^+$
[c] Rb^+
[d] $[NEt_4]^+$ and/or $[K([2.2.2]crypt)]^+$ counterion

examples of the second class are outlined into more detail in the subsequent text; selected molecular structures are shown in Figs. 5 and 6.

The group of binary intermetalloid clusters composed of transition metal and pnictogen elements is less diverse than according examples with tetrel element. The tendency of pnictogen elements to form electron precise, polycyclic cages with considerably strong covalent bonds rather than molecules with delocalized bonding, is already visible in the architectures of the homoatomic Zintl anions. The most popular ones, the nortricyclane-like structures of Pn_7^{3-} and the so-called ufosane-type anions Pn_{11}^{3-}, consequently accord with the Zintl–Klemm–Busmann *pseudo*-element concept. [89–119] However, some further species have been known, like Pn_2^{2-} [154], Pn_4^{2-} [155–161], or Pn_5^- [162–164], which show other bonding characteristics including aromatic behavior. In reactions of compounds bearing those anions with transition metal complexes, the Zintl anions prefer acting as a ligand with allocated electron pairs. Several examples of corresponding complexes, predominantly of the general type $[(\eta^x\text{-}Pn_7)_yM_zL_n]^{3-}$ ($x = 1,\ldots, 4$, $y = 1$ or 2, $z = 1$ or 2, $n = 0,\ldots, 3$), are to be found in the literature (see Fig. 6 for some examples) [13, 131, 139, 140]. The transition between those complexes and binary intermetalloid clusters are, however, seamless. A large number of $\{P_7\}$ cages that were functionalized by (element) organic groups and mixed $(P_{7-x}As_x)^{3-}$ have been reported, which are not explicitly referred to in this article, and a couple of hetero-main group cages $(E_xP_y)^{q-}$ (E=Tr, Tt) [165].

The first molecule that is situated at the border of a complex with polypnictide ligands and an intermetalloid cluster comprising pnictogen atoms is $[Nb@As_8]^{3-}$ (Fig. 5b) [166], which was, however, synthesized unwantedly at first. Following the *pseudo*-element concept, a Nb(V) cation is surrounded by an $\{As_8\}^{8-}$ crown. An

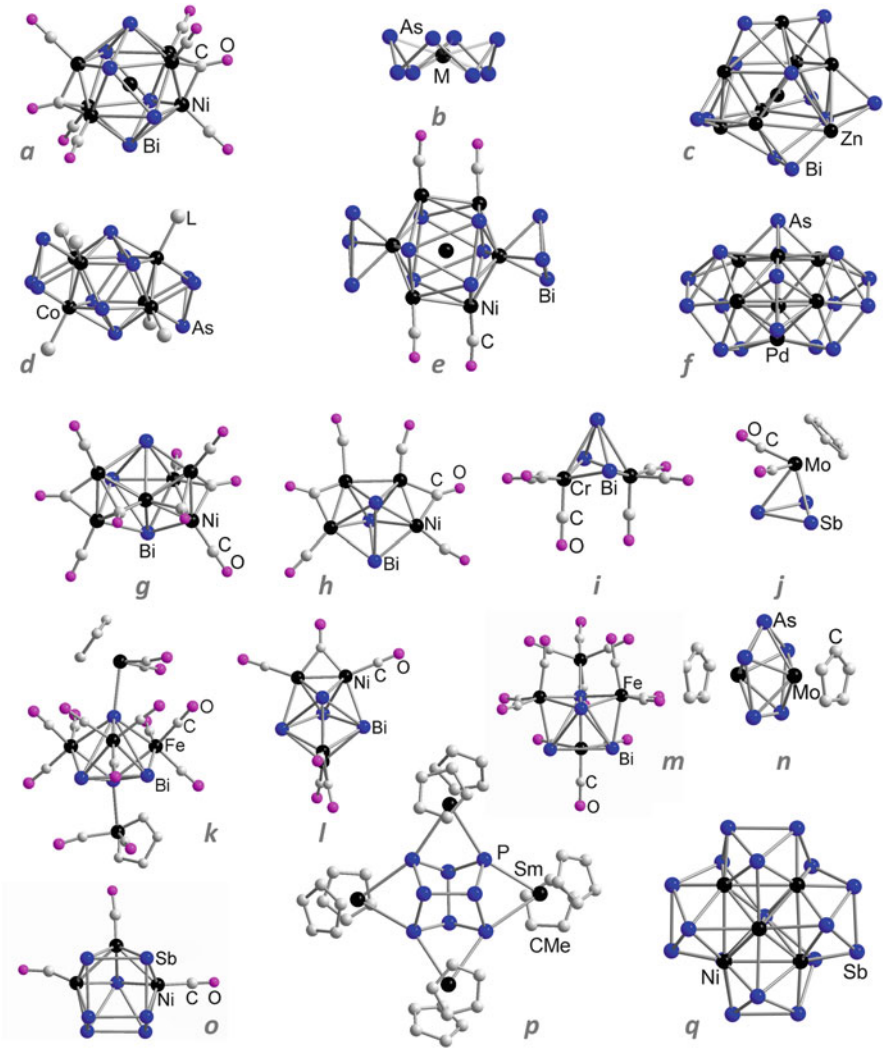

Fig. 5 Examples for molecular structures of binary transition metal–pnictogen intermetalloid clusters (**a**–**f**) or heterometallic clusters or transition metal complexes with pnictogen polyanions as ligands (**g**–**q**) – except for those based on seven-atom pnictogen cages, which are shown in Fig. 6 (For details, see the text and Table 2)

isoelectronic and isostructural $[Mo@As_8]^{2-}$ anion, with an even higher charged, interstitial Mo(VI) cation is known as well [133]. As simple electron count would result in a 16-electron complex in this case, additional electron donation from As p orbitals has been proposed that serve to fulfill the 18-electron rule at the central metal atom. As can be gathered from these two examples, pnictogen elements are capable of stabilizing higher charged, electron-deficient interstitial atoms – again as a consequence of their higher tendency to form nonmetallic, rather localized bonds.

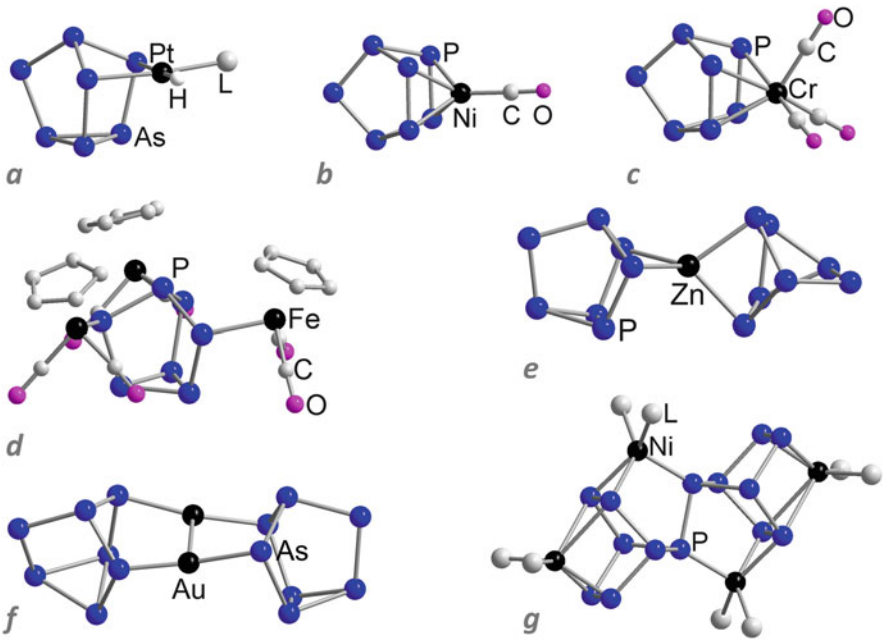

Fig. 6 Examples for molecular structures of transition metal complexes based on pnictogen polyanions with seven atoms as ligands (**a**–**g**) (For details, see Table 2)

Nevertheless, most of the binary intermetalloid clusters comprising pnictogen atoms have been formed so far with electron-rich transition metals. In all of these cases, a complete rearrangement of the Zintl anion precursor took place – except for Bi compounds, most often as bottom-up synthesis based on Bi_2^{2-} anions in solution occured. In $[Pd_7As_{16}]^{4-}$ (Fig. 5f) [139], a distorted, monocapped trigonal prism $\{Pd_7\}$, composed of six Pd(I) atoms and one Pd(III) atom with square planar coordination, is surrounded by two $\{As_5\}^-$ rings, which are isoelectronic with the Cp^- (cyclopentadienyl) anion, two $\{As_2\}^{2-}$ dumbbells, and two $\{As\}^{3-}$ atoms. Several complexes are further known that bear As_7^{3-} units as ligands to transition metal atoms. These are given in Table 2, and selected ones are shown in Fig. 5, which are, however, not discussed in detail here. Besides, a binary complex with formal Sn^{2+} as central atom, $[(As_7)Sn(\eta^2\text{-}As_7)]^{4-}$ [167], and further hetero-main group cages $(E_xAs_y)^{q-}$ (E=Tr, Tt) were reported [165], and several $\{As_7\}$ cages with (element) organic decoration are not mentioned here.

Another extraordinary example is the $[As@Ni_{12}@As_{20}]^{3-}$ anion [134], obtained by reaction of K_3As_7, $[P^nBu_4]Br$ and $[Ni(cod)_2]$ in *en*. The cluster is isoelectronic and isostructural with the $[Sn@Cu_{12}@Sn_{20}]^{12-}$ anion (Fig. 1n) [65], which was generated in solid-state reactions eight years later. Analogous to the latter, the onion-like aggregate incorporates a single {As} atom, enclosed in a $\{Ni_{12}\}$ icosahedron, which itself is located within an $\{As_{20}\}$ pentagon dodecahedron as its dual

polyhedron. As another unusual feature of this anion, it crystallizes as an $[P^nBu_4]^+$ salt, hence, without any alkali metal (complex) counterions.

$[Ni_5Sb_{17}]^{4-}$ (Fig. 5q) [146] represents the only ligand-free intermetalloid cluster that comprises antimony atoms known to date. A part of the cluster is structurally related to $[Pd_7As_{16}]^{4-}$ (see above). As with Pn=As, complexes with Sb_7^{3-} acting as ligands have been reported, which are listed in Table 2 but not discussed here.

Bismuth as a metal does not rely so much on rather localized, covalent bonding only and is therefore capable of forming a number of intermetalloid and heterometallic clusters. Many of them represent carbonyl-coordinated clusters like $[Ni_4Bi_3(CO)_6]^{3-}$, $[Bi_4Ni_4(CO)_6]^{2-}$, $[Ni_6Bi_3(CO)_9]^{3-}$, and $[Ni_{0.33}@Bi_6Ni_6(CO)_8]^{4-}$ (Figs. 5a, g, h, l) [142], which can be described as more or less spherical molecules with the CO groups acting as terminal, μ-bridging or μ^3-bridging ligands. The only carbonyl-free example of a binary intermetalloid cluster involving Bi atoms has been $[Zn@Zn_8Bi_4@Bi_7]^{5-}$ (Fig. 5c) [147] so far. In this *closo*-type cluster, a {Zn} atom is incorporated in a distorted $\{Zn_8Bi_4\}$ icosahedron, which is capped by seven further Bi atoms. To achieve the total number of 50 valence electrons (for 26 skeleton electrons), the icosahedron contributes with [(4 × 5 valence electrons from Bi) + (8 × 2 valence electrons from Zn =)] 36 valence electrons, two further electrons are gained from the interstitial Zn atom, five is from the charge, and one electron is donated from each of the seven Bi ligands. The latter is a quite unusual donor behavior of a pnictogen atom, which, however, was rationalized by means of quantum chemical analyses.

With increasing cluster size of intermetalloid clusters comprising heavier pnictogen elements As, Sb, and Bi, the bonding situation seems to become more complex, and the clear tendency to form two-electron two-center bonds vanishes. This is a trend to be continued when proceeding to ternary intermetalloid clusters (see next section).

3 Ternary Heterometallic and Intermetalloid Clusters

As mentioned in the introduction, tetrahedral anions like Tt_4^{4-} would enlarge the variety of starting materials in the style of the highly diverse chemistry of P_4 and As_4 [168–176], which has so far not been realized to a great extent due to the high atomic charges and consequently poor solubility of these homoatomic species. However, this can be overcome by isoelectronic replacement of a (formally) charged tetrel atom by a (formally) neutral pnictogen atom, which largely enhances the solubility of the resulting tetrahedral anions $(Tt_2Pn_2)^{2-}$. The replacement can also be viewed in the inverse direction, in the sense that a tetrahedral Pn_4 moiety is partially substituted with Tt(−I) or Tr(−II) atoms within tetrahedral anions $(Tt_2Pn_2)^{2-}$ or $(TrPn_3)^{2-}$. Such anions have been reported as $[K([2.2.2]crypt)]^+$ salts for the following elemental combinations: Sn/Sb [177], Sn/Bi [178, 179], Pb/Sb [180], Pb/Bi [181], Ga/Bi, and In/Bi [197]. Beside lower charge and higher solubility, the binary anions within the starting material allow for an even larger

electronic and structural diversity to be transferred into the resulting heterotrimetallic product clusters. We mention in passing that the isoelectronic replacement can also lead to an increase of the charge, as realized for the binary triel/tetrel tetrahedron $(TlSn_3)^{5-}$ in the solid phase $Na_5(TlSn_3)$ [182]. However, the even poorer solubility of this phase and its homologs definitely inhibits the use of the anions for reactions in solution, still leaving an option for reactions in high-temperature fluxes, which had indeed been realized.

The vast majority of ternary intermetalloid clusters have so far been accessed by reactions of the $[K([2.2.2]crypt)]^+$ salts of the quoted binary Tt/Pn and Tr/Pn Zintl anions with diverse transition metal or lanthanide complexes. The resulting clusters show a variety of molecular structures, all of which differ from those that were obtained upon reactions with homoatomic Zintl anions, owing to the change in electronic and coordination prerequisites. Crystallographic analyses turned out to be difficult, since most of the clusters are spheroidal and thus tend to exhibit rotational disorder in the crystal. Furthermore, in some cases, different clusters of the same charge co-crystallize on the same crystallographic positions. Hence, even if the involved main group elements are not direct or second next neighbors in the periodic table (which systematically cannot be discriminated by X-rays), assignment of the different atom types can be very challenging. For this, a meticulous analysis utilizing further spectroscopic and spectrometric methods, such as ESI-MS (electrospray mass spectrometry), EDX (energy-dispersive X-ray spectroscopy), μ-RFA (micro X-ray fluorescence analysis), IR (infrared spectroscopy), or NMR spectroscopy, as well as complementary magnetic measurements and quantum chemical investigations, most commonly using density functional theory (DFT) methods, is inevitable to prevent mistakes and to draw a comprehensive picture. Table 3 gives an overview of all structurally characterized ternary assemblies of the combinations M/Tr/Tt, M/Tr/Pn, and M/Tt/Pn. The list comprises intermetalloid clusters as well as heterometallic complexes.

3.1 *M/Tr/Tt-Based Clusters*

The underrepresentation of triel elements in Zintl anion chemistry is reflected in the only small number of intermetalloid and heterometallic clusters with the involvement of triel element atoms. This is valid in particular for clusters with homoatomic triel moieties but also in the case of the highly charged triel/tetrel elemental combinations. Hence, until today, $[Ni@Sn_9Tl]^{3-}$ (Fig. 7a) [183] remains the only example of an intermetalloid cluster with the elemental combination M/Tr/Tt that has been isolated as a crystalline salt. Further, different from the M/Tt/Pn and M/Tr/Pn clusters described below, it was not obtained upon reaction of a binary Zintl anion with a Ni complex but from K_4Sn_9, [2.2.2]crypt, $[Ni(cod)_2]$, and TlCp. $[Ni@Sn_9Tl]^{3-}$ can be explained by terms of a cluster extension of the endohedrally filled mono-capped square antiprism of $[Ni@Sn_9]^{3-}$, which coexists with the ternary cage in the solid state. In the ternary cluster, Tl represents one cap of a

Table 3 Overview of structurally characterized ternary intermetalloid or heterometallic clusters and complexes with binary Zintl anions as ligands (with increasing number of main group (semi-) metal atoms for each of the categories) that were extracted as single crystal from solution as $[K([2.2.2]crypt)]^+$ salts

Formula	Tr/Tt reactant Tr/Pn reactant Tt/Pn reactant	References	Figure no.
$[Ni@Sn_9Tl]^{3-}$	K_4Sn_9, TlCp	[183]	Fig. 7a
$[Sm@Ga_2HBi_{11}]^{3-}/[Sm@Ga_3H_3Bi_{10}]^{3-}$	$(GaBi_3)^{2-}$	[184]	Fig. 13a
$[(La@In_2Bi_{11})(\mu\text{-}Bi)_2(La@In_2Bi_{11})]^{6-}$	$(InBi_3)^{2-}$	[185]	Fig. 13d
$[V@Ge_8As_4]^{3-}$	$K_8Ge_8As_6V$	[186]	Fig. 10a
$[Nb@Ge_8As_6]^{3-}$	$K_{10}Ge_{10}As_{10}Nb$	[186]	Fig. 10a
$[Ta@Ge_6As_4]^{3-}$	$K_8Ge_8As_8Ta$	[187]	Fig. 11
$[Ta@Ge_8As_4]^{3-}$	$K_8Ge_8As_8Ta$	[187]	Fig. 11
$[Ta@Ge_8As_6]^{3-}$	$K_8Ge_8As_8Ta$	[187]	Fig. 11
$[Sn_2Sb_5(ZnPh)_2]^{3-}$	K_8SnSb_4	[177]	Fig. 8a
$[Ni_2@Sn_7Bi_5]^{3-}$	$(Sn_2Bi_2)^{2-}$	[188]	Fig. 9a
$[Pd_3Sn_8Bi_6]^{4-}$	$(Sn_2Bi_2)^{2-}$	[189]	Fig. 9c
$[Zn@Zn_5Sn_3Bi_3@Bi_5]^{4-}$	$(Sn_2Bi_2)^{2-}$	[190]	Fig. 8b
$[La@Sn_7Bi_7]^{4-}/[La@Sn_4Bi_9]^{4-}$	$(Sn_2Bi_2)^{2-}$	[191]	Fig. 10a
$[Ce@Sn_7Bi_7]^{4-}/[Ce@Sn_4Bi_9]^{4-}$	$(Sn_2Bi_2)^{2-}$	[191]	Fig. 10a
$[Eu@Sn_6Bi_8]^{4-}$	$(Sn_2Bi_2)^{2-}$	[192]	Fig. 10a
$[Ni_2@Pb_7Bi_5]^{3-}$	$(Pb_2Bi_2)^{2-}$	[181]	Fig. 9a
$[Pd@Pd_2Pb_{10}Bi_6]^{4-}$	$(Pb_2Bi_2)^{2-}$	[193]	Fig. 9b
$[Zn@Zn_5Pb_3Bi_3@Bi_5]^{4-}$	$(Pb_2Bi_2)^{2-}$	[181]	Fig. 8b
$[La@Pb_7Bi_7]^{4-}/[La@Pb_4Bi_9]^{4-}$	$(Pb_2Bi_2)^{2-}$	[194]	Fig. 10a
$[La@Pb_6Bi_8]^{3-}/[La@Pb_3Bi_{10}]^{3-}$	$(Pb_2Bi_2)^{2-}$	[194]	Fig. 10a
$[Ce@Pb_3Bi_{10}]^{3-}$	$(Pb_2Bi_2)^{2-}$	[194]	Fig. 10a
$[Nd@Pb_6Bi_8]^{3-}/[Nd@Pb_3Bi_{10}]^{3-}$	$(Pb_2Bi_2)^{2-}$	[194]	Fig. 10a
$[Sm@Pb_3Bi_{10}]^{3-}$	$(Pb_2Bi_2)^{2-}$	[194]	Fig. 10a
$[Gd@Pb_3Bi_{10}]^{3-}$	$(Pb_2Bi_2)^{2-}$	[194]	Fig. 10a
$[Tb@Pb_3Bi_{10}]^{3-}$	$(Pb_2Bi_2)^{2-}$	[194]	Fig. 10a

bicapped square antiprismatic structure. Formally and regarding the total charge of the cluster, the Tl atom has to be counted as Tl^-, in accordance with the Wade–Mingos rules for a *closo*-type 22 skeleton electron cage. The interstitial Ni atom is situated slightly off-center, approaching the Sn cap by 0.32 Å (thereby widening the surrounding Sn_4 square), in spite of a noticeable Ni–Tl interaction. A homologous species, $[Ni@Ge_9Tl]^{3-}$, was observed in mass spectrometry investigations of the corresponding reaction solution with K_4Ge_9 as reactant, but the cluster could not be crystallized. A species without interstitial transition metal atom is found in the binary $[(\eta^3\text{-}Ge_9)In(\eta^3\text{-}Ge_9)]^{5-}$ anion (Fig. 7b), in which the triel atom possesses a formal +3 charge, however, instead of the formal –2 charge in the first. Here, the *hetero*atom is furthermore coordinated via a triangular face of the $\{Ge_9\}$ cages [195].

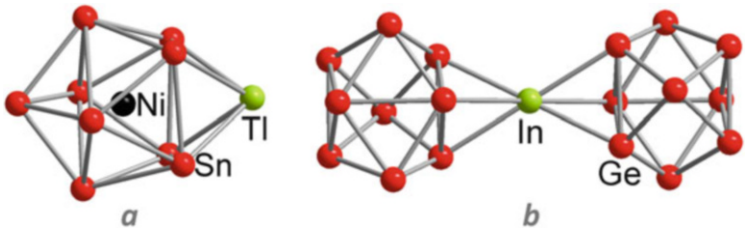

Fig. 7 Molecular structures of $[Ni@Sn_9Tl]^{3-}$, as the only known ternary intermetalloid cluster with a M/Tr/Tt elemental combination, with the triel atom possessing a formal –2 charge (**a**), and the molecular structure of a binary anion, which also comprises a Tr/Tt elemental combination, $[(\eta^3\text{-}Ge_9)In(\eta^3\text{-}Ge_9)]^{5-}$, however, with the triel atom in a formal positive oxidation state and without interstitial atom (**b**)

3.2 M/Tt/Pn-Based Clusters

In all of the following cases, binary Zintl anions have served as precursor molecules for the formation of ternary intermetalloid clusters in solution. First studies were undertaken on the ternary solid compound K_8SnSb_4 [196] comprising the highly charged $(SnSb_4)^{8-}$ analogs of the *ortho*-stannate anion. For first insights into its extraction behavior, it was treated with *en*/[2.2.2]crypt or with liquid ammonia, respectively. In the first case, the tetrahedral anion $(Sn_2Sb_2)^{2-}$ crystallized as its $[K([2.2.2]crypt)]^+$ salt; in the second case, a novel nortricyclane-type $(Sn_3Sb_4)^{6-}$ anion was obtained in $[K_6(NH_3)_9](Sn_3Sb_4)$. First, as one would expect, the highly charged anion of the precursor phase was not retained in solution. Second, a rearrangement into the tetrahedral binary anion seems to be preferred in *en*, and, third, binary nortricyclane-like cages are likewise stable for the Tt/Pn elemental combination. Here, an extraction of the K_8SnSb_4 in *en*/[2.2.2]crypt was carried out in the presence of $[ZnPh_2]$ to check the reactivity of the tetrahedral anion in situ. This led to the formation and isolation of the $[K([2.2.2]crypt)]^+$ salt of $[Sn_2Sb_5(ZnPh)_2]^{3-}$(Fig. 8a) [177]. This anion was thus the first step on the way toward ternary intermetalloid clusters of the elemental combination $[M@Tt_xPn_y]^{n-}$. In this molecule, two $\{ZnPh\}^+$ fragments are η^2 coordinated by a nortricyclane-type $\{Sn_2Sb_5\}^{5-}$ anion, which in the sum fully complies with the Zintl–Klemm–Busmann concept. Since Sn and Sb are indistinguishable by X-ray diffraction, DFT calculation were carried out to determine the most stable isomer of the $\{Sn_2Sb_5\}^{5-}$ cage for this complex. According to these, it became clear that the negatively charged Sn atoms avoid neighboring positions with each other and that they prefer three-bonded positions. The calculations also indicated that the interaction of the binary anion with the $\{ZnPh\}^+$ moieties is only sigma type (Fig. 8a). This is different from the ligand behavior of $\eta^4\text{-}Ge_9^{4-}$ [37], which coordinates to a $\{ZnPh\}^+$ fragment by both sigma-type and pi-type interactions (Fig. 4b).

Although the K_8SnSb_4 phase was shown to produce the desired precursor anion in solution, the use of ternary Zintl phases as starting material suffers from a couple of disadvantages. In many cases, they form as mixed phases, hence, supporting side

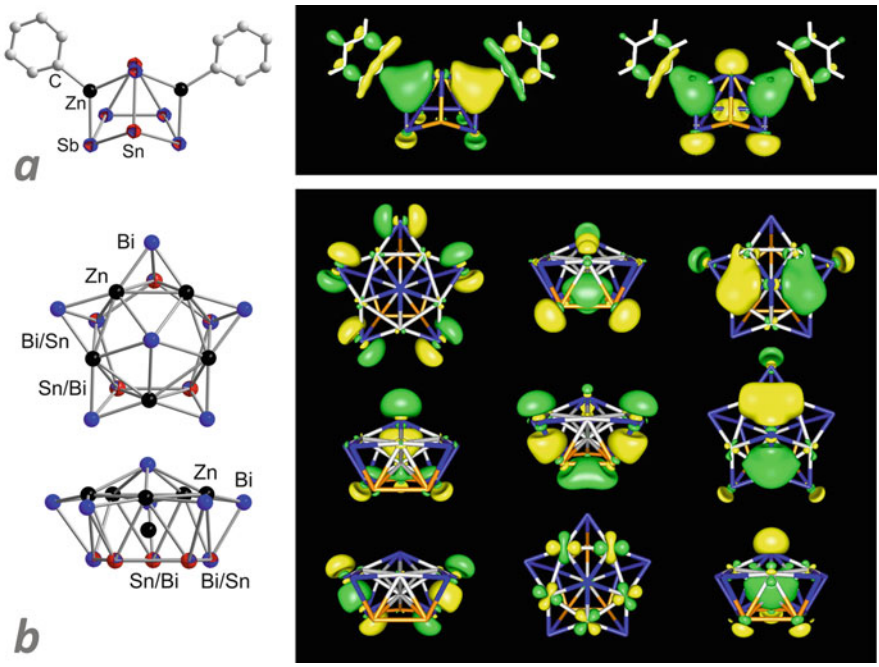

Fig. 8 Molecular structures of $[Sn_2Sb_5(ZnPh)_2]^{3-}$, along with an illustration of the sigma-type bonding of the Sn/Sb polyanion to the $\{ZnPh\}^+$ fragment (**a**). Molecular structure of $[Zn@Zn_5Tt_3Bi_3@Bi_5]^{4-}$ in two views and cluster orbitals indicating the coexistence of rather localized electron density with delocalized cluster orbitals (**b**). *Two-colored atoms* indicate disorder of the respective Tt and Pn atoms in the crystal structure. Orbital plots reproduced with permission from Wiley-VCH

reactions in an undesired or at least uncontrollable manner. Second, the solubility is always (relatively) low, and dissolution usually gives rise to a rearrangement into anions comprising different ratios of the main group elements than the original solid, such as the 1:4 ratio in K_8SnSb_4. Consequently, this does not represent an atom–economic approach. For provision of pure and well-soluble precursor materials, the use of $[K([2.2.2]crypt)]^+$ salts seemed to be the best choice again. The first $[K([2.2.2]crypt)]^+$ salts of binary Zintl anions of tetrel and pnictogen elements were published in the 1980s by Corbett: $[K([2.2.2]crypt)]_2(Tt_2Pn_2)\cdot en$ (Tt/Pn: Sn/Bi or Pb/Sb) [178, 180]. The Sn/Bi anion and its Pb/Bi homolog, which was only recently isolated [181], showed to be excellent starting materials for the formation of ternary intermetalloid clusters with novel structures. The reactions with Tt=Sn or Pb led to topologically identical results in most cases; the binary combination of Pb and Bi is advantageous in providing better solubility and producing higher yields.

Several complexes of d^{10} transition metal atoms, that is, $[ZnPh_2]$, $[Ni(cod)_2]$, $[Pd(PPh_3)_4]$, and $[Pd(dppe)_2]$ (dppe=diphenylphosphinoethane), were tested in reactions with $[K([2.2.2]crypt)]_2(Tt_2Bi_2)\cdot en$ (Tt=Sn, Pb) in *en*. Six different compounds containing four different ternary intermetalloid clusters with new architectures,

$[Zn@Zn_5Tt_3Bi_3@Bi_5]^{4-}$ [181, 190], $[Ni_2@Tt_7Bi_5]^{3-}$ [181, 188], $[Pd_3@Sn_8Bi_6]^{4-}$ [189], and $[Pd@Pd_2Pb_{10}Bi_6]^{4-}$ [193], were obtained.

Structurally and electronically, $[Zn@Zn_5Tt_3Bi_3@Bi_5]^{4-}$ (Fig. 8b) [181, 190] shows similarities to the binary cluster $[Zn@Zn_8Bi_4@Bi_7]^{5-}$ described above [147]. As the latter, the ternary clusters are based on a Zn-centered deltahedral structure and can be explained in terms of Wade–Mingos rules. However, the 11-atom $\{Zn_5Tt_3Bi_3\}$ shell around the interstitial Zn atom does not form icosahedral *closo*-type cages but uncapped *nido*-type fragments of it. These are based on a pentagonal antiprism, comprising a $\{Tt_3Bi_2\}$ pentagon and a $\{Zn_5\}$ pentagon, being capped by a single Bi atom above the $\{Zn_5\}$ ring. Five further Bi atoms cap the antiprism, thereby bridging all of the Zn–Zn edges with a third, longer contact to the Tt or Bi atom of the respective $\{Zn_2(Tt/Bi)\}$ triangular face. For complying with Wade–Mingos rules, a total number of $(2 \times 11 + 4) = 26$ skeleton electrons are needed, which add up to a total number of 48 valence electrons upon consideration of two *exo*-electrons per cluster atom. The atoms that form the $\{Zn_5Tt_3Bi_3\}$ shell provide 37 electrons, [$(5 \times 2) = 10$ valence electrons from 5 Zn atoms + $(3 \times 4) =$ 12 valence electrons from 3 Tt atoms + $(3 \times 5) = 15$ valence electrons from 3 Bi atoms]. The central Zn atom and the 4– charge add another six electrons for a sum of 43 valence electrons so far. For accomplishment of the expected number of 48 valence electrons, each of the five capping Bi atoms is thus regarded as one-electron donors, as in the binary cluster, which was rationalized by population analyses here. Quantum chemical analyses helped to analyze the bonding situation, which indicates a coexistence of two-center and three-center bonds with delocalized cluster orbitals (Fig. 8b).

The $[Ni_2@Tt_7Bi_5]^{3-}$ anions (Tt=Sn, Pb, Fig. 9a) [181, 188] are composed of two face-sharing square antiprisms, which meet at a central "Tt(0)"$_4$ square. The two external four rings comprise three "Tt(−I)" and five "Bi(0)" atoms. These are disordered over the eight positions, with the most stable Tt versus Bi distribution achieved with largest distances between the three Tt atoms, according to DFT calculations. A $\{Ni_2\}$ dumbbell is embedded within this cluster. In spite of a rather close proximity of the two Ni atoms (2.444(2) Å for Tt=Sn, 2.499(6) Å for Tt=Pb), no bonding interaction seems to be present between them according to the calculations. They are not in need of it, as the interaction with the eight nearest atoms of the $\{Sn_7Bi_5\}^{3-}$ cluster allows for provision of eight electrons for each of the Ni atoms, thus, completing the desired 18-electron shells. Thus far, it could not be clarified why the clusters form reproducibly in the way they do – and why the involvement of different elements of the same group sometimes produces the same results and sometimes not. Quantum chemical studies usually rationalized the observed structures as being the preferred ones in comparison with other species, but the underlying formation processes are still widely unknown. It seems to be obvious – still not explaining the findings – that a majority of tetrel atoms within a cluster are found in structures that resemble binary M/Tt clusters, whereas clusters with a majority of pnictogen atoms are rather similar to binary M/Pn clusters.

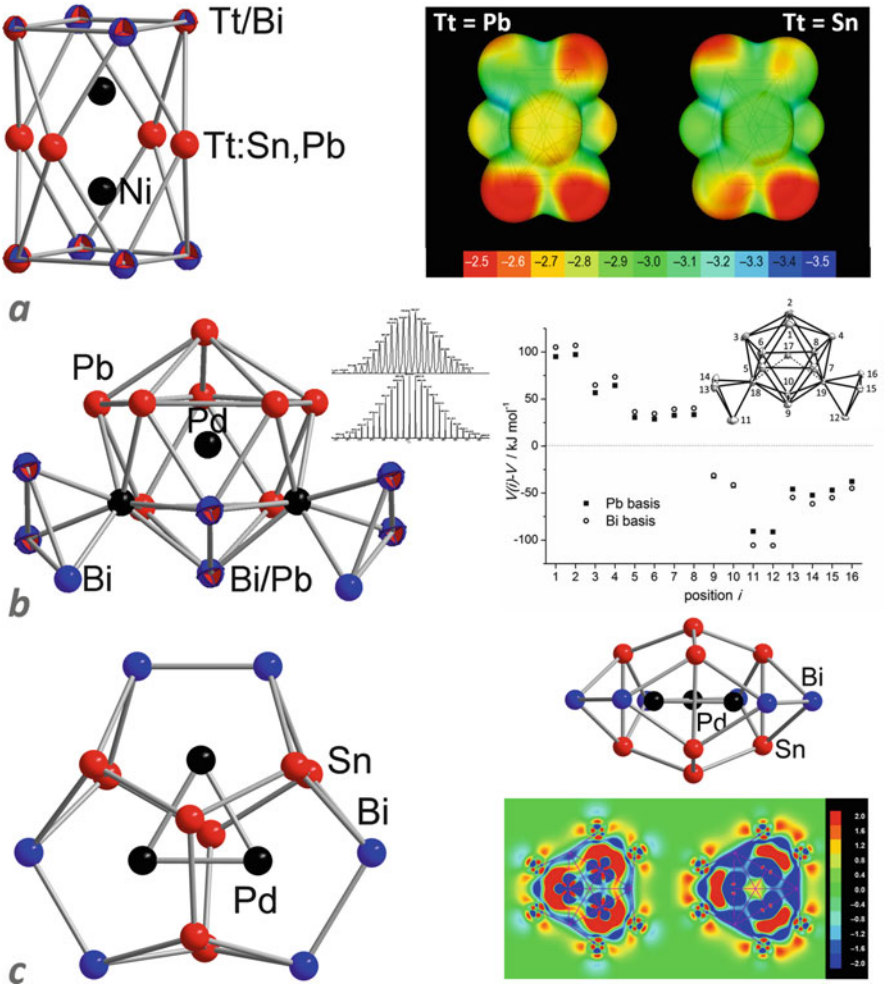

Fig. 9 Molecular structure of $[Ni_2@Tt_7Bi_5]^{3-}$ (Tt = Sn, Pb), along with a plot of the electrostatic surface potential (reproduced with permission from the Royal Society of Chemistry) indicating a somewhat more balanced situation in the Tt = Pb case, which was made responsible in part for the better solubility of anions based on Pb/Bi instead of Sn/Bi (**a**). Molecular structure of $[Pd@Pd_2Pb_{10}Bi_6]^{4-}$ and measured (*top*) and simulated ESI mass peak; the diagram to the *right* (reproduced with permission from Wiley-VCH) illustrates the output of the perturbation theory treatment of the cluster anion that served to assign Pb or Bi atoms, respectively, to places *i*, with potentials $V(i)$ being larger or smaller, respectively, than the potential V calculated with a mean atomic charge (**b**). Molecular structure of the $[Pd_3@Sn_8Bi_6]^{4-}$ in two views and plot of the difference electron densities (reproduced with permission from the American Chemical Society) for two possible models of charge assignment, "$\{[Pd_3]^0@[Sn_8Bi_6]^{4-}\}^{4-}$" or "$\{[Pd_3]^{2-}@[Sn_8Bi_6]^{2-}\}^{4-}$," with better match of the first (**c**). Two-colored atoms indicate disorder of the respective Tr and Pn atoms in the crystal structure

The transfer from Ni as interstitial atom type toward its heavier congener Pd comes along with two significant changes: again, other cluster structures are observed, and one obtains different structures for Tt=Sn and Tt=Pb instead of identical ones. $[Pd@Pd_2Pb_{10}Bi_6]^{4-}$ (Fig. 9b) [193], which was obtained upon reaction of the $(Pb_2Bi_2)^{2-}$ anion with an Pd(0) complex, and which represents the heaviest ternary intermetalloid cluster anion known to date, can be also deduced from an icosahedron; it therefore possesses a strong relation to the binary cluster $[Pd@Pb_{12}]^{2-}$ and its homologs [23, 24, 59, 76–79]. However, the ternary cluster again differs in that it bears a more complicated structure. It can be described as a Pd-centered $\{Pd_2Pb_{10-x}Bi_x\}$ icosahedron. Additionally, two $\{Bi_{3-x}Pb_x\}$ triangles are attached in a η^3 manner to the two Pd atoms of the icosahedron. The Pb/Bi ratio was determined by mass spectrometry, EDX spectroscopy, and quantum chemical studies including first-order perturbation theory. The latter also served to determine the most plausible distributions of the two atom types over the cluster positions and thus to identify the most probable isomers. The three lowest-energy isomers possess C_{2v}, C_s, or C_2 symmetry, depending on the position of four Bi atoms on six possible positions. Most probably, and in agreement with ^{207}Pb NMR spectroscopic data (DMF solution, –5°C), the three isomers coexist. Wade–Mingos rules apply for this cluster, as well, independent of the distribution of Pb and Bi atoms over the cluster positions. In all cases, the $\{Pd_2Pb_{10-x}Bi_x\}^{(2-x)-}$ icosahedron turns out to be a *closo*-type cluster if the two $\{PdBi_{3-x}Pb_x\}^{(3+x)-}$ fragments are viewed as 14-electron *pseudo*-Pb fragments each. Indeed, as rationalized by population analyses, $\{Bi_3\}^-$ ligands (or the mixed-metallic homologs) can be considered as four-electron donors, adding up to 14 electrons for the quoted tetrahedral fragment. Since the central Pd atom does not contribute to the cluster electrons, the total number of valence electrons is 70 [$=2 \times 14 + 10 \times 4 + 2$], as needed for a *closo*-type icosahedron that comprises two transition metal atoms. Accordingly, 26 skeleton electrons [$= 70 - 10 \times 2 - 2 \times 12$] are finally achieved this way.

A completely different result is obtained if the reaction quoted above is carried out with $(Sn_2Bi_2)^{2-}$ instead of its heavier homolog: although the cluster anion $[Pd_3@Sn_8Bi_6]^{4-}$ (Fig. 9c) [189] also comprises three Pd atoms in its formula, none of the structural characteristics resembles that of the Pd/Pb/Bi cluster described above. It possesses an oblate shape, with the three Pd atoms located within the $\{Sn_8Bi_6\}$ shell with smaller distances to the Bi atoms. The shell may be described by an assembly of three $\{Sn_2Bi_2\}$ butterfly-like fragments that are linked by Bi–Bi bond formation into a donutlike structure, which is doubly capped by two further Sn atoms. Uniquely, the assignment of Sn and Bi atoms was unambiguous in the single-crystal X-ray diffraction study of this compound. However, it was not possible to explain the bonding situation within the cluster structure by means of any known electron-counting concept. For this, difference electron calculations were carried out to distinguish between two possible models: "$\{[Pd_3]^0@[Sn_8Bi_6]^{4-}\}^{4-}$" or "$\{[Pd_3]^{2-}@[Sn_8Bi_6]^{2-}\}^{4-}$." None of the two models matches perfectly the total electron density calculated for the entire cluster, but a better fit was obtained for the model that keeps the Pd atoms neutral. This example indicates once more that it seems reasonable in general to describe these heterometallic clusters as "superatoms" or "superions" of

different electron configurations, rather than talking about localized or semi-localized bonding.

By use of the binary anions $(Tt_2Bi_2)^{2-}$, the incorporation of lanthanide atoms into intermetalloid cluster chemistry was achieved for the first time. The studies were carried with $[K([2.2.2]crypt)]_2(Tt_2Bi_2)\cdot en$ (Tt=Sn, Pb) and lanthanide complexes of the type $[Ln(CpMe_4H)_3]$ (Ln=La, Ce, Nd, Gd, Sm, Eu, Tb). These investigations lead to the formation of a number of compounds in which two anionic clusters occur – separately or together in double salts – with $[K([2.2.2]crypt)]^+$ counterions. The $[M@Tt_xBi_y]^{z-}$ clusters represent non-deltahedral polyhedra with 13 vertices ($x+y=13$) [191, 194] or 14 vertices ($x+y=14$) [186, 191, 194], respectively, and nine faces each – so-called enneahedra (Fig. 10a). In the 14-atom cage, three squares are connected via three bonds to form a 12-atom donutlike ring. Above and below this ring, a 13th and a 14th atom are placed that connect the three apices of the squares that direct toward them. This way, the cluster is constructed by six pentagonal and three square faces. The 13-atom cage can be described by a basal square face that is connected to four pentagonal faces, which share their edges and bind to a common 13th atom at the apex of the cluster. It is worth mentioning that despite a high degree of Tt/Bi disorder in these cages, the apex and the four adjacent atoms are always and exclusively Bi atoms, which was confirmed by quantum chemical investigations. Isomers with Tt atoms occupying one or several of these positions are significantly higher in energy. This is due to the specific electronic situation within this cluster "cap" (see below). Both types of clusters contain one interstitial Ln(III) atom each, and the two main group metal polyhedra are structurally highly related: if the apical Bi atom is (formally) replaced by a dumbbell, one ends up with the 14-atom enneahedron. The coexistence of the two cluster types in solution was furthermore demonstrated by means of ^{139}La NMR studies (Fig. 10b). Depending on the size of the interstitial Ln(III) atom, the ratio of 13-to-14-atom cages differs significantly. The larger the size of the Ln(III) atom, the larger is the 14:13 ratio, as confirmed by ESI mass spectrometric analyses of solutions of the solid material (Fig. 10c). The only example of an enneahedral cage that embedded a Ln(II) atom has so far been the anion $[Eu@Sn_6Bi_8]^{4-}$ [192].

The extraction of the quaternary solid mixtures K/Ge/As/V, K/Ge/As/Nb, or K/Ge/As/Ta in *en* in the presence of [2.2.2]crypt also allowed for the crystallization of salts of ternary cluster anions – although no binary anion salt and no transition metal compound were employed. Similar as reported above for the serendipitous formation of $[Nb@As_8]^{3-}$ or $[Mo@As_8]^{3-}$ [133, 166], the metallophilicity of As obviously helped in the oxidation of elemental Nb, V, or Ta powder – or even the Nb or Ta tube material. The products contained intermetalloid clusters with 12 vertex atoms, $[V@Ge_8As_4]^{3-}$ or $[Ta@Ge_8As_4]^{3-}$, respectively, or the metal-centered 14-vertex enneahedra $[Nb@Ge_8As_6]^{3-}$ or $[Ta@Ge_8As_6]^{3-}$, respectively [186, 187]. The cluster with 14 shell atoms is topologically identical to the Ln-centered ones described above – indicating its relatively high stability. The Nb compound furthermore represents the second example beside the Eu compounds that contains exclusively the larger cluster type as anion, whereas the cluster co-crystallizes together with the cluster exhibiting a 12-atom cage in the case of

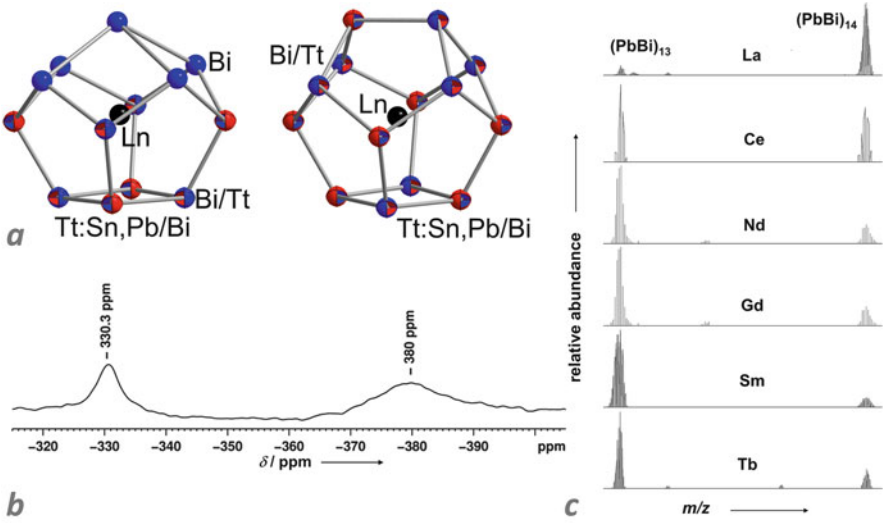

Fig. 10 Molecular structure of the two (usually co-crystallizing enneahedral intermetalloid cluster anion types $[Ln@Tt_{13-x}Bi_x]^{x-}$ and $[Ln@Tt_{14-x}Bi_x]^{(11-x)-}$ (Ln = lanthanoid(III); Tt = Sn, Pb; (**a**) and picture of the development of the ESI mass peaks of solutions of the solid material for Ln cations of decreasing sizes (from *top*; (**b**)). ^{139}La NMR spectrum of an *en* solution of $[K([2.2.2]crypt)]_3[La@Pb_6Bi_8]_{0.038}$ $[La@Pb_3Bi_{10}]_{0.962}$ recorded at 333 K (**c**). Two-colored atoms indicate disorder of the respective Tr and Pn atoms in the crystal structure. Spectra reproduced with permission from Wiley-VCH

M=Ta. The 12-atom cages have the same topology as the $[Ru@Ge_{12}]^{3-}$ cluster quoted above, however, with a binary $\{Ge_8As_4\}$ composition and with an interstitial group 5 atom instead of Ru [24]. Moreover, for M=V or Ta, they can be fully explained by means of the *pseudo*-element concept and are diamagnetic. These clusters obtained with V, Nb and Ta have been the first examples for interstitial clusters with such highly charged transition metal atoms inside the main group atom shell. As a very uncommon species, the experiments with Ta also evolved the intermediate anionic complex $[Ta@Ge_6As_4]^{3-}$ (Fig. 11) which allowed for some insight in the successive formation processes of non-deltahedral intermetalloid clusters starting out from the binary anions and the early, *pseudo*-catalytic role of the interstitial transition metal atom therein.

The electronic situations of the three highly related, non-deltahedral clusters with 12, 13, or 14 vertex atoms are discussed in detail in the chapter on "Quantum Chemical Investigations of Clusters of Heavy Metal Atoms" by F. Weigend. We refer to this article for details, but it state here that the clusters with a 12-atom or 14-atom shell can be explained by the *pseudo*-element concept, with all tetrel atoms being formally negatively charged and therefore three bonded, each bearing one lone pair. The description of the M-centered cages with 13 atoms, however, is much more complicated, in that the cluster is reduced overall and in that the pnictogen atoms occur in three different situations here that can be formally described as "Pn

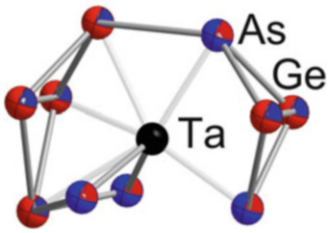

Fig. 11 Molecular structure of the $[Ta@Ge_6As_4]^{3-}$ anion in $[K([2.2.2]crypt)]_3[Ta@Ge_6As_4] \cdot 2tol$, which is supposed to be a key species in the cluster formation cascade toward non-deltahedral intermetalloid clusters

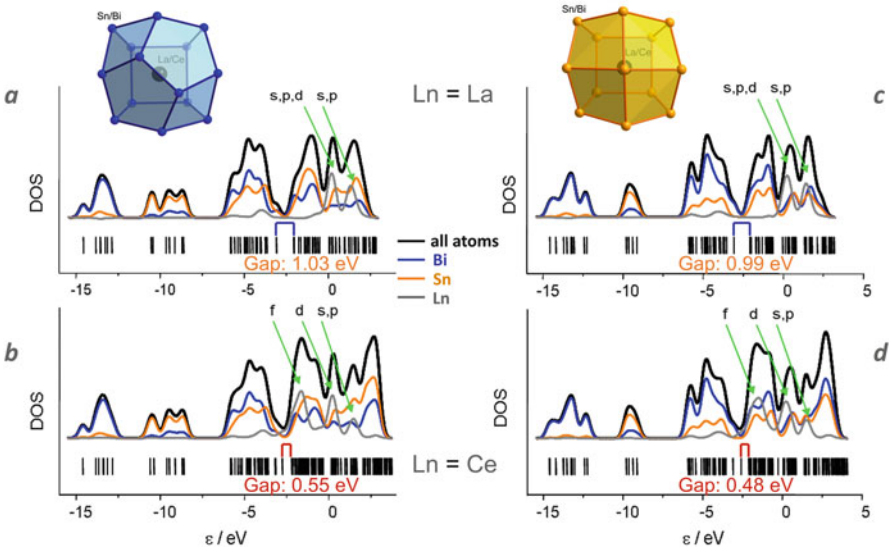

Fig. 12 Electronic properties of the clusters $[Ln@Sn_7Bi_7]^{4-}$ (**a**, **b**) and $[Ln@Sn_9Bi_4]^{4-}$ (**c**, **d**) with Ln = La(III) (**a**, **c**) or Ce(III) (**b**, **d**), as calculated by means of DFT methods, given as simulated density of states (DOS) versus the frontier orbital region of the MO scheme. Major contributions of Ln atomic orbitals to the MOs are indicated by *arrows* (Reproduced with permission from the American Chemical Society)

(I)," "Pn(−I)," and "Pn(0)." The interaction with the lanthanide or transition metal atom (ion) is predominantly ionic, with a somewhat higher covalent contribution within the M@13-atom clusters. All experimental measurement or calculations of physical properties on the lanthanide compounds have so far indicated the clusters as being lanthanide-doped semimetallic cages. Accordingly, the magnetic behavior represents widely that of the interstitial ions, and electronic properties are characterized by the energy of the (empty or partially filled) f orbitals in relation to the HOMO–LUMO gap of the empty Tr/Pn shells (Fig. 12).

3.3 M/Tr/Pn-Based Clusters

In a reaction of $[K([2.2.2]crypt)]_2(GaBi_3)$·*en* or $[K([2.2.2]crypt)]_2(InBi_3)$·*en* [197] with $[Sm(CpMe_4H)_3]$ or $[La(CpMe_4H)_3]$, in *en*, two new compounds with ternary intermetalloid were observed, $[K([2.2.2]crypt)]_3[Sm@Ga_2HBi_{11}]_{0.9}[Sm@Ga_3H_3Bi_{10}]_{0.1} \cdot en \cdot tol$ [184] (anions in Fig. 13a) or $[K([2.2.2]crypt)]_6[(La@In_2Bi_{11})(\mu\text{-}Bi)_2(La@In_2Bi_{11})] \cdot 3en \cdot 3tol$ (anion in Fig. 13d), respectively [185]. All of the three clusters possess a binary 13-atom main group elemental cage that accord to the general formulae "$\{Tr_2Pn_{11}\}^{7-}$" or "$\{Tr_3Pn_{10}\}^{9-}$" and are topologically identical with the Tt/Pn 13-atom cages described above. Again, a Ln(III) atom is located in the barycenter of the approximately C_{4v} symmetric cages. However, some significant differences come along with the substitution of formal "Tr(−II)" atoms for the isoelectronic "Tt(−I)" atoms in the M/Tt/Pn cluster anions: the high charge overload at the triel atoms induces a considerable Lewis basicity at these sites of the cages, which needs to be compensated for both a balanced electronic situation and a charge that allows for crystallization with $[K([2.2.2]crypt]^+$: it is apparent that all of the cluster anions that have been crystallized with this cation complex until now carry total negative charges of 2–4, not higher, as only in these cases a stable crystal structure is realized. The high charge of the triel polyanions has been one of the reasons why such clusters have not been isolated from solution so far – except in these heteroatomic and heteropolar cases, which help to reduce the charge. The La/In/Bi cluster hence bears two "μ-Bi(I)" bridges that partially neutralize the "In(−II)" sites to form two "In(−I)–Bi(−I)–In(−I)" bridges and this way connect two of the "$\{La@In_2Bi_{11}\}^{4-}$" clusters. In the sum, one obtains an $[(La@In_2Bi_{11})(\mu\text{-}Bi)_2(La@In_2Bi_{11})]^{6-}$ anion, with no rotational disorder due to its anisotropic shape and with an ordinary 3– charge at each of the cluster halves. In the Sm/Ga/Bi cluster, the charge overload at the Ga atoms is even more dramatic. Therefore, the Ga(−II) atoms are in the position to deprotonate the solvent *en*, such that the Ga(−II) atoms are (partially) protonated in the two co-crystallizing species $[Sm@Ga_2HBi_{11}]^{3-}$ and $[Sm@Ga_3H_3Bi_{10}]^{3-}$. Due to the common disorder within 8 of the 13 atomic positions, also the H atoms are disordered, which made their detection highly challenging and required the combination of a variety of different analytical methods (Fig. 13b, c). The cluster furthermore showed to be supportive in C–C bond formation as octamethylfulvene, deriving from the released $CpMe_4H$ ligands, was detected as a by-product in this reaction. Whether or not this activity is catalytic is to be determined in the future.

4 Summary and Concluding Remarks

This chapter defined and summarized the known intermetalloid and heterometallic clusters. These combine main group (semi-)metal polyanions and transition metal atoms or complexes, with the first acting as lateral and/or surrounding ligands to the

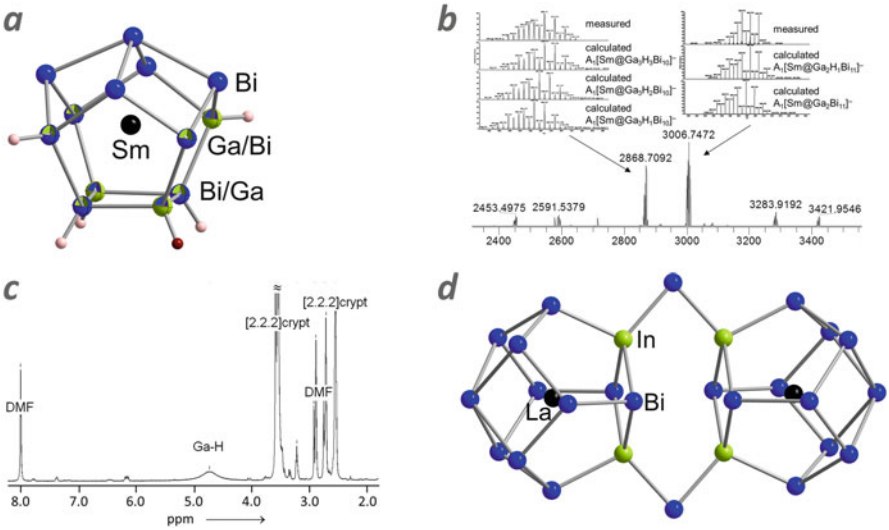

Fig. 13 Overlay of the molecular structures of the ternary intermetalloid clusters $[Sm@Ga_2HBi_{11}]^{3-}$ and $[Sm@Ga_3H_3Bi_{10}]^{3-}$(**a**), along with the ^1H NMR spectrum in DMF solution demonstrating the presence of a Ga–H bond (**b**) and the ESI mass spectrum that shows the coexistence of both clusters (**c**). Molecular structure of $[(La@In_2Bi_{11})(\mu\text{-}Bi)_2(La@In_2Bi_{11})]^{6-}$, representing a "$Bi^+$-bridged" dimer of ternary 13-atom cages (**d**). Spectra reproduced with permission from Wiley-VCH

latter. Upon relatively straightforward synthetic approaches, a large variety of structures have been observed. Interestingly, topological relations between the cluster architectures were observed even for different elemental combinations, whereas similar elemental combinations can lead to very different cluster structures. Accordingly, different bonding situations need to be assigned to such clusters, most of which comply with either the Zintl–Klemm–Busmann *pseudo*-element concept or with the Wade–Mingos rules. Still, some exceptions exist that needed an exclusive type of theoretical treatment and according description of their electronic features. The article intended to introduce the reader into the highly diverse world of multimetallic clusters and their synthetic approach, which is still not at its limit considering the unexplored elemental combinations.

Acknowledgments The authors thank the Deutsche Forschungsgemeinschaft (GRK 1782) and the Verband der Chemischen Industrie (VCI scholarship for B.W.) for financial support. We thank Florian Weigend, Werner Massa, Rodoplphe Clérac, Rainer Pöttgen, and the technical staff within Fachbereich Chemie for highly appreciated help during our studies on binary and ternary Zintl clusters.

References

1. Zintl E, Goubeau J, Dullenkopf W (1931) Z Phys Chem Abt A 154:1–46
2. Laves F (1941) Z Naturwissenschaften 29:244–255
3. Fässler TF (2007) Angew Chem Int Ed 46:2572–2575
4. Guloy AM, Ramlau R, Tang Z, Schnelle W, Baitinger M et al (2006) Nature 443:320–323
5. Kanatzidis MG, Armatas GS (2006) Science 313:817–820
6. Sun D, Riley AE, Cadby AJ, Richmann EK, Korlann SD et al (2006) Nature 441:1126–1130
7. Butovskii MV, Döring C, Bezugly V, Wagner FR, Grin Y et al (2010) Nat Chem 2:741–744
8. Schnepf A, Schnöckel H (2002) Angew Chem Int Ed 41:3533–3552
9. Schnöckel H (2010) Chem Rev 110:4125–4163
10. Fässler TF, Hoffmann SD (2004) Angew Chem Int Ed 43:6242–6247
11. Fässler T (2011) Struct Bond 140:91–132
12. Scharfe S, Kraus F, Stegmaier S, Schier A, Fässler TF (2011) Angew Chem Int Ed 50: 3630–3670
13. Turbervill RSP, Goicoechea JM (2014) Chem Rev 114:10807–10828
14. Klemm W, Busmann E (1963) Z Anorg Allg Chem 319:297–311
15. Wade K (1976) Adv Inorg Chem Radiochem 18:1–67
16. Mingos DMP, Slee T, Zhenyang L (1990) Chem Rev 90:383–402
17. Witte J, von Schnering HG (1964) Z Anorg Allg Chem 327:260–273
18. Goicoechea JM, Sevov SC (2006) J Am Chem Soc 128:4155–4161
19. Goicoechea JM, Sevov SC (2005) Angew Chem Int Ed 44:4026–4028
20. Esenturk EN, Fettinger J, Eichhorn BW (2006) Polyhedron 25:521–529
21. Sun ZM, Zhao YF, Li J, Wang LS (2009) J Clust Sci 20:601–609
22. Zhou B, Denning MS, Kays DL, Goicoechea JM (2009) J Am Chem Soc 131:2802–2803
23. Wang JQ, Stegmaier S, Fässler TF (2009) Angew Chem Int Ed 48:1998–2002
24. Espinoza-Quintero G, Duckworth JCA, Myers WK, McGrady JE, Goicoechea JM (2014) J Am Chem Soc 136:1210–1213
25. Jin X, Espinoza-Quintero G, Below B, Arcisauskaite V, Goicoechea JM et al (2015) J Organomet Chem 792:149–153
26. Goicoechea JM, Sevov SC (2005) J Am Chem Soc 128:7676–7677
27. Waibel M, Raudaschl-Sieber G, Fässler TF (2011) Chem Eur J 17:13391–13394
28. Waibel M, Henneberger T, Fässler TF (2012) Chem Commun:8676–8678
29. Stegmaier S, Waibel M, Henze A, Jantke LA, Karttunen AJ et al (2012) J Am Chem Soc 134: 14450–14460
30. Zhou B, Goicoechea JM (2010) Chem Eur J 16:11141–11150
31. Wang Y, Qin Q, Wang J, Sanga R, Xu L (2014) Chem Commun:4181−4183
32. Schenk C, Schnepf A (2009) Chem Commun:3208–3210
33. Li F, Sevov SC (2015) Inorg Chem 54:8121–8125
34. Schenk C, Henke F, Santiso-Quinones G, Krossing I, Schnepf A (2008) Dalton Trans:4436–4441
35. Schenk C, Schnepf A (2007) Angew Chem Int Ed 46:5314–5316
36. Henke F, Schenk C, Schnepf A (2009) Dalton Trans:9141–9145
37. Scharfe S, Fässler TF (2010) Eur J Inorg Chem 2010:1207–1213
38. Goicoechea JM, Sevov SC (2006) Organometallics 25:4530–4536
39. Zhou B, Denning MS, Jones C, Goicoechea JM (2009) Dalton Trans:1571–1578
40. Spiekermann A, Hoffmann SD, Kraus F, Fässler TF (2007) Angew Chem Int Ed 46: 1638–1640
41. Spiekermann A, Hoffmann SD, Fässler TF, Krossing I, Preiss U (2007) Angew Chem Int Ed 46:5310–5313
42. Renner G, Kircher P, Huttner G, Rutsch P, Heinze K (2001) Eur J Inorg Chem 2001:973–980
43. Kircher P, Huttner G, Heinze K, Renner G (1998) Angew Chem Int Ed 37:1664–1666
44. Rios D, Sevov SC (2010) Inorg Chem 49:6396–6398
45. Schnepf A, Schenk C (2006) Angew Chem Int Ed 45:5373–5376

46. Nienhaus A, Hauptmann R, Fässler TF (2002) Angew Chem Int Ed 41:3213–3215
47. Boeddinghaus MB, Hoffmann SD, Fässler TF (2007) Z Anorg Allg Chem 633:2338–2341
48. Denning MS, Goicoechea JM (2008) Dalton Trans:5882–5885
49. He H, Klein W, Jantke LA, Fässler TF (2014) Z Anorg Allg Chem 640:2864–2870
50. Hlukhyy V, Stegmaier S, van Wüllen L, Fässler TF (2014) Chem Eur J 20:12157–12164
51. Hlukhyy V, He H, Jantke LA, Fässler TF (2012) Chem Eur J 18:12000–12007
52. Gillett-Kunnath MM, Paik JI, Jensen SM, Taylor JD, Sevov SC (2011) Inorg Chem 50: 11695–11701
53. Kesanli B, Fettinger J, Gardner DR, Eichhorn BW (2002) J Am Chem Soc 124:4779–4786
54. Kesanli B, Halsig JE, Zavalij P, Fettinger JC, Lam YF et al (2007) J Am Chem Soc 129: 4567–4574
55. Scharfe S, Fässler TF, Stegmaier S, Hoffmann SD, Ruhland K (2008) Chem Eur J 14: 4479–4483
56. Scharfe S (2010) Untersuchungen zur Reaktivität von Zintl-Anionen der Tetrele in Lösung. PhD Thesis, Technische Universität München, München
57. Benda CB, Waibel M, Köchner T, Fässler TF (2014) Chem Eur J 20:16738–16746
58. Krämer T, Duckworth JCA, Ingram MD, Zhou B, McGrady JE et al (2013) Dalton Trans:12120−12129
59. Wang JQ, Stegmaier S, Wahl B, Fässler TF (2010) Chem Eur J 16:1793–1798
60. Benda CB, Waibel M, Fässler TF (2015) Angew Chem Int Ed 54:522–526
61. Prabusankar G, Kempter A, Gemel C, Schröter MK, Fischer RA (2008) Angew Chem Int Ed 47:7234–7237
62. Esenturk EN, Fettinger JC, Eichhorn BW (2006) J Am Chem Soc 128:12–13
63. Kocak FS, Zavalij P, Lam YF, Eichhorn BW (2008) Inorg Chem 47:3515–3520
64. Sun ZM, Xiao H, Li J, Wang LS (2007) J Am Chem Soc 129:9560–9561
65. Stegmaier S, Fässler TF (2011) J Am Chem Soc 133:19758–19768
66. Burns RC, Corbett JD (1982) J Am Chem Soc 104:2804–2810
67. Kesanli B, Fettinger J, Eichhorn BW (2001) Chem Eur J 7:5277–5528
68. Eichhorn BW, Haushalter RC (1988) J Am Chem Soc 110:8704–8706
69. Campbell J, Mercier HPA, Franke H, Santry DP, Dixon DA et al (2002) Inorg Chem 41: 86–107
70. Yong L, Hoffmann SD, Fässler TF (2005) Z Krist New Cryst St 220:53–57
71. Zhou B, Denning MS, Chapman TAD, Goicoechea JM (2009) Inorg Chem 48:2899–2907
72. Downing DO, Zavalij P, Eichhorn BW (2010) Eur J Inorg Chem 2010:890–894
73. Wang JQ, Wahl B, Fässler TF (2010) Angew Chem Int Ed 49:6592–6595
74. Yong L, Boeddinghaus MB, Fässler TF (2010) Z Anorg Allg Chem 636:1293–1296
75. Esenturk EN, Fettinger J, Eichhorn BW (2005) Chem Commun:247–249
76. Zhou B, Krämer T, Thompson AL, McGrady JE, Goicoechea JM (2011) Inorg Chem 50: 8028–8037
77. Wang Y, Wang LL, Ruan HP, Luo BL, Sang RL et al (2015) Chin J Struct Chem 34: 1253–1258
78. Esenturk EN, Fettinger J, Eichhorn BW (2006) J Am Chem Soc 128:9178–9186
79. Esenturk EN, Fettinger J, Lam YF, Eichhorn BW (2004) Angew Chem Int Ed 43:2132–2134
80. Yong L, Hoffmann SD, Fässler TF, Riedel S, Kaupp M (2005) Angew Chem Int Ed 44: 2092–2096
81. Eichhorn BW, Haushalter RC (1990) J Chem Soc Chem Commun:937–939
82. Yong L, Hoffmann SD, Fässler TF (2005) Eur J Inorg Chem 2005:3663–3669
83. Zhou B, Denning MS, Chapman TAD, McGrady JE, Goicoechea JM (2009) Chem Commun:7221–7223
84. Goicoechea JM, McGrady JE (2015) Dalton Trans:6755−6766
85. Zhang X, Li G, Gao Z (2001) Rapid Commun Mass Spectrom 15:1573–1576
86. Gillett-Kunnath MM, Petrov I, Sevov SC (2010) Inorg Chem 49:721–729
87. Gillett-Kunnath MM, Oliver AG, Sevov SC (2011) J Am Chem Soc 133:6560–6562

88. Gillett-Kunnath MM, Muñoz-Castro A, Sevov SC (2012) Chem Commun:3524–3526
89. Manriquez V, Hönle W, von Schnering HG (1986) Z Anorg Allg Chem 539:95–109
90. Santandrea RP, Mensing C, von Schnering HG (1986) Thermochim Acta 98:301–311
91. von Schnering HG (1981) Angew Chem Int Ed Engl 20:33–51
92. Meyer T, Hönle W, von Schnering HG (1987) Z Anorg Allg Chem 552:69–80
93. Dahlmann W, von Schnering HG (1972) Naturwissenschaften 59:420
94. Dahlmann W, von Schnering HG (1973) Naturwissenschaften 60:429
95. Hönle W, Buresch J, Peters K, Chang JH, von Schnering HG (2002) Z Kristallogr New Cryst Struct 217:485–486
96. Hönle W, Buresch J, Peters K, Chang JH, von Schnering HG (2002) Z Kristallogr New Cryst Struct 217:487–488
97. Hönle W, Buresch J, Wolf J, Peters K, Chang JH et al (2002) Z Kristallogr New Cryst Struct 217:489–490
98. Schmettow W, von Schnering HG (1977) Angew Chem Int Ed Engl 16:857
99. Emmerling F, Röhr C (2002) Z Naturforsch B 57:963–975
100. Dorn FW, Klemm W (1961) Z Anorg Allg Chem 309:189–203
101. Hirschle C, Röhr C (2000) Z Anorg Allg Chem 626:1992–1998
102. Perla LG, Oliver AG, Sevov SC (2015) Inorg Chem 54:872–875
103. Wichelhaus W, von Schnering HG (1973) Naturwissenschaften 60:104
104. von Schnering HG, Hönle W (1988) Chem Rev 88:243–273
105. Korber N, Daniels J, von Schnering HG (1996) Angew Chem Int Ed Engl 35:1107–1110
106. Korber N, Richter F (1996) Chem Commun:2023–2024
107. Korber N, Daniels J (1996) Z Anorg Allg Chem 622:1833–1838
108. Korber N, von Schnering HG (1996) Chem Ber 129:155–159
109. Knettel D, Reil M, Korber N (2001) Z Naturforsch B 56:965
110. Dai FR, Xu L (2007) Chin J Struct Chem 26:45–48
111. Korber N, Daniels J (1996) Polyhedron 15:2681–2688
112. Belin CHE (1980) J Am Chem Soc 102:6036–6040
113. Von Schnering HG, Somer M, Kliche G, Hönle W, Meyer T et al (1991) Z Anorg Allg Chem 601:13–30
114. Emmerling F, Röhr C (2003) Z Anorg Allg Chem 629:467–472
115. Hanauer T, Korber N (2006) Z Anorg Allg Chem 632:1135–1140
116. Reber AC, Ugrinov A, Sen A, Qian M, Khanna SN (2009) Chem Phys Lett 473:305–311
117. Bolle U, Tremel W (1992) J Chem Soc Chem Commun:91–93
118. Zhai J, Xu L (2011) Chin J Struct Chem 30:1091–1094
119. García F, Less RJ, Naseri V, McPartlin M, Rawson JM et al (2008) Chem Commun:859–861
120. Charles S, Eichhorn BW, Rheingold AL, Bott SG (1994) J Am Chem Soc 116:8077–8086
121. Charles S, Eichhorn BW, Bott SG (1993) J Am Chem Soc 115:5837–5838
122. Weinert B, Eulenstein AR, Ababei R, Dehnen S (2014) Angew Chem Int Ed 53:4704–4708
123. Gascoin F, Sevov SC (2001) Inorg Chem 40:5177–5181
124. Rodriguez-Fortea A, Canadell E (2003) Inorg Chem 42:2759–2763
125. Knapp CM, Westcott BH, Raybould MAC, McGrady JE, Goicoechea JM (2012) Angew Chem Int Ed 51:9097–9100
126. Scherer OJ, Sitzmann H, Wolmershauser G (1985) Angew Chem Int Ed Engl 24:351–353
127. Ahlrichs R, Fenske D, Fromm K, Krautscheid H, Krautscheid U et al (1996) Chem Eur J 2: 238–244
128. Charles S, Fettinger JC, Bott SG, Eichhorn BW (1996) J Am Chem Soc 118:4713–4714
129. Kesanli B, Charles S, Lam YF, Bott SG, Fettinger JC et al (2000) J Am Chem Soc 122: 11101–11107
130. Konchenko SN, Pushkarevsky NA, Gamer MT, Köppe R, Schnöckel H et al (2009) J Am Chem Soc 131:5740–5741
131. Knapp C, Zhou B, Denning MS, Rees NH, Goicoechea JM (2010) Dalton Trans:426–436

132. Knapp CM, Jackson CS, Large JS, Thompson AL, Goicoechea JM (2011) Inorg Chem 50: 4021–4028
133. Eichhorn BW, Mattamana SP, Gardner DR, Fettinger JC (1998) J Am Chem Soc 120: 9708–9709
134. Moses MJ, Fettinger JC, Eichhorn BW (2003) Science 300:778–780
135. Knapp CM, Westcott BH, Raybould MAC, McGrady JE, Goicoechea JM (2012) Chem Commun 48:12183–12185
136. Foust AS, Foster MS, Dahl LF (1969) J Am Chem Soc 91:5631–5633
137. Rheingold AL, Foley MJ, Sullivan PJ (1982) J Am Chem Soc 104:4727–4729
138. Eichhorn BW, Haushalter RC, Huffman JC (1989) Angew Chem Int Ed Engl 28:1032–1033
139. Moses MJ, Fettinger J, Eichhorn BW (2002) J Am Chem Soc 124:5944–5945
140. Chaki NK, Mandal S, Reber AC, Qian M, Saavedra HM et al (2010) ACS Nano 4:5813–5818
141. Breunig HJ, Rösler R, Lork E (1997) Angew Chem Int Ed Engl 36:2819–2821
142. Goicoechea JM, Hull MW, Sevov SC (2007) J Am Chem Soc 129:7885–7893
143. Breunig HJ, Burford N, Rösler R (2000) Angew Chem Int Ed 39:4148–4150
144. Pan FX, Li LJ, Wang YJ, Guo JC, Zhai HJ et al (2014) J Am Chem Soc 137:10954–10957
145. Bolle U, Tremel W (1994) J Chem Soc Chem Commun:217−219
146. Moses MJ, Fettinger JC, Eichhorn BW (2007) Inorg Chem 46:1036–1038
147. Goicoechea JM, Sevov SC (2006) Angew Chem Int Ed 45:5147–5150
148. Perla LG, Sevov SC (2015) Inorg Chem 54:8401–8405
149. Benda CB, Köchner T, Schäper R, Schulz S, Fässler TF (2014) Angew Chem Int Ed 53: 8944–8948
150. Qin Q, Zhou L, Wang Y, Sang R, Xu L (2014) Dalton Trans:5990−5993
151. Xu L, Ugrinov A, Sevov SC (2001) J Am Chem Soc 123:4091–4092
152. Whitmire KH, Churchill MR, Fettinger JC (1985) J Am Chem Soc 107:1056–1057
153. Gröer T, Scheer M (2000) Organometallics 19:3683–3691
154. Xu L, Bobev S, El-Bahraoui J, Sevov SC (2000) J Am Chem Soc 122:1838–1839
155. Kraus F, Aschenbrenner JC, Korber N (2003) Angew Chem Int Ed 42:4030–4033
156. Kraus F, Korber N (2005) Chem Eur J 11:5945–5959
157. Kraus F, Korber N (2006) Inorg Chem 45:1117–1123
158. Hanauer T, Kraus F, Reil M, Korber N (2006) Monatsh Chem 137:147–156
159. Critchlow SC, Corbett JD (1984) Inorg Chem 23:770–774
160. Cisar A, Corbett JD (1977) Inorg Chem 16:2482–2487
161. Kuznetsov AN, Fässler TF (2002) Z Anorg Allg Chem 628:2537–2541
162. Baudler M, Düster D, Ouzounis D (1987) Z Anorg Allg Chem 544:87–94
163. Baudler M, Akpapoglou S, Ouzounis D, Wasgestian F, Meinigke B et al (1988) Angew Chem Int Ed Engl 27:280–281
164. Milyukov VA, Kataev AV, Sinyashin OG, Hey-Hawkins E (2006) Russ Chem Bull Int Ed 55:1297–1299
165. Knapp CM, Large JS, Rees NH, Goicoechea JM (2011) Dalton Trans 40:735–745
166. von Schnering HG, Wolf J, Weber D, Ramirez R, Meyer T (1986) Angew Chem Int Ed Engl 25:353–354
167. Haushalter RC, Eichhorn BW, Rheingold AL, Geib S (1988) J Chem Soc Chem Commun 1027−1028
168. Schwarzmaier C, Noor A, Glatz G, Zabel M, Timoshkin AY et al (2011) Angew Chem Int Ed 50:7283–7286
169. Crossairt BM, Piro NA, Cummins CC (2010) Chem Rev 110:4164–4177
170. Caporali M, Gonsalvi L, Rossin A, Peruzzini M (2010) Chem Rev 110:4178–4235
171. Ginsberg AP, Lindsell WE (1971) J Am Chem Soc 93:2082–2084
172. Masuda JD, Schoeller WW, Donnadieu B, Bertrand G (2007) J Am Chem Soc 129: 14180–14181
173. Masuda JD, Schoeller WW, Donnadieu B, Bertrand G (2007) Angew Chem Int Ed 46: 7052–7055

174. Heinl S, Peresypkina E, Timoshkin AY, Mastrorilli P, Gallo V et al (2013) Angew Chem Int Ed 52:10887–10891
175. Schwarzmaier C, Timoshkin AY, Scheer M (2013) Angew Chem Int Ed 52:7600–7603
176. Köchner T, Engesser TA, Scherer H, Plattner DA, Steffani A et al (2012) Angew Chem Int Ed 51:6529–6531
177. Lips F, Schellenberg I, Pöttgen R, Dehnen S (2009) Chem Eur J 15:12968–12973
178. Critchlow SC, Corbett JD (1982) Inorg Chem 21:3286–3290
179. Lips F, Raupach M, Massa W, Dehnen S (2011) Z Anorg Allg Chem 637:859–863
180. Critchlow SC, Corbett JD (1985) Inorg Chem 24:979–981
181. Ababei R, Heine J, Hołyńska M, Thiele G, Weinert B et al (2012) Chem Commun:11295–11297
182. Blase W, Cordier G (1990) Z Kristallogr 193:319–320
183. Rios D, Gillett-Kunnath MM, Taylor JD, Oliver AG, Sevov SC (2011) Inorg Chem 50: 2373–2377
184. Weinert B, Müller F, Harms K, Dehnen S (2014) Angew Chem Int Ed 53:11979–11983
185. Weinert B, Weigend F, Dehnen S (2012) Chem Eur J 18:13589–13595
186. Mitzinger S, Broeckaert L, Massa W, Weigend F, Dehnen S (2015) Chem Commun:3866–3869
187. Mitzinger S, Broeckaert L, Massa W, Weigend F, Dehnen S (2016) Nat Commun 7:10480
188. Lips F, Dehnen S (2011) Angew Chem Int Ed 50:955–959
189. Lips F, Clérac R, Dehnen S (2011) J Am Chem Soc 133:14168–14171
190. Lips F, Dehnen S (2009) Angew Chem Int Ed 48:6435–6438
191. Lips F, Hołyńska M, Clérac R, Linne U, Schellenberg I et al (2012) J Am Chem Soc 134: 1181–1191
192. Lips F, Clérac R, Dehnen S (2011) Angew Chem Int Ed 50:960–964
193. Ababei R, Massa W, Harms K, Xie X, Weigend F et al (2013) Angew Chem Int Ed 52: 13544–13548
194. Ababei R, Massa W, Weinert B, Pollak P, Xie X et al (2015) Chem Eur J 21:386–394
195. Hansen DF, Zhou B, Goicoechea JM (2012) J Organomet Chem 721–722:53–61
196. Eisenmann B, Klein J (1988) Z Naturforsch 43b:1156–1160
197. Xu L, Sevov SC (2000) Inorg Chem 39:5383–5389

Struct Bond (2017) 174: 135–200
DOI: 10.1007/430_2015_5004

Published online: 10 July 2016

Metalloid Clusters

Andreas Schnepf

Abstract Metalloid cluster compounds of the general formulae M_nR_m ($n > m$; M=metal like Al, Au, Sn, etc.; R=ligand like S-C_6H_4-COOH, N($SiMe_3$)$_2$, etc.) represent a novel group of cluster compounds localized within the nanoscaled area between molecules and the solid state, opening our eyes to the complexity and the fundamental principles of the dissolution and the formation of metals. Only in recent years, synthetic routes were established to get access to this most complex group of metal atom clusters. Here, the synthetic routes and the structure and bonding of metalloid clusters of group 13 and group 14 are discussed, showing that within this, also technologically important nanoscaled regime novel motives are realized, partly comparable to arrangements known from the elemental metals themselves. However, also completely novel and unpredicted structures are realized, indicating that the knowledge of the nanoscaled regime of metals is still in its infancy. Consequently, the synthesis and characterization of metalloid clusters can be used to establish a sound structural basis for metal nanoparticles not only for bare metals but for all metals of the periodic table.

Keywords Aluminum • Gallium • Germanium • Metal • Nanoscale • Tin

Contents

Dedicated to Professor Hansgeorg Schnöckel on the occasion of his 75th birthday.

A. Schnepf (✉)
Institute of Inorganic Chemistry, University Tübingen, Auf der Morgenstelle 18, 72076 Tübingen, Germany
e-mail: andreas.schnepf@uni-tuebingen.de

1 Introduction

The majority of elements on the periodic table are metals and their chemistry, especially their formation and dissolution, belong to the oldest technical chemical processes. Thereby, the synthesis of metals plays a central role in the evolution of mankind, and thus complete periods are named according to the metals used there for the first time (Copper Age, 4,300–2,200 B.C.; Bronze Age, 2,200–1,000 B.C.; Iron Age, 1,000–40 B.C.). However, to date, awareness of metals beyond bulk metals and their stable compounds (e.g., salts, oxides, sulfides, in solution or in bulk) is limited. Basic knowledge of the intermediates in the formation and breaking of metal–metal bonds are mostly unknown even though this process plays a vital role in the evolution of mankind.

The dearth of understanding the intermediate states of metals can be attributed to the lack of useful starting materials and accessible synthetic routes to synthesize molecular compounds localized in this intermediate range. Additionally, when such compounds are identified, the high reactivity and their metastable character hinder isolation for further investigations. Molecular compounds exhibiting a direct metal-to-metal bond, such as $Re_2Cl_8^{2-}$, were classified by F. A. Cotton as metal atom clusters [1, 2]. His quite general definition includes many different kinds of clusters, e.g., naked metal atom clusters, which are present under ultrahigh-vacuum conditions, as well as "saltlike" clusters, in which also nonmetal atoms are associated intimately with the cluster. However, it is quite obvious that a naked metal atom cluster, exclusively held together by metal–metal bonds, is different from a saltlike cluster, where partly no direct metal-to-metal bond is present.

Consequently, a more specific term is necessary to further divide the general term of metal atom clusters. Thereby, metal clusters, which contain both ligand-bearing and naked metal atoms that are only bound to other metal atoms, were named by Schnöckel et al. as *metalloid* clusters [3–6] or, more generally, *elementoid* clusters, to express, in accordance with the Greek word ειδος (ideal, prototype), that the ideal form or the motif of the solid structure of the metal or element can be recognized in the topology of the metal atoms in the cluster. In general, such metalloid clusters contain more direct metal–metal contacts than metal–ligand contacts and can be described, on first glance, by the general formula

M_nR_m ($n > m$; M=metal like Al, Au, Sn, etc.; R=ligand like S-C_6H_4-COOH, $N(SiMe_3)_2$, etc.) and are the central topic of this contribution. These metalloid clusters are ideal model compounds to shed light on the borderland between molecules and the solid state of metals at a molecular level as when n increases, the clusters resemble more and more the bulk metal itself. Thereby, the average oxidation state of the metal atoms inside the cluster approaches the value zero, of the bulk phase. Additionally, as the size of such metalloid cluster compounds is within the nanometer range, research in this field, beside the fundamental aspect as outlined above, gains a technological aspect in the field of nanotechnology.

Hence, due to recent progress in the field of nanotechnology, the size range between molecules and the solid state has become the focus of various research efforts [7, 8]. In particular, elucidation of the structural and electronic properties and photodynamics for materials of this size range can have great scientific impact with applications in solar energy harvesting [9, 10], optoelectronic technologies [11, 12], sensors [13], and biological and medical imaging [14]. Additionally, it was recently shown that field effect transistors can be built using silicon nanowires [15]. The nanoscaled area is especially of interest for metals or semimetals as drastic changes take place on going from oxidized species (e.g., oxides, halides, nonconducting; $AlCl_3$, $AuCl_3$, GeO_2, etc.) via metalloid clusters of the general formula M_nR_m ($n > m$; M=metal like Al, Au, Sn, etc.; R=ligand like S-C_6H_4-COOH, $N(SiMe_3)_2$, etc.) to the bulk elemental phase (e.g., metal, conducting; semimetal, semiconducting; elemental Al, Au, or Ge) [16]. This behavior is quite different with respect to "saltlike" cluster compounds, e.g., a heterocubane $Li_4Cl_4{\cdot}4D$ (D=$OP(NMe_2)_3$, Et_2O) structure [17, 18] can be already seen as a cutout of the rock salt structure. Hence, in the case of "saltlike" clusters, even small clusters with only a small number of metal atoms (ions) exhibit a similar structure like the bulk material, e.g., MO_6 octahedra in poly-oxo-metallates (M=V, Ni, Mo, W) [19, 20] or hexagonal closed packed (A-B-A) assemblies of selenium ions with copper ions in tetrahedral sites in $(Cu_2Se)_n$ clusters [21].

This difference between "saltlike" and metalloid clusters is that in the case of the metalloid clusters, the oxidation state of the metal atoms inside the cluster changes, drawing closer to the value zero, as the cluster gets larger. In the case of the saltlike and naked clusters, the oxidation state of the metal atoms (ions) is always the same, irrespective of the metal atom being within a cluster, a molecule, or the solid state. This interrelation between the different classes of cluster compounds including the group of negatively charged Zintl-type clusters is shown in Fig. 1.

The highly mixed valence situation in the case of metalloid clusters leads to the most complex bonding situation in the field of metal atom clusters, and often a structural approach onto a solid structure is realized as it was first of all shown by Schnöckel et al. for the elements Al and Ga [22]. However, novel structural motives are realized even within large metalloid cluster compounds as lately described for the structurally characterized metalloid clusters $Al_{50}Cp^*_{12}$ **1** (Cp^*=C_5Me_5) [23, 24] and Au_{102}[*p*-MBA]$_{44}$ **2** (*p*-MBA=*p*-mercaptobenzoic acid) [25]. In both compounds (Fig. 2), different polyhedral arrangements are found in the center of

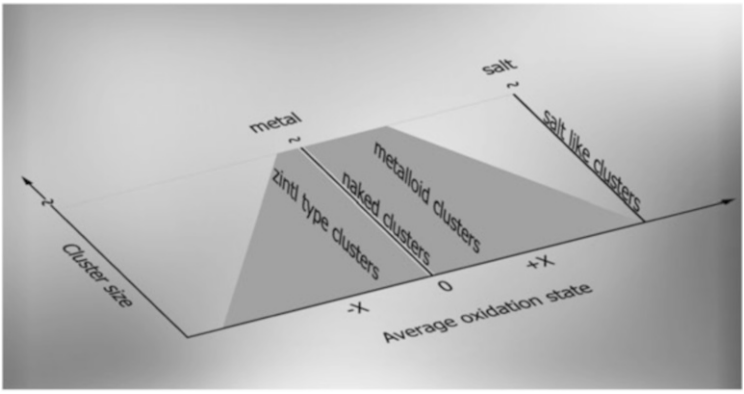

Fig. 1 Interrelation between different types of metal atom clusters with respect to average oxidation state of the metal atoms and cluster size

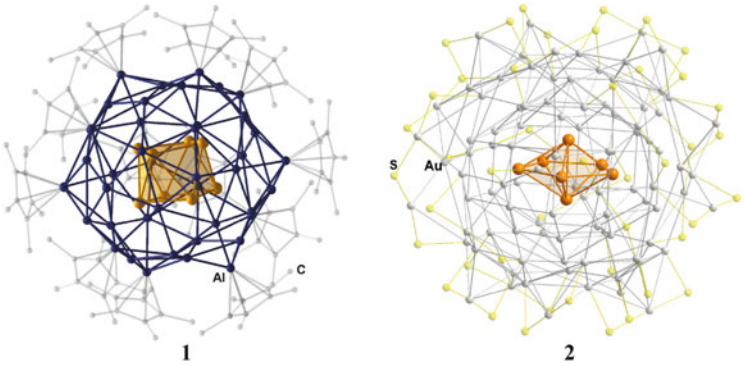

Fig. 2 Molecular structure of the metalloid cluster compounds $Al_{50}Cp^*_{12}$ **1** ($Cp^*=C_5Me_5$, without hydrogen atoms) and $Au_{102}[p\text{-MBA}]_{44}$ **2** (*p*-MBA=*p*-mercaptobenzoic acid; only the sulfur atom is shown). The central Al_8 square antiprism for **1** and the Au_7 pentagonal bipyramid for **2** are highlighted by a polyhedral presentation in *orange*

the cluster, i.e., in the case of **1** a square antiprismatic Al_8 unit and in the case of **2** a pentagonal bipyramidal Au_7 unit [26].

So, although the diameter of the metal core is within the nanometer range – ca. 1 nm for **1** and 1.4 nm for **2** within both cluster compounds – no central metal atom is present, as it would be expected for a simple cutout of the solid-state structure of elemental gold or aluminum, both exhibiting a cubic closed packed (ccp) structure. This circumstance demonstrates that the simple assumption that the arrangement of the metal atoms within a nanoscaled metalloid cluster can be seen as a cutout of the solid-state structure [27] is questionable, even for metalloid clusters with diameters in the nanometer range. However, somewhere in the nanometer range, a structural transition to the solid-state structure should take place as the fcc

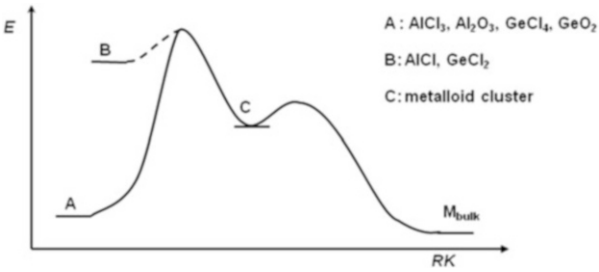

Scheme 1 Schematic development of the energy during the synthesis of a metal from oxidized starting materials

structure is adopted, e.g., by gold nanoparticles with a diameter larger than 2 nm [28].

As a consequence of the structural uncertainty in the case of metals or semimetals, the structural characterization of metalloid cluster compounds is the first step to establish a useful basis for structure–property relations of metal nanoparticles. Or in other words, the synthesis and characterization of metalloid clusters open our eyes to the complexity and the fundamental principles of a simple-seeming chemistry, for example, the dissolution and the formation of metals. However, obtaining structural information on these metal cluster compounds is not trivial, and many highly sophisticated methods were established, even for naked metal atom clusters in the gas phase (gas-phase drift measurements or electron diffraction measurements together with quantum chemical calculations have been used to get structural information about small naked gold or tin clusters in the gas phase [29, 30]). The best experimentally available structural information comes from single-crystal X-ray structure analysis. The drawback of this technique is the fact that the compound must be obtained first in the form of single crystals, which is not trivial, as metalloid clusters are metastable intermediates on the way to the bulk phase as emphasized in Scheme 1. Thus, special synthetic methods have been established, which are described in Sect. 3.

Although everything outlined in the introduction holds true for all metals, we will focus in the following on metalloid clusters of the main group elements of group 13 and 14 to keep the focus of this book. For recent developments in the field of metalloid clusters of noble metals like gold or silver, see, e.g., [31, 32].

2 Solid-State Structure of Aluminum, Gallium, Germanium, and Tin

As metalloid clusters are ideal model compounds for the area between molecular compounds and the solid state of the corresponding metal, a short survey of the solid-state structures of the elements discussed within this contribution is given, whereby group 13 and group 14 metals are discussed separately.

2.1 The Modifications of the Elements Al and Ga

For aluminum, the situation is quite simple as only one modification, the metallic face-centered cubic (fcc) arrangement of the Al atoms, has been identified so far. However, ab initio calculations indicate that in principle, a nonmetallic allotrope, like observed for boron, might be possible [33]. This aspect is discussed in Sect. 4.1.3. In contrast to aluminum, seven modifications are structurally proven for gallium indicating a higher structural diversity which might be also expected within metalloid gallium clusters and which is indeed realized as discussed in Sect. 4.2. To classify the arrangement of the gallium atoms within different metalloid gallium clusters, the most prominent structural features of the normal-pressure modifications α-, β-, γ-, and δ-Ga and the high-pressure modifications Ga II and Ga III are shown in Fig. 3. Additionally, Ga IV with fcc packing of the gallium atoms like in α-aluminum is observed at very high pressure [34].

A characteristic feature of α-Ga (coordination number 1+2+2+2) is the formation of a short Ga–Ga bond (245 pm) of every Ga atom with one of its seven neighbors. Therefore, α-Ga is also described as a molecular metal with Ga_2 dumbbells. For the low-temperature phases β-, γ-, and δ-Ga, the following characteristic units are observed: a ladder structure (coordination number 2+2+2+2) for β-gallium, Ga_7-rings that stack to form tubes, and a centered Ga_n "wire," observed for γ-Ga, and interpenetrating Ga_{12} icosahedra for δ-Ga.

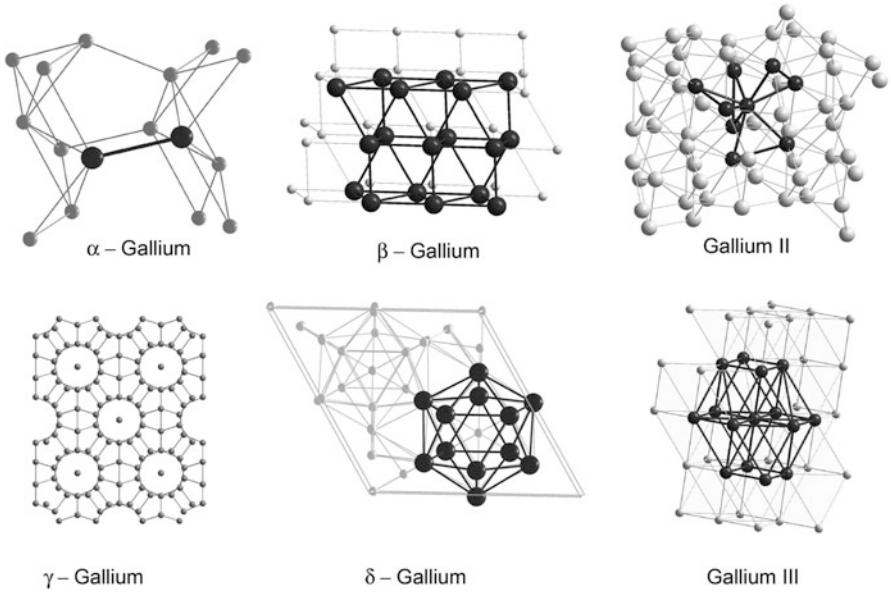

Fig. 3 Sections of the normal-pressure solid-state modifications α-, β-, γ-, and δ-gallium and the high-pressure modifications Ga II and Ga III

In all these cases (α-, β-, γ-, and δ-gallium), *pseudo*molecular units can be discerned, indicating, similar to the lighter congener boron, a degree of covalent bonding. In contrast to this, higher coordination numbers are realized within the high-pressure modifications Ga II–Ga IV, leading to a more metallic character like the homologues aluminum or indium.

2.2 The Modifications of the Elements Ge and Sn

Elemental germanium normally crystallizes in a cubic diamond lattice (α-germanium, Ge(*cF*8)), where every germanium atom is tetrahedrally bound to four other germanium atoms with a Ge–Ge distance of 245 pm [35]. Additionally, several high-pressure modifications of germanium have been structurally characterized [36]. After pressure release, the normal-pressure modifications γ-Ge (Ge(*tP*12)) and δ-Ge (Ge(*cI*16)) have been obtained [37, 38]. In both allotropes (γ- and δ-Ge), the germanium atoms are still fourfold coordinated, but the bond angles deviate considerably from the ideal tetrahedral angle of 109.5°. γ-Ge crystallizes in a three-dimensional arrangement with five- and seven-membered rings, while δ-Ge comprises six-membered rings (Fig. 4).

Lately, a novel element modification, Ge(*cF*136), was identified [39], which is obtained by the oxidation of the Zintl-anion Ge_9^{4-} by an ionic liquid. In Ge(*cF*136), all germanium atoms are fourfold coordinated and are arranged in the clathrate(II) form, where two different polyhedra are present: a pentagonal dodecahedron built up of

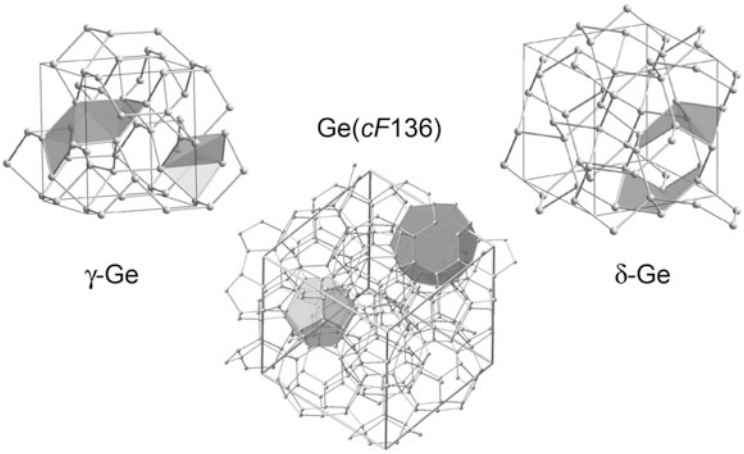

Fig. 4 Cutout of the solid-state structures of γ-germanium (*left*), δ-germanium (*right*), and Ge(*cF*136) (*middle*). The five- and seven-membered rings (γ-Ge) as well as the six-membered rings (δ-Ge) are emphasized via a polyhedral presentation. In the case of Ge(*cF*136), the Ge_{20} pentagonal dodecahedron (*bright*) and the Ge_{28} hexakaidecahedron (*dark*) are emphasized via a polyhedral presentation

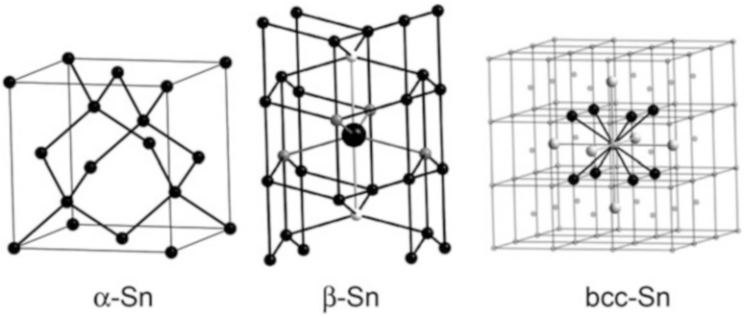

Fig. 5 Cutout of the different solid-state structures of tin. *Left*, unit cell of α-tin. *Middle*, cutout of the solid-state structure of β-tin. The coordination number of 4+2 is emphasized by *light gray* (4) and *white* (2) neighbor atoms. *Right*, unit cell of the bcc-type tin modification. The coordination number 8+6 is emphasized by *dark* (8) and *bright* (6) spheres

20 atoms and a hexakaidecahedron exhibiting 28 atoms (Fig. 4). Additionally, the reaction of the Zintl phase Mg_2Ge with $GeCl_4$ gives "mesostructured germanium with cubic pores" [40], whereas the oxidation of the Zintl ion $(Ge_9^{2-})_n$ with ferrocenium hexafluorophosphate in the presence of a surfactant (cetyltriethylammonium bromide) leads to "hexagonal nanoporous germanium" [41].

For elemental tin, two different well-characterized normal-pressure modifications with a phase transition temperature of 13.2°C are known [35]. Below 13.2°C, tin crystallizes in a cubic diamond lattice (*α-tin*) with a Sn–Sn single bond length of 281 pm (Fig. 5 left). At temperatures above 13.2°C, tin crystallizes in a tetragonal lattice (*β-tin*), where the coordination number of every Sn atom increases from 4 to 4 +2 so that every tin atom is now located in a distorted octahedral arrangement. Due to the increase of the coordination number, the Sn–Sn distances increase as well to 301.6 pm and 317.5 pm, respectively (Fig. 5 middle). At high pressure, two other modifications of tin have been clearly identified to date. At 10 GPa, a modification is realized where the tin atoms show a body-centered tetragonal (bct) arrangement with Sn–Sn distances of 297 pm [42]. At 120 GPa, a structural modification is observed, where the tin atoms form a body-centered cubic (bcc) structure, a well known arrangement for metals like tungsten or iron (Fig. 5 right) [43]. The Sn–Sn distances are 284.6 pm in the first and 328.7 pm in the second coordination sphere.

With respect to the behavior at high pressure, tin differs from the lighter congeners Si and Ge, where the phase transition sequence *diamond* → *β-tin* → *bct* → *bcc* is not observed. However, for all the elements Si, Ge, and Sn, the solid-state structure with a diamond lattice is thermodynamically most favorable (for tin below 13°C). Consequently, between the elements, there are both similarities and differences, which also hold true for metalloid clusters, and as expected among these clusters, the motif of the solid structure of the metal or element might be already recognized in the topology of the metal atoms in the cluster.

3 Synthesis

As metalloid clusters are like any metal nanoparticle metastable and prone to the formation of the metal itself, special synthetic routes are necessary for their synthesis. Thereby, kinetic stabilization is necessary, which is often realized by applying bulky ligands. These bulky ligands shield the metal core in a way that further growing to the elemental state is arrested and the metalloid clusters are kinetically stabilized so that they can be isolated, characterized, and further manipulated. As the average oxidation state of the metal atoms within a metalloid cluster compound is in between 0 and 1, reduction of a suitable starting material (e.g., $AlCl_3$ or $GeCl_4$) might be a possible synthetic route, a similar procedure as used for the synthesis of metals from the corresponding ore, e.g., reduction of Fe_2O_3 with CO to elemental iron [44]. However, the formation of metals from oxidized species is normally performed under drastic reaction condition, e.g., reduction of Fe_2O_3 takes place above 1000°C, and thus an isolation of intermedially formed metalloid clusters (Scheme 1) in preparative scale is not possible via this route. Nevertheless, applying a metastable starting material (B in Scheme 1) for the reduction leads to less drastic reaction conditions so that intermedially formed metalloid clusters (C in Scheme 1) might be accessible via kinetic stabilization.

However, when the starting material (oxidized compound) is easily reduced to the elemental state, as it is the case for noble metals, the reaction conditions might be already mild, and consequently the first metalloid cluster synthesized was the metalloid gold-cluster $Au_{55}(PPh_3)_{12}Cl_6$ **3** [27, 45]. However, although **3** is easily obtained via the reduction of $(PPh_3)AuCl$ with B_2H_6, its structural characterization is missing to date as it cannot be obtained in a crystalline form. Nevertheless, 26 years after the synthesis of the Au_{55} cluster **3**, the metalloid gold-cluster $Au_{102}[p\text{-MBA}]_{44}$ **2** (*p*-MBA=*p*-mercaptobenzoic acid) was obtained via a similar synthetic route, i.e., reduction of $HAuCl_4$ with $NaBH_4$ in the presence of *p*-mercaptobenzoic acid [25, 46]. Thereby, **2** was successfully crystallized and could be structurally characterized, revealing the unusual feature of a central Au_7 unit as discussed in the introduction (Fig. 2). After this breakthrough, a variety of metalloid gold clusters could be isolated and structurally characterized [32], and quite recently the structure of a metalloid gold cluster with 133 gold atoms in the cluster core was solved via single-crystal X-ray structure analysis [47].

However, the focus of this contribution is on metalloid main group clusters of group 13 and 14, where this synthetic route is not easily transferrable as Al, Ga, Ge, and Sn exhibit a more positive reduction potential and thus more drastic conditions are necessary, which is counterproductive with respect to kinetic stabilization of intermedially formed metalloid clusters. Nevertheless, a variety of metalloid clusters especially of group 14 is obtained via this route, whereby the naked tetrel atoms that exhibit the oxidation state zero are introduced via two main routes: (a) ligand stripping via reductive elimination (Scheme 2) or (b) complete dehalogenation of a halide precursor (Scheme 3).

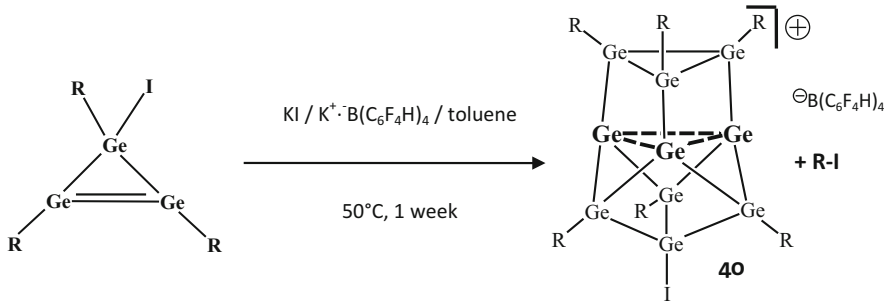

Scheme 2 Reaction scheme for the synthesis of **40** [48]. The naked germanium atoms (*bold*) might result from reductive elimination of RI (R=Si*t*Bu$_3$)

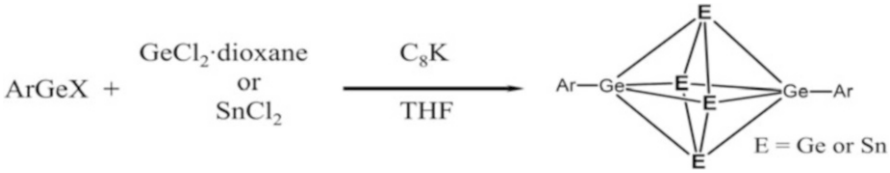

Scheme 3 Reaction scheme for the synthesis of Ge_6Ar_2 **29** (Ar = 2,6-Dipp$_2$-C$_6$H$_3$; Dipp = 2,6-*i*Pr$_2$-C$_6$H$_3$) and $Ge_4Sn_2Ar_2$ **29a** [49, 50]. The naked tetrel atoms are *bold*

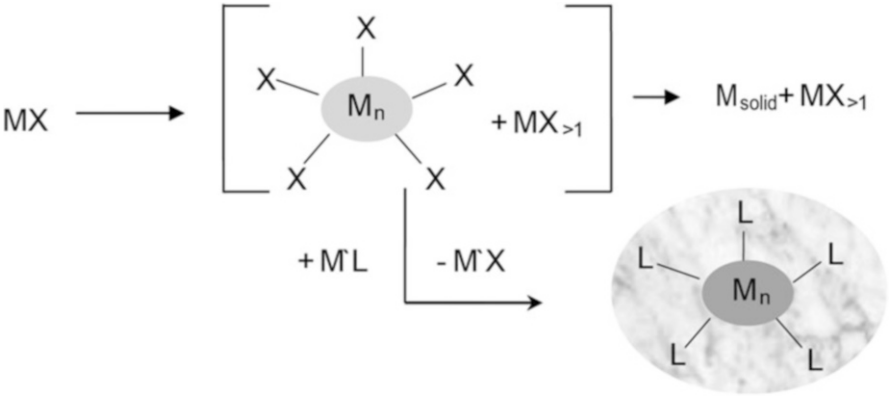

Scheme 4 Schematic presentation of the synthesis of a metalloid cluster compound applying the disproportionation reaction of a monohalide (X=halide-like Cl; L=bulky ligand-like *t*Bu)

Beside these more classical synthetic routes, the most successful synthetic route to metalloid cluster compounds starts from metastable compounds, e.g., halides in low oxidation states [51, 52] that disproportionate into the thermodynamically stable products at low temperature. When the disproportionation reaction takes place at low temperatures, which means temperatures well below 0°C, intermedially formed clusters might be trapped by substituting the halide by a bulky ligand as exemplified in Scheme 4.

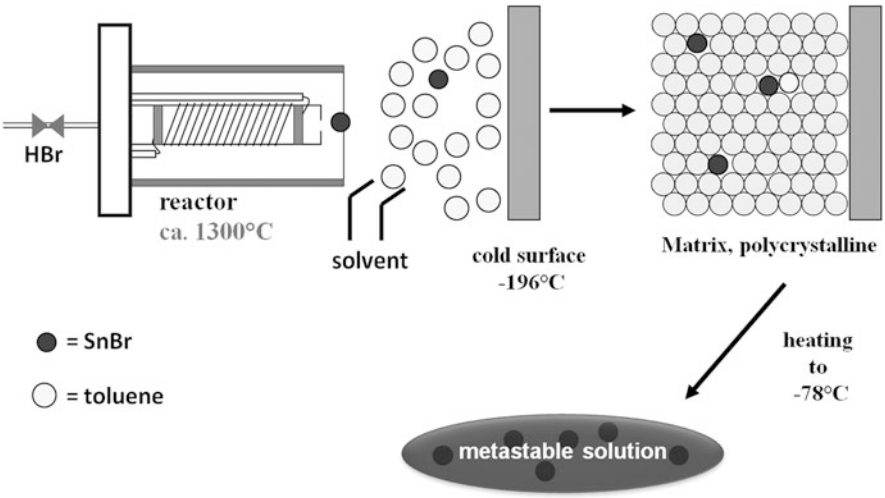

Scheme 5 Principle of the matrix isolation technique applied for the preparative co-condensation, whereby the high-temperature molecule is used in larger quantities

In the case of group 13 and group 14, the only metastable halides useful for this synthetic route are the respective monohalides, which are obtained in the form of metastable solutions via the synthetic route of the preparative co-condensation technique [53]. The experimental realization of this idea has been described many times [51, 52, 54, 55], and the principal procedure will be described here only briefly. As the monohalides (AlX, GaX, GeX, and SnX) are high-temperature gas-phase compounds, they must be transferred into a synthetically useful form of, e.g., a metastable solution first. This is realized via the preparative co-condensation technique, as sketched in Scheme 5. Hence, the high-temperature molecule (dark circle in Scheme 5) is first synthesized in a reactor at high temperature and low pressure. Afterward, the high-temperature molecule is condensed together with an inert solvent (bright circle in Scheme 5) at a cold surface (−196°C). Thereby, the solvent freezes, and the high-temperature molecules are trapped within the solid matrix at low temperatures. After the co-condensation reaction is finished, the solid matrix is heated, e.g., with dry ice to −78°C, and after melting of the matrix, one might obtain a metastable solution of the high-temperature molecule now at low temperature.

Hence, the preparative co-condensation technique gives access to completely novel reagents based on high-temperature gas-phase molecules as already outlined by Moskovits and Ozin: "*By using cryogenic techniques on a routine basis, chemists are no longer restricted to conventional methods of solving a synthetic problem. The chemist can now devise experiments taking advantage of starting materials that might be regarded as esoteric or even unattainable from a synthetic point of view*" [56].

However, finding the right solvent and donor component for the co-condensation reaction to give a metastable solution is challenging, and toluene is predominantly used as inert solvent, to which different donor molecules like thf, Et_2O, NEt_3, $PnBu_3$, etc. are added. During the co-condensation reaction, normally between 20 and 40 mmol of the monohalide is produced, while 100–200 ml of solvent mixture is used. The solubilized monohalides subsequently disproportionate in the temperature range between −60°C and +80°C depending on the kind of the halide and donor as well as on the concentration of the donor with respect to the corresponding monohalide. Consequently, these metastable MX solutions (M=Al, Ga, Ge, Sn) are the ideal starting point for the chemistry described in the following sections, directly indicating that novel reagents can open new avenues in chemistry.

4 Structure and Bonding of Metalloid Clusters of Aluminum and Gallium and their Interrelation to Solid-State Structures

In the following chapter, the structure and bonding of selected examples of metalloid clusters of aluminum and gallium are discussed mainly focusing on the interrelation to the solid-state structures. Thereby, only such metalloid clusters are discussed that exhibit only aluminum or only gallium atoms in the cluster core. Hence, metalloid clusters exhibiting also nonmetal atoms like phosphorous or semimetal atoms like silicon will be excluded. However, for further reading, books and reviews are recommended [57, 58].

4.1 Metalloid Aluminum Clusters

4.1.1 Small Clusters

The smallest metalloid aluminum cluster is $\{Al_7[N(SiMe_3)_2]_6\}^-$ **4**, which is obtained by the reaction of an Al(I)Cl solution with $LiN(SiMe_3)_2$ [5, 6]. The molecular structure of the anionic cluster can be described as a central aluminum atom bound to two $Al_3[N(SiMe_3)_2]_3$ moieties. This sandwich-like description might lead to the formulation of the compound as a central Al^{3+} ion to which two aromatic $\{Al_3[N(SiMe_3)_2]_3\}^{2-}$ units are bound. A similar aromatic compound is known for gallium $[Ga_3Ar_3]^{2-}$ (Ar = 2,6-Mes_2-C_6H_3; Mes = 2,4,6-Me_3-C_6H_2) which is obtained via the reductive dehalogenation of $GaArCl_2$ with elemental sodium [59]. However, quantum chemical calculations indicate that the description of the central aluminum atom in **4** as an Al^{3+} ion is not useful [5, 6] and thus the description of **4** as a sandwich compound is not feasible. Another explanation of

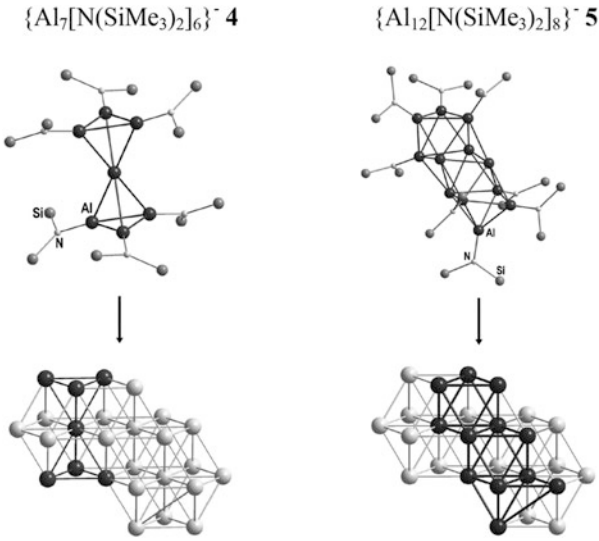

Fig. 6 Molecular structures of $\{Al_7[N(SiMe_3)_2]_6\}^-$ **4** and $\{Al_{12}[N(SiMe_3)_2]_8\}^-$ **5** ($SiMe_3$ groups not shown) and their topological relationship to the structure of solid α-aluminum

the arrangement of the aluminum atoms in **4** can be seen as a structural approach to the solid-state structure of α-aluminum (Fig. 6).

However, the Al–Al distances inside **4** vary between 260 and 280 pm and are therefore slightly shorter than in elemental aluminum, where an Al–Al distance of 286 pm is found. This shortening can be addressed to a certain contribution of covalent bonding inside the cluster core leading to more localized bonding electrons with respect to the bulk metal and therefore to shorter Al–Al bonds. A similar description for the arrangement of the aluminum atoms in the cluster core holds true for the metalloid cluster $\{Al_{12}[N(SiMe_3)_2]_8\}^-$ **5** [60], in which the arrangement of the aluminum atoms also resembles that of α-aluminum as emphasized in Fig. 6. **5** is also obtained by the reaction of a metastable AlCl solution with $LiN(SiMe_3)_2$. However, this time, the synthesis is performed at room temperature, while **4** is obtained by a reaction at −25°C, directly indicating that different cluster sizes might be obtained during the disproportionation reaction of the metastable halide solution, depending on the applied reaction conditions. The significant role of the applied halide is obvious from the metalloid cluster $[Al_{14}[N(SiMe_3)_2]_6I_6]^-$ **6**, which is obtained from a reaction of $LiN(SiMe_3)_2$ with a more stable AlI solution. Thereby, the reaction mixture is heated several times to 55°C, and **6** is isolated with $[Li(OEt_2)_4]^+$ as counter ion [61, 62]. The main structural units of **6** are two staggered, approximately Al-centered Al_6 rings, which might be called a "wheel-rim-type" structure (Fig. 7). The central Al atoms deviate somewhat from the planes of the rings and show an Al–Al distance of 273 pm. The other Al–Al distances range from 257 pm (between Al atoms with iodine ligands) to 291 pm (between Al atoms with $N(SiMe_3)_2$ ligands) and are therefore in the same range as found in **4** and **5**. The interrelation of the "wheel-rim-type" structure of **6** to the metal becomes

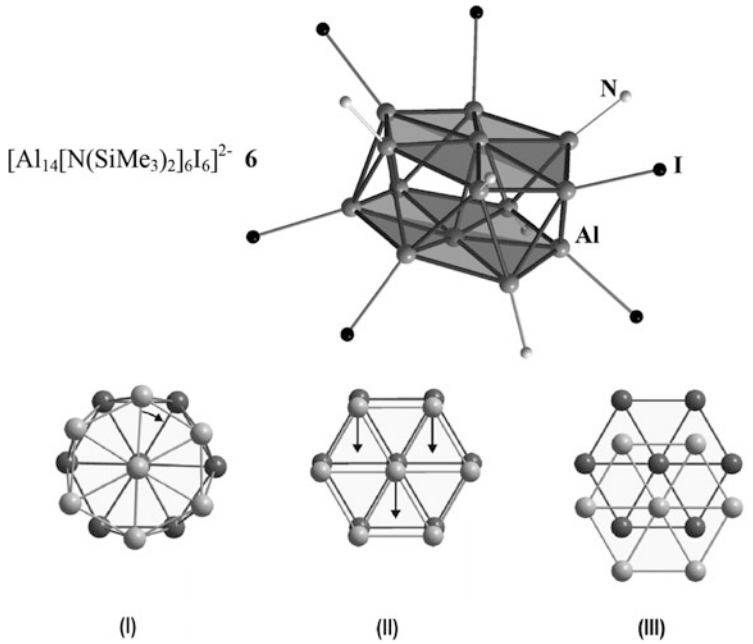

Fig. 7 Molecular structure of $[Al_{14}[N(SiMe_3)_2]_6I_6]^-$ **6** without $SiMe_3$ groups and relationships to Al metal (transformation of the position of the Al atoms of **6** in direction of the close packing in the bulk metal)

obvious by a 30° rotation of the two centered Al_6 rings (I in Fig. 7) followed by a shift of the centered six-membered rings toward each other (II in Fig. 7).

4.1.2 $\{Al_{69}[N(SiMe_3)_2]_{18}\}^{3-}$ and $\{Al_{77}[N(SiMe_3)_2]_{20}\}^{2-}$

The first examples **4–6** already indicate that the arrangement of aluminum atoms in the cluster core of a metalloid aluminum cluster resembles that found in elemental aluminum, however, still showing significant differences with respect to bond distance and coordination number. This effect might be due to the cluster size as the number of naked metal atoms is still small with respect to ligand-bound ones. This situation is completely different among the largest metalloid aluminum clusters characterized so far, $\{Al_{69}[N(SiMe_3)_2]_{18}\}^{3-}$ **7** [63] and $\{Al_{77}[N(SiMe_3)_2]_{20}\}^{2-}$ **8** [64], which are obtained by a reaction of $LiN(SiMe_3)_2$ with a metastable AlCl and AlI solution at 60°C, respectively. The molecular structures (Fig. 8) of **7** and **8** strikingly show the importance of the synthesis and structural characterization of metalloid clusters for understanding of the formation and dissolution of metals, especially as the differences between **7** and **8** are too small to be observed with common nanoscopic methods (e.g., AFM, atomic force microscopy). Hence,

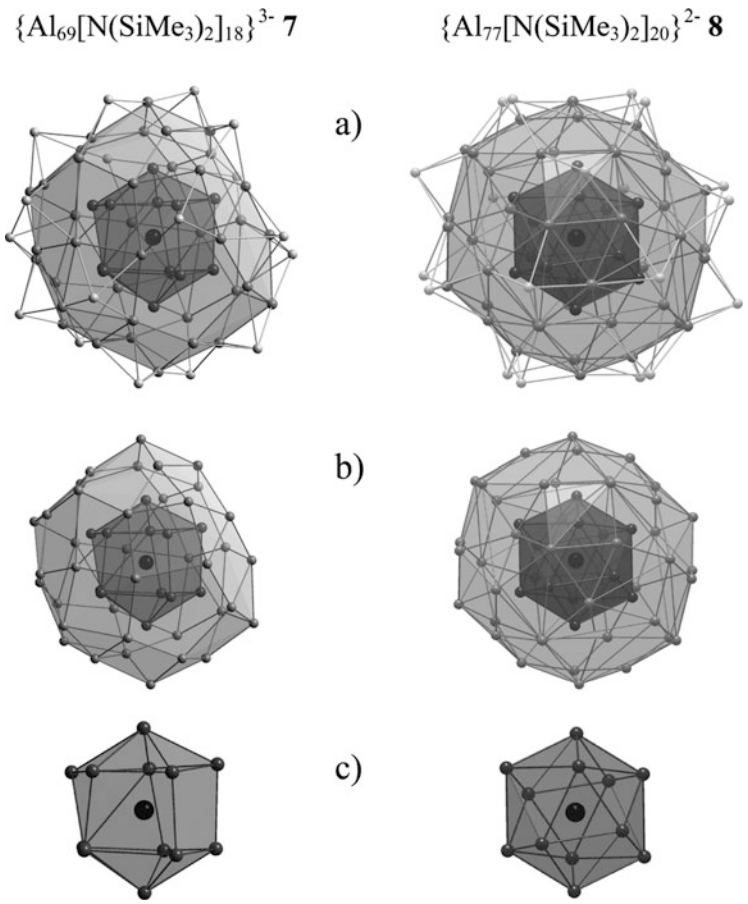

Fig. 8 Comparison of the arrangement of the Al atoms in the metalloid clusters $\{Al_{69}[N(SiMe_3)_2]_{18}\}^{3-}$ **7** and $\{Al_{77}[N(SiMe_3)_2]_{20}\}^{2-}$ **8**; the outer shell Al atoms form 2c2e bonds to $N(SiMe_3)_2$ groups which are omitted for clarity. (**a**) Complete shell-like arrangement of all Al atoms: **7** (1+12+38+18 Al atoms) and **8** (1+12+44+20 Al atoms). (**b**) Inner two shells omitting the ligand-bearing Al atoms. (**c**) Arrangement of the inner Al_{13} unit

single-crystal X-ray structure analysis was absolutely necessary to reveal the differences.

Both clusters have nearly the same size, where 69 or 77 aluminum atoms are present in a shell of 18 and 20 $N(SiMe_3)_2$ groups, respectively. Additionally in both clusters, the aluminum atoms are arranged in "shells," whereby in both cases, a central aluminum atoms is surrounded by 12 nearest aluminum atoms.

The coordination number and the Al–Al distances decrease from the center (278 pm) to the outer shells (268 pm). Hence, the Al–Al bonds become more localized ongoing from the center to the outside of the cluster. Despite this similarities of **7** and **8**, there are significant differences of both clusters:

1. The Al_{13} core of **7** can be described as a distorted D_{5h} structure, often described as decahedral [65], whereas the central Al atom in the Al_{77} cluster **8** has an icosahedral coordination sphere that is distorted in the direction of a cuboctahedron (Fig. 8). However, in both clusters, the Al–Al distances from the center to the first Al_{12} shell and those within this shell are nearly identical [66].
2. The second shell in **7** consists only of 38 aluminum atoms, while the one in **8** exhibits 44 aluminum atoms.
3. The number of ligands attached to the cluster differs significantly.

As the arrangement in the cluster core of **7** and **8** is substantially different, this shows that even small changes in the cluster shell lead to changes in the topology of the metal framework at the center, which should also affect the physical properties. A similar situation was recently found in gold chemistry where the arrangement of the gold atoms in the metalloid clusters $Au_{130}(SPh\text{-}COOH)_{50}$ [67] and $Au_{133}(SPh\text{-}t\text{Bu})_{52}$ [47] differs substantially, although only small changes in the ligand shell are present, further underlining that the arrangement of the metal atoms in the cluster core is very sensitive to the ligand shell. This finding additionally implies that different surface reactions may lead to different topological changes within the interior of the metal down to the nanometer range.

In order to understand the topology and the packing density of **7** and **8** with respect to metallic aluminum, the atomic volume of the "naked" Al atoms in **7** and **8** was calculated [68] and compared to the volume of a hypothetical molecular Al_{55} section of the fcc Al metal lattice [63, 66]. The calculations thereby reveal that the atomic volume increases from **7** to **8** to elemental aluminum, indicating that the driving force is the formation of the most compact arrangement with the highest possible coordination number 12. Therefore, the arrangement of the naked Al atoms in **7** and **8** is less compact with shorter (more molecular) Al–Al contacts and lower coordination numbers with respect to bulk elemental aluminum.

4.1.3 Icosahedral Clusters

All previously discussed metalloid Al clusters show that the arrangement of the Al atoms inside these clusters can be described as a structural approach to the solid-state structure of α-aluminum, whereby the observed distortions reflect the adaptation of the cluster core to the $(AlR)_n$ shell. However, also structures are realized that do not resemble fcc aluminum, indicating that there may be different solid-state structures such as a hypothetical nonmetallic β-aluminum modification as discussed in this section.

As the stability of a metastable Al(I) halide solution significantly depends on the applied donor, the donor stabilized $Al_4Br_4{\cdot}4NEt_3$ is obtained in the presence of the strong donor NEt_3 [69–72]. Weaker donors such as thf or thp lead to the clusters $Al_{22}Cl_{20}{\cdot}12L$ (L=thf or thp) **9** [33] and $Al_{22}Br_{20}{\cdot}12thf$ **10** [73, 74], representing the first polyhedral Al subhalides with a unique cluster core (Fig. 9). The icosahedral

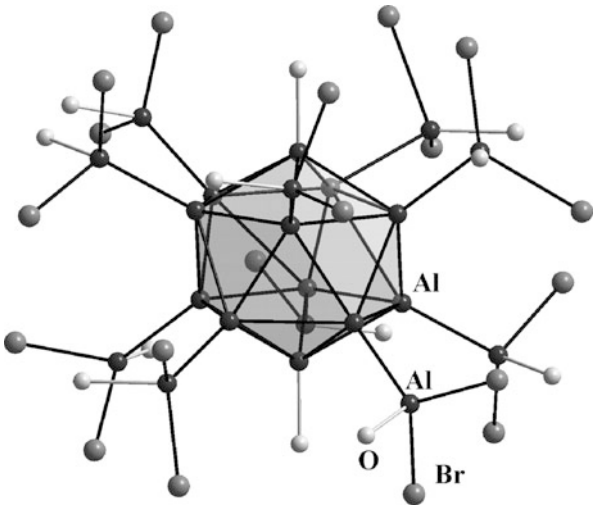

Fig. 9 Molecular structure of $Al_{22}Br_{20}{\cdot}12thf$ **10**. From the thf molecules, only the directly bound oxygen atom is shown, and the central Al_{12}-icosahedra is shown in a polyhedral presentation

Al_{12} core in **9** and **10** is reminiscent of the polyhedral Al_{12} cluster $[Al_{12}(i\text{Bu})_{12}]^{2-}$ in which every aluminum atom is directly bound to the carbon atom of an *i*Bu ligand [75, 76]. In contrast to this, within the Al_{22} halides **9** and **10,** 10 more Al atoms are directly bound to an Al atom of the icosahedral Al_{12} cluster core, presenting a unique configuration. Additionally, each of the outer 10 Al atoms is bound to two halide atoms and saturated by a donor molecule (thf, thp). The apex and base atoms in the Al_{12} icosahedron are not "naked" as they are coordinated by one donor molecule, each. Consequently, three different kinds of aluminum atoms are present in **9** and **10**, which is confirmed by solid-state ^{27}Al NMR and XPS measurements [33]. The average Al–Al distance within the central Al_{12} icosahedra is around 270 pm, which is slightly longer than the average Al–Al distance to the outer aluminum atoms of 253 pm being in the range of normal Al–Al single bonds. Additionally, the average Al–Br bond length is within 230 pm in the normal range for single bonds. Since both **9** and **10** have more metal–metal than metal–ligand bonds, **9** and **10** are metalloid clusters where the type of metal atom topology is surprising and has no precedent in elemental aluminum.

However, the α-boron structure, which consists of a network of molecular icosahedral cluster units connected by boron–boron bonds, has a similar topological motif. Consequently, as metalloid clusters are molecular intermediates on the way to the bulk phase of the corresponding element, **9** and **10** may be intermediates on the way to a hypothetical nonmetallic Al modification with a structure similar to α-boron. This scenario was corroborated by ab initio calculations, which reveal that an energy-consuming expansion of the closest packed Al atoms in elemental aluminum by about 30% (ca. 33 kJ/mol^{-1}) leads to a situation where a structure analogous to that of α-boron is energetically more stable than the expanded fcc lattice [33]. As a "contraction" in the direction of the bulk metal actually takes place during disproportionation, as shown in the discussion of the Al_{69} and Al_{77} clusters

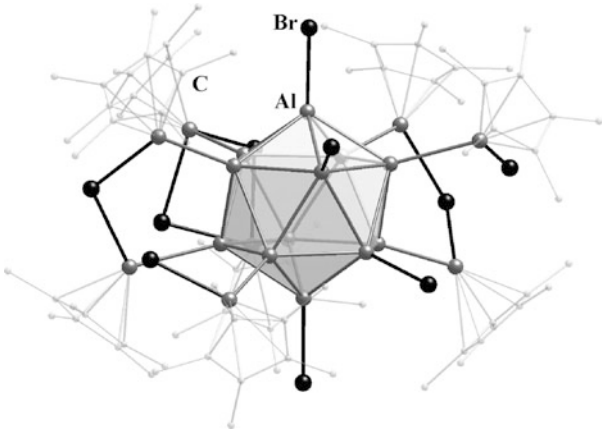

Fig. 10 Molecular structure of $Al_{20}Cp^*_8Br_{10}$ **11a** without hydrogen atoms. The central icosahedron is shown in a polyhedral presentation

7 and **8** (cf. Sect. 4.1.2), the intermediate existence of a β-Al modification with a larger atom volume cannot be excluded. Additionally, mixed substituted aluminum clusters $Al_{20}Cp^*_8Br_{10}$ **11a** and $Al_{20}Cp^*_8Cl_{10}$ **11b** are known [77, 78] that also exhibit a central Al_{12} core indicating that the structural motive of an Al_{12} icosahedra is favorable in the cluster regime. However, one major difference between the halide compounds **9** and **10** and the partially substituted compounds **11a** and **11b** is that in both **11a** and **11b**, halide atoms are directly bound to Al atoms of the central Al_{12} icosahedron (base and apex Al atoms of the central Al_{12} icosahedra in Fig. 10).

The central Al_{12} icosahedron is thus bound to four halogen atoms, six Al(II)BrCp* units, and two Al(I)Cp* moieties. This arrangement leads to a total of 26 skeletal electrons ($2e^-$ for the halide and Al(II)BrCp* bearing aluminum atoms and $3e^-$ for the Al(I)Cp* coordinated aluminum atoms), nicely in accordance with Wade's rules [79], so that **11a** and **11b** exhibit the bonding situation of a *closo* structure. As also within the halides **9** and **10** as well as within the fully substituted cluster anion $Al_{12}[i\text{Bu}]_{12}^{2-}$, 26 skeletal electrons are present a direct relation is obvious, indicating that the intermedial appearance of an $Al_{12}X_{12}$ species during the disproportionation reaction of AlX is feasible [77, 78].

Up to now, it seems as if the disproportionation reaction always leads to metalloid aluminum clusters, where the arrangement in the cluster core more or less resembles that of α-aluminum or the hypothetical β-aluminum. However, also novel structures are available, i.e., an Al_8 moiety in the center of the metalloid Al cluster $Al_{50}Cp^*_{12}$ **1** as discussed in the following.

4.1.4 The Al_{50} Cluster

The synthesis of the $Al_{50}Cp^*_{12}$ cluster **1** (Fig. 11) [23, 24] further demonstrates that the stability of the halide and the reactivity of the ligand source play a vital role during the synthesis of a metalloid cluster from the disproportionation reaction of a metastable subhalide. Hence, when the reaction of AlX and $MgCp^*_2$ is performed

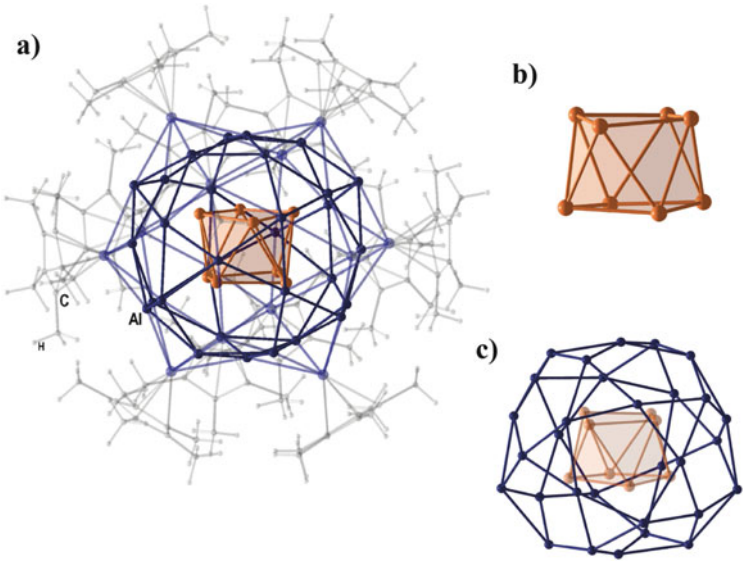

Fig. 11 (**a**) Representation of the $Al_{50}Cp^*_{12}$ molecule **1**. (**b**) Ball and stick model for the Al_8 core. (**c**) Ball and stick model for the Al_8 core and the surrounding icosidodecahedral Al_{30} shell; in all cases, the central Al_8 core is in a polyhedral presentation

at −78°C, the only isolable product is $[AlCp^*]_4$ [80]. When the reaction is performed at higher temperatures (−30°C), beside the substitution also a disproportionation takes place:

$$73AlBr + MgCp^*_2 \rightarrow [AlCp^*]_4 + 8[MgCp^*Br]_2 + Al_{50}Cp^*_{12} + 19AlBr_3.$$

Consequently, beside the Al(I) compound $[AlCp^*]_4$, also the aluminum-rich metalloid cluster $Al_{50}Cp^*_{12}$ **1** is formed, being thereby the largest organometallic aluminum cluster only containing Al, C, and H.

As outlined in the introduction, the center of **1** consists of an Al_8 moiety. This Al_8 moiety exhibits a distorted tetragonal antiprism geometry (Fig. 11); a similar arrangement is found in the $Ga_8[C_{13}H_9]_8^{2-}$ ion [81]. The Al_8 center in **1** is surrounded by 30 Al atoms that form an icosidodecahedron with 12 pentagonal and 20 trigonal faces. Every pentagonal face is capped by an AlCp* unit, whose 12 Al atoms form a very regular icosahedron with Al–Al distances of 500 pm. Every aluminum atom in the AlCp* unit is coordinated by 10 atoms (5Al and 5C) in a "mixed sandwich" form. Unusually the average Al−Al bond lengths in **1** increase from the center Al_8 unit (266 pm), over the Al_{30} unit (281 pm), to the capping AlCp* units (287 pm). The Al−C and the C−C bond lengths in the AlCp* units are similar to those in $(AlCp^*)_4$ [82, 83] indicative of similar bonding. The fivefold symmetry of the outer shell, which is also reflected in the second Al_{42} shell (Fig. 11), is merely broken by the Al_8 unit in the center. The relative energy of the neutral compound **1** compared to metal atoms and bulk metal was determined

by model calculations, showing that **1** can be seen as an intermediate in the formation of bulk material starting from aluminum atoms in the gas phase [23, 24].

4.2 Metalloid Gallium Clusters

In contrast to aluminum, gallium exhibits a great variety of normal- and high-pressure modifications and thus has a larger structural basis for the gallium atoms within metalloid clusters. The flexibility of gallium atoms to perform different connectivities is reflected in the great variety of structural motifs of metalloid gallium clusters. This aspect in the field of metalloid gallium clusters was nicely visualized by a cover picture of *Dalton Transactions* **2005**, 19 (Fig. 12), showing

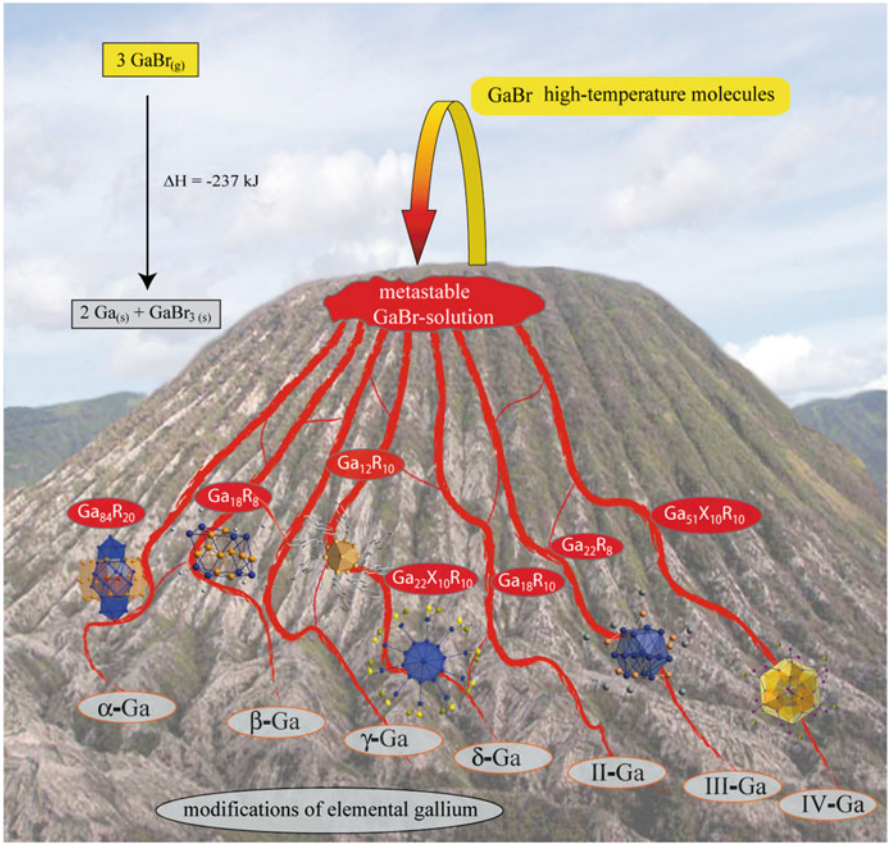

Fig. 12 This cartoon illustrates in a simple manner the hypothetical routes to the formation of different modifications of bulk gallium via different metalloid gallium clusters as snapshots of this highly complex process of self-organization strategies with the high-temperature molecules GaX (Image reproduced by permission of H. Schnöckel [16] and The Royal Society of Chemistry from *Dalton Trans.*, 2005, 3131–3136, DOI: 10.1039/B507002N.)

the different routes of the disproportionation reaction from metastable gallium monohalides to the different modifications.

This image conveys the selectivity of the disproportionation reaction course, which is also reflected experimentally as some metalloid clusters are obtained in remarkably high yield. This selectivity is expressed in the cover picture where only little connections between the different routes onto the different solid-state modifications are shown. During the last years, a great variety of metalloid Ga_nR_m clusters have been synthesized starting from metastable Ga(I) halides, containing nearly each number of Ga atoms up to 26 (e.g., Ga_{18} **14** [84], **16** [85], Ga_{19} **17** [86], Ga_{22} **18–20** [87–92], Ga_{24} **21** [93, 94], and Ga_{26} **22** [95, 96]). Hence, the following discussion highlights a representative selection of such metalloid clusters, starting from the small metalloid cluster $Ga_8[C(SiMe_3)_3]_6$ **12** and ending with the largest metalloid gallium cluster $\{Ga_{84}[N(SiM_3)_2]_{20}\}^{4-}$ **23**. Thereby, the presentation is focused on the structural aspects and their relation to the solid-state structures. For full-length discussions, see, e.g., [57] or [58].

4.2.1 Small Metalloid Gallium Clusters: Ga_8- and Ga_{12} Clusters

One of the smallest metalloid gallium clusters is $Ga_8[C(SiMe_3)_3]_6$ **12** [97, 98] showing a structural resemblance to α-Ga exhibiting non Wade-like bonding. The structure of **12** can be described as two Ga_4R_3 tetrahedra directly bound together by an unsupported Ga–Ga bond (Fig. 13). In **12**, 13 metal–metal bonds and only six metal–ligand bonds are formed. Consequently, the Ga_8R_6 cluster **12** can be seen as a prototypic compound with a 2e2c metal-to-metal bond as both atoms participating in the Ga–Ga bond do so without bridging atoms and are exclusively bonded to other metal atoms of the same type. The bond strength was thereby classified by

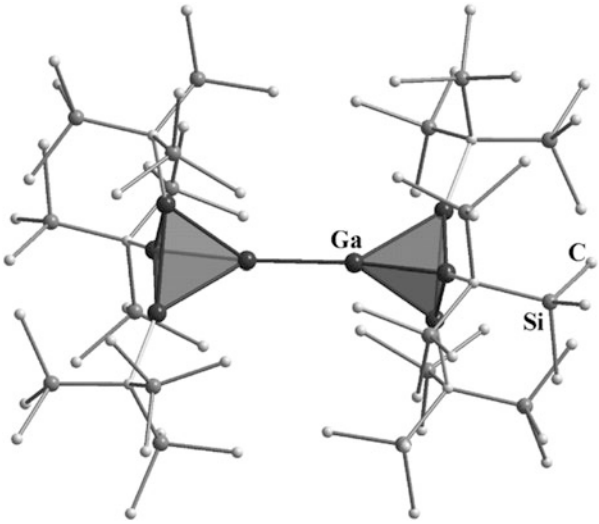

Fig. 13 Molecular structure of $[Ga_8R_6]$ **12** ($R=C(SiMe_3)_3$) without hydrogen atoms; the central Ga_8 is emphasized via a polyhedral presentation

theoretical calculations as lying between that of a classical 2e2c bond and a 2e3c bond [99].

The Ga_8R_6 cluster thus represents the first model compound for a metal atom contact [100] in the form of a nano-metal wire, whereby the Ga–Ga distance in the Ga_2 unit is with 261 pm comparable to the Ga–Ga distance in the Ga_n wire within δ-gallium (Ga–Ga 260 pm) (such a metal atom wire was lately extended by the synthesis of L*ZnZnZnL* (L*=N(Ar*)(Si*i*Pr$_3$) (Ar* = 2,6-(CHPh$_2$)$_2$-4-Me-C$_6$H$_2$) exhibiting a central linear Zn_3 unit with direct Zn-Zn bonds, shielded by the extremely bulky L* ligand. However, in the case of the Zn_3 compound, only the central Zn atom exhibits metal–metal bonds only [101, 102]). In comparison to aluminum chemistry, **12** might be also called the "answer" of the element Ga to the Al_7R_6 cluster **4** which is the smallest metalloid cluster of the element Al. In the latter cluster, only one metal atom connects two tetrahedral moieties, while in the Ga_8R_6 cluster **12**, analogous to the structure of α-Ga, a Ga_2 moiety is the connecting unit.

The metalloid cluster anion $Ga_{12}[C_{13}H_9]_{10}^{2-}$ **13** is obtained from a reaction of a metastable Ga(I)Br solution with fluorenyllithium ($LiC_{13}H_9$) and exhibits an icosahedral structure that is elongated in the direction of the naked gallium atoms (Fig. 14) [103, 104]. Hence, within the Ga_5 rings, relatively short Ga–Ga distances around 259 pm are present, while the average distance between the Ga_5 rings is 268 pm, significantly longer and comparable to the Ga–Ga distances to the naked gallium atoms of 265 pm. The distance between these two "naked" Ga atoms amounts to 527 pm. At first glance, **13** is reminiscent of a classical icosahedral species, e.g., $B_{12}H_{12}^{2-}$, for which bonding follows Wade's rules.

However, a closer look reveals that the icosahedral *closo* structure observed for **13** does not follow Wade's rules, as $2n+4$ skeletal electrons would predict a *nido* structure. Indeed, DFT calculations for the model compound $Ga_{12}(CH_3)_{10}^{2-}$ confirm that Wade's rules are not a suitable model to describe bonding for **13** [103, 104]. Conversely, the following interpretation seems to be more adequate: after removal of two R^- substituents, a hypothetical $Ga_{12}R_8$ species containing the same oxidation number as for the Ga atoms in **13** is formed. Such $M_{12}R_8$ species are indeed known for In [105, 106] and Al [60] (cf. Sect. 4.1.1), in which the metal

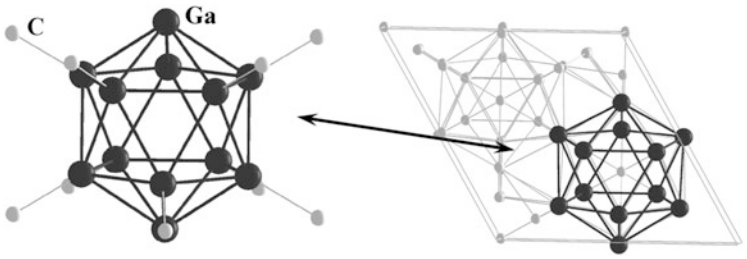

Fig. 14 Molecular structure of $[Ga_{12}(C_{13}H_9)_{10}]^{2-}$ **13** (of the fluorenyl ligands, only the C atom directly bound to the Ga atoms are shown for the sake of clarity) and highlighted substructure in δ-gallium

atom core corresponds – although slightly distorted – to the closest packing of the metals. In case of gallium, via the addition of two R^- ligands, a different structure is realized, which corresponds to the topology of δ-gallium (Fig. 14).

4.2.2 Average-Sized Metalloid Gallium Clusters: Ga_{18}- to Ga_{22} Clusters

Starting from metastable Ga(I) bromide solutions, the reaction with an equimolar amount of $NaSitBu_3$ dissolved in thf gives the gallium cluster compounds $[Ga_{18}(SitBu_3)_8]$ **14** and $[Ga_{22}(SitBu_3)_8]$ **15c** in different relative amounts, together with the by-product $tBu_3Si\text{-}SitBu_3$ depending on the reaction conditions [84]. This might formally be described by the following reaction equation:

$$18\,GaBr + 18\,NaR \rightarrow [Ga_{18}R_8] + 18\,NaBr + 5(R)_2$$
$$22\,GaBr + 22\,NaR \rightarrow [Ga_{22}R_8] + 22\,NaBr + 7\,(R)_2$$

The fact that two different clusters are obtained exhibiting the same number and kind of ligands gives the opportunity to enlighten ordering principles in this complicated area of metalloid cluster compounds. The structures of the clusters are significantly different as shown in Fig. 15. While the Ga_{18} cluster possesses a ladderlike structure of three Ga_6 layers, the Ga_{22} cluster exhibits a Ga-centered

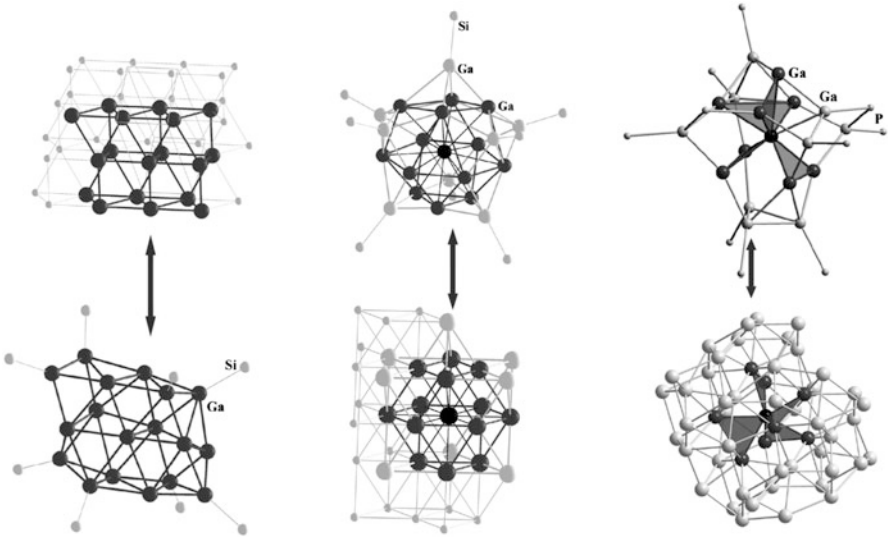

Fig. 15 The topological correlation of the Ga atom in the clusters **15c**, **14**, and **16** and the different Ga modifications. Of the ligands, only the directly bound atom is shown for the sake of clarity. *Left*, $Ga_{18}[Si(tBu)_3]_8$ **14**: cluster (*bottom*) and the low-temperature β-Ga modification (*top*). Middle $Ga_{22}[Si(tBu)_3]_8$ **15c**: cluster (*top*) and the high-pressure Ga(III) modification (*bottom*). *Right*, $Ga_{18}(PtBu_2)_{10}$ **16**: cluster (*top*) and the high-pressure Ga(II) modification (*bottom*)

structure with a central gallium atom with the high coordination number of 13, leading to long average Ga–Ga distances of 294 pm. Such high coordination numbers are observed for gallium only in the high-pressure modifications Ga(II), Ga(III), and Ga(IV), and the arrangement of the gallium atoms in **15c** resembles those found in Ga(III). Beside this, the ladderlike arrangement of the gallium atoms in **14** resembles the arrangement found in the normal-pressure modification β-Ga (Fig. 15).

Hereby the following question arises: Can we explain this different behavior or, in other words, can we identify the driving force for the resemblance to one or the other solid-state structure?

In the case of the Ga_{18} and the Ga_{22} cluster **14** and **15c**, there is the same number of $GaSitBu_3$ units surrounding the naked gallium atoms. Hence in the case of **14** and **15c**, the same "box" of eight $GaSitBu_3$ ligands surrounds 10 and 14 naked Ga atoms, respectively (the distance between adjacent Si atoms of the ligands is in both cases ca. 7.7 Å). Consequently, putting more atoms into a similar box leads to a higher density, and as a result, the 14 atoms arrange like in the high-pressure modification Ga(III), while the 10 atoms arrange as seen within the normal-pressure modification β-gallium.

This explanation based on structural arguments only was further corroborated by DFT calculations demonstrating that the experimentally determined increase in density of 5% from β-Ga to Ga(III) is indeed identical to that of the Ga atoms of $[Ga_{18}(SitBu_3)_8]$ **14** and $[Ga_{22}(SitBu_3)_8]$ **15c** [84]. This first example shows that a comparison of similar clusters is a suitable way to get an idea about ordering principles. Thus, further comparison of the $Ga_{18}(SitBu_3)_8$ compound **14** to another Ga_{18} cluster shielded by 10 $PtBu_2$ ligands: $[Ga_{18}(PtBu_2)_{10}]^{3-}$ **16** [85] is reasonable. However, in this case, the clusters have the same number of gallium atoms, while the ligands show only little similarities. Furthermore, the $PtBu_2$ ligands form a special shell via additional P-donor bonds; thus, the central Ga_n feels a compression by the outer shell, due to the bridging character of the $PtBu_2$ ligands [107–110] (a similar situation is observed within a metalloid germanium cluster cf. Sect. 5.3).

Therefore, for the $Ga_{18}(PtBu)_{10}^{3-}$ cluster **16**, a high density could be expected, and thus a resemblance to a high-pressure modification might be expected and is indeed observed. Hence, the arrangement of the 18 gallium atoms in the cluster core resembles that found in the high-pressure modification Ga(II) as exemplified in Fig. 15. These results nicely show that characteristics of the element itself are already realized within metalloid clusters corroborating their intermedial character between molecules and the solid state.

A metalloid cluster that is localized between the neutral Ga_{18} and Ga_{22} clusters is the anionic metalloid cluster $\{Ga_{19}[C(SiMe_3)_3]_6\}^-$ **17**, where the arrangement of the gallium atoms resembles that of the high-pressure modification Ga(III) [86]. The 19 Ga atoms are thereby arranged within three sandwiched Ga_6 rings with the central planar ring containing the central Ga atom (Fig. 16). The upper and lower Ga_6 rings are folded and contain three ligand-bearing Ga atoms each. The distances from the central Ga atom to the "naked" six Ga atoms in the central planar ring amount to 274 pm, whereas longer distances of 295 pm to the three upper and

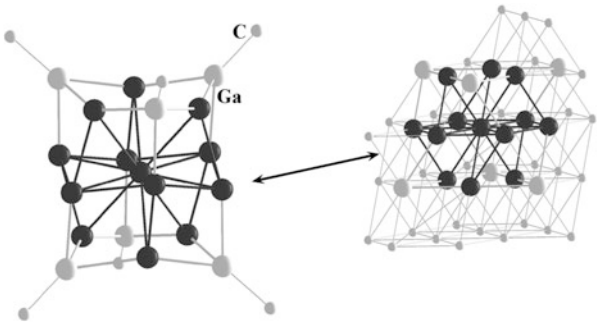

Fig. 16 Molecular structure of $[Ga_{19}(CSiMe_3)_6]^-$ **17** without $SiMe_3$ groups and highlighted substructure in Ga(III)

three lower Ga atoms are observed, completing the geometry of the distorted anticuboctahedron of "naked" Ga atoms. Consequently, **17** is the first centered metalloid gallium cluster, where the central gallium atom exhibits the coordination number 12, as in a "real" metal (very recently a second metalloid triel cluster of a similar composition: $In_{19}R_6$ (R=B(NDippCH)$_2$; Dipp = 2,6-*i*Pr$_2$-C$_6$H$_3$) could be obtained, where the central indium atom also exhibits the coordination number 12, whereby now the 12 indium atoms form a coboctahedron being thus an ideal cutout of a fcc lattice: [111]). **17** also shows two other remarkable characteristics: (1) **17** is the only metalloid cluster from which it has been possible to measure a ^{69}Ga-NMR spectrum in solution (−134 ppm) [86] and (2) is the largest metalloid cluster for which ESI mass spectra have been obtained [112, 113]. The gas-phase investigations of the structurally characterized metalloid gallium cluster **17** indicate that the naked Ga_n cluster core is stabilized by $GaC(SiMe_3)_3$ ligands and not by $C(SiMe_3)_3$ ligands. The dissociation of $\{Ga_{19}[C(SiMe_3)_3]_6\}^-$ **17** via collision-induced dissociation experiments thereby leads, after the elimination of six $GaC(SiMe_3)_3$ groups, to the remarkably stable Ga_{13}^- anion. The extraordinary stability of the electronically closed-shell anion Ga_{13}^- with respect to the jellium model [114–116] is obvious from the large value of the electron affinity of 3.3 eV of the neutral Ga_{13} cluster, which for comparison is close the value of 3.45 eV of the fluorine atom.

Refocusing on the clusters exhibiting 22 gallium atoms, a large structural variety is obvious as to date three different arrangements are known as shown in Fig. 17. Thereby, the neutral metalloid clusters $Ga_{22}R_8$ (R=Si(SiMe$_3$)$_3$ **15a** [87, 88], Ge(SiMe$_3$)$_3$ **15b** [89], and Si*t*Bu$_3$ **15c** [84]) and the anionic one $Ga_{22}R_{10}^{2-}$ **18** (R=N(SiMe$_3$)$_2$) [90, 91] exhibit a central gallium atom with a high coordination number (13 for **15a** – **15c** and 11 for **18**). Additionally in both cluster types, the average Ga–Ga distance shrinks from the center to the exterior indicating that the bonding becomes more localized (more molecular) from the center to the outer shell. The structural differences between both clusters might be ascribed to the presence of a different number of ligand-bearing gallium atoms.

In contrast to **15a**, **15b**, **15c**, and **18**, there are Ga_{22} clusters that exhibit an icosahedral Ga_{12} core without a central gallium atom $[Ga_{22}Br_2\{N(SiMe_3)_2\}_{10}Br_{10}]^{2-}$ **19** and $[Ga_{22}Br\{N(SiMe_3)_2\}_{10}Br_{10}]^{3-}$ **20** [92]. Each of these two Ga_{22} cluster

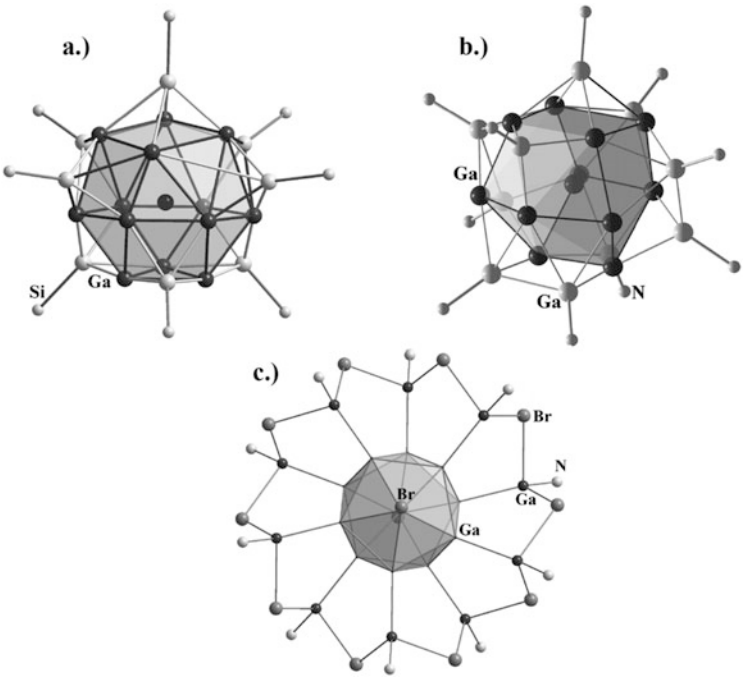

Fig. 17 Three different arrangements of 22 Ga atoms in the cluster species (**a–c**) without $SiMe_3$ or *t*Bu groups: (**a**) $Ga_{22}R_8$ (R=Si(SiMe$_3$)$_3$ **15a**, Ge(SiMe$_3$)$_3$ **15b**, Si*t*Bu$_3$ **15c**); the central Ga atom has a coordination number 13, and the coordination polyhedron is shown via a polyhedral presentation. (**b**) $\{Ga_{22}[N(SiMe_3)_2]_{10}\}^{2-}$ **18**; the central Ga atom has a coordination number of 11. (**c**) $\{Ga_{22}[N(SiMe_3)_2]_{10}Br_{12}\}^{2-}$ **19** (projection along the *top* and *bottom* Ga atoms); the central empty Ga_{12} polyhedron is shown via a polyhedral presentation

anions has an icosahedrally shaped Ga_{12} core, which is directly connected via short (240 pm) 2c2e bonds to ten further Ga atoms. The terminal gallium atoms in **19** are further bound to $N(SiMe_3)_2$ ligands and bridged through ten Br atoms. The difference between **19** and **20** is that in the case of **20**, only one of the remaining gallium atoms of the Ga_{12} icosahedra is bound to a terminal Br atom, while in the case of **19**, both gallium atoms are bound to a bromine atom, leading to a more symmetric arrangement. The average Ga–Ga distance in the central Ga_{12} icosahedra in **19** and **20** is 260 pm and thus comparable to the average Ga–Ga distance found in the icosahedral metalloid cluster $Ga_{12}[C_{13}H_8]_{10}^{2-}$ **13**, so in both cases, an arrangement similar to δ-Ga is obvious. However, in **19** and **20**, shorter Ga–Ga distances with respect to those in δ-Ga (282 pm) are observed, which is due to the more molecular (more localized) bonding in the clusters. Additionally, the structure of **19** and **20** is quite similar to that found in the binary halide $[Al_{22}X_{20}]$ (**9** and **10**), and thus **19** and **20** might be derivatives formed from a hypothetical halide precursor $[Ga_{22}Br_{20}]$, which might be present in solution. The compound that comes closest to $Al_{22}Br_{20}$·12thf **10** is $Ga_{24}Br_{22}$·10thf **21**, which is obtained from a donor-poor

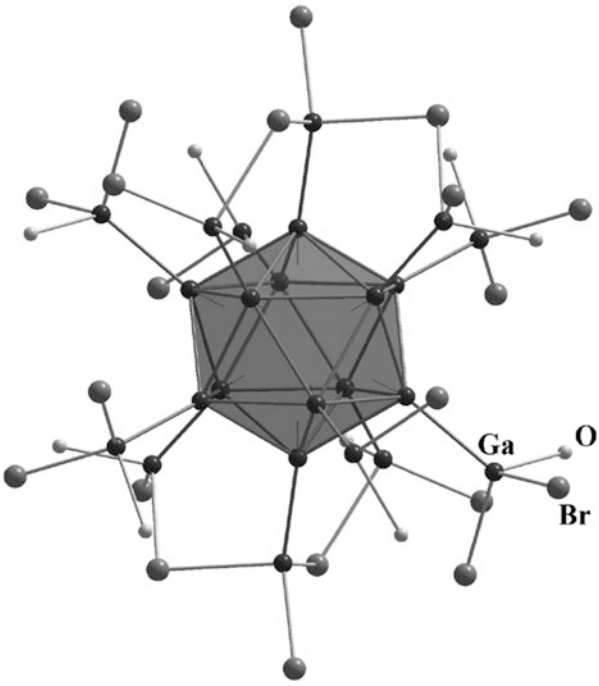

Fig. 18 Molecular structure of $Ga_{24}Br_{22}{\cdot}10thf$ **21** (from the thf molecules, only the oxygen atoms directly bound to the gallium atom are shown)

GaBr solution (toluene/thf), which is slowly warmed from −78°C to room temperature over several days [93, 94]. During the synthesis, the thf concentration has to be kept low so that the equilibrium **1** is driven from the hypothetical $Ga_{10}Br_{10}{\cdot}10thf$ toward $Ga_{24}Br_{22}{\cdot}10thf$ **21**.

$$2Ga_{10}Br_{10} \cdot 10thf + 5GaBr \rightarrow Ga_{24}Br_{22} \cdot 10thf(\mathbf{21}) + GaBr_3 + 14thf \quad (1)$$

In **21**, the Ga–Ga distances in the central Ga_{12} icosahedra vary between 255 and 267 pm, similar to all other clusters exhibiting an icosahedral Ga_{12} core. However, in contrast to **19**, **20**, and **13**, all gallium atoms of the central Ga_{12} core are bound via short (240 pm) 2c2e bonds to external gallium atoms (Fig. 18).

However, compared to the central Ga_{12}-icosahedron, the external Ga_{12}-icosahedron is strongly distorted due to the varied substitution of the Ga atoms: two para-positioned Ga atoms are bound to three Br atoms, one terminal, and the other two shared with neighboring gallium atoms. All other external Ga atoms bind to two bromine and the oxygen atom from the thf molecule. Quantum chemical calculations give an atomic volume for the Ga_{24} core that is 3% lower than the one calculated for the Al atoms in the $Al_{22}X_{20}$ cluster **9** and **10**. As the atomic radius of Ga is also smaller than the one of Al, the icosahedral structure in **21** might also be seen as a structural approach to an α-boron-type structure of gallium.

Before we will come to the largest metalloid gallium cluster characterized so far, we will shortly introduce the anionic metalloid Ga_{26} cluster $\{Ga_{26}[Si(SiMe_3)_3]_8\}^{2-}$

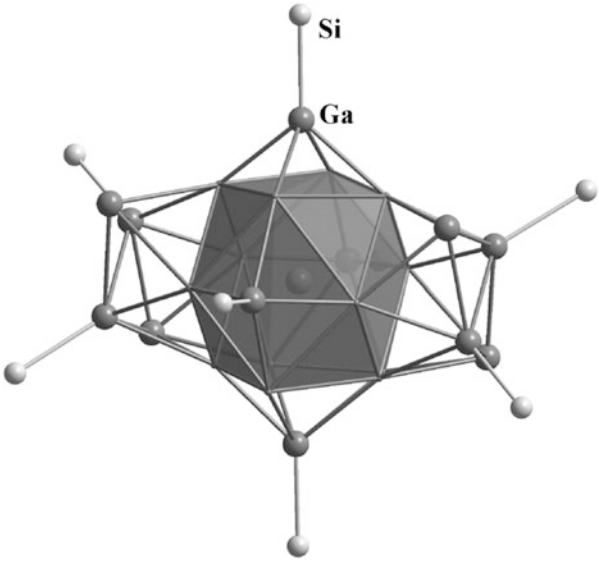

Fig. 19 Molecular structure of $[Ga_{26}R_8]^{2-}$ **22** (R=Si(SiMe$_3$)$_3$); SiMe$_3$ groups are omitted for clarity. The distorted Ga_{13} "13-vertex polyhedron" is emphasized via a polyhedral presentation

22 which is obtained from a metathesis reaction of the supersonically produced "GaI" [117] with LiSi(SiMe$_3$)$_3$ [95, 96]. The molecular structure as shown in Fig. 19 might be described as follows: a central gallium atom is surrounded by 13 gallium atoms leading to a distorted Ga_{13} "13-vertex polyhedron" exhibiting two pentagonal, four tetragonal, and eight trigonal faces. The two pentagonal and two of the tetragonal faces are capped by a GaR unit with average Ga–Ga distances of 260–272 pm, while the remaining two tetragonal faces are bound to Ga_4R_2 units each. Hence, the surrounding at the central gallium atom is again reminiscent to the high-pressure modification Ga(III) with its distorted cuboctahedral 8–4 coordination. It should be noted that also a Wade-like bonding discussion has been presented for **22** [118].

4.2.3 Large Metalloid Gallium Clusters: $\{Ga_{84}[N(SiMe_3)_2]_{20}\}^{x-}$ ($X = 3,4$)

When a metastable GaBr solution (toluene/thf) is reacted with LiN(SiMe$_3$)$_2$ and the reaction mixture is afterward heated to 50–60°C for a couple of hours, the Ga_{84} cluster $\{Ga_{84}[N(SiMe_3)_2]_{20}\}^{4-}$ **23** [119, 120] is obtained in form of black crystals, which exhibit a metallic luster. The molecular structure of **23** is illustrated in Fig. 20 in a similar fashion to that of the multishell aluminum cluster $\{Al_{77}[N(SiMe_3)_2]_{20}\}^{2-}$ **8**. Briefly, in the center of **23** a Ga_2 unit is present – a unique situation in the whole field of metal cluster chemistry – exhibiting a short Ga–Ga distance of 233.5 pm. This distance is nearly as short as the so-called Ga–Ga triple bond of 232 pm in $Ga_2R_2^{2-}$ [R=(2,4,6-*i*Pr$_3$C$_6$H$_2$)$_2$C$_6$H$_3$] [121]. However, the Ga–Ga distance in the typical Ga_2 moiety of α-gallium is 244.8 pm,

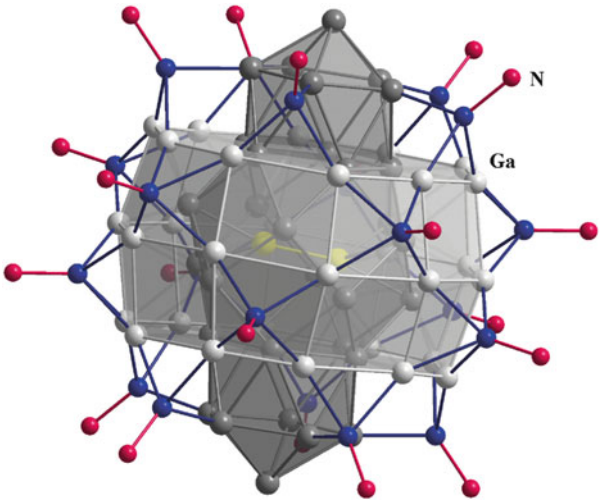

Fig. 20 Molecular structure of $[Ga_{84}R_{20}]^{4-}$ **23** (R=N(SiMe$_3$)$_2$; only the N atoms (*red*) directly bound to the Ga atoms are shown). There are 2 (*yellow*) + 32 (*dark gray*) + 30 (*light gray*) = 64 "naked" and 20 ligand-bearing (*blue*) gallium atoms

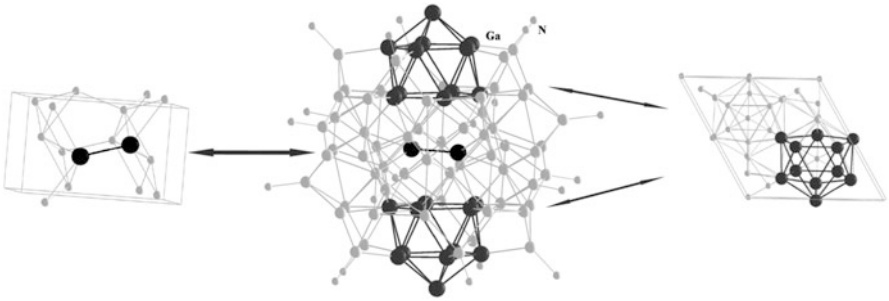

Fig. 21 The topological correlation between the Ga atoms in $Ga_{84}[N(SiMe_3)_2]_{20}^{4-}$ **23**: cluster (*middle*) and the room temperature modification α-gallium (*left*) and the low-temperature modification δ-gallium (*right*)

as a consequence of the higher coordination number (7 instead of 5 in **23**). That means, for the first time the central Ga_2 unit in **23** represents a small but typical section of the thermodynamically stable α-allotrope (Fig. 21).

The Ga_2 unit is surrounded by a Ga_{32} shell in the form of a football with icosahedral caps. The icosahedral caps thereby resemble the structure of δ-gallium or of the clusters $[Ga_{22}R_{10}X_{11/12}$ **19**, **20**]. The apex and base atoms of the Ga_{32} unit are naked and are oriented toward each other in the crystal in an unusual fashion, leading to special physical properties as discussed below. The Ga_2Ga_{32} unit is surrounded by a meandering belt of 30 Ga atoms that are also naked. Finally, the entire Ga_{64} framework is protected by 20 GaR groups (R=N(SiMe$_3$)$_2$).

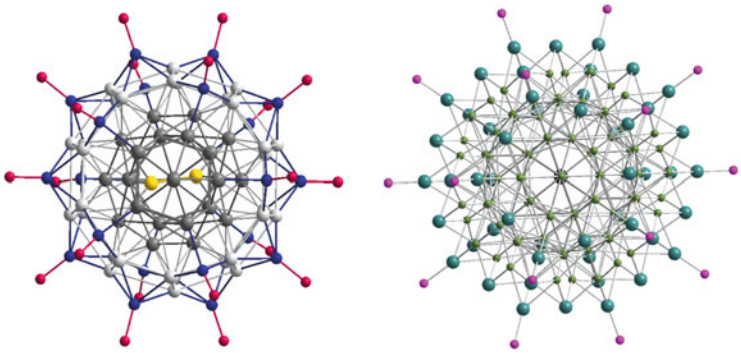

Fig. 22 Projection of the metalloid Ga_{84} cluster **23** (*left*) and $PtPd_{164}(CO)_{72}(PPh_3)_{20}$ (*right*), to show their similar arrangement of metal atoms with respect to the fivefold axis. In both clusters, 20 Ga–N and 20 Pd–P units represent the outer sphere. In $PtPd_{164}(CO)_{72}(PPh_3)_{20}$, however, there are 72 additional CO to connect the different cluster shells: $(Pt/Pd_{12}/Pd_{30}/Pd_{12}/(CO)_{12}/Pd_{60}/Pd_{30}/Pd_{20}/[P(Ph_3)_{20}]$

Hence, in the case of **23** for the first time, a structure is observed, where an arrangement similar to two different solid-state structures (α- and δ-gallium) is realized within one cluster, showing the high structural diversity and flexibility of elemental gallium (Fig. 21).

Thereby, the arrangement of **23** seems to be quite favorable as the compound can be obtained in nearly quantitative yield, leading after crystallization to a nearly colorless solution. The high *pseudo*symmetry of **23** is clearly shown in Fig. 22, where a nearly fivefold symmetry as found in quasicrystals is obvious only violated by the central Ga_2 unit. Besides crystals containing only $Ga_{84}R_{20}^{4-}$ **23** species, another oxidation state of the Ga_{84} unit could be observed in a crystalline compound, where now $Ga_{84}R_{20}^{3-}$ cluster species **23a** are present, exhibiting a slightly different arrangement in the ionic lattice [122].

With respect to the number of "naked" nonligand-bearing metal atoms, the Ga_{84} cluster **23** is the largest cluster of this type, which has been structurally characterized. With its 64 naked Ga atoms, it is even larger than the $PtPd_{164}$ cluster [123], as well as an Au_{102} [25] or Au_{133} [47] cluster**.** In the Au_{133} cluster, only 55 "naked" Au atoms build up the cluster core, and there are only 43 "naked" metal atoms in the $Pt@Pd_{42}$-core of the $PtPd_{164}$ cluster. Therefore, in both cases of metalloid clusters of precious metals, the ligands not only form a protecting shell for the cluster core but also act as the glue between the inner and outer Pd and Au shells of these metalloid cluster compounds.

Though there are obvious structural similarities between these clusters, e.g., fivefold symmetry and the similar arrangement of the 20 outer ligands (Fig. 22), metalloid clusters of group 13 are incomprehensibly mostly ignored during discussion of metalloid clusters of precious metals. However, the Ga_{84} cluster units show several special structural peculiarities, also in comparison to many other metalloid clusters:

1. In the cluster center, a Ga_2 dumbbell with a very short Ga–Ga distance of 234 pm is present.
2. The 42 (84/2) crystallographically different Ga atoms (the cluster is centrosymmetric) are, in principle, also chemically different; i.e., this cluster represents a molecule with the highest degree of mixed valency, which is also reflected in a great variety of different ^{71}Ga-NMR shifts [124]. This situation is thereby different with respect to precious metal atom clusters, e.g., $PtPd_{164}$ [123], where the synthesis and the structure indicate that the metal atoms do not change their zero-valent character!

Another distinctive property of the Ga_{84} cluster compound is the fact that crystals containing the Ga_{84}^{4-} units show a metallic luster indicating special physical properties, e.g., electric conductivity. Indeed four-point conductivity measurements on single crystals down to 1.5 K show electric conductivity and below 7 K superconductivity [125]. Magnetic [126], muon spin resonance (μSR) [127] and ^{71}Ga NMR measurements [124, 128] show that the Ga_{84} compound exhibits type II superconductivity. Additionally, the ^{71}Ga NMR measurements show that within the crystal, two different phases are present; a nonconducting (nc) and a conducting phase (c), whereby only the conducting phase becomes superconducting. The difference between the (c) and the (nc) phase can be traced back to an ordered or a non-ordered arrangement of the Ga_{84} clusters within the crystal lattice (Fig. 23). Thereby, toluene molecules, that are localized between different Ga_{84} clusters in the crystal lattice, play a vital role as removal of toluene leads to a loss of the perfect arrangement and thus to a loss of the electrical conductivity (Fig. 23). Hence, the arrangement of the clusters with respect to each other has a strong impact on the physical properties of the bulk crystal. Additionally, the ratio (nc) to (c) inside the crystal strongly influences the upper critical field (B_{c2}) which is necessary to completely suppress the superconducting state. Thereby, B_{c2} changes from 0.25 T to 5 T with constant T_c values for samples, in which the conducting phase amounts to 90% and 10%, respectively, a behavior also known from superconducting alloys and of "dirty" superconductors, for instance, superconducting materials with a certain amount of nonmagnetic impurities [129].

Consequently with respect to elemental gallium, which is a type I superconductor with $T_c = 1.1$ K and a low critical field of $B_c \approx 6 \cdot 10^{-3}$ T, the behavior of the Ga_{84} cluster is extremely different. The findings for the Ga_{84} cluster additionally demonstrate that the orientation of the cluster in the solid state can have a strong impact on the physical properties. This fact only becomes obvious as the Ga_{84} cluster **23** is obtained in a crystalline state, highlighting that crystallization of **23** is the first and most important step to establish a sustainable basis for further investigations.

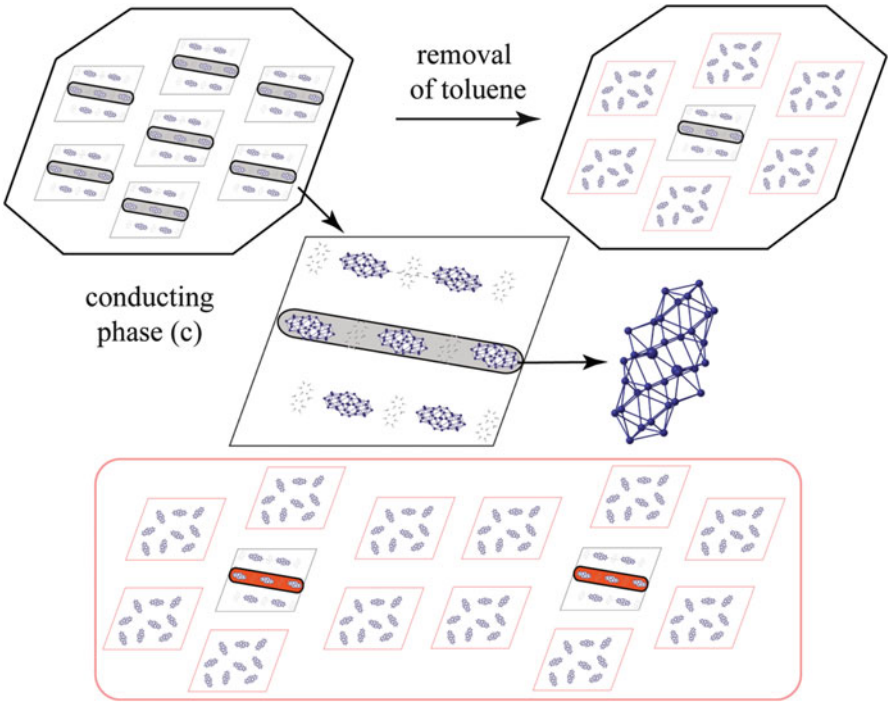

Fig. 23 Schematic presentation of the conducting (c) phase (*gray*) within the crystallites with perfect arrangement of Ga_{84} clusters. Destruction of the perfect order by removal of toluene molecules (*upper part*). Superconductivity via intergrain Josephson coupling between the remaining c-phases of different crystallites (*lower part*, *red surrounding*)

5 Structure and Bonding of Metalloid Clusters of Germanium and Tin and their Interrelation to Solid-State Structures

In the following, the structure and bonding of metalloid clusters of germanium and tin are discussed again with focus on the interrelation to solid-state structures. However, in the case of the tetrel germanium and tin, the number and the size of the clusters are much smaller with respect to the triel aluminum and gallium, and only one example of a multishell cluster $Sn_{15}Ar^*_6$ **51** (Ar*=$NSiMe_3$Dipp; Dipp=2,6-*i*Pr_2-C_6H_3) is known [130, 131]. Therefore, the structure and bonding are more localized within the molecular regime and can be partly described by molecular-based models like Wade's rules [79]. Additionally, there is a strong correlation to the naked Zintl-type clusters, whose structure and bonding also follow Wade's rules [132–134], and recently it has been shown that metalloid clusters can indeed be synthesized from Zintl anions by attaching ligands to the tetrel core [135]. Nevertheless, already in this size, regime interrelations to

solid-state structures occur. This relationship further underlines the intermediate character of metalloid clusters, rendering them to essential model compounds for the area between molecules and the solid state of metals or semimetals. Herein, in contrast to the procedure for the triel elements aluminum and gallium (cf. Sect. 4), the metalloid clusters of germanium and tin will be discussed together, beginning with the smallest Ge_5Ar_4 cluster **24** (Ar = 2,6-Mes_2-C_6H_3; Mes = 2,4,6-Me_3-C_6H_2) and ending with the largest structurally characterized metalloid tetrel cluster $Sn_{17}[Ga(ddp)]_6$ **52** (ddp=$HC(CMeNDipp)_2$; Dipp = 2,6-*i*Pr_2-C_6H_3) [150, 136].

5.1 Small Clusters with Less than Ten Tetrel Atoms

5.1.1 Metalloid E_5R_4 Clusters

The smallest metalloid germanium cluster, Ge_5Ar_4 **24**, exhibits five germanium atoms and is obtained via the reductive coupling of the germylene Ge(Cl)Ar in the presence of $GeCl_2$·dioxane with potassium graphite (Eq. 2) [137]. **24** exhibits only one naked germanium atom, and its structure is best described as a butterfly arrangement of a $(GeR)_4$ moiety, with a fold angle of 134° which is capped by a naked germanium atom, leading to two short Ge–Ge distances of 246 pm and two long Ge–Ge distances of 303 pm.

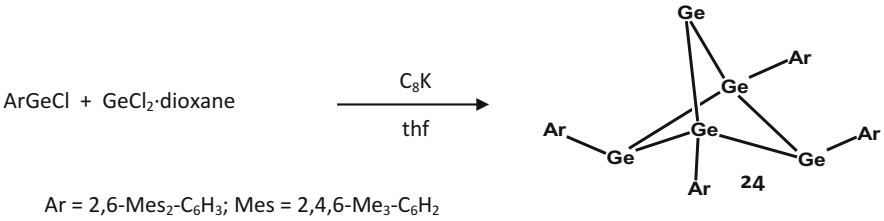

(2)

The bonding inside **24** can be described as follows: the naked germanium atom forms two 2c2e bonds bearing a lone pair of electrons. The two four-coordinated germanium atoms exhibit a classical bonding, and the three-coordinated germanium atoms form three 2c2e bonds and have additional electron density at one vertex. This description, further supported by quantum chemical calculations on the model compound Ge_5Me_4, leads to the formulation of three resonance forms A, B, and C (Scheme 6). The zwitterionic forms A and C represent a classical bonding situation having only paired electrons, while form B represents a singlet biradicaloid form, showing that **24** might be a member of this new and growing class of the main group of compounds [138–140]. Such a biradicaloid bonding situation is frequently observed in the case of metalloid germanium clusters to be seen in the following.

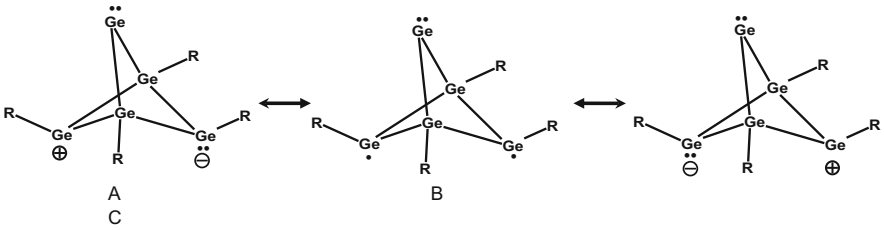

Scheme 6 Possible resonance forms for the presentation of the bonding situation in Ge_5Ar_4 **24** (Ar = 2,6-Mes_2-C_6H_3; Mes = 2,4,6-Me_3-C_6H_{22})

Another possible arrangement for a metalloid E_5R_4 species is realized in silicon chemistry where the reductive coupling of R_3Si-$SiBr_2Cl$ with C_8K in thf gives the spiro compound $Si_5(SiR_3)_4$ **25** (R=*t*$BuMe_2Si$) in 3.5% yield along with the cyclotrisilene $Si_3R_3SiR_3$, which is the main product of the reaction (Eq. 3).

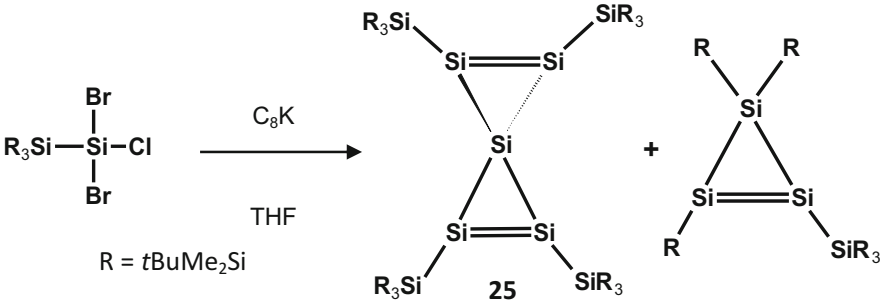

(3)

In the case of silicon, the biradicaloid bonding is avoided, leading to a compound that exhibits two short Si–Si double bonds of 218.6 pm and longer Si–Si single bonds to the spiro silicon atom of 232 pm. However, in **24**, the biradicaloid bonding might also be avoided forming a Ge–Ge bond between the two germanium atoms with coordination number three, as it is observed within the polyhedral cluster compound Ge_4Si*t*$Bu_2(SiMe$*t*$Bu_2)_4$ **26** (Fig. 24) (interestingly, the photolysis of **26** gives the metalloid cluster $Ge_9(Si$*t*$Bu_2)_2(SiMe$*t*$Bu_2)_4$ where, like in the silicon compound **25**, a spiro germanium atom is present and which was described as a tetraradicaloid species [141]). Additionally quite recently, another isomer of a Ge_5R_4 species was found in the so-called pyramidane $Ge_5[SiMe$*t*$Bu_2]_4$ **27**, where now the naked germanium atom is bound to a more planar $Ge_4[SiMe$*t*$Bu_2]_4$ four-membered ring, leading to Ge–Ge bonds from the naked to the ligand-bound germanium atoms of 255 and 277 pm, closer in distance than in **24** [142, 143]. The structural characterization of the metalloid clusters **24** and **27** enlightens the influence of the ligand on the structure and bonding of a cluster compound, due to their similar composition but with different structure. Thereby, it became obvious that the orientation of the ligand plays a vital role [142, 143]. This

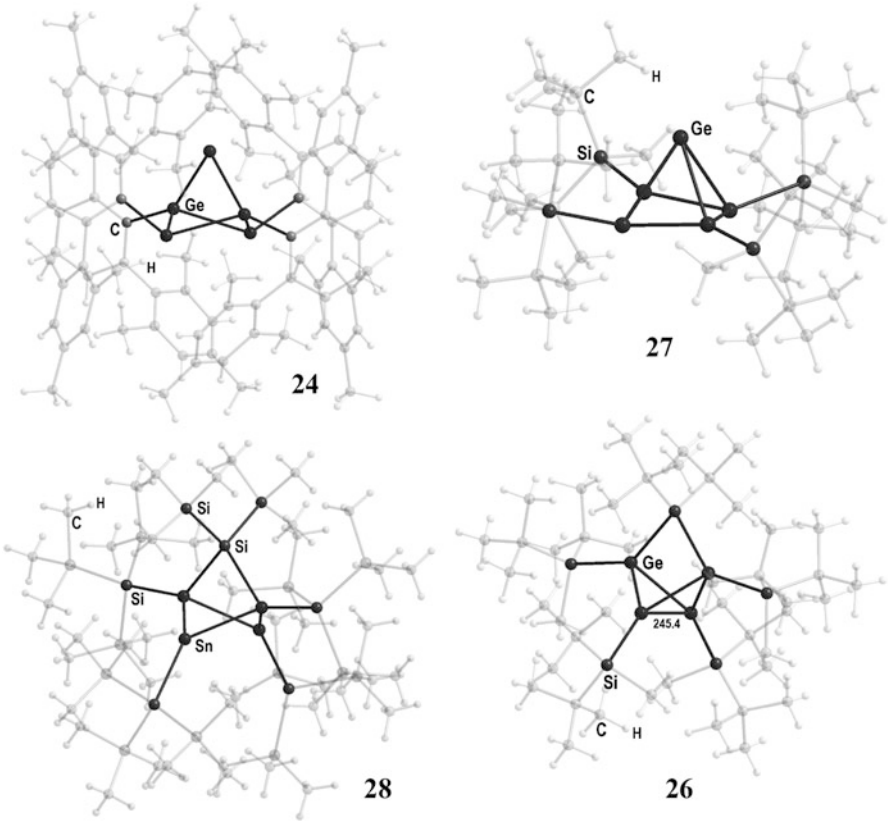

Fig. 24 Molecular structure of Ge_5Ar_4 **24** (Ar = 2,6-Mes_2-C_6H_3; Mes = 2,4,6-Me_3-C_6H_2) (*top left*), $Ge_5(SiMe\mathit{t}Bu_2)_4$ **27** (*top right*), $Sn_4Si(SiMe_3)_2[Si(SiMe_3)_3]_4$ **28** (*bottom left*), and $Ge_4Si\mathit{t}Bu_2(SiMe\mathit{t}Bu_2)_4$ **26** (*bottom right*). From the ligands, only the directly bound atom is shown solid, while the rest is shown transparent for clarity

aspect was addressed in detail during the discussion of the structurally similar tin cluster compound $Sn_4Si(SiMe_3)_2[Si(SiMe_3)_3]_4$ **28** (Fig. 24) [144, 145].

In case of **28**, the polyhedral arrangement of the four tin and the silicon atom is similar to the one found for the five germanium atoms in the metalloid germanium cluster compounds **24** and **27**. The most interesting aspect of these clusters to compare is the bonding of the tetrel atoms with coordination number 3. This focus is warranted because the arrangement of the ligand at these atoms differs significantly (Fig. 24); i.e., the geometry of the three-coordinated atoms is best described as nearly planar for **28** (sum of bonding angles, 350°), while it is pyramidal in the case of **24** (sum of bonding angles, 309°). The change in orientation is thereby induced by the steric bulk of the $Si(SiMe_3)_3$ ligands as the capping silicon atom in **28** also involves bulky $SiMe_3$ groups. The geometric arrangement of the ligands has a strong influence on the bonding within the cluster core as it was

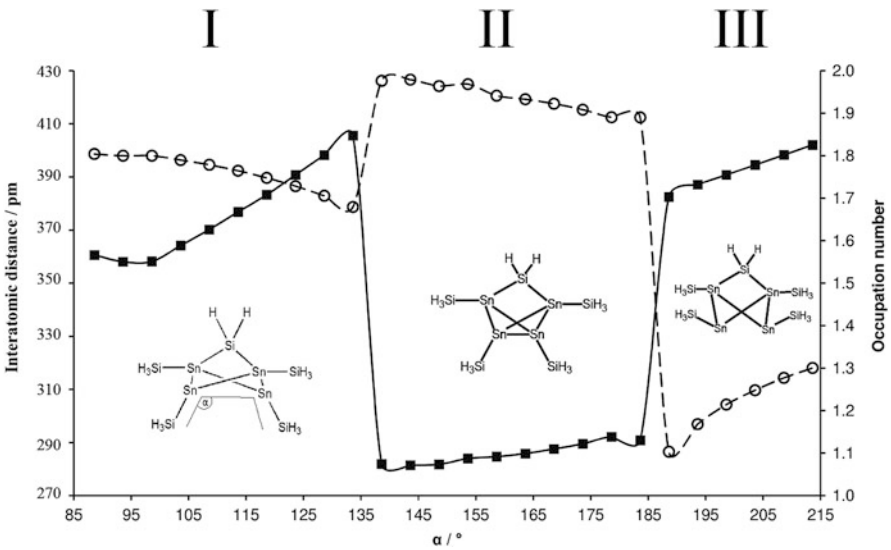

Fig. 25 Angular dependence of the tin–tin bond distance between Sn1 and Sn2 in **28H** (*filled square*) and the occupation number n_1 obtained from the CASSCF calculation of the singlet state (*open circle*); the structure of **28H** in the different regions I (singlet biradicaloid), II (classical bonding), and III (biradical bonding) is also shown

shown by quantum chemical CASSCF (*complete active space self-consistent field*) calculations on the model compound $Sn_4(SiH_3)_4SiH_2$ **28H** (Fig. 25).

As seen in Fig. 25, the bonding between the two Sn atoms with coordination number 3 changes from singlet biradicaloid (I) via a classical bound system (II) to a biradical system (III) by changing the angle α from 85 to 215° – α describes the orientation of the ligand with respect to the Sn–Sn vector. The results of the CASSCF calculations thus clearly show that the orientation of the ligand directly affects the bonding between the two tin atoms with coordination number 3. The transition between the different bonding areas (I–III) is thereby quite abrupt, i.e., small changes in α lead to a drastic change in bonding and thus in chemical behavior. This unexpected result is of general interest for various applications such as catalytic processes, involving unsaturated or cluster compounds [146].

5.1.2 Metalloid E_xR_2: Clusters ($x = 6, 7$)

The metalloid cluster compound $Ge_6Ar^*_2$ **29** as well as the mixed congener $Ge_2Sn_4Ar^*_2$ **29a** (Ar^*=C_6H_3-2,6-$Dipp_2$; Dipp=C_6H_3-2,6-iPr_2) are both synthesized via the same reaction strategy, i.e., reductive coupling of Ar*GeCl by C_8K in the presence of $GeCl_2$ or $SnCl_2$, respectively [49, 50]. Hence, the E(II) halides are completely reduced and inserted into the cluster compound as naked atoms. The arrangement of the six tetrel atoms inside both cluster compounds is best described

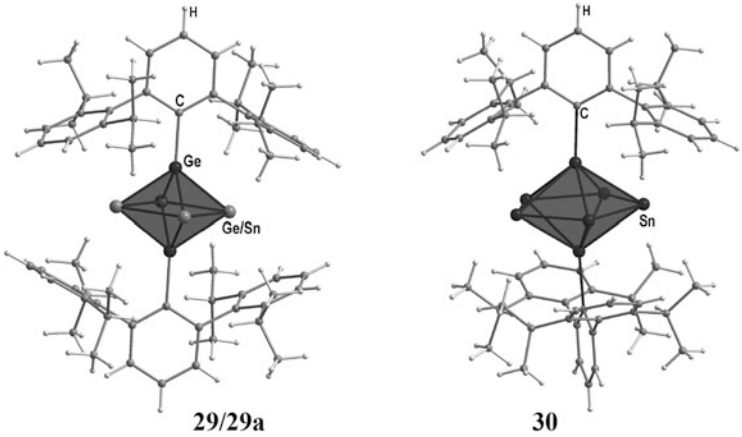

Fig. 26 Molecular structure of Ge_6Ar_2 **29** and $Ge_2Sn_4Ar_2$ **29a** (*left*) and $Sn_7Ar^*_2$ **30a** (Ar*=C_6H_3-2,6-$Dipp_2$; Dipp=C_6H_3-2,6-$i Pr_2$). The central polyhedral arrangement of the six (**29**) and seven (**30**) tetrel atoms is emphasized via a polyhedral presentation

as a flattened octahedron since two different sets of bond lengths are found inside the cluster cores (Fig. 26). In **29**, the average Ge–Ge distance between ligand-bound and naked germanium atoms is with 251 pm significantly shorter than the average Ge–Ge distance of 288 pm between naked germanium atoms. Thus, the germanium atoms with the higher coordination numbers form the shorter Ge–Ge bonds. This relatively unusual behavior can be explained by assuming that the naked germanium atoms bear a lone pair of electrons providing only two electrons for cluster bonding. For the ligand-bound germanium atoms, this lone pair of electrons is split, and one electron is used for a 2c2e bond to a ligand, and the other one is used for cluster bonding. Hence, the ligand-bound germanium atoms provide three electrons for cluster bonding, leading to shorter Ge–Ge bonds. This counting leads to a total of 14 cluster bonding electrons for **29** and **29a**, which is the required number for a *closo*-type cluster compound ($2n + 2 = 14$ for $n = 6$) according to Wade's rules [79].

Consequently, **29** and **29a** fit to Wade's rules as is normally the case for the Zintl ions [132–134]. Additionally, the average Ge–Ge distance in **29** of 263 pm is directly comparable to those calculated for the model Zintl ion Ge_6^{2-} (269 pm) [147]. Another interpretation of the bonding in **29** omits the E–E bonding in the central four-membered ring so that every E atom bears a lone pair forming two 2c2e bond, resembling the bonding of a germylene or stannylene. This description is supported by ^{119}Sn NMR measurements on **29a**, where a signal at $\delta = 1584$ ppm is found [49, 50], a region most commonly associated with two-coordinated Sn (II) species [148]. A slight variance of the tetrel core is observed within the metalloid tin clusters Sn_7R_2 (R=Ar*=C_6H_3-2,6-$Dipp_2$ **30a** [149]; R=GaCl(ddp); ddp=$HC(CMeNDipp)_2$ **30b** [136, 150]; Dipp = 2,6-$i Pr_2$-C_6H_3), which are synthesized via reductive coupling routes, both containing a central pentagonal bipyramidal Sn_7 core (Fig. 26). Thereby, all Sn–Sn distances in the polyhedral Sn_7 cluster

core vary in a narrow range between 295 and 303 pm. As the cluster bonding electrons in **30a** and **30b** amount to 20, both *closo* compounds are again in line with Wade's rules. However, metalloid clusters may not necessarily follow Wade's rules as to be seen in the following section.

5.1.3 E_8R_x Clusters ($x = 8, 6$)

Group 14 cluster compounds of the general formula E_8R_6 are known for all heavier tetrel atoms, except lead; hence, the change of bonding can be analyzed descending group 14 from Si to Sn. The silicon compound $Si_8(SitBu_3)_6$ **31** is synthesized from the fully substituted tetrahedral cluster via oxidation and reduction steps as outlined in Fig. 27 [151, 152]. The molecular structure of **31** (Fig. 27) exhibits two $Si_3(SitBu_3)_3$ triangles in anticonfiguration, with Si–Si bond lengths of 240 pm which are within the normal region for a single bond in polyhedral cluster compounds [153]. Between the two three-membered rings, a Si_2 dumbbell of two naked silicon atoms is localized, featuring a short Si–Si bond of 229 pm. The silicon atoms of the central dumbbell form three additional Si–Si bonds: two Si–Si bonds of 233 pm to two silicon atoms of one Si_3 triangle and one long Si–Si bond of 275 pm to one silicon atom of the opposite Si_3-triangle. The central Si_2 dumbbell is the most

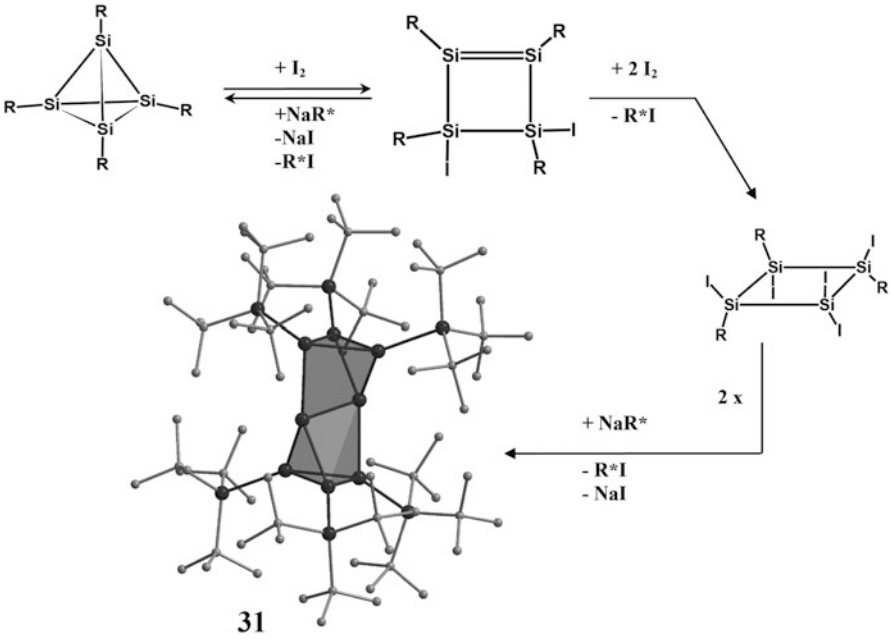

Fig. 27 Reaction pathway from tetrahedrane Si_4R_4 to the metalloid cluster compound Si_8R_6 **31** (R=Si*t*Bu$_3$), whose molecular structure is shown without hydrogen atoms and where the central Si_8 unit is emphasized via a polyhedral presentation

unusual feature in **31**. This rare arrangement leads to the question as to why the central Si_2 unit is not oriented perpendicular to the three-membered Si_3R_3 rings, which would lead to an ideal tetrahedral environment for each silicon atom as it is the case for the carbon compound $C_8(SiMe_3)_6$ [154, 155]. Steric effects are not responsible for this arrangement as in the directly linked tetrahedral structure steric hindrance would even be reduced. Therefore, electronic effects are responsible for the central silicon atoms being inverse tetrahedrally bonded.

E_8R_6 cluster compounds of germanium are synthesized via the synthetic route, using the disproportionation reaction of the Ge(I) halide GeBr. This route yields two germanium cluster compounds of formulae Ge_8R_6 ($Ge_8[N(SiMe_3)_2]_6$ **32** [156, 157] and $Ge_8[C_6H_3\text{-}2,6\text{-}(OtBu)_2]_6$ **33** [158]), whose structures are depicted in Fig. 28. Both structures can be described as a cube-like arrangement of eight germanium atoms, where two germanium atoms are naked, while the remaining six bear ligands. The naked germanium atoms are located on opposite sides of the cube. Hence, the arrangement of the tetrel atoms in the cluster is completely different with respect to the one found in the silicon compound **31**.

The bonding in **32** and **33** might be described by the three resonance forms depicted in Scheme 7, which is similar to the description of the bonding in the smallest metalloid cluster of germanium Ge_5Ar_4 **24** (Sect. 5.1.1). However, in the case of the Ge_8 clusters **32** and **33**, only the charged structure for the anionic part (Ge^-) is favorable. For the cationic part (Ge^+), the arrangement is energetically

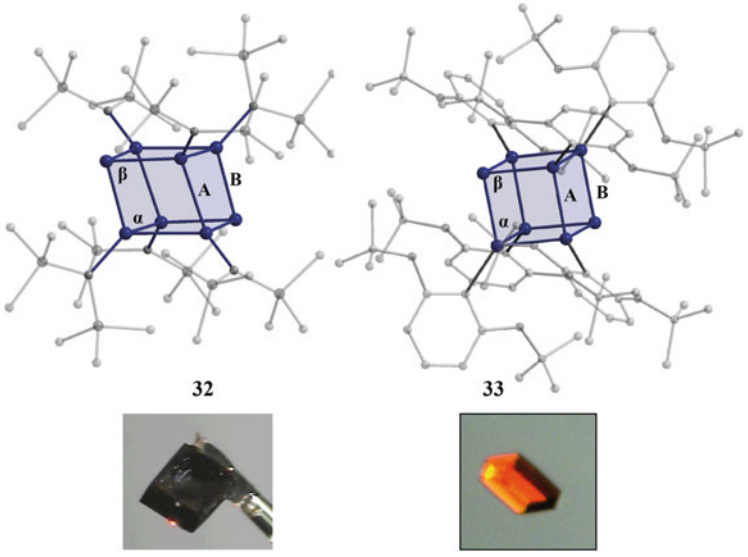

Fig. 28 *Top*, molecular structure of the metalloid cluster compounds $Ge_8[N(SiMe_3)_2]_6$ **32** (*left*) and $Ge_8[C_6H_3(OtBu)_2]_6$ **33** (*right*) without hydrogen atoms. The central Ge_8 core is emphasized by a polyhedral presentation. **32**, $A = 267$ pm, $B = 250$ pm, $\alpha = 101°$, $\beta = 82°$; **33**, $A = 251$ pm, $B = 249$ pm, $\alpha = 92°$, $\beta = 87°$; *bottom*, photo of crystals of the cluster compounds $Ge_8[N(SiMe_3)_2]_6$ **32** (*left*); and $Ge_8[C_6H_3(OtBu)_2]_6$ **33** (*right*)

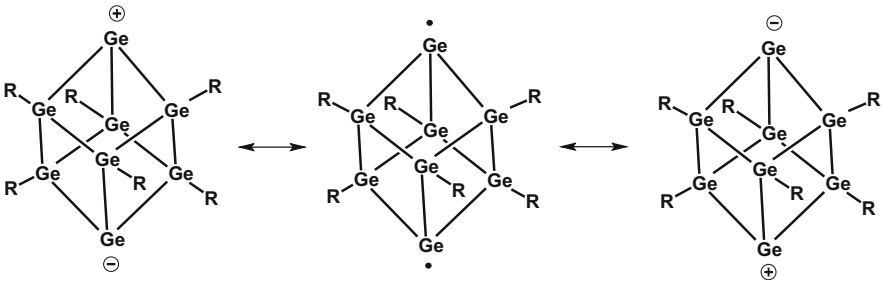

Scheme 7 Possible resonance forms for the presentation of the bonding situation in $Ge_8[N(SiMe_3)_2]_6$ **32** ($R = N(SiMe_3)_2$)

unfavorable as a germyl cation should exhibit a planar structure as it was recently shown for the free germyl cations R_3Ge^+ (R=Si*t*Bu$_3$ [159, 160], R = 2,6-(O*t*Bu)$_2$-C_6H_3 [161]). The triplet biradical form is also ruled out as no *electron paramagnetic resonance* (EPR) signal is observed for **32**, and the singlet state is the ground state according to quantum chemical calculations on the model compound $Ge_8(NH_2)_6$ **32a** [156, 157]. However, it should be noted that the triplet state of **32a** is only 96.5 kJ/mol higher in energy, a value normally calculated for singlet biradicaloids [162].

As both clusters **32** and **33** exhibit the same Ge_8R_6 formula, the influence of the ligand onto the structure and bonding can directly be observed. A closer look onto the arrangement of the germanium atoms shows significant differences: in the case of the aryl-substituted compound **33**, the arrangement is nearly perfectly cubic, i.e., the Ge–Ge distances vary in the small range from 249 pm to 252 pm, and the Ge–Ge–Ge angles inside the cluster amount to $90 \pm 1°$. In contrast to this, the cubic arrangement in **32** is strongly distorted as two different Ge–Ge distances (250 pm (Ge–GeR) and 267 pm (GeR–GeR)) are found inside the cluster core and the Ge–Ge–Ge angles vary from 74° to 102°.

The observed differences are the result of a different bonding inside the cluster core, induced by the different kind of ligands, attached to the cluster core. This finding is corroborated by quantum chemical calculations on model compounds Ge_8R_6 (R=PH_2, NH_2, CH_3, C_6H_5) [158] revealing that a ligand possessing a free pair of electrons on the hetero atom directly bound to the germanium atom leads to a higher degree of delocalization of bonding electrons inside the cluster core. On the other hand, a ligand with no free electron pair at the hetero atom bound to germanium results in more localized bonding electrons inside the cluster core. Consequently, the ligand attached to the cluster core is not only necessary to kinetically stabilize the cluster so that it can be isolated, but it also has an influence on the bonding and the properties of the cluster, e.g., directly seen in the different crystal color of **32** and **33** (Fig. 28).

This finding can also be of importance for nanotechnology where little is known about the influence of ligands (environment) on the physical properties of a group 14 nanoparticle. The results on the metalloid germanium clusters **32** and **33** seem to

be valid for corresponding Sn compounds too, i.e., within the metalloid cluster $Sn_8(Si\mathit{t}Bu_3)_6$ [163], preliminary data on the molecular structure show a nearly undistorted cubic arrangement of the eight Sn atoms inside the cluster core. Hence, again a ligand ($Si\mathit{t}Bu_3$), where the directly bound atom (Si) does not bear a lone pair, leads to an undistorted cubic arrangement. However, the main difference between germanium and tin within a metalloid E_8R_6 cluster is due to quantum chemical calculations that for germanium the neutral compound is energetically favored and for tin the dianionic one [156, 157]. The structure of such a dianionic Sn_8 compound $[Sn_8(Si\mathit{t}Bu_3)_6]^{2-}$ was obtained via single-crystal X-ray structure analysis, showing a nearly undistorted cubic arrangement of eight tin atoms [163].

The discussed results so far show that the nature as well as the orientation of the ligand has a strong influence on the properties of a metalloid cluster compound. However, as to be expected, the number of ligands strongly influences the bonding inside the cluster core as the average oxidation state of the tetrel atoms is changed and additionally localized bonds are formed to the stabilizing ligands. This aspect is addressed by the metalloid Sn_8 cluster Sn_8Ar_4 **34** ($Ar = 2,6\text{-}Mes_2C_6H_3$; $Mes = 2,4,6\text{-}Me_3C_6H_2$) [164, 165] which is synthesized via a reductive coupling reaction of $[(ArSn(\mu\text{-}Cl)]_2$ with potassium and where only four ligands are bound to the Sn_8 core. The structure of **34** (Fig. 29) can be described as a strongly distorted cubic arrangement, since the Sn–Sn distances inside the cluster core vary from 285 to 302 pm.

The distortion of the cubic core leads additionally to Sn–Sn contacts along the diagonal of the four-membered faces (dashed lines in Fig. 29) of 311 pm. Consequently, with respect to the metalloid cluster $Sn_8(Si\mathit{t}Bu_3)_6$, the elimination of two

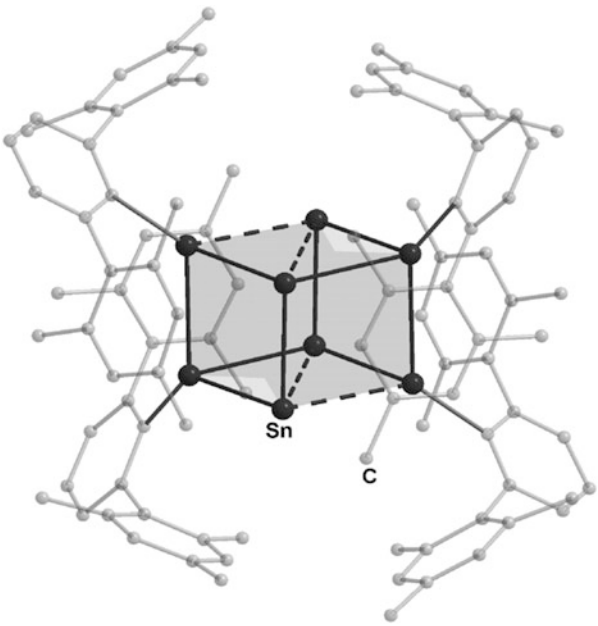

Fig. 29 Molecular structure of Sn_8Ar_4 **34** ($Ar = 2,6\text{-}Mes_2C_6H_3$; $Mes = 2,4,6\text{-}Me_3C_6H_2$); hydrogen atoms are omitted for clarity. The central strongly distorted Sn_8 cube is shown via a polyhedral presentation; all Sn–Sn bonds longer than 300 pm are presented by *dashed lines*

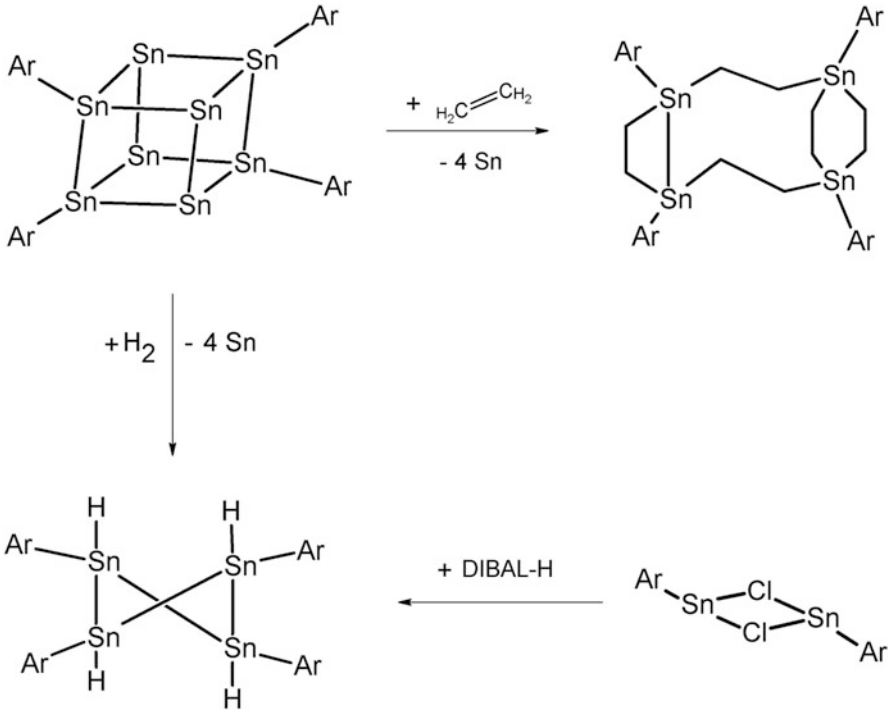

Scheme 8 Reactions of Sn_8Ar_4 **34** with excess ethylene or H_2 and the reaction of $(SnArCl)_2$ with DIBAL-H in a 1:4 ratio (Ar = 2,6-Mes_2-C_6H_4; Mes = 2,4,6-Me_3-C_6H_2)

more ligands leads to a distortion of the cubic arrangement in that way that additional Sn–Sn contacts are formed.

The distortion additionally leads to very different Sn–Sn bonds inside the cluster core. Thus, two naked tin atoms form two long (311 and 302 pm) and two short (285 and 288 pm) Sn–Sn bonds. The other two naked tin atoms form three short Sn–Sn bonds (285, 287 and 289 pm) and one long Sn–Sn contact of 311 pm. The shielding of the Sn_8 core by only four ligands additionally leads to an open cluster core so that **34** can be further reacted with small molecules like H_2 or ethylene, leading to cluster degradation as summarized in Scheme 8 [166, 167].

5.1.4 E_9R_3 Clusters: Radicals and Anions

Metalloid cluster compounds with nine tetrel atoms inside the cluster core are known for germanium and tin, having the same formula E_9R_3. The germanium compound is an anion $\{Ge_9[Si(SiMe_3)_3]_3\}^-$ **35** that is isolated with different counter ions $(Li(THF)_4)^+$ or $[K(2.2.2\text{-crypt})]^+$) as orange crystals [135, 168, 169]. In the case of tin, a neutral $Sn_9(Ar^t)_3$ **36** (Ar^t = 2,6-$Trip_2$-C_6H_3; Trip = 2,4,6-*i*Pr_3-C_6H_2) [170, 171] and an anionic compound $\{Sn_9[Si(SiMe_3)_3]_3\}^-$ **37** [172] are known.

The neutral tin compound **36** is obtained via thermolysis of the hydride precursor $[Ar'Sn(\mu\text{-}H)]_2$ in hot toluene. Conversely, the anionic germanium compound $\{Ge_9[Si(SiMe_3)_3]_3\}^-$ **35** is isolated from the reaction of GeBr with $LiSi(SiMe_3)_3$ [168, 169] or by the reaction of the Zintl-anion Ge_9^{4-} with $ClSi(SiMe_3)_3$ [135]. In contrast to this, the disproportionation reaction of a Sn(I)halide in the presence of $LiSi(SiMe_3)_3$ gives access to the more open Sn_9 cluster $\{Sn_9[Si(SiMe_3)_3]_2\}^{2-}$ **38** [173], where the tin atoms exhibit the formal oxidation state zero as it is the case for isostructural germanium clusters of formula $Ge_9R_2^{2-}$which are obtained from the Zintl-anion Ge_9^{4-} [174–179]. The nine tin atoms in **38** are arranged in the form of a monocapped square antiprism, in which two opposite tin atoms of the lower Sn_4 ring are bound to $Si(SiMe_3)_3$ ligands (Fig. 30).

The capped Sn_4 square is distorted to a rectangle, in which the longest Sn–Sn distances, around 322 pm, are found (dashed lines in Fig. 30). All other tin–tin distances within the cluster core are in the normal range for tin clusters and vary between 289 and 306 pm. Due to the open ligand shell, **38** easily reacts with $Cl\text{-}Si(SiMe_3)_3$ to give $\{Sn_9[Si(SiMe_3)_3]_3\}^-$ **37**, the heavier congener of **35**, where now three $Si(SiMe_3)_3$ ligands are bound to the Sn_9 core (Fig. 30). In **37**, the nine tin atoms are arranged in the *nido* form of a monocapped square antiprism, i.e., **37** and

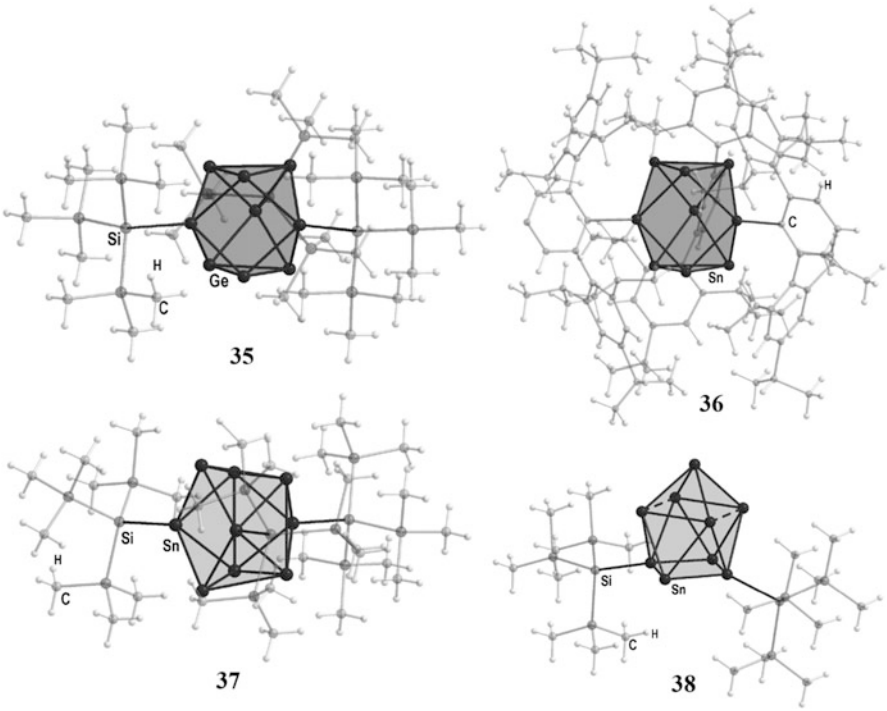

Fig. 30 Molecular structure of $\{Ge_9[Si(SiMe_3)_3]_3\}^-$ **35** (*top left*), $Sn_9(Ar')_3$ **36** ($Ar' = 2,6\text{-}Trip_2\text{-}C_6H_3$; $Trip = 2,4,6\text{-}i Pr_3\text{-}C_6H_2$) (*top right*), $\{Sn_9[Si(SiMe_3)_3]_3\}^-$ **37** (*bottom left*), and $\{Sn_9[Si(SiMe_3)_3]_2\}^{2-}$ **38** (*bottom right*). The central E_9 units are highlighted via a polyhedral presentation

38 are in line with Wade's rules as in both cases 22 skeletal electrons are present ($2n+4$, $n=9$). However, calculations show that the energy difference between the *closo* and the *nido* form is less than 10 kJ/mol [172], i.e., inside the cluster core a highly flexible system is present. This flexibility is also obvious from the arrangement of the nine tetrel atoms in $\{Ge_9[Si(SiMe_3)_3]_3\}^-$ **35** and $Sn_9Ar^{t}_3$ **36**, where a tricapped trigonal prismatic arrangement is realized, where each capping tetrel atom bears a ligand (Fig. 30). However, in **35** and **36**, the tricapped trigonal prismatic structure is strongly distorted so that a large height-to-edge ratio of 1.27 for **35** and 1.37 for **36** is realized. This large e:h ratio is to be expected as a D_{3h} symmetric nine atom cluster with 20 skeletal electrons (i.e., for a *closo* compound) possesses a LUMO (lowest unoccupied molecular orbital) which is bonding along the edges and antibonding along the heights [180]. In **35** and **36**, this LUMO is occupied with one or two electrons leading to the observed distortion toward large e:h ratios.

In the case of the germanium compound **35**, the open-ligand shell as well as the high-yield synthesis gives access to a variety of further investigations (Fig. 31). Thereby, buildup reactions were possible, leading to transition metal linked "dimeric" nineteen atomic clusters of composition $\{MGe_{18}[Si(SiMe_3)_3]_6\}^X$ ($X=1^-$, M=Cu, Ag, Au; X=0, M=Zn, Cd, Hg) [181–184]. Recently, a compound exhibiting a linear chain buildup of two copper atoms and two Ge_9R_3 units $\{Ge_9[Si(SiMe_3)_3]_3\}$-Cu-$\{Ge_9[Si(SiMe_3)_3]_3\}$-Cu-PPh_3 was synthesized [185], showing the potential of **35** for the synthesis of novel materials [186]. Additionally, **35** can be used in coordination chemistry, e.g., as a $2e^-$ donor ligand in the anionic compound $\{(CO)_5Cr\text{-}Ge_9[Si(SiMe_3)_3]_3\}^-$ [187]. Further CO elimination gives $\{(CO)_3Cr\text{-}Ge_9[Si(SiMe_3)_3]_3\}^-$, where a cluster enlargement has taken place, leading to a bicapped square antiprismatic Ge_9Cr cluster core. The heavier congeners $\{(CO)_3M\text{-}Ge_9[Si(SiMe_3)_3]_3\}^-$ (M=Mo, W) are directly accessible by the reaction of **35** with $W(CO)_3(CH_3CN)_3$ and $Mo(CO)_3(EtCN)_3$, respectively [188]. Finally, the addition of a fourth ligand leads to the neutral compound $Ph_3Sn\text{-}Ge_9[Si(SiMe_3)_3]_3$ [189, 190].

These results impressively show that a fruitful chemistry emerges due to the open-ligand shell. Additionally, further research concerning the physical and chemical properties of $\{Ge_9[Si(SiMe_3)_3]_3\}^-$ **35** was performed. Thereby, femtosecond transient absorption spectroscopy in thf reveals photodetachment of an electron from **35** in solution [191]. Additionally, gas-phase measurements of the fragmentation properties of **35** as well as of its redox chemistry have been carried out [192, 193]. Thereby, it was shown that the weakest bond within the cluster is the one to the $Si(SiMe_3)_3$ ligand – the whole dissociation pathways of **35** in the gas phase are summarized in Fig. 32.

This dissociation route is thereby quite different with respect to results for metalloid cluster compounds of group 13, where the $\{Ga_{19}[C(SiMe_3)_3]_6\}^-$ cluster **17** eliminates $Ga[C(SiMe_3)_3]$ units and not the ligand alone as it is the case for $\{Ge_9[Si(SiMe_3)_3]_3\}^-$ **35**. This different behavior might be the outcome of the different element–element bonding in the cluster being in the case of germanium much stronger due to greater covalent bonding character. The dissociation

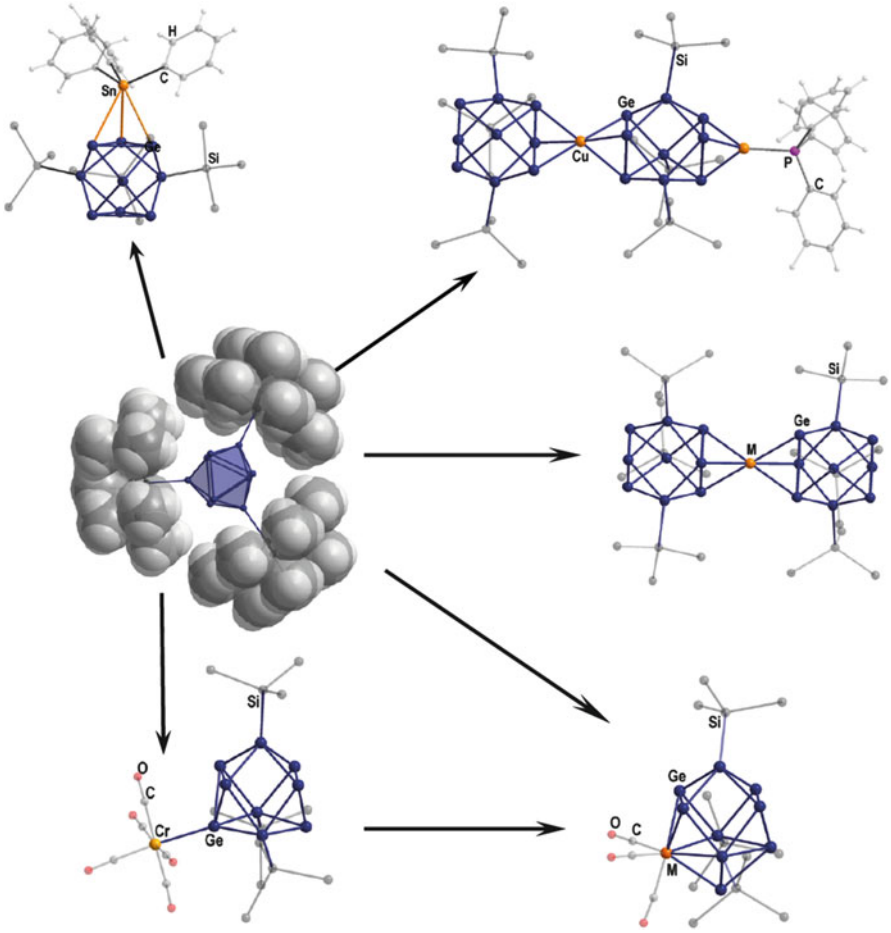

Fig. 31 Reaction routes for further buildup reactions of the metalloid germanium cluster $\{Ge_9[Si(SiMe_3)_3]_3\}^-$ **35** (in the molecular structure of **35**, the ligands are shown via a space filling model, and the central Ge_9 unit is highlighted via a polyhedral presentation). In the products, the methyl groups are omitted for clarity

experiments in the gas phase additionally reveal that ligand dismantling can take place at the cluster core, leading to mixed metalloid clusters like $\{Ge_9Si(SiMe_3)_3\}^-$ **35d1i.** Such a scenario seems possible during the synthesis of metalloid clusters in solution (cf. Sect. 5.2). In the case of the neutral tin compound $Sn_9(Ar^t)_3$ **36** (Ar^t = 2,6-$Trip_2$-C_6H_3; Trip = 2,4,6-*i*Pr_3-C_6H_2), further reactions have not been viable to date. However, recently the structurally similar metalloid tin cluster $[Sn_{10}(Ar)_3]^+$ **39** (Ar = 2,6-$Mes_2C_6H_3$; Mes = 2,4,6-$Me_3C_6H_2$) could be synthesized by a reductive coupling reaction of ArSnCl with C_8K in the presence of $AlCl_3$ [194, 194]. The molecular structure of **39** can be described as a $Sn_9(Ar)_3$ moiety as in **36**, where an additional tin atom is capping one of the heights of the central trigonal prism (Fig. 33).

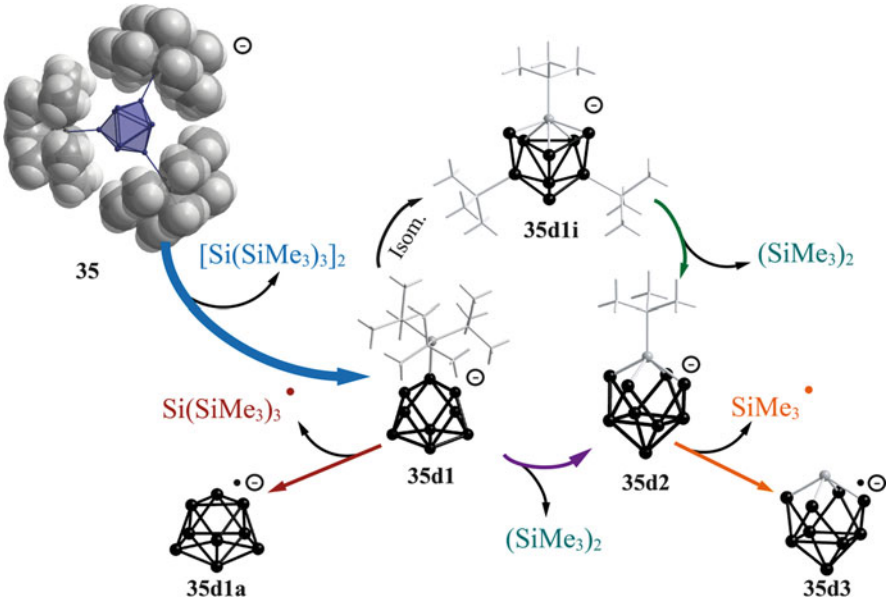

Fig. 32 Schematic drawing of the experimentally found reaction pathways for the dissociation of $\{Ge_9[Si(SiMe_3)_3]_3\}^-$ **35** in the gas phase

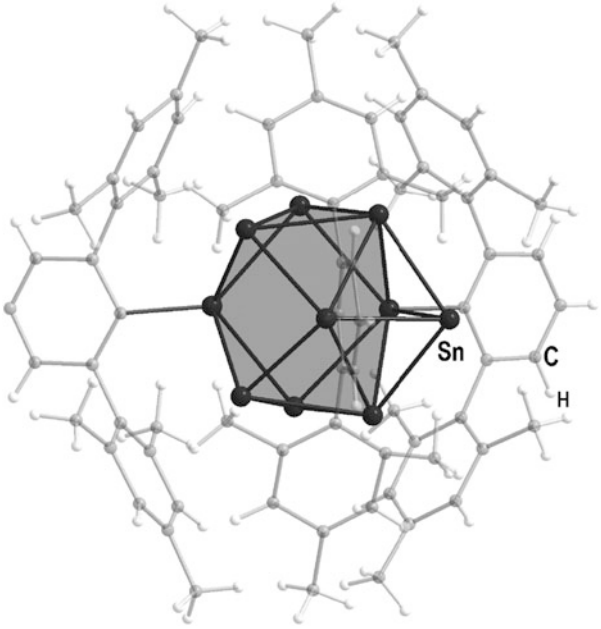

Fig. 33 Molecular structure of the cationic compound $\{Sn_{10}Ar_3\}^+$ **39** (Ar = 2,6-$Mes_2C_6H_3$; Mes = 2,4,6-$Me_3C_6H_2$). The ligands are shown partly transparent for clarity. The central Sn_9 unit is shown in a polyhedral presentation, in which the capping Sn atom (*on the right*) is not included

The addition of the tin atom leads to strong distortions of the Sn_9 moiety such that the two triangles of naked tin atoms are no longer parallel to each other, i.e., the relatively uniform height in **36** of approximately 400 pm splits into distances of 382, 394, and 451 pm. The longest distance of 451 pm is hereby the one, which is capped by the additional tin atom.

5.2 *Metalloid Tetrel Clusters Exhibiting Ten Tetrel Atoms: Approaching the Elemental Structure?*

To date, three metalloid cluster compounds of germanium with ten germanium atoms in the cluster core are known: $[Ge_{10}(Si\mathit{t}Bu_3)_6I]^+$ **40** [48], $\{Ge_{10}Si[Si(SiMe_3)_3]_4(SiMe_3)_2Me\}^-$ **41** [196], and $[(thf)_2Na]_6Ge_{10}[Fe(CO)_4]_8$ **42** [194, 195]. The clusters are synthesized via different synthetic routes. The cationic compound $[Ge_{10}(Si\mathit{t}Bu_3)_6I]^+$ **40** is synthesized from germacyclopropene $Ge_3(Si\mathit{t}Bu_3)_3I$, which is reacted for one week with a mixture of the potassium salts $KI/KB(C_6F_4H)_4$ in toluene at 50°C (c.f. Scheme 2) [48]. For the formation of **40**, it is assumed that the naked germanium atoms derive from a reductive elimination of $\mathit{t}Bu_3SiI$, which is found as a by-product in the reaction mixture. The anionic cluster compound $\{Ge_{10}Si[Si(SiMe_3)_3]_4(SiMe_3)_2Me\}^-$ **41** is synthesized together with the metalloid Ge_9 species $\{Ge_9[Si(SiMe_3)_3]_3\}^-$ **35** by a reaction of GeCl with $LiSi(SiMe_3)_3$ [196]. The neutral cluster $[(thf)_2Na]_6Ge_{10}[Fe(CO)_4]_8$ **42** is synthesized by a reaction of GeBr with $Na_2Fe(CO)_4$ and is isolated in the form of nearly black crystals [194, 195]. Hence, from a synthetic point of view, **41** and **42** might be similar. However, from a structural point of view, the cluster cores of the two metalloid Ge_{10} cluster compounds $[Ge_{10}(Si\mathit{t}Bu_3)_6I]^+$ **40** and $\{Ge_{10}Si[Si(SiMe_3)_3]_4(SiMe_3)_2Me\}^-$ **41** are very similar as it can be seen in Fig. 34.

This similarity is unusual, as significant differences between both compounds are present: firstly, the average oxidation state of the germanium atoms inside the cluster core is 0.8 in the case of **40** and 0.4 in the case of **41**. Secondly, one compound is a cation, while the other compound is an anion. Thirdly, and most importantly, the ligands in both metalloid clusters are bound to different germanium atoms (Fig. 34). Despite all these differences, the germanium atoms inside both compounds are arranged in a similar way, showing that this arrangement is favorable for a metalloid cluster compound with 10 germanium atoms in the cluster core. A reason for this preference might be the fact that in both compounds, an adamantine arrangement of the ten germanium atoms is present, as emphasized in Fig. 34 by a polyhedral presentation. Consequently here, for the first time, a topological approach onto the structure of elemental α-germanium is realized, which is more pronounced in the case of **41** where the average oxidation state of the germanium atoms is 0.4, much closer to the value 0 of the element. The structural feature of **40** and **41** was additionally observed in the cluster anion $Au_3Ge_{45}^{9-}$ that was synthesized from the Zintl-anion Ge_9^{4-} showing that this

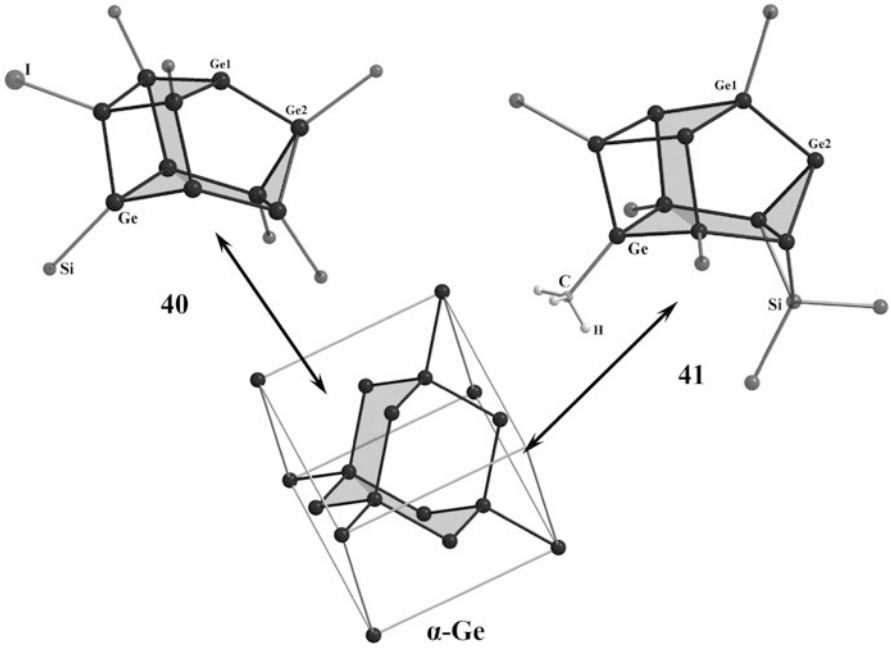

Fig. 34 Molecular structure of $[Ge_{10}(SitBu_3)_6I]^+$ **40** (*top left*) and $\{Ge_{10}Si[Si(SiMe_3)_3]_4(SiMe_3)_2Me\}^-$ **41** (*top right*) without $SiMe_3$ groups. The adamantine-like arrangement of the germanium atoms inside the cluster core is emphasized by a polyhedral presentation and compared to the arrangement in α-Ge, where a unit cell (cell edges in *gray*) is shown and where the comparable structure is also highlighted by a polyhedral presentation

arrangement of germanium atoms is important in the borderland between molecules and the solid state [197, 198].

However, such a structural transition must not necessarily occur when ten germanium atoms are present inside the cluster core, which is obvious when we take the structure of the third metalloid Ge_{10} cluster: $[(thf)_2Na]_6Ge_{10}[Fe(CO)_4]_8$ **42** into account [194, 195].

The arrangement of the ten germanium atoms in **42** is completely different with respect to **40** and **41**. Thereby, a unique polyhedral arrangement is realized that exhibits two different sites – a cubic part on the one side and an icosahedron part on the other side as emphasized in Fig. 35. In accordance to the description of the centaur of the Greek mythology (half human and half horse), a polyhedron built of two different polyhedra (here, half cube and half icosahedron) was named a centaur polyhedron [199], and therefore the polyhedron built up of the ten germanium atoms in **42** can be named a centaur polyhedron. A centaur polyhedron is a completely unknown structural motive in germanium chemistry, and so the reason for the formation of **42** was questionable. Quantum chemical calculations additionally reveal that in the different sides of the centaur polyhedron, also different

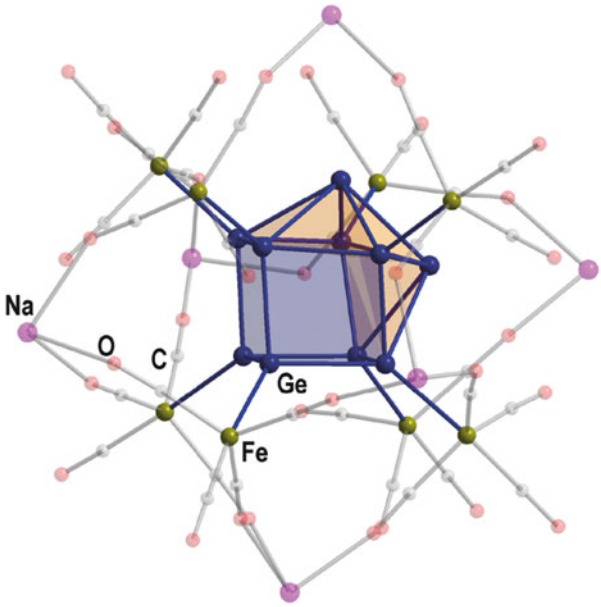

Fig. 35 Molecular structure of $(thf)_{18}Na_6Ge_{10}[Fe(CO)_4]_8$ **42** without coordinated thf molecules. The central germanium atoms and the surrounding sodium atoms are *dark colored*. The different parts of the centaur polyhedra of the central Ge_{10} unit are emphasized by a polyhedral presentation where the cubic part is *blue* and the icosahedral part is *orange*

bonding situations are present. Thereby, at the cubic side, three center bonding components with *shared electron numbers* (SENs) of 0.058 to 0.086 were calculated, while the SENs in the icosahedral part are in the range of 0.278–0.284 (SENs for bonds are a reliable measure of the strength of covalent bonding. For example, the SEN for the Ge–Ge single bond in the model compound R_3GeGeR_3 ($R{=}NH_2$) is 1.04.). Thus, the bonding inside **42** can be described as localized in the cubic part and delocalized in the icosahedral part of the centaur polyhedron.

Such a bonding situation is unique in the field of metalloid cluster compounds as, for example, in the large multishell metalloid clusters of group 13, e.g., $\{Al_{77}[N(SiMe_3)_2]_{20}\}^{2-}$ **8** the bonding changes from the inner to the outer side but not from one side to the other. The outstanding structure of **42** made a classification quite complicated, and it seems as if this structural unit (centaur polyhedron) is an unusual singular result. However, more recent reports indicate this structural unit is not unique in tin chemistry: a great variety of metalloid tin clusters are obtained via the synthetic route of the disproportionation reaction of a Sn(I)halide, leading to the neutral metalloid cluster compound of tin $Sn_{10}[Si(SiMe_3)_3]_6$ **43** [200] as well as to the charged ones $\{Sn_{10}[Si(SiMe_3)_3]_5\}^-$ **44** [201] and $\{Sn_{10}[Si(SiMe_3)_3]_4\}^{2-}$ **45** [202], where the arrangement of the tin atoms in the cluster core can be described by a more or less distorted centaur polyhedron (Fig. 36).

Thereby, in the case of $Sn_{10}[Si(SiMe_3)_3]_6$ **43**, it could be shown by a comparison of bond distances, electronic situation, and Sn Mößbauer spectroscopy that a correlation to a phase transition is present [200]. Thus, the change of bond distances

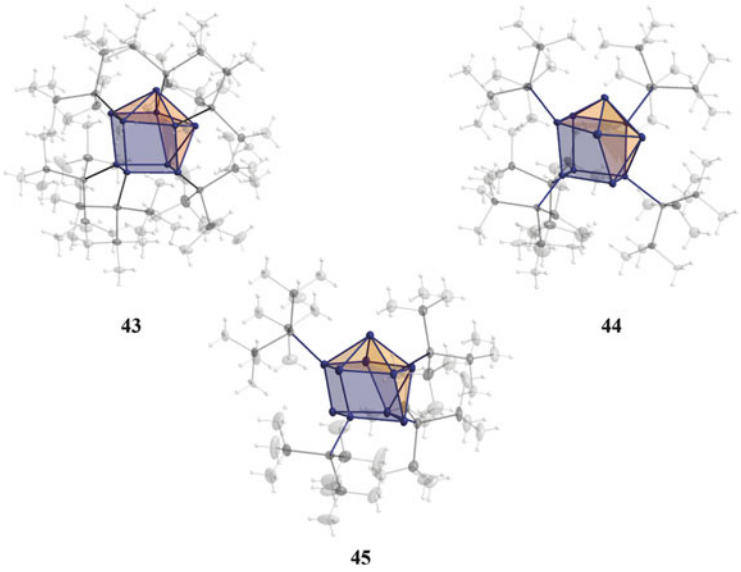

Fig. 36 Molecular structure of $Sn_{10}[Si(SiMe_3)_3]_6$ **43** (*left*), $\{Sn_{10}[Si(SiMe_3)_3]_5\}^-$ **44** (*right*), and $\{Sn_{10}[Si(SiMe_3)_3]_4\}^{2-}$ **45** (*middle*). The different parts of the centaur polyhedra of the central Sn_{10} unit are emphasized by a polyhedral presentation where the cubic part is *blue* and the icosahedral part is *orange*. The $Si(SiMe_3)_3$ ligands are shown semitransparent for clarity

as well as electronic properties from the cubic (localized bonding electrons, short Sn–Sn bonds) to the icosahedral part of the centaur polyhedron (delocalized bonding electrons, long Sn–Sn distances) can be correlated with a phase transition from α- to β-tin. This correlation only becomes obvious for tin as α- and β-tin are stable at normal pressure with a phase transition temperature of 13.2°C [35]. In the case of germanium, β-germanium is a high-pressure modification which is stable above 11 GPa [203], leading to shorter Ge–Ge distances [204].

However, the centaur polyhedral arrangement of the ten germanium atoms in **42** also hints to a phase transition from α- to β-germanium ongoing from the cubic to the icosahedral part. Consequently, also in the case of the tetrels, an arrangement is realized within a metalloid cluster at normal conditions that is realized for the element only at high pressure. This behavior is also obvious in larger clusters as discussed in the following. However, before discussing larger clusters, we will briefly take a look at the metalloid tin clusters exhibiting ten tin atoms, which seems to be a favorable number for metalloid tin clusters. All metalloid Sn_{10} clusters **43**, **44**, and **45** are synthesized by the reactions of a metastable Sn(I)halide precursors with $LiSi(SiMe_3)_3$. Thereby, the yield of the isolated cluster compound can be unusually high, e.g., **45** is obtained in 80 % yield taking the disproportionation reaction into account. This yield is unusual for the complicated reaction system, starting from a binary halide and ending up with a metalloid tin cluster (Scheme 4).

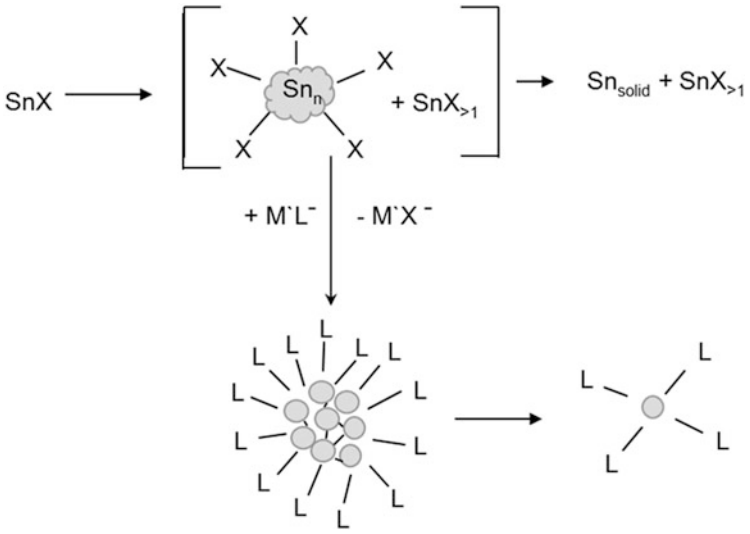

Scheme 9 Principle reaction scheme for the synthesis of a metalloid tin cluster via the disproportionation reaction of a Sn(I) halide (ML=ligand source, e.g., $LiSi(SiMe_3)_3$)

However, recent results from gas-phase measurements [205] as well as theoretical calculations [206] have shown that larger naked tin clusters can be described as an aggregation of smaller units. If such a behavior is also valid for ligand-stabilized metalloid clusters, this leads to an essential alteration of the general reaction scheme (Scheme 4) for the formation of metalloid tin clusters applying the disproportionation reaction of a metastable subhalide (Scheme 9): firstly, as previously described the disproportionation reaction leads to larger clusters on the way to the bulk phase. However, now these intermediates might be seen as an agglomeration of smaller units. Afterward, the substitution of the halides by bulky ligands leads to a product mixture of ligand-stabilized metalloid tin clusters of different sizes. These clusters may also be described as an agglomeration of smaller units as indicated by loosely bound spheres in Scheme 9. In a subsequent step, now disaggregation takes place, leading to smaller clusters of similar size with an open-ligand shell as not enough ligand is available for complete shielding. Consequently, the reaction does not lead to larger metalloid clusters but to smaller ones with an open-ligand shell. The clusters are thereby obtained in high yield and combined with the accessibility of the open-ligand shell; this might be the starting point for further investigations. However, initial results indicate that further reactions applying metalloid tin clusters are more complicated as also ligand elimination and dismantling can take place.

Hence, the reaction of $\{Sn_{10}[Si(SiMe_3)_3]_4\}^{2-}$ **45** with $ZnCl_2$ does not lead to a connection of metalloid tin clusters but to ligand elimination leading to the very open metalloid tin cluster $\{Sn_{10}[Si(SiMe_3)_3]_3\}^-$ **46**, whose molecular structure is

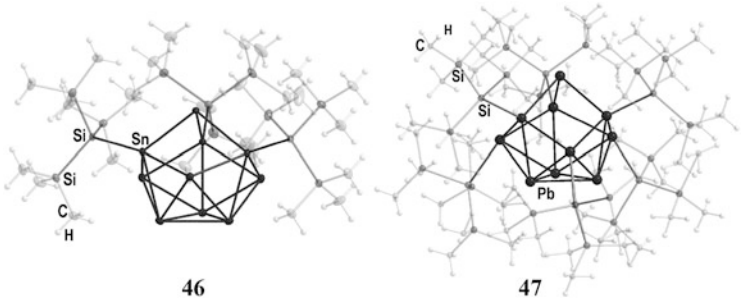

Fig. 37 Molecular structure of $\{Sn_{10}[Si(SiMe_3)_3]_3\}^-$ **46** (*left*) and $Pb_{10}[Si(SiMe_3)_3]_6$ **47** (*right*). The $Si(SiMe_3)_3$ ligands are shown semitransparent for clarity

shown in Fig. 37 [207]. The arrangement of the ten tin atoms inside the cluster core of **46** is best described as a combination of three different layers, starting with a Sn_3 triangle with slightly elongated Sn–Sn bonds (300 pm). This triangle is topped by a puckered six-membered ring in chair conformation containing three naked as well as the three ligand-bound tin atoms. The bond distances within this puckered six-membered ring are with 289–299 pm in the range of normal Sn–Sn single bonds as found in α-tin (288 pm). This six-membered ring is capped by the remaining naked tin atom in that way that short tin–tin bonds of 287 ± 1 pm to the three ligand-bound tin atoms are formed. This description of the arrangement of the ten tin atoms within **46** is in line with the one used to describe the arrangement of lead atoms within the metalloid lead cluster $Pb_{10}[Si(SiMe_3)_3]_6$ **47**, where all lead atoms in the six-membered ring are bound to a ligand [208, 209].

Hence, such an arrangement seems favorable for metalloid cluster compounds of the heaviest group 14 elements. Recently, it was shown that ligand dismantling can also occur during the synthesis of a metalloid cluster applying the disproportionation reaction of a metastable tin(I) halide, leading again to a metalloid tin cluster with ten tin atoms in the cluster core $\{Sn_{10}Si(SiMe_3)_2[Si(SiMe_3)_3]_4\}^{2-}$ **48** [210]. The Sn_{10} cluster core of **48** (Fig. 38) can again be described as a distorted centaur polyhedral arrangement, where the Sn–Sn distances are again longer in the icosahedral part (average value, 298.5 pm) and shorter in the cubic part (average value, 292.4 pm).

In the cubic area, two tin atoms are bound to the silicon atom of the bridging $Si(SiMe_3)_2$ group with Sn–Si distances of 260 and 266 pm, within the same range as the other Sn–Si distances in **48**. The $Si(SiMe_3)_2$ group thereby originates from the degradation of a $Si(SiMe_3)_3$ ligand, as it is frequently observed in cluster chemistry when $Si(SiMe_3)_3$ is used as a ligand, e.g., during the synthesis of $\{(SiMe_3)_2SiE_4[Si(SiMe_3)_3]_3\}^-$, (E=Ga [211, 212], Al [213]), and $\{Ge_{10}Si[Si(SiMe_3)_3]_4(SiMe_3)_2Me\}^-$ **41** [196].

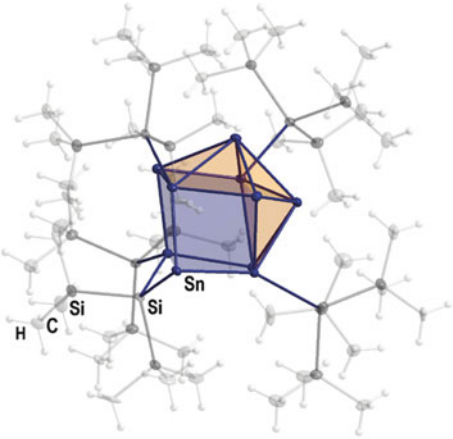

Fig. 38 Molecular structure of $\{Sn_{10}Si(SiMe_3)_2[Si(SiMe_3)_3]_4\}^{2-}$ **48**. The different parts of the centaur polyhedra of the central Sn_{10} unit is emphasized by a polyhedral presentation where the cubic part is blue and the icosahedral part is orange. The $Si(SiMe_3)_3$ ligands are shown 50 % transparent for clarity

5.3 Metalloid Ge and Sn Clusters Exhibiting More than Ten Tetrel Atoms

In the case of the largest metalloid clusters of germanium and tin, novel structural motifs are again realized with connectivity's known from high-pressure modifications. In the case of the metalloid germanium cluster $Ge_{12}[FeCp(CO)_2]_8[FeCpCO]_2$ **49**, which is obtained by the reaction of a metastable Ge(I)Br solution with $KFeCp(CO)_2$ [214, 215], the 12 germanium atoms are not arranged in the form of a simple polyhedron, but a structure is realized which can be described at first glance as two face-shared Ge_8 cubes. This arrangement is thus quite different with respect to the metalloid lead cluster $Pb_{12}[Si(SiMe_3)_3]_6$, where the twelve lead atoms are arranged in the form of a distorted icosahedron [208, 209].

The Ge_{12} core in **49** is completely shielded by eight terminally bound $FeCp(CO)_2$ units and two bridging FeCp(CO) ligands. The bridging FeCp(CO) ligand is thereby bound tightly to the Ge_{12} core, leading to short Ge–Fe distances of 230 and 240 pm. Beside this, the terminally bound $FeCp(CO)_2$ ligands show longer Ge–Fe distances with an average value of 246 pm. The Ge–Ge distances in the cluster core vary between 249 and 260 pm, being in a normal range for metalloid germanium clusters [216]. The arrangement of the 12 germanium atoms is unique in the field of metalloid tetrel clusters. However, a comparable arrangement of germanium atoms is found in the high-pressure modification of germanium Ge(II) [Ge(*tI*4)] [203], where a similar Ge_{12} unit is present as emphasized in Fig. 39.

This structural similarity indicates that the arrangement of the 12 germanium atoms within the cluster core of **49** can be seen as a structural approach to the solid-state structure Ge(II), which is only stable at a pressure of 10.8 GPa. This high-pressure-like arrangement might thereby be induced by the dense-packed ligand shell as it is the case for the metalloid gallium cluster $Ga_{18}(PtBu_2)_{10}$ **16** (cf. Sect. 4.2.2). Such a structural resemblance to a high-pressure modifications is

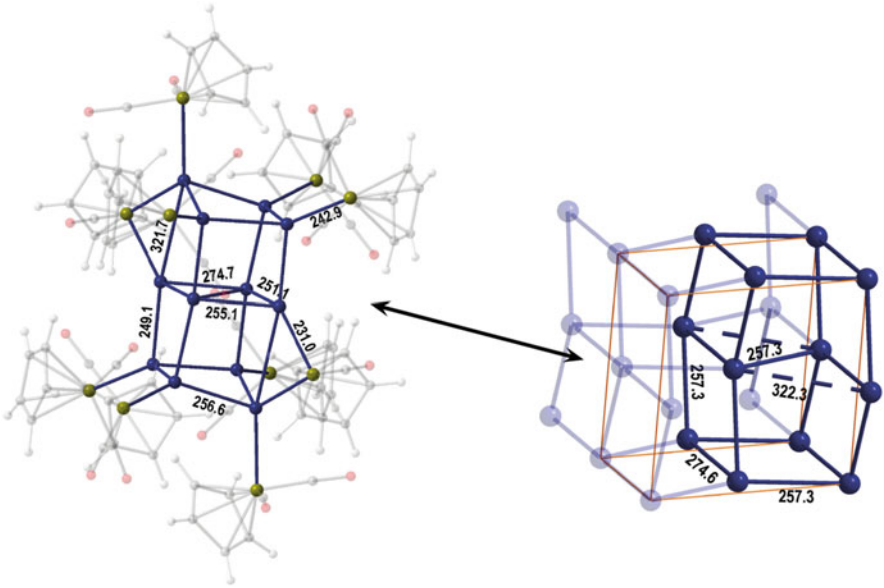

Fig. 39 Comparison of the arrangement of the germanium atoms within $Ge_{12}[FeCp(CO)_2]_8[FeCpCO]_2$ **49** (*left*) and the solid-state structure of Ge(II) [Ge(*tI4*)] (*right*)

also realized in $Sn_{15}[NDippSiMe_3]_6$ (Dipp=C_6H_3,2,6-*i*Pr_2) **51** [130, 131], where the arrangement of the 15 tin atoms can be seen as a cutout of a bcc packing (vide supra) that is known for elemental tin at a pressure of 45 ± 5 GPa [43].

However, more open structures are possible as seen in the largest structurally characterized metalloid cluster compound of germanium $[Li(thf)_2]_3Ge_{14}R_5$ (R=$Si(SiMe_3)_3$ **50** [217] and R=$Ge(SiMe_3)_3$ **50a** [218]) synthesized by the reaction of GeBr with LiR. Both compounds are structurally similar, and in the following, we will only discuss **50**. In the case of **50**, only five out of the 14 germanium atoms of the cluster core are bound to a ligand via a Ge–Si single bond. Additionally, to three germanium atoms, a lithium cation is coordinated which is additionally saturated by two thf molecules. The five ligands together with the thf molecules completely shield the cluster core of 14 germanium atoms as to be seen in the space filling model shown in Fig. 40. The 14 germanium atoms inside the cluster core are arranged in a unique way. Most noteworthy is the fact that the 14 germanium atoms build up an empty polyhedron that is not spherical but flattened, as the shortest Ge–Ge distance between two opposite germanium atoms is 414 pm, while the longest one is 658 pm (Fig. 41).

The polyhedron is built up of six pentagonal faces and three tetragonal faces that are distorted to a butterfly arrangement leading to a diagonal Ge–Ge contact of 285.6 pm. The other Ge–Ge distances inside **50** are in between 246 and 256 pm, which is in the range for a normal Ge–Ge single bond. This description is further corroborated by quantum chemical calculations that hint to classical 2c2e bonds for

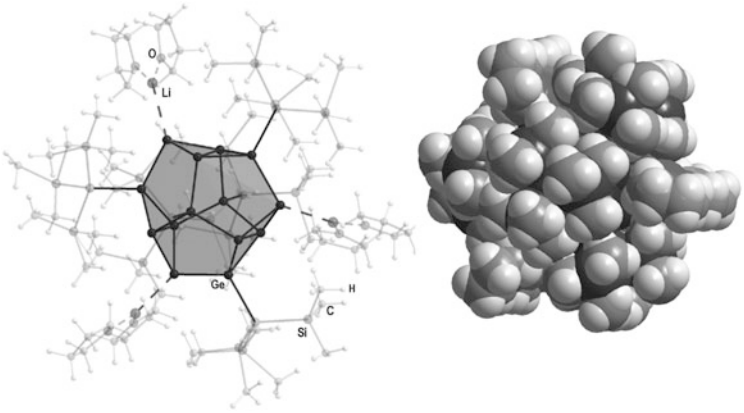

Fig. 40 *Left*, molecular structure of the metalloid germanium cluster compounds $[Li(thf)_2]_3Ge_{14}[Si(SiMe_3)_3]_5$ **50**. The arrangement of the central 14 germanium atoms is emphasized by a polyhedral presentation. *Right*, space filling model of **50**

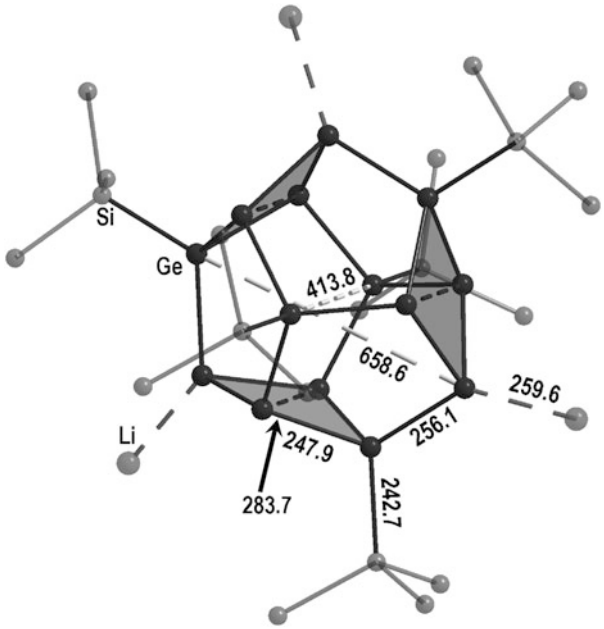

Fig. 41 Molecular structure of the metalloid germanium cluster compound $[Li(thf)_2]_3Ge_{14}[Si(SiMe_3)_3]_5$ **50** without CH_3 groups and thf molecules. The inner dimensions of the empty polyhedron are marked. The three tetragonal faces are highlighted by a polyhedral presentation, and the interesting dashed Ge–Ge bond between the low-coordinated germanium atoms of 283.7 pm is marked by an *arrow*

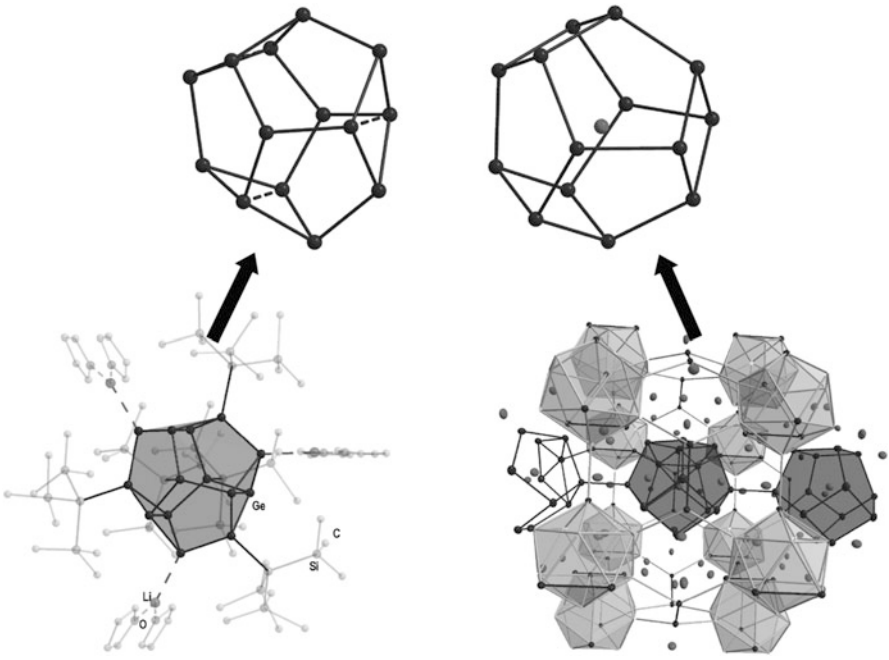

Fig. 42 *Left*, arrangement of the 14 germanium atoms in $[Li(thf)_2]_3Ge_{14}[Si(SiMe_3)_3]_5$ **50** and the molecular structure of **50** without hydrogen atoms. *Right*, arrangement of the 14 tin atoms in the Zintl phase $Na_{29}Zn_{24}Sn_{32}$ together with a larger cutout of this Zintl phase

these short bonds as the SENs (*shared electron numbers*) for the two center bonding components are similar to those found for a normal Ge–Ge single bond. However, most interesting is the bonding within the tetragonal face, especially the bond between the low-coordinated germanium atoms (Fig. 42). This issue was investigated by CASSCF (*complete active space self-consistent field*) calculations indicating that the bond strength between the two germanium atoms is reduced to 40 % in comparison to a typical Ge–Ge single bond. Additionally, the calculations show that the bond exhibits a biradical character.

Thus, **50** can be seen as a singlet hexaradicaloid species being the extension of the biradicaloid character onto a larger cluster compound. As metalloid clusters are model compounds for the area between molecules and the solid state, the multiradicaloid character of **50** might be also of importance for nanoparticles as well as surfaces, where unsaturated germanium atoms are present. Thus, a multiradicaloid character might be the reason for different physical as well as chemical properties of nanoparticles in comparison to the bulk phase; e.g., the reactivity of a reconstructed Ge(100)-2 × 1 surface with unsaturated organic compounds like 1,5-cyclooctadiene is normally traced back to the presence of possible "multiple" Ge–Ge bonds [219]. However, the radicaloid character would also lead to a higher reactivity (for reconstructed Si(100)-2 × 1 surfaces, the significance of radicals was lately shown for the cooperative bifluorination or bichlorination [220]).

This high reactivity is also obvious for **50** which decomposes after the $Li(thf)_2$ units are eliminated by the addition of a complexing reagent for Li^+ like TMEDA. Thereby, the intermedially assumed trianion $\{Ge_{14}[Si(SiMe_3)_3]_5\}^{3-}$ deprotonates the solvent (thf) giving the monoanion $\{Ge_{14}[Si(SiMe_3)_3]_5H_2\}^-$, which was identified by mass spectrometry [217]. Interestingly, this monoanion decomposes after collision in the gas phase to give $\{Ge_9[Si(SiMe_3)_3]_3\}^-$ **35** and $Ge_5[Si(SiMe_3)_3]_2H_2$. The calculated structure of the neutral cluster $Ge_5[Si(SiMe_3)_3]_2H_2$ is similar to the one of the smallest metalloid germanium cluster Ge_5Ar_4 **24**, which exhibits a biradicaloid bonding character. Hence, in the gas phase, a direct connection between a singlet biradicaloid and a singlet hexaradicaloid system is present indicating that such a bonding is important in the nanoscaled area between molecules and the solid state.

As already mentioned, the E_{14} polyhedron found in **50** is unique in the field of metalloid cluster compounds. However, comparable Sn_{14} polyhedra were found in the Zintl phase $Na_{29}Zn_{24}Sn_{32}$ (Fig. 42) [221, 222], and additionally a comparable polyhedra is observed in the molecular Zintl-anion $[Eu@Sn_6Bi_8]^{4-}$ [223, 224]. Nevertheless, there are significant differences, and the most obvious one is the fact that all other compounds exhibit an additional atom in the center of the polyhedron. Thus, the structure of the metalloid cluster **50** shows that even the heavier congeners of carbon can build up larger empty polyhedra without a stabilizing atom in the center. Consequently, also fullerene-like compounds might be accessible, and **50** can be seen as a first step into this direction.

However, another interpretation is also probable taking into account the novel solid-state structure of germanium, Ge(*cF*136): the germanium atoms in Ge(*cF*136) are arranged in a clathrate(II) form (vide supra). Hence, Ge(*cF*136) exhibits the structural motif of a pentagon dodecahedron and a hexacaidecahedron. In both polyhedra, the structure of three adjacent pentagonal faces is present, which is also a central structural motif of **50** (Fig. 43). Consequently, the arrangement of the

Fig. 43 Comparison of the substructure of three adjacent pentagonal faces inside the Ge_{14} polyhedron (*top*) of $[Li(thf)_2]_3Ge_{14}[Si(SiMe_3)_3]_5$ **50** with the substructure of Ge(cF136), hexacaidecahedron (*left*), and pentagon dodecahedron (*right*)

germanium atoms in **50** can be seen as a structural approach onto the solid-state structure of Ge(*cF*136) or maybe another clathrate-like arrangement.

Which interpretation fits best has to be clarified by future experiments and theoretical calculations, giving more insight into the area between the molecular and the solid state.

In the case of larger metalloid tin clusters, the first and only structurally characterized multishell cluster of group 14 is realized: $Sn_{15}R_6$ (R=NDipp($SiMe_3$) **51**; NDipp($SiMe_2Ph$) **51a**, Dipp=C_6H_3, s2,6-*i*Pr_2) [130, 131]. The clusters are synthesized via different synthetic routes: while **51** is synthesized via a reductive coupling reaction, **51a** is synthesized via thermolysis of a suitable precursor. However, the molecular structure of both clusters is essentially the same as in both structures, the arrangement of the tin atoms (Fig. 44) can be described as a body-centered arrangement of 15 tin atoms, being the first metalloid group 14 cluster compounds having a central tetrel atom. The naked tin atoms form a body-centered distorted cube, where each of the six faces of the cube is capped by a ligand-bound tin atom.

This arrangement cannot be compared with the structure of elemental tin (neither gray nor white). However, the arrangement is similar to the arrangement in a high-pressure modification found at 45 ± 5 GPa [43]. Hence, **51** is another example of a metalloid cluster compound, where the arrangement is similar to the one found in a high-pressure modification of the corresponding element. In **51**, the tin–tin distances from the central tin atom to the eight tin atoms of the cube have an average value of 318 pm that is longer than the average value in metallic β-tin, indicating that the bonding electrons are strongly delocalized that might be expected due to the "metallic" arrangement of the tin atoms in **50**. The average tin–tin distance of the ligand-bound tin atoms is 301 pm, much shorter, i.e., the

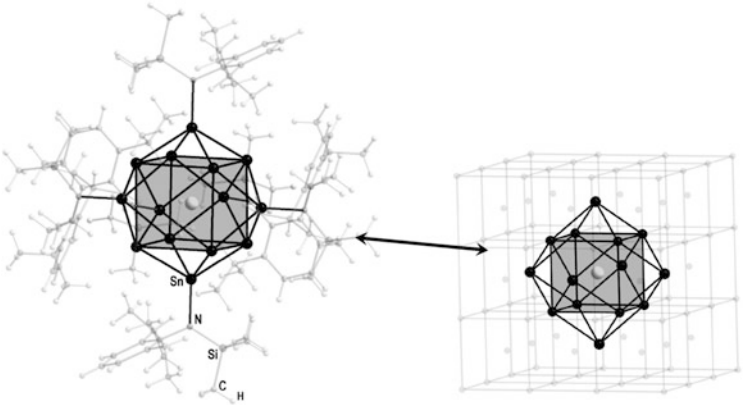

Fig. 44 Molecular structure of $Sn_{15}R_6$ (R=NArSiMe_3; Ar=C_6H_3, 2,6-*i*Pr_2) **51**; hydrogen atoms are omitted for clarity. The central atom is *bright gray*, and the cube of naked atoms is highlighted by a polyhedral presentation

tin–tin bonds get more localized ongoing from the center to the ligand shell, a similar behavior as observed for the multishell metalloid triel clusters.

Beside this multishell arrangement, the tin atoms in the largest metalloid tetrel cluster $Sn_{17}[GaCl(ddp)]_4$ **52** (ddp=HC(CMeNDipp)$_2$; Dipp = 2,6-*i*Pr$_2$-C$_6$H$_3$) are quite differently arranged. **52** is obtained by the reduction of $SnCl_2$ with Ga(ddp) and is obtained as dark red crystals beside the Sn_7 cluster $Sn_7[GaCl(ddp)]_2$ **30a** (Fig. 26), which is obtained in the form of orange crystals. **30a** is structurally similar to Sn_7Ar_2 **30**; hence, a pentagonal bipyramidal arrangement is realized, where the central Sn_5 ring is capped by two SnGaCl(ddp) units leading also to similar Sn–Sn bond lengths.

The structure of the Sn_{17} cluster **52** (Fig. 45) is best described as two Sn_9 units that are fused together by a central tin atom. The central tin atom thus has the highest coordination number of eight, leading to the longest tin–tin distances inside **52** of 309.8 pm. The other tin–tin distances inside the cluster vary in a range as it is normally observed for polyhedral tin clusters like **30a**.

The arrangement of the tin atoms in **52** further underlines that larger tin clusters can be seen as an aggregation of smaller units. Electron count for **52** assuming that every naked tin atom bears a lone pair contributing two electrons for cluster bonding, while the central tin atom contributes all four valence electrons and the ligand-bound tin atoms contribute three electrons for cluster bonding leads to a total number of 40 electrons for cluster bonding. 40 electrons is thereby the correct number for shell closing according to the jellium model [114–116], which is also used to describe the bonding inside the metalloid gallium cluster $Ga_{22}R_8$ **15** [225] or the silicon-centered metalloid aluminum cluster $SiAl_{14}Cp^*_6$ [226]. Additionally, 20 electron pairs are in line with the *mno* rules for condensed polyhedra [227], i.e., two individual polyhedra ($m = 2$) in a structure with 17 vertices ($n = 17$) should share only one vertex ($o = 1$) exhibiting $m + n + o = 20$ electron pairs. The Sn_{17} core is structurally as well as electronically similar to the Zintl-type

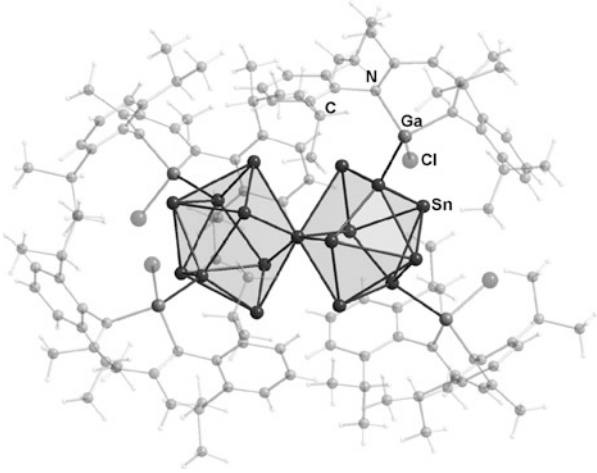

Fig. 45 Molecular structure of $Sn_{17}[GaCl(ddp)]_4$ **52** (ddp=HC(CMeNDipp)$_2$; Dipp = 2,6-*i*Pr$_2$-C$_6$H$_3$). The substructure of a Sn_9 unit is emphasized by a polyhedral presentation

cluster $[Ni_2@Sn_{17}]^{4-}$ **53,** where also 40 bonding electrons are present and where a nickel atom is localized inside the Sn_9 units [228]. Thus, as it was the case for the small polyhedral metalloid clusters (cf. Sect. 5.1.2), a strong correlation to the naked Zintl ions is also present in the case of larger clusters that can be described as an aggregation of smaller units. However, as the bonding might be also described by bonding models that assume complete delocalization like the jellium model, this further underlines the intermediate character of metalloid clusters between molecules and the solid state.

6 Summary and Concluding Remarks

Metalloid cluster compounds of the general formula M_nR_m ($n > m$; M=metal like Al, Au, Sn, etc.; R=ligand like S-C_6H_4-COOH, $N(SiMe_3)_2$, etc.) represent a novel group of cluster compounds localized within the nanoscaled area between molecules and the solid state, opening our eyes to the complexity and the fundamental principles of the dissolution and the formation of metals. Thereby, novel structural motifs are realized like the central square antiprismatic Al_8 unit in $Al_{50}Cp^*_{12}$ **1**, the pentagonal bipyramid Au_7 unit in $Au_{102}([p\text{-MBA}]_{44}$ **2**, or the empty Ge_{14} polyhedron in $[Li(thf)_2]_3Ge_{14}[Si(SiMe_3)_3]_5$ **50**, indicating a high complexity of the simple-seeming process of formation or dissolution of metals. Additionally, the results give fundamental impact on nanotechnology as now a defined structural basis is present to establish structure–property relations in this new industrial field, indicating that the simple-seeming idea that a metal nanoparticle can just be seen as a cutout of the solid-state structure is not true, even for clusters/particles with diameters in the nanometer range.

However, the so far obtained molecular compounds indicate that the arrangement of the metal atoms in a metalloid clusters already partly resembles possible arrangements of the elemental metals themselves. Thereby, also structural motifs are realized at normal conditions found in the solid state only at extreme conditions. Additionally, the arrangement within a metalloid cluster also hints to possible new solid-state structures like the icosahedral arrangement of the twelve aluminum atoms inside $Al_{22}Br_{20}\cdot 12thf$ **10** hint to a possible α-boron like arrangement for aluminum. However, the synthesis and structural characterization of the so far obtained metalloid clusters are just a first step to an understanding of the properties of nanoscaled metals.

Consequently in the future, beside the synthesis of more metalloid clusters to broaden the structural basis, it will be necessary to take a closer look at the properties of these metalloid cluster compounds. This is a challenge as some of these compounds are only obtained in small amount and secondly some clusters are very sensitive, e.g., crystals of the metalloid cluster $\{Ge_9[Si(SiMe_3)_3]_3\}^-$ **35** ignite when exposed to air. Additionally, the properties of crystals of the metalloid gallium cluster $[Ga_{84}(N(SiMe_3)_2)_{20}]^{4-}$ **23** show that also the arrangement of a metalloid cluster in the solid state can have a vital influence on the measured

properties. Nevertheless, although research in this field is complex and time-consuming, it is worth doing as it is the only way to shed light on this fascinating area between molecules and solid state of metals that gains increasing technological significance due to progress in the field of nanotechnology.

Acknowledgments I thank Prof. Dr. Hansgeorg Schnöckel, Dr. Claudio Schrenk, and Dr. Samantha DeCarlo for the helpful discussions and suggestions and Dr. Claudio Schrenk and Marion Schnepf for the support in developing the figures and schemes.

References

1. Cotton FA (1964) Inorg Chem 3:1217–1220
2. Cotton FA (1966) Q Rev Chem Soc 20:389–401
3. Schnepf A, Schnöckel H (2002) Angew Chem 114:3682–3704
4. Schnepf A, Schnöckel H (2002) Angew Chem Int Ed 41:3532–3554
5. Purath A, Köppe R, Schnöckel H (1999) Angew Chem 111:3114–3116
6. Purath A, Köppe R, Schnöckel H (1999) Angew Chem Int Ed 41:2926–2928
7. Goesmann H, Feldmann C (2010) Angew Chem 122:1402–1437
8. Goesmann H, Feldmann C (2010) Angew Chem Int Ed 49:1362–1395
9. Pelton M, Tang Y, Bakr OM, Stellacci F (2012) J Am Chem Soc 134:11856–11859
10. Holmes AL, Huetges J, Reckmann A, Muthuswamy E, Meerholz K, Kauzlarich SM (2015) J Phys Chem 119:5671–5678
11. Wheeler LM, Levij LM, Kortshagen UR (2013) J Phys Chem Lett 4:3392–3396
12. Yi C, Tofanelli MA, Ackerson CJ, Knappenberger KL (2013) J Am Chem Soc 135: 18222–18228
13. Carolan D, Doyle H (2015) Nanoscale 7:5488–5494
14. Vaughn DD II, Schaak R (2013) Chem Soc Rev 42:2861–2879
15. Yang P (2008) Dalton Trans 4387–4391
16. Schnöckel H (2005) Dalton Trans 3131–3136
17. Barr D, Clegg W, Mulvey RE, Snaith R (1984) Chem Commun 79–80
18. Mitzel NW, Lustg C (2001) Z Naturforsch B 56:443–445
19. Long DL, Tsunashima R, Cronin L (2010) Angew Chem 122:1780–1803
20. Long DL, Tsunashima R, Cronin L (2010) Angew Chem Int Ed 49:1736–1758
21. Corrigan JF, Fuhr O, Fenske D (2009) Adv Mater 21:1867–1871
22. Schnepf A, Schnöckel H (2002) Group 13 chemistry – from fundamentals to application. In: Shapiro PY, Atwood DA (eds) ACS Symposium Series Nr. 822, pp 154–167
23. Vollet J, Hartig JR, Schnöckel H (2004) Angew Chem 116:3248–252
24. Vollet J, Hartig JR, Schnöckel H (2004) Angew Chem Int Ed 43:3186–3189
25. Jadzinsky PD, Calero G, Ackerson CJ, Bushnell DA, Kornberg RD (2007) Science 318: 430–433
26. Schnöckel H, Schnepf A, Whetten RL, Schenk C, Henke P (2011) Z Anorg Allg Chem 637: 15–23
27. Schmid G, Boese R, Pfeil R, Bandermann F, Calis GHM, van der Velden JWA (1981) Chem Ber 114:3634–3642
28. Qian H, Zhu Y, Jin R (2012) Proc Natl Acad Sci U S A 109:696–700
29. Lechtken A, Neiss C, Kappes MM, Schooss D (2009) Phys Chem Chem Phys 11:4344–4350
30. Oger E, Kelting R, Weis P, Lechtken A, Schooss D, Crawford NRM, Ahlrichs R, Kappes MM (2009) J Chem Phys 130:124305-1–124305-10
31. Li G, Jin R (2013) Acc Chem Res 46:1749–1758

32. Jin R (2015) Nanoscale 7:1549–1565
33. Klemp C, Bruns M, Gauss J, Häusermann U, Stößer G, van Wüllen L, Jansen M, Schnöckel H (2001) J Am Chem Soc 123:9099–9106
34. Schulte O, Holzapfel WB (1997) Phys Rev B 55:8122–8128
35. Wiberg N, Wiberg E, Holleman A (eds) (2007) Holleman-Wiberg Lehrbuch der Anorganischen Chemie, 102nd edn. de Gruyter & Co, Berlin, pp 1002–1041
36. Villars P (1997) Pearson's handbook of crystallographic data for intermetallic phases, Desk Edition. ASM International, Materials Park
37. Nelmes RJ, McMahon MI, Wright NG, Allan DR, Loveday JS (1993) Phys Rev B 48: 9883–9886
38. Kasper JS, Richards SM (1964) Acta Crystallogr 17:752–755
39. Guloy AM, Ramlau R, Tang Z, Schnelle W, Baitinger M, Grin Y (2006) Nature 443:320–323
40. Armatas GS, Kanatzidis MG (2006) Nature 441:1122–1125
41. Sun D, Riley AE, Cadby AJ, Richmann EK, Korlann SD, Tolbert SH (2006) Nature 441: 1126–1130
42. Barnett JD, Bean VE, Hall HT (1966) J Appl Phys 37:875–877
43. Desgreniers S, Vohra YK, Ruoff AL (1989) Phys Rev B 39:10360
44. Wiberg N, Wiberg E, Holleman A (eds) (2007) Holleman-Wiberg Lehrbuch der Anorganischen Chemie. de Gruyter & Co, Berlin, pp 1637–1642
45. Schmid G (1990) Inorg Synth 27:214–218
46. Heinecke CL, Ni TW, Malola S, Mäkinen V, Wong OA, Häkkinen H, Ackerson CJ (2012) J Am Chem Soc 134:13316–13322
47. Dass A, Theivendran S, Nimmala PR, Kumara C, Jupally VJ, Fortunelli A, Sementa L, Barcaro G, Zuo X, Noll BC (2015) J Am Chem Soc 137:4610–4613
48. Sekiguchi A, Ishida Y, Kabe Y, Ichinohe M (2002) J Am Chem Soc 124:8776–8777
49. Richards AF, Hope H, Power PP (2003) Angew Chem 115:4205–4208
50. Richards AF, Hope H, Power PP (2003) Angew Chem Int Ed 42:4071–4074
51. Dohmeier C, Loos D, Schnöckel H (1996) Angew Chem 108:141–161
52. Dohmeier C, Loos D, Schnöckel H (1996) Angew Chem Int Ed Engl 35:129–149
53. Timms PL (1976) Cryochemistry. Wiley, New York, pp 62–36
54. Schnöckel H, Schnepf A (2001) Adv Organomet Chem 47:235–281
55. Köppe R, Schnepf A (2002) Z Anorg All Chem 628:2914–2918
56. Ozin GA, Moskovits M (1976) Cryochemistry. Wiley, New York
57. Schnöckel H, Schnepf A (2011) In: Aldridge S, Downs AJ (eds) The group 13 metals aluminium, gallium, indium and thallium. Wiley-VCH, Weinheim, pp 402–487
58. Schnöckel H (2010) Chem Rev 110:4125–4163
59. Li XW, Pennington WT, Robinson GH (1995) J Am Chem Soc 117:7578–7579
60. Purath A, Köppe R, Schnöckel H (1999) Chem Commun 1933–1934
61. Köhnlein H, Stößer G, Baum E, Möllhausen E, Huniar U, Schnöckel H (2000) Angew Chem 112:828–830
62. Köhnlein H, Stößer G, Baum E, Möllhausen E, Huniar U, Schnöckel H (2000) Angew Chem Int Ed 39:799–801
63. Köhnlein H, Purath A, Klemp C, Baum E, Krossing I, Stösser G, Schnöckel H (2001) Inorg Chem 40:4830–4838
64. Ecker A, Weckert E, Schnöckel H (1997) Nature 387:379–381
65. Yi JY (2000) Phys Rev B 61:7277–7279
66. Köhnlein H, Schnöckel H (2002) Polyhedron 21:489–501
67. Chen Y, Zeng C, Liu C, Kirschbaum K, Gayathri C, Gil RR, Rosi NL, Jin R (2015) J Am Chem Soc 137:10076–10079
68. Foresmann JB, Keith TA, Wiberg KB, Snoonian J, Frisch MJ (1996) J Phys Chem 100: 16098–16104
69. Mocker M, Robl C, Schnöckel H (1994) Angew Chem 106:1860–1861
70. Mocker M, Robl C, Schnöckel H (1994) Angew Chem Int Ed Engl 33:1754–1755

71. Ecker A, Schnöckel H (1996) Z Anorg Allg Chem 622:149–152
72. Ecker A, Schnöckel H (1998) Z Anorg Allg Chem 624:813–816
73. Klemp C, Köppe R, Weckert E, Schnöckel H (1999) Angew Chem 111:1851–1855
74. Klemp C, Köppe R, Weckert E, Schnöckel H (1999) Angew Chem Int Ed 38:1739–1743
75. Hiller W, Klinkhammer KW, Uhl W, Wagner J (1991) Angew Chem 103:182–183
76. Hiller W, Klinkhammer KW, Uhl W, Wagner J (1991) Angew Chem Int Ed Engl 30:179–180
77. Vollet J, Burgert R, Schnöckel H (2005) Angew Chem 117:7117–7121
78. Vollet J, Burgert R, Schnöckel H (2005) Angew Chem Int Ed 44:6956–6960
79. Wade K (1976) Adv Inorg Chem Radiochem 18:1
80. Huber M, Henke P, Schnöckel H (2009) Chem Eur J 15:12180–12183
81. Schnepf A, Stößer G, Schnöckel H (2000) Z Anorg Allg Chem 626:1676–1680
82. Dohmeier C, Robl C, Tacke M, Schnöckel H (1991) Angew Chem 103:594–595
83. Dohmeier C, Robl C, Tacke M, Schnöckel H (1991) Angew Chem Int Ed Engl 30:564–565
84. Donchev A, Schnepf A, Stößer G, Baum E, Schnöckel H, Blank T, Wiberg N (2001) Chemistry 7:3348–3353
85. Steiner J, Schnöckel H (2006) Chemistry 12:5429–5433
86. Schnepf A, Stößer G, Schnöckel H (2000) J Am Chem Soc 122:9178–9181
87. Schnepf A, Weckert E, Linti G, Schnöckel H (1999) Angew Chem 111:3578–3581
88. Schnepf A, Weckert E, Linti G, Schnöckel H (1999) Angew Chem Int Ed 38:3381–3383
89. Linti G, Rodig A (2000) Chem Commun 127–128
90. Schnepf A, Stößer G, Schnöckel H (2002) Angew Chem 114:1959–1962
91. Schnepf A, Stößer G, Schnöckel H (2002) Angew Chem Int Ed 41:1882–1884
92. Schnepf A, Köppe R, Weckert E, Schnöckel H (2004) Chemistry 10:1977–1981
93. Duan T, Baum E, Burgert R, Schnöckel H (2004) Angew Chem 116:3252–32555
94. Duan T, Baum E, Burgert R, Schnöckel H (2004) Angew Chem Int Ed 43:3190–3192
95. Rodig A, Linti G (2000) Angew Chem 112:3076–3078
96. Rodig A, Linti G (2000) Angew Chem Int Ed 39:2952–2954
97. Schnepf A, Köppe R, Schnöckel H (2001) Angew Chem 113:1287–1289
98. Schnepf A, Köppe R, Schnöckel H (2001) Angew Chem Int Ed 40:1241–1243
99. Köppe R, Schnöckel H (2000) Z Anorg Allg Chem 626:1095–1099
100. Scheer E, Agrait N, Cuevas JC, Yeyati AL, Ludoph B, Martin-Rodero A, Bollinger GR, van Ruitenbeek JM, Urbina C (1998) Nature 394:154–157
101. Hicks J, Underhill EJ, Kefalidis CE, Maron L, Jones C (2015) Angew Chem 127: 10138–10142
102. Hicks J, Underhill EJ, Kefalidis CE, Maron L, Jones C (2015) Angew Chem Int Ed 54: 10000–10004
103. Schnepf A, Stößer G, Köppe R, Schnöckel H (2000) Angew Chem 112:1709–1711
104. Schnepf A, Stößer G, Köppe R, Schnöckel H (2000) Angew Chem Int Ed 39:1637–1639
105. Wiberg N, Blank T, Nöth H, Ponikwar W (1999) Angew Chem 111:887–890
106. Wiberg N, Blank T, Nöth H, Ponikwar W (1999) Angew Chem Int Ed Engl 38:839–841
107. Steiner J, Stößer G, Schnöckel H (2003) Angew Chem 115:2016–2019
108. Steiner J, Stößer G, Schnöckel H (2003) Angew Chem Int Ed 42:1971–1974
109. Steiner J, Stößer G, Schnöckel H (2004) Angew Chem 116:305–309
110. Steiner J, Stößer G, Schnöckel H (2004) Angew Chem Int Ed 43:302–305
111. Protchenko AV, Dange D, Blake MP, Schwarz AD, Jones C, Mountford P, Aldridge S (2014) J Am Chem Soc 136:10902–10905
112. Weiss K, Schnöckel H (2003) Z Anorg Allg Chem 629:1175–1183
113. Weiss K, Köppe R, Schnöckel H (2002) Int J Mass Spectrom 214:383–395
114. Brack M (1993) Rev Mod Phys 65:677–732
115. Martin TP (1996) Phys Rep 273:199–241
116. de Heer WA (1993) Rev Mod Phys 65:611–676
117. Green MLH, Mountford P, Smout G, Speel S (1990) Polyhedron 22:2763–2765

118. Fehlner T, Halet JF, Saillard JY (2007) Molecular Clusters. Cambridge University Press, Cambridge, pp 73–76
119. Schnepf A, Schnöckel H (2001) Angew Chem 113:734–737
120. Schnepf A, Schnöckel H (2001) Angew Chem Int Ed 40:712–715
121. Su J, Li XW, Crittendon RC, Robinson GH (1997) J Am Chem Soc 119:5471
122. Schnepf A, Jee B, Schnöckel H, Weckert E, Meents A, Lübbert D, Herrling E, Pilawa B (2003) Inorg Chem 42:7731–7733
123. Mednikov EG, Jewell MC, Dahl LF (2007) J Am Chem Soc 129:11619–11630
124. Bakharev ON, Bono D, Brom HB, Schnepf A, Schnöckel H, de Jongh LJ (2006) Phys Rev Lett 96:117002/1–117002/4
125. Hagel J, Kelemen MT, Fischer G, Pilawa B, Wosnitza J, Dormann E, Löhneysen HV, Schnepf A, Schnöckel H, Neisel U, Beck J (2002) J Low Temp Phys 129:13–142
126. Bono D, Bakharev ON, Schnepf A, Hartig J, Schnöckel H, de Jongh LJ (2007) Z Anorg Allg Chem 633:2173–2177
127. Bono D, Schnepf A, Hartig J, Schnöckel H, Nieuwenhuys GJ, Amato A, de Jongh LJ (2006) Phys Rev Lett 97:077601/1–077601/4
128. Bakharev ON, Zelders N, Brom HB, Schnepf A, Schnöckel H, de Jongh LJ (2003) Eur Phys J D 24:101–104
129. Buckel W, Kleiner R (2013) Superconductivity: fundamentals and applications, 7th edn. Wiley-VCH, Weinheim
130. Brynda M, Herber R, Hitchcock PB, Lappert MF, Nowik I, Power PP, Protchenko AV, Ruzicka A, Steiner J (2006) Angew Chem 118:4439–4443
131. Brynda M, Herber R, Hitchcock PB, Lappert MF, Nowik I, Power PP, Protchenko AV, Ruzicka A, Steiner J (2006) Angew Chem Int Ed 45:4333–4337
132. Scharfe S, Kraus F, Stegmaier S, Schier A, Fässler TF (2011) Angew Chem 123:3712–3754
133. Scharfe S, Kraus F, Stegmaier S, Schier A, Fässler TF (2011) Angew Chem Int Ed 50: 3630–3670
134. Sevov SC, Goicoechea JM (2006) Organometallics 25:5678–5692
135. Li F, Sevov SC (2012) Inorg Chem 51:2706–2708
136. Prabusankar G, Kempter A, Gemel C, Schröter MK, Fischer RA (2008) Angew Chem 120: 7344–7347
137. Richards AF, Brynda M, Olmstead MM, Power PP (2004) Organometallics 23:2841
138. Gordon MS, Nguyen KA, Carroll MT (1991) Polyhedron 10:1247
139. Grützmacher H, Breher F (2002) Angew Chem 114:4178
140. Grützmacher H, Breher F (2002) Angew Chem Int Ed 41:4006
141. Ito Y, Lee VY, Gornitzka H, Goedecke C, Frenking G, Sekiguchi A (2013) J Am Chem Soc 135:6770–6773
142. Lee VY, Ito Y, Gapurenko OA, Sekiguchi A, Minkin VL, Minyaev RM, Gornitzka H (2015) Angew Chem 127:5746–5749
143. Lee VY, Ito Y, Gapurenko OA, Sekiguchi A, Minkin VL, Minyaev RM, Gornitzka H (2015) Angew Chem Int Ed 54:5654–5657
144. Schrenk C, Kubas A, Fink K, Schnepf A (2011) Angew Chem 123:7411–7415
145. Schrenk C, Kubas A, Fink K, Schnepf A (2011) Angew Chem Int Ed 50:7237–7277
146. Power PP (2010) Nature 463:171–177
147. King RB, Silaghi-Dumitrescu I, Kun A (2002) J Chem Soc Dalton Trans 3999
148. Wrackmeyer B (2008) In: Davies AG, Gielen M, Pannell KH, Tiekink ERT (eds) Tin Chemistry. Wiley-VCH, Weinheim, pp 17–52
149. Rivard E, Steiner J, Fettinger JC, Giuliani JR, Augustine MP, Power PP (2007) Chem Commun 4919–4921
150. Prabusankar G, Kempter A, Gemel C, Schröter MK, Fischer RA (2008) Angew Chem Int Ed 47:7234–7237
151. Fischer G, Huch V, Mayer P, Vasisht SK, Veith M, Wiberg N (2005) Angew Chem 117:8096

152. Fischer G, Huch V, Mayer P, Vasisht SK, Veith M, Wiberg N (2005) Angew Chem Int Ed 44:7884
153. Unno M (2014) Struct Bond 156:49–84
154. Tanaka M, Sekiguchi A (2005) Angew Chem 117:5971
155. Tanaka M, Sekiguchi A (2005) Angew Chem Int Ed 44:5821
156. Schnepf A, Köppe R (2003) Angew Chem 115:940
157. Schnepf A, Köppe R (2003) Angew Chem Int Ed 42:911
158. Schnepf A, Drost C (2005) Dalton Trans 20:3277
159. Sekiguchi A, Fukawa T, Lee VY, Nakamoto M, Ichinohe M (2003) Angew Chem 115: 1175–1177
160. Sekiguchi A, Fukawa T, Lee VY, Nakamoto M, Ichinohe M (2003) Angew Chem Int Ed 42: 1143–1145
161. Schenk C, Drost C, Schnepf A (2009) Dalton Trans 5:773–776
162. Breher F (2007) Coord Chem Rev 251:1007–1043
163. Wiberg N, Lerner HW, Wagner S, Nöth H, Seifert T (1999) Z Naturforsch 54B:877–880
164. Eichler BE, Power PP (2001) Angew Chem 113:818–819
165. Eichler BE, Power PP (2001) Angew Chem Int Ed 40:796–797
166. Vasko P, Wang S, Tuononen HM, Power PP (2015) Angew Chem 127:3873–3876
167. Vasko P, Wang S, Tuononen HM, Power PP (2015) Angew Chem Int Ed 54:3802–3805
168. Schnepf A (2003) Angew Chem Int Ed 115:2728–2729
169. Schnepf A (2003) Angew Chem Int Ed 42:2624–2625
170. Richardson AF, Eichler BE, Brynda M, Olmstead MM, Power PP (2005) Angew Chem 117: 2602–2605
171. Richardson AF, Eichler BE, Brynda M, Olmstead MM, Power PP (2005) Angew Chem Int Ed 44:2546–2549
172. Schrenk C, Neumaier M, Schnepf A (2012) Inorg Chem 51:3989–3995
173. Schrenk C, Winter F, Pöttgen R, Schnepf A (2012) Inorg Chem 51:8583–8588
174. Ugrinov A, Sevov SC (2002) J Am Chem Soc 124:2442–2443
175. Ugrinov A, Sevov SC (2003) J Am Chem Soc 125:14059–14064
176. Ugrinov A, Sevov SC (2004) Chem Eur J 10:3727–3733
177. Hull MW, Sevov SC (2007) Angew Chem 119:6815–6818
178. Hull MW, Sevov SC (2007) Angew Chem Int Ed 46:6695–6698
179. Hull MW, Sevov SC (2009) J Am Chem Soc 131:9026–9037
180. O'Neill ME, Wade K (1983) Polyhedron 2:963–966
181. Schenk C, Schnepf A (2007) Angew Chem 119:5408–5410
182. Schenk C, Schnepf A (2007) Angew Chem Int Ed 46:5314–5316
183. Schenk C, Henke F, Santigo G, Krossing I, Schnepf A (2008) Dalton Trans 33:4436–4441
184. Henke F, Schenk C, Schnepf A (2009) Dalton Trans 42:9141–9145
185. Li F, Sevov SC (2015) Inorg Chem 54:8121–8125
186. Schnepf A (2008) Eur J Inorg Chem 1007–1018
187. Schenk C, Schnepf A (2009) Chem Commun 22:3208–3210
188. Henke F, Schenk C, Schnepf A (2011) Dalton Trans 40:6704–6710
189. Li F, Munoz-Castro A, Sevov SC (2012) Angew Chem 124:8709–8712
190. Li F, Munoz-Castro A, Sevov SC (2012) Angew Chem Int Ed 51:8581–8584
191. Klinger M, Schenk C, Henke F, Clayborne PA, Schnepf A, Unterreiner AN (2015) Chem Commun 51:12278–12281
192. Koch K, Schnepf A, Schnöckel H (2006) Z Anorg All Chem 632:1710–1716
193. Schenk C, Henke F, Neumaier M, Olzmann M, Schnöckel H, Schnepf A (2010) Z Anorg Allg Chem 636:1173–1182
194. Schnepf A, Schenk C (2006) Angew Chem 118:5499–5502
195. Schnepf A, Schenk C (2006) Angew Chem Int Ed 45:5373–5376
196. Schnepf A (2007) Chem Commun 192–194

197. Spiekermann A, Hoffmann SD, Fässler TF, Krossing I, Preiss U (2007) Angew Chem 119: 5404–5407
198. Spiekermann A, Hoffmann SD, Fässler TF, Krossing I, Preiss U (2007) Angew Chem Int Ed 46:5310–5313
199. Rocaniere C, Laval JP, Dehaudt P, Gaudreau B, Chotard A, Suard E (2004) J Solid State Chem 177:1758–1767
200. Schrenk C, Schellenberg I, Pöttgen R, Schnepf A (2010) Dalton Trans 39:1872–1876
201. Schrenk C, Helmlinger J, Schnepf A (2012) Z Anorg Allg Chem 638:589–593
202. Schrenk C, Winter F, Pöttgen R, Schnepf A (2015) Chemistry 21:2992–2997
203. Menoni CS, Hu JZ, Spain IL (1986) Phys Rev B 34:362–368
204. Schwarz U (2002) Z Krstallogr 219:376–390
205. Lechtken A, Drebov N, Ahlrichs R, Kappes MM, Schooss D (2010) J Chem Phys 132:211102
206. Li H, Chen W, Wang F, Sun Q, Guo ZX, Jia Y (2013) Phys Chem Chem Phys 15:1813–1836
207. Schrenk C, Gerke B, Pöttgen R, Clayborne A, Schnepf A (2015) Chemistry 21:8222–8228
208. Klinkhammer KW, Xiong Y, Yao S (2004) Angew Chem 116:6328–6331
209. Klinkhammer KW, Xiong Y, Yao S (2004) Angew Chem Int Ed 43:6202–6204
210. Schrenk C, Schnepf A (2013) Main Group Metal Chem 36:161–167
211. Linti G, Köstler W, Piotrowski H, Rodig A (1998) Angew Chem 110:2331–2333
212. Linti G, Köstler W, Piotrowski H, Rodig A (1998) Angew Chem Int Ed 37:2209–2211
213. Vollet J, Stösser G, Schnöckel H (2007) Inorg Chim Acta 360:1298–1304
214. Schenk C, Henke F, Schnepf A (2013) Angew Chem 125:1883–1887
215. Schenk C, Henke F, Schnepf A (2013) Angew Chem Int Ed 52:1834–1838
216. Schnepf A (2010) New J Chem 34:2079–2092
217. Schenk C, Kracke A, Fink K, Kubas A, Klopper W, Neumaier M, Schnöckel H, Schnepf A (2011) J Am Chem Soc 133:2518–2524
218. Schenk C, Schnepf A (2008) Chem Commun 4643–4645
219. Prayongpan P, Stripe DS, Greenlief CM (2008) Surf Sci 602:571–578
220. Harikumar KR, Leung L, McNab IR, Polanyi JC, Lin H, Hofer WA (2009) Nat Chem 1: 716–721
221. Kim SJ, Hoffman SD, Fässler TF (2007) Angew Chem 119:3205–3209
222. Kim SJ, Hoffman SD, Fässler TF (2007) Angew Chem Int Ed 46:3144–4148
223. Lips F, Clerac R, Dehnen S (2011) Angew Chem 123:991–995
224. Lips F, Clerac R, Dehnen S (2002) Angew Chem Int Ed 50:960–964
225. Schebarchov D, Gaston N (2011) Phys Chem Chem Phys 13:21109–21115
226. Purath A, Dohmeier C, Ecker A, Köppe R, Krautscheid H, Schnöckel H, Ahlrichs R, Stoermer C, Friedrich J, Jutzi P (2000) J Am Chem Soc 122:6955–6959
227. Jemmis ED, Balakrishnarajan MM, Pancharatna PD (2002) Chem Rev 102:93–144
228. Esenturk EN, Fettinger JC, Eichhorn BW (2006) J Am Chem Soc 128:12–13

Struct Bond (2017) 174: 201–268
DOI: 10.1007/430_2016_4

Published online: 21 July 2016

Metal Oxido Clusters of Group 13–15 Elements

Michael Mehring

Dedicated to Professor Hansgeorg Schnöckel on the occasion of his 75th birthday.

Abstract Solution-based approaches towards metal oxides are based on hydrolysis and condensation processes starting from precursor solutions. Metal oxido clusters represent important intermediates within these processes, and a detailed understanding of their (structural) chemistry adds to the knowledge about how to control structure, particle size, and morphology of the final hydrolysis products. The present review focuses on structural aspects of metal oxido clusters which are composed of more than ten metal atoms and contain at least one oxido ligand within the cluster structure, however where necessary smaller clusters and hydroxido clusters are also included. In addition to fully inorganic metal oxido clusters, those stabilized by organic ligands and in addition selected organometallic examples are also discussed. The group 13–15 elements Al, Ga, In, Ge, Sn, Pb, Sb, and Bi are considered in this review, complemented by some examples of Ce, U, and Pu. Large metal oxido clusters of the latter with diameters of about 2 nm show remarkable resemblance of their metal oxido core structures with those of bismuth, which is attributed to the fact that the trivalent and tetravalent metal oxides of these elements tend to form structures which can be deduced from the fluorite structure type. Intriguing examples are represented by various bismuth oxido clusters which exhibit a $\{Bi_{38}O_{45}\}$ core structure, stabilized by a variety of ligands at the periphery. For gallium, two large metal oxido clusters have been reported which also show an interesting relationship to a parent gallium oxide, whereas for aluminum two tridecanuclear cluster types dominate the literature, the metal hydroxido clusters and cationic Keggin-type ions, neither of which is related to structures of

M. Mehring (✉)
Technische Universität Chemnitz, Institut für Chemie, Koordinationschemie, 09107 Chemnitz, Germany
e-mail: michael.mehring@chemie.tu-chemnitz.de

aluminum oxide. However, the structural chemistry of the group 13–15 metal oxido clusters is quite different from the heteropolyanionic nature of polyoxometalates and compared to the latter is often less intensely addressed. Thus, the review provides an overview on the growing number of large group 13–15 metal oxido clusters including information on reported synthesis conditions, yields, and analytics.

Keywords Condensation • Hydrolysis • Main group elements • Metal oxido clusters • Nucleation • Structure

Contents

1 Introduction

Metal oxides are among the most important materials with regard to technological and industrial applications, and there is still growing interest in this versatile class of compounds. Many metal oxides exhibit interesting physical properties in combination with thermal stability, hardness, and chemical resistance and thus are used in the fields of optics, magnetism, or electrics [1–4]. The chemical resistance is also a key point for the widespread use of metal oxides as (porous) catalyst supports in the chemical and petrochemical industry [5]. In addition metal oxides might also act as catalytically active components themselves or catalyst promoters. Semiconducting metal oxides have been reported to be the most efficient photocatalysts for water splitting and water purification [6, 7], and they play an important role for the microelectronics industry [2–4]. They serve as dielectric materials, miniaturized batteries, capacitors, sensors, and actuators.

The accelerated development in the abovementioned emerging applications is directly linked to the access to metal oxides of different size, shape, and morphology, and thus control of micro- and nanostructure formation as well as control of phase formation and polymorphism is an important challenge. A variety of synthetic techniques is available to address this challenge, which is often referred to as "controlled fabrication" and "synthesis by design" of well-defined structures, particles, and thin films with dimensions on the micrometer down to the nanometer scale [2, 8]. Among these approaches for synthesis and structuring, physical vapor deposition (PVD), chemical vapor deposition (CVD), and atomic layer deposition (ALD) have been shown to be very versatile, but especially with regard to

commercial applications on larger-scale solution-based processes at ambient temperatures without the need for high vacuum are promising alternatives [3, 7, 9, 10]. Methods such as (co)precipitation, sol–gel processes and spray deposition are striking examples [1, 8, 11]. Solution-based approaches offer various ways to manipulate the deposition process chemically, and it becomes possible to overcome the problem of thermodynamic control which is inherent for high-temperature solid-state approaches toward metal oxides. Metastable phases become accessible, and texture control is feasible for many systems starting from precursor solutions [8]. The key point is the control of the evolution of network structures and thus of the precipitation process. The latter and even colloid formation both are results of hydrolysis and inorganic polycondensation. Hydrolysis of metal ions and inorganic compounds and condensation of hydroxylated species determine the nucleation and growth of (nano)particles and thus determine final properties such as size, size distribution, shape, morphology, etc. Having this knowledge in mind, the first steps of hydrolysis starting from hydrated metal cations have been intensely investigated on a molecular scale for decades. In addition nucleation and growth have been thoroughly studied, and nucleation theories were developed, but often with regard to coarser models without a look at the molecular scale. A detailed understanding for structure formation after the first steps of hydrolysis and condensation but prior to formation of solid nanoparticles is still in its infancy for metal oxides. The gap is certainly filled by a complex solution chemistry of metal oxido clusters, which up to now is still poorly understood. Even isolated polymetallic oxido clusters are difficult to analyze due to several reasons, e.g., ligand dynamics and equilibria in solution depending on concentration, stability, solvation, and solubility or simply the lack of analytical techniques for unambiguous structure elucidation. Analytical techniques such as NMR, IR, ESI-mass spectrometry, extended X-ray absorption fine-edge spectroscopy, diffraction techniques, or analytics for molecular weight determination were used for characterization, but are difficult to interpret and often inconclusive. There is a need to identify possible structural motifs unambiguously first in order to develop model systems which are suited to support assumptions made based on analytics from solution. Therefore at the current stage isolation, characterization and structure elucidation in the solid state of large metal oxido clusters loom large in speciation in hydrolysis processes. A more detailed knowledge about the structure and chemistry of metal oxido clusters will be beneficial for the understanding of hydrolysis processes and the development of novel synthetic approaches toward metal oxide polymorphs with defined size, shape, and texture. In addition detailed knowledge on metal oxido clusters might also be helpful to better understand geological processes. This holds true for certainly all metal oxido clusters, and only a small section will be covered in this essay on the group 13 elements Al, Ga, and In; the group 14 elements Ge, Sn, and Pb; and the group 15 elements Sb and Bi. The main focus will be given to molecular structures of metal oxido clusters with at least ten metal atoms and at least one oxido group being present within the cluster assembly. In addition to fully inorganic metal oxido clusters, those stabilized by organic ligands as well as examples bearing metal–carbon bonds are included. Examples of metal oxido clusters that are part of

extended network structures are not covered. Most of the clusters addressed here are either neutral or cationic in nature and thus differ from the extensively studied and reviewed class of anionic polyoxometalates (POMs). An enormous number of POMs were synthesized and characterized [12–16], and their structural characterization revealed three types of structures that dominate the chemistry of these heteropolyanions, the Keggin-type $[XM_{12}O_{40}]^{n-}$, the Wells–Dawson-type $[X_2M_{18}O_{62}]^{n-}$, and the Anderson-type $[XM_6O_{24}]^{n-}$ structures (M, metal; X, metal or heteroelement). Cationic and neutral metal oxido clusters have been addressed to a lesser extent, but play a dominant role in the chemistry of metal oxido clusters of main group elements. In the following chapters, an overview on main group oxido clusters of group 13–15 elements will be presented.

2 Aluminum, Gallium, and Indium

The aqueous solution chemistry of the trivalent group 13 metal cations aluminum, gallium, and indium has been studied intensively over the past decades. It was demonstrated that the hydrolysis and condensation behavior of these elements are very complex. However, the high natural abundance of aluminum on the one hand and the technological importance together with environmental issues on the other hand made this element the most widely studied one among the group 13 elements. Aluminum does not belong to the essential elements for humans, but has great impact on health risks. Its widespread industrial use, e.g., in form of the metal oxide as catalyst support, gate dielectric, and abrasive, as inorganic additives in cosmetics, or as metal for packaging and construction of lightweight component parts, leads to the release of large quantities of the element to the environment including bioavailable forms, which is a current severe human health risk [17]. Several recent review articles summarize different facets of aluminum chemistry with regard to hydrolysis and condensation processes including the chemistry of rather small coordination compounds but also that of metal oxido clusters [18–21]. Another important industrial field of aluminum is connected with organometallic compounds. Their hydrolysis products are represented by alkylalumoxanes, the hydrolysis products of trialkylaluminum compounds, which, for example, serve as polymerization catalysts [22, 23]. The most prominent example is methylalumoxane (MAO), which is part of very efficient catalysts used for the polymerization of ethylene and propylene [24]. The nature and structure of the active catalysts are quite difficult to analyze and often unknown, but a large number of oligomeric model compounds have been investigated [20]. By contrast the number of isolated and fully characterized examples of distinct metal oxido alkoxides is rather small, although aluminum alkoxides have found widespread applications, for example, in sol–gel chemistry.

In comparison to studies on aluminum, the heavier group 13 elements gallium and indium have been studied and reviewed to a much lesser extent [19, 21], which presumably is a result of lower natural abundance and limited use in technological

applications on a large scale. This might change drastically in the future if the photovoltaic industry will establish thin film solar cells based on copper–indium–gallium selenide, but already nowadays an increasing demand for the metal oxides of indium and gallium with regard to the fabrication of nanostructured semiconductors is noticed.

The present review is focused on large metal oxido clusters with a minimum of ten metals (Tables 1 and 2); however, a look to the basic structural moieties of some smaller metal oxido clusters is essential for a better understanding of the general *Aufbau principles*. The coordination environment for the oxido ligands in clusters is typically μ_3-O, whereas the μ-O coordination is quite rarely found (Fig. 1). Larger clusters, especially with relation to the formation of nanoclusters and finally the solid metal oxide/hydroxides which are obtained upon hydrolysis/condensation, should in addition contain μ_4-oxido ligands as is observed in the Keggin-type $\{Al_{13}\}$ clusters [18]. It is worth to note that the μ_4-coordination at the oxido ligand is often significantly distorted in metal oxido alkoxides, whereas almost ideal coordination is present as basic structural unit in the center of Keggin-type clusters.

The number of fully characterized examples of large metal oxido clusters of group 13 is quite limited so far. Going from aluminum and gallium to indium, one might expect a growing extent of examples with oxygen of higher coordination number due to the larger size of the cation and thus larger cavities within the clusters. Intriguing examples which demonstrate this size effect are the adamantane-type structures $[R_4M_4(\mu\text{-}O)_2(\mu\text{-}OH)_4]$ [M=Al, Ga; R=C(SiMe$_3$)$_3$] [56] and $[R_4In_4(\mu_4\text{-}O)(\mu\text{-}OH)_6]$ [R=C(SiMe$_3$)$_3$] [57], which are very close in structure with the four metal atoms occupying the vertices of a tetrahedron but only the larger indium allows for the incorporation of an μ_4-oxido ligand within the tetrahedral cavity (Fig. 2). Noteworthy, an adamantane-type structural motif was also observed in compounds such as $[\{Ge_4(\mu\text{-}O)_2(\mu\text{-}OH)_4\}\{W(CO)_5\}_4]$ [58] and $[(p\text{-}ClC_6H_4Sb)_4(\mu\text{-}O_6)(Hnaphpz)_4]$ (H_2naphpz=2-[1H-pyrazol-5(3)-yl]naphthalene-1-ol) [59] and represents a quite common structural unit in metal oxido cluster chemistry.

Several pentanuclear cluster compounds of the general type $[(RIn)_5(\mu_5\text{-}O)(\mu\text{-}OR')_8]$ (R,R'=alkyl) with a central μ_5-oxido ligand were reported [34, 60], which is a typical structure for clusters with trivalent metals (Figs. 1 and 3). Other examples of this type include the metal oxido clusters $[M_5(\mu_5\text{-}O)(\mu\text{-}OR)_8X_5]$ (R=alkyl, X=alkoxide, halide, siloxide) for metals such as Fe, Sc, Y, and La [61–70] and are also documented for aluminum and gallium, e.g., $[(i\text{BuOAl})_5(\mu_5\text{-}O)(\mu\text{-}Oi\text{Bu})_8]$ [71], $[(FAl)_5(\mu_5\text{-}O)(\mu\text{-}Oi\text{Pr})_8]$ [32], $[(HAl)_5(\mu_5\text{-}O)(\mu\text{-}Ot\text{Bu})_8]$ [72], $[(HAl)_4(ClAl)(\mu_5\text{-}O)(\mu\text{-}Oi\text{Pr})_8]$ [73], and $[(ClGa)_5(\mu_5\text{-}O)(\mu\text{-}OEt)_8]$ (Fig. 3) [33]. The largest indium oxido cluster reported so far is the decanuclear $[(MeIn)_5(\mu_5\text{-}O)(OEt)_6(OH)_2]_2$, which is composed of two alkoxides with a basic pentanuclear cluster core, similar to those described above. The compound was obtained upon reaction of $InMe_3$ with ethanol and most likely provides $[(MeIn)_5(\mu_5\text{-}O)(OEt)_8]$ first, which hydrolyzes and finally dimerizes to give the decanuclear indium oxido cluster (Fig. 4) [34].

Table 1 Examples of aluminum and gallium oxido alkoxides with nuclearity above ten (excluding Keggin-type clusters). Synthesis conditions, isolated yield, and analytics are given

Compound	Synthesis	η/%	Analytics	References
$[Al_{10}(\mu_4\text{-}O)_2(\mu_3\text{-}O)_4(\mu\text{-}OiPr)_2(OiPr)_{16}(NH_3)_8]$	Ammonolysis of $Al(OiPr)_3$ in toluene in an ammonia flow	75	^{1}H-, ^{13}C-, ^{27}Al-NMR, IR, MS, XRD	[25]
$[(iBu_2Al)_6(iBuAl)_4(\mu_3\text{-}O)_6(\mu\text{-}H)_2]$	Thermolysis of $(iBu_2AlOAliBu_2)_2$	10	^{1}H-NMR, ^{27}Al MAS NMR, XRD	[26]
$[Al_{10}F_{16}(\mu_4\text{-}O)_2(\mu\text{-}OiPr)_{10}(py)_4](py)_{4.17}$	Reaction of $Al(OiPr)_3$ with HF in pyridine (py)	n.r.	XRD	[27]
$[Al_{11}(\mu_4\text{-}O)_2(\mu_3\text{-}O)_2(\mu\text{-}O)_2(\mu\text{-}OnPr)_{10}(\mu\text{-}OiPr)_2(\mu\text{-}ROH)_2(OiPr)_8(OR)]$ R=*i*Pr, *n*Pr	Reaction of $Al(OiPr)_3$ and $Ta(OiPr)_5$ in *i*PrOH and *n*PrOH, decomposition of bimetallic complexes	Low	EA, XRD	[28]
$[t\text{BuAl}(\mu_3\text{-}O)]_{12}$	Heating of $[(t\text{Bu})_2\text{Al(OH)}]$ in hexane	n.r.	EI-MS, ^{1}H-NMR	[22]
$[(t\text{BuGa})_{12}(\mu_3\text{-}O)_8(\mu\text{-}O)_2(\mu\text{-}OH)_4]$	$[t\text{Bu}_2\text{Ga(Spy)}]$ in toluene in an atmosphere of dry oxygen (H-Spy=2-mercaptopyridine)	70	^{1}H-NMR, IR, XRD	[29]
$[(\text{MeGa})_{12}(\mu_3\text{-}O)_8(\mu\text{-}OH)_6](B(C_6F_5)_4)_2(C_6H_5Cl)_2(H_2O)_2$	Reaction of $[t\text{BuC(N}i\text{Pr)}_2]\text{GaMe}_2$ with $(Ph_3C)[B(C_6F_5)_4]$ in benzene	n.r.	^{1}H-NMR, XRD	[30]
$[(\{o\text{-}C_6H_4OMe\}\text{Ga})_{12}(\mu_3\text{-}O)_8(\mu\text{-}O)_2(\mu\text{-}OH)_4]\ (thf)_4$	Hydrolysis of $[\text{Ga}(o\text{-}C_6H_4OMe)_3]_2$ (TMEDA) · 3 toluene in THF	n.r.	MS, XRD	[31]
$[(i\text{PrGa})_{12}(\mu_3\text{-}O)_8(\mu\text{-}O)_2(\mu\text{-}OH)_4](H_2O)_2$	Hydrolysis of $\text{Ga}i\text{Pr}_3$ in thf	n.r.	XRD	[31]
$[(\{p\text{-Tolyl}\}\text{Ga})_{12}(\mu_3\text{-}O)_8(\mu\text{-}OH)_6][\text{GaBr}_{4-n}(p\text{-tolyl})_n](thf)_6$ ($n = 1, 2$)	Hydrolysis of in situ-prepared $[\text{Ga}(p\text{-tolyl})_3]_2$	n.r.	MS, XRD	[31]
$[Al_{16}F_{20}(\mu_4\text{-}O)_4(\mu\text{-}OiPr)_{20}]$	Hydrolysis of $AlF_x(OiPr)_{3-x}$ in *i*PrOH with water	Low	XRD	[32]
$[Ga_{12}(\mu_4\text{-}O)_2(\mu_3\text{-}O)_5(\mu\text{-}OEt)_{10}Cl_{12}(py)_4]$	Reaction of $GaCl_3$ with NaOEt in toluene and addition of pyridine	n.r.	^{1}H-NMR, IR, MS, EA, XRD	[33]
$[(\text{MeIn})_{10}(\mu_5\text{-}O)_2(\mu_3\text{-}OEt)_4(\mu\text{-}OEt)_8(\mu_3\text{-}OH)_4](thf)_2$	Alcoholysis of $InMe_3$ with EtOH in thf (heating)	62	^{1}H-, ^{13}C-NMR, Mp, EA, IR, EI-MS, XRD	[34]

n.r. not reported

Table 2 Examples of Keggin-type clusters of gallium and aluminum. Synthesis conditions, isolated yield, analytics, and Keggin-type assignment are given

Compound	Synthesis	η/%	Analytics	Keggin-motif	References
$[Al_{12}(OH)_{14}(H_2O)_{12}Cl/F/AlO_4/Si_5O_{16}]$	Structure motif in the mineral zunyite	n.r.	XRD	α	[35, 36]
$(NH_4)_7[Al_{13}(\mu_4\text{-}O)_4(\mu\text{-}OH)_{24}(H_2O)_{12}](SO_4)_7(H_2O)_x$	Hydrolysis of $AlCl_3$ with $NH_{3(aq)}$ and $(NH_4)_2SO_4$ in water	n.r.	XRD	ε	[37]
$[Al_{13}(\mu_4\text{-}O)_4(\mu\text{-}OH)_{25}(H_2O)_{10}(SO_4)](SO_4)_2(H_2O)_{20}$	Hydrolysis of $AlCl_3$ with NaOH and Na_2SO_4 in water	n.r.	XRD	ε	[38]
$[Al_{13}(\mu_4\text{-}O)_4(\mu\text{-}OH)_{24}(H_2O)_{12}][Na(18\text{-crown-}6)(H_2O)_2L_2(H^+)_w]_{0.5}{}^{x-}[\{L(H^+)_y\}]_z(H_2O)_{29}$ ($x+z=7$) L=*p*-sulfonatocalix[4]arene	Hydrolysis of $AlCl_3$ with NaOH and addition of Na_4L and 18-crown-6 ether	65%	^{27}Al-NMR, XRD	ε	[39]
$Na[Al_{13}(\mu_4\text{-}O)_4(\mu\text{-}OH)_{24}(H_2O)_{12}](SO_4)_4(H_2O)_{19}$	Hydrolysis of $AlCl_3 \cdot 6\ H_2O$ in the presence of Na_2SO_4 in water	n.r.	XRD	δ	[40]
$Na[Al_{13}(\mu_4\text{-}O)_4(\mu\text{-}OH)_{24}(H_2O)_{12}](2,6\text{-NDS})_4(H_2O)_{13.5}$ 2,6-NDS: 2,6-napthalene disulfonate	Hydrolysis of $AlCl_3 \cdot 6\ H_2O$ with NaOH in water, heating at 80°C, addition of NDS	21%	^{27}Al MAS NMR, TGA, XRD	δ	[41]
$[Al_{13}(\mu_4\text{-}O)_4(\mu\text{-}OH)_{25}(H_2O)_{11}](SO_4)_3(H_2O)_{14}$	Hydrolysis of $AlCl_3 \cdot 6\ H_2O$ in the presence of glycine, addition of $Ca(OH)_2$, $CaCl_2 \cdot 2\ H_2O$, and glycine, 140–145°C for 6 days, H_2SO_4/Na_2SO_4	47–78%	^{27}Al liquid and solid NMR, ICP-OES, XRD	γ	[42]
$(pipzH_2)(H_3O)[Al_{15}(\mu_3\text{-}O)_4(\mu_3\text{-}OH)_6(\mu\text{-}OH)_{14}(hpdta)_4](pipz)(H_2O)_{41}$ pipz: piperazine; hpdta: 2-hydroxypropane-1,3-diamine-*N*,*N*,*N*′*N*′-tetraacetate	Hydrolysis of $Al(NO_3)_3 \cdot 9\ H_2O$ in the presence of H_5hpdta and piperazine in water	n.r.	EA, IR, XRD	Zeotype	[43]
$[Al_{26}(\mu_4\text{-}O)_8(\mu\text{-}OH)_{50}(H_2O)_{20}](2,6\text{-NDS})_6(H_2O)_{12.4}$	Hydrolysis of $AlCl_3 \cdot 6\ H_2O$ with NaOH in water, addition of NDS	4%	^{27}Al MAS NMR, XRD	2 × δ	[41]
$[Al_{30}(\mu_4\text{-}O)_8(\mu\text{-}OH)_{56}(H_2O)_{26}](2,6\text{-NDS})_8Cl_2(H_2O)_{40}$ 2,6-NDS: 2,6-napthalene disulfonate	Hydrolysis of $AlCl_3 \cdot 6\ H_2O$ with NaOH in water, addition of NDS	25%	^{27}Al MAS NMR, XRD	2 × δ	[41]

(continued)

Table 2 (continued)

Compound	Synthesis	η/%	Analytics	Keggin-motif	References
$[Al_{30}(\mu_4\text{-}O)_8(\mu\text{-}OH)_{56}(H_2O)_{24}](SO_4)_9$	Hydrolysis of $AlCl_3$, NaOH, and K_2SO_4 in water	n.r.	^{27}Al-NMR, XRD	2 × δ	[44]
$[Al_{32}(\mu_4\text{-}O)_8(\mu\text{-}OH)_{60}(H_2O)_{28}(SO_4)_2](SO_4)_7Cl_2(H_2O)_{30}$	Hydrolysis of $AlCl_3$, NaOH, and Na_2SO_4 in water	n.r.	XRD	2 × δ	[38]
$[(Al(IDA)H_2O)_2(Al_{30}(\mu_4\text{-}O)_8(\mu\text{-}OH)_{60}(H_2O)_{22})](2,6\text{-NDS})_4(SO_4)_2Cl_4(H_2O)_{40}$ IDA: iminodiacetate; 2,6-NDS: 2,6-napthalene disulfonate	Hydrolysis of $AlCl_3$ with NaOH in water, crystallization in the presence of NaIDA and NDS	23%	XRD	2 × δ	[45]
$[Al_{13}(\mu_3\text{-}OH)_6(\mu\text{-}OH)_{18}(H_2O)_{24}](NO_3)_{15}$	Hydrolysis of $Al(NO_3)_3 \cdot 9\ H_2O$ in the presence of $(nBu)_2NNO$ in MeOH	60%	TGA, PXRD, XRD	"Flat" Al_{13}	[46]
$Na[Ga(\mu_4\text{-}O)_4Al_{12}(\mu\text{-}OH)_{24}(H_2O)_{12}](SO_4)_4(H_2O)_{10}$	Hydrolysis of $AlCl_3$ and Ga with NaOH in water, addition of Na_2SO_4	n.r.	XRD	ε	[47, 48]
$[Ge(\mu_4\text{-}O)_4Al_{12}(\mu\text{-}OH)_{24}(H_2O)_{12}](SeO_4)_4(H_2O)_{14}$	Hydrolysis of $AlCl_3 \cdot 6\ H_2O$ with NaOH/GeO_2 in water, addition of Na_2SeO_4	n.r.	^{27}Al MAS NMR, XRD	ε	[49]
$[Ga_2Al_{18}(\mu_4\text{-}O)_8(\mu\text{-}OH)_{36}(H_2O)_{12}](2,7\text{-NDS})_4(H_2O)_{30.5}$ 2,7-NDS: 2,7-napthalene disulfonate	Hydrolysis of $AlCl_3 \cdot 6\ H_2O$ with NaOH in water, addition of $GaCl_3$, addition of NDS	30%	ESI-MS, EA, ^{71}Ga-NMR, XRD	2 × ε	[50]
$[W_2Al_{28}(\mu_4\text{-}O)_8(\mu_3\text{-}O)_4(\mu\text{-}O)_4O_2(\mu\text{-}OH)_{48}(H_2O)_{24}][H_2W_{12}O_{40}]_2(H_2O)_{55}$	Reaction of $[Al_{30}O_8(OH)_{56}(H_2O)_{26}](SO_4)_9$ with $Na_6H_2W_{12}O_{40}$	n.r.	EA,XRD	2 × δ	[51]
$[(Zn(NTA)H_2O)_2(Al(NTA)(\mu\text{-}OH)_2)_2(Al_{30}(\mu_4\text{-}O)_8(\mu_3\text{-}OH)_6(\mu\text{-}OH)_{54}(H_2O)_{20}](2,6\text{-NDS})_5(H_2O)_{64}$ 2,6-NDS: 2,6-napthalene disulfonate	Hydrolysis of $AlCl_3$ with NaOH in water, $ZnCl_2$, and NTA, crystallization in the presence of NDS	9%	SEM/EDX, ICP-OES, IR, XRD	2 × δ	[45]
$[Ga_{13}O_4(OH)_{24}(H_2O)_{12}]^{7+}$; chloride and nitrate solutions	Hydrolysis of $GaCl_3$ with NaOH in water	n.r.	^{71}Ga-NMR, EXAFS	ε	[52, 53]

$[Ga_{30}(\mu_4\text{-}O)_{12}(\mu_3\text{-}O)_4(\mu_3\text{-}OH)_4(\mu\text{-}OH)_{42}(H_2O)_{16}](2,6\text{-}NDS)_6$ 2,6-NDS: 2,6-napthalene disulfonate	Hydrolysis of $GaCl_3$ with NaOH in water, crystallization in the presence of NDS	n.r.	XRD	Subunit $\beta\text{-}Ga_2O_3$	[54]
$[Ga_{32}(\mu_4\text{-}O)_{12}(\mu_3\text{-}O)_8(\mu\text{-}O)_7(\mu\text{-}OH)_{39}(H_2O)_{20}](pyH\subset C_{36}H_{36}N_{24}O_{12})_3(NO_3)_6(H_2O)_{53}$ py: pyridine	Hydrolysis of $Ga(NO_3)_3 \cdot 8\ H_2O$ with Cucurbit[6]uril in water, pyridine	72%	XRD	Subunit $\beta\text{-}Ga_2O_3$	[55]

n.r. not reported

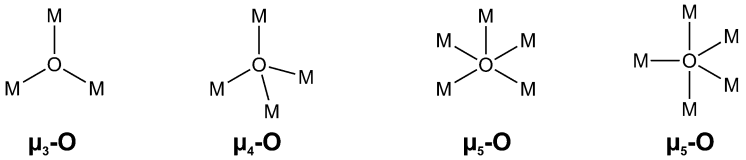

Fig. 1 Typical coordination geometries of oxido ligands as found in group 13 metal oxido clusters. The μ_4-O coordination is usually distorted, and μ_5-O coordination is typically found to be in between tetragonal pyramidal and trigonal bipyramidal

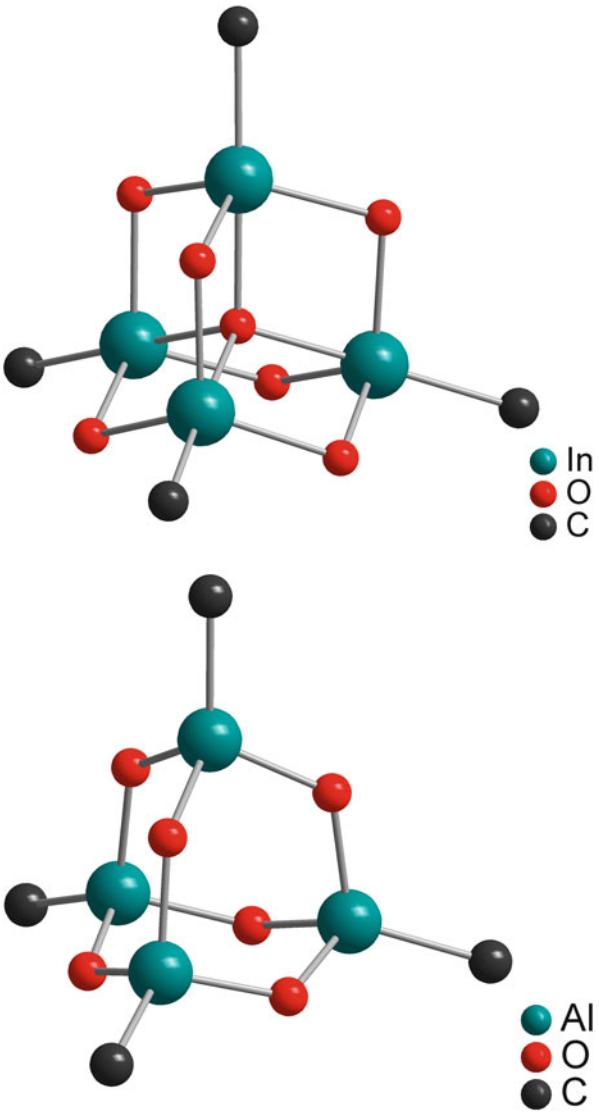

Fig. 2 Ball-and-stick model of adamantane-type metal(III) oxido core structures of organometallic molecules of the type $[R_4M_4(\mu_4\text{-}O)(\mu\text{-}OH)_6]$ (*top*) and $[R_4M_4(\mu\text{-}O)_2(\mu\text{-}OH)_4]$ (*bottom*) with and without central μ_4-oxido ligands assigned, respectively. Hydrogen atoms are not given, and groups R are represented by one carbon atom only [56, 57]

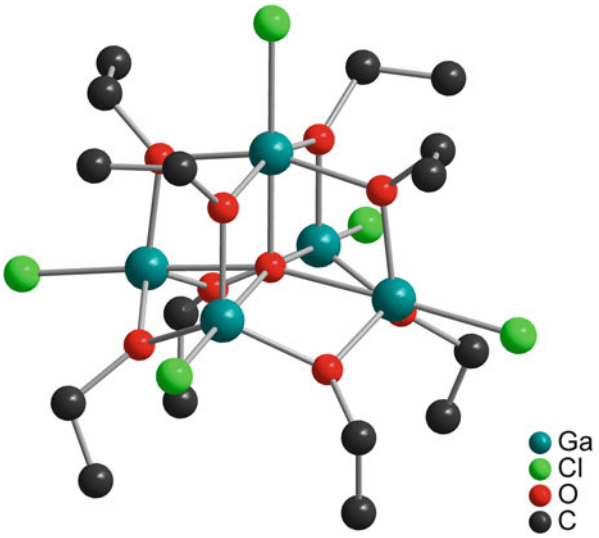

Fig. 3 Ball-and-stick model representing the molecular structure of $[(ClGa)_5(\mu_5\text{-}O)(\mu\text{-}OEt)_8]$. Hydrogen atoms are not given [33]

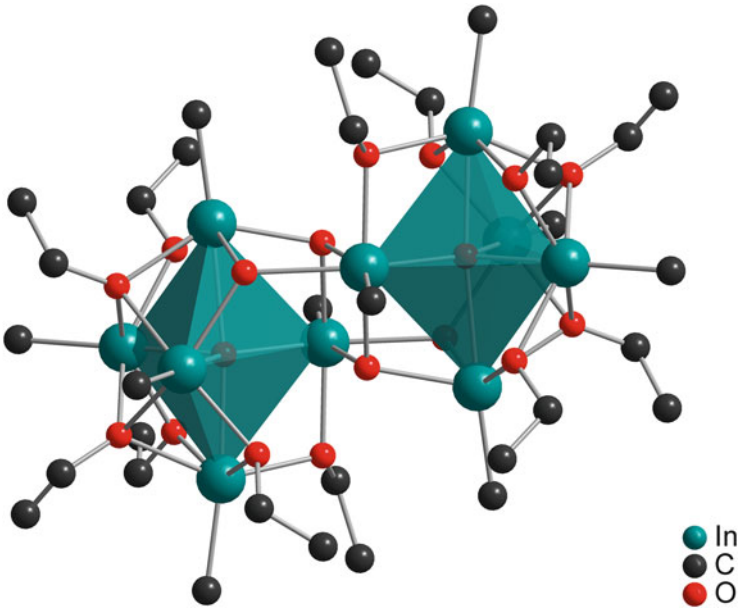

Fig. 4 Ball-and-stick model representing the molecular structure of the decanuclear indium oxido cluster $[(MeIn)_5(\mu_5\text{-}O)(\mu_3\text{-}OEt)_2(\mu\text{-}OEt)_4(\mu_3\text{-}OH)_2]_2$, which is best described as dimer of the above described pentanuclear clusters of the general type $[(RM)_5(\mu_5\text{-}O)(\mu_3\text{-}OR')_4(\mu\text{-}OR')_4]$ (R,R′=alkyl). Hydrogen atoms are not given [34]

Another example in which the pentanuclear units constitute a basic building block is represented by the oxido alkoxido cluster $[Ga_{12}(\mu_4\text{-}O)(\mu_3\text{-}O)_5(\mu\text{-}OEt)_{10}Cl_{12}(py)_4]$, which is best described as being built of two pentanuclear anionic $[Ga\{ClGa(py)\}(ClGa)_3(\mu_4\text{-}O)(\mu_3\text{-}O)_2(\mu\text{-}OEt)_5Cl]^-$ moieties with close resemblance to the basic core structure of $[(ClGa)_5(\mu_5\text{-}O)(\mu\text{-}EtO)_8]$. These building blocks are connected via an oxido ligand bound to two Ga atoms of the building unit and two bridging $[GaCl(py)]^{2+}$ cations bound to two oxido ligands of each cluster [33]. Similar kinds of metal oxido clusters with two connected pentanuclear core structures have been reported for $[Al_{11}(\mu_4\text{-}O)_2(\mu_3\text{-}O)_2(\mu\text{-}O)_2(\mu\text{-}O\textit{n}Pr)_{10}(\mu\text{-}O\textit{i}Pr)_2(\mu\text{-}ROH)_2(O\textit{i}Pr)_8(OR)]$ (R=*i*Pr, *n*Pr) [28] and $[Al_{10}(\mu_4\text{-}O)_2(\mu_3\text{-}O)_2(\mu\text{-}OEt)_{14}(\mu\text{-}OEt)_8]$ [74], which both are described to result from "controlled hydrolysis." Schmidbaur and coworkers presented another interesting large aluminum oxido alkoxide upon studies on the ammonolysis of aluminum triisopropoxide. Unexpectedly, the reaction did not give a product as result of ammonolysis, but the novel cluster $[Al_{10}(\mu_4\text{-}O)_2(\mu_3\text{-}O)_4(\mu\text{-}O\textit{i}Pr)_2(O\textit{i}Pr)_{16}(NH_3)_8]$ as a result of partial hydrolysis was observed [25]. Traces of water present in ammonia gas are sufficient to provide the compound in high yield. The cluster might be best described as being composed of the hexanuclear core $[Al_6(\mu_4\text{-}O)_2(\mu_3\text{-}O)_4(\mu\text{-}O\textit{i}Pr)_2(O\textit{i}Pr)_4(NH_3)_8]$, which is coordinated by four molecules $Al(O\textit{i}Pr)_3$ via the bridging oxygen atoms. The μ_4-oxido ligands show a typical distorted coordination geometry as mentioned above.

Recently, Kemnitz and coworkers started to study the sol–gel chemistry of aluminum alkoxides in anhydrous hydrogen fluoride [27, 32] and did observe the formation of aluminum oxido clusters. The source of the oxido ligands was not determined analytically, but the authors rule out partial hydrolysis and favor ether formation. Exemplarily, two large aluminum oxido alkoxido fluorido clusters are mentioned, $[Al_{16}F_{20}(\mu_4\text{-}O)_4(\mu\text{-}O\textit{i}Pr)_{20}]$ and $[Al_{10}F_{16}(\mu_4\text{-}O)_2(\mu\text{-}O\textit{i}Pr)_{10}(py)_4]$ (py=pyridine) (Figs. 5 and 6) [27, 32]. The former might be described as being built up by four interconnected building units $[Al_4F_5(\mu_4\text{-}O)(\mu\text{-}O\textit{i}Pr)_5]$, and quite similarly the latter is composed of two times the same building block connected via fluorido ligands and two $AlF_3(py)_2$ fragments. Both examples exhibit μ_4-oxido ligands which show a coordination mode between tetrahedral and seesaw type.

In principle, most of the oxido clusters reported might be formally constructed by a combination of the two basic cyclic fragments M_2O_2 and M_3O_3 (Fig. 7). This is nicely demonstrated by the following series: hexanuclear $[(t\text{BuAl})_6(\mu_3\text{-}O)_4(\mu_3\text{-}OH)_4]$ (Fig. 8) [29] and $[t\text{BuAl}(\mu_3\text{-}O)]_6$ [22], nonanuclear $[t\text{BuAl}(\mu_3\text{-}O)]_9$, the postulated dodecamer $[t\text{BuAl}(\mu_3\text{-}O)]_{12}$ [22], and the unusual decanuclear aluminum oxido cluster $[(i\text{Bu}_2\text{Al})_6(i\text{BuAl})_4(\mu_3\text{-}O)_6(\mu\text{-}H)_2]$ [26]. They are exclusively built up by a combination of edge-sharing M_2O_2 and M_3O_3 fragments. Noteworthy, the basic hexanuclear metal oxido hydroxido cage structure $[(t\text{BuAl})_6(\mu_3\text{-}O)_4(\mu_3\text{-}OH)_4]$ might be constructed by eight edge-sharing Al_2O_2 rings. The resulting hexanuclear unit is a typical structural motif of a variety of metal oxido clusters and, for example, is also observed in clusters such as $[Bi_6(\mu_3\text{-}O)_4(\mu_3\text{-}OH)_4]^{6+}$ [75, 76] and $[Sn_6(\mu_3\text{-}O)_4(\mu_3\text{-}OH)_4]$ [77].

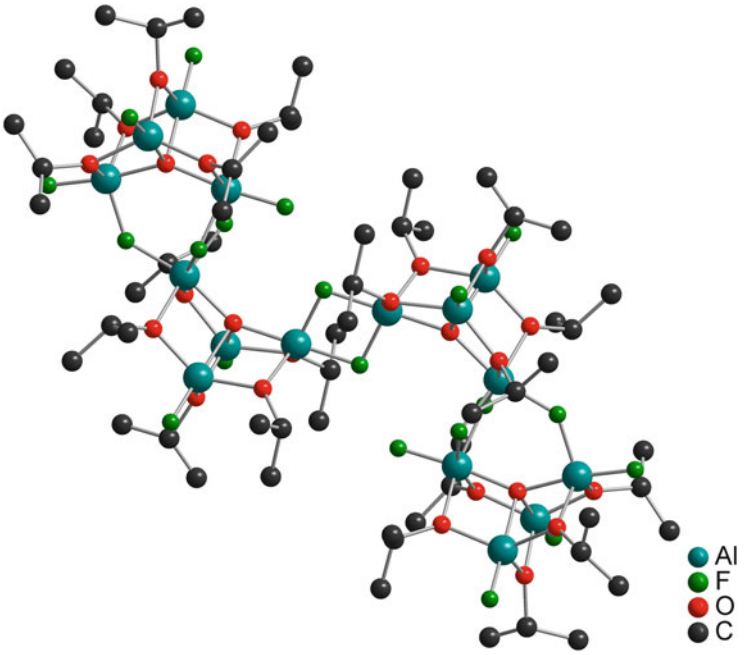

Fig. 5 Ball-and-stick model representing the molecular structure of the hexadecanuclear metal oxido fluorido cluster $[Al_{16}F_{20}(\mu_4\text{-}O)_4(\mu\text{-}O\textit{i}Pr)_{20}]$, which is composed of four $[Al_4F_5(\mu_4\text{-}O)(\mu\text{-}O\textit{i}Pr)_5]$ fragments. Hydrogen atoms are not given [32]

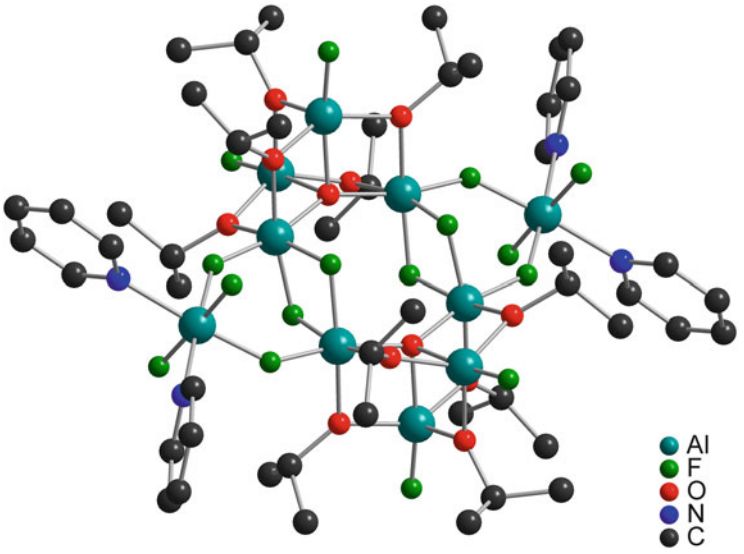

Fig. 6 Ball-and-stick model representing the molecular structure of the decanuclear metal oxido fluorido cluster $[Al_{10}F_{16}(\mu_4\text{-}O)_2(\mu\text{-}O\textit{i}Pr)_{10}(py)_4]$, which is composed of two $[Al_4F_5(\mu_4\text{-}O)(\mu\text{-}O\textit{i}Pr)_5]$ fragments and two bridging $AlF_3(py)_2$ moieties. Hydrogen atoms are not given [27]

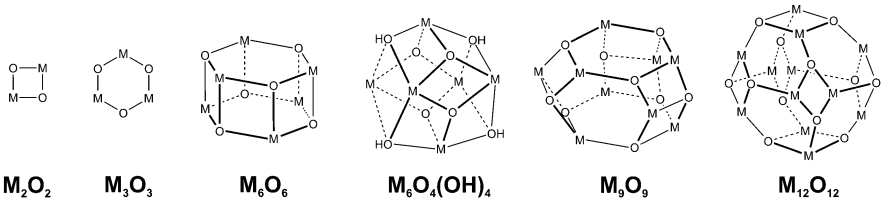

Fig. 7 Typical metal oxido moieties as reported for group 13 metal oxido clusters. The clusters are built up by a combination of M_2O_2 and M_3O_3 subunits

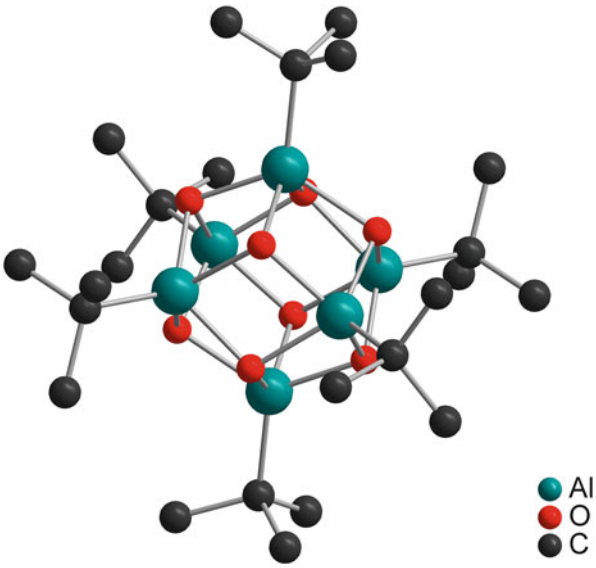

Fig. 8 Ball-and-stick model representing the molecular structure of a hexanuclear metal oxido hydroxido cluster as reported for $[(t\text{BuAl})_6(\mu_3\text{-O})_4(\mu_3\text{-OH})_4]$. Hydrogen atoms are not shown [29]

On the basis of mass spectrometry, the formation of the dodecanuclear aluminum oxido cluster $[t\text{BuAlO}]_{12}$ was proposed [22], but evidence based on single-crystal X-ray structure analysis is still missing. Instead, three similar organogallium oxido hydroxido clusters were isolated and structurally characterized, cationic $[(\text{RGa})_{12}(\mu_3\text{-O})_8(\mu\text{-OH})_6]^{2+}$ (R=Me, *p*-tolyl) and neutral $[(\text{RGa})_{12}(\mu_3\text{-O})_8(\mu\text{-O})_2(\mu\text{-OH})_4]$ (R=*t*Bu, o-C_6H_4OMe), and there is evidence for further examples with variation of the organic substituent (Fig. 9) [29–31]. Twelve fused six-membered $[Ga_3O_3]$ rings constitute the polyhedral galloxane framework with gallium being tetracoordinated. Analysis of the positions occupied by the gallium atoms reveals the formation of an icosahedral structure, which seems to be a quite stable arrangement allowing for protonation without disturbing the core structure. Although being speculative, it might be considered that aluminum also forms such oxido hydroxido clusters rather than $[t\text{BuAlO}]_{12}$ as was postulated. The dodecanuclear cluster $[t\text{BuAlO}]_{12}$ might easily form under EI-MS conditions from $[(\text{RAl})_{12}(\mu_3\text{-O})_8(\mu\text{-O})_2(\mu\text{-OH})_4]$ by elimination of water.

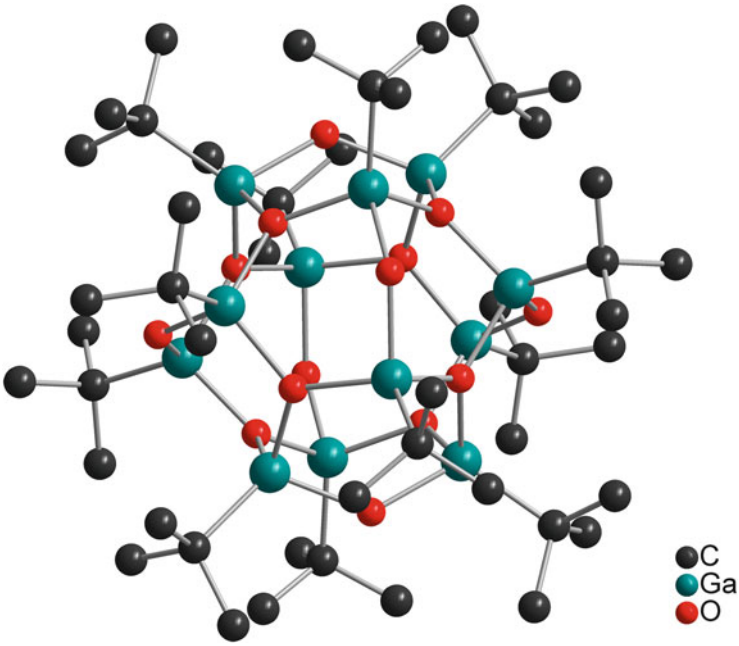

Fig. 9 Ball-and-stick model representing the molecular structure of the neutral dodecanuclear organogallium oxido cluster $[(t\text{BuGa})_{12}(\mu_3\text{-O})_8(\mu\text{-O})_2(\mu\text{-OH})_4]$. Hydrogen atoms are not shown [29]

A variety of polycations of aluminum is accessible via aqueous synthetic routes, but the number of clusters with more than ten atoms is still limited [18, 19]. The first report on such large polynuclear aluminum oxido clusters dates back to 1960, when Johansson et al. described the hydrolysis/condensation of aluminum salts in aqueous solution. A ε-type Keggin structure for an aluminum oxido cluster containing 13 aluminum atoms in $(NH_4)_7[Al_{13}O_4(OH)_{24}(H_2O)_{12}](SO_4)_7$ was obtained and structurally characterized for the first time [37]. Thirty years later, analytical evidence by NMR spectroscopy was presented for the gallium analogue of the polycation [52]; however, a single-crystal structure analysis was not reported to date. The basic structural motif of the Keggin-type clusters is the central tetracoordinated metal cation, $M(\mu_4\text{-O})_4$, surrounded by twelve edge-sharing hexacoordinate metal oxido units, all together resulting in a polycation of charge 7+, best described as $[M(\mu_4\text{-O})_4\{M'(\mu\text{-OH})_2(H_2O)\}_{12}]^{7+}$. The metals M and M' may vary to give heterobimetallic oxido clusters such as $[Ga(\mu_4\text{-O})_4\{Al(\mu\text{-OH})_2(H_2O)\}_{12}]^{7+}$ or $[Ge(\mu_4\text{-O})_4\{Al(\mu\text{-OH})_2(H_2O)\}_{12}]^{8+}$, and additional examples were claimed [47, 49]. However, there is an ongoing discussion as to which elements can be incorporated because evidence by single-crystal structure analyses is still rare. With regard to structural aspects of the three-dimensional cluster, it must be kept in mind that even for one sole metal, five isomers (α-, β-, γ-, δ- and ε-form) exist which are assigned to the five Baker–Figgis isomers of the Keggin ion

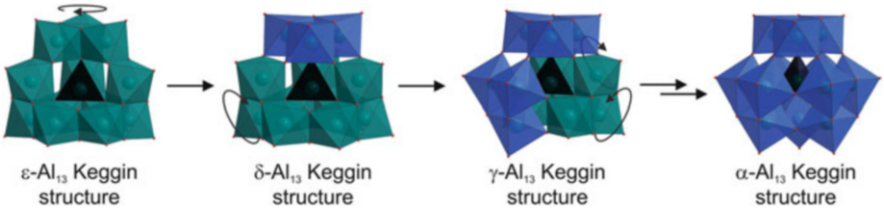

Fig. 10 Four Baker–Figgis isomers (α, γ, δ, and ε) of the Keggin ion and their transformation processes by rotation of metal oxido triads relative to the ε-isomer are shown. The missing (theoretical) β-isomer is obtained by rotation of only the front triad of the γ-isomer. Note that the ε-isomer shows edge-sharing of the triads, whereas the α-isomer shows corner-sharing, exclusively. The figure was created according to the style in [42]

(Fig. 10). The clusters might be described as being composed of four trinuclear metal oxido clusters, which are bound to a central tetrahedrally coordinated metal atom. The isomers result from different positions of the triads with regard to each other. Several of these tridecanuclear clusters were isolated and characterized (Table 2) [18]. The ε-isomer is the most stable one, is accessible in combination with different counterions, and was also detected in soils. Its synthesis is quite easy, whereas the other isomers are much more difficult to synthesize. However, the α-isomer is realized as part of the mineral zunyite [35, 36], the single-crystal structure analysis of the δ-isomer was presented in 2000 [40], and that of the γ-isomer was reported in 2013 (Fig. 11) [42]. Thus, only the β-isomer has still to be isolated and fully structurally characterized. Although not synthesized so far, recent theoretical calculations of the energetics for Keggin-type aluminate cations show that this should be a feasible task [78].

In addition to the tridecanuclear Keggin-type oxido hydroxido clusters, tridecanuclear aluminum hydroxides of the type $[Al_{13}(\mu_3\text{-}OH)_6(\mu\text{-}OH)_{18}(H_2O)_{24}]^{15+}$ were reported (Fig. 12), which have been isolated as both chloride and nitrate salts [46, 79, 80]. They might be regarded as "flat" counterparts of the Keggin-type clusters without showing condensation reactions and thus lack metal oxido units. In addition to those clusters which are stabilized by inorganic ligands, several examples containing organic ligands coordinated to the periphery were reported, e.g., $[Al_{13}(\mu_3\text{-}OH)_6(\mu\text{-}OH)_{12}(heidi)_6(H_2O)_6](NO_3)_3$ (H_3heidi=hydroxyethyliminodiacetic acid) [19, 81]. These "flat" hydroxido clusters are best described as being built up by a central hexacoordinated aluminum cation which is connected via six μ_3-hydroxido ligands to six additional octahedral aluminum atoms. The resulting seven octahedra are edge-sharing and make up the flat central $\{Al_7\}$ core, best described as $[Al_7(\mu_3\text{-}OH)_6(\mu\text{-}OH)_6]^{9+}$, quite similar to the well known heptanuclear Anderson-type polyoxometalates. In addition six hexacoordinate aluminum cations of the type $[Al(\mu\text{-}OH)_2(H_2O)_4]^+$ are bonded to the flat core via two μ-hydroxido ligands each, in alternating positions above and below the flat central core. The overall charge amounts to +15, which, compared to the $\{Al_{13}\}$-Keggin-type clusters with only a +7 charge, is quite high. Charge compensation is realized by a large variety of anionic ligands. This structural motif seems to be quite common and stable.

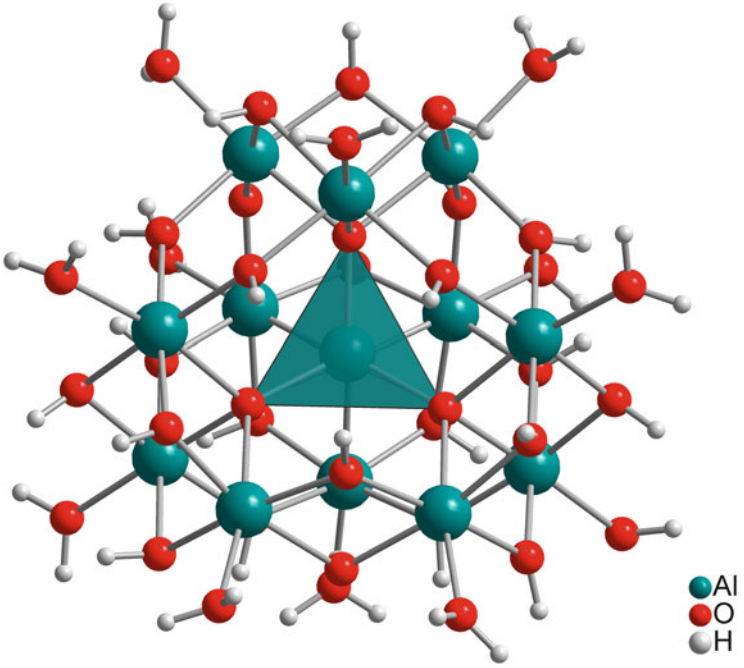

Fig. 11 Ball-and-stick model of a typical Keggin-type cluster (γ-form), $[Al(\mu_4\text{-}O)_4Al_{12}(\mu\text{-}OH)_{25}(H_2O)_{11}](SO_4)_3(H_2O)_{14}$. The tetrahedral AlO_4 unit is highlighted in teal; the other aluminum atoms show hexacoordination AlO_6. Two water molecules show an occupancy of ½. Sulfate and the non-coordinating water molecules are not shown [42]

Examples for gallium do exist as well, e.g., $[Ga_{13}(\mu_3\text{-}OH)_6(\mu\text{-}OH)_{18}(H_2O)_{24}](NO_3)_{15}$ [82]. In addition, a larger pentadecanuclear aluminum hydroxido cluster was reported, the structure of which might also be reduced to a heptanuclear $\{Al_7\}$ core structure, in this case described as $[Al_7(\mu_3\text{-}O)_4(\mu_3\text{-}OH)_6(\mu\text{-}OH)_2]^{5+}$, which represents the deprotonated form of $[Al_7(\mu_3\text{-}OH)_6(\mu\text{-}OH)_6]^{9+}$, to which four dinuclear $[Al_2(OH)_2(hpdta)]^{2-}$ moieties ($H_5hpdta{=}HOCH_2[CH_2N(CH_2COOH)_2]_2$) are coordinated. The negative total charge of the cluster $[Al_{15}(\mu_3\text{-}O)_4(\mu_3\text{-}OH)_6(\mu\text{-}OH)_{14}(hpdta)_4]^{3-}$, which self-assembles into a three-dimensional network, is compensated by oxonium and piperazinium ions [43].

Although analytical evidence for a variety of other polynuclear aluminum cations does exist [1, 18, 19], crystallization of hydrolysis products of aluminum and gallium provided only a handful of well-characterized clusters with more than fifteen metal atoms. In the case of aluminum, examples with 26, 30, and 32 metal atoms were structurally characterized, with all of them being built up by a combination of two Keggin-type $\{Al_{13}\}$ clusters. The most simple combination is found

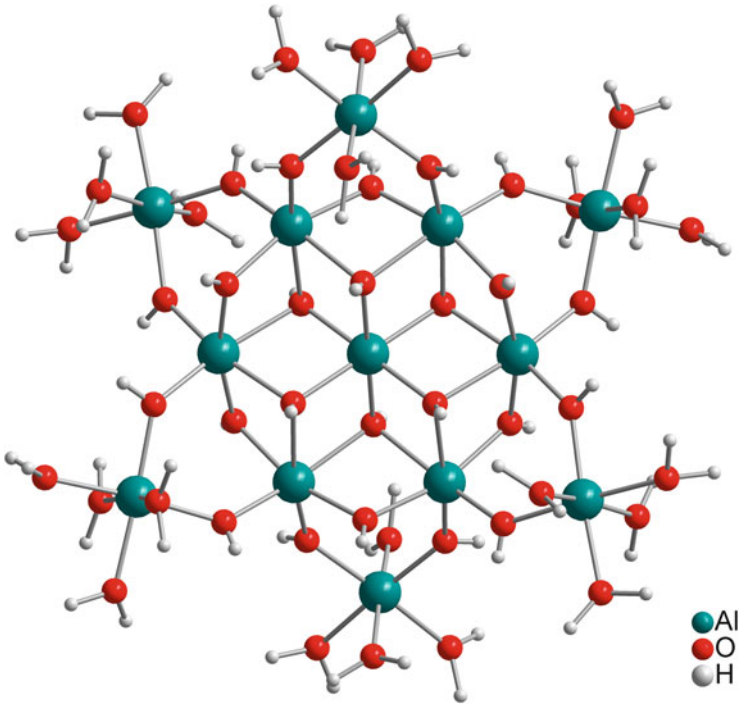

Fig. 12 Ball-and-stick model representing the molecular structure of the "flat" tridecanuclear cluster $[Al_{13}(\mu_3\text{-}OH)_6(\mu\text{-}OH)_{18}(H_2O)_{24}]^{15+}$, which was isolated as nitrate salt. The non-coordinating nitrates are omitted for clarity. The aluminum atoms show exclusively hexacoordination [46]

in $[Al_{26}(\mu_4\text{-}O)_8(\mu\text{-}OH)_{50}(H_2O)_{20}](2,6\text{-NDS})_6$ (2,6-NDS=2,6-naphtalene disulfonate), in which two Keggin-type δ-{Al_{13}} clusters condense via peripheral coordinated water molecules to result in two bridging hydroxyl groups and thus in two vertex-sharing octahedral Al centers (Fig. 13) [41].

The connectivity in the {Al_{30}} and {Al_{32}} clusters differs in such a way that additional aluminum hydroxide moieties are attached to the {Al_{13}} clusters and thus provide a link for the two Keggin-type clusters (Fig. 14). Three reports on structural analyses of Al_{30} clusters exist, two of them are about the sulfate salt $[Al_{30}(\mu_4\text{-}O)_8(\mu\text{-}OH)_{56}(H_2O)_{26}](SO_4)_9$ and another one on a disulfonate/chloride salt $[Al_{30}(\mu_4\text{-}O)_8(\mu\text{-}OH)_{56}(H_2O)_{26}]Cl_2(2,6\text{-NDS})_8(2,6\text{-NDS})_8$ (2,6-NDS=2,6-naphtalene disulfonate) [40, 44]. However, the polycations are identical and show two AlO_6 units that connect the Keggin-type δ-{Al_{13}} clusters via corner-sharing hydroxido ligands each and two AlO_6 units that are bonded via an edge to the Keggin-type cluster and vertex sharing with the two other bridging AlO_6 units. According to Taulelle and coworkers, the core structure might be rewritten as $[(\delta\text{-}Al_{13})_2\{Al_4(OH)_8(H_2O)_6\}]^{18+}$ [44]. Interestingly, it is possible to substitute two bridging aluminum atoms by tungsten atoms to give the heterobimetallic cluster $[W_2Al_{28}(\mu_4\text{-}O)_8(\mu_3\text{-}O)_4(\mu\text{-}O)_4O_2(\mu\text{-}OH)_{48}(H_2O)_{24}]^{12+}$ [51]. The structure of the largest homometallic

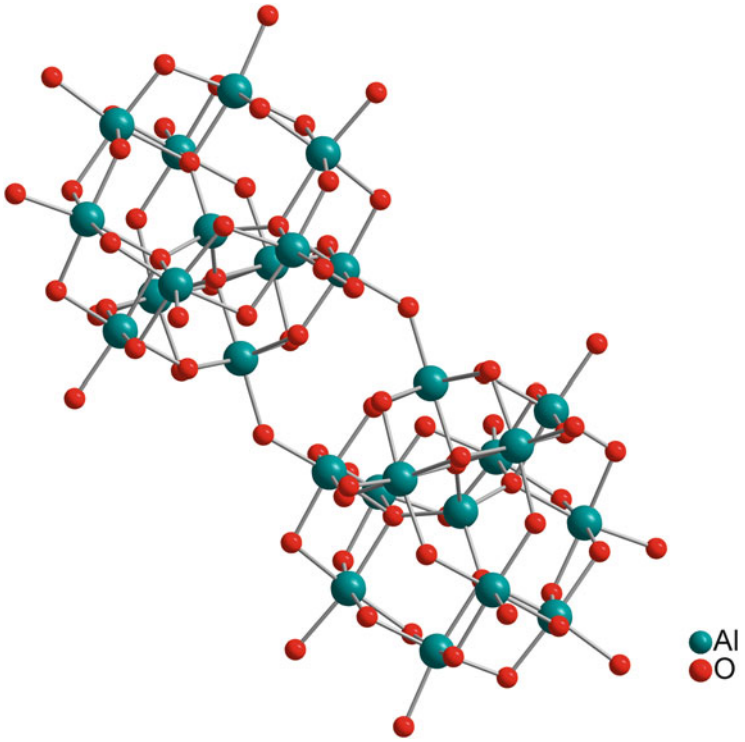

Fig. 13 Ball-and-stick model representing the molecular structure of the aluminum oxido cluster $[Al_{26}(\mu_4\text{-}O)_8(\mu\text{-}OH)_{50}(H_2O)_{20}]^{12+}$, which was isolated as 2,6-naphtalene disulfonate salt. The non-coordinating sulfonates are omitted for clarity. Hydrogen positions were not determined. The high-nuclearity cluster represents a condensation product of two Keggin-type δ-$\{Al_{13}\}$ clusters. Hydrogen atoms are not given [41]

clusters $\{Al_{32}\}$ – $[Al_{32}(\mu_4\text{-}O)_8(\mu\text{-}OH)_{60}(H_2O)_{28}(SO_4)_2]Cl_2(SO_4)_7$ and $[\{Al(IDA)(H_2O)\}_2Al_{30}(\mu_4\text{-}O)_8(\mu\text{-}OH)_{60}(H_2O)_{22}]Cl_4(2,6\text{-}NDS)_4(SO_4)_2$ (H_2IDA=imidoacetic acid) – differs from $\{Al_{30}\}$ clusters only by additionally coordinated $[Al(OH)_2(H_2O)_3(SO_4)]^-$ and $[\{Al(IDA)(H_2O)\}_2]^+$ fragments, respectively, to each Keggin-type unit. Similarly, it was observed that additional ligand-stabilized metals might attach to the cluster core as demonstrated by the isolation of the $\{Zn_2Al_{32}\}$ cluster $[\{(Zn(NTA)H_2O\}_2\{Al(NTA)(\mu\text{-}OH)_2\}_2Al_{30}(\mu_4\text{-}O)_8(\mu_3\text{-}OH)_{54}(\mu\text{-}OH)_6(H_2O)_{20}](2,6\text{-}NDS)_5$ (H_3NTA=nitriloacetic acid) [45]. With regard to large heterobimetallic clusters, a recent example with unprecedented structure was reported by Forbes and coworkers, $[Ga_2Al_{18}(\mu_4\text{-}O)_8(\mu\text{-}OH)_{36}(H_2O)_{12}]^{18+}$ (Fig. 15). The cluster represents a cationic variation on the Wells–Dawson topology and is a rare example which does not belong to the family of Keggin-type ions among the aluminum oxido hydroxido clusters [50].

As mentioned above, there is a lack of structural evidence for the formation of a gallium $\{Ga_{13}\}$ cluster with Keggin-type structure, but formation of the flat $\{Ga_{13}\}$

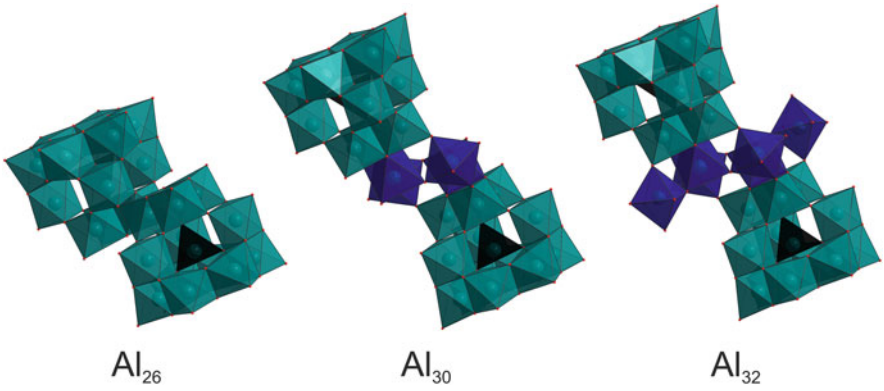

Fig. 14 Visualization of the aluminum oxido polyhedra (AlO_6, *teal*; bridging AlO_6, *dark blue*; AlO_4 *black*) as found in $[Al_{26}(\mu_4\text{-}O)_8(\mu\text{-}OH)_{50}(H_2O)_{20}]^{12+}$, $[Al_{30}(\mu_4\text{-}O)_8(\mu\text{-}OH)_{56}(H_2O)_{26}]^{9+}$, and $[Al_{32}(\mu_4\text{-}O)_8(\mu\text{-}OH)_{60}(H_2O)_{28}(SO_4)_2]^{16+}$, which all show the Keggin-type cluster as basic structural motif [38, 41, 44]

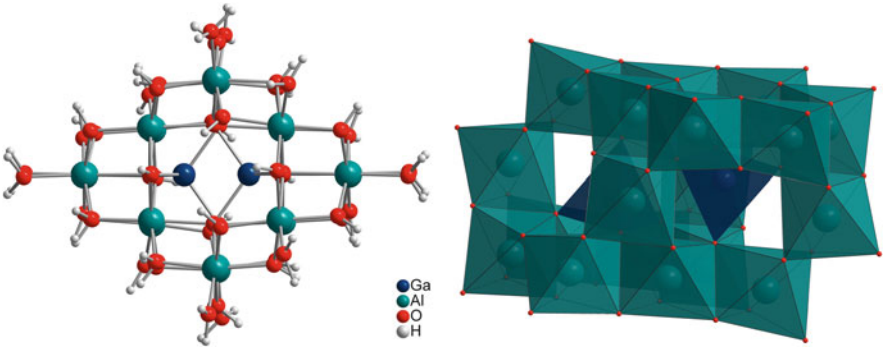

Fig. 15 Ball-and-stick model and view of the metal oxido polyhedra representing the molecular structure of the heterometallic cluster $[Ga_2Al_{18}(\mu_4\text{-}O)_8(\mu\text{-}OH)_{36}(H_2O)_{12}]^{18+}$, which was isolated with non-coordinating 2,6-naphtalene disulfonates [50]

hydroxido cluster $[Ga_{13}(\mu_3\text{-}OH)_6(\mu\text{-}OH)_{18}(H_2O)_{24}]^{15+}$ was presented in 2005 by Fedin and coworkers [55]. The same group did also show that a polynuclear gallium oxido cluster is accessible as single crystal with 32 gallium atoms, $[Ga_{32}(\mu_4\text{-}O)_{12}(\mu_3\text{-}O)_8(\mu\text{-}O)_7(\mu\text{-}OH)_{39}(H_2O)_{20}]^{3+}$, the structure of which is different from the $\{Al_{32}\}$ cluster (Fig. 16). However, some structural resemblance with the basic structural units of the Keggin-type clusters becomes obvious. Two pairs of corner-sharing tetrahedral GaO_4 units exist with each of the other corners being connected to three octahedrally coordinated edge-sharing GaO_6 units. Noteworthy, this arrangement shows some structural relationship to lacunary Keggin-type units but might also be regarded as a cutout of the structure of $\beta\text{-}Ga_2O_3$ (Fig. 16) [83]. The cluster structure is being complemented by additional $[Ga(\mu\text{-}OH)_2(H_2O)_2]^+$ units to result

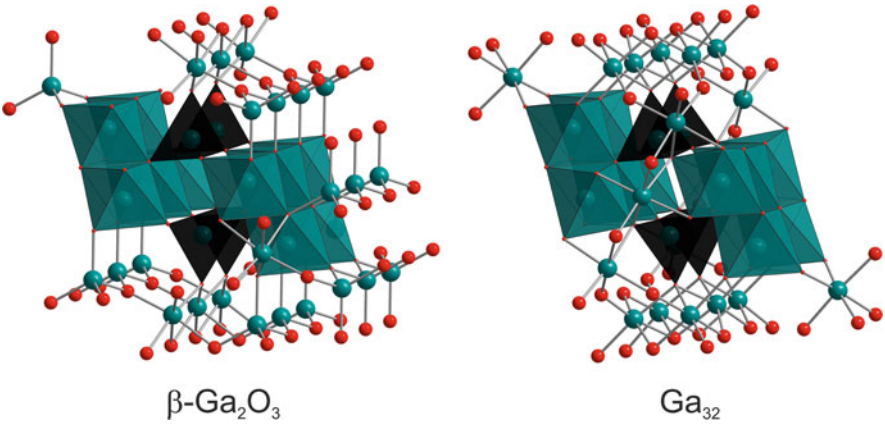

Fig. 16 Comparison of the metal oxido framework of the cluster $[Ga_{32}(\mu_4\text{-}O)_{12}(\mu_3\text{-}O)_8(\mu\text{-}O)_7(\mu\text{-}OH)_{39}(H_2O)_{20}]^{3+}$ and a cutout of $\beta\text{-}Ga_2O_3$. Hydrogen atoms are not given. Octahedral gallium coordination GaO_6 is given in *teal* and tetrahedral coordination GaO_4 in *black* [83]. The figure was created according to the style in [55]

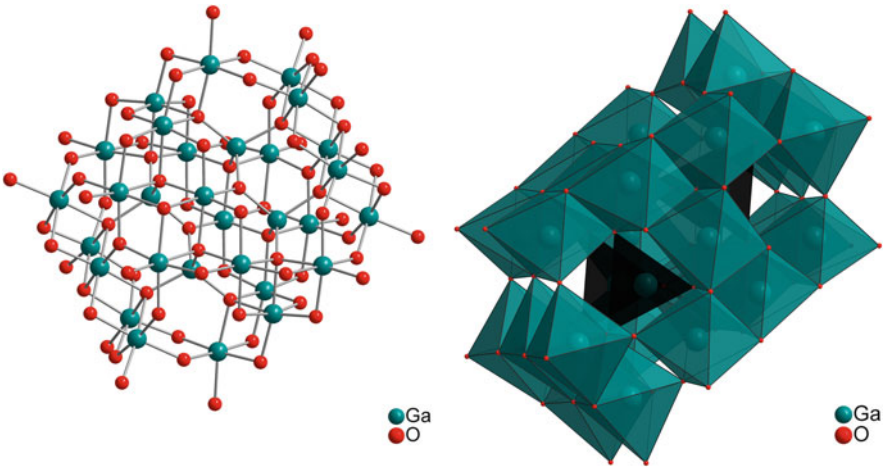

Fig. 17 Ball-and-stick model (without hydrogen atoms) and view of the metal oxido polyhedra representing the molecular structure of $[Ga_{30}(\mu_4\text{-}O)_{12}(\mu_3\text{-}O)_4(\mu_3\text{-}OH)_4(\mu\text{-}OH)_{42}(H_2O)_{16}]^{12+}$. Hydrogen atoms are not given [54]

in the $\{Ga_{32}\}$ polycation, which was crystallized with the help of cucurbit[6]uril forming strong hydrogen bonds within the supramolecular arrangement [55]. A quite similar cluster was reported recently by Forbes and coworkers, $[Ga_{30}(\mu_4\text{-}O)_{12}(\mu_3\text{-}O)_4(\mu_3\text{-}OH)_4(\mu\text{-}OH)_{42}(H_2O)_{16}]^{12+}$ crystallizing with 2,6-naphthalene disulfonate as counteranion and lacking two gallium atoms in the periphery with regard to the $\{Ga_{32}\}$ cluster (Fig. 17) [54].

3 Germanium, Tin, and Lead

The aqueous solution chemistry of the tetravalent group 14 metal cations germanium, tin, and lead is of considerable interest, especially with regard to industrial use and the environmental impact of these elements [84]. Among these elements, reports on germanium are relatively sparse. Early studies focus on the formation of small species such as $[GeO(OH)_3]^-$ or $[GeO_2(OH)_2]^{2-}$, which dominate at low concentrations, but also larger aggregates such as $[\{Ge(OH)_4\}_8(OH)_3]^{3-}$ and clusters such as $[Ge_8O_{16}(H_2O)_5(OH)_3]^{3-}$ were postulated [85]. Up to now full structural characterization including single-crystal X-ray structure analyses of such molecular germanium oxido clusters is still missing, but the formation of diverse germanium oxido building blocks is manifested in the isolation of numerous open-framework germanates [86, 87]. Examples of distinct homometallic molecular germanium oxido clusters are restricted to clusters with less than ten atoms, e.g., $[Ge_6O_8(CMe_2CH_2COMe)_6(H_2O)_2][GeBr_3]_2$ (Fig. 18) [88]. The hexanuclear germanium oxido cluster was unexpectedly observed as byproduct upon reaction of Ge(I)Br with acetone and was formed in addition to the major product $Br_3GeCMe_2CH_2COMe$. Other examples of homometallic germanium oxido clusters are represented by the octanuclear alkoxide $[Ge_8(\mu_3\text{-}O)_6(OC_6H_3t\text{Bu-2-Me-4})_4]$ [89], the neutral tungsten complex $[\{Ge_4(\mu\text{-}O)_2(\mu\text{-}OH)_4\}\{W(CO)_5\}_4]$ [58], and the anionic clusters $[\{Ge_6(\mu_3\text{-}O)_6(\mu\text{-}OH)_2\}\{Cr(CO)_5\}_6]^{2-}$ and $[\{Ge_6(\mu\text{-}O)_2(\mu_3\text{-}O)_4(OR)_2\}\{W(CO)_5\}_6]^{2-}$ (R=H, Et) [90]. Some evidence for metal oxido clusters of Si/Ge in solution prior to crystallization of germanium-containing zeolithes and oligomer formation in hydrolyzed germanium ethoxide solutions was found based on ESI-MS [91–93]. However, the chemistry of germanium oxido clusters is mainly unexplored so far.

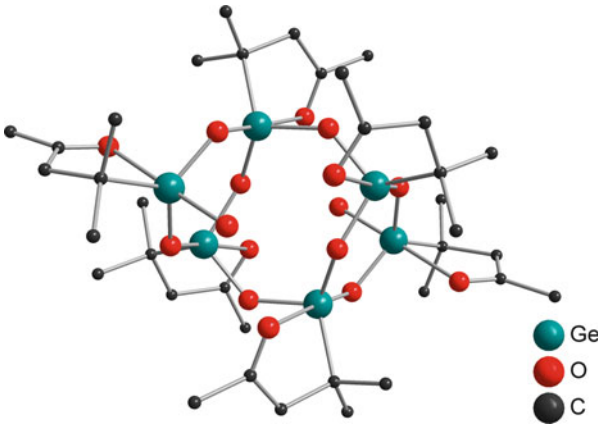

Fig. 18 Ball-and-stick model representing the molecular structure of the hexanuclear germanium oxido cluster $[Ge_6O_8(CMe_2CH_2COMe)_6(H_2O)_2]^{2+}$. The $[GeBr_3]^-$ counteranions and hydrogen atoms are not shown [88]

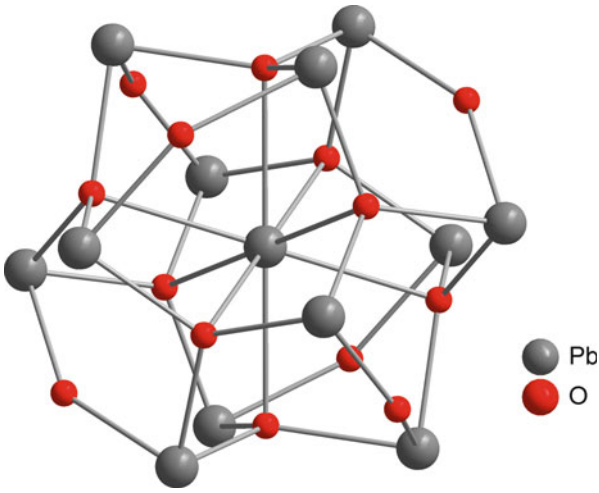

Fig. 19 Ball-and-stick model representing the lead oxido cluster structure $[Pb_{13}O_8(OH)]^{4+}$, which was isolated as insoluble nitrate salt. The hydroxido groups are coordinated to two lead atoms [95]

Given the industrial importance and the environmental impact of the element tin, the data reported on isolated inorganic molecular clusters is also limited. Early reports focus on small soluble complexes such as $[Sn(OH)_6]^{2-}$ for tin(IV) and $[Sn(H_2O)_3]^{2+}$, $[SnOH(H_2O)_2]^{+}$, $[Sn_3(OH)_4]^{2+}$, $[Sn(OH)_3]^{-}$, and $[Sn_2O(OH)_4]^{2-}$ for tin(II) [94]. Further hydrolysis of the cationic tin(II) species $[Sn_3(OH)_4]^{2+}$ upon increase of the pH results in the formation of the hexanuclear tin oxido hydroxide $[Sn_6O_4(OH)_4]$, which shows the highest nuclearity within the series of molecular tin oxido hydroxides [94]. Larger clusters have not been isolated from aqueous solutions, and similarly for lead, large molecular homometallic oxido clusters with more than ten metal atoms are scarce. The only example for lead is represented by $[Pb_{13}O_8(OH)_6]^{4+}$, which was obtained by hydrothermal synthesis as insoluble crystalline material with four nitrate ions (Fig. 19) [95]. The structure might be described as built from eight OPb_4 tetrahedra which share a common central Pb atom. By contrast several early reports on primary hydrolysis products and clusters of the type $[Pb_xO_y(OH)_z]^{n+}$, mainly insoluble basic nitrates and building blocks in heterometallic oxides, exist [96–102]. It was concluded that the aqueous chemistry of lead is dominated over a large pH range by hydrolysis products of low nuclearity such as $[Pb_4(OH)_4]^{4+}$ and $[Pb_6O(OH)_6]^{4+}$ (Fig. 20) [96, 102–104]. Noteworthy, the hexanuclear neutral lead oxido cluster $[Pb_6O_4(OH)_4]$ (Fig. 20) [105], the heavier analogue of the abovementioned tin cluster $[Sn_6O_4(OH)_4]$ [77], was not characterized so far, although calculations point to its stability and corresponding alkoxides of the general formula $[Pb_6(\mu_3\text{-}O)_4(\mu_3\text{-}OR)_4]$ were isolated [106–110].

It might be assumed that a rich structural chemistry should exist for tin oxido alkoxides because (1) similarities in the coordination chemistry of tetravalent titanium and tin exist and (2) a wealth of structures was reported in the past decades for titanium [111, 112] and (3) of the economic interest in tin alkoxides, for example, as precursors for the synthesis of semiconducting tin oxide-based materials [113]. Similarly to titanium, the controlled hydrolysis of tin alkoxides should

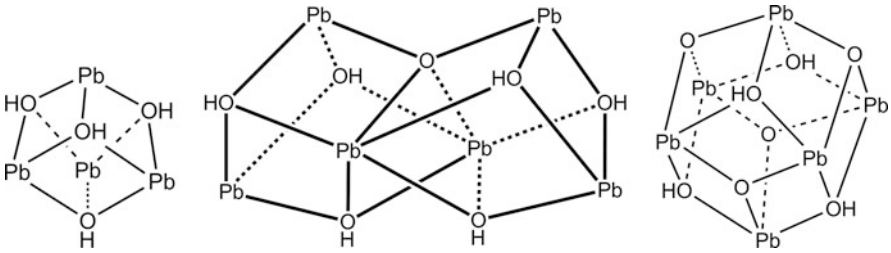

Fig. 20 Model structures for the cationic tetranuclear lead clusters $[Pb_4(OH)_4]^{4+}$, $[Pb_6O(OH)_6]^{4+}$, and hexanuclear $[Pb_6O_4(OH)_4]$. Similar tetranuclear $\{Ln_4(OH)_4\}$ subunits are well known for the lanthanides, and the hexanuclear motif $[Pb_6O_4(OH)_4]$ is realized by several elements such as tin, bismuth, and uranium

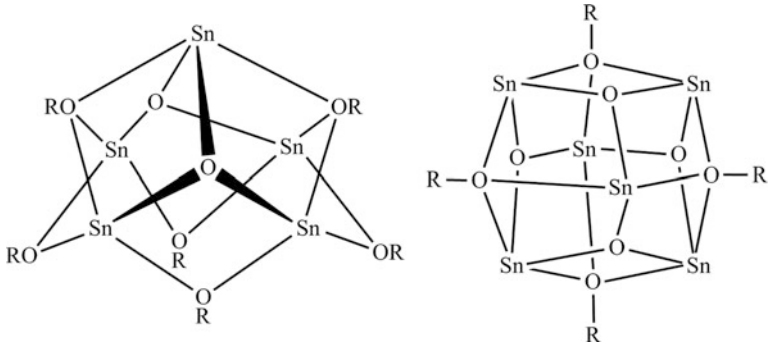

Fig. 21 Model structures for pentanuclear and typical hexanuclear tin oxido alkoxides

give tin oxido alkoxido clusters of diverse nuclearity as partial hydrolysis products on their way to bulk tin oxide. The isolation of model compounds might help to better understand the processes of nucleation and growth of tin oxide particles and complement other studies on crystal growth at later stages that rely on analytical methods such as powder X-ray diffraction (PXRD), transmission electron microscopy (TEM), and scanning electron microscopy (SEM) [114]. However, only a few examples of tin oxido alkoxides have been fully characterized, the majority of which shows nuclearities below ten.

A basic structural motif of tin oxido clusters is the Sn_3O_4 moiety that might be described as lacunary, tin deficient, Sn_4O_4 cube and is realized in both tin (II) and tin(IV) compounds. In the case of tin(II) oxido alkoxides, two of these trinuclear moieties are connected to give the most prominent structural motif, which is the hexanuclear $[Sn_6(\mu_3\text{-}O)_4(\mu_3\text{-}OR)_4]$ cluster (Fig. 21). The hexanuclear core structure has been reported for a large variety of substitutents R and is derived from the aqueous hydrolysis product $[Sn_6O_4(OH)_4]$ (Table 3).[77] The removal of one tin-containing moiety gives rise to the pentanuclear tin oxido alkoxides of the type $[Sn_5(\mu_3\text{-}O)_2(\mu\text{-}OR)_6]$, but other types of pentanuclear clusters

Table 3 Examples of tin oxido alkoxides and hydroxides with nuclearities from four to ten. Synthesis conditions, isolated yield, and analytics are given

Compound	Synthesis	η/%	Analytics	References
$[Sn_4(\mu_3\text{-}O)_2(\mu\text{-}OEt)_4(OEt)_6(\eta^2\text{-}acac)_2]$	Alcoholysis of $Sn(OtBu)_4$ in EtOH/toluene; crystallization from *n*-hexane	26	XRD, IR, ^{1}H-, ^{119}Sn-NMR	[115]
$[Sn_4O(OSiMe_3)_8]$	Oxidation of $[Sn(OSiMe_3)_2]_2$ with O_2 in THF	90	XRD, IR, ^{1}H-, ^{13}C-, ^{119}Sn-NMR, EA	[116]
$[LSnOSn(OH)_2OSnL{\cdot}LSnOH]$ $[L{=}N(CH_2CMe_2O)_2(CH_2CH_2O)]$	Hydrolysis of [LSnO*t*Bu] in CD_2Cl_2	n.r.	XRD, ^{1}H-, ^{13}C-, ^{119}Sn-NMR, ESI-MS	[117]
$[Sn_5(\mu_3\text{-}O)_2(\mu\text{-}OCH_2CMe_3)_6]$	Hydrolysis of $Sn(OCH_2CMe_3)_2$ in THF/H_2O	52	XRD, IR, ^{1}H-, ^{13}C-, ^{119}Sn-, ^{17}O-NMR, EA	[118]
$[Sn_6O_4(OH)_4]$	Hydrolysis of "in situ"-prepared $SnSO_4$ with NH_3/H_2O	n.r.	XRD	[77, 119]
$[Sn_6(\mu_3\text{-}O)_4(\mu_3\text{-}OMe)_4]$	Hydrolysis of $Sn(OMe)_2$ in benzene/H_2O	n.r.	PXRD, EA, MS, IR	[120, 121]
$[Sn_6(\mu_3\text{-}O)_4(\mu_3\text{-}OEt)_4]$	Hydrolysis of $Sn(OEt)_2$ in toluene	n.r.	XRD, MS, IR, EA	[121, 122]
$[Sn_6(\mu_3\text{-}O)_4(\mu_3\text{-}O*i*Pr)_4]$	Electrochemical synthesis starting from tin in *i*PrOH	n.r.	EA, IR	[121]
$[Sn_6(\mu_3\text{-}O)_4(\mu_3\text{-}OtBu)_4]$	Reaction of tin with *t*BuOH; crystallization from toluene	n.r.	XRD, ^{1}H-, ^{13}C-, ^{119}Sn-NMR, EA	[123]
$[Sn_6(\mu_3\text{-}O)_4(\mu_3\text{-}OSiMe_3)_4]$	Thermolysis of $[Sn(OSiMe_3)_2]_2$	99	^{1}H-, ^{13}C-, ^{119}Sn-NMR, IR, MS, UV, EA	[116, 124]
$[Sn_6(\mu_3\text{-}O)_4(\mu_3\text{-}OSiMe_3)_4\{Fe(CO)_4\}]$	Reaction of $[Sn_6(\mu_3\text{-}O)_4(\mu_3\text{-}OSiMe_3)_4]$ with $[Fe_2(CO)_9]$ in toluene; crystallization from benzene/acetonitril	50	XRD, ^{1}H-, ^{13}C-, ^{119}Sn-NMR, IR, EA	[124]
$[Sn_6(\mu_3\text{-}O)_4(\mu_3\text{-}OSiMe_3)_4\{Fe(CO)_4\}_2]$	Reaction of $[Sn_6(\mu_3\text{-}O)_4(\mu_3\text{-}OSiMe_3)_4]$ with $[Fe_2(CO)_9]$ in toluene; crystallization from benzene/acetonitril	35	XRD, ^{1}H-, ^{13}C-, ^{119}Sn-NMR, IR, EA	[124]
$[Sn_6(\mu_3\text{-}O)_4(\mu_3\text{-}OH)_4\{Mn(CO)_2Cp^*\}_6]$	Hydrolysis of $[\{Cp^*(CO)_2Mn\}_2Sn]$ in THF and crystallization from THF/Et_2O/*n*-pentane	52	XRD,^{1}H-, ^{119}Sn-NMR, IR, EA	[125]
$[Sn_6(\mu_3\text{-}O)_4(\mu_3\text{-}OH)_4\{W(CO)_5\}_6]$	Hydrolysis of $SnCl_2$/$Na_2[W_2(CO)_{10}]$ in THF	2	XRD, IR	[126]
$[Sn_6(\mu_3\text{-}O)_4(\mu_3\text{-}OH)_4\{Cr(CO)_5\}_6]$ · 3THF	Hydrolysis of $\{Cr(CO)_5\}SnCl_2$/$K_2[Cr(CO)_5]$ in THF	n.r.	XRD, EA, IR	[127]
$[Sn_6(\mu_3\text{-}O)_4(\mu_3\text{-}OCH_2CH_2NMe_2)_4]$	Alcoholysis of $[Sn_6O_4(OMe)_4]$ with $HOCH_2CH_2NMe_2$	86	XRD, ^{1}H-, ^{13}C-, ^{119}Sn-NMR, EA	[122]

(continued)

Table 3 (continued)

Compound	Synthesis	η/%	Analytics	References
$[Sn_6(\mu_3\text{-}O)_4(\mu\text{-}OCH_2CMe_3)_4]$	Hydrolysis of $Sn(OCH_2CMe_3)_2$ in THF/H_2O	60	XRD, IR, ^{1}H-, ^{13}C-, ^{17}O-, ^{119}Sn-NMR, EA	[118]
$[Sn_6O_6(OAc)_6(O\mathit{t}Bu)_6]$	Ester elimination; reaction of $Sn(O\mathit{t}Bu)_4$ and $Sn(OAc)_4$ in toluene	n.r.	XRD,^{1}H-, ^{119}Sn-NMR	[128]
$[Sn_3(\mu_3\text{-}O)(\mu\text{-}OH)(\mu\text{-}OR)_3(OR)_6(HOR)]_2$ (R=$OCH_2C_4H_3S$)	Alcoholysis of $Sn(O\mathit{t}Bu)_4$ with 2-thiophenemethanol; crystallization from toluene/*n*-hexane	53	XRD, IR, EA	[129]
$[\{(PhCH_2Sn)_6(\mu_4\text{-}O)(\mu_2\text{-}OH)_{11}(H_2O)\}(OTf)_5]$	Crystallization of a mixture of HOTf and $\{(PhCH_2)_2SnO\}_6\{(PhCH_2)_2SnOH)_2(CO_3)\}_2$ in acetonitrile/CH_2Cl_2/toluene	n.r.	XRD	[130]
$[(2,4,6\text{-}i\mathrm{Pr}_3C_6H_2Sn)_6(OH)_4(\mu\text{-}O)(\mu_3\text{-}O)_4(\mu\text{-}OH)]$	Hydrolysis of $2,4,6\text{-}i\mathrm{Pr}_3C_6H_2Sn(CCMe)_3$ in THF/H_2O and crystallization from $CHCl_3$	n.r.	XRD,^{1}H-NMR, IR	[131]
$[Sn_7(\mu_3\text{-}OH)(\mu_3\text{-}O)_3(\mu_3\text{-}OEt)_3\{W(CO)_5\}_7][PPh_4]_2$	Alcoholysis of $SnCl_2/Na_2[W_2(CO)_{10}]$ in ethanol; crystallization in the presence of PPh_4^+ from EtOH	9	XRD, ^{1}H-, ^{13}C-, ^{31}P-NMR, IR, EA	[126]
$[(i\mathrm{PrSn})_9(\mu_3\text{-}O)_8(\mu\text{-}OH)_6Cl_5]\cdot 6DMSO$	Hydrolysis of $i\mathrm{PrSn}(OH)_2Cl \cdot 0.75H_2O$ in DMSO	n.r.	XRD	[132]
$[(FcSn)_9Cl_5(\mu_3\text{-}O)_8(\mu_2\text{-}OH)_6] \cdot 5CHCl_3$ (Fc: ferrocenyl)	Hydrolysis of $FcSnCl_3$/NaSePh in THF; crystallization from $CHCl_3$/*n*-pentane	n.r.	XRD,^{1}H-, ^{13}C-, ^{119}Sn-NMR, IR	[133]
$[Sn_{12}O_8(OH)_4(OEt)_{28}(HOEt)_4]$	Alcoholysis of $[Sn(Oi\mathrm{Pr})_4\cdot HOi\mathrm{Pr}]_2$ in $EtOH/H_2O$	<1	XRD,^{1}H-, ^{13}C-, ^{119}Sn-NMR	[134]

n.r. not reported

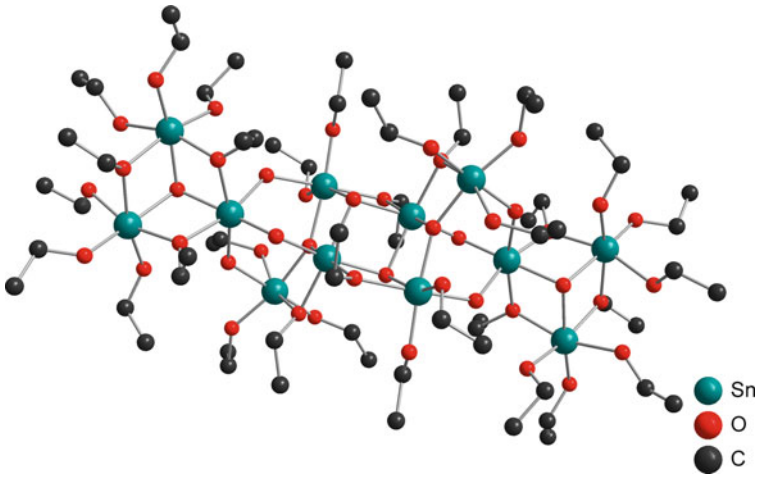

Fig. 22 Ball-and-stick model representing the molecular structure of the dodecanuclear tin oxido alkoxide $[Sn_{12}O_8(OH)_4(OEt)_{28}(HOEt)_4]$. Hydrogen atoms are omitted [134]

were also realized as was demonstrated for $[LSnOSn(OH)_2OSnL{\bullet}2LSnOH]$ $[L{=}N(CH_2CMe_2O)_2(CH_2CH_2O)]$, a hydrolysis product of an 1-alkoxido-stannatrane. The tin oxido hydroxido core of this tin oxido cluster is stabilized by an intramolecular donor-stabilizing ligand [117].

The largest tin oxido alkoxido cluster contains twelve tin atoms and was reported by Ribot et al. in 2008 (Fig. 22) [134]. In addition to the molecular structure of $[Sn_{12}O_8(OH)_4(OEt)_{28}(HOEt)_4]$, its dynamics in solution were studied, nicely demonstrating the value of such clusters as model compounds to study exchange reactions at surfaces. The molecular structure is best described as being built up from a row of two pairs of nonequivalent building blocks, each of them being composed of three tin atoms connected via μ_3-oxido ligands. The trinuclear Sn_3O_4 building blocks, which constitute a typical structural motif as mentioned above, are assembled via hydroxido bridges. A similar situation of hydroxido-bridged Sn_3O_4 units was presented recently for hexanuclear $[Sn_3(\mu_3\text{-}O)(\mu\text{-}OH)(\mu\text{-}OCH_2C_4H_3S)_3(OCH_2C_4H_3S)_6(HOCH_2C_4H_3S)]_2$ [129] and $[Sn_4(\mu_4\text{-}O)(OSiMe_3)_8]$, which might be described as a $[Sn_3(\mu_3\text{-}O)(\mu\text{-}OSiMe_3)_3]^+$ moiety with tin(II) atoms and to which a tin(IV)-containing anion $[Sn(OSiMe_3)_5]^-$ is attached [116].

A reason for the scarcity of reports on fully characterized large tin oxido clusters is most likely related to low solubility and difficulties of crystallization. The introduction of organic ligands bound to tin gives access to more soluble organometallic compounds and produced an enormous wealth of fully characterized examples, especially of diorganotin oxido compounds but also of monoorganotin oxido clusters (Table 4) [135–144]. The chemistry of tetraorganodistannoxanes of the general type $[R_2XSnOSnXR_2]_2$ (R=alkyl, aryl; X=halogen, OH, OR, NCO, etc.) has been thoroughly reviewed, and thus only a brief comment is made here

Table 4 Selected examples of organotin oxido clusters with nuclearity above ten. Synthesis conditions, isolated yield, and analytics are given

Compound	Synthesis	η/%	Analytics	References
$[\{(PhCH_2)_2SnO\}_6\{(PhCH_2)_2SnOH)_2(CO_3)\}_2]$	Reaction of $(PhCH_2)_2SnO$ with $(CH_3)_2CO_3$ in toluene/methanol	44	XRD, ^{1}H-, ^{13}C-, ^{119}Sn-NMR, IR, ESI-MS, EA	[130]
$[\{(PhCH_2)_{10}(SnO)_3(SnOH)_2\}HPO_4]_2$	Alcoholysis of $(PhCH_2)_2SnCl_2$ in EtOH/Na_2HPO_4	75	XRD, EA, IR	[152]
$[\{(PhCH_2)_{10}(SnO)_3(SnOH)_2\}SO_4]_2{\cdot}4H_2O$	Alcoholysis of $(PhCH_2)_2SnCl_2$ in EtOH/Na_2SO_4	78	XRD, EA, IR	[152]
$[\{(n\mathrm{Bu})_{10}(SnO)_3(SnOH)_2\}NO_3]_2$	Alcoholysis of $(nBu)_2SnCl_2$ in EtOH/$NaNO_3$	70	XRD, EA, IR	[152]
$[(R_2SnO)_3(R_2SnOH)(R_2SnOEt)(CO_3)]_2$ ($R=C_6H_5CH_2$)	Alcoholysis of $(PhCH_2)_2SnCl_2$ in EtOH	13	XRD, EA	[153]
$[(R_2SnO)_3(R_2SnOH)_2(CO_3)]_2$ ($R=C_6H_5CH_2$)	Alcoholysis of $(PhCH_2)_2SnCl_2$ in EtOH/NaOEt	15	XRD, EA, IR	[153]
$[(R_2SnO)_3(R_2SnOH)_2(L^1/L^2)]_2$ (L^1=1,1´--ferrocenedicarboxylic acid; L^2 =hexanedicarboxylic acid, $R=C_6H_5CH_2$)	Reaction of $[(R_2SnO)_3(R_2SnOH)_2(CO_3)]_2$ [$R=C_6H_5CH_2$] with L^1 and L^2	L^1, 70 L^2, 80	XRD, EA, ^{119}Sn-NMR	[153]
$[(2,4,6\text{-}i\mathrm{Pr}_3\text{-}C_6H_2Sn)_7Sn_3(4\text{-}MeC_6H_4SO_3)_2(\mu\text{-}OH)_{16}(OH)_3(\mu_3\text{-}O)_3(\mu_4\text{-}O)(4\text{-}MeC_6H_4SO_3)_4]$	Hydrolysis of 2,4,6-$i\mathrm{Pr}_3C_6H_2Sn(CCMe)_3$ in toluene/THF/H_2O in the presence of $4\text{-}MeC_6H_4SO_3H$	40	XRD, ^{1}H-NMR, ^{119}Sn-CP-MAS NMR, IR, EA	[154]
$[C_{36}H_{55}Cl_6N_3O_7Sn_{10}]{\cdot}C_6H_6$	Hydrolysis of $[Ar(H)NSnCl]_2$ (Ar=2,6-$i\mathrm{Pr}_2C_6H_3$)	n.r.	XRD	[155]
$[Sn(\mu\text{-}OH)_6\{(PhCH_2Sn)_{10}(\mu_4\text{-}O)_2(\mu\text{-}OH)_{16}(H_2O)_2(OTf)_2\}(OTf)_6]$	Reaction of $\{(PhCH_2)_2SnO\}_6\{(PhCH_2)_2SnOH)_2(CO_3)\}_2$ with HOTf in acetonitril	n.r.	XRD	[130]
$[(ArSn)_8(\mu_4\text{-}O)_2(\mu_3\text{-}O)_8(\mu\text{-}O)_4(\mu\text{-}OH)_8\{Sn(OH)\}_4]$ Ar=2,4,6-$i\mathrm{Pr}_3C_6H_2$	Hydrolysis of $ArSn(C_3H_3)_3$ in H_2O/THF	20	XRD, ^{1}H-, ^{119}Sn-NMR, ^{119}Sn-CP-MAS NMR, IR, EA	[131]

$[\{(n\text{BuSn})_{12}(\mu_3\text{-O})_{14}(\mu\text{-OH})_6\}(\text{OH})_2]\cdot 4\text{HO}i\text{Pr}$	Hydrolysis of $n\text{BuSn}(\text{O}i\text{Pr})_3$ in $i\text{PrOH}/\text{H}_2\text{O}$	67	XRD, ^{119}Sn-NMR, EA	[148]
$[\{(\text{nBuSn})_{12}(\mu_3\text{-O})_{14}(\mu\text{-OH})_6\}\text{Cl}_2]\cdot 2\text{H}_2\text{O}$	Hydrolysis of $n\text{BuSnCl}_3$ in $\text{KOH}/\text{H}_2\text{O}$ and crystallization from acetone/acetonitril	84	XRD, ^{119}Sn-NMR, EA, ESI-MS	[156]
$[\{(i\text{PrSn})_{12}(\mu_3\text{-O})_{14}(\mu\text{-OH})_6\}\text{Cl}_2]\cdot\text{L}$; [$\text{L}^1$ $=3\text{H}_2\text{O}$; L^2=2 DMF; $\text{L}^3=4\text{H}_2\text{O}\cdot 4$DMPU]	Hydrolysis of $i\text{PrSn}(\text{OH})_2\text{Cl}\cdot 0.75\ \text{H}_2\text{O}$ in the presence of $\text{L}^n(n=1\text{–}3)$	n.r.	XRD (L^1-L^3), EA ($\text{L}^{1,2}$)	[157]
$[\{(n\text{BuSn})_{12}(\mu_3\text{-O})_{14}(\mu\text{-OH})_6\}(\text{O}_3\text{SC}_6\text{H}_4\text{CH}_3)_2]\cdot\text{C}_4\text{H}_8\text{O}_2$	Reaction of nBuSnO(OH) with *p*-toluene sulfonic acid in toluene; crystallization from 1,4-dioxane/water	50	XRD, EA, ^{1}H-, ^{119}Sn-NMR, ^{119}Sn-CP-MAS NMR	[158]
$[(\text{Me}_3\text{SiCH}_2\text{Sn})_{12}(\mu_3\text{-O})_{14}(\mu\text{-OH})_6\text{Cl}_2]\cdot 2\text{CHCl}_3$	Method 1: hydrolysis of $\text{Me}_3\text{SiCH}_2\text{SnCl}_3$ and Me_3SiCl in toluene/$\text{NH}_3/\text{H}_2\text{O}$ Method 2: hydrolysis of $\text{Me}_3\text{SiCH}_2\text{SnCl}_3$ in $\text{H}_2\text{O}/\text{KOH}$, crystallization from CHCl_3	93 85	XRD, ^{1}H-, ^{13}C-, ^{29}Si-, ^{119}Sn-NMR, IR, EA, Mössbauer, XRD	[159]
$[\{(\text{PhCH}_2\text{Sn})_{12}(\mu_3\text{-O})_{14}(\mu\text{-OH})_6\}(\text{OTf})_2]$	Reaction of $[(\text{R}_2\text{SnO})_3(\text{R}_2\text{SnOH})_2(\text{CO}_3)]_2$ [R=PhCH_2] with HOTf in CD_3CN	31	XRD, ^{1}H-, ^{13}C-, ^{19}F-, ^{119}Sn-NMR, IR, EA, ESI-MS	[160]
$[i\text{PrSn})_{11}(\text{VO})\text{O}_{14}(\text{OH})_6]\text{Cl}\cdot 2\text{DMF}\cdot\text{H}_2\text{O}$	Hydrolysis of $i\text{PrSn}(\text{OH})_2\text{Cl}\cdot 0.75\text{H}_2\text{O}$, $\text{H}_2\text{N}(\text{CH}_2)_2\text{NH}_2$ and $\text{VOSO}_4\ 5\text{H}_2\text{O}$ in DMF	68	XRD	[151]
$[\{(i\text{PrSn})_{12}\text{O}_{14}(\text{OH})_6\}\{(i\text{PrSn})_3(\text{VO})_4\text{O}_{10}(\text{OH})_3\}]\cdot 4$DMSO	Hydrolysis of $i\text{PrSn}(\text{OH})_2\text{Cl}$ and VO(acac)_2 in $\text{DMSO}/\text{H}_2\text{O}$/hydrazine	n.r.	XRD	[161]
$[(\text{Ph}_3\text{Sn})_2(\text{PhSn})_{10}\text{Sn}_2(\mu\text{-O})_8(\mu_3\text{-O})_{18}(\text{C}_7\text{HCl}_3\text{O}_3)_2]$	Hydrothermal reaction of 3,5,6-trichlorosalicylic acid ($\text{C}_7\text{HCl}_3\text{O}_3\text{H}_2$) and $(\text{Ph}_3\text{Sn})_2\text{O}$ in MeOH, crystallization from Et_2O	65	XRD, ^{1}H-, ^{13}C-, ^{119}Sn-NMR, IR, EA	[150]
$[\{\text{Sn}(\text{CH}_2)_3\text{Sn}\}_6(\text{ClCH}_2\text{CO}_2)_{14}(\text{OH})_2\text{O}_{10}]$	Hydrolysis of $[(\text{ClCH}_2\text{CO}_2)_2(\text{OH})\text{Sn}(\text{CH}_2)_3\text{Sn}(\text{OH})(\text{O}_2\text{CCH}_2\text{Cl})_2]_n$ in CH_2Cl_2/hexane	39	XRD, EA	[146]
$[\{\text{R(Cl)Sn}(\text{CH}_2)_3\text{Sn(Cl)}(\text{CH}_2)_3\text{Sn(Cl)R}\}\text{O}_{1.5}]_4$(R=$\text{CH}_2\text{SiMe}_3$)	Reaction of $\text{RSnCl}_2(\text{CH}_2)_3\text{SnCl}_2(\text{CH}_2)_3\text{SnCl}_2\text{R}$ with$(t\text{Bu}_2\text{SnO})_3$ in CH_2Cl_2, crystallization from CHCl_3	96	XRD, ^{1}H-, ^{13}C-, ^{119}Sn-NMR, EA	[145]
$[\text{Sn}_7\text{O}_5(\text{SnR}_2)_2]_2$ (R=2-mercaptonicotinic acid)	Reaction of $n\text{Bu}_2\text{SnCl}_2$ with Na-2-mercapto-nicotinic acid in benzene, crystallization from hexane	64	XRD, ^{119}Sn-NMR, EA	[147]

(continued)

Table 4 (continued)

Compound	Synthesis	η/%	Analytics	References
$[\{(PhCH_2Sn)_{12}(\mu\text{-}O)_{14}(\mu\text{-}OH)_6\}\{((PhCH_2)_2Sn)_6(\mu\text{-}L)_4(\mu\text{-}OH)_2\}]\cdot 2C_4H_8O\cdot 2C_2H_5OH\cdot 2H_2O$ (H_3L=3,5-pyrazoledicarboxylic acid)	Alcoholysis of $[\{((PhCH_2)_2Sn)_6(\mu\text{-}L)_4(\mu\text{-}OH)_2\}\{((PhCH_2)_2SnCl)_2\}]_n$ and collidine in MeOH, crystallization from THF/MeOH/EtOH	11	XRD, IR, EA	[162]

n.r. not reported

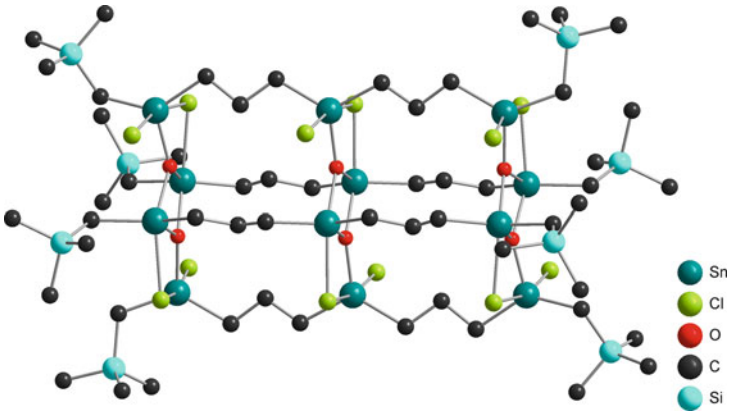

Fig. 23 Ball-and-stick model representing the molecular structure of the dodecanuclear ladder-type organotin oxido cluster $[\{R(Cl)Sn(CH_2)_3Sn(Cl)(CH_2)_3Sn(Cl)R\}O_{1.5}]_4$ [R=CH_2SiMe_3]. Hydrogen atoms are omitted [145]

[138]. The basic structural motif is their so-called ladder-type arrangement as a result of alternating μ_3-oxido ligands, which, unlike in the Sn_3O_4-type clusters, bridge three tin atoms within the same plane of the $Sn_4X_4O_2$ unit. In addition to the rather simple molecular structures of $[R_2XSnOSnXR_2]_2$, several supramolecular assemblies have been reported upon variation of R and X. For example, Jurkschat and coworkers reported the trimethylene-bridged ladder-type compound $[\{R(Cl)Sn(CH_2)_3Sn(Cl)(CH_2)_3Sn(Cl)R\}O_{1.5}]_4$ [R=CH_2SiMe_3] [145], which contains twelve tin atoms and was prepared starting from $[Me_3SiCH_2(Cl_2)SnCH_2]_2CH_2$ in a simple hydrolysis step (Fig. 23). Another type of tin oxido clusters containing twelve tin atoms, which also relies on a ladder-type arrangement, was observed upon hydrolysis of trimethylene-bridged diorganotin carboxylates and is represented by the formula $[(Sn(CH_2)_3Sn)_6O_{10}(OH)_2(ClCH_2COO)_{14}]$ (Fig. 24) [146]. In addition Ma et al. isolated a ladder-type-based macrocycle $[(nBu_2Sn)_{18}O_{10}L_8]$ (H_2L=2-mercaptonicotinic acid), which is composed of 18 tin atoms (Fig. 25) [147].

Several monoorganotin oxido clusters of the type $[(RSn)_{12}(\mu_3\text{-}O)_{14}(\mu\text{-}OH)_6]^{2+}$ (R=alkyl, aryl) have been reported to be hydrolysis products of monoorganotin trichlorides, trialkoxides, and trialkynides and were used as building blocks for tin-containing organic–inorganic hybrid materials (Fig. 26) [148, 149]. The spherical structural arrangement of the macrocation is quite stable, and this cluster type might be called a "magic tin oxido cluster" within the monoorganotin oxido cluster series. The dicationic nature allows for the synthesis of a variety of derivatives with all types of anionic counteranions, and even the additional modification by triorganotin moieties was observed to give the tetradecanuclear cluster $[(Ph_3Sn)_2(PhSn)_{10}(LSn)_2(\mu_3\text{-}O)_{18}(\mu\text{-}O)_8]$ (L=3,5,6-trichlorosalicylate) [150]. In addition the substitution of a tin atom by vanadium to give $[(i\text{PrSn})_{11}(VO)(\mu_3\text{-}O)_{14}(\mu\text{-}OH)_6]^{2+}$ was reported [151]. Thus, the nano-building block allows

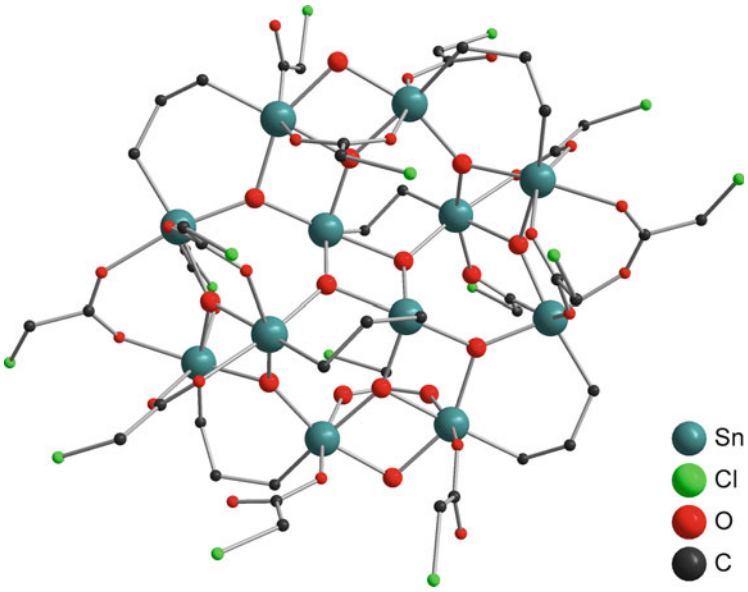

Fig. 24 Ball-and-stick model representing the molecular structure of a "flat" dodecanuclear organotin oxido cluster $[(Sn(CH_2)_3Sn)_6O_{10}(OH)_2(ClCH_2COO)_{14}]$. Hydrogen atoms are omitted [146]

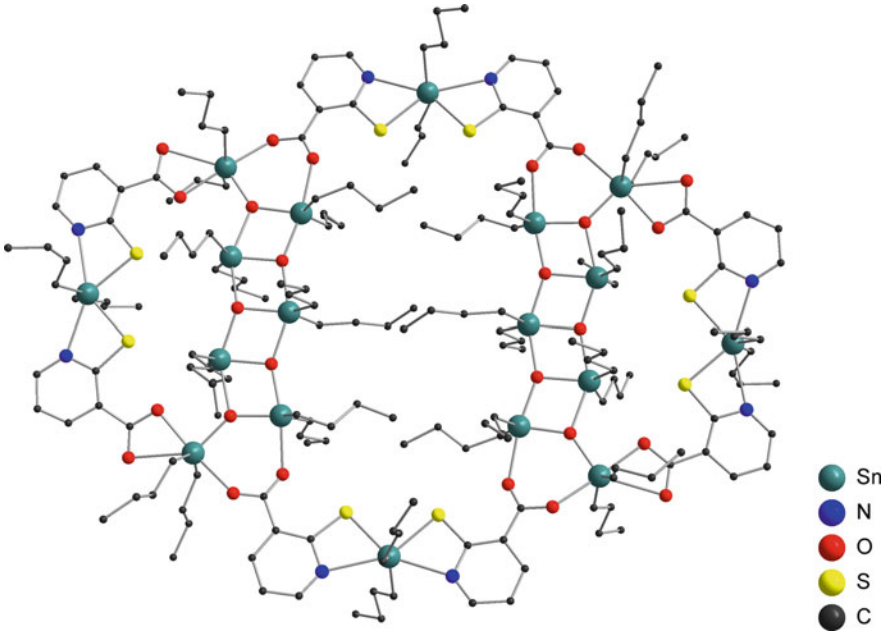

Fig. 25 Ball-and-stick model representing the molecular structure of the octadecanuclear ladder-type organotin oxido cluster $[(n\mathrm{Bu}_2\mathrm{Sn})_{18}O_{10}L_8]$ (H_2L=2-mercaptonicotinic acid). Two hexanuclear ladder-type units are bridged via four mononuclear diorganotin moieties. Hydrogen atoms are omitted [147]

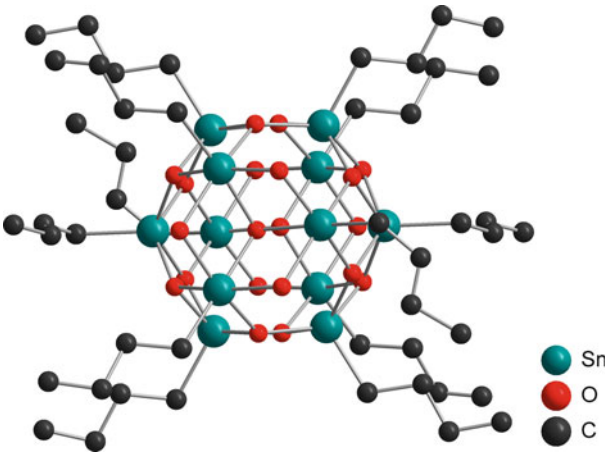

Fig. 26 Ball-and-stick model representing the molecular structure a typical cationic dodecanuclear organotin oxido cluster, the spherical cation $[(n\text{BuSn})_{12}(\mu_3\text{-O})_{14}(\mu\text{-OH})_6]^{2+}$. Hydrogen atoms are not shown [148]

modification of its molecular and electronic structure, which explains the still ongoing interest in this type of tin oxido clusters, which were first introduced by Puff and Reuter in 1989 (Table 4) [157].

As a result of weak bonds between lead and carbon, organolead oxido clusters are virtually unknown, but some lead oxido alkoxides similar to tin exist. For example, the hexanuclear core structure of lead(II) oxido alkoxides of the type $[Pb_6(\mu_3\text{-O})_4(\mu_3\text{-OR})_4]$ [106–110], which are derived from hypothetical $[Pb_6(\mu_3\text{-O})_4(\mu_3\text{-OH})_4]$ [105], are present as basic motif of the heteronuclear metal oxido cluster $[Pb_6Nb_4(\mu_4\text{-O})_4(\mu_3\text{-OEt})_4(\mu\text{-OEt})_{12}(OEt)_8]$ [108], so far the largest cluster in the series of lead oxido alkoxides (Fig. 27). The cluster might be described to be composed of a $[Pb_6O_4(OEt)_4]$ core to which four molecules $Nb(OEt)_4$ are attached via μ_4-oxido ligands. A different hexanuclear core structure was reported for $[(PbO)_6(R_2Si_2O_3)_2]$ [R=(2,6-*i*$Pr_2C_6H_3$)N($SiMe_3$)], in which the hexanuclear core $\{Pb_6O_2\}$ is encapsulated by a bulky silanolate (Fig. 28) [163]. Additional lead oxido silanolates/alkoxides such as tetranuclear $[Pb_4(\mu_4\text{-O})(OSiPh_3)_6]$ [110], heptanuclear $[Pb_7(\mu_4\text{-O})(\mu_3\text{-O})(\mu\text{-OSiMe}_3)_{10}]$ [164], and heptanuclear $[Pb_7(\mu_4\text{-O})_4(\mu_3\text{-O})_4(\mu_3\text{-OMe})_4(\mu\text{-I})_4]I_2$ [165] were reported, while clusters of higher nuclearity are unknown for homometallic species.

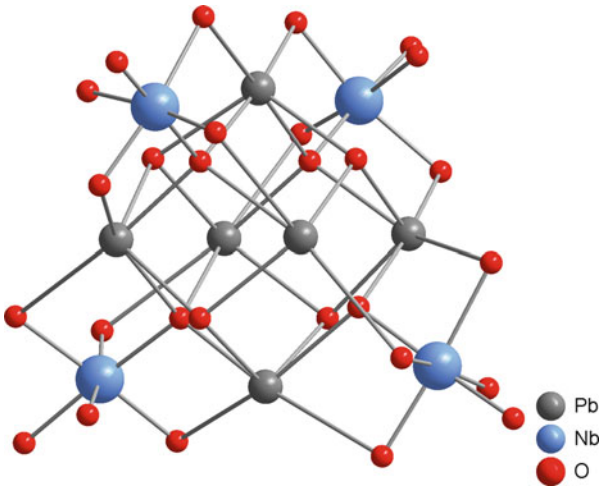

Fig. 27 Ball-and-stick model representing the heteronuclear metal oxido framework of $[Pb_6Nb_4(\mu_4\text{-}O)_4(\mu_3\text{-}OEt)_4(\mu\text{-}OEt)_{12}(OEt)_8]$. The central structural unit is composed of a hexanuclear $[Pb_6O_8]$ unit as it was postulated for $[Pb_6O_4(OH_4]$. Carbon and hydrogen atoms were not located [108]

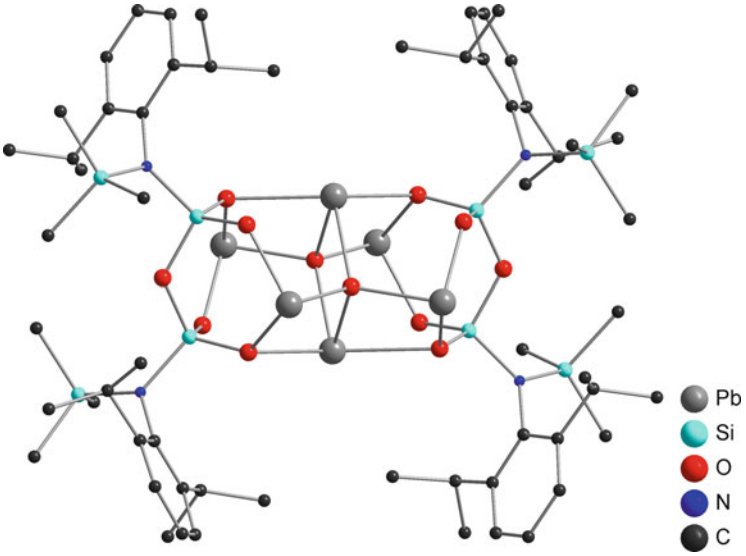

Fig. 28 Ball-and-stick model representing the molecular structure of $[(PbO)_6(R_2Si_2O_3)_2]$ [R= (2,6-*i*$Pr_2C_6H_3$)N($SiMe_3$)]. The central hexanuclear lead oxido unit is captured by two bulky organosilanolates. Hydrogen atoms are not shown [163]

4 Antimony and Bismuth

The metal oxides of antimony and bismuth show a very low solubility in aqueous solution, and the hydrolysis products are observed as hydrates of various forms. For antimony the anhydrides Sb_2O_3 and Sb_2O_5 but also the mixed valent compound Sb_2O_4 are easily accessible, whereas for bismuth exclusively Bi_2O_3 is observed upon hydrolysis. The low solubility and the redox behavior of antimony might have hampered detailed studies on hydrolysis products at later stages of nucleation in aqueous solution so far. Under strongly basic conditions, the antimonates $[Sb(OH)_4]^-$ and $[Sb(OH)_6]^{3-}$ present the primary species at early stages of hydrolysis. It is assumed that under acidic conditions, hydrated SbO^+ is formed [166, 167], but it is very likely that polymetaloxido cations are generated similarly to bismuth. Based on early reports on the hydrolysis behavior of bismuth salts, the presence of the hydrated bismuthyl-ion BiO^+ in aqueous solution was postulated, later on described as $[Bi_6(OH)_8]^{10+}$ [168–172], which finally turned out to be $[Bi_6O_4(OH)_4]^{6+}$ [75, 76, 173]. The latter hexanuclear cluster is realized in a large number of hydrolysis products with diverse counteranions (Fig. 29, Table 5), is formed in aqueous solution under acidic conditions, and is assumed to form via hydrated forms of $[Bi(OH)_2]^+$, $[Bi_2(OH)_4]^{2+}$, and $[Bi_3(OH)_5]^{4+}$ [94, 171]. A change of the conditions to higher pH values is assumed to give nonanuclear species of the general type $[Bi_9O_n(OH)_m]^{z+}$ [168, 190], which indeed has been realized in the cluster cations $[Bi_9O_8(OH)_6]^{5+}$ and $[Bi_9O_8(OEt)_6]^{5+}$, both crystallizing as perchlorate salt [189]. Nonanuclear bismuth oxido clusters were also realized with ligands such as triflate [191], carboxylate [192], diketonate [193], silanolate [194], aryloxide [195], and alkoxide [189, 196] but show a different molecular structure (Tables 6 and 7). The cation $[Bi_9O_8(OH)_6]^{5+}$ and the related ethoxide are build up by three corner-sharing $\{Bi_5\}$ subunits, whereas the other nonanuclear clusters are comprised of a hexanuclear $\{Bi_6\}$ oxido unit, to which three bismuth moieties are

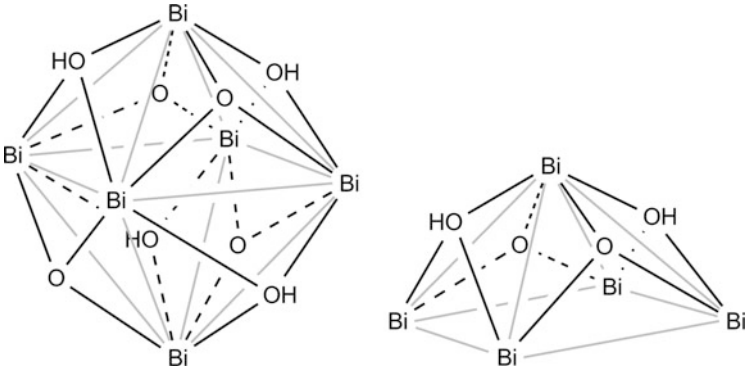

Fig. 29 Model structures for the typical hexanuclear bismuth oxido hydroxido motif $[Bi_6O_4(OH)_4]^{6+}$ and a pentanuclear metal oxido subunit as it is found in clusters such as $[Bi_9O_8(OH)_6]^{5+}$, with three of the subunits being corner-sharing

Table 5 Selected examples of inorganic bismuth oxido clusters with nuclearities between six and ten. Synthesis conditions, isolated yield, and analytics are given

Inorganic Compounds	Synthesis	η/%	Analytics	References
$[Bi_6O_4(OH)_4(NO_3)_6] \cdot HO$	(1) Heating of $[Bi_6O_4(OH)_4(NO_3)_6(H_2O)_2] \cdot 2\ H_2O$	n.r.	XRD, PXRD, CA, TGA	[75, 174–177]
	(2) Hydrothermal synthesis from $Bi(NO_3)_3 \cdot 5\ H_2O$ in H_2O			
$[Bi_6O_4(OH)_4(NO_3)_6(H_2O)_2] \cdot 2\ H_2O$	(1) Hydrolysis of $Bi(NO_3)_3 \cdot 5\ H_2O$ in diluted HNO_3	n.r.	XRD, PXRD, Raman	[76, 175–177]
	(2) Hydrothermal synthesis from $Bi(NO_3)_3 \cdot 5\ H_2O$ in H_2O	84		
$[Bi_6O_4(OH)_4](OH)(NO_3)_5 \cdot 0.5\ H_2O$	Hydrolysis of $Bi(NO_3)_3 \cdot 5\ H_2O$ in diluted HNO_3 with NaOH	n.r.	PXRD, CA, IR, ^{1}H-NMR, UV/Vis	[173, 175, 176]
$[Bi_6O_4(OH)_4(NO_3)_5(H_2O)](NO_3)$	Crystallization of $[Bi_6O_4(OH)_4(NO_3)_6(H_2O)_2] \cdot 2H_2O$ from water	n.r.	XRD, PXRD, EA, IR	[178]
$[Bi_6O_4(OH)_4(NO_3)_6(H_2O)_2] \cdot H_2O$	Hydrolysis of $Bi(NO_3)_3 \cdot 5\ H_2O$ in diluted HNO_3 with NaOH; crystallization by diffusion of acetone into solution	64	XRD, EA, IR	[178]
$[Bi_6O_4(OH)_4]_{0.5}[Bi_6O_5(OH)_3]_{0.5}(NO_3)_{5.5}$ often denoted as "$[Bi_6O_4(OH)_4](NO_3)_6$"	(1) Hydrolysis of Bi_2O_3 in HNO_3/H_2O/EtOH	n.r.	XRD, PXRD, CA, TGA, Raman	[177, 179]
	(2) Evaporation of solvent from $[Bi_6O_5(OH)_3(NO_3)_3]_2(NO_3)_4 \cdot 6\ H_2O$ solution	n.r.	XRD, PXRD, Raman	[177, 180]
	(3) Hydrolysis of $Bi(NO_3)_3 \cdot 5\ H_2O$ with urea in H_2O	n.r.	XRD, PXRD, PND, CA, TGA, IR, ^{1}H-MAS NMR, XRF	[175–177]
$[Bi_6O_5(OH)_3(NO_3)_3]_2(NO_3)_4 \cdot 6\ H_2O$	(1) Hydrolysis of $Bi(NO_3)_3 \cdot 5\ H_2O$ in diluted HNO_3 with NaOH	n.r.	XRD, PXRD, CA, TGA, IR, ^{1}H-MAS NMR, XRF, Raman	[175–177, 181]
	(2) Hydrolysis of $Bi(NO_3)_3 \cdot 5\ H_2O$ with urea in H_2O			
	(3) Hydrolysis of $Bi(NO_3)_3 \cdot 5\ H_2O$ in H_2O			
$[Bi_6O_5(OH)_3(NO_3)_4(H_2O)]_2(NO_3)_2 \cdot 4\ H_2O$	Hydrolysis of $Bi(NO_3)_3 \cdot 5\ H_2O$ in H_2O and diffusion of EtOH	44	XRD, EA, IR, UV/Vis, FE	[182]
$[Bi_6O_6(OH)](NO_3)_5 \cdot 2.5\ H_2O$	Reaction of elemental bismuth in diluted HNO_3	n.r.	PXRD, CA, TGA	[175, 183]

$[Bi_6O_6(OH)_2](NO_3)_4 \cdot 2\ H_2O$	Reaction of elemental bismuth in diluted HNO_3	n.r.	PXRD, CA, TGA	[175, 176, 183]
$[Bi_6O_6(OH)_3](NO_3)_3 \cdot 1.5\ H_2O$	(1) Reaction of elemental bismuth in diluted HNO_3	n.r.	PXRD, CA, TGA, ^{1}H-MAS NMR	[175, 176, 183]
	(2) Hydrothermal synthesis from $Bi(NO_3)_3 \cdot 5\ H_2O$ and H_2O or $[Bi_6O_5(OH)_3(NO_3)_3]_2(NO_3)_4 \cdot 6\ H_2O$ and H_2O			
$[Bi_6O_4(OH)_4](NO_3)_{12}(HOC_2H_4NH_3)_6$	Reaction of $Bi(NO_3)_3$ with ethanolamine in water	–	XRD	[184]
$[Bi_6O_4(OH)_4][B_{12}H_{12}]_3 \cdot 10\ H_2O$	Reaction of Bi_2O_3 with $(H_3O)_2[B_{12}H_{12}]$ in H_2O	n.r.	XRD, DTA/TG	[185]
$[Bi_6O_4(OH)_4](ClO_4)_6 \cdot 7\ H_2O$	Reaction of Bi_2O_3 with $HClO_4$ in water	n.r.	XRD, ND, CA, IR, Raman	[186–188]
$[Bi_9O_8(OH)_6](ClO_4)_5$	Hydrolysis of $BiOClO_4$ in H_2O/NaOH and tris(hydroxymethyl)ethane	46	XRD, PXRD, CA, ^{1}H-, ^{17}O-NMR, MALDI-MS, MS	[189]
$[Bi_9O_8(OEt)_6(EtOH)](ClO_4)_5 \cdot 4\ EtOH$	Ethanolysis of $[Bi_9O_8(OH)_6](ClO_4)_5$	91	XRD, ^{1}H-, ^{13}C-NMR, IR	[189]

n.r. not reported

Table 6 Selected examples of ligand-stabilized bismuth oxido clusters with nuclearities between six and ten. Synthesis conditions, isolated yield, and analytics are given

Ligand-stabilized Compounds	Synthesis	η/%	Analytics	References
$[Bi_6O_4(OH)_4(tfa)_6]_2[Bi(tfa)_3]_3$ (Htfa: trifluoroacetic acid)	Hydrolysis of $Bi(tfa)_3$ in H_2O	n.r.	XRD, IR	[197]
$[Bi_6O_6(OH)_2(tfa)_4]_2[Bi(tfa)_3]_4$ (tfa: trifluoroacetic acid)	Hydrolysis of $Bi(tfa)_3$ in H_2O	n.r.	XRD, IR	[197]
$[Bi_6O_4(OH)_4(OTf)_6(MeCN)_6]$ · 2 MeCN (HOTf: trifluoromethane sulfonic acid)	Reaction of $[Bi_6O_4(OH)_4(NO_3)_6]$ · H_2O with (1) CF_3SO_3H or (2) $Me_3SiO_3SCF_3$ in toluene; crystallization from $MeCN/CHCl_3$	55	SC-XRD, PXRD, EA, ^{1}H-, ^{13}C-NMR, IR	[198]
$[Bi_6O_4(OH)_4(O_3SNH_2)_6]$	Hydrolysis of $Bi(NO_3)_3$ · 5 H_2O with sulfamic acid in H_2O	n.r.	PXRD, EA, IR, DTA-TGA	[199]
$[Bi_6O_4(OH)_4(O_3SNH_2)_6]$ · H_2O	Reaction of Bi_2O_3 with sulfamic acid in H_2O	78	XRD, EA, IR, MS	[200]
$[Bi_6O_4(OH)_4(H_2O)_2]$ $[(CH_2)_2(SO_3)_2]_3$	Hydrothermal synthesis from Bi_2O_3 and ethanedisulfonic acid in H_2O	90	XRD, PXRD, IR, TGA	[191]
$[Bi_6O_4(OH)_4(H_2O)_6](NTf_2)_6$ (NTf_2: bis(trifluoromethanesulfonyl)amide)	Hydrolysis of $Bi(NTf_2)_3$ in H_2O/*p*-xylene with heptanoic acid	n.r.	XRD	[201]
$[Bi_6O_5(BTC)_2(HBTC)]$ (H_3BTC=1,3,5-benzenetricarboxylic acid)	Hydrothermal synthesis from $Bi(NO_3)_3$ · 5 H_2O, H_3BTC, NaOH and H_2O	n.r.	XRD, PXRD, EA, IR, TGA	[202]
$[Bi_9O_7(HSal)_{13}(Me_2CO)_5]$ · 1.5 Me_2CO (H_2Sal: salicylic acid)	Hydrolysis of $Bi(HSal)_3$ (acidolysis of $BiPh_3$ with salicylic acid in toluene and crystallization from acetone)	n.r.	XRD, ^{1}H-, ^{13}C-NMR, IR, MALDI-MS	[192]
$[Bi_9O_7(hfac)_{13}]$ (hfac: hexafluoroacetylacetonate)	Reaction of $BiPh_3$ with hexafluoroacetylacetone and hexafluoropentane-2,2,4,4-tetraol	90	XRD, PXRD, EA, ^{1}H-, ^{19}F-NMR, IR, MS, UV/Vis	[193]
$[Bi_9O_8(OH)_6](OTf)_5$ (HOTf: trifluoromethane sulfonic acid)	Hydrothermal synthesis from Bi_2O_3 and CF_3SO_3H in H_2O	89	XRD, PXRD, IR, TGA	[191]

n.r. not reported

attached via three faces of the octahedral $\{Bi_6\}$ unit (Figs. 29 and 30).The tendency of bismuth to form polynuclear species as result of hydrolysis and condensation is high, and mononuclear species of the general type $[Bi(OH)_n(H_2O)_{6-n}]^{3-n}$ are only observed in highly diluted solutions, with the number of n depending on the pH of the solution [168].

The hexanuclear metal oxido unit $[M_6O_{4+x}(OH)_{4-x}]^{(6-x)+}$ is a quite common structural building block in the metal oxido cluster chemistry of large metal cations.

Table 7 Selected examples of bismuth oxido alkoxides and silanolates with nuclearity between six and ten. Synthesis conditions, isolated yield, and analytics are given

Alkoxides and Siloxides	Synthesis	η/%	Analytics	References
$[Bi_2Na_4O(OtBu)_8]$	Reaction of $Bi(OtBu)_3$ with $NaOtBu$ in benzene	15	XRD, ^{1}H-NMR	[203]
$[Bi_2Na_4O(OC_6F_5)_8(thf)_4]$	Reaction of $[Bi(OC_6F_5)_3 \cdot C_7H_8]_2$ with $NaOC_6F_5$ in THF	79	XRD, EA, ^{19}F-NMR, IR	[204]
$[Bi_2Na_4O(OSiMe_3)_8]$	(1) Reaction of $BiCl_3$ with $NaOSiMe_3$ in toluene	9	XRD, EA, IR	[194, 205]
	(2) Reaction of $[Bi(OSiMe_3)_3]$ with $NaOSiMe_3$ in toluene	76		
$[Bi_4Na_2O_2(OC_6F_5)_{10}(thf)_2]$	Reaction of $BiCl_3$ with $NaOC_6F_5$ in THF	n.r.	XRD	[196, 206]
$[Bi_4Li_2O_2\{O\text{-}2\text{-}(CH_2CH{=}CH_2)C_6H_4\}_{10}]$	Alcoholysis of $Bi[N(SiMe_3)_2]_3$ with 2-allylphenol; Li source not given	<5%	XRD	[207]
$[Bi_6O_3(OC_6H_3\text{-}2,6\text{-}Cl_2)_{12}] \cdot 2\ C_6H_5CH_3 \cdot Et_2O \cdot 2,6\text{-}Cl_2C_6H_3OH$	Alcoholysis of $BiPh_3$ with 2,6-dichlorophenol in toluene and crystallization from hexane/THF/Et_2O	23	XRD, EA	[208]
$[Bi_6O_3(OC_6F_5)_{12}(C_6H_5CH_3)]$	(1) Hydrolysis or ether elimination of $[Bi(OC_6F_5)_3(C_6H_5CH_3)]_2$ in CH_2Cl_2	89	XRD, EA, ^{19}F-NMR	[196]
	(2) Alcoholysis of $BiPh_3$ with HOC_6F_5 in CH_2Cl_2	80		
	(3) Hydrolysis or ether elimination of $[Bi(OC_6F_5)_3(C_6H_5CH_3)]_2$ in THF and crystallization from toluene	n.r.		
$[Bi_9O_7(OC_6F_5)_{13}(thf/C_6H_5CH_3)_2]$	Hydrolysis or ether elimination from $[Bi(OC_6F_5)_3(C_6H_5CH_3)]_2$	n.r.	XRD, EA, ^{19}F-NMR	[195, 196, 206]
$[Bi_9O_7(OCH(CF_3)_2)_{13}]$	Alcoholysis of $BiPh_3$ with $(CF_3)_2CHOH$	10	XRD, EA, ^{1}H-, ^{19}F-NMR, IR	[209]
$[Bi_9O_7(OSiMe_3)_{13}] \cdot 0.5\ C_7H_8$	Hydrolysis of $[Bi(OSiMe_3)_3]$ in toluene	100	XRD, EA, IR	[194]

n.r. not reported

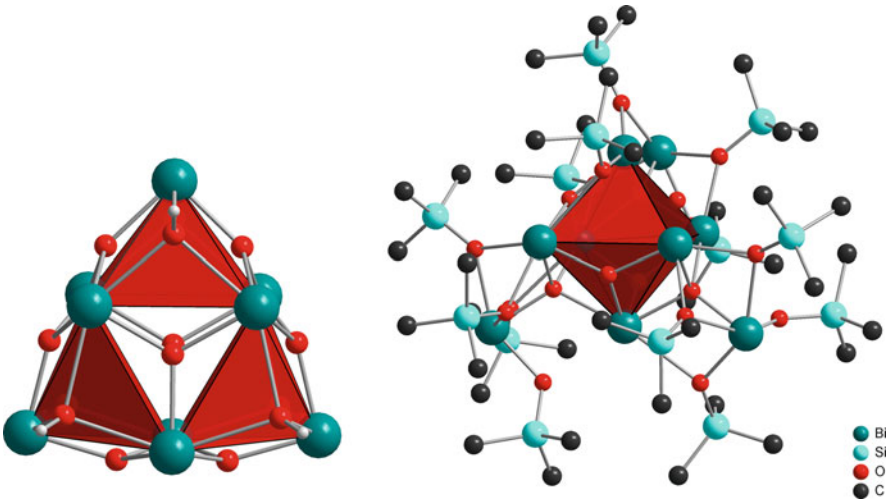

Fig. 30 Ball-and-stick model representing the molecular structures of two different nonanuclear bismuth oxido clusters. The cluster $[Bi_9O_8(OH)_6]^{5+}$ (*left*) is composed of three corner-sharing pentanuclear $\{Bi_5\}$ subunits, and the silanolate is composed of the hexanuclear $\{Bi_6O_8\}$ subunit $[Bi_6O_7(OSiMe_3)]^{3+}$, which is coordinated to three bismuthates of the type $[Bi(OSiMe_3)_4]^-$ [189, 194]

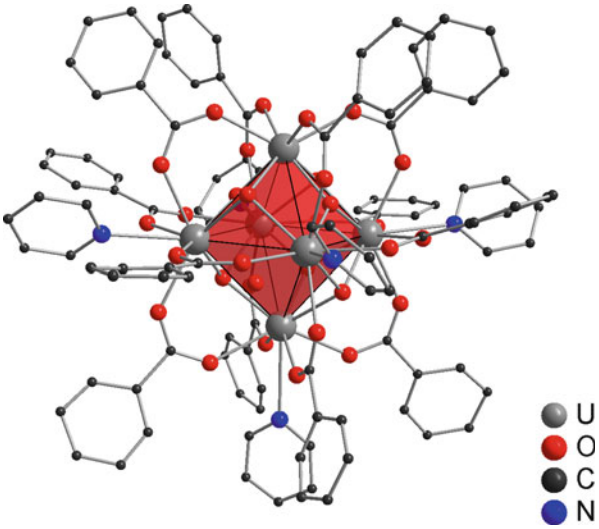

Fig. 31 Ball-and-stick model representing the molecular structure of the hexanuclear uranium oxido cluster $[U_6O_4(OH)_4(PhCOO)_{12}(py)_5]$. The almost identical $[M(\mu_3\text{-}O)_4(\mu_3\text{-}OH)_4]$ core is reported for several bismuth oxido clusters (see Tables 5 and 6) [210]

For example, the molecular uranium oxido cluster $[U_6O_4(OH)_4(PhCOO)_{12}(py)_5]$ (py=pyridine) [210] as given in Fig. 31 shows a core structure which is almost identical to the bismuth examples given in Fig. 29 and Tables 5 and 6. Structural

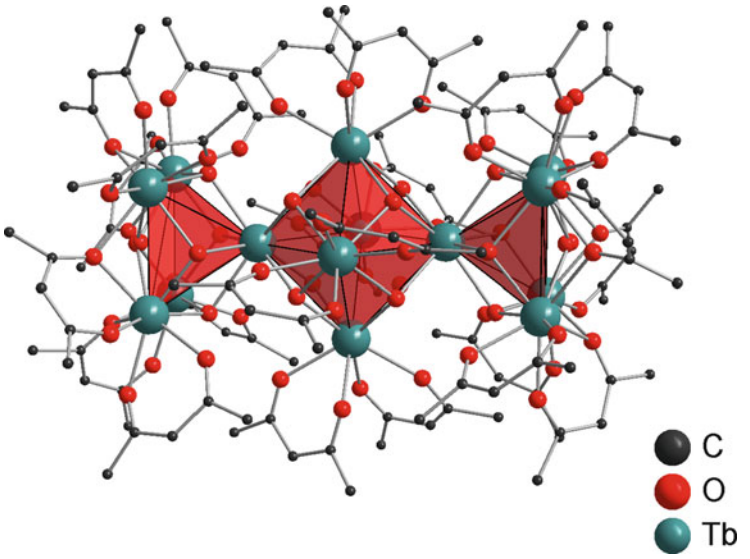

Fig. 32 Ball-and-stick model representing the molecular structure of the tetradecanuclear lanthanide hydroxido cluster $[Tb_{14}(OH)_{18}(acac)_{24}]$. Hydrogen atoms are not shown. The central hexanuclear $\{Ln_6\}$ cluster is connected via two corners to a pentanuclear $\{Ln_5\}$ cluster each. Both cluster fragments constitute typical structures as found in bismuth oxido chemistry as well [212]

units of the type $\{U_6O_8\}$ were also reported as part of extended networks or discrete clusters such as $[U_6O_8(OTf)_{12}(H_2O)_3]\cdot 23H_2O$ (OTf=triflate) [211]. Similar hexanuclear core structures are also observed in lanthanides of the types $[Ln_{14}(OH)_{18}(acac)_{24}]$ (Ln=Dy, Tb, Eu; acac=acetylacetonate (Fig. 32) [212, 213], $[Ln_{14}O(OH)_{20}(IN)_{22}(Cu_6Cl_4(H_2O)_8]\cdot 6\ H_2O$ (Ln=Y, Gd, Dy; HIN=isonicotinic acid) [214], $[Ln_6O(OH)_8(NO_3)_6(H_2O)_{12}](NO_3)_2\cdot x\ H_2O$ (Ln=Sm, Dy, Er) [215], and $[Ln_6O(OH)_8(H_2O)_{24}](ClO_4)_8\cdot xH_2O$ (Ln=Nd, Gd) [216], but the degree of condensation is drastically reduced. Noteworthy, the oxido ligand as observed in the latter three examples constitutes the center of the octahedral cluster, which is also observed in some bismuth oxido clusters, e.g., in $[Bi_2Na_4O(OR)_8]$ (R=$SiMe_3$, *t*Bu, C_6F_5) [194, 203, 204] and in the central octahedral unit in $\{Bi_{38}O_{45}\}$ clusters such as $[Bi_{38}O_{45}(hfac)_{24}]$ [193] (hfac=hexafluoroacetylacetonate) or $[Bi_{38}O_{45}(NO_3)_{20}(dmso)_{28}](NO_3)_4$ [178], among others.

In comparison to bismuth and other main group metals, inorganic polyantimony oxido clusters without covalent linkage to an organic ligand are almost unknown. However, the report on the three-dimensional network structure of $[Sb_4O_4(OH)_2]$ $[O_3SCH_2CH_2SO_3]$ is a clear hint that cations of the type $[Sb_4O_4(OH)_2]^{2+}$ exist in aqueous solution [217]. By contrast other examples of inorganic antimony oxido clusters are of anionic nature. A serendipitous but pioneering work was reported in 1994 by Fenske et al. that described a hexanuclear cluster of the type $[Sb_6(\mu_3\text{-}O)_2(\mu\text{-}O)_8Cl_{14}]^{4-}$ with all antimony atoms being hexacoordinate (Fig. 33). The basic structural arrangement is best described as oxygen-bridged lacunary Sb_3O_4

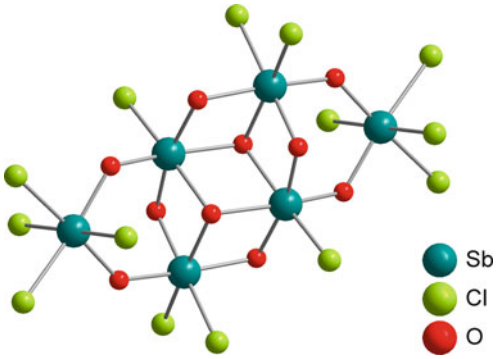

Fig. 33 Ball-and-stick model representing the molecular structure of the hexanuclear antimonate $[Sb_6(\mu_3\text{-}O)_2(\mu\text{-}O)_8Cl_{14}]^{4-}$ [218]

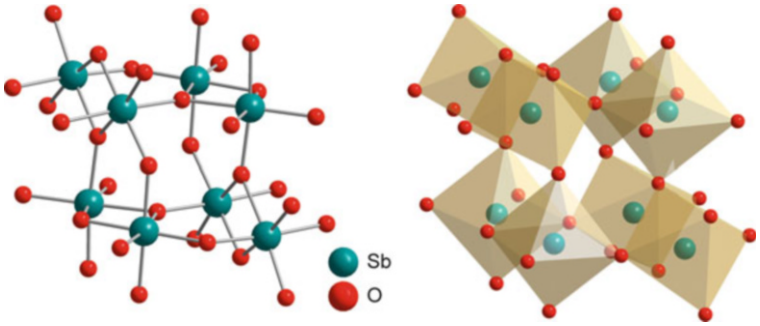

Fig. 34 Ball-and-stick model and polyhedral view representing the molecular structure of the octanuclear antimony oxido hydroxido cluster $[Sb_8O_{12}(OH)_{20}]^{4-}$ [219]

cubes, which are known from tin oxido and diorganoantimony compounds [218]. Shortly afterwards, Nakano et al. did show that the hydrolysis of $KSb(OH)_6$ in aqueous solution in the presence of $[t\text{Bu}_4\text{N}]OH$ provided a material that after crystallization from chloroform turned out to be the first discrete polyantimony oxido hydroxido cluster $[Sb_8O_{12}(OH)_{20}]^{4-}$ (Fig. 34) [219]. The antimony atoms are octahedrally coordinated, and the resulting octahedra are edge-sharing with one next neighbor to give dimerized units of the type $\{Sb_2O_{10}\}$, which themselves are corner-sharing with two neighboring $\{Sb_2O_{10}\}$ units.

Later on the cluster was reacted with the silanol $HOSiMe_2t\text{Bu}_2$, and upon cluster degradation tetranuclear $[Sb_4O_6(OH)_4(OSiMe_2t\text{Bu})_6]^{2-}$ was obtained. The structure of the silanolate-stabilized antimony oxido cluster $[Sb_4O_6(OH)_4\{OSiMe_2t\text{Bu}\}_6]^{2-}$ might be described to be composed of four edge-sharing octahedral SbO_6 moieties that form a planar Sb_4O_{16} core [220]. Hydrolysis is expected to provide the new antimonite $[Sb_4O_6(OH)_{10}]^{2-}$, which might be regarded as being a slightly reorganized tetranuclear cutout of $[Sb_8O_{12}(OH)_{20}]^{4-}$, with four edge-sharing octahedral SbO_6 units. Characterization of the discrete anion $[Sb_4O_6(OH)_{10}]^{2-}$ is not

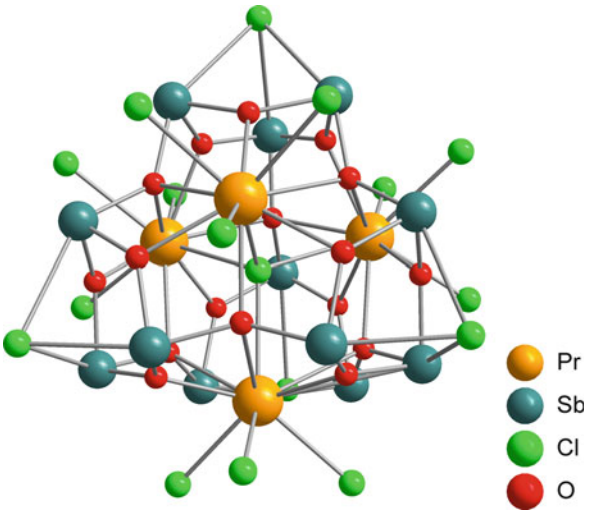

Fig. 35 Ball-and-stick model representing the molecular structure of the heteronuclear metal oxido cluster[$Pr_4Sb_{12}(\mu_4\text{-}O)_6(\mu_3\text{-}O)_{12}(\mu_4\text{-}Cl)(\mu_3\text{-}Cl)_4Cl_{12}]^{5-}$ [222]

reported so far. Another almost planar antimony oxido arrangement is found in $[Sb_6O_4(NCS)_{12}]^{2-}$ that similarly forms a central Sb_4O_4 ladder-type arrangement to which another antimony-containing moiety, here $Sb(NCS)_3$, is coordinated at the peripheral oxygen atoms [221]. The largest discrete antimony-containing oxido cluster was observed under hydrothermal synthesis conditions starting from Pr $(OAc)_3{\cdot}3H_2O$, $SbCl_3$ and 2-methylpyridine in water and turned out to be a heteronuclear cluster of the type $[Pr_4Sb_{12}(\mu_4\text{-}O)_6(\mu_3\text{-}O)_{12}(\mu_4\text{-}Cl)(\mu_3\text{-}Cl)_4Cl_{12}]^{5-}$ in combination with monoprotonated 2-methylpyridine as cation (Fig. 35) [222]. The structure is best described as being composed of a praseodymium tetrahedron built up around a μ_4-chlorido ligand and itself being encapsulated in a truncated $\{Sb_{12}\}$ cage. The anion is of nearly perfect T_d symmetry and quite robust. Thus it has been used as cluster-type building block to build up inorganic–organic hybrid frameworks under solvothermal conditions [222–225].

As mentioned above, the tetranuclear antimony oxido cluster $[Sb_4O_6(OH)_{10}]^{2-}$ is not reported to date, but structural analogs are found among the organometallic antimony oxido clusters. A series of soluble diorganoantimony oxides of the type $[(R_2Sb)_4(\mu_3\text{-}O)_2(\mu\text{-}O)_4]$ (R=alkyl, aryl), which show a Sb-O-core structure as anticipated for the antimonate $[Sb_4O_6(OH)_{10}]^{2-}$, was reported [226, 227]. Diverse other organoantimony oxido clusters with nuclearity up to ten have been reported; selected examples are (1) $[(R_2Sb)_4O_4(O_2)_2]$ (R=Ph, o-tolyl) with four antimony atoms occupying a square [226, 228, 229]; (2) a series of adamantane-like clusters, e.g., tetranuclear $[(p\text{-}ClC_6H_4Sb)_4O_6(Hnaphpz)_4]$ (H_2naphpz, 2-[1H-pyrazol-5(3)-yl]naphthalene-1-ol) [59]; (3) carboxylates, e.g., tetranuclear $(Ph_2Sb)_4O_4(OH)_2(O_2CR)_2$ (R=2-$(CHO)C_6H_4$, 2,3-$F_2C_6H_3$, 4-$CF_3C_6H_4$) [230]; (4) organosilanolate-stabilized clusters, e.g., hexanuclear $[(Ph_2Sb)_4Sb_2(Ph_2SiO_2)_2O_2(OH)_2]$ [231]; (5) phosphonate-stabilized clusters, e.g., nonanuclear $[(Ph_2Sb)_2(PhSb)_7O_{11}(OH)_2(cycPO_2)_4(H_2O)_2]$

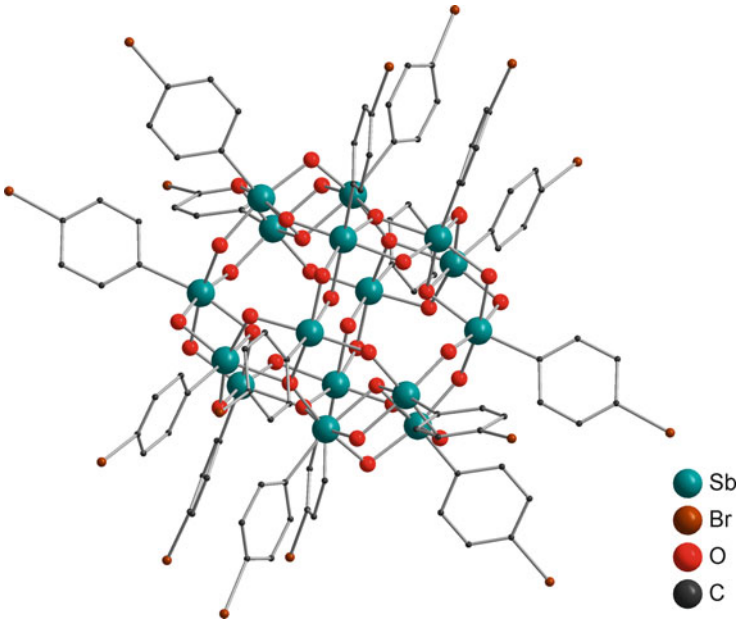

Fig. 36 Ball-and-stick model representing the molecular structure of the organometallic cluster [(p-X-$C_6H_4Sb)_{16}O_{28}(OH)_8$] (X=Cl, Br). Hydrogen atoms are not shown [234]

(cycPO_2H=1,1,2,3,3-pentamethyltrimethylenephosphinic acid) [232]; or (6) terphenyl-stabilized clusters, e.g., decanuclear [(2,6-Mes$C_6H_3Sb)_4(ClSb)_4$ $(HOSb)_2O_{14}$] [233]. Examples with more than ten antimony atoms are scarce and restricted to monoorganoantimony derivatives, which might be regarded as condensation products of organostibonic acids. For example, hexadecanuclear antimony oxido clusters of the type [(p-X-$C_6H_4Sb)_{16}O_{28}(OH)_8$] (X=Cl, Br) were isolated starting from the corresponding arylstibonic acid in toluene under reflux in the presence of 3,5-dimethylpyrazole (Fig. 36) [234]. This cluster is unique among the polyantimony oxido compounds and the only homometallic example of such large size.

Several other heterometallic condensation products of aryl stibonic acids $ArSbO_3H_2$ of high nuclearity, which incorporate diverse metal atoms within the metal oxido core structure, have been reported. They are usually obtained under solvothermal or reflux conditions in the presence of amines and metal salts and form quite different molecular structures besides quite similar nuclearity. The additional cations play the role of templates, and interesting antimony oxido clusters, for example, as found in the tetradecanuclear heterovalent Sb(V)/Sb(III) compound $(Ph_3Te)_2[Na_2(H_2O)_2(p$-Br-$C_6H_4Sb)_{10}Sb_4(Ph_2Te)_4O_{30}(OH)_4]$, were reported [235]. The latter cluster seems to be unique, whereas a series of structurally related dodecanuclear clusters was reported, the structures of which show some intriguing dependency on the incorporated metal. With medium-sized cations such as Na^+ and K^+ clusters of the general type $[M_2H_{10-x}(ArSb)_{12}O_{30}]^{x-}$ (M=Na, K) were

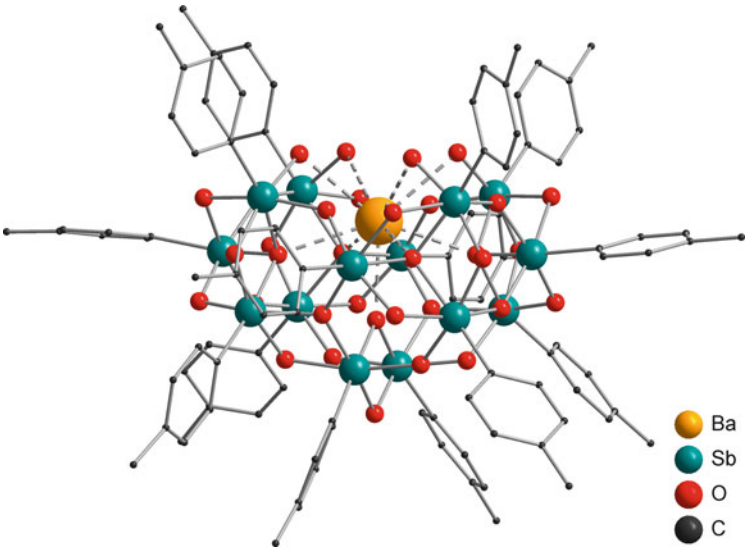

Fig. 37 Ball-and-stick model representing the molecular structure of a bowl-shaped organoantimony oxido cluster, which captures a barium cation $[BaH_{10}(p\text{-}MeC_6H_4Sb)_{14}O_{34}]$. Hydrogen atoms are not shown [238]

isolated. They show an irregular hexagonal antiprism composed of twelve Sb atoms, e.g., in $[K_2H_8(p\text{-}ClC_6H_4Sb)_{12}O_{30}]^{2-}$ [236, 237]. Larger cations such as Rb^+ and Ba^{2+} show the tendency to form open, bowl-shaped $\{Sb_{14}\}$ metal oxido units, in which the cation is placed above or partially within the opening of the bowl (Fig. 37). This structural arrangement seems to be a very prominent one, because different element compositions have been realized and the stability of the molecular clusters was demonstrated by electrospray mass spectrometry, e.g., $[BaH_{10}(p\text{-}MeC_6H_4Sb)_{14}O_{34}]$, $(PhCH_2NMe_3)_xRb[RbH_{10-x}(p\text{-}ClC_6H_4Sb)_{14}O_{34}]$, $Rb_2[RbH_9(p\text{-}ClC_6H_4Sb)_{14}O_{34}]$, $Rb[RbH_{10}(p\text{-}MeC_6H_4Sb)_{14}O_{34}]$, and $Rb[RbH_9(p\text{-}MeC_6H_4Sb)_{14}O_{33}Br]$ [238, 239].

In the case of the lighter cation Li^+, the condensation products of arylstibonic acids allow the capture of the cation in the center of the antimony oxido cage structure, and thus for $[LiH_3(p\text{-}MeC_6H_4Sb)_{12}O_{28}]^{4-}$ a $\{LiSb_{12}O_{28}\}$ cage is observed, which shows the geometry of a γ-Keggin ion (Fig. 38) [238]. Remarkably, the Keggin-type arrangement is also observed for other heteronuclear antimony oxido clusters, which incorporate a transition metal instead of lithium. In addition transition metals might coordinate to the outer sphere of the cluster, which adopts a ε-Keggin-type structure, e.g., in $[Co(p\text{-}XC_6H_4Sb)_{12}O_{28}\{Co(H_2O)_3\}_4]Cl_2$ (X=Me, Cl) [240], $(PhCH_2NMe_3)_2[Zn(p\text{-}ClC_6H_4Sb)_{12}O_{28}(ZnCl)_4]Cl_2$ [240], $[Mn(PhSb)_{12}O_{28}\{Mn(H_2O)_3\}_2\{Mn(H_2O)_2(AcOH)\}_2]$ [241], and $[Mn(PhSb)_{12}O_{28}\{Mn(H_2O)_6(C_5H_5N)_{1.5}(MeCN)_{1.5}\}]$ [241], whereas the lack of additional transition metals in the periphery of $[BaCoH_4(p\text{-}MeC_6H_4Sb)_{12}O_{28}]$ [240] gave a δ-Keggin-type structure. These polyantimony oxido clusters were described as "reverse"

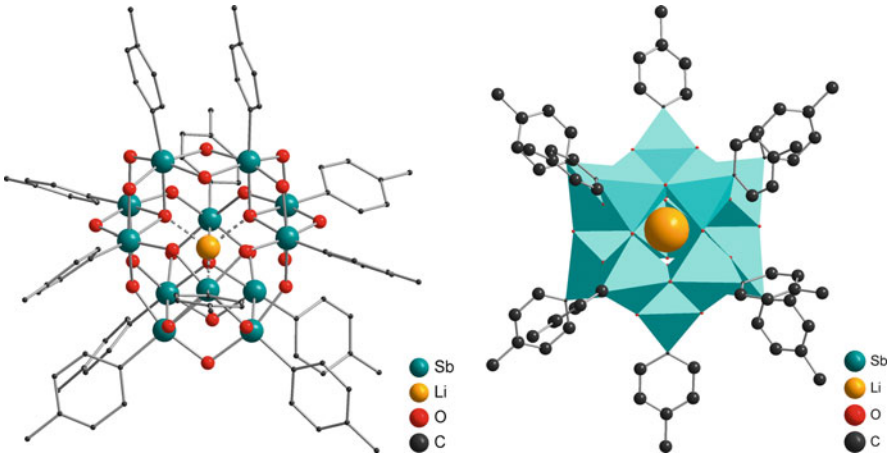

Fig. 38 Ball-and-stick model and polyhedral view of the molecular organoantimony oxido cluster, which captures a lithium cation $[LiH_3(p\text{-}MeC_6H_4Sb)_{12}O_{28}]^{4-}$. The cluster adopts a typical γ-Keggin-type arrangement. Hydrogen atoms are not shown [238]

Keggin ions by Baskar et al. [241], because the positions, which are occupied by the main group element (E) and the transition metal (TM), are in a reverse order as compared to traditional Keggin-type polyoxometalates $[ETM_{12}O_{40}]^{2-}$.

The aqueous chemistry of bismuth is dominated by complexes and clusters with nuclearities below ten. Hexanuclear clusters of the type $[Bi_6O_{4+x}(OH)_{4-x}]^{(6-x)+}$ might be regarded as "magic bismuth oxido clusters" of high stability with an octahedral arrangement of the bismuth atoms, denoted as $\{Bi_6\}$. Compounds such as $[Bi_{12}O_8(cit)_8]^{12-}$ (H_4cit=citric acid) [242] and $[Bi_{18}O_{12}(OH)_{12}(O_3S\text{-}Cam)_{24}(H_2O)_{14}]$ (HO_3S-Cam=*S*-(+)-10-camphorsulfonic acid) might be expected to be large bismuth oxido clusters based on their molecular formula; however, their molecular structures can be cut into two and three, respectively, subunits of $\{Bi_6\}$ clusters that are encapsulated by the organic ligands. Even the dodecanuclear cluster $[Bi_{12}O_{10}(OH)_6(NO_3)_6](NO_3)_4$ might be formally degraded into two hexanuclear clusters of the type $[Bi_6O_5(OH)_3(H_2O)]^{5+}$ which dimerize by bismuth oxygen coordination to give two neighboring octahedra [182]. The latter cluster is an interesting and unique example that visualizes a primary hydrolysis/condensation step of octahedral bismuth oxido nitrates in aqueous solution, which are easily formed and usually obtained upon hydrolysis of bismuth nitrate. However, they are often ill-defined and reported as so-called basic bismuth subnitrates, often without further specification. The composition of the hydrolysis products is best described as $[Bi_6O_{4+x}(OH)_{4-x}](NO_3)_{6-x}$, sometimes also formulated as hydrated $BiO(NO_3)$. In these compounds there is quite a high degree of variation for the exact composition, and unusual disorder might occur as was illustrated by a detailed study of Christensen and Lebech in 2012 [177]. Formerly, a prominent basic bismuth nitrate was described as $[Bi_6O_{4.5}(OH)_{3.5}](NO_3)_{5.5}\cdot H_2O$, which finally turned out to be

$[Bi_6O_4(OH)_4]_{0.54(1)}[Bi_6O_5(OH)_3]_{0.46(1)}(NO_3)_{5.54(1)}$ based on Rietveld refinement of synchrotron data. Noteworthy, the compound is composed of two cations of different charge but similar shape, and thus disordered packing of the cations is observed. Careful control of the crystallization process gives access to basic bismuth nitrates with either $[Bi_6O_4(OH)_4]^{6+}$ or $[Bi_6O_5(OH)_3]^{5+}$ cations and varying degree of hydration (Table 5). These hexanuclear bismuth oxido nitrates rapidly form in concentrated solutions and show a very low solubility in water, but they are soluble in DMSO and thus, in principle, become available for functionalization at the periphery, but they also show a strong tendency toward further condensation in solution. Several studies were carried out in order to substitute the nitrates by other ligands such as carboxylates and sulfonates, but only in rare cases the hexanuclear core structure is retained. For example, upon reaction of $[Bi_6O_4(OH)_4(NO_3)_6]\cdot H_2O$ with CF_3SO_3H, the water-soluble triflate $[Bi_6O_4(OH)_4(OTf)_6(MeCN)_6]$ was isolated [198]. However, most often further condensation reactions take place, and regardless whether $[Bi_6O_{4+x}(OH)_{4-x}](NO_3)_{6-x}$ or bismuth nitrate – with in situ formation of $\{Bi_6\}$ – were chosen as starting materials, bismuth oxido clusters with a nuclearity of 38 were observed. These clusters with the bismuth oxido core structure $\{Bi_{38}O_{45}\}$ are suggested to present another class of stable "magic bismuth oxido clusters," and their stability was demonstrated by electrospray mass spectrometry on several compounds even with molecular masses above 10 daltons [243–246]. Nevertheless, a full substitution of the nitrates at the periphery is rarely observed, and in several experiments none of the nitrates were substituted. Instead bismuth oxido clusters with variation in the bonding mode of the nitrates to the cluster core $\{Bi_{38}O_{45}\}$ and a varying number of coordinated solvent molecules DMSO were isolated (Table 8). An instructive example is the isolation of several bismuth oxido nitrates upon slight changes of the reaction conditions. The cluster $[Bi_{38}O_{45}(NO_3)_{20}(dmso)_{28}](NO_3)_4 \cdot 4$ DMSO was isolated as product of hydrolysis starting from $[Bi_6O_4(OH)_4(NO_3)_6] \cdot H_2O$ in DMSO [244], but crystallization of a second crop of crystals was observed, which after slight changes of the crystallization conditions turned out to be $[\{Bi_{38}O_{45}(NO_3)_{24}(dmso)_{26}\}\cdot 4DMSO]$ $[\{Bi_{38}O_{45}(NO_3)_{24}(dmso)_{24}\}\cdot 4DMSO]$ [178]. Addition of sodium benzoate provides the partially substituted derivative $[\{Bi_{38}O_{45}(NO_3)_{20}(OBz)_4(dmso)_{24}\}\cdot 4DMSO]$ $[\{Bi_{38}O_{45}(NO_3)_{24}(dmso)_{26}\}\cdot 4DMSO]$ [247]. Several other mixed ligand $\{Bi_{38}O_{45}\}$ nitrates with ligands such as sulfonates and carboxylates were reported and are given in Table 8. Noteworthy, the solubility of these large bismuth oxido nitrates is in most cases higher than that of the hexanuclear bismuth oxido nitrates, which is attributed to the coordinated DMSO molecules and partial substitution by organic ligands. Both prevent the large clusters from aggregation via bridging nitrate ligands as it is observed for the hexanuclear basic bismuth nitrates. A typical example of a $\{Bi_{38}O_{45}\}$ nitrate is shown in Fig. 39.

A rare case of full substitution of the nitrates was observed for methacrylate-substituted $\{Bi_{38}O_{45}\}$, $[Bi_{38}O_{45}(OMc)_{24}(dmso)_9(H_2O)_2]\cdot 2DMSO\cdot 5H_2O$ (OMc=methacrylate) [249], which shows significantly higher solubility in organic solvents such as THF and alcohols than most of the other bismuth oxido clusters (Fig. 40). The cluster is accessible starting from $[Bi_6O_4(OH)_4(NO_3)_6]\cdot H_2O$ in

Table 8 Selected examples of bismuth oxido nitrate clusters based on a $\{Bi_{38}O_{45}\}$ core. Synthesis conditions, isolated yield, and analytics are given

Bismuth oxido nitrates	Synthesis	η/%	Analytics	References
$[Bi_{38}O_{45}(NO_3)_{20}(dmso)_{28}](NO_3)_4 \cdot 4$ DMSO	Hydrolysis of $[Bi_6O_4(OH)_4(NO_3)_6] \cdot H_2O$ in HNO_3/DMSO; crystallization upon diffusion of THF or acetone into solution or evaporation of DMSO	72	XRD, EA, ESI-MS, TGA	[178, 244]
$[\{Bi_{38}O_{45}(NO_3)_{24}(dmso)_{26} \cdot 4$ DMSO]-$[\{Bi_{38}O_{45}(NO_3)_{24}(dmso)_{24}\} \cdot 4$ DMSO]	Hydrolysis of $[Bi_6O_4(OH)_4(NO_3)_6] \cdot H_2O$ in HNO_3/DMSO; crystallization upon diffusion of THF or acetone into solution	34	XRD, EA, IR	[178]
$[\{Bi_{38}O_{45}(NO_3)_{24}(dmso)_{26}\} \cdot 2$ DMSO]-$[\{Bi_{38}O_{45}(NO_3)_{24}(dmso)_{24}\} \cdot 0.5$ DMSO	Hydrolysis of $Bi(NO_3)_3 \cdot 5\ H_2O$ in DMSO in the presence of sodium methacrylate	49	XRD, EA, IR	[178]
$[\{Bi_{38}O_{45}(NO_3)_{20}(OBz)_4(dmso)_{24}\} \cdot 4$ DMSO]-$[\{Bi_{38}O_{45}(NO_3)_{24}(dmso)_{26}\} \cdot 4$ DMSO] (OBz: benzoate)	Hydrolysis of $Bi(NO_3)_3 \cdot 5\ H_2O$ in DMSO in the presence of sodium benzoate	28	XRD, PXRD, EA, IR, UV/Vis, DLS	[247]
$[\{Bi_{38}O_{45}(OH)_2(NO_3)_{24}(dmso)_{23}(H_2O)_2\} \cdot 2$ DMSO $\cdot H_2O][\{Bi_{38}O_{45}(NO_3)_{22}(O_2CPy)_2\ (dmso)_{24}(H_2O)_2\} \cdot 8$ DMSO $\cdot 2\ H_2O](HO_2CPy$: 4-pyridinecarboxylic acid)	Hydrolysis of $[Bi_6O_4(OH)_4(NO_3)_6] \cdot H_2O$ in DMSO in the presence of HO_2CPy	6	XRD, EA, IR	[248]
$[\{Bi_{38}O_{45}(OH)_2(O\textit{p}Ts)_8(NO_3)_{12}(dmso)_{26}\}(NO_3)_2 \cdot 2$ DMSO $\cdot 2\ H_2O]$ $[\{Bi_{38}O_{45}(OH)_2(O\textit{p}Ts)_8(NO_3)_{12}(dmso)_{24}\}(NO_3)_2 \cdot 4$ DMSO](HO*p*Ts: 4-toluenesulfonic acid)	Hydrolysis of $[Bi_6O_4(OH)_4(NO_3)_6] \cdot H_2O$ in DMSO in the presence of HO*p*Ts	27	XRD, EA, ESI-MS, TGA	[244, 248]
$[\{Bi_{38}O_{45}(O_3SC_4H_7)_8(NO_3)_{14}(dmso)_{19.5}(H_2O)_2\}]$-$[\{Bi_{38}O_{45}(O_3SC_4H_7)_{10}(NO_3)_{16}(dmso)_{16}\ (H_2O)_2\}] \cdot 3\ H_2O \cdot 3$ DMSO	Hydrolysis of $[Bi_6O_4(OH)_4(NO_3)_6] \cdot H_2O$ in DMSO in the presence of sodium 2-methylprop-2-ene-1-sulfonate	68	XRD, EA, ^{1}H-, ^{13}C-NMR, IR, ESI-MS, TGA	[245]
$[Bi_{38}O_{45}(O_3SC_6H_{13})_{14}(NO_3)_{10}(dmso)_{28}]$	Hydrolysis of $[Bi_6O_4(OH)_4(NO_3)_6] \cdot H_2O$ in DMSO in the presence of sodium hexane-1-sulfonate	41	PXRD, EA, ^{1}H-, ^{13}C-NMR, IR, ESI-MS, TGA	[245]
$[Bi_{38}O_{45}(O_3SC_8H_{17})_{16}(NO_3)_8(dmso)_{12}]$	Hydrolysis of $[Bi_6O_4(OH)_4(NO_3)_6] \cdot H_2O$ in DMSO in the presence of sodium octane-1-sulfonate	64	EA, ^{1}H-, ^{13}C-NMR, IR, ESI-MS, TGA	[245]

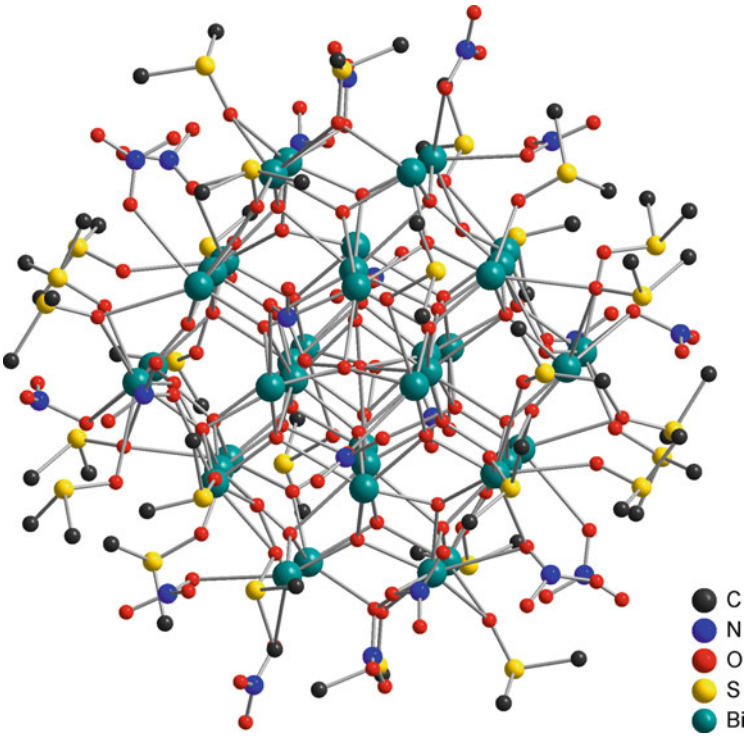

Fig. 39 Ball-and-stick model representing the molecular structure of a typical $\{Bi_{38}O_{45}\}$ cluster, $[Bi_{38}O_{45}(NO_3)_{20}(dmso)_{28}]^{4+}$, which crystallizes as nitrate salt with additional DMSO. Hydrogen atoms are not shown [244]

DMSO and sodium methacrylate, and its core structure is almost identical with that of $[Bi_{38}O_{45}(NO_3)_{20}(dmso)_{28}]^{4+}$.

In order to avoid systematically the presence of nitrates in bismuth oxido clusters, nitrate-free precursors and conditions have to be used for the hydrolysis/condensation step. This strategy was applied in the synthesis of the two first examples of $\{Bi_{38}O_{45}\}$ clusters. In 2006 Dikarev et al. reported the formation of $[Bi_{38}O_{45}(hfac)_{24}]$, which was formed via the nonanuclear cluster $[Bi_9O_7(hfac)_{13}]$ (hfac=hexafluoroacetylacetonate) as a result of hydrolysis and condensation [193]. Simultaneously, Andrews et al. reported on the isolation of $[Bi_{38}O_{44}(HSal)_{26}(Me_2CO)_{16}(H_2O)_2]$ (H_2Sal=salicylic acid) and the intermediate formation of $[Bi_9O_7(HSal)_{13}(Me_2CO)_5]$ starting from $Bi(Hsal)_3$ [192], both clusters being supposed to be quite stable hydrolysis products of bismuth tris-salicylate and are suggested to be model compounds of the ill-defined bismuth subsalicylate, which is used as an ingredient in commercial Pepto-Bismol. The latter pharmaceutical is used to treat duodenal and peptic ulcers, ulcerative colitis, and diarrhea, and thus there is an ongoing interest in this class of compounds [192, 246, 250–252]. The formation of nonanuclear bismuth oxido clusters, which in both studies

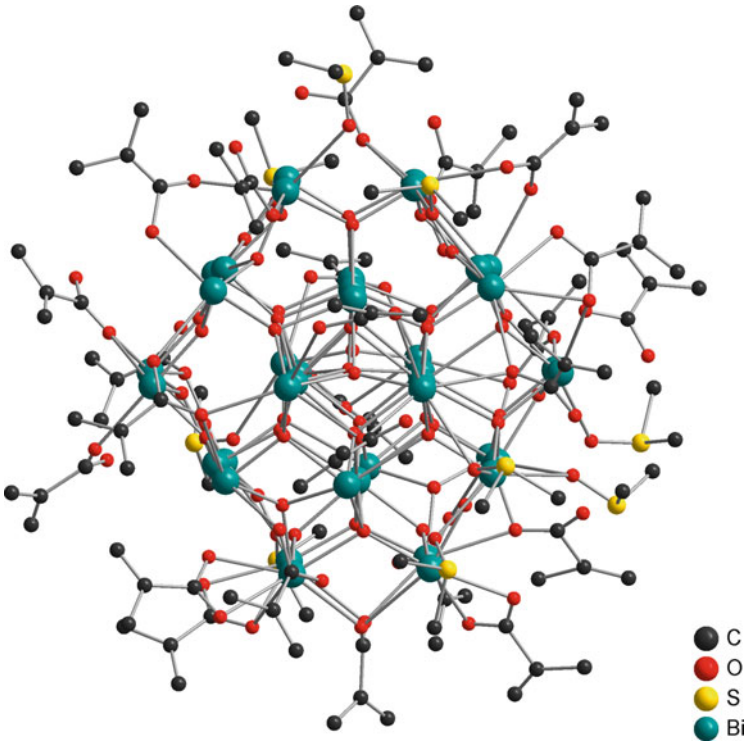

Fig. 40 Ball-and-stick model representing the molecular structure of the "fully" methacrylate-substituted bismuth oxido cluster $[Bi_{38}O_{45}(OMc)_{24}(dmso)_9(H_2O)_2]$. Hydrogen atoms are not shown [249]

were observed first, is well in line with earlier reports of Tytko, who postulated hexa- and nonanuclear bismuth oxido clusters to be stable intermediates in the hydrolysis process [168]. The larger clusters based on the $\{Bi_{38}O_{45}\}$ core seem to mark the next step of stable intermediates within the growth process of bismuth oxido species. Noteworthy, even bismuth oxide might be used as starting material to synthesize $\{Bi_{38}O_{45}\}$-based clusters. Andrews et al. reported the reaction of Bi_2O_3 with 2,4,6-mesitylenesulfonic acid to give an insoluble precipitate in water, which was crystallized from *m*-xylene to give a compound of the composition $[Bi_{38}O_{45}(O_3SMes)_{24}(H_2O)_{14}]$ in form of a *m*-xylene solvate [200]. Nevertheless, all $\{Bi_{38}O_{45}\}$ clusters reported so far were isolated from organic solvents or at least mixtures of them with water. The solubility of the clusters with high-molecular mass and molecular diameters of about 2 nm is limited in aqueous solution, and a proof for their existence in aqueous solution is still missing.

With regard to the bismuth oxido core structure, one aspect should be highlighted. The bismuth oxido core structures of all $\{Bi_{38}O_{45}\}$ clusters as given in Tables 8 and 9 are almost identical besides that $[Bi_{38}O_{44}(HSal)_{26}(Me_2CO)_{16}(H_2O)_2]$ [192] contains only 44 oxygen atoms.

Table 9 Selected examples of ligand-stabilized bismuth oxido clusters with nuclearities between $\{Bi_{10}\}$ and $\{Bi_{38}\}$. Synthesis conditions, isolated yield, and analytics are given

Ligand-stabilized bismuth oxido clusters	Synthesis	η/%	Analytics	References
$[Bi_{10}O_8(O_2C\text{-}C_6H_4\text{-}2\text{-}NO_2)_{14}(EtOH)_x\cdot(EtOH)_y\ (H_2O)_z]$	Ethanolysis of $BiPh_3$ in the presence of 2-nitrobenzoic acid	n.r.	XRD, EA, IR, MS	[253]
$(NH_4)_{12}[Bi_{12}O_8(Cit)_8](H_2O)_{10}$ (H_4Cit=citric acid)	Hydrolysis of BiHCit with NH_3 in H_2O	42	XRD, EA, CA, ^{13}C-NMR	[242, 254]
$[(t\text{BuPO}_3)_{10}(t\text{BuPO}_3\text{H})_2Bi_{14}O_{10}(C_6H_3)_3(H_2O)_4]$	Acidolysis of $BiPh_3$ with $t\text{BuPO}_3H_2$ in THF	66	XRD, EA, IR	[255]
$[\{(2,6\text{-}i\text{Pr}_2C_6H_3O)PO_3\}_{10}\{(2,6\text{-}i\text{Pr}_2C_6H_3O)PO_2OH\}_2$ $(Bi_{14}O_{10})\cdot 2\ CH_3OH]\cdot 3\ C_6H_{12}\cdot 3\ CH_3OH\cdot 2\ H_2O$	Acidolysis of $BiPh_3$ with 2,6-diisopropylphenylphosphate in toluene; crystallization from MeOH/CH_2Cl_2/cyclohexane	85	XRD, EA, ^{1}H-, ^{31}P-NMR, IR, ESI-MS, TGA	[256]
$[Bi_{18}O_{12}(OH)_{12}(O_3S\text{-Cam})_{18}(H_2O)_2]\cdot 13\ H_2O$ (HO_3S-Cam=*S*-(+)-10-camphorsulfonic acid)	Hydrolysis of Bi_2O_3 in H_2O in the presence of *S*-(+)-10-camphorsulfonic acid	100	XRD, EA, ^{1}H-, ^{13}C-NMR, IR	[200]
$[Bi_{22}O_{26}(HSal)_{14}]$ (H_2Sal=salicylic acid)	Reaction of $[Bi_{22}O_{26}(OSiMe_2t\text{Bu})_{14}]$ with salicylic acid in THF	77	PXRD, EA, IR, ESI-MS	[257]
$[Bi_{22}O_{26}(HSal^{4Me})_{14}]$ (H_2Sal^{4Me}=4-methylsalicylic acid)	Reaction of $[Bi_{22}O_{26}(OSiMe_2t\text{Bu})_{14}]$ with 4-methylsalicylic acid in THF	76	PXRD, EA, ^{1}H-NMR, IR, ESI-MS	[243]
$[Bi_{34}O_{22}(BHA)_{22}(H\text{-BHA})_{14}(dmso)_6]$ (H_2BHA=benzohydroxamic acid)	Hydrolysis of $[Bi_2(BHA)_3]$ in DMSO/toluene	55	XRD, EA, ^{1}H-, ^{31}P-NMR, IR	[258]
$[Bi_{38}O_{44}(HSal)_{26}(Me_2CO)_{16}(H_2O)_2]\cdot 4\ Me_2CO$ (H_2Sal=salicylic acid)	Acidolysis of $BiPh_3$with salicylic acid in toluene; crystallization from acetone	n.r.	XRD, EA, ^{1}H-, ^{13}C-NMR, IR, MS	[192]
$[Bi_{38}O_{44}(HSal)_{26}(Me_2CO)_{16}(H_2O)_4]\cdot 3\ Me_2CO$ (H_2Sal=salicylic acid)	Acidolysis of $BiPh_3$with salicylic acid in toluene; crystallization from acetone	n.r.	XRD	[257]
$[Bi_{38}O_{44}(HSal)_{26}(dmf)_{18}(H_2O)_4]$ (H_2Sal=salicylic acid)	Hydrolysis of [Bi(HSal)(Sal)(H_2O)] (mechanochemically from $Bi_2O_3$and salicylic acid) in DMF	n.r.	XRD	[250]
$[Bi_{38}O_{45}(HSal)_{22}(OH)_2(dmso)_{16.5}]\cdot DMSO\cdot H_2O$ (H_2Sal=salicylic acid)	Hydrolysis of $[Bi_{22}O_{26}(HSal)_{14}]$ in DMSO	90	XRD, EA, TGA, IR, ESI-MS	[257]

(continued)

Table 9 (continued)

Ligand-stabilized bismuth oxido clusters	Synthesis	η/%	Analytics	References
$[Bi_{38}O_{45}(HSal^{4Me})_{24}(dmso)_{14}(H_2O)_2] \cdot 4\ H_2O$ (H_2Sal^{4Me}=4-methylsalicylic acid)	Hydrolysis of $Bi(HSal^{4Me})_3$ or $[Bi_{22}O_{26}(HSal^{4Me})_{14}]$ in DMSO	38/92	XRD, EA, TGA, ^{1}H-NMR, ^{1}H-DOSY, IR, ESI-MS	[246]
$[Bi_{38}O_{45}(OMc)_{24}(dmso)_9(H_2O)_2] \cdot 2$ DMSO $\cdot 5\ H_2O$ (HOMc=methacrylic acid)	Hydrolysis of $[Bi_6O_4(OH)_4(NO_3)_6] \cdot H_2O$ in DMSO in the presence of sodium methacrylate	78	XRD, EA, ^{1}H-, ^{13}C-NMR, IR, DLS	[248, 249]
$[Bi_{38}O_{45}(HSal)_{22}(OMc)_2(dmso)_{15}(H_2O)] \cdot$ DMSO $\cdot$ $2\ H_2O$ (HOMc=methacrylic acid, H_2Sal: salicylic acid)	Reaction of $[Bi_{38}O_{45}(OMc)_{24}(dmso)_9(H_2O)_2]$ with salicylic acid in THF; crystallization from DMSO	54	XRD, EA, IR	[259]
$[Bi_{38}O_{45}(OMc)_{22}(O_3SC_6H_4CH{=}CH_2)_2(dmso)_6(H_2O)_{1.5}]$ $\cdot 2.5\ H_2O$	Reaction of $[Bi_{38}O_{45}(OMc)_{24}(dmso)_9(H_2O)_2]$ with sodium 4-vinylbenzenesulfonate in DMSO	11	XRD, EA, IR	[259]
$[Bi_{38}O_{45}\{O_2CC_6H_3\text{-}3,5\text{-}(NO_2)_2\}_{20}(OH)_4(dmso)_{16}] \cdot$ 4 DMSO $\cdot$ 11 H_2O	Reaction of $BiPh_3$ with 3,5-dinitrobenzoic acid in toluene; crystallization from DMSO	21	XRD, EA, IR	[260]
$[Bi_{38}O_{45}\{O_2CC_6H_3\text{-}3,5\text{-}(NO_2)_2\}_{20}(O_2CMe)_2(OH)_2$ $(dmf)_{10}] \cdot 15$ DMF $\cdot 20\ H_2O$	Reaction of $BiPh_3$ with 3,5-dinitrobenzoic acid in toluene; crystallization from EtOAc/DMF	15	XRD, EA, IR	[260]
$[Bi_{38}O_{45}(OVal\text{-}Boc)_{22}(OH)_2]$ (HOVal valine, Boc=*tert*-butyloxycarbonyl)	Reaction of $[Bi_{22}O_{26}(OSiMe_2tBu)_{14}]$ with *N*-Boc-protected valine in THF; crystallization from EtOH	53	PXRD, EA, IR, ESI-MS, DLS, CD-spectroscopy	[257]
$[Bi_{38}O_{45}(OPhe\text{-}Boc)_{22}(OH)_2]$ (HOPhe=phenylalanine)	Reaction of $[Bi_{22}O_{26}(OSiMe_2{}^tBu)_{14}]$ with *N*-Boc-protected phenylalanine in THF; crystallization from EtOH	81	PXRD, EA, IR, ESI-MS, DLS, CD-spectroscopy	[257]
$[Bi_{38}O_{45}(OBz)_{24}(dmso)_{21}]$ (HOBz: benzoic acid)	Hydrolysis of $[Bi_6O_4(OH)_4(NO_3)_6] \cdot H_2O$ in DMSO in the presence of sodium benzoate	32	PXRD, EA, ^{1}H-, ^{13}C-NMR, IR	[248]
$[Bi_{38}O_{45}(O_3S\text{-}Mes)_{24}(H_2O)_{14}] \cdot C_8H_{10}$ (HO_3S-Mes=2,4,6-mesitylenesulfonic acid)	Reaction of Bi_2O_3 with 2,4,6-mesitylenesulfonic acid in H_2O; crystallization from mesitylene	58	XRD, EA, ^{1}H-, ^{13}C-NMR, IR	[200]
$[Bi_{38}O_{45}(hfac)_{24}]$ (hfac =hexafluoroacetylacetonate)	Hydrolysis of $[Bi_9O_7(hfac)_{13}]$ with coordinating solvent in CH_2Cl_2 and diffusion of hexane	30	XRD, EA, ^{1}H-, ^{19}F-NMR, IR, UV/Vis	[193]

n.r. not reported

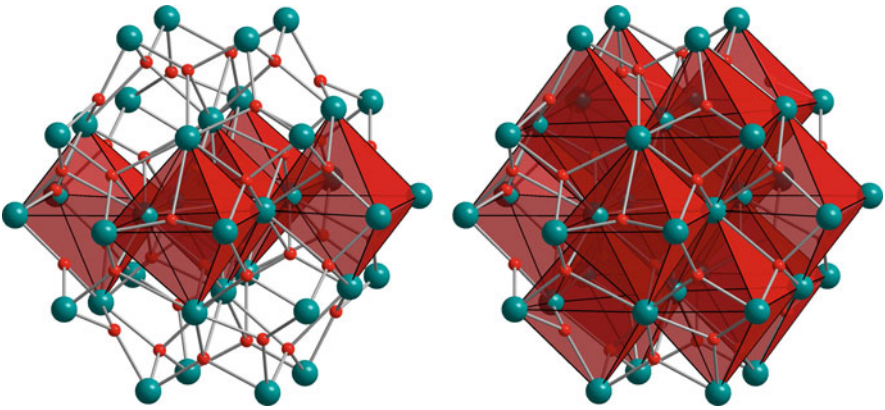

Fig. 41 Ball-and-stick model and polyhedral view representing the bismuth oxido cluster core $\{Bi_{38}O_{45}\}$. *Left*: five edge-sharing octahedra are shown, which are created by bismuth atoms of the three middle layers. *Right*: full view showing the 13 edge-sharing octahedra. The structure can be deduced from the fluorite structure type [261]

Surprisingly, the central oxygen atom is missing as compared to, e.g., $[Bi_{38}O_{45}(hfac)_{24}]$ [193] or $[Bi_{38}O_{45}(OMc)_{24}(dmso)_9(H_2O)_2]$ [249], but Mansfeld et al. did confirm the result with their report on $[Bi_{38}O_{44}(HSal)_{26}(Me_2CO)_{16}(H_2O)_4]$ [257] and André et al. by publication of the X-ray single-crystal structure analysis of $[Bi_{38}O_{44}(HSal)_{26}(dmf)_{18}(H_2O)_4]$ [250]. It is far from clear why the oxygen atom is missing in the center of these bismuth oxido clusters, while in similar carboxylates such as $[Bi_{38}O_{45}(HSal^{4Me})_{24}(dmso)_{14}(H_2O)_2]$ (H_2Sal^{4Me}=4-methylsalicylic acid) [246], $[Bi_{38}O_{45}(HSal)_{22}(OH)_2(dmso)_{16.5}]$ [257], and $[Bi_{38}O_{45}(HSal)_{22}(OMc)_2(dmso)_{15}(H_2O)]$ [259], the expected $\{Bi_{38}O_{45}\}$ core structure is observed. Mehring and coworkers pointed out that this core structure is very stable and best described as being composed of edge-sharing $[Bi_6O_8]$-polyhedra, which are composed of six octahedral Bi atoms with the eight O atoms located over all of the triangular faces similar to the hexanuclear bismuth oxido clusters of the type $[Bi_6O_{4+x}(OH)_{4-x}]^{(6-x)+}$ (Fig. 41) [261]. This structural concept is based on a dense hexagonal packing of bismuth atoms and seems to be a principal structure concept in bismuth oxido cluster chemistry and of metal oxido clusters with large metals in general. For example, in uranium(IV) and plutonium(IV) clusters, a similar f.c.c. packing of the metals is observed, and noteworthy three clusters with 38 metal atoms have been reported, $[U_{38}O_{56}Cl_{18}(bz)_{24}(THF)_8]\cdot 8THF$ (Fig. 42) [262], $Li_{14}[Pu_{38}O_{56}Cl_{54}(H_2O)_8]$ [263], and $Li_2[Pu_{38}O_{56}Cl_{42}(H_2O)_{20}]\cdot 15H_2O$ [264], all of them showing a similar basic $[M_{38}O_{56}]^{40+}$ core structure. There is a close structural resemblance of these metal oxido core structures with the $[Bi_{38}O_{45}]^{24+}$

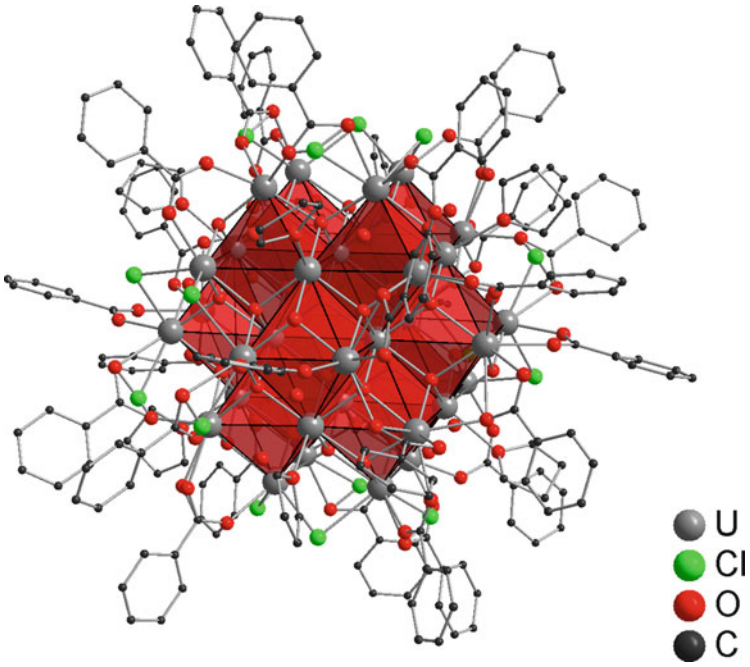

Fig. 42 Ball-and-stick model and polyhedral view of the molecular structure of the uranium oxido cluster $[U_{38}O_{56}Cl_{18}(bz)_{24}(THF)_8]$ (bz=benzoate). The metal oxido core structure $[M_{38}O_{56}]^{40+}$ is comprised of 38 uranium atoms and is very similar to $\{Bi_{38}O_{45}\}$. Hydrogen atoms are not shown [262]

core, which is built up by edge-sharing $\{M_6\}$-polyhedra (Fig. 41). The metal oxido structures of the large metals can be deduced from the fluorite structure type.

In addition to the large number of $\{Bi_{38}O_{45}\}$ bismuth oxido clusters, examples of lower nuclearity have been observed while using ligands for the cluster stabilization such as phosphonates, phosphates, hydroxamates, alkoxides, and siloxides. The recently reported hydroxamate $[Bi_{34}O_{22}(BHA)_{22}(H\text{-}BHA)_{14}(dmso)_6]$ (H_2BHA=benzohydroxamic acid) [258] fits into the general concept of bismuth layers as a result of a f.c.c. packing of the bismuth atoms and thus edge-sharing $\{Bi_6\}$ units in bismuth oxido clusters. This arrangement is close to that found for cubic δ- and tetragonal β-Bi_2O_3, in which the oxygen atoms occupy ¾ of the tetrahedral voids. Both solid-state structures might be constructed starting from a fluorite cell, which is also the basis to construct the metal oxido core of the polynuclear metal oxido clusters. In accordance with the above described structural

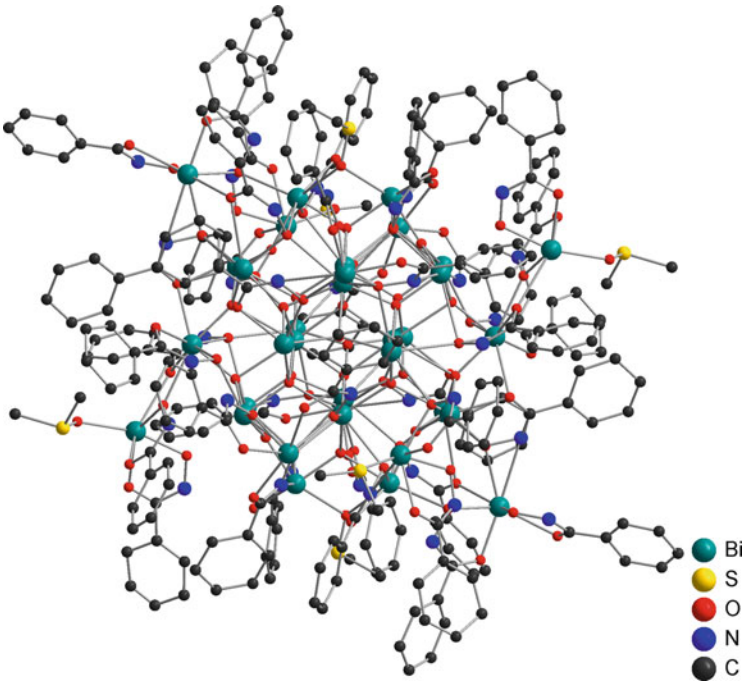

Fig. 43 Ball-and-stick model representing the molecular structure of the hydroxamate cluster $[Bi_{34}O_{22}(BHA)_{22}(H\text{-}BHA)_{14}(DMSO)_6]$. The central metal oxido cluster is based on a $\{Bi_{24}\}$ core. Hydrogen atoms are not shown [258]

concept, the hydroxamate $[Bi_{34}O_{22}(BHA)_{22}(H\text{-}BHA)_{14}(dmso)_6]$ was described as being composed of a $\{Bi_{24}O_{22}\}$ core structure, which is encapsulated by ten additional bismuth atoms via oxygen coordination. These outer sphere bismuth atoms are coordinated to mono- or di-anionic hydroxamate ligands, which in combination with DMSO form the hydrophobic organic shell (Fig. 43) [258].

Similarly, the molecular structures of the large homometallic bismuth oxido silanolates and alkoxides $[Bi_{18}O_{18}(OSiMe_3)_{18}]$ [194], $[Bi_{20}O_{18}(OSiMe_3)_{24}]$ [194], $[Bi_{22}O_{26}(OSiMe_2tBu)_{14}]$ [266], and $[Bi_{32}O_{40}(OH)_4(O\text{-}2,6\text{-}Ph_2C_6H_3)_{12}]$ [207] as well as the heterometallic clusters $[Bi_{33}NaO_{38}(OSiMe_3)_{24}]$ [194] and $[Bi_{50}Na_2O_{64}(OH)_2(OSiMe_3)_{22}]$ [194] fit with the above described Aufbau principle of edge-sharing $\{Bi_6\}$ octahedra as basic motif with a silanolate/alkoxide shell making up the hydrophobic nature (Table 10). For example, the bismuth oxido cluster $[Bi_{22}O_{26}(OSiMe_2tBu)_{14}]$ is composed of six of these octahedra (Fig. 44).

Table 10 Selected examples of bismuth oxido alkoxides and siloxides with nuclearity above 10. Synthesis conditions, isolated yield, and analytics are given

Bismuth oxido alkoxides and siloxides	Synthesis	η/%	Analytics	References
$[Bi_{10}Na_5O_7(OH)_6(OSiMe_3)_{15}] \cdot 1.5\ C_7H_8$	Hydrolysis of $[Bi_2Na_4O(OSiMe_3)_8]$ in toluene	n.r.	XRD, EA, IR	[205]
$[Bi_{12}O_4\{O_3SiN(SiMe_3)(2,6\text{-}iPr_2C_6H_3)\}_8Cl_4(thf)_8]$	Reaction of $Bi(NMe_2)_3$/"$Bi(NMe_2)_2Cl$" with $(HO)_3SiR$ in hexane/THF [R=N(SiMe$_3$)(2,6-*i*Pr$_2$C$_6$H$_3$)]	23	XRD, EA, ^{29}Si-NMR, IR	[265]
$[Bi_{14}Na_8O_{18}(OSiMe_3)_{14}(thf)_4] \cdot C_6H_6$	Hydrolysis of $[Bi_2Na_4O(OSiMe_3)_8]$ in THF/benzene	n.r.	XRD, EA, IR	[205]
$[Bi_{15}Na_3O_{18}(OSiMe_3)_{12}] \cdot C_7H_8$	Hydrolysis of $[Bi_2Na_4O(OSiMe_3)_8]$ (crystallization from filtrate of $[Bi_{10}Na_5O_7(OH)_6(OSiMe_3)_{15}]$ solution)	n.r.	XRD, EA, IR	[205]
$[Bi_{18}O_{18}(OSiMe_3)_{18}] \cdot 2\ C_7H_8$	Hydrolysis of $Bi(OSiMe_3)_3$ in toluene (from filtrate of $[Bi_{20}O_{18}(OSiMe_3)_{24}]$ solution)	8	XRD, EA, IR	[194]
$[Bi_{18}Na_4O_{20}(OSiMe_3)_{18}]$	Reaction of $BiCl_3$with $NaOSiMe_3$ in THF; crystallization from toluene	n.r.	XRD	[194]
$[Bi_{20}O_{18}(OSiMe_3)_{24}] \cdot 3\ C_7H_8$	Hydrolysis of $Bi(OSiMe_3)_3$ in toluene	11	XRD, EA, IR	[194]
$[Bi_{22}O_{26}(OSiMe_2tBu)_{14}] \cdot 2\ C_6H_6$	Hydrolysis of $Bi(OSiMe_2tBu)_3$ in benzene	99	XRD, EA, IR	[266]
$[Bi_{32}O_{40}(OH)_4(O\text{-}2,6\text{-}Ph_2C_6H_3)_{12}]$	Alcoholysis of $Bi[N(SiMe_3)_2]_3$ with 2,6-diphenylphenol	n.r.	XRD	[207]
$[Bi_{33}NaO_{38}(OSiMe_3)_{24}] \cdot 3\ C_7H_8$	Reaction of $BiCl_3$ with $NaOSiMe_3$ in THF; crystallization from toluene	n.r.	XRD	[194]
$[Bi_{50}Na_2O_{64}(OH)_2(OSiMe_3)_{22}] \cdot 2\ C_7H_8 \cdot 2\ H_2O$	Reaction of $BiCl_3$with $NaOSiMe_3$ in THF; crystallization from toluene/moisture	n.r.	XRD	[194]

n.r. not reported

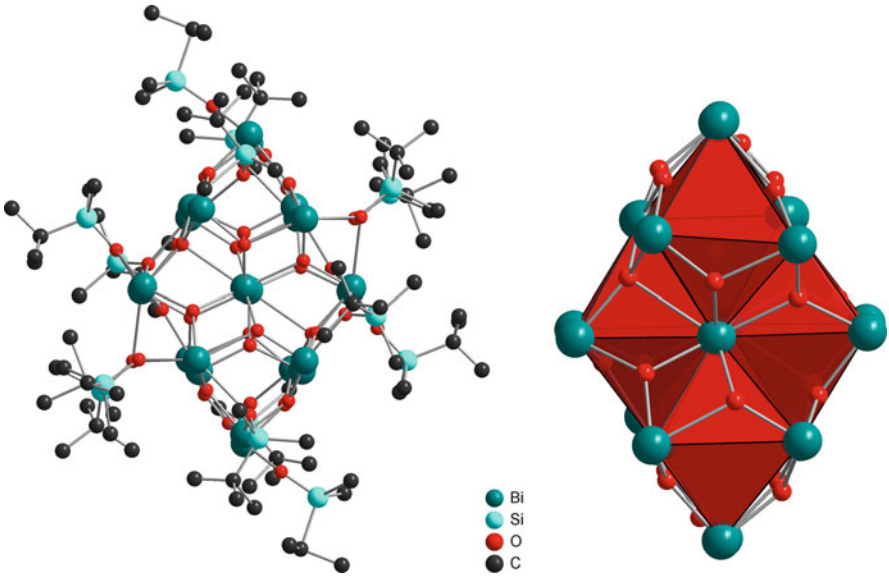

Fig. 44 Ball-and-stick model and polyhedral view of the molecular structure of the bismuth oxido cluster $[Bi_{22}O_{26}(OSiMe_2tBu)_{14}]$. The cluster is composed of six edge-sharing $\{Bi_6\}$ units. Hydrogen atoms are not shown [266]

Noteworthy, a cerium cluster of the same nuclearity and following the same structural concept was reported. The mixed valence cerium oxido cluster $[Ce_{22}O_{20}(OH)_4(ib)_{26}(tme)_4]$ (Hib=isobutyric acid, H_3tme: 1,1,1-tris (hydroxymethyl)ethane) is composed of six Ce(III) and 16 Ce(IV) atoms forming a metal oxido core of the type $\{Ce_{22}O_{24}\}$, which is covered by twenty six anionic ligands protecting the cluster (Fig. 45) [267]. The cluster structure might be regarded as a cutout of the fluorite structure type of cerium(IV) oxide.

Bismuth and sodium cations show quite similar radii of their cations which allow substitution within the metal atom sublattice without substantial distortion of the structures. To date $[Bi_{50}Na_2O_{64}(OH)_2(OSiMe_3)_{22}]$ is the largest bismuth oxido-based cluster, and despite several reports on various substituted $\{Bi_{38}O_{45}\}$ clusters in the last decade, those on larger ones are still missing (Fig. 46) [194]. The $\{Bi_{50}Na_2\}$ cluster is built up by the same Aufbau principle as discussed for the $\{Bi_{22}\}$ and $\{Bi_{38}\}$ clusters before.

In contrast to the less sensitive $\{Bi_{38}O_{45}\}$ nitrates, sulfonates, and carboxylates, the bismuth silanolates are very sensitive toward moisture, which makes their

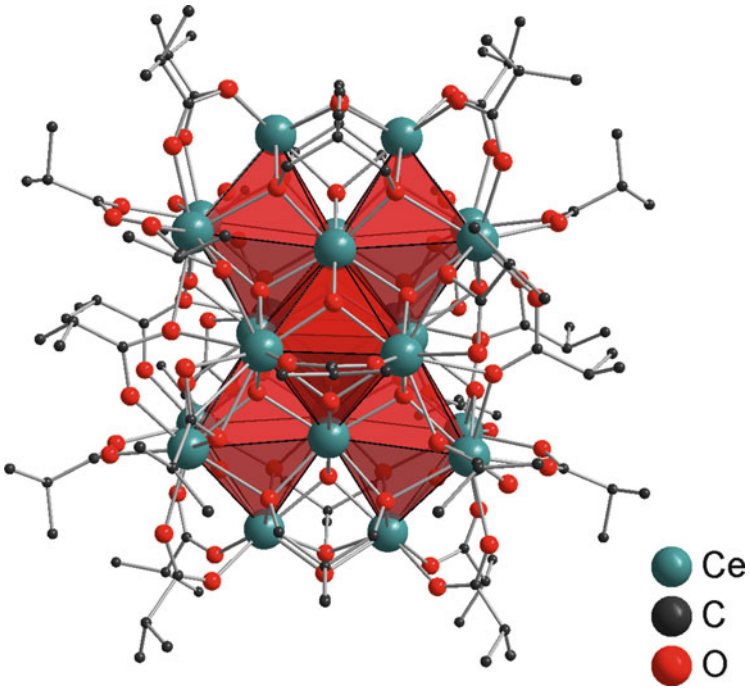

Fig. 45 Ball-and-stick model and polyhedral view of the molecular structure of the cerium oxido cluster $[Ce_{22}O_{20}(OH)_4(ib)_{26}(tme)_4]$ (Hib=isobutyric acid, H_3tme=1,1,1-tris(hydroxymethyl)ethane). Similar to $[Bi_{22}O_{26}(OSiMe_2tBu)_{14}]$, the cluster is composed of six edge-sharing $\{Bi_6\}$ units. The structure is rotated by 90° with regard to the representation of $[Bi_{22}O_{26}(OSiMe_2tBu)_{14}]$ in Fig. 44. Hydrogen atoms are not shown [267]

handling more difficult but also offers the possibility to use the silanolates as starting materials for the synthesis of other bismuth oxido clusters. For example, the synthesis of $[Bi_{22}O_{26}(HSal^{4Me})_{14}]$ (H_2Sal^{4Me}=4-methylsalicylic acid) was reported starting from $[Bi_{22}O_{26}(OSiMe_2tBu)_{14}]$ [246], which otherwise was not isolated but was shown to be an intermediate on the hydrolysis/condensation route toward $[Bi_{38}O_{45}(HSal^{4Me})_{24}(dmso)_{14}(H_2O)_2]$ by NMR, ESI-MS and single-crystal X-ray diffraction.

Several ligands were so far successfully attached to the bismuth oxido cluster core $\{Bi_{38}O_{45}\}$, but examples for phosphonates, phosphinates and phosphates were not reported. To date two polynuclear bismuth oxido compounds exist. The

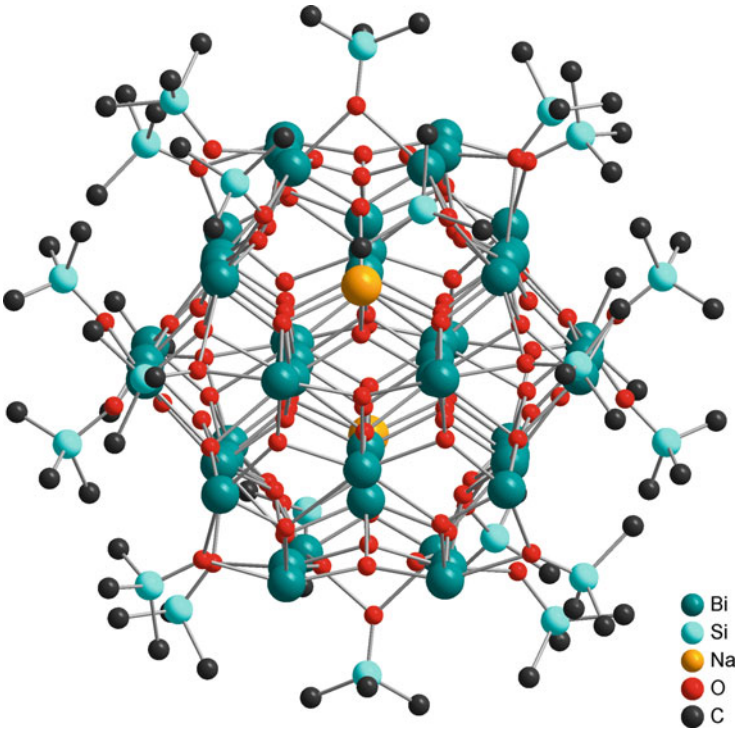

Fig. 46 Ball-and-stick model representing the molecular structure of the bismuth oxido silanolate $[Bi_{50}Na_2O_{64}(OH)_2(OSiMe_3)_{22}]$, the largest cluster within the bismuth series so far. Hydrogen atoms are not shown [194]

phosphonate $[t\text{BuPO}_3)_{10}(t\text{BuPO}_3\text{H})_2\text{Bi}_{14}\text{O}_{10}(\text{C}_6\text{H}_6)_3(\text{H}_2\text{O})_4]$ [255] and the phosphate $[\{(2,6\text{-}i\text{Pr}_2\text{C}_6\text{H}_3\text{O})\text{PO}_3\}_{10}\{(2,6\text{-}i\text{Pr}_2\text{C}_6\text{H}_3\text{O})\text{PO}_2\text{OH}\}_2\text{Bi}_{14}\text{O}_{10}(\text{CH}_3\text{OH})_2]$ [256] both show the same bismuth oxido core structure, which does not follow the Aufbau principle as described above (Fig. 47). The core structure is based on a $Bi_{14}O_{10}$-buidling block, which is captured by the ligands to form a rugby ball-like structure. The first steps of condensation seem to be similar to other bismuth species, which is indicated by the presence of ladder-type $\{Bi_4O_6\}$ subunits, but the multidentate nature of the ligands and its strong binding capacity seem to hamper cluster growth.

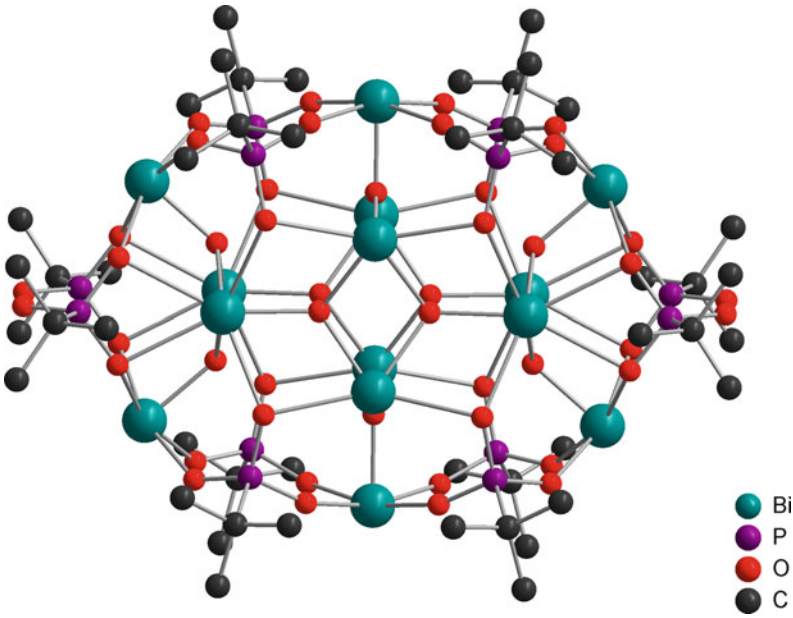

Fig. 47 Ball-and-stick model representing the molecular structure of the bismuth oxido phosphonate $[t\mathrm{BuPO_3})_{10}(t\mathrm{BuPO_3H})_2\mathrm{Bi_{14}O_{10}}(\mathrm{C_6H_6})_3(\mathrm{H_2O})_4]$. Coordinated water and benzene molecules are omitted and hydrogen atoms not given [255]

5 Summary and Concluding Remarks

Metal oxides are accessible via various solution-based approaches starting from simple inorganic precursors, but with regard to control of structure, particle size, and morphology, most approaches are based on empirical studies rather than controlled synthesis. It must also be kept in mind that usually postmodification of the as-prepared precipitate by heating to high temperatures is necessary, e.g., to complete condensation reactions and/or to remove water, carbon, and other elements, and is crucial for structure formation, particle growth, and morphology. A further step toward the realization of a synthetic concept at low temperatures, which might be called "synthesis by design", is the understanding of nucleation and growth of metal oxido species on a molecular scale. Many early studies on aqueous solution chemistry of metal salts exist, and various complexes of low nuclearity which are formed prior to nucleation have been postulated and were also verified in many cases. However, a detailed picture at later stages of hydrolysis/condensation processes is still lacking, and only a limited number of examples of well-characterized group 13–15 metal oxido clusters with more than ten atoms are known. The present review summarizes these examples and shows some common trends but also demonstrates the diversity of metal oxido clusters as reported so far. Especially, for germanium but also for antimony, the data on purely inorganic clusters are scarce even for those of lower nuclearity. The most relevant example for antimony might be $[\mathrm{Sb_8O_{12}(OH)_{20}}]^{4-}$, which is constructed by edge- and

corner-sharing octahedral SbO_6 units. However, isolation of the three-dimensional network structure $[Sb_4O_4(OH)_2][O_3SCH_2CH_2SO_3]$ might be regarded as an indication for the presence of cationic species in aqueous solution upon change of conditions such as the pH value. The solution chemistry becomes even more complex if organometallic oxido clusters are included in studies on structure formation. For example, antimony shows condensation products of high nuclearity which are derived from organostibonic acids such as $[(p\text{-}ClC_6H_4Sb)_{16}O_{28}(OH)_8]$. There is also a wealth of organometallic tin oxido compounds, especially in the oxidation state IV, and also aluminum and gallium reveal a large number of organometallic oxido clusters. Prominent examples of such clusters of these elements are $[RAlO]_n$ (R=alkyl, $n = 6$, 9, 12), $[(t\text{BuGa})_{12}(\mu_3\text{-}O)_8(\mu\text{-}O)_2(\mu\text{-}OH)_4]$, and $[(n\text{BuSn})_{12}(\mu_3\text{-}O)_{14}(\mu\text{-}OH)_6]^{2+}$. These organometallic compounds are of limited use as model compounds for hydrolysis studies, but might serve as precursors for metal oxides. However, postmodification for carbon removal is necessary after processing, and pure oxides are difficult to obtain. Nevertheless, in applications where residual carbon is tolerated, organometallic compounds might offer the advantage of a high solubility in organic solvents.

The most important inorganic metal oxido clusters of aluminum are the "flat" $[Al_{13}(\mu_3\text{-}OH)_6(\mu\text{-}OH)_{18}(H_2O)_{24}]^{15+}$ and the Keggin-type clusters $[Al_{13}(\mu_4\text{-}O)_4(\mu\text{-}OH)_{24}(H_2O)_{12}]^{7+}$. The latter were shown to condense to give larger aggregates such as $[Al_{26}(\mu_4\text{-}O)_8(\mu\text{-}OH)_{50}(H_2O)_{20}]^{12+}$, which still are based on Keggin-type structures and do not show structural relationship to aluminum oxide. This is quite similar to the structural chemistry of polyoxometalates which is based on structures such as the Keggin-type $[XM_{12}O_{40}]^{n-}$, the Wells–Dawson-type $[X_2M_{18}O_{62}]^{n-}$, and the Anderson-type $[XM_6O_{24}]^{n-}$ (M, metal; X, metal or heteroelement) with none of them representing a cutout of the corresponding natural metal oxides. For aluminum, it might be speculated that amorphous hydrolysis products are composed of mainly Keggin-type-related aluminum oxido hydroxide building blocks. By contrast, for gallium two examples, $[Ga_{32}(\mu_4\text{-}O)_{12}(\mu_3\text{-}O)_7(\mu_3\text{-}OH)_8(\mu\text{-}OH)_{39}(H_2O)_{20}]^{11+}$ and $[Ga_{30}(\mu_4\text{-}O)_{12}(\mu_3\text{-}O)_4(\mu_3\text{-}OH)_4(\mu\text{-}OH)_{42}(H_2O)_{16}]^{12+}$, were detected which are structurally related to $\beta\text{-}Ga_2O_3$ and might represent intermediates or nucleation germs for the bulk material. In contrast to the group 13 elements, such large inorganic tin oxido clusters were not reported so far, with $[Sn_{12}O_8(OH)_4(OEt)_{28}(HOEt)_4]$ being an exception. The most prominent clusters are those based on $[Sn_6(\mu_3\text{-}O)_4(\mu_3\text{-}OH)_4]$, which could be regarded as a primary octahedral building block $\{M_6O_8\}$ of a f.c.c. packing of metals and oxygen atoms attached to the triangular faces. This motif represents a cutout of the fluorite structure type. Other metals also show this octahedral building block including organometallic compounds and for large metals such as bismuth, cerium, uranium, and plutonium become increasingly important. In metal oxido clusters of these elements, the $\{M_6O_8\}$ units become edge-sharing, as in the fluorite-type metal oxides, and large clusters such as $[Ce_{22}O_{20}(OH)_4(ib)_{26}(tme)_4]$, $[Bi_{22}O_{26}(OSiMe_2t\text{Bu})_{14}]$, $[U_{38}O_{56}Cl_{18}(bz)_{24}(THF)_8]$, $Li_{14}[Pu_{38}O_{56}Cl_{54}(H_2O)_8]$, and $[Bi_{38}O_{45}(NO_3)_{20}(dmso)_{28}](NO_3)_4{\cdot}4$ DMSO. Several other bismuth oxido clusters with 38 metal atoms have been isolated, but larger ones, with the heteronuclear cluster $[Bi_{50}Na_2O_{64}(OH)_2(OSiMe_3)_{22}]$ being the only exception, are not reported despite tremendous research efforts. It might be speculated that these nanoscaled and more or

less spherical clusters of approximately 2 nm in diameter represent a very stable metal oxido unit with substantial solubility. Increasing the cluster size by addition of metal oxido units to the $\{Bi_{38}O_{45}\}$ core while maintaining a symmetrical spherical arrangement might result in a very low solubility which is unfavorable for crystallization under thermodynamic control. It is suggested that amorphous hydrolysis products might be mainly composed of these $\{Bi_{38}O_{45}\}$-based clusters, which explains that upon short time of heating, metastable β-Bi_2O_3 is easily formed. The latter bismuth oxide adopts a tetragonal distorted defect fluorite structure type. In general it is proposed that those metal oxides, which adopt fluorite-type structures, follow a similar *Aufbau principle* as was described for bismuth oxido clusters.

Although nucleation and growth of metal oxides have been studied for decades, the chemistry at early stages of structure formation is still in its infancy. Most of the work is based on the analysis of small complexes and a limited number of crystal structures of larger metal oxido clusters. It seems to be necessary to enlarge the structural database of metal oxido clusters on the one hand and on the other hand to intensify research on the characterization of clusters including their dynamic behavior in solution. For example, electrospray mass spectrometric analyses for bismuth provided first results on cluster growth, and EXAFS studies as well as high-energy X-ray scattering for PDF analysis (pair distribution function) on actinides proved to be very fruitful to study structure formation. These activities should be enhanced including other elements and additional analytics such as NMR, IR, and other in situ X-ray techniques and should be accompanied by theoretical investigations.

Acknowledgments The author thanks Felix Dannenberg, Lydia Wrobel, Lutz Mertens, Marcus Weber, Ronny Fritzsche, and Ana-Maria Preda for assistance with preparation of figures and tables and comments on the manuscript. The Deutsche Forschungsgemeinschaft, especially in the frame of the DFG priority program 1415, DAAD, and Fonds der Chemischen Industrie is thanked for continuing financial support.

References

1. Jolivet J-P, Henry M, Livage J, Bescher E (2000) Metal oxide chemistry and synthesis: from solution to solid state. Wiley, Hoboken
2. Rodríguez J, Fernández-García M (2007) Synthesis, properties, and applications of oxide nanomaterials. Wiley, Hoboken
3. Jones AC, Hitchman ML (2008) Chemical vapour deposition: precursors, processes and applications. Royal Society of Chemistry, Cambridge
4. Fernandez-Garcia M, Martinez-Arias A, Hanson JC, Rodriguez JA (2004) Chem Rev 104:4063–4104
5. Fierro JLG (2005) Metal oxides: chemistry and applications. CRC Press, Boca Raton
6. Kudo A, Miseki Y (2009) Chem Soc Rev 38:253–278
7. Knapp CE, Carmalt CJ (2016) Chem Soc Rev 45:1036–1064
8. Niederberger M, Pinna N (2009) Metal oxide nanoparticles in organic solvents: synthesis, formation, assembly and application. Springer, London
9. Marchand P, Carmalt CJ (2013) Coord Chem Rev 257:3202–3221
10. Hatanpää T, Ritala M, Leskelä M (2013) Coord Chem Rev 257:3297–3322
11. Sui R, Charpentier P (2012) Chem Rev 112:3057–3082
12. Mingos DMP, Fischer S, Kurad D, Mehmke J, Tytko KH (1999) Bonding and charge distribution in polyoxometalates: a bond valence approach. Springer, Berlin Heidelberg

13. Pope M, Müller A (2001) Polyoxometalate chemistry from topology via self-assembly to applications. Springer, Dordrecht
14. Borrás-Almenar JJ, Coronado E, Müller A, Pope M (2003) Polyoxometalate molecular science. Springer, Dordrecht
15. Sécheresse F (2013) Polyoxometalate chemistry, World Scientific Series in Nanoscience and Nanotechnology. Vol 8, World Scientific Publishing Co. Pte. Ltd. Singapore
16. Ruhlmann L, Schaming D (2015) Trends in polyoxometalates research: chemistry research and applications. Nova Science Pub Inc, New York
17. Krewski D, Yokel RA, Nieboer E, Borchelt D, Cohen J et al (2007) J Toxicol Environ Health Part B 10:1–269
18. Casey WH (2006) Chem Rev 106:1–16
19. Mensinger ZL, Wang W, Keszler DA, Johnson DW (2012) Chem Soc Rev 41:1019–1030
20. Roesky HW, Walawalkar MG, Murugavel R (2001) Acc Chem Res 34:201–211
21. Barron AR (1993) Comments Inorg Chem 14:123–153
22. Mason MR, Smith JM, Bott SG, Barron AR (1993) J Am Chem Soc 115:4971–4984
23. Pasynkiewicz S (1990) Polyhedron 9:429–453
24. Sinn H, Kaminsky W (1980) Adv Organomet Chem 18:99–149
25. Tripathi UM, Schier A, Schmidbaur H (1998) Z Naturforsch B 53:434–437
26. Wu F-J, Simeral LS, Mrse AA, Eilertsen JL, Negureanu L et al (2007) Inorg Chem 46:44–47
27. Dimitrov A, Koch J, Troyanov SI, Kemnitz E (2009) Eur J Inorg Chem 5299–5301
28. Starikova ZA, Kessler VG, Turova NY, Tcheboukov DE, Suslova EV et al (2004) Polyhedron 23:109–114
29. Landry CC, Harlan CJ, Bott SG, Barron AR (1995) Angew Chem Int Ed 34:1201–1202
30. Swenson DC, Dagorne S, Jordan RF (2000) Acta Crystallogr Sect C Cryst Struct Commun 56:1213–1215
31. McKinlay RM, Dalgarno SJ, Nichols PJ, Papadopoulos S, Atwood JL et al (2007) Chem Commun 2393–2395
32. König R, Scholz G, Veiczi M, Jäger C, Troyanov SI et al (2011) Dalton Trans 40:8701–8710
33. Suslova EV, Kessler VG, Gohil S, Turova NY (2007) Eur J Inorg Chem 5182–5188
34. Chamazi NN, Heravi MM, Neumüller B (2006) Z Anorg Allg Chem 632:2043–2048
35. Baur WH, Ohta T (1982) Acta Crystallogr Sect B Struct Sci 38:390–401
36. Pauling L (1933) Z Kristallogr 84:442–452
37. Johansson G, Gullman L-O, Kjekshus A, Söderquist R (1960) Acta Chem Scand 14:771–773
38. Sun Z, Wang H, Tong H, Sun S (2011) Inorg Chem 50:559–564
39. Drljaca A, Hardie MJ, Raston CL (1999) J Chem Soc Dalton Trans 3639–3642
40. Rowsell J, Nazar LF (2000) J Am Chem Soc 122:3777–3778
41. Abeysinghe S, Unruh DK, Forbes TZ (2012) Cryst Growth Des 12:2044–2051
42. Smart SE, Vaughn J, Pappas I, Pan L (2013) Chem Commun 49:11352–11354
43. Schmitt W, Baissa E, Mandel A, Anson CE, Powell AK (2001) Angew Chem Int Ed 40:3577–3581
44. Allouche L, Gérardin C, Loiseau T, Férey G, Taulelle F (2000) Angew Chem Int Ed 39:511–514
45. Abeysinghe S, Unruh DK, Forbes TZ (2013) Inorg Chem 52:5991–5999
46. Gatlin JT, Mensinger ZL, Zakharov LN, MacInnes D, Johnson DW (2008) Inorg Chem 47:1267–1269
47. Parker WON, Millini R, Kiricsi I (1997) Inorg Chem 36:571–575
48. Görz H, Schönherr S, Pertlik F (1991) Monatsh Chem 122:759–764
49. Lee AP, Phillips BL, Olmstead MM, Casey WH (2001) Inorg Chem 40:4485–4487
50. Fairley M, Corum KW, Johns A, Unruh DK, Basile M et al (2015) Chem Commun 51:12467–12469
51. Son JH, Kwon Y-U, Han OH (2003) Inorg Chem 42:4153–4159
52. Bradley SM, Kydd RA, Yamdagni R (1990) J Chem Soc Dalton Trans 413–417
53. Michot LJ, Montargès-Pelletier E, Lartiges BS, La d'Espinose Caillerie J-B, Briois V (2000) J Am Chem Soc 122:6048–6056
54. Casey W, Olmstead M, Hazlett C, Lamar C, Forbes T (2015) Inorganics 3:21–26

55. Gerasko OA, Mainicheva EA, Naumov DY, Kuratieva NV, Sokolov MN et al (2005) Inorg Chem 44:4133–4135
56. Schnitter C, Roesky HW, Albers T, Schmidt H-G, Röpken C et al (1997) Chem Eur J 3:1783–1792
57. Al-Juaid SS, Buttrus NH, Eaborn C, Hitchcock PB, Roberts ATL et al (1986) J Chem Soc Chem Commun 908–909
58. Kitschke P, Mertens L, Rüffer T, Lang H, Auer AA et al (2015) Eur J Inorg Chem 4996–5002
59. Jami AK, Baskar V (2012) Dalton Trans 41:12524–12529
60. Chitsaz S, Neumüller B (2001) Z Anorg Allg Chem 627:2451–2459
61. Seisenbaeva GA, Gohil S, Suslova EV, Rogova TV, Turova NY et al (2005) Inorg Chim Acta 358:3506–3512
62. Reis DM, Nunes GG, Sa EL, Friedermann GR, Mangrich AS et al (2004) New J Chem 28:1168–1176
63. O'Keefe BJ, Monnier SM, Hillmyer MA, Tolman WB (2001) J Am Chem Soc 123:339–340
64. Veith M, Grätz F, Huch V, Gütlich P, Ensling J (2004) Z Anorg Allg Chem 630:2329–2336
65. Kusserow M, Spandl J (2006) Z Anorg Allg Chem 632:885–892
66. Poncelet O, Sartain WJ, Hubert-Pfalzgraf LG, Folting K, Caulton KG (1989) Inorg Chem 28:263–267
67. Turevskaya EP, Belokon AI, Starikova ZA, Yanovsky AI, Kiruschenkov EN et al (2000) Polyhedron 19:705–711
68. Westin G, Kritikos M, Wijk M (1998) J Solid State Chem 141:168–176
69. Kritikos M, Moustiakimov M, Wijk M, Westin G (2001) J Chem Soc Dalton Trans 1931–1938
70. Bradley DC, Chudzynska H, Frigo DM, Hammond ME, Hursthouse MB et al (1990) Polyhedron 9:719–726
71. Abrahams I, Bradley DC, Chudzynska H, Motevalli M, Sinclair RA (2002) J Chem Soc Dalton Trans 259–266
72. Cesari M (1980) Gazz Chim Ital 110:365–369
73. Carmalt CJ, Mileham JD, White AJP, Williams DJ (2002) New J Chem 26:902–905
74. Yanovsky AI, Turova NY, Kozlova NI, Struchkov YT (1987) Koord Khim 13:149–154
75. Lazarini F (1979) Acta Crystallogr Sect B Struct Sci 35:448–450
76. Lazarini F (1979) Cryst Struct Commun 8:69–74
77. Howie RA, Moser W (1968) Nature 219:372–373
78. André Ohlin C, Rustad JR, Casey WH (2014) Dalton Trans 43:14533–14536
79. Seichter W, Mögel H-J, Brand P, Salah D (1998) Eur J Inorg Chem 795–797
80. Wang W, Wentz KM, Hayes SE, Johnson DW, Keszler DA (2011) Inorg Chem 50:4683–4685
81. Jordan PA, Clayden NJ, Heath SL, Moore GR, Powell AK et al (1996) Coord Chem Rev 149:281–309
82. Rather E, Gatlin JT, Nixon PG, Tsukamoto T, Kravtsov V et al (2005) J Am Chem Soc 127:3242–3243
83. Åhman J, Svensson G, Albertsson J (1996) Acta Crystallogr Sect C Cryst Struct Commun 52:1336–1338
84. Baes CF, Mesmer RS (1977) Ber Bunsen-Ges Phys Chem 81:245–246
85. Ingri N (1963) Acta Chem Scand 17:597–617
86. Andrew Ken I, Xiaodong Z (2013) Nanoporous materials: synthesis and applications. CRC Press, Boca Raton, pp 319–350
87. Lin Z-E, Yang G-Y (2010) Eur J Inorg Chem 2895–2902
88. Schnepf A (2005) Eur J Inorg Chem 2120–2123
89. Green RA, Moore C, Rheingold AL, Weinert CS (2009) Inorg Chem 48:7510–7512
90. Renner HG, Rutsch P (2001) Z Naturforsch B 56:1328–1339
91. Schaack BB, Schrader W, Schuth F (2009) J Phys Chem B 113:11240–11246
92. Zink S, Eichner T, Schnell M, Woenckhaus J (2005) Z Phys Chem 219:1355–1371
93. Cristoni S, Armelao L, Gross S, Seraglia R, Tondello E et al (2002) Rapid Commun Mass Spectrom 16:733–737

94. Wiberg N (2007) Lehrbuch der Anorganischen Chemie. Walter de Gruyter Co, Berlin
95. Li Y, Krivovichev SV, Burns PC (2001) J Solid State Chem 158:74–77
96. Grimes SM, Johnston SR, Abrahams I (1995) J Chem Soc Dalton Trans 2081–2086
97. Yeom YH, Kim Y, Seff K (1997) J Phys Chem B 101:5314–5318
98. Yeom YH, Kim Y, Seff K (1999) Microporous Mesoporous Mater 28:103–112
99. Haag-Bruhl C, Fuess H, Lightfoot P, Cheetham AK (1988) Acta Crystallogr Sect C Cryst Struct Commun 44:8–11
100. Hill R (1985) Acta Crystallogr Sect C Cryst Struct Commun 41:998–1003
101. Keller H-L (1983) Angew Chem 95:318–319
102. Olin A, Soderquist R (1972) Acta Chem Scand 26:3505–3514
103. Spiro TG, Templeton DH, Zalkin A (1969) Inorg Chem 8:856–861
104. Johansson G, Olin A (1968) Acta Chem Scand 22:3197–3201
105. Bengtsson LA, Hoffmann R (1993) J Am Chem Soc 115:2666–2676
106. Teff DJ, Huffman JC, Caulton KG (1996) J Am Chem Soc 118:4030–4035
107. Papiernik R, Hubert-Pfalzgraf LG, Massiani MC (1991) Polyhedron 10:1657–1662
108. Papiernik R, Hubert-Pfalzgraf LG, Daran J-C, Jeannin Y (1990) J Chem Soc Chem Commun 695–697
109. Yanovsky AI, Turova NY, Turevskaya EP, Struchkov YT (1982) Koord Khim 8:153–156
110. Gaffney C, Harrison PG, King TJ (1980) J Chem Soc Chem Commun 1251–1252
111. Rozes L, Sanchez C (2011) Chem Soc Rev 40:1006–1030
112. Coppens P, Chen Y, Trzop E (2014) Chem Rev 114:9645–9661
113. Hampden-Smith MJ, Wark TA, Brinker CJ (1992) Coord Chem Rev 112:81–116
114. Zhuang Z, Huang F, Lin Z, Zhang H (2012) J Am Chem Soc 134:16228–16234
115. Verdenelli M, Parola S, Hubert-Pfalzgraf LG, Lecocq S (2000) Polyhedron 19:2069–2075
116. Barbul I, Johnson AL, Kociok-Köhn G, Molloy KC, Silvestru C et al (2013) ChemPlusChem 78:866–874
117. Zöller T, Jurkschat K (2013) Inorg Chem 52:1872–1882
118. Boyle TJ, Alam TM, Rodriguez MA, Zechmann CA (2002) Inorg Chem 41:2574–2582
119. Abrahams I, Grimes SM, Johnston SR, Knowles JC (1996) Acta Crystallogr Sect C Cryst Struct Commun 52:286–288
120. Harrison PG, Haylett BJ, King TJ (1978) J Chem Soc Chem Commun 112–113
121. Turova NY, Suslova EV, Kessler VG, Belokon AI (2007) Russ J Inorg Chem 52:1682–1686
122. Hollingsworth N, Horley GA, Mazhar M, Mahon MF, Molloy KC et al (2006) Appl Organomet Chem 20:687–695
123. Zöller T, Iovkova-Berends L, Dietz C, Berends T, Jurkschat K (2011) Chem Eur J 17:2361–2364
124. Sita LR, Xi R, Yap GPA, Liable-Sands LM, Rheingold AL (1997) J Am Chem Soc 119:756–760
125. Schiemenz B, Ettel F, Huttner G, Zsolnai L (1993) J Organomet Chem 458:159–166
126. Kircher P, Huttner G, Zsolnai L, Driess A (1998) Angew Chem Int Ed 37:1666–1668
127. Schiemenz B, Antelmann B, Huttner G, Zsolnai L (1994) Z Anorg Allg Chem 620:1760–1767
128. Caruso J, Hampden-Smith MJ, Rheingold AL, Yap G (1995) J Chem Soc Chem Commun 157–158
129. Leonhardt C, Brumm S, Seifert A, Cox G, Lange A et al (2013) ChemPlusChem 78:1400–1412
130. Plasseraud L, Cattey H, Richard P (2010) Z Naturforsch B 65:1293–1300
131. Prabusankar G, Jousseaume B, Toupance T, Allouchi H (2006) Angew Chem Int Ed 45:1255–1258
132. Puff H, Reuter H (1989) J Organomet Chem 368:173–183
133. You Z, Möckel R, Bergunde J, Dehnen S (2014) Chem Eur J 20:13491–13496
134. Ribot F, Martinez-Ferrero E, Boubekeur K, Hendrickx PMS, Martins JC et al (2008) Inorg Chem 47:5831–5840
135. Sanchez C, de AA, Soler-Illia GJ, Ribot F, Lalot T, Mayer CR et al (2001) Chem Mater 13:3061–3083
136. Gómez-Romero P, Sanchez C (2005) Functional hybrid materials. Wiley, Hoboken

137. Ribot F (2008) Tin chemistry. Wiley, Hoboken, pp 69–92
138. Jurkschat K (2008) Tin chemistry. Wiley, Hoboken, pp 201–230
139. Chandrasekhar V, Gopal K, Sasikumar P, Thirumoorthi R (2005) Coord Chem Rev 249:1745–1765
140. Holmes RR, Day RO, Swamy KCK, Schmid CG, Burton SD et al (1989) Main Group Met Chem 12:291–303
141. Holmes RR (1989) Acc Chem Res 22:190–197
142. Chandrasekhar V, Singh P, Gopal K (2008) Tin chemistry. Wiley, Hoboken, pp 93–116
143. Chandrasekhar V, Singh P, Gopal K (2007) Appl Organomet Chem 21:483–503
144. Chandrasekhar V, Gopal K, Thilagar P (2007) Acc Chem Res 40:420–434
145. Mehring M, Schürmann M, Reuter H, Dakternieks D, Jurkschat K (1997) Angew Chem Int Ed 36:1112–1114
146. Zobel B, Costin J, Vincent BR, Tiekink ERT, Dakternieks D (2000) J Chem Soc Dalton Trans 4021–4022
147. Ma CL, Jiang Q, Zhang RF, Wang DQ (2003) Dalton Trans 2975–2978
148. Banse F, Ribot F, Toledano P, Maquet J, Sanchez C (1995) Inorg Chem 34:6371–6379
149. Sanchez C, Rozes L, Ribot F, Laberty-Robert C, Grosso D et al (2010) C R Chim 13:3–39
150. Wang Q-F, Ma C-L, He G-F, Li Z (2013) Polyhedron 49:177–182
151. Kastner G, Reuter H (2000) J Organomet Chem 598:381–386
152. Ma C, Zhang J, Jiang Q, Zhang R (2004) Inorg Chim Acta 357:2791–2797
153. Zheng G-L, Ma J-F, Yang J, Li Y-Y, Hao X-R (2004) Chem Eur J 10:3761–3768
154. Prabusankar G, Jousseaume B, Toupance T, Allouchi H (2007) Dalton Trans 3121–3123
155. Padělková Z, Havlík A, Švec P, Nechaev MS, Růžička A (2010) J Organomet Chem 695:2651–2657
156. Dakternieks D, Zhu H, Tiekink ERT, Colton R (1994) J Organomet Chem 476:33–40
157. Puff H, Reuter H (1989) J Organomet Chem 373:173–184
158. Eychenne-Baron C, Ribot F, Steunou N, Sanchez C, Fayon F et al (2000) Organometallics 19:1940–1949
159. Beckmann J, Jurkschat K, Kaltenbrunner U, Rabe S, Schürmann M et al (2000) Organometallics 19:4887–4898
160. Plasseraud L, Cattey H, Richard P (2011) Z Naturforsch B 66:262–268
161. Izaaryene M, Reuter H (2011) Phosphorus Sulfur Silicon Relat Elem 186:1364–1366
162. Chandrasekhar V, Thirumoorthi R (2009) Organometallics 28:2096–2106
163. Nehete UN, Chandrasekhar V, Jancik V, Roesky HW, Herbst-Irmer R (2004) Organometallics 23:5372–5374
164. Weinert CS, Guzei IA, Rheingold AL, Sita LR (1998) Organometallics 17:498–500
165. Shi Y-J, Xu Y, Chen X-T, Xue Z, You X-Z (2002) Eur J Inorg Chem 3210–3213
166. Vasil'ev VP, Shorokhova VI (1972) Elektrokhimiya 8:185–190
167. Dawson JL, Wilkinson J, Gillibrand MI (1970) J Inorg Nucl Chem 32:501–517
168. Tytko K-H (1979) Chem Unserer Zeit 13:184–194
169. Olin A (1957) Acta Chem Scand 11:1445–1456
170. Granér F, Olin A, Sillén LG (1956) Acta Chem Scand 10:476
171. Frei V, Mages G, Wendt H (1973) Ber Bunsen-Ges Phys Chem 77:243–247
172. Dragulescu C, Nimara A, Julean I (1972) Chim Anal 2:239–242
173. Gattow G, Schott D (1963) Z Anorg Allg Chem 324:31–47
174. Sundvall B (1979) Acta Chem Scand Ser A Phys Inorg Chem 33:219–224
175. Christensen AN, Chevallier MA, Skibsted J, Iversen BB (2000) J Chem Soc Dalton Trans 265–270
176. Christensen AN, Jensen TR, Scarlett NVY, Madsen IC, Hanson JC et al (2003) Dalton Trans 3278–3282
177. Christensen AN, Lebech B (2012) Dalton Trans 41:1971–1980
178. Miersch L, Rüffer T, Schlesinger M, Lang H, Mehring M (2012) Inorg Chem 51:9376–9384
179. Henry N, Mentré O, Abraham F, MacLean EJ, Roussel P (2006) J Solid State Chem 179:3087–3094

180. Henry N, Evain M, Deniard P, Jobic S, Mentré O et al (2003) J Solid State Chem 176:127–136
181. Lazarini F (1978) Acta Crystallogr Sect B Struct Sci 34:3169–3173
182. Liu B, Zhou W-W, Zhou Z-Q, Zhang X-Y (2007) Inorg Chem Commun 10:1145–1148
183. Brčić BS, Kolar D, Lazarini F, Malešič M (1973) Monatsh Chem 104:365–375
184. Cherkasova TG, Golubenko NA, Tatarinova ES (2005) Russ J Inorg Chem 50:1378–1380
185. Zimmermann LW, Schleid T (2011) Z Anorg Allg Chem 637:1903–1908
186. Sundvall B (1974) Acta Chem Scand Ser A Phys Inorg Chem 28:1036–1037
187. Sundvall B (1980) Acta Chem Scand Ser A Phys Inorg Chem 34:93–98
188. Sundvall B (1983) Inorg Chem 22:1906–1912
189. Thurston JH, Swenson DC, Messerle L (2005) Chem Commun 4228–4230
190. Dragulescu C, Nimara A, Julean I (1974) Rev Roum Chim 19:1455–1459
191. Rogow DL, Fei H, Brennan DP, Ikehata M, Zavalij PY et al (2010) Inorg Chem 49:5619–5624
192. Andrews PC, Deacon GB, Forsyth CM, Junk PC, Kumar I et al (2006) Angew Chem Int Ed 45:5638–5642
193. Dikarev EV, Zhang H, Li B (2006) Angew Chem Int Ed 45:5448–5451
194. Mehring M, Mansfeld D, Paalasmaa S, Schürmann M (2006) Chem Eur J 12:1767–1781
195. Jones CM, Burkart MD, Whitmire KH (1992) J Chem Soc Chem Commun 1638–1639
196. Whitmire KH, Hoppe S, Sydora O, Jolas JL, Jones CM (2000) Inorg Chem 39:85–97
197. Kugel B, Frank W (2002) Z Anorg Allg Chem 628:2178
198. Miersch L, Rüffer T, Lang H, Schulze S, Hietschold M et al (2010) Eur J Inorg Chem 4763–4769
199. Zahariev A, Parvanova V, Kaloyanov N (2010) Thermochim Acta 502:90–93
200. Andrews PC, Busse M, Junk PC, Forsyth CM, Peiris R (2012) Chem Commun 48:7583–7585
201. Kawamura M, Cui D-M, Shimada S (2006) Tetrahedron 62:9201–9209
202. Feyand M, Köppen M, Friedrichs G, Stock N (2013) Chem Eur J 19:12537–12546
203. Veith M, Yu E-C, Huch V (1995) Chem Eur J 1:26–32
204. Jolas JL, Hoppe S, Whitmire KH (1997) Inorg Chem 36:3335–3340
205. Mehring M, Paalasmaa S, Schürmann M (2005) Eur J Inorg Chem 4891–4901
206. Whitmire KH, Jones CM, Burkart MD, Chris Hutchison J, McKnight AL (1992) Mater Res Soc Symp Proc 271:149–154
207. Kou X, Wang X, Mendoza-Espinosa D, Zakharov LN, Rheingold AL et al (2009) Inorg Chem 48:11002–11016
208. James SC, Norman NC, Orpen AG, Quayle MJ, Weckenmann U (1996) J Chem Soc Dalton Trans 4159–4161
209. Andrews PC, Junk PC, Nuzhnaya I, Spiccia L (2008) Dalton Trans 2557–2568
210. Mougel V, Biswas B, Pecaut J, Mazzanti M (2010) Chem Commun 46:8648–8650
211. Nocton G, Burdet F, Pécaut J, Mazzanti M (2007) Angew Chem Int Ed 46:7574–7578
212. Li X-L, He L-F, Feng X-L, Song Y, Hu M et al (2011) CrystEngComm 13:3643–3645
213. Wang R, Song D, Wang V (2002) Chem Commun 368–369
214. Zhang M-B, Zhang J, Zheng S-T, Yang G-Y (2005) Angew Chem Int Ed 44:1385–1388
215. Giester G, Unfried P, Zak Z (1997) J Alloys Compd 257:175–181
216. Wang R, Carducci MD, Zheng Z (2000) Inorg Chem 39:1836–1837
217. Swanson CH, Shaikh HA, Rogow DL, Oliver AG, Campana CF et al (2008) J Am Chem Soc 130:11737–11741
218. Fenske D, Garbe R, Dehnicke K (1994) Z Naturforsch B 49:983–986
219. Nakano H, Ozawa Y, Yagasaki A (1995) J Am Chem Soc 117:12007–12008
220. Kusaka Y, Ozawa Y, Yagasaki A (2001) Inorg Chem 40:2634–2635
221. Bertazzi N, Alonzo G, Saiano F, Battaglia LP (1995) Z Anorg Allg Chem 621:2070–2074
222. Hu B, Feng M-L, Li J-R, Lin Q-P, Huang X-Y (2011) Angew Chem Int Ed 50:8110–8113
223. Hu B, Zou G-D, Feng M-L, Huang X-Y (2012) Dalton Trans 41:9879–9881
224. Zou G-D, Wang Z-P, Song Y, Hu B, Huang X-Y (2014) Dalton Trans 43:10064–10073
225. Zou G-D, Zhang G-G, Hu B, Li J-R, Feng M-L et al (2013) Chem Eur J 19:15396–15403
226. Breunig HJ, Probst J, Ebert KH, Lork E, Cea-Okuvares R et al (1997) Chem Ber 130:959–961

227. Bordner J, Doak GO, Everett TS (1986) J Am Chem Soc 108:4206–4213
228. Betz R, Lindner C, Klufers P, Mayer P (2009) Acta Crystallogr Sect E Struct Rep 65:m253–m254
229. Breunig HJ, Krüger T, Lork E (2002) J Organomet Chem 648:209–213
230. Yin H, Wu Q, Hong M, Li W (2012) Z Anorg Allg Chem 638:725–729
231. Kishore PVVN, Baskar V (2014) Inorg Chem 53:6737–6742
232. Chandrasekhar V, Thirumoorthi R (2009) Organometallics 28:2637–2639
233. Beckmann J, Heek T, Takahashi M (2007) Organometallics 26:3633–3635
234. Jami AK, Prabhu MSR, Baskar V (2010) Organometallics 29:1137–1143
235. Srungavruksham NK, Baskar V (2015) Dalton Trans 44:6358–6362
236. Clark CJ, Nicholson BK, Wright CE (2009) Chem Commun 923–925
237. Nicholson BK, Clark CJ, Wright CE, Groutso T (2010) Organometallics 29:6518–6526
238. Nicholson BK, Clark CJ, Wright CE, Telfer SG, Groutso T (2011) Organometallics 30:6612–6616
239. Nicholson BK, Clark CJ, Jameson GB, Telfer SG (2013) Inorg Chim Acta 406:53–58
240. Nicholson BK, Clark CJ, Telfer SG, Groutso T (2012) Dalton Trans 41:9964–9970
241. Baskar V, Shanmugam M, Helliwell M, Teat SJ, Winpenny REP (2007) J Am Chem Soc 129:3042–3043
242. Asato E, Katsura K, Mikuriya M, Turpeinen U, Mutikainen I et al (1995) Inorg Chem 34:2447–2454
243. Sattler D, Schlesinger M, Mehring M, Schalley CA (2013) ChemPlusChem 78:1005–1014
244. Miersch L, Schlesinger M, Troff RW, Schalley CA, Rüffer T et al (2011) Chem Eur J 17:6985–6990
245. Miersch L, Rüffer T, Schaarschmidt D, Lang H, Troff RW et al (2013) Eur J Inorg Chem 1427–1433
246. Schlesinger M, Pathak A, Richter S, Sattler D, Seifert A et al (2014) Eur J Inorg Chem 4218–4227
247. Schlesinger M, Weber M, Rüffer T, Lang H, Mehring M (2014) Eur J Inorg Chem 302–309
248. Miersch L (2012) Dissertation thesis, Technische Universität Chemnitz (Chemnitz, Germany)
249. Miersch L, Rüffer T, Mehring M (2011) Chem Commun 47:6353–6355
250. André V, Hardeman A, Halasz I, Stein RS, Jackson GJ et al (2011) Angew Chem Int Ed 50:7858–7861
251. Sun H (2010) Biological chemistry of arsenic, antimony and bismuth. Wiley, Hoboken
252. Boyd TD, Kumar I, Wagner EE, Whitmire KH (2014) Chem Commun 50:3556–3559
253. Andrews PC, Deacon GB, Junk PC, Kumar I, MacLellan JG (2009) Organometallics 28:3999–4008
254. Asato E, Katsura K, Mikuriya M, Fujii T, Reedijk J (1992) Chem Lett 21:1967–1970
255. Mehring M, Schürmann M (2001) Chem Commun 2354–2355
256. Chandrasekhar V, Metre RK, Suriya Narayanan R (2013) Dalton Trans 42:8709–8716
257. Mansfeld D, Miersch L, Rüffer T, Schaarschmidt D, Lang H et al (2011) Chem Eur J 17:14805–14810
258. Pathak A, Blair VL, Ferrero RL, Mehring M, Andrews PC (2014) Chem Commun 50:15232–15234
259. Schlesinger M, Miersch L, Rüffer T, Lang H, Mehring M (2013) Main Group Met Chem 36:11–19
260. Chandrasekhar V, Metre RK, Sahoo D (2014) Eur J Inorg Chem 164–171
261. Mehring M (2007) Coord Chem Rev 251:974–1006
262. Falaise C, Volkringer C, Vigier J-F, Beaurain A, Roussel P et al (2013) J Am Chem Soc 135:15678–15681
263. Söderholm L, Almond PM, Skanthakumar S, Wilson RE, Burns PC (2008) Angew Chem Int Ed 47:298–302
264. Wilson RE, Skanthakumar S, Söderholm L (2011) Angew Chem Int Ed 50:11234–11237
265. Nehete UN, Roesky HW, Jancik V, Pal A, Magull J (2007) Inorg Chim Acta 360:1248–1257
266. Mansfeld D, Mehring M, Schürmann M (2005) Angew Chem Int Ed 44:245–249
267. Malaestean IL, Ellern A, Baca S, Kögerler P (2012) Chem Commun 48:1499–1501

Struct Bond (2017) 174: 269–320
DOI: 10.1007/430_2016_5

Published online: 21 July 2016

Large Metal Chalcogenide Clusters and Their Ordered Superstructures via Solvothermal and Ionothermal Syntheses

Tetyana I. Levchenko, Yining Huang, and John F. Corrigan

Dedicated to Prof. Dr. Hansgeorg Schnöckel on the occasion of his 75th birthday.

Abstract Nanometre-scale metal chalcogenide clusters and materials derived from their regular spatial organization via covalent or other bonding interactions represent an important area of research, encompassing intricate structures and unique size-related electronic and physical properties. This chapter will summarize the structure and bonding principles in these systems, focusing on high nuclearity and discrete metal chalcogenide clusters, and will review the recent progress in their preparation using solvothermal and ionothermal approaches.

Keywords Discrete clusters • Ionothermal • Metal chalcogenides • Molecular clusters • Non-covalent bonding • Non-tetrahedral clusters • Solvothermal • Superlattice • Superstructure • Tetrahedral clusters

Contents

T.I. Levchenko, Y. Huang (✉), and J.F. Corrigan (✉)
Department of Chemistry and Centre for Advanced Materials and Biomaterials Research (CAMBR), The University of Western Ontario, London, ON, Canada N6A 5B7
e-mail: yhuang@uwo.ca; jfcorrig@uwo.ca

1 Introduction

Polynuclear metal chalcogenides ME (where M = metal, E = group 16 element heavier than oxygen) often possess unique structures due to the bonding modes inherent to the chalcogen sites [1–7]. Metal chalcogenide clusters with well-defined sizes and chemical composition can contain tens to hundreds of metal core atoms, organized with a high level of symmetry, reaching several nanometres in size [6, 8–10]. Many of these nanoclusters can be prepared and isolated as single crystals, making it possible to obtain complete structural information through single-crystal X-ray diffraction [11]. Other powerful tools, such as electron tomography, can help significantly in the analysis of cluster (super)structures [12–15]. Knowledge of the exact structure of such clusters provides valuable insight into structure–property relationship in nanodimensional systems without obscuring effects of size polydispersity and structure ambiguity, often inherent to colloidal nanoparticles. Generally, clusters of semiconductor metal chalcogenides have size-related electronic and photophysical properties due to quantum confinement effects [16–18]. Thus, a systematic blue shift of the optical absorption band is observed with decreasing CdSe cluster size [19, 20]. The properties of the clusters can also be tuned by the substitution of M and E, by combining several different metals or chalcogens, with site-selective distribution of the components in a cluster core, and/or fitting organic ligands on a cluster surface. Long-range order is present with certain secondary structures (1D, 2D and 3D arrangements), maintained by electrostatic (Coulomb) interactions and/or relatively weak (e.g. van der Waals) forces or, alternatively, by covalent bonding (with or without auxiliary organic linkers) between metal chalcogenide clusters [21]. Such multilevel, hierarchical structures of metal chalcogenide clusters have multiple attractive features: materials containing metal chalcogenide clusters can be engineered at several different length scales, from atomic level (size and composition of cluster core) to the superstructure level (intercluster bonding type and connectivity patterns), which provides an additional opportunity to control their properties [22]. Moreover, hybrid materials can be created based on molecular-level integration of anionic metal chalcogenide clusters

with cations having special functions [23, 24], or even by the combination (crystallization) of cluster superstructures with other advanced materials. One of the recent examples of the latter is the cluster-based material $(C_5H_{12}N)_{12}[Zn_4Ga_{14}Sn_2Se_{35}]$@reduced graphene oxide, where $C_5H_{12}N$ is piperidinium cation [25]. The properties of the materials containing metal chalcogenide clusters encompass such research areas as photophysics, photoelectrochemistry, photocatalysis, etc., as they are promising candidates for application as advanced energy conversion materials and bio-labels [26–30].

Historically, a coordination chemistry approach has been used for the preparation and crystallization of metal chalcogenide clusters from solutions [1, 6, 9]. This powerful approach utilizes different sources of chalcogenides and surface chalcogenolates (among them silylated reagents $E(SiMe_3)_2$ and $RESiMe_3$) [11] and has been proven to give access to, for instance, unprecedented large sizes (e.g. $[Ag_{490}S_{188}(S^tC_5H_{11})_{114}]$) [31] as well as opportunities for unique surface functionalization (e.g. ferrocene (fc) decorated $[Ag_{74}S_{19}(dppp)_6(fc(C\{O\}OCH_2CH_2S)_2)_{18}]$, where *dppp*=1,3-bis(diphenylphosphino)propane) [32] to group 11 metal chalcogenide clusters. Materials containing metal chalcogenide clusters have also been prepared by solid-state chemistry approaches from high-temperature reactions in polychalcogenide flux (e.g. a series of discrete clusters $[M_4Sn_4S_{17}]^{10-}$ with M=Mn, Fe, Co, Zn in a K_2S_x flux) [33, 34]. More recently, solvothermal approaches have been exploited [35, 36], conducting synthesis using relatively simple reagents (e.g. elemental forms and inorganic salts) in an appropriate organic solvent in a sealed vessel at moderately high temperature and autogenous pressure. A related approach, utilizing ionic liquids as reaction media is also a focus of research efforts for the preparation of metal chalcogenide clusters [37]. During the last decade solvothermal and ionothermal approaches have yielded, for example, new metal chalcogenide clusters with unprecedented structures [38–40], the ability for precise and uniform one-atom doping of clusters with vacant sites [41, 42] and the preparation of large, discrete clusters, previously accessible only in covalently bonded 2D and 3D superlattices [43, 44].

Several research groups have been developing solvothermal and ionothermal approaches towards the preparation of large metal chalcogenide clusters and materials derived from their regular spatial organization. The general synthetic routes and the structures and properties of these materials will be summarized in this review. Note that the main focus is on discrete clusters (mainly tetrahedral) and their non-covalent 3D superstructures, while extended framework superstructures (both zeolite and metal-organic framework analogues with inorganic linkers and organic ligand connection between clusters, respectively) were previously covered in several reviews [45–48]. Relatively large metal chalcogenide clusters, mainly containing ≥ 8 metal sites in the core, are the focus herein.

2 Bonding in Metal Chalcogenide Clusters

2.1 Metal–Chalcogen Bonding

Chalcogenides E^{2-} form stable bonds with many metals, adopting several different bridging coordination modes, with μ_3 and μ_4 being the most common [2, 4, 6]. Thus, the coordination number of sulfur reaches 4 even with a relatively large metal cation such as Cd^{2+}. The ability to bridge metals with high coordination numbers is attributed to the large ionic radii, high polarizability, more delocalized electron orbitals and the anionic nature of chalcogenide ligands [6]. The bridging ability increases on going down group 16 from sulfur to selenium to tellurium [3, 5, 7]. Metal cations in cluster chalcogenides can be in one particular oxidation state (M^{2+}, M^{3+} or M^{4+}) or different combinations of two cations (e.g. M^{3+}/M^{+} or M^{4+}/M^{2+}) or exhibit even more complex composition. A recent example of such multinary compounds is a family of discrete $M_{20}E_{35}$ clusters, combining, for instance, five metals with different oxidation states (i.e. Cu, Zn, Mn, Ga and Sn) in one cluster, as confirmed by EDX analysis; for clusters with quaternary composition (e.g. $[Cu_2Ga_{16}Sn_2Se_{35}]^{12-}$ or $[Zn_4Ga_{14}Sn_2Se_{35}]^{12-}$), single-crystal structure refinement results are in good agreement with atomic absorption spectroscopy analysis [49]. As a consequence of the high bridging ability of E^{2-} with high coordination numbers for M^{x+}, in many metal chalcogenide frameworks, cations and anions both adopt tetrahedral coordination, which makes tetrahedral unit $\{ME_4\}$ the most basic building block in these materials. A distinct structural feature is the overall tetrahedral shape of many such clusters. The covalent character of bonding in the tetrahedral units $\{ME_4\}$ reflects the relative position of the composing metals in the periodic table. Most often, metals in these tetrahedral clusters belong to groups 12, 13 and 14 (e.g. Zn, Cd, Hg; Ga, In; Ge, and Sn) and late first-row transition metals (e.g. Mn, Fe, Co and Cu); however, this does not exclude the possibility of doping by other metals (e.g. Li). Many of the tetrahedral metal chalcogenide clusters, originally prepared by other approaches, have been reproduced solvothermally. Even more clusters have proven accessible by solvothermal and ionothermal approaches, including those with completely new structure types. The group 11 metal chalcogenide clusters, prepared by coordination chemistry approaches, are numerous and structurally diverse [50–52], but such discrete clusters are typically not accessible via solvothermal or ionothermal approaches. Although large cluster cores composed of tetrahedral units $\{ME_4\}$ and an overall tetrahedral shape are characteristic to metal chalcogenides, some examples are also known for oxides (e.g. tetrahedral clusters $[Mn^{II}{}_{29}Mn^{III}{}_6O_{56}]^{36-}$ or $[Ln_{20}O_{11}]^{38+}$, where Ln=lanthanoid metal) [53, 54]. With adamantoid (cubic) (Fig. 1, left) and barrelanoid (hexagonal) (Fig. 1, right) crystalline cages both being possible with the tetrahedral coordination of atoms (corresponding to zinc blende and wurtzite crystal structures, respectively, well known for bulk crystalline metal chalcogenides), the recognized structural variations of tetrahedral metal chalcogenide cluster arise from different combinations of cubic and hexagonal cages in the ME

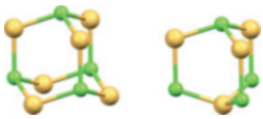

Fig. 1 Adamantoid or cubic (*left*), barrelanoid or hexagonal (*right*) crystalline cages. M sites are shown as *green spheres* and E as *yellow-orange*

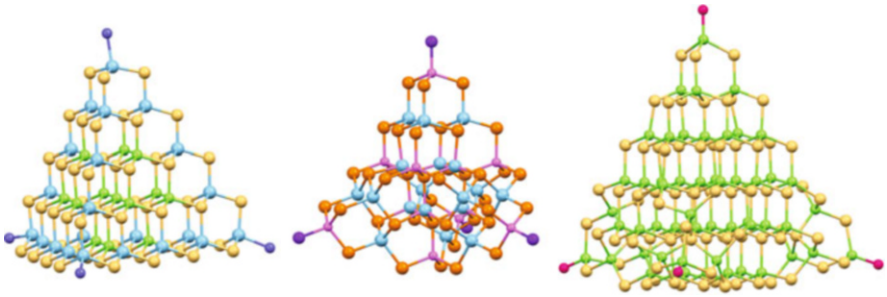

Fig. 2 The core structures of the largest discrete clusters prepared in the three tetrahedral cluster series: (basic) supertetrahedral cluster $[Cd_{13}In_{22}S_{52}(mim)_4]^{12-}$, where *mim* = 1-methylimidazole (*left*); penta supertetrahedral cluster $[Cu_{11}In_{15}Se_{16}(SePh)_{24}(PPh_3)_4]$ (*centre*); capped supertetrahedral clusters $[Cd_{54}S_{32}(SPh)_{48}(H_2O)_4]^{4-}$ (*right*). [43, 55, 56]. If not stated otherwise, M^{2+} sites are shown as *green*; M^{3+}, *light blue*; M^{4+}, *blue*; M^{+}/M^{2+} transition metal sites, *magenta*; S, *yellow-orange*; Se, *orange*; Te, *brown*; C, *light grey*; O, *pink*; N, *violet*; and P, *purple* in all figures throughout the review. Atoms and bonds in the cluster core are typically shown as *spheres and sticks*, respectively, while in ligands and other species atoms and bonds are shown as *capped sticks*

frameworks. Thus, by the nature of intra-cluster connectivity, tetrahedral metal chalcogenide clusters can be classified as belonging to three particular structural series, (basic) supertetrahedral, penta supertetrahedral and capped supertetrahedral (Fig. 2) [47, 57]; these are considered in detail below in Sects. 2.3, 5.2 and 5.3. Although large, non-tetrahedral clusters [6, 9] are less often prepared via solvothermal and ionothermal syntheses, some fascinating examples of discrete ring- and cagelike frameworks formed by vertex and edge sharing of basic tetrahedra $\{ME_4\}$ have been reported recently. These clusters are discussed below in Sects. 2.5, 5.5 and 5.6.

2.2 *Local Electroneutrality in the Cluster Core*

One of the most important factors affecting the size and connectivity of metal chalcogenide clusters is the charge on the constituent metal cations. As the tetrahedral clusters display a clear structural relationship with the corresponding

crystalline solids, they are found to obey the same rules surrounding their bonding. Generally, the charge of metal cations appearing in particular sites of tetrahedral metal chalcogenide clusters is found to follow Pauling's electrostatic valence rule. According to this rule, in order to keep *local electroneutrality* (local charge balance), the sum of the strengths of the electrostatic bonds to E^{2-} anion should be equal to the charge on the anion, i.e. 2. The electrostatic bond strength can be calculated as the ratio of the charge on adjacent metal cations to its coordination number. From this it follows, for example, that each tetrahedral E^{2-} site could be either surrounded by four tetrahedral M^{2+} or two tetrahedral M^{3+} plus two tetrahedral M^{+}. More specific cases are addressed below when considering the tetrahedral cluster series. Pauling's electrostatic valence rule works most obviously for the inner sites in the cluster, although it is not always applicable to surface sites (at vertexes, edges and faces of tetrahedral clusters). This is because E^{2-} sites on the surface may receive additional bond valence from cationic species that are not part of the cluster. A few exceptions to Pauling's electrostatic valence rule (e.g. a tetrahedral cluster with a core E^{2-} site bonded to four M^{3+}) [58] can be rationalized considering cluster stabilization from additional lattice species.

2.3 Series of Tetrahedral Clusters

In a basic *supertetrahedral* series, each molecular cluster consists of a regular tetrahedral-shaped fragment of the zinc blende-type lattice (cubic, adamantoid cages) (Fig. 3). Larger clusters in this series are formed by fusion of adamantoid cages only. This is the most fundamental type of connectivity; other series of clusters can be geometrically derived from the basic supertetrahedral building units. The difference between clusters within the series lies in the size of the framework. This is reflected in conventional notation for the clusters in the supertetrahedral series, T_n, where the integer n indicates the number of individual $\{ME_4\}$ tetrahedra along each edge (Fig. 3). The integer n is also equivalent to the number of metal layers within a particular cluster. Thus, a T_3 cluster with a $M_{10}E_{20}$ core contains four fused adamantoid cages and has three $\{ME_4\}$ tetrahedra along each edge (or three metal layers) (Fig. 3, top right). The composition of an idealized core M_xE_y of any T_n cluster is strictly defined (see formulae in Table 1). It can be seen that the number of E sites in a T_n cluster is equal to the number of M sites in the next larger $T_{(n+1)}$ cluster. The peculiarity of large T_n clusters is the presence of tetrahedrally coordinated (inner) anions, while smaller clusters (T_1, T_2 and T_3) consist of μ- and μ_3-anions only. To maintain the local electroneutrality, in large metal chalcogenide clusters containing two or more types of metal cations, site-selective distribution of metals will be one that better balances the tetrahedrally coordinated anion sites E^{2-}, which occur inside clusters $\geq T_4$. In multinary clusters with more than one type of chalcogenide (e.g. both Se and S), the appearance of E, E′, M and M′ at inner or surface sites may be governed by multiple factors [59]. The largest reported discrete supertetrahedral clusters are T_5; for instance,

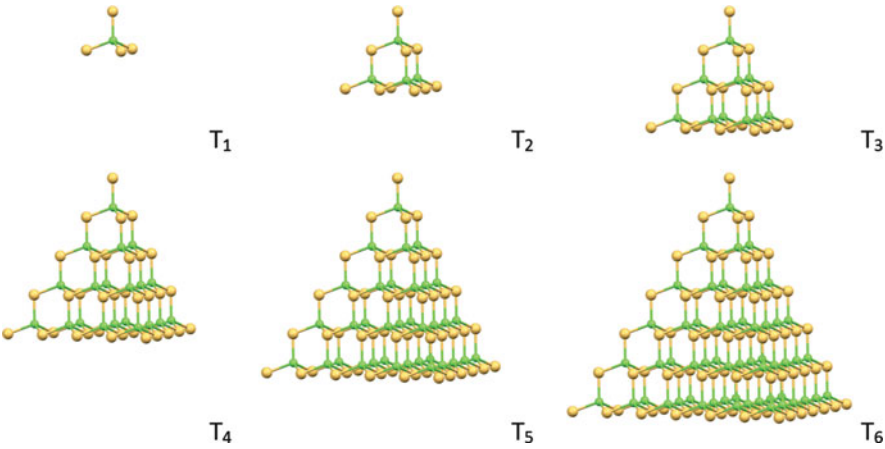

Fig. 3 Tetrahedrally shaped fragments of regular zinc blende (cubic) crystalline lattice as idealized structures of supertetrahedral T_n clusters. Such clusters up to T_5 were synthesized and structurally characterized, while T_6 remains a hypothetical structure

Table 1 Series of tetrahedral metal chalcogenide clusters[a]

Name	(Basic) **supertetrahedral**	**Penta** supertetrahedral	**Capped** supertetrahedral
Notation	T_n	P_n	C_n
$n = 1$	ME_4	M_8E_{17}	$M_{17}E_{32}$
$n = 2$	M_4E_{10}	$M_{26}E_{44}$	$M_{32}E_{54}$
$n = 3$	$M_{10}E_{20}$		$M_{54}E_{84}$
$n = 4$	$M_{20}E_{35}$		
$n = 5$	$M_{35}E_{56}$		
Cluster stoichiometry [b]	M_xE_y,[c] where $x = [n(n+1)(n+2)]/6$; $y = [(n+1)(n+2)(n+3)]/6$	M_xE_y, where $x = 4[n(n+1)(n+2)]/6 + [(n+1)(n+2)(n+3)]/6$; $y = 4[(n+1)(n+2)(n+3)]/6 + [n(n+1)(n+2)]/6$	M_xE_y, where $x = [n(n+1)(n+2)]/6 + [4(n+1)(n+2)]/2 + 4$; $y = [(n+1)(n+2)(n+3)]/6 + [4(n+2)(n+3)]/2 + 4$

[a]Adapted from [47]

[b]Stoichiometry of discrete clusters is summarized. The overall stoichiometry of the superstructures of covalently connected clusters (e.g. corner-sharing case) varies depending on the pattern of connectivity

[c]Colours in formulae are used to emphasize the structural relation between clusters with the same n in the different series: the parts of expression correspond to the number of metal (green) and chalcogen (orange) atoms in the idealized basic supertetrahedral T_n unit M_xE_y. For instance, the composition of an idealized penta supertetrahedral P_n cluster can be derived by taking four times the expression for a T_n unit and one for an anti-T_n unit, where the latter has the metal and chalcogen positions exchanged in comparison to a regular one

$[Cd_{13}In_{22}S_{52}L_4]^{12-}$ cluster, where L is neutral organic ligand 1-methylimidazole, *mim*, capping four cluster vertexes through In−N coordination bonds (Fig. 2, left); this was prepared using solvothermal methods [43].

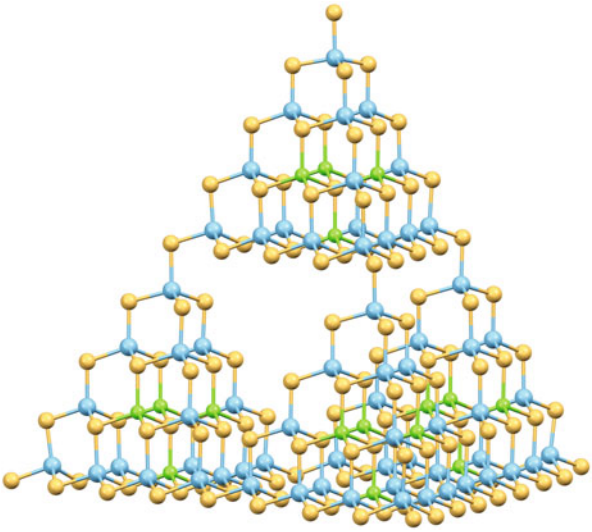

Fig. 4 Hierarchical $T_{4,2}$ cluster $[Cd_{16}In_{64}S_{134}]^{44-}$ as an example of clusters with a void in the core; it can be viewed as four T_4 units covalently assembled into T_2 cluster or as T_8 cluster with the void of T_4 size inside [61]

Clusters with a void or cavity in the core, i.e. hierarchical and coreless clusters, can be considered as structure variations of a supertetrahedral series rather than a separate connectivity type. *Hierarchical* supertetrahedral clusters (denoted $T_{p,q}$) consist of four supertetrahedral T_p units assembled (through vertex sharing by bridging E^{2-} or ER^- sites) into a self-closed T_q cluster with a central void of size T_p. Hierarchical $T_{p,q}$ clusters can also be viewed as T_n-like clusters of a larger size ($n = p*q$) with a well-defined tetrahedral void in a core, created by the systematic absence of M and E atoms. In hierarchical clusters, the presence of an inner tetrahedral void ensures a decrease of the coordination number of some of the internal anions; the structure is favourable under conditions of an appropriate combination of constituent elements and a structure-directing agent that optimizes both local and total charge balances. Hierarchical clusters with large T_p units (and, consequently, large voids) are rare, as T_n clusters preferentially self-assemble into extended lattices (an extraordinary example is dual hierarchical covalently bonded 3D superstructure $T_{5,\infty}$ [60]) instead of forming discrete self-closed $T_{p,q}$ clusters. An example of large hierarchical cluster is the solvothermally prepared discrete $T_{4,2}$ $[Cd_{16}In_{64}S_{134}]^{44-}$ (Fig. 4) [61]. More recently, solvothermal synthesis also resulted in the preparation of the anionic $T_{2,2}$ cluster $[M_{16}Se_{34}]^{x-}$ (M=Ge/In mixed sites) covalently linked with T_3 clusters in a 3D framework [62]. Hierarchical supertetrahedral clusters can be prepared while systematically hosting a particular chemical species (e.g. alkali metal cations) [63].

The other set of clusters with a central void are *coreless* clusters, having in their otherwise regular T_n lattice a single metal tetrahedral site vacant, surrounded by four core E^{2-} ions. Examples are the solvothermally prepared coreless T_5 $[Cd_6In_{28}S_{56}]^{12-}$ which are arranged in a covalently bonded 2D superstructure [64] and coreless T_5 $[In_{34}S_{56}]^{6-}$ which form a covalently bonded 3D co-assembly

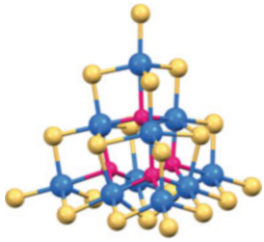

Fig. 5 Stuffed supertetrahedral cluster $[Sn_{10}S_{20}O_4]^{8-}$: an extra O atom is present in each of the four cubic cages of the regular T_3 unit [66]

with regular T_3 $[In_{10}S_{18}]^{6-}$ units [65]. These large clusters with one metal cation missing appear since such a structure allows for a reduction in the coordination number of four inner chalcogenide anions from four to three, helping to maintain local electroneutrality. The void in as-prepared coreless clusters is occupied by various (highly disordered) guest species [64]. At the same time, a coreless structure provides a unique possibility for precise doping with carefully chosen metal cations (e.g. by Cu^+ or Mn^{2+}), which was shown to change dramatically the photophysical properties versus the pristine metal chalcogenide frameworks [41, 42].

Similar to the main structural feature in coreless clusters that results from metal atom elimination, uncommon *stuffed* clusters can be viewed as a product of the addition of extra atoms to regular T_n frameworks. Recent examples of solvothermally prepared stuffed clusters include $[Sn_{10}S_{20}O_4]^{8-}$ and $[Sn_{10}Se_{20}O_4]^{8-}$ with extra oxygen atoms in each cubic cage of the T_3 units (Fig. 5); both S- and Se-containing analogues are covalently linked in co-assemblies of clusters of different sizes [66, 67]. The formation of such oxychalcogenide units allows for the stabilization of a Sn^{4+}-containing T_3 framework, which is otherwise unlikely to form: according to Pauling's electrostatic valence rule, μ_3-E^{2-} sites do not match with tetrahedral Sn^{4+} sites and the largest possible supertetrahedral cluster in the pure system $M_x{}^{4+}E_y$ is T_2.

Penta supertetrahedral cluster series (denoted P_n) are formed by coupling four T_n supertetrahedral units onto the faces of an anti-supertetrahedral unit of the same order. The central anti-supertetrahedral unit has the M and E positions exchanged in comparison to a regular one; e.g. anti-T_2 unit has composition $\{E_4M_{10}\}$ (Fig. 6, top left). In this way, P_n clusters contain both cubic and hexagonal cages, and the latter appear on fused faces (Fig. 6, top centre). Thus, in a P_1 cluster four hexagonal cages are sharing a single tetrahedral E site, also each containing three M sites of the same $\{EM_4\}$ unit. In a P_2 cluster there are three hexagonal cages on each of four faces of anti-T_2 unit, twelve in total (Fig. 6, top right). The structural relation between P_n and T_n with the same n is reflected in the composition of an idealized P_n core M_xE_y (see formulae in Table 1), as formulae can be derived using the known composition law for T_n. The largest solvothermally prepared penta supertetrahedral cluster P_2 with composition $[Li_4In_{22}S_{44}]^{18-}$ exhibits corner sharing in a covalently bonded 3D structure [68]. This large cluster contains four tetrahedrally coordinated S^{2-} sites, located in the central anti-T_2 unit. To satisfy Pauling's electrostatic valence rule,

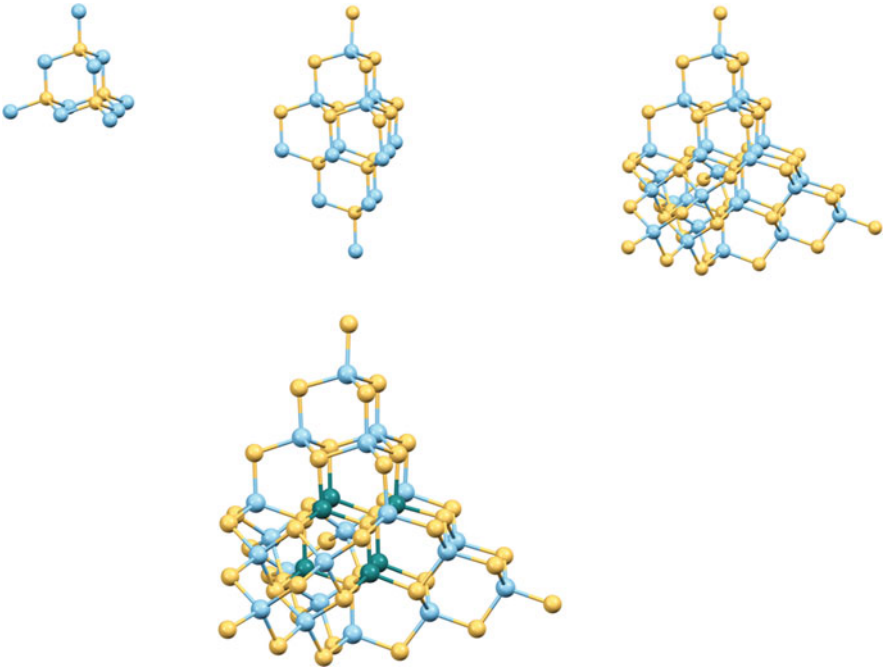

Fig. 6 Anti-T_2 building unit with a composition $\{E_4M_{10}\}$ (*top left*), in which the M and E positions are exchanged in comparison to a regular T_2 unit $\{M_4E_{10}\}$. Face-to-face coupling of a T_2 and an anti-T_2 supertetrahedral unit (each containing a cubic cage) creates three hexagonal cages (*top centre*). Penta supertetrahedral cluster P_2 (*top right*) can be viewed as a combination of four T_2 units and one central anti-T_2 unit; partial occupancy of some cites by metals of different valence is ignored here. Anionic P_2 cluster $[Li_4In_{22}S_{44}]^{18-}$ (*bottom*) contains six inner metal sites with partial occupancy Li/In (shown as *dark cyan*) to satisfy Pauling's electrostatic valence rule [68]

each such S^{2-} site should be surrounded by two Li^+ and two In^{3+}, giving together a bond valence sum of +2. These two metals are statistically distributed over six symmetry equivalent inner metal sites (located in central anti-T_2 unit) with 2/3 occupancy by Li^+ and 1/3 occupancy by In^{3+} (Fig. 6, bottom) [68]. In the discrete cluster of the same size P_2, prepared using a coordination chemistry approach [55], a statistical distribution of Cu^+ and In^{3+} cations over six symmetry equivalent inner metal sites was also found (Fig. 2, centre). With four vertex metal positions in the central anti-T_2 unit, as well as four metal positions at P_2 cluster vertexes solely occupied by Cu^+, results of elemental analysis are in a good agreement with the disordered model and a neutral formula $[Cu_{11}In_{15}Se_{16}(SePh)_{24}(PPh_3)_4]$, featuring $PhSe^-$ ligands on edges and PPh_3 ligands at cluster vertexes [55].

Capped supertetrahedral cluster series (denoted C_n) consist of a core, which is a regular fragment of the cubic lattice, and four hexagonal (barrelanoid) cages capping the vertexes. Another way to view clusters of the C_n series, better showing their relation with T_n series, is as follows: a regular supertetrahedral unit T_n at the core is covered on each face with a single "layer" of vertex-sharing basic $\{ME_4\}$ units (see Fig. 7, top centre) and each vertex is completed by a $\{M_4E_4\}$ group to form a hexagonal cage. In this way, the composition of an idealized C_n core can be derived using formulae for T_n with the same n (Table 1). The structural feature of C_n clusters is the open cleft that runs along each of the tetrahedral edges (see Fig. 7, bottom). Like in T_n clusters, the number of E sites in a C_n cluster is equal to the number of M sites in the next larger $C_{(n+1)}$ in the series. In C_n clusters, each hexagonal cage (more precisely, a M_4E_5 unit) at one of four vertexes can also be independently rotated (around the threefold axis of the tetrahedron) by 60°. This results in additional variation (isomerism) in the capped supertetrahedral series, denoted as $C_{n,m}$ where m refers to the number of corners that have been rotated from their original position in the parent C_n. This variant does not usually change either cluster or superstructure properties significantly, so vertex rotation will not be mentioned below while referring the cluster type and size. Discrete capped supertetrahedral clusters with sizes up to C_3 were synthesized solvothermally; some examples are $[Cd_{54}S_{32}(SPh)_{48}(H_2O)_4]^{4-}$ (Fig. 2, right) and $[Cd_{54}Se_{32}(SPh)_{48}(H_2O)_4]^{4-}$ (Fig. 7, bottom) [56]. The core of these C_3 clusters is formed by ten tetra-coordinated cadmium and twenty tetra-coordinated chalcogenide sites in a cubic arrangement (forming a regular T_3 unit) (Fig. 7, top left). The inner tetrahedron is covered on each face with seven $\{CdE_4\}$ units fused through vertexes by rows 2-3-2 to form a single cubic sheet (Fig. 7, top centre), resulting in four times three μ_3-E^{2-} sites (twelve in total). Capping each vertex with a hexagonal cage (Fig. 7, top right) increases the number of edge μ-PhS^- sites to eight per each of the six edges (48 in total).

From the description above, it can be seen that in the vast majority of these tetrahedral clusters, the number of E sites exceeds the number of M sites; this follows from having the tetrahedral $\{ME_4\}$ unit as a building block. The presence of an inner anti-T_n unit (derived from a $\{EM_4\}$ unit) in the structure of P_n cluster series is an exception. Interestingly, the preparation and structural characterization of several large tetrahedral "quantum dots" with crystalline CdSe cores corresponding entirely to anti-T_n clusters was recently reported [69]. The metal chalcogenide core structure with unusual metal-terminated {111} facets was derived using a combination of single and powder X-ray diffraction data and atomic pair distribution function analysis. These quantum dots have approximate formulae $Cd_{35}Se_{20}X_{30}L_{30}$, $Cd_{56}Se_{35}X_{42}L_{42}$ and $Cd_{84}Se_{56}X_{56}L_{56}$, with benzoate and *n*-butylamine ligands (X = O_2CPh, L = H_2N-Bu), and can be viewed as anti-T_4, anti-T_5 and anti-T_6, respectively.

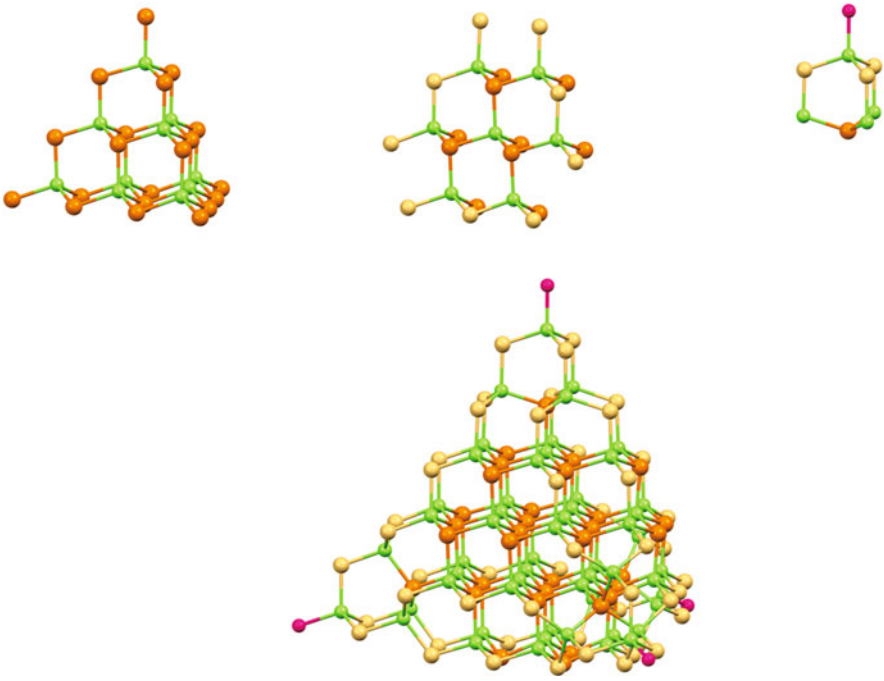

Fig. 7 The core T_3 unit (*top left*), a single cubic sheet (*top centre*) that covers each face of the central tetrahedron and a hexagonal cage (*top right*) that caps each vertex in the C_3 cluster $[Cd_{54}Se_{32}(SPh)_{48}(H_2O)_4]^{4-}$ (*bottom*). The open cleft along each of the six edges of the tetrahedral C_3 cluster is formed by S (shown as *yellow-orange spheres*) and Cd (*green*) atoms. Carbon atoms of PhS^- ligands are omitted for clarity [56]

2.4 Ligands on Tetrahedral Clusters

Some metal chalcogenide clusters, such as those with group 13 and 14 metals, may be prepared as purely inorganic (anionic) frameworks. This is in accordance with Pauling's electrostatic valence rule, as tetrahedrally coordinated M^{3+} or M^{4+} cations can balance edge or corner E^{2-} anions with low coordination numbers. For metal chalcogenide clusters with surface M^{2+} sites, the sum of the strengths of the electrostatic bonds to edge or vertex E^{2-} sites is too low to reach local electroneutrality. To overcome this, the coordination numbers of such E^{2-} sites are found to increase. In other words, clusters require the incorporation of an encapsulating and stabilizing shell of organic ligands. The ligands on a metal chalcogenide core also kinetically protect the cluster and prevent further condensation to the thermodynamically favoured infinite crystalline lattice of the related solid. Organic ligands serving in this capacity include various phosphines PR_3, amines (especially, N-containing aromatic heterocycles), halides (Hal) and organochalcogenolate anions RE^- [6, 9]. While the majority of these ligands replace surface E^{2-} sites, creating M−P, M−N and M−Hal coordination, chalcogenolates

at edges and vertexes do not alter the M_xE_y stoichiometry of the idealized cluster core. For chalcogenolate ligands the most common bonding mode is the doubly bridging μ; triply and higher bridging coordination modes are more often observed for selenolate and tellurolate ligands than for thiolates, reflecting their larger size. In discrete metal chalcogenide systems with mixed ligands, bridging chalcogenolate ligands preferentially occupy edge positions, while other ligands are bonded to metals at vertex positions.

In coordination chemistry approaches for cluster formation, the use of coordinating and chelating solvents to increase the solubility of reactants and/or products simultaneously can lead to the preparation of metal chalcogenide clusters containing solvent molecules as ligands (e.g. pyridine, dmf) [70, 71]. Higher reactivity under solvothermal or ionothermal conditions may also cause some side reactions to occur. Consequently, products of the decomposition/conversion of solvent (or additive) may serve as ligands. Examples include the coordination of dimethylamine from DMF, piperidine from dipiperidinomethane and 1-butyl-2-methyl-imidazole, Bim, from 1-butyl-2,3-dimethylimidazolium chloride, [Bmmim]Cl [44, 49, 72, 73]. An interesting case of ligand conversion during hydrothermal synthesis is the hydrolysis of the cyano group of 3-pyridinecarbonitrile, which resulted in the preparation of 1D covalently bonded clusters $[Zn_8S(SPh)_{13}L(H_2O)]$, with bidentate L = 3-carboxypyridyl bridging two adjacent clusters via M−N and M−O coordination (Fig. 8) [74]. Another possibility for "by-product" ligands to appear in the coordination sphere of metals is from the reaction of solvent with some precursor (e.g. $MeOCS_2^-$ ligand formed from reaction of MeOH and CS_2, used as sulfur source) [75]. The concept of intentional ligand modification during the assembly of metal chalcogenide clusters via solvothermal and ionothermal approaches has been developed recently, aiming at broadening the range of possible ligands and gaining access to new moieties that are unreachable under milder synthetic conditions. In this vein, a C−S cross-coupling reaction under hydrothermal conditions was systematically studied for in situ ligand reactions between mono-halide-substituted pyridines (L=Hal-C_5H_4N) and thiophenol during the preparation of $[Zn_8S(SPh)_{14}L_2]$ [76]. Varying the nature and position of the halide substituent allowed to observe that ligands containing iodine as a substituent were, unexpectedly, unreactive under the conditions explored, despite the fact that iodide is the best leaving group in comparison to F^-, Cl^- or Br^-. The lack of reactivity of iodide-substituted pyridines was attributed to the higher energy barrier for iodide elimination during the hydrothermal process in comparison to the other halide-substituted pyridines. It was also found that with a ligand containing the substituent in the ortho-position, no crystalline product was obtained, whereas the use of ligands with substituents in meta- and para-positions (e.g. 3-chloropyridine and 4-chloropyridine) led to the crystallization of clusters with in situ prepared ligands at the vertexes (L=*m*-$C_6H_5SC_5H_4N$ and *p*-$C_6H_5SC_5H_4N$, respectively). Such selectivity was attributed to the spatial hindrance induced by the cluster $[Zn_8S(SPh)_{14}L_2]$. Overall, the successful one-pot-synthesis of clusters with tailored ligands demonstrates the potential of in situ ligand-generating reactions under solvothermal and ionothermal conditions in constructing functional metal

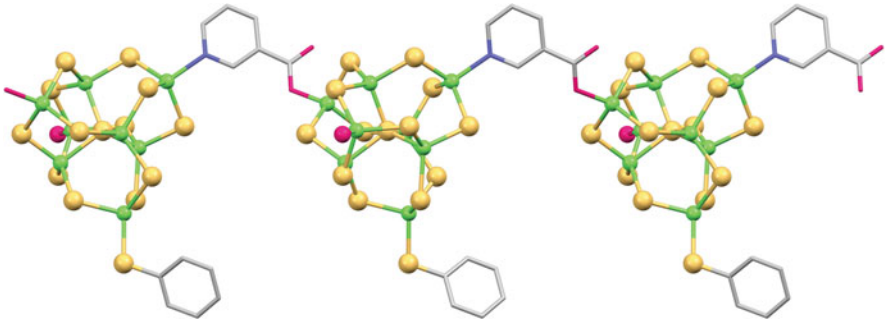

Fig. 8 A fragment of the 1D covalently bonded cluster chain of $[Zn_8S(SPh)_{13}L(H_2O)]$ with L = 3-carboxypyridyl, a bidentate ligand formed in situ by hydrolysis of the cyano group of 3-pyridinecarbonitrile. Carbon atoms of PhS^- ligands, except the one on the cluster vertex, are omitted for clarity [74]

chalcogenide clusters, simultaneously building a new bridge between coordination chemistry and synthetic organic chemistry.

The selection and in-situ design of ligands provide potential to modify metal chalcogenide clusters on several levels, tailoring cluster size and composition by adjusting the coordinating ability of the ligands and regulating superstructure topology by changing cluster–cluster interactions. The latter can be illustrated on the example of the neutral C_2 clusters $[Cd_{32}S_{14}(SR)_{36}L_4]$, where R is either the phenyl [70] or the 2-hydroxypropyl [77] group and L is dmf or water respectively. The strong influence of ligands on the superstructure packing is such that the thiophenolate-stabilized Cd32 clusters crystallize into cubic superstructure (space group *P32*) sustained by van der Waals ligand–ligand intercluster interactions, whereas the thiopropanol-stabilized Cd32 clusters crystallize into a double layer superstructure (space group $R\bar{3}$) with a continuous network of hydrogen bonding. As another important function, an increased solubility of clusters due to the presence of organic surface ligands (especially those with modified properties, such as fluorinated ligands [78–80]) can also enhance the crystallization of clusters into superlattices [81]. The recent preparation of various mononuclear metal complexes with the perfluorinated chalcogenolate ligands [82, 83] that potentially can be used as precursors for the large cluster synthesis lays the foundation for future progress in this field.

Ligands are also known to influence the photophysical properties of metal chalcogenide clusters. For instance, phenylchalcogenolate ligands were reported to quench CdE clusters emission at room temperature, which was attributed to the existence of non-radiative relaxation mechanism that involves vibrating modes of the bridging μ-PhE^- ligands [20]. In contrast to this, the replacement of PhE^- by Hal^- ligands results in red shifts and significant enhancements of the emission [84] and absorption [85] peaks. Moreover, optical properties of clusters can be affected by trapping of organic species in ligand shell via cation–π interactions [86], which may potentially be used in various sensing systems. Generally, the electronic and

photophysical properties of smaller clusters were found to be more sensitive to changes in the ligand shell. The influence of ligands becomes less pronounced with increasing cluster size; this was observed experimentally and confirmed by theoretical calculations at DFT and TDDFT levels for tetrahedral clusters belonging to different series (e.g. see [87]). The incorporation of ligands with special functionality (such as those containing ferrocene derivatives) can also introduce electrochemical functionality onto the clusters [88–90]. Ligand exchange reactions provide even more opportunities for tailoring metal chalcogenide clusters; the approach was proven to be efficient for the preparation of neutral $Cd_{10}E_x$ clusters with dendritic thiolate ligands [91] or with poly(ethylene glycol) units directly attached to the core [92], featuring high solubility in organic solvents and water, respectively, as well as modified photophysical properties.

2.5 Non-tetrahedral Clusters

Non-tetrahedral clusters possess diverse frameworks and have no obvious structural similarity with the corresponding bulk crystalline metal chalcogenides [6, 9]. In this review (see Sects. 5.5 and 5.6), the focus will be on the discrete assemblies where basic tetrahedral $\{ME_4\}$ units are joined together into polymeric fragments through sharing of vertexes and/or edges so as to form one or several rings. For instance, large, "double-decker" rings and complex cages have been prepared recently using solvothermal and ionothermal approaches. Metal cations here belong to groups 13 (In^{3+}) and 14 (Ge^{4+}, Sn^{4+}), or transition metals (Mn^{2+}), and E is a heavier (Se, Te) chalcogen. Such clusters can be viewed as molecular analogues of polymeric 1D chains [93, 94], typical for compounds of group 13 and 14 elements, and more unusual 1D ribbons [95], also prepared under solvothermal and ionothermal conditions. Complex vertex-linkage or the coexistence of vertex- and edge-linked basic tetrahedral $\{ME_4\}$ units was previously also found in some 3D metal chalcogenides [96, 97]. The tendency of the repeating fragments, composed of linked $\{MSe_4\}$ or $\{MTe_4\}$ units, to cyclize can be attributed to the larger atomic size and, as a consequence, the higher structural flexibility of Se^{2-} and Te^{2-} in comparison with S^{2-}. These clusters are typically charge-balanced, templated and stabilized by bulky imidazolium-based cations or other organic amines (see Sect. 5.6).

3 Bonding in Materials Containing Metal Chalcogenide Clusters

3.1 Bonding in Cluster Superstructures

Crystalline solids containing spatially organized metal chalcogenide clusters can be categorized into several classes depending on the nature of the bonding in the superstructure. Clusters may form covalently linked "continuous" frameworks of various types (i.e. 3D networks, 2D layers or 1D chains), or alternatively, with an absence of such interconnected species, metal chalcogenide clusters are "isolated" or "discrete" (0D) in their crystalline superstructures.

The covalent linkage of clusters can be realized through inorganic bridges (most often, corner-sharing clusters connected at vertexes with a single E^{2-} or RE^{-} bridge) [98, 99] or through the use of organic multidentate ligands (e.g. bi- or even tetradentate tetrahedral linkers) [100–102]. In some superstructures, both inorganic and organic connectivities can coexist [103], and such covalent linkages can also be realized via more unusual species, e.g. metal complexes [104, 105]. Superstructures with covalent linkages between tetrahedral clusters have been extensively studied and several reviews were published [47, 48]. They are not the main subject of this review and only selected cases (featuring exceptional clusters, prepared under solvothermal or ionothermal conditions) are discussed in the following sections. Large tetrahedral metal chalcogenide clusters (e.g. T_4 and T_5), covalently linked into superstructures, are well established, while the preparation of the corresponding discrete analogues remained a formidable challenge until recently.

An interesting type of bonding in such superstructures is realized when metal chalcogenide clusters form dimers, i.e. two clusters are linked via covalent bonds, and then such dimers are self-assembled into a non-covalent superstructure. This type of bonding of two clusters was achieved, for example, under solvothermal conditions using 1,2-di(4-pyridyl)ethylene (*dpe*) ligands as the organic linker, covalently bonding two vertices of two T_3 clusters (Fig. 9) [106]. In each "half" of such T_3-T_3 two-cluster anion $[Ga_{10}S_{17}HL_2\text{-}dpe\text{-}Ga_{10}S_{17}HL_2]^{6-}$, the remaining two vertexes are terminated by L=3,5-dimethylpyridine, while the fourth vertex contains a SH^{-} anion. Total electroneutrality is achieved via 3,5-dimethylpyridinium cations. The self-assembly into a non-covalent superstructure (space group $P\bar{1}$) is realized though π–π interactions between aromatic rings and N−H···S hydrogen bonding between protonated organic cations and surface S atoms in clusters. Even more sophisticated coupling is realized in solvothermally prepared crystalline solids containing a C_1–C_1 two-cluster neutral component, double bridged by the more flexible bifunctional organic ligand 1,3-di(4-pyridyl) propane (*dpp*) $[Cd_{17}Se_4(SPh)_{26}\text{-}(dpp)_2\text{-}Cd_{17}Se_4(SPh)_{26}]$ (Fig. 10) [107]. Such dimers are subsequently assembled into a non-covalent superstructure (space group $P2_1/c$). Non-covalent superstructures, containing cluster dimers, allow the intercluster connectivity with organic linkers to adjust system performance

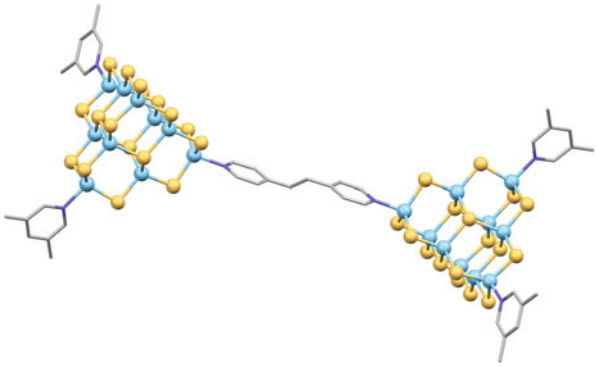

Fig. 9 Two-cluster anion $[Ga_{10}S_{17}HL_2$-*dpe*-$Ga_{10}S_{17}HL_2]^{6-}$, where L = 3,5-dimethylpyridine [106]

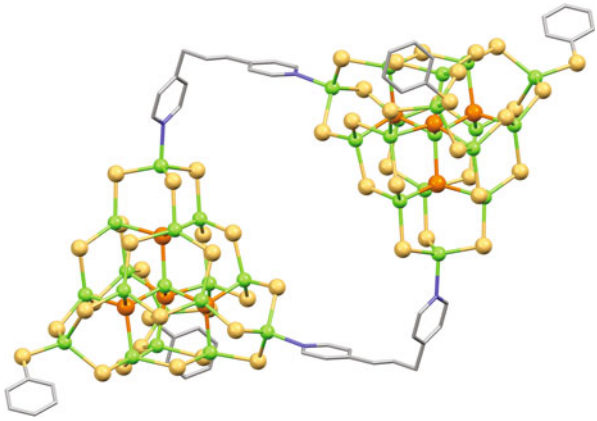

Fig. 10 Two-cluster doubly bridged neutral aggregate $[Cd_{17}Se_4(SPh)_{26}$-$(dpp)_2$-$Cd_{17}Se_4(SPh)_{26}]$. Carbon atoms of PhS^- ligands, except those on vertexes, are omitted for clarity [107]

(through the combination of the size-related properties of nanodimensional clusters with functionality of bifunctional ligands), at the same time preserving the solubility of individual components.

As opposed to covalent intercluster bonding, metal chalcogenide clusters can be considered as being discrete molecular entities when the superstructure is formed only via electrostatic bonding and/or other cluster–cluster interactions, e.g. hydrogen bonding and dispersion (van der Waals) forces. In such cases, the superstructures of metal chalcogenide clusters can be referred to as molecular crystals [21]. Such superstructures of smaller clusters prepared by a coordination chemistry approach are especially well documented [70, 77, 108–117]. In contrast, the preparation of progressively larger, discrete metal chalcogenide clusters (with several composition restrictions related with maintaining both local and total electroneutrality, in addition to low solubility of formed clusters) requires special conditions for superlattice formation. Recent successes (e.g. a superlattice of discrete "full-core" T_5 clusters) [43, 44] are closely connected with developing solvothermal and ionothermal approaches together with a better understanding of the role of various factors associated with these synthetic routes.

Since anionic clusters dominate this area, discrete ionic superstructures are most likely to form. Less common, neutral metal chalcogenide clusters, typically with phenylchalcogenolate ligands and/or aromatic ring-containing structure-directing and stabilizing species, can form discrete superstructures through relatively weak ligand–ligand and ligand–template–ligand interactions. The intercluster bonding (for instance, hydrogen or π–π interactions) is such that connection between the building blocks into a superstructure is reversible [118–121]. The key factor is whether superstructure disassembly (e.g. via dissolving in a suitable solvent) would be possible in such a way that the core and ligand shell of individual clusters does not change. Several cases of complete recrystallization of superstructures consisting of large discrete clusters were reported under relatively mild solvothermal conditions. Disassembly of the crystalline solid, while clusters went into solution at elevated temperature and pressure, was followed by recurring superstructure formation upon cooling [41, 122].

The solubility of the discrete large tetrahedral clusters broadens their potential for application, making possible, for instance, solution processing to achieve new advanced materials. Thus, mesostructured materials and even porous gels and aerogels were prepared using small metal chalcogenide clusters (e.g. $[Ge_4S_{10}]^{4-}$) as building blocks; such materials may be useful in photocatalysis or in the removal of heavy metals from water [123]. The production of semiconductor-doped thin-film materials for optics and electronics has also been proposed [70]. Thus, polyvinylcarbazole films, functionalized by $[Cd_{32}S_{14}(SPh)_{36}(dmf)_4]$, can be spin-coated from a pyridine solution.

The nature of the bonding in superstructures is known to influence the physical properties of cluster assembly. In some cases, the effect of connectivity of the clusters is less pronounced in comparison with the effect of cluster size and composition, as it can be followed, for example, for the optical properties of the systems [41, 49]. In other cases, these (inter)cluster features are found to be of comparable importance: it was shown that the photocurrent response of solvothermally prepared material containing a 3D covalent framework of $[Cd_{32}S_{14}(SPh)_{40}]^{4-}$ clusters (corner sharing through PhS^- ligands) synthetically integrated with a metal-complex dye is seven times larger than that of the material where the identical clusters are discrete. This was attributed to the facilitated transfer of photo-induced electrons in the 3D framework [75].

3.2 Topology of Superstructures

For topological consideration on the level of superstructure, it is convenient to view each tetrahedral cluster as a tetrahedral pseudo-atom (T) or, alternatively, to consider only the positions of the barycentres of the clusters. The covalent linkage of four-vertex-connected tetrahedral clusters (often realized by a single E^{2-} bridge) is known to give a limited number of topologies for 3D superstructures [47], which is related to the limited flexibility of the T−E−T angles [46, 124]. The common

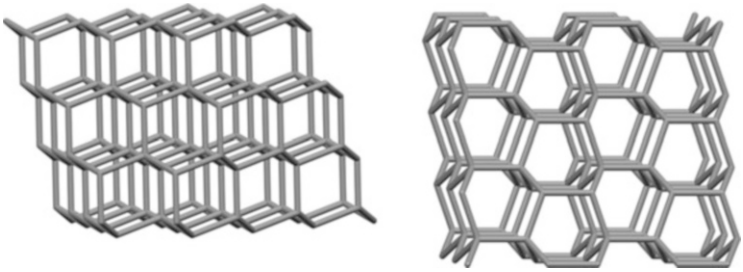

Fig. 11 Examples of 3D superstructure topologies formed from discrete tetrahedral clusters: idealized cubic diamond (*left*) and hexagonal diamond (*right*) superstructures. Clusters are not shown; lines are connecting the barycentres of the clusters

topological types for covalently linked large tetrahedral clusters are (cubic) single and double diamond, as well as cubic carbon nitride. In the latter, four connected clusters are combined with tri-connected S^{2-} sites that bridge the corners of three adjacent clusters [125]. The covalent linkage of tetrahedral clusters with auxiliary organic ligands L, most often pyridyl-based ones, helps to increase the flexibility of the T−L−T connection, which potentially broadens the range of the possible topologies. The cluster connectivity in such cases rarely reaches four and the coordination polymers are most often prepared as 1D and 2D superstructures. An exception is a series of 3D four connected covalent superlattices where T_3 or T_4 units are linked by imidazolate ligands [126].

The wide variety of the nature and relative weakness of interactions leading to the formation of superstructures from discrete clusters leads to the remarkable diversity in connectivities and makes it more difficult to generalize corresponding topological types. Various distortions also complicate this assignment. For instance, considering the barycentre positions, superlattices with distorted cubic diamond and hexagonal diamond topologies have been often reported for large anionic tetrahedral clusters (Fig. 11) (e.g. see [44]). This means that intra- and inter-cluster connectivities are the same, and the clusters behave like artificial atoms in zinc blende- and wurtzite-like crystal structures.

Unlike 2D and 3D covalent superstructures formed via corner sharing through inorganic linker, where topologies combining two tetrahedral clusters of different size, structure or composition are not that rare (e.g. P_1-T_2, T_2-T_5, or $T_{2,2}$-T_3 hybrid covalent superstructures) [58, 62, 65, 127–129], there are a limited number of examples of superstructures combining two different discrete clusters. Thus, ionic superstructure with a cubic $[Cd_8L_{12}(NO_3)(dmf)_8]^{3+}$ cluster as a cation and a dumbbell-shaped $[Cd_6L_{14}]^{2-}$ cluster as an anion (L = 2,5-dimethylphenylthiolate) was prepared under ambient conditions [130]. Even more unusual cases of two-cluster-anion superstructures via solvothermal preparation (e.g. co-crystallization of tetrahedral T_4 $[Cu_4In_{16}S_{35}H_4]^{14-}$ and cubic $[Cu_{12}S_8]^{4-}$ discrete anionic clusters) [122] are considered below.

In the superstructures of neutral discrete clusters, multilevel organization often takes place with the participation of several different interactions. Thus

neighbouring clusters may be arranged into layer-like formation via intercluster N−H···E or C−H···E hydrogen bonding, with such layers further combined into superstructure through van der Waals forces [131].

3.3 Total Electroneutrality in Superstructures

As opposed to the local electroneutrality, *total electroneutrality* (global charge balance) refers to the overall charge density match between clusters and charge-balancing species. As was discussed above, local electroneutrality generally follows Pauling's electrostatic valence rule, making relatively straightforward calculations possible (e.g. using Brown's bond valence model) [132, 133] to explain/predict the arrangement of metal cations of different valence in particular cluster. In contrast, with total electroneutrality there are many different factors (among them, partial atomic charges on cluster core atoms and protonation ability of charge-balancing species) to be taken into account simultaneously, making any attempt of its quantitative representation more difficult. Thus, an additional stabilization of superstructures assembled via electrostatic (Coulomb) forces can be achieved while charge-balancing species are also capable of other interactions with clusters, e.g. N−H···E and C−H···E hydrogen bonding, π–π, anion-π and hydrophobic interactions. Aromatic quaternary ammonium cations and protonated organic amines are most important in this capacity. Some effects related with maintaining total electroneutrality are discussed below.

Even in solvothermally prepared covalently bonded 3D and 2D superstructures of clusters, where charge-balancing species are most often highly disordered, alternating the charge-balancing cations was reported to cause changes in cluster arrangement, varying from different unit cell parameters to the different packing of clusters in a superstructure. For instance, the use of the larger Et_4N^+ cation instead of Me_4N^+ results in a change of stacking pattern for the 2D covalently bonded superstructure of T_5 clusters $[Cu_5In_{30}S_{54}]^{13-}$ (space groups *Pm* and *C2/c*, respectively) [134]. It was proposed that even small quaternary alkyl ammonium cations may show structure-directing effect in addition to charge compensation. Different protonated organic amines with well-known structure-directing ability may display even more remarkable effects: thus, under the same synthetic conditions, the addition of dipiperidinomethane instead of 1,4-bis(3-aminopropyl)piperazine leads to the solvothermal preparation of a 3D covalent superstructure of two clusters, T_3 and coreless T_5 as $[In_{10}S_{20}]^{10-}$ and $[In_{34}S_{56}]^{10-}$, respectively, versus that of the single T_4 cluster as $[Zn_4In_{16}S_{35}]^{14-}$ (space groups $I4_1/a$ and $I4_1/acd$) [65, 135]. It is interesting that a source of a M^{2+} *d*-block metal is present in the reaction mixtures probed with all amines, but M^{2+} only becomes incorporated into T_4 clusters. The formation of superstructures with substantially different charge densities (the overall framework negative charge per metal site is −0.273 vs. −0.5 for T_3–coreless T_5 and T_4, respectively) was discussed in terms of the charge densities of the incorporated protonated amine molecules, approximated by their

C/N ratio (5.5 vs. 2.5 for dipiperidinomethane and 1,4-bis(3-aminopropyl)piperazine, respectively). Such an approximation is rough and cannot be generalized; for instance, the same 3D covalent superstructure of T_4 clusters $[Zn_4In_{16}S_{35}]^{14-}$ (space group $I\overline{4}2d$) was also reported with other protonated amine species, including 4,4′-trimethylenedipiperidine which has a C/N ratio of 6.5 [135].

In superstructures containing discrete clusters, additional interactions helping in stabilizing negative charges are of even greater significance. Their assembly may depend to a large extent not only on the electrostatic interactions but on hydrogen bonding as well. Though N−H···S or N−H···Se hydrogen bonding is weaker in comparison with N−H···O that is known to direct the assembly of oxide frameworks (e.g. zeolites), charge-balancing protonated organic amines in 0D superstructures of metal chalcogenide clusters are often found to be ordered and shown to play an important role in cluster formation and crystallization. A close match of charge density, geometry and additional interactions should exist between anionic clusters and cationic species in superstructures to make the formation of particular discrete clusters more favourable. The preparation of covalently bonded 3D frameworks is typically more tolerant of small variations in the size and shape of amines. For example, varying the protonation ability or steric hindrance by using similar amines (piperidine derivatives and related compounds) under the same solvothermal conditions was shown to result in the formation of different superstructures [49]. Thus, comparing *o*-, *m*- and *p*-methyl piperidines with the unsubstituted one indicates that the substituent in the *p*-position gives a superstructure of discrete T_4 clusters $[Zn_4Ga_{14}Sn_2Se_{35}]^{12-}$ with a significantly larger unit cell parameter (19.2020(3) Å vs. 18.8951(1) Å for substituted and unsubstituted piperidine, respectively, space group $I\overline{4}3m$). The weaker bonding in the superstructure containing protonated *p*-methyl piperidine is reflected, for instance, in the faster dissolution rate and increased solubility of the product, as well as in its band gap change. Both *o*- and *m*-methyl piperidines lead to the formation of related 3D covalently bonded T_4 clusters (space group $I4_1/acd$) as minor and exclusive products, respectively. It was concluded that *m*-position substitution creates the highest steric hindrance in comparison with *o*- or *p*-positions, not allowing such an arrangement of protonated amines around the discrete cluster, while hydrogen bonding allows for additional stabilization [49].

4 Synthetic Approaches: Solvothermal and Ionothermal Routes

Generally, a solvothermal approach refers to conducting reactions in an appropriate solvent with the aid of suitable additives in a sealed vessel at elevated temperature and autogenous pressure. If the process is done in water, the process is differentiated as hydrothermal, and in the case of other (organic) solvents, it is referred to as solvothermal. Some organic solvents widely used for the preparation of metal

chalcogenide clusters are methanol, acetonitrile, DMF and organic amines. The importance of the latter (e.g. N-containing aromatic heterocycles) as solvents and additives is related to the fact that organic amines can act as ligands, stabilizers and (in a protonated form) charge-balancing species for large anionic metal chalcogenide clusters. The most recently explored variation, ionothermal process, utilizes more thermally and chemically stable ionic liquids as a reaction medium. Reaction vessels may vary from sealed thick-walled glass tubes to stainless steal autoclaves with an inert lining or inner container; a combination of the sealed in glass tube with an autoclave with some liquid for counter pressure is also possible. Under solvothermal conditions a supercritical state can be achieved, when the liquid–vapour boundary disappears and the fluid achieves properties of both the liquid and the gas though for many reactions it is not necessary and rarely applied.

In a typical solvothermal or ionothermal process, the reagents are mixed with suitable additives in a chosen reaction medium and heated to moderately high temperature for a period of time from several hours to several days, cooled to room temperature with a desired rate, and products are isolated. Syntheses of metal chalcogenide clusters by these approaches are typically performed with small-scale reactions (product weight from tens to hundreds of mg). Reported yields (% based on a metal source used) vary, although they are generally higher for smaller clusters (e.g. ~65% for P_1 [74, 136] or even ~90% for T_3 [106]) but decreasing for larger systems. Optimization of reaction conditions (such as alternating metal or chalcogen source, addition of auxiliary solvents, changing reaction time or temperature [44, 59]) can help to enhance product purity and yield.

Although smaller metal chalcogenide clusters may be used as precursors for solvothermal or ionothermal conversion into larger ones [137, 138], the synthesis often starts with simple elementary forms and inorganic salts and involves redox chemistry for cluster formation. Various clusters with different sizes and compositions can be present in solution simultaneously, while upon cooling and crystallization, equilibrium shifts in favour of one (or more) product(s). In comparison with a solid state chemistry approach, where performing the reactions in molten media (e.g. polychalcogenide flux) requires high temperatures ($>300^{\circ}C$, often 500–650°C), the solvothermal approach offers a significant reduction in the reaction temperatures (typically $\leq 200^{\circ}C$). The flexibility of the solvothermal approach also allows an adaption to large-scale synthesis or a combination with other techniques, e.g. microwave-assisted synthesis. The combination of elevated temperature and pressure during solvothermal synthesis often allows increased solubility of precursors, promoting diffusion in reaction mixtures, improving selectivity of conversion, speeding up reactions and facilitating crystallization of the product. Performing such synthesis in ionic liquids shares some advantages with those done in traditional organic solvents (solvothermal approach), where reaction media may simultaneously act as a structure-directing agent and as a template. In this vein, ionic liquids with voluminous quaternary ammonium and imidazolium-based cations are of particular interest [37, 139]. At the same time, the negligible vapour pressure of ionic liquids makes the use of autoclaves (and associated equipment cost and safety measures) unnecessary. Generally, reaction pathway and outcome

may be quite different under solvothermal and ionothermal conditions, and selection of the particular synthetic approach for each system depends on multiple factors.

5 Structures of Materials Containing Metal Chalcogenide Clusters

5.1 General Comments

As was described above, there are certain limitations and conditions for metal chalcogenide cluster formation related to maintaining local and total electroneutrality. Since the preparation of discrete tetrahedral metal chalcogenide clusters meets particular (different) restrictions depending on cluster composition, i.e. the type of metal cations present, it is reasonable to consider solvothermal and ionothermal routes to (1) clusters with M^{2+} cations exclusively and (2) clusters with M^{3+} cations, both exclusively or doped with M^{4+}, M^{2+} or M^{+} cations, separately. Reactions where tetrahedral clusters are taken as starting reagents resulting in the preparation of new clusters are also discussed separately. As the distinct group, discrete non-tetrahedral metal chalcogenide clusters with M^{2+}, M^{3+} and M^{4+} cations (and mixes) are described as well.

5.2 Tetrahedral Clusters with M^{2+} Cations

M^{2+} cations of later d-block metals have been widely used for preparing metal chalcogenide clusters. Large, discrete tetrahedral clusters made of entirely group 12 metals are known for all tetrahedral cluster series. Moreover, only M^{2+} cations have been reported to yield any C_n clusters, and the largest known solvothermally prepared cluster is C_3, containing 54 metal sites.

The adjacent tetrahedral M^{2+} sites are ideal to charge-balance the inner (tetrahedral) E^{2-}, which is essential for the formation of the core of large clusters. At the same time M^{2+} cations are not adequate for low-coordinated edge and vertex E^{2-} sites. Such sites tend to be occupied by chalcogenolate RE^{-} groups (most often, PhE^{-}). Even with this substitution, maintaining the total electroneutrality of the clusters becomes problematic when cluster size gets larger, as the negative charge of the clusters increases considerably. This can be illustrated on C_n cluster series with M^{2+} cations [107], from C_2 to (theoretical) C_5 showing the negative charge increase of idealized clusters from 4 to 22:

C_2 $[M_{32}E_{14}(EPh)_{40}]^{4-}$
C_3 $[M_{54}E_{32}(EPh)_{52}]^{8-}$
C_4 $[M_{84}E_{59}(EPh)_{64}]^{14-}$
C_5 $[M_{123}E_{96}(EPh)_{76}]^{22-}$

Note that M^{2+} cations in combination with a specific cluster geometry in the C_n series (i.e. higher ratio between low-coordinated edge and vertex and high-coordinated inner E sites) are much more favourable for preparing large tetrahedral clusters in comparison with other cluster series, where the negative charge would increase even more dramatically. This can be seen by comparing clusters with approximately the same number of metal and chalcogenide sites in the different series, e.g. C_2 [$M_{32}E_{54}$] and T_5 [$M_{35}E_{56}$]. With M^{2+} cations and all edge and vertex chalcogenide sites occupied by PhE^-, the stoichiometry of these clusters is $[M_{32}E_{14}(EPh)_{40}]^{4-}$ and $[M_{35}E_{28}(EPh)_{28}]^{14-}$, respectively. The difference in negative charge (4 vs. 14) explains why there are multiple examples of C_2 clusters with exclusively M^{2+} cations, while the corresponding T_5 clusters are not yet known.

Thus, key synthetic strategies for large clusters with M^{2+} cations are (1) decreasing and/or (2) stabilizing the large negative charge. The first strategy can be realized by replacing four vertex negatively charged RE^- ligands with neutral ones (e.g. P-, N- or O-containing). The second requires using adequate charge-balancing species with charge density and geometry match, as well as complementary interactions (e.g. hydrogen, π–π and anion-π bonding) allowing them to perform roles of structure-directing and template agents for superlattice crystallization.

A number of M^{2+}-containing tetrahedral clusters have been originally prepared by coordination chemistry approach and then were reproduced under solvothermal conditions. An example is the discrete neutral P_1 cluster $[Cd_8Se(SePh)_{12}Cl_2L_2]$, where two vertexes are occupied with neutral ligands L=PCy_3, tricyclohexylphosphine, and the other two with Cl^- [140]. In this way, such a P_1 cluster consists of a tetrahedral anti-T_1 {$SeCd_4$} central unit capped by two tetrahedral {$CdSe_3L$} and two tetrahedral {$CdSe_3Cl$} units, with alkylphosphine or halogenide ligands replacing Se in regular T_1 {$CdSe_4$} unit. Using $[Cd_4(SePh)_8]_\infty$ and $CdCl_2$ precursors with methanol as a solvent allowed rather unusual short reaction times and low temperatures (1 h at 130°C, respectively) in this case; very slow cooling to room temperature (0.3°C/min) helped product crystallization. A similar approach, based on "corner capping" with neutral ligands, was reported for the preparation of neutral discrete P_1 clusters $[Zn_8S(SPh)_{14}L_2]$ using a series of substituted pyridine ligands, e.g. L=3-aminopyridine [136], or fused-ring heterocyclic N-containing aromatic ligands, e.g. L=4,7-phenanthroline, 5-aminoquinoline or 3-(2-thienyl)-pyridine (Fig. 12) [74]. Varying the capping ligands was shown to influence cluster–cluster interactions (leading to crystallization in different space groups belonging to triclinic or monoclinic crystal systems) and modification of the optical properties of the clusters. For instance, in room temperature PL spectra obtained in DMSO solutions, an emission band for $[Zn_8S(SPh)_{14}L_2]$ with L=3-(2-thienyl)-pyridine is substantially narrower and blue shifted in comparison with the corresponding band for the clusters with L=5-aminoquinoline (~350 and 476 nm, respectively). In contrast, no emission was observed at room temperature for the clusters with L=4,7-phenanthroline [74], which demonstrates that photophysical properties of such clusters can be strongly influenced by ligands.

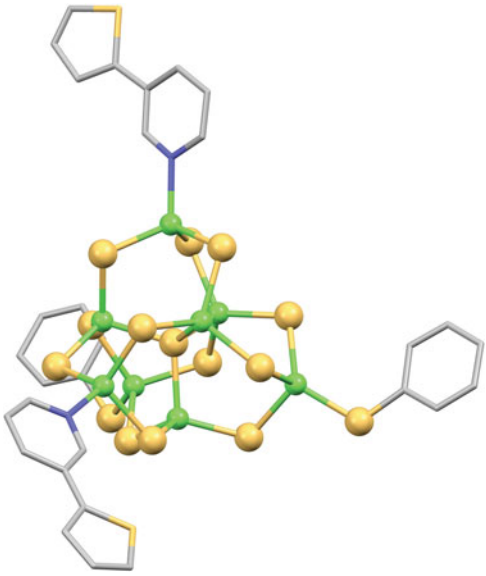

Fig. 12 Neutral P_1 cluster $[Zn_8S(SPh)_{14}L_2]$, where L = 3-(2-thienyl)pyridine. Carbon atoms of PhS^- ligands, except those on vertexes, are omitted for clarity [74]

The "corner capping" with neutral ligands, occurring through the formation of M−O bonds at all four vertexes of a tetrahedral cluster, was also used to decrease the charge of even larger frameworks, resulting in the crystallization of discrete tetra-anionic C_3 clusters $[Cd_{54}S_{32}(SPh)_{48}(H_2O)_4]^{4-}$ and $[Cd_{54}Se_{32}(SPh)_{48}(H_2O)_4]^{4-}$ [56]. Water ligands (replacing PhS^- sites at each vertex) arise from the use of the mixed solvent system (acetonitrile–water) for solvothermal synthesis with $[Cd_4(SePh)_8]_\infty$ and thiourea/selenourea precursors. These large tetrahedral clusters (edge length 1.97 nm as measured between vertex metal sites) crystallize into noncentrosymmetric superlattices, either primitive or face-centred (space groups *P23* or $F\,\overline{43}c$, respectively) (Fig. 13). $[Cd_{54}Se_{32}(SPh)_{48}(H_2O)_4]^{4-}$ has μ_3- and μ_4-Se^{2-} sites that were formed by replacing thiourea with selenourea, while all edge ligands are μ-PhS^-. Anionic clusters were prepared with a variety of charge-balancing alkylammonium cations, i.e. tetramethylammonium, Me_4N^+; tetraphenylphosphonium, Ph_4P^+; and *n*-octyltrimethylammonium, $C_{11}H_{26}N^+$. These disordered species, along with disordered solvent molecules, occupy the large voids between Cd54 units.

The solvothermal preparation of various clusters belonging to the C_n series made it convenient to follow the influence of size and composition of clusters on their optical properties. Thus, a systematic blue shift of the low-energy absorption peak (from 353 through 327 to 291 nm) was observed with cluster size decrease from $[Cd_{54}S_{32}(SPh)_{48}(H_2O)_4]^{4-}$ through $[Cd_{32}S_{14}(SPh)_{40}]^{4-}$ to $[Cd_{17}S_4(SPh)_{26}\ (H_2NCSNH_2)_2]$. The effect of cluster composition (for a given $[Cd_{54}E_{32}(SPh)_{48}\ (H_2O)_4]^{4-}$ cluster size) was demonstrated by a red shift (from 353 to 393 nm) upon changing from sulfur to the heavier selenium in the cluster core [56].

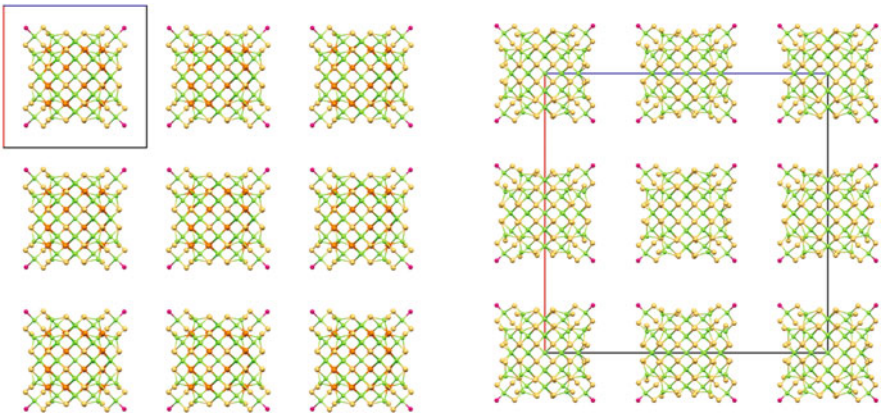

Fig. 13 Fragments of cubic superlattices of C_3 clusters: primitive for $[Cd_{54}Se_{32}(SPh)_{48}(H_2O)_4]^{4-}$ with space group *P23* (*left*) and face-centred for $[Cd_{54}S_{32}(SPh)_{48}(H_2O)_4]^{4-}$ with space group $F\,\overline{43}c$ (*right*). Carbon atoms of PhS^- ligands, as well as disordered charge-balancing species and crystallized solvent molecules, are omitted for clarity. Viewed along the *b* direction; cell axis *a* shown *red* and axis *c* *blue* [56]

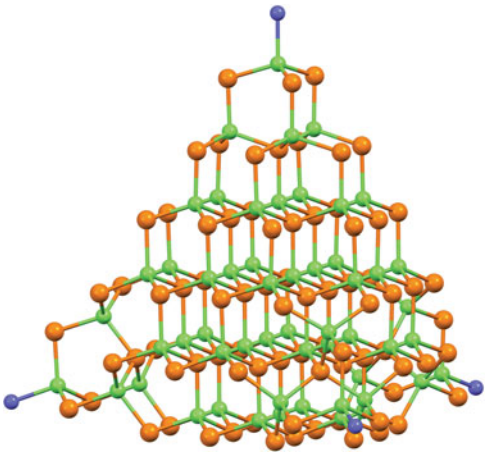

Fig. 14 $Cd_{54}Se_{80}$ structure of the anionic C_3 cluster $[Cd_{54}Se_{32}(SePh)_{48}(dmf)_4]^{4-}$ (Levchenko TI, Huang Y, Corrigan JF, unpublished results)

The use of $(Me_4N)_2[Cd(EPh)_4]$ as a single source precursor in DMF solvent allowed for the solvothermal preparation of the all-selenium analogue $[Cd_{54}Se_{32}(SePh)_{48}(dmf)_4]^{4-}$ (Fig. 14) (Levchenko TI, Huang Y, Corrigan JF, unpublished results) and even larger CdS clusters (with the size as large as C_4 and C_5 mentioned above) [141], although orientation flexibility of the latter within the superlattice hampers single-crystal characterization. Based on series of analyses, including TEM and electron tomography, these clusters break the trend in the capped tetrahedral series and have a truncated tetrahedral shape [141, 142].

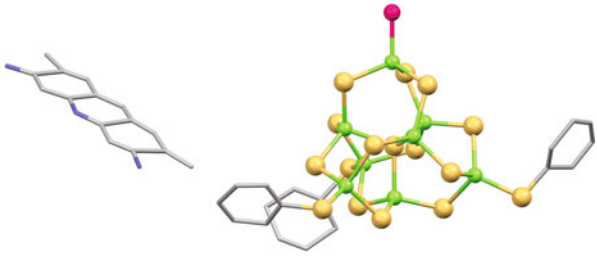

Fig. 15 Ion-pair charge transfer salt $[C_{15}H_{16}N_3]^+[Zn_8S(SPh)_{15}H_2O]^-$. Carbon atoms of PhS^- ligands, except those on vertexes, are omitted for clarity [23]

The co-crystallization of anionic metal chalcogenide clusters with counterions having special functions (e.g. organic chromophores) enables uniform molecular-level integration of inorganic and organic components to obtain new functional materials with synergistic properties. For example, the solvothermally prepared combination of the discrete P_1 anionic cluster $[Zn_8S(SPh)_{15}H_2O]^-$ with the fluorescent dye acridine yellow G through the formation of ion-pair charge transfer salt $[C_{15}H_{16}N_3][Zn_8S(SPh)_{15}H_2O]$ gives rise to the new crystalline material (space group *C2/c*) (Fig. 15), in which the metal chalcogenide framework serves as the electron donor and augments the colour of the fluorescent dye [23]. Experiments on labelling bacteria (e.g. *E. coli*) using a suspension of this material show that a combination of fluorescent dye and metal chalcogenide cluster was efficient for staining under confocal microscopy conditions with minimal photobleaching over time, while fluorescent imaging of bacteria with acridine yellow G on its own was much less stable.

Although the co-crystallization of metal chalcogenide clusters and optically active species can also be achieved using conventional synthesis [143–145], such integration was shown to be enhanced even under mild-temperature solvothermal conditions. Moreover, an additional feature in the latter case is the possibility to realize a "one-pot synthesis", when the assembly of large anionic clusters is combined with their co-crystallization with functional cations. When such cations represent fused-ring aromatic compounds, they can play an even more complex role, combining additional functionality, charge balancing and superlattice stabilization (e.g. through π–π interactions with PhE^- ligands of clusters). This was realized, for instance, with the solvothermal preparation of the discrete T_3 cluster $[Zn_{10}S_4(SPh)_{15}Cl]^{4-}$, co-crystallized with methylviologen cation dye ($[C_{12}H_{14}N_2]^{2+}$ or MV^{2+}) to give ion-pair charge transfer salt $(MV)_2[Zn_{10}S_4(SPh)_{15}Cl]$ [24]. The resulting crystalline material shows a remarkable red shift (>200 nm) of a broad absorption band in solid-state spectra in comparison with that of the individual components; such a shift was assigned to a charge transfer from the electron-rich metal chalcogenide cluster anions to MV^{2+} cations. Similar integration with the MV^{2+} cation was achieved for discrete C_1 clusters $[Cd_{17}Se_4(SPh)_{24}Br_4]^{2-}$ [146]; cyclic voltammetry showed a low-potential shift of the MV^{2+} cations in this ion-pair charge transfer salt in comparison with $MVBr_2$, which indicates that strong cation–anion interaction was preserved even upon dissolving in DMF. Examination of photocurrent responses of $(MV)[Cd_{17}S_4(SPh)_{24}Br_4]$ and $(MV)[Cd_{17}Se_4(SPh)_{24}Br_4]$

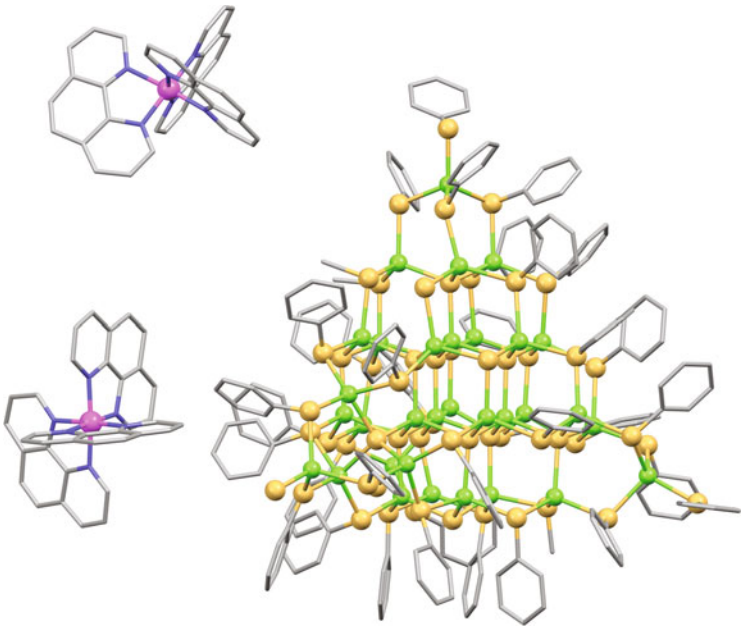

Fig. 16 Ion-pair charge transfer salt $[Fe(phen)_3]_2[Cd_{32}S_{14}(SPh)_{40}]$ [147]

showed that the current intensities of the ion-pair charge transfer salts are significantly larger than those of the similar clusters $[Cd_{17}E_4(SPh)_{28}]^{2-}$ with $(Me_4N)^+$ cations; the MV^{2+} cation was found to play different roles in electron transfer under visible light or UV irradiation [146].

Optically active metal-chelate dyes (e.g. complexes of M^{2+} with 1,10-phenanthroline, *phen*, or 2,2′-bipyridine, *bpy*, ligands) further extend the approach for the assembly of integrated materials through cation–anion interactions involving tetrahedral metal chalcogenide clusters. Bulky cations $[M(phen)_3]^{2+}$ and $[M(bpy)_3]^{2+}$, formed in situ during the solvothermal process, are comparable in size with large tetrahedral clusters and can additionally play the role of space-filling (template) species. Geometry match in this case is accompanied by charge density match: compared to widely used quaternary ammonium cations and protonated organic amines, the metal-chelate dyes possess both a large size and relatively low charge density, which fits the low charge density of large anionic tetrahedral clusters belonging to the C_n series. Hydrophobic and π–π interactions between fused-ring N-containing aromatic ligands of such cationic species and surface PhE^- ligands of anionic clusters also contribute to superlattice stabilization. Thus, the discrete C_2 anionic clusters $[Cd_{32}S_{14}(SPh)_{40}]^{4-}$ were solvothermally prepared and integrated with the metal-chelate dye cations $[Fe(phen)_3]^{2+}$ (Fig. 16) [147]. The use of a bulkier ligand (namely, 3,4,7,8-tetramethyl-1,10-phenanthroline, *tmphen*) instead of *phen* as in $[Fe(phen)_3]_2[Cd_{32}S_{14}(SPh)_{40}]$ leads to crystallization of $[Fe(tmphen)_3]_2[Cd_{32}S_{14}(SPh)_{40}]$, having different packing of the same tetrahedral clusters (space groups $P2_1/c$ and $P\overline{1}$, respectively). The optical properties and

photoelectrochemical performance of the composite material can be tuned by varying the cluster size, changing the type of metal centres or organic chelating ligands; for instance, the advantage of Ru^{2+} over Fe^{2+} in metal-complex dyes was demonstrated [75].

5.3 Tetrahedral Clusters with M^{3+} and Mixed Cations

In contrast to M^{2+} cations, the formation of discrete tetrahedral clusters composed entirely of trivalent metal ions is limited to relatively small species. The observation that clusters having interstitial chalcogenide atoms (e.g. larger than T_3) are unlikely to form is in accordance with Pauling's electrostatic valence rule, as the adjacent tetrahedrally coordinated M^{3+} sites would overburden the total bond valence of tetrahedrally coordinated E^{2-} sites. Therefore, access to large tetrahedral clusters with M^{3+} cations requires the presence of lower valence metals (M^{2+} or M^{+}) in the inner sites to maintain the local electroneutrality. A classical example is the T_4 cluster $[Cd_4In_{16}S_{35}]^{14-}$ present in 3D covalent superstructures [148]. At the same time, M^{3+} cations usually provide enough bond valence to balance low-coordinated surface E^{2-} sites, which eliminates (or decreases) the need for surface ligands. That is why tetrahedral clusters with M^{3+} surface sites can exist as "naked" species, although ligands at vertexes are still useful to prevent covalent linkage into 3D and 2D condensed frameworks. The common challenge for the preparation of large tetrahedral clusters, already addressed while discussing systems with M^{2+} cations, is related with maintaining the total electroneutrality, as the negative charge of the clusters increases with their size increase. The incorporation of lower valence metals into a M^{3+} system, unavoidable to keep the local electroneutrality in large tetrahedral clusters, simultaneously complicates maintaining the total electroneutrality by contributing to an increase in negative charge. This can be illustrated by comparison of the (hypothetical) binary and (isolated) ternary cluster compositions, e.g. T_4 $[In_{20}E_{35}]^{10-}$ vs. T_4 $[Cd_4In_{16}E_{35}]^{14-}$ and T_5 $[In_{35}E_{56}]^{7-}$ vs. T_5 $[Cd_{13}In_{22}E_{56}]^{20-}$.

The synthetic strategies used with mixed-metal systems based on M^{3+} cations are also related to (1) decreasing and/or (2) stabilizing the large negative charge, as was discussed above for M^{2+} systems, while the arsenal of solutions is more diverse and includes both similar routes (as "corner capping" the cluster with neutral ligands) and those specific to mixed systems. Thus, introducing M^{4+} cations onto surface (most often, vertex) sites helps in reducing the overall cluster negative charge, also providing more flexibility to adjust charge density of the system. A general way towards large tetrahedral clusters here assumes varying the ratio between multiple metal ions in different oxidation states (e.g. $M^{4+}/M^{3+}/M^{2+}$, $M^{4+}/M^{3+}/M^{+}$ or even $M^{4+}/M^{3+}/M^{2+}/M^{+}$) and meticulous selection of charge-balancing species with geometrical, charge density and mutual interaction match. The preparation of tertiary (and more complex) metal chalcogenides can often be complicated by phase separation, with M^{4+}, M^{3+} or M^{2+} cations forming stable

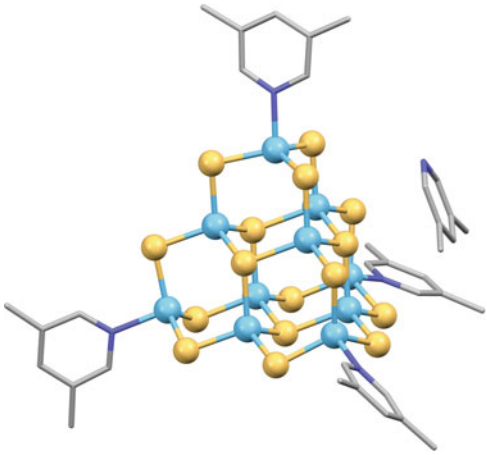

Fig. 17 Anionic T_3 cluster $[Ga_{10}S_{16}L_4]^{2-}$ charge-balanced and stabilized by $2H^+$-L, where L = 3,5-dimethylpyridine [149]

chalcogenides on their own. Solvothermal and ionothermal synthesis with suitable additives (charge-balancing, structure-directing and space-filling species, with possibility to blend all those functions in just one compound) provide favourable conditions to facilitate integration of different metal cations into the same cluster. Some particular cases illustrating the mentioned synthetic strategies and approaches, starting from those common between M^{2+} and M^{3+} tetrahedral cluster systems, are described below.

The "corner capping" with neutral N-containing aromatic ligands in a purely M^{3+} system was achieved, for example, in the preparation of the discrete anionic T_3 cluster $[Ga_{10}S_{16}L_4]^{2-}$, where all four vertexes are occupied by L=3,5-dimethylpyridine, covalently attached via the formation of Ga−N bonds [149]. Each anionic cluster is charge-balanced and additionally stabilized with two monoprotonated 3,5-dimethylpyridine cations; despite the disorder of the cationic species, the orientation of the heterocyclic aromatic ring parallel to cluster faces can be distinguished (Fig. 17).

The idea of using fused-ring heterocyclic N-containing additives to corner-cap, charge-balance and stabilize large tetrahedral clusters also resulted in the solvothermal preparation of several discrete clusters with size from T_3 to T_5 and edge lengths reaching 1.55 nm (as measured between vertex metal sites) [43]. Prior to this work, T_5 clusters were known only in 3D and 2D covalently linked superstructures. In the discrete anionic T_5 cluster $[Cd_{13}In_{22}S_{52}L_4]^{12-}$, four vertexes are capped by L=1-methylimidazole (*mim*), ligands, and negative charge of the cluster is balanced by protonated forms of organic superbase 1,8-diazabicyclo-[5.4.0]undec-7-ene (DBU) and Li^+ cations. The Cd^{2+} sites in the inner fragment $\{Cd_{13}S_4\}$, containing four tetrahedrally coordinated S^{2-} sites, are mandated by local electroneutrality requirement, while edge and corner In^{3+} sites alleviate the otherwise low-coordinated surface S^{2-} sites. The orientational disorder of *mim* ligands and charge-balancing H^+-DBU species did not allow their precise location to be determined in the superstructure of the T_5 cluster (space group $I4_1/amd$),

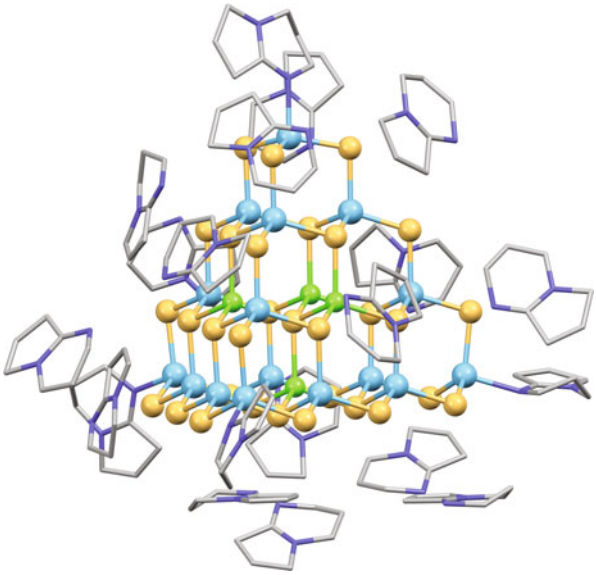

Fig. 18 Anionic T_4 cluster $[Cd_4In_{16}S_{31}L_4]^{6-}$ charge-balanced and stabilized by H^+-L species, where L = 1,5-diazabicyclo[4.3.0]non-5-ene, DBN (all neighbouring DBN are shown, forming a "cocoon" around the cluster) [43]

although their presence was confirmed with a series of analyses. Single-crystal X-ray diffraction analysis of the smaller T_4 anionic cluster $[Cd_4In_{16}S_{31}L_4]^{6-}$, prepared by the same "superbase route", allowed location of the capping ligands L=1,5-diazabicyclo[4.3.0]non-5-ene (DBN) at vertexes and charge-balancing H^+-DBN species, which create a stabilizing "cocoon" around the cluster (space group $I4_1/a$, see Fig. 18).

The T_5 cluster $[Cd_{13}In_{22}S_{52}(mim)_4]^{12-}$ exhibits distinct, broad emission in the solid state at room temperature with the maximum observed at 512 nm (fwhm ~70 nm); a band gap of 2.87 eV was calculated from the diffuse reflectance UV−vis data. Both absorption and emission bands were found to be red shifted in comparison with those of smaller clusters (e.g. T_4 $[Cd_4In_{16}S_{31}(DBN)_4]^{6-}$ with a band gap 3.27 eV) as result of both size increase and composition change [43].

Other derivatives of imidazolium salts were also useful to provide access to extra-large supertetrahedral metal chalcogenide clusters in a "corner capping" approach. Performing syntheses in the ionic liquid [Bmmim]Cl (where Bmmim=1-butyl-2,3-dimethylimidazolium) allowed the combination of charge-decreasing (partially), charge-balancing and charge-stabilizing functions in one compound, which also served as the reaction medium. This resulted in the preparation of several discrete anionic T_5 clusters, including $(Bmmim)_{12}(NH_4)[Cu_5In_{30}S_{52}(SH)_2Cl_2]$ and the first Ga-based T_5 cluster $(Bmmim)_8(NH_4)_3[Cu_5Ga_{30}S_{52}(SH)_2(Bim)_2]$ [44]. In the latter, the corner-capping ligand Bim (1-butyl-2-methyl-imidazole) is generated by in situ decomposition of the IL. The relatively unusual precursor, $[H^+\text{-en}]_2[Ga_4S_7(en)_2]$, was separately prepared by solvothermal synthesis in ethylenediamine (en) and used as the Ga source, with In_2S_3 as the In source. In T_5 clusters with mixed M^+ and M^{3+} cations, the central metal site, surrounded by four tetrahedrally coordinated S^{2-}, should be a

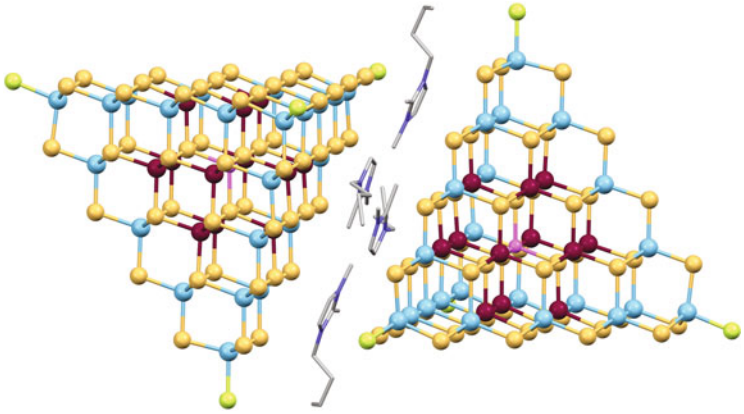

Fig. 19 $[Bmmim]^+$ cations between two anionic T_5 clusters $[Cu_5In_{30}S_{52}(SH)_2Cl_2]^{13-}$: the imidazolium rings are parallel to the surfaces of neighbouring clusters and anion–π interactions are suggested to exist. Vertex sites with partial occupancy SH/Cl are shown as *lime-green* in colour; metal sites Cu/Ga as *maroon* [44]

Cu^+ cation, and each inner tetrahedrally coordinated S^{2-} anion should be bonded with two Cu^+ and two M^{3+} cations in order to maintain local electroneutrality. According to this, in each cluster one Cu^+ cation occupies solely the central metal site, while four Cu^+ cations are statistically distributed along with M^{3+} cations in the other 12 metal sites of the inner $\{M_{13}S_4\}$ fragment (Fig. 19). Most of the $[Bmmim]^+$ cations are located between the tetrahedral faces of two T_5 clusters, and the imidazolium rings of $[Bmmim]^+$ cations are oriented such to be parallel to the nearby cluster face (Fig. 19). The closest distances between S^{2-} on the face of the cluster and the centre of imidazolium rings are such that the presence of anion–π interaction was assumed. C−H···S hydrogen bonding and anion–π interactions also help to stabilize the large anionic clusters.

Both In- and Ga-based T_5 clusters show emission in solid state at room temperature but the obtained spectra are remarkably different. Thus, $[Cu_5In_{30}S_{52}(SH)_2Cl_2]^{13-}$ shows a distinct asymmetric emission band at 540 nm (fwhm ~50 nm), while $[Cu_5Ga_{30}S_{52}(SH)_2(Bim)_2]^{11-}$ shows an unusual broad emission band at 630 nm with fwhm of ~180 nm. Calculated from the diffuse reflectance UV−vis data, band gaps are 2.28 and 3.68 eV for $[Cu_5In_{30}S_{52}(SH)_2Cl_2]^{13-}$ and $[Cu_5Ga_{30}S_{52}(SH)_2(Bim)_2]^{11-}$, respectively, exhibiting a blue shift compared to the bulk $CuInS_2$ (1.53 eV) and $CuGaS_2$ (2.40 eV) [44].

An approach to decrease the charge of anionic clusters, complementary to the use of the "corner capping" neutral organic ligands, was realized via covalent termination of the cluster vertexes with complex metal cations. In this case, instead of replacing the vertex E^{2-} sites in tetrahedral clusters, longer E-ML_n units are formed with participation of four vertex E atoms, where M is a transition metal and L organic ligand. Thus in the discrete T_3 cluster $[Zn_2Ga_4Sn_4Se_{20}]^{8-}$, introducing Sn^{4+} cations onto four vertex sites contributed to a decrease in the negative

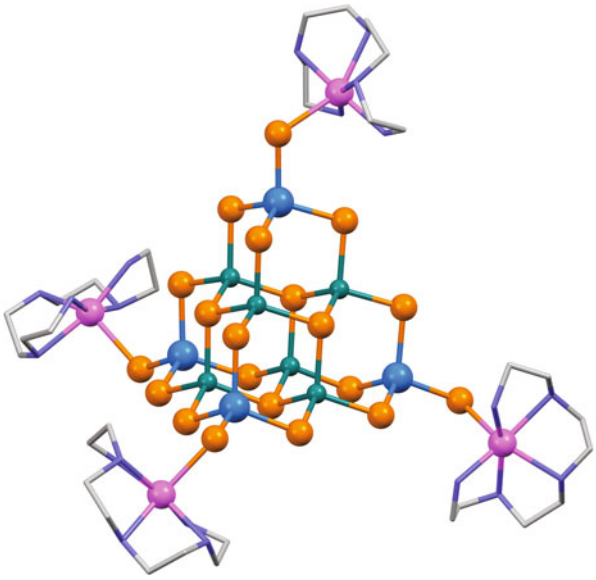

Fig. 20 The neutral cluster with covalently bonded metal complexes [Mn(*tepa*)]$_4$[$Zn_2Ga_4Sn_4Se_{20}$]. Metal sites with partial occupancy Zn/Ga are shown as *dark cyan* [131]

charge, while the attachment of four metal complexes $[Mn(L)]^{2+}$ with the polydentate organic ligand L = $C_8H_{23}N_5$, tetraethylenepentamine (*tepa*), covalently terminates all cluster vertexes and charge-balances the framework [131]. In the in situ formed metal complex $[Mn(tepa)]^{2+}$, the Mn atom is coordinated with five N sites from the organic ligand and one vertex Se site of the tetrahedral cluster, thus having a distorted octahedral environment. Hence, the distribution of Mn^{2+} and Zn^{2+} cations in the clusters (octahedral and tetrahedral coordination, respectively) results from the different coordination abilities of these metals. The ligand *tepa* also serves as the reaction medium in the solvothermal synthesis. The resulting neutral clusters with pendent metals, [Mn(*tepa*)]$_4$[$Zn_2Ga_4Sn_4Se_{20}$] (Fig. 20), assemble into a superlattice (space group $P\,\overline{4}b2$) with different levels of ordering provided by different intercluster forces: hydrogen bonding N−H···Se between *tepa* ligands on one cluster and Se sites on the face of the adjacent cluster give a layered arrangement parallel to the (001) plane, while the layers are further packed into 3D superlattice through van der Waals interactions. Hence, the metal complexes [Mn(*tepa*)]$^{2+}$ at the four cluster vertexes not only allow charge balance but also act as structure-directing agents for superstructure assembly.

The isostructural [Mn(*teta*)]$_4$[$Mn_2Ga_4Sn_4S_{20}$], also covalently terminated with metal-complex cations ML_n, was solvothermally prepared using the shorter $C_6H_{18}N_4$, triethylenetetramine (*teta*), as both solvent and polydentate ligand [150]. Further shortening the length of the organic ligand in the metal-complex cation (L = $C_4H_{13}N_3$, diethylenetriamine (*dien*)) changes not only the hydrogen bonding-governed assembly of clusters into a superstructure (space group *C*2/*c*) but

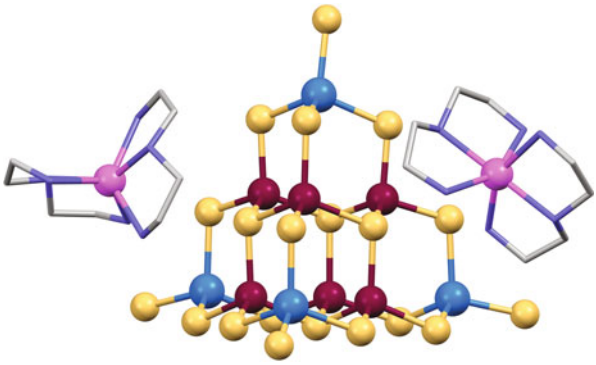

Fig. 21 The anionic T_3 cluster $[Mn_2Ga_4Sn_4S_{20}]^{8-}$ with metal-complex cations $[Mn(dien)_2]^{2+}$. Metal sites with partial occupancy Mn/Ga are shown as *maroon* [150]

the cluster composition itself, leading to formation of discrete anionic T_3 clusters $[Mn_2Ga_4Sn_4S_{20}]^{8-}$ charge-balanced and stabilized by $[Mn(dien)_2]^{2+}$ cations (Fig. 21) with additional hydrogen N−H···S bonding (in the absence of covalent bonding) between negatively charged cluster and positively charged metal-complex. However, the use of a bidentate ligand as an extreme case of shortening ($L = C_2H_8N_2$, ethylenediamine (*en*)) under similar reaction conditions results in the formation of a covalently bonded 1D superstructure, where anionic clusters $[Mn_2Ga_4Sn_4S_{20}]^{8-}$ are interlinked by two pairs of unsaturated metal-complex cations $[Mn_2(en)_5]^{4+}$ via Sn–S–Mn covalent bonds.

While metal-complex cations such as $[M(phen)_3]^{2+}$ and $[M(bpy)_3]^{2+}$ are used to template, charge-balance and stabilize the formation of anionic metal chalcogenide clusters, enhanced optical properties (due to cation–anion charge transfer) are also incorporated. Such integrated materials are formed to a great extent in a similar manner as was discussed above for pure M^{2+} systems (with surface PhE^- ligands), except here there are no additional π–π and hydrophobic surface interactions in the case of naked T_n clusters. Some discrete anionic clusters prepared under solvothermal conditions using this approach are the In^{3+}-containing T_3 clusters $[Ni(phen)_3]_3[In_{10}S_{20}H_4]$ (Fig. 22, left) [73] and $[Ni(bpy)_3]_3[In_{10}S_{20}H_4]$ [144], where *phen* and *bpy* ligands on three metal complex cations provide steric hindrance and an aromatic environment to template and stabilize the metal chalcogenide frameworks (Fig. 22, right). Similarly, the iron-doped T_4 cluster $[Fe(bpy)_3]_3[Fe_4In_{16}S_{35}H_2]\cdot 4H^+$-*tea*$\cdot 2H^+$-*bpy* can be prepared, with additional charge balance with protonated triethylamine (*tea*) and protonated bipyridine [151].

In the examples addressed above, decreasing and balancing the charge and stabilization of large anionic clusters was achieved by (1) covalent capping/terminating of cluster vertexes by neutral and cationic groups and/or by (2) non-covalent (e.g. ionic and hydrogen bonding or van der Waals forces) interactions with different species, i.e. P- or N-containing organic ligands and transition metal complexes with N-containing aliphatic or aromatic chelating ligands; often several routes are realized simultaneously. A particular case where stabilization of clusters is achieved via non-covalent interactions with only protonated forms of organic amines can also take place. Many protonated amines provide more flexibility in

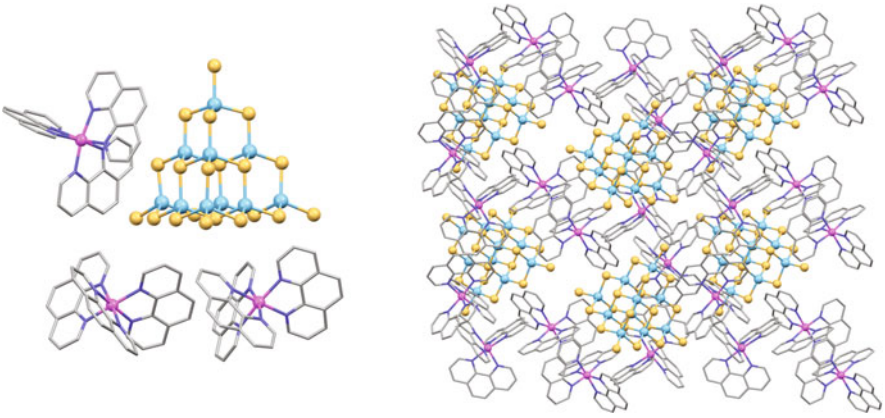

Fig. 22 The anionic T_3 cluster $[In_{10}S_{20}H_4]^{6-}$ with three metal–complex cations $[Ni(phen)_3]^{2+}$ (*left*); superstructure of the clusters, charge-balanced, templated and stabilized by metal complexes (viewed along the *b* direction) (*right*). Co-crystallized solvent molecules are omitted for clarity [73]

templating and charge-balancing of anionic metal chalcogenide clusters, in comparison, for example, with rigid metal-complex cations with *phen* and *bpy* ligands. Thus, the series of discrete anionic T_4 clusters $[M_xGa_{18-x}Sn_2E_{35}]^{12-}$, where $x = 2$ or 4; M = Mn, Cu and Zn; E = S and Se, was solvothermally prepared using piperidine (*pr*, $C_5H_{11}N$) as the reaction solvent [49]. Stabilization of the clusters is achieved, on the one hand, by varying the ratio between precursors (complex composition including M^+, M^{2+}, M^{3+} and M^{4+} metal sources) allowing charge tuning of the cluster and, on the other hand, by a perfect match of charge density, geometry and mutual interactions (electrostatic and hydrogen bonding) between the highly ordered protonated piperidine cations and the anionic clusters in the superstructure. Theoretical calculations at the DFT level show that the $[Cu_2Ga_{16}Sn_2Se_{35}]^{12-}$ cluster has more negative charge centres at the Se^{2-} vertexes of the tetrahedron and at the central Se^{2-} site of each edge. In the superstructure of such clusters (space group $I\,\overline{4}3m$; body-centred cubic packing in unit cell), two piperidinium cations interact with Se^{2-} at each edge centre and three piperidinium cations – with each vertex Se^{2-} with the formation of strong electrostatic interactions and additional N−H···Se hydrogen bonds, so each discrete T_4 cluster is surrounded by and bonded with 24 piperidinium cations (Fig. 23). Since each piperidinium cation interacts with two adjacent metal chalcogenide clusters, it provides a total charge balance $(H^+\text{-}pr)_{12}[Cu_2Ga_{16}Sn_2Se_{35}]^{12-}$ for each cluster. The remarkable stability of such protonated amine-cluster "ion pair" was confirmed by the miniscule change of electrical conductivity upon dissolving the crystalline product in piperidine. While solvothermal synthesis was performed under similar reaction conditions but using other amines (piperidine derivatives and related compounds) possessing stronger protonation ability and/or higher steric hindrance,

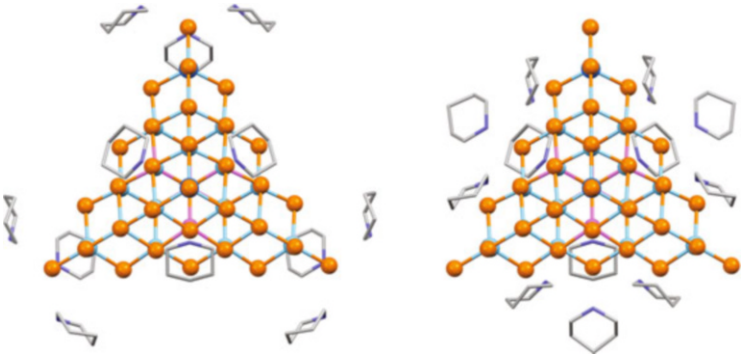

Fig. 23 The anionic T_4 cluster $[Cu_2Ga_{16}Sn_2Se_{35}]^{12-}$ surrounded by 24 protonated piperidine molecules: those bonded to cluster vertexes (*left*) and the centres of edges (*right*) through N−H···Se hydrogen bonding are shown separately [49]

only the formation of 3D covalent superstructures took place, which proves the importance of a multilateral match between the protonated amine and cluster.

Solvothermal reactions in a mixed solvent system containing water and the organic "superbase" amine DBU allowed the preparation of very unusual large In^{3+}-containing cluster $[In_{38}S_{65}(H_2O)_6]^{16-}$ stabilized by H^+-DBU [38]. This cluster is covalently bonded via dimeric $[In_2S(H_2O)_2]^{4+}$ units into a 2D framework (space group *Pnma*). The structure of the cluster $[In_{38}S_{65}(H_2O)_6]^{16-}$ with an overall tetrahedral shape (Fig. 24, left) is different from well-known T_n, P_n or C_n structures and can be described as a combination of an octahedral core unit $\{In_{10}S_{13}\}$ (Fig. 24, right) with four tetrahedral T_2 corners $\{In_4S_{10}\}$ and four hexagonal rings $\{In_3S_3\}$ as faces. There are very few examples known for clusters containing both octahedral and tetrahedral coordination for metal sites; one example is the smaller anionic cluster $[Mn_6Ge_4Se_{17}(H_2O)_6]^{6-}$ [152]. In the $[In_{38}S_{65}(H_2O)_6]^{16-}$, the core unit of the cluster $\{In_{10}S_{13}\}$ possesses an octahedral crystalline lattice of NaCl type and features a central μ_6-S^{2-} site. Six H_2O molecules complete the six In^{3+} sites at the face centre of the octahedral core unit. Four corner $\{In_4S_{10}\}$ T_2 units are attached to the core unit $\{In_{10}S_{13}\}$ via bonding between three S^{2-} sites on one face of the T_2 unit and the corner In^{3+} site of the central moiety, which enables all ten In^{3+} sites within the core to have an octahedral coordination. Therefore, both In^{3+} and S^{2-} sites in this framework have local coordination geometries that are unusual for tetrahedral metal chalcogenide clusters. A calculation of bond valence sums gives 2.078 for the central μ_6-S^{2-} site; such a value was previously considered unlikely to be found in stable systems as local electroneutrality is not maintained. Another rare exception to Pauling's electrostatic valence rule in tetrahedral metal chalcogenide clusters is observed in the smaller covalently bonded P_1 cluster $[In_8S_{17}H]^{9-}$ with a μ_4-S^{2-} site (calculated bond valence sum 2.28 instead of required 3) in the central anti-T_1 unit $\{SIn_4\}$ [58]. From the number of both metal and chalcogen sites, the 2D covalently bonded cluster $[In_{38}S_{65}(H_2O)_6]^{16-}$ (proposed notation TO_2 meant to stress the mixed tetrahedral (T)/octahedral (O) configuration of the core) exceeds the size of the discrete

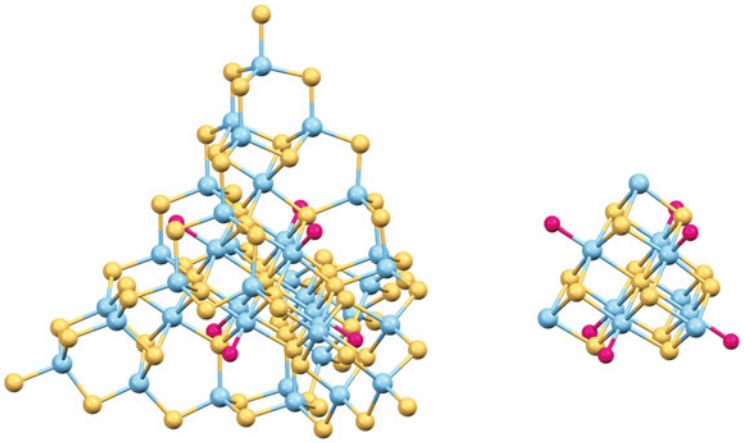

Fig. 24 The anionic TO_2 cluster $[In_{38}S_{65}(H_2O)_6]^{16-}$ (*left*); separately shown is the octahedral core unit $\{In_{10}S_{13}\}$ in the same orientation (*right*) [38]

supertetrahedral T_5 clusters (e.g. $[Cu_5In_{30}S_{52}(SH)_4]^{13-}$) [41]. Both of these tetrahedral metal chalcogenide clusters were formed due to a stabilizing "cocoon" of protonated organic "superbases", H^+-DBU and H^+-DBN/H^+-PR, respectively.

To conclude the overview of M^{3+}-based tetrahedral metal chalcogenide clusters, it is worth mentioning the very unusual system where stabilization of a superstructure consisting of two different discrete anionic clusters is achieved with participation of protonated amines. Here, solvothermal synthesis in ethylenediamine results in the preparation of a binary superstructure, combining the tetrahedral T_4 $[Cu_4In_{16}S_{35}H_4]^{14-}$ and cubic $[Cu_{12}S_8]^{4-}$ discrete clusters (Fig. 25, left), with only protonated ethylenediamine species compensating the (high) charge of both anions [122]. It was proposed that $[Cu_{12}S_8]^{4-}$ clusters may act as template during the formation and crystallization of $[Cu_4In_{16}S_{35}H_4]^{14-}$. The overall ratio between these two anionic clusters in superlattice is 1:2 and each $[Cu_{12}S_8]^{4-}$ is located in a cavity formed by six adjacent $[Cu_4In_{16}S_{35}H_4]^{14-}$ (Fig. 25, right).

The red crystals of $[Cu_4In_{16}S_{35}H_4]_2[Cu_{12}S_8]\cdot 32H^+$-*en* (space group $R\bar{3}$) are stable in their mother liquor in the sealed container, while they quickly degenerate to black product upon isolation from the solution [122]. The blackened crystals absorb intensely in the near-IR diapason; the absorption properties were found to be even better for the annealed product. Such remarkable near-infrared absorption properties along with photocurrent response may allow future application as a near-infrared protective material.

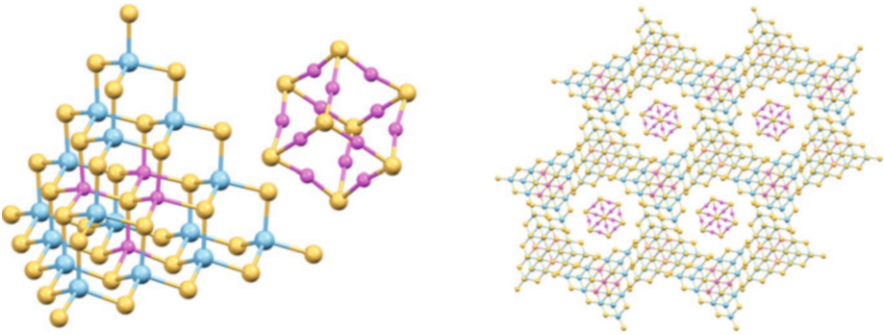

Fig. 25 Tetrahedral T_4 $[Cu_4In_{16}S_{35}H_4]^{14-}$ and cubic $[Cu_{12}S_8]^{4-}$ discrete anionic clusters (*left*); fragment of packing in binary superstructure, where cubic $[Cu_{12}S_8]^{4-}$ reside in hexagonal spaces formed by tetrahedral $[Cu_4In_{16}S_{35}H_4]^{14-}$ clusters from different layers (viewed along the *c* direction) (*right*). Charge-balancing H^+-*en* species are mostly disordered and omitted for clarity [122]

5.4 Reactions of Large Tetrahedral Clusters

Recently, several cases of "solvothermal insertion" have been described, where discrete tetrahedral clusters with available cavities envelop a size-fitting metal cation, leading to the formation of a new product. Precise doping is possible due to the two-step strategy, assuming (1) solvothermal preparation and isolation of host cluster crystals, followed with (2) metal insertion into the core and crystallization of a new host–guest cluster, again enhanced under solvothermal conditions. Using soluble clusters as a host is essential, as attempts of metal cation diffusion into coreless clusters covalently bonded into rigid 3D or 2D superstructures were reported to be incomplete and inhomogeneous. Doping with a single metal ion (realizing highly ordered distribution of multiple metal components in a tetrahedral cluster) is very unlikely to be achieved in a one-step preparation as multinary cluster systems often show statistical distribution of several metals over multiple possible sites to satisfy the local electroneutrality requirement. For instance, discrete T_5 clusters $[Cu_5In_{30}S_{52}(SH)_4]^{13-}$ have only one central Cu site and yet 12 inner sites partially occupied by Cu^+ (1/3 probability) and In^{3+} (2/3 probability). In contrast to this, monocopper doping into an In^{3+}-based T_5 cluster was achieved in the two-step strategy, with metal solvothermal insertion into discrete coreless T_5 cluster $[Cd_6In_{28}S_{52}(SH)_4]^{12-}$ (space group $I4_1/amd$) (Fig. 26, left) realized at relatively mild temperature (150 °C) in mixed solvent (DBN, PR and H_2O), leading to the preparation of the discrete T_5 cluster $[CuCd_6In_{28}S_{52}(H_2O)_4]^{7-}$ (crystallized in the same space group $I4_1/amd$) (Fig. 26, right) [41]. The yield for the Cu^+ insertion is ~70% based on the host cluster; the driving force for the reaction is proposed to be the reduction of the charge of anionic host. Also interesting is that metal insertion is accompanied by four-vertex HS^- sites being replaced with neutral water ligands, further decreasing the overall cluster charge. In a similar way, a single Mn^{2+} was inserted into the open T_5 $[Cd_6In_{28}S_{52}(SH)_4]^{12-}$ or $[Zn_6In_{28}S_{52}(SH)_4]^{12-}$ clusters, resulting in host–guest T_5 cluster with drastically

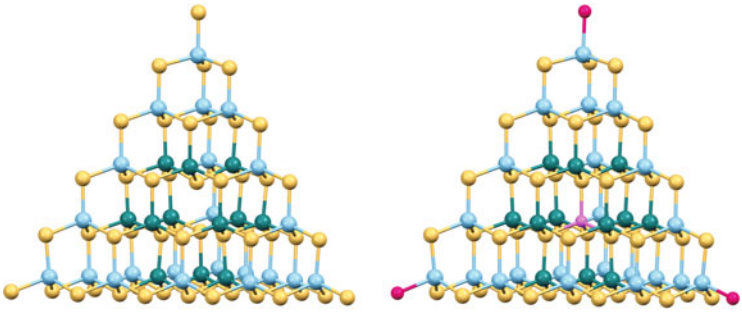

Fig. 26 Discrete coreless T_5 $[Cd_6In_{28}S_{52}(SH)_4]^{12-}$ (*left*) as a host cluster and discrete T_5 cluster $[CuCd_6In_{28}S_{52}(H_2O)_4]^{7-}$ (*right*) as a product of "solvothermal insertion" reaction. Metal sites with partial occupancy Cd/In are shown as *dark cyan* [41]

changed optical properties [42]. Thus, the Mn^{2+}-doped material shows a prominent red emission at room temperature with maximum at 630 nm, which is significantly red shifted in comparison with both host clusters with weak green emission (~490 nm), and traditional Mn^{2+}-doped chalcogenides of group 12 metals with orange emission (~585 nm). An alkali metal cation (Cs^+ or Rb^+) was also ionothermally inserted into the central cavity of the hierarchical $T_{2,2}$ cluster $[In_8Sn_8Se_{34}]^{12-}$ with polyselenium Se_4 chains interconnecting the clusters into a covalent 2D superstructure in a one-step process [63]. The larger size of the negatively charged cavity in the host cluster (with a "missing" $\{EM_4\}$ unit in the centre in comparison with just a single M site in coreless T_5 examples above) fits alkali metal cations but not alkaline earth (Ca^{2+}, Sr^{2+}) or transition (Mn^{2+}, Cu^{2+}) metals.

5.5 *Non-tetrahedral Clusters with M^{2+} Cations*

Metal chalcogenide clusters with overall tetrahedral shape are the most common for large M^{2+} systems, especially those prepared by solvothermal approach, with only a few examples of other arrangements. One group of non-tetrahedral clusters includes relatively small, cagelike assemblies formed by group 12 metals where basic tetrahedra $\{ME_4\}$ are linked by vertex sharing. For instance, the discrete cubic cluster $[Cd_8L_{14}(dmf)_6(NO_3)]^+$ was prepared by a coordination chemistry approach using the fluorine-substituted ligand L = 3-fluorophenylthiolate [81]. In this "double four-ring" cationic cluster, eight Cd^{2+} are arranged at eight corners of a cube and bridged by twelve 3-fluorophenylthiolate ligands with S atoms being slightly out from the centre of each cubic edge. Corner Cd^{2+} sites within the cube are bonded to 3-fluorophenylthiolate, *dmf* and NO_3^- ligands. The related cubic $[Cd_8(SPh)_{12}]^{4+}$ cluster (Fig. 27) was previously prepared solvothermally as a 3D covalently bonded MOF, linked by in situ generated tetradentate 1,2,4,5-tetra (4-pyridyl)benzene ligands, coordinated to cube vertexes via the formation of

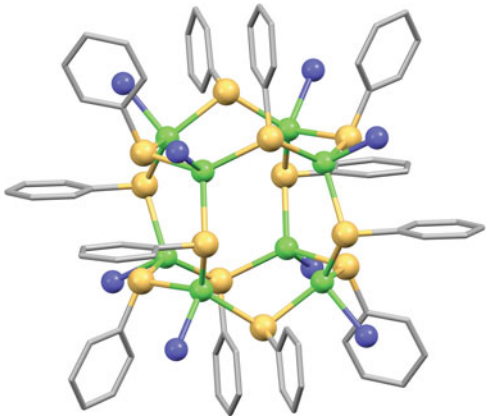

Fig. 27 Cationic cubic $[Cd_8(SPh)_{12}]^{4+}$ cluster in 3D covalently bonded coordination polymer. Only N atoms from 1,2,4,5-tetra (4-pyridyl)benzene ligands are shown. A trapped anion is omitted for clarity [153]

Cd−N bonds [153]. Both cagelike cationic clusters are found to contain trapped anions (NO_3^- or SO_4^{2-}), which come from starting reagents and may additionally play the role of template and structure-directing species. The structurally related $[Hg_8(\mu_8\text{-}S)(SCH_3)_{12}]^{2+}$ cluster has an enclosed μ_8-S inside its cage [154]. It should be mentioned that such positively charged molecular clusters (as well as 3D covalently bonded frameworks of such clusters) are usually not accessible via solvothermal or ionothermal approaches. The likely reason is the difficulties with charge balancing and stabilization of the clusters and their superstructure in this case.

5.6 *Ring- or Cagelike Clusters with M^{3+}, M^{4+} and Mixed Cations*

Discrete ring-shaped clusters, as well as cagelike assemblies in which metal cations are bridged by group 16 elements (oxygen or chalcogen), are relatively widespread for transition metals (e.g. some transition metal sulphide rings, giant oxomolybdate, oxothiomolybdate and polyoxometalate wheels or cages) [155–158]. In contrast, such large clusters are rather unusual for group 13 and 14 metals.

Unlike the large tetrahedral metal chalcogenide clusters which represent regular fragments of related solid-state ME, ring- and cagelike clusters possess laced structures: basic tetrahedral $\{ME_4\}$ units are combined into polymeric formations (linear and branched, respectively) via vertex and/or edge sharing. The higher structural flexibility of the heavier chalcogenides allows geometrical adjustment in forming arching fragments. Chalcogenide sites are generally low coordinate (mostly μ-, seldom μ_3-E^{2-}); local charge balance is maintained with high-valence metal ions. While the M:E ratio in these ring- and cagelike clusters is higher in comparison with large tetrahedral clusters (~1:2.0 vs. ~ 1:1.7, respectively), the presence of M^{3+} and M^{4+} cations contributes to a decrease of the negative charge. Tracery-like frameworks allow for an arrangement of a large number of

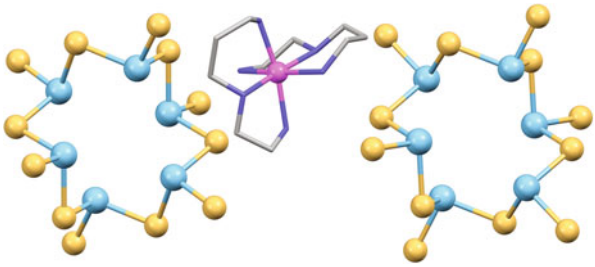

Fig. 28 Ring-shaped anionic clusters $[Sb_6S_{12}]^{6-}$ with metal-complex cation $[Ni(aepa)_2]^{2+}$ [159]

charge-balancing species around the anionic cluster without steric hindrance. The effect of structure-directing and templating agents on the assembly of these structures is suggested to be of a great importance. A few known examples of their solvothermal and ionothermal preparation are described below.

The previously unknown group 15 metal ring-shaped anionic cluster $[Sb_6S_{12}]^{6-}$ (formed by six corner-sharing SbS_3 pyramids) was solvothermally prepared using the multidentate amine *N*-(aminoethyl)-1,3-propanediamine (*aepa*) as a reaction solvent [159]. In situ formed $[Ni(aepa)_2]^{2+}$ complexes serve to charge-balance, template and stabilize the ring-shaped clusters into a superstructure formed through hydrogen bonding and van der Waals interactions (space group $R\overline{3}$, featuring two crystallographically independent ring-shaped anions with slightly different geometric parameters; see Fig. 28).

The much larger and structurally sophisticated cluster $[In_{18}Te_{30}(dach)_6]^{6-}$ was solvothermally prepared in a mixed solvent of 1,2-diaminocyclohexane (*dach*) and water [39]. As opposed to single-chain rings like in the $[Sb_6S_{12}]^{6-}$ anion, this cluster has a double-decker ring or wheel topology (Fig. 29). The structure of the highly symmetrical $In_{18}Te_{30}$ wheel (point group pseudo-D_{3d} when ignoring the *dach* ligands) can be viewed as a combination of six $\{In_2Te_6\}$ (representing two edge-sharing basic tetrahedra ME_4) with six $\{InTe_3N_2\}$ units. The latter unit is formed from the basic ME_4 tetrahedron, while one E site is replaced by two N from the chelating amine *dach*; it contains an unusual five-coordinated In^{3+} cation that possesses trigonal bipyramidal geometry. The organic ligand *dach* can be considered as "decorating", in contrast with bridging ligands (e.g. μ-chalcogenolates) in some well-known [160, 161] or recently reported [162, 163] metal chalcogenide rings. The $2H^+$-*dach*·H_2O unit, assembled by hydrogen bonding, was found positioned as an axle with H_2O molecule located exactly at the centre of the $In_{18}Te_{30}$ wheel. This unit is proposed to act as a template in the formation of the anionic cluster, while metal-complex cations $[Mn(dach)_3]^{2+}$ provide additional charge-balancing, templating and stabilization of the superstructure with overall composition $[Mn(dach)_3]_2[In_{18}Te_{30}(dach)_6]\cdot 2H^+$-*dach*·$H_2O$ (space group *Pnnm*).

The analogous wheel-shaped cluster $[In_{18}Te_{30}(dapn)_6]^{6-}$, where *dapn* = 1,3-diaminopropane, was prepared with such metal-complex cations as $[Fe(phen)_3]^{2+}$ or $[Ni(phen)_3]^{2+}$ and isolated as air-stable crystals [164]. Unlike the $[In_{18}Te_{30}(dach)_6]^{6-}$ anion, where *dach* is chelated to the In^{3+} giving $\{InTe_3N_2\}$ units, *dapn* was found to react as a monodentate ligand giving $\{InTe_3N\}$ units with tetrahedral geometry in $[In_{18}Te_{30}(dapn)_6]^{6-}$ cluster. In the superstructures with composition

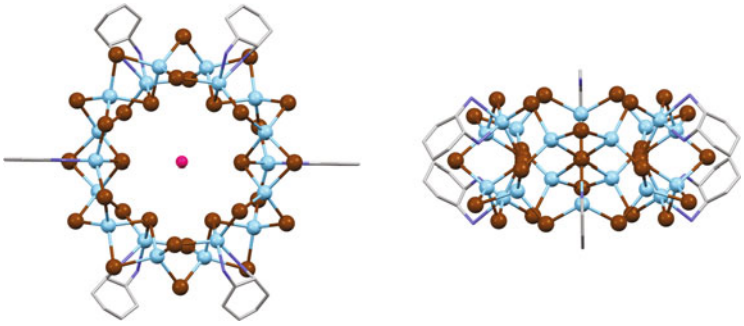

Fig. 29 Two different orientations of wheel-shaped $[In_{18}Te_{30}(dach)_6]^{6-}$ anionic cluster with H_2O molecule in the central $2H^+$-*dach*·H_2O unit (H^+-*dach* not shown) acting as template for the wheel assembly [39]

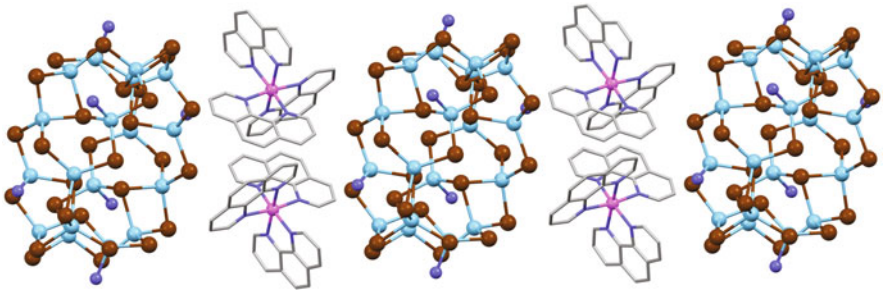

Fig. 30 Fragment of packing of anionic clusters $[In_{18}Te_{30}(dapn)_6]^{6-}$ and metal-complex cations $[Ni(phen)_3]^{2+}$, forming dimers through π–π interactions. Dangling *dapn* ligand fragments, except N atoms bonded to In, are omitted for clarity [164]

$[M(phen)_3]_2[In_{18}Te_{30}(dapn)_6]\cdot 2H^+$-*dapn*·*dapn* with M = Fe or Ni (space group $P\bar{1}$), clockwise (Δ) $[M(phen)_3]^{2+}$ cation couples with anticlockwise (Λ) $[M(phen)_3]^{2+}$ through π–π interactions forming dimeric species. Such positively charged dimers are about the same size as the wheel-shaped anionic cluster $[In_{18}Te_{30}(dapn)_6]^{6-}$ and bonded with the latter through electrostatic and additional anion–π interactions (Fig. 30). The solvothermal synthesis of $[In_{18}Te_{30}(dapn)_6]^{6-}$ required substantially higher temperature and much longer reaction time in comparison with that of $[In_{18}Te_{30}(dach)_6]^{6-}$: the optimized reaction conditions are 180°C/28–30 days and 140°C/4 days, respectively. This can be related to the use of elemental indium instead of $InCl_3$ and/or different properties of *dapn* as solvent (e.g. bp 140°C) in comparison with mixed system *dach*:H_2O = 7:3 (with bp of *dach* ~80°C). *Dapn* ligands are significantly disordered, while chelating and relatively more rigid *dach* molecules were located and refined using single-crystal X-ray analysis.

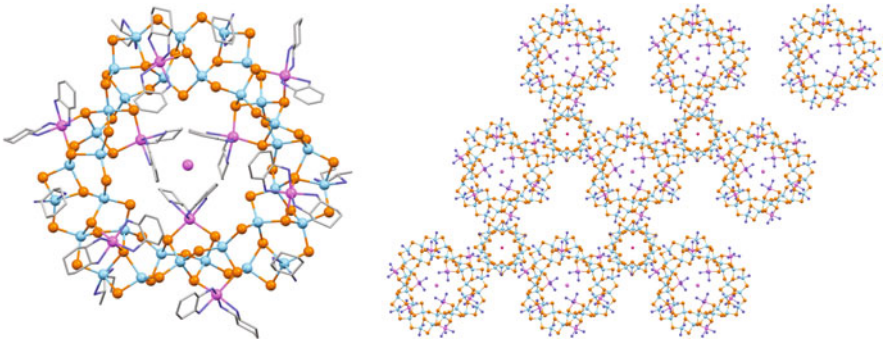

Fig. 31 Triangular ring-shaped anionic cluster $[Mn_9In_{33}Se_{60}(dach)_{24}]^{3-}$ with the central Mn^{2+} cation acting as template and structure-directing agent (*left*). A fragment of packing in the binary superstructure combining larger $[Mn_9In_{33}Se_{60}(dach)_{24}]^{3-}$ and smaller $[In_{18}Se_{30}(dach)_6]^{6-}$ ring-shaped clusters; *dach* ligands, except N atoms, are omitted for clarity (*right*). Clusters are shown along the *c* direction [165]

The combination of a mixed solvent of *dach* and H_2O with [Bmim]Br (Bmim=1-butyl-3-methyl-imidazolium) allowed for the solvothermal preparation of the binary superstructure, combining wheel-shaped $[In_{18}Se_{30}(dach)_6]^{6-}$ with the triangular double-decker ring $[Mn_9In_{33}Se_{60}(dach)_{24}]^{3-}$ clusters in a 1:2 ratio (Fig. 31, right) [165]. While the first cluster is the Se-containing analogue of $[In_{18}Te_{30}(dach)_6]^{6-}$, the second is a novel discrete ring structure possessing a different topology and containing both M^{3+} group 13 and M^{2+} transition metal cations. The tangled structure of this triangular ring can be viewed as a complex combination of 27 basic $\{InSe_4\}$ tetrahedral and 6 $\{InSe_3N_2\}$ trigonal bipyramidal units through either vertex- or edge-sharing (Fig. 31, left). The outer diameter of resulting $In_{33}Se_{60}$ ring was calculated as ~2.5 nm (while measuring between two opposite Se^{2-} sites). The $In_{33}Se_{60}$ ring is further decorated by 9 $\{Mn(dach)_2\}$ bridging units (distorted octahedral geometry for Mn), with three units on the inside, three on the outside and the other three on a same face as the ring. The discrete clusters of $[Mn_9In_{33}Se_{60}(dach)_{24}]^{3-}$ are discernible on TEM images. The charge balance in the two-anion superstructure is achieved with combination of $[Mn(dach)_3]^{2+}$, Mn^{2+}, H^+-*dach* and Cl^-. The overall composition (deduced from both single-crystal X-ray diffraction data and a set of auxiliary analyses) is $Mn_2[Mn(dach)_3]_3[Mn_9In_{33}Se_{60}(dach)_{24}]_2[In_{18}Se_{30}(dach)_6]\cdot(H^+\text{-}dach)_{11}Cl_9\cdot 7H_2O$, space group $R\,\overline{3}c$. The assembly of the triangular double-decker ring $[Mn_9In_{33}Se_{60}(dach)_{24}]^{3-}$ is proposed to be structure-directing and templated by a Mn^{2+} cation in the centre of the ring through Mn···N inverse second-sphere coordination. The ionic solvent [Bmim]Br takes part in the formation of large ring-shaped anions by increasing the solubility of the products, but is not present in the final compound.

Probing the optical properties of the material containing $[Mn_9In_{33}Se_{60}(dach)_{24}]^{3-}$ and $[In_{18}Se_{30}(dach)_6]^{6-}$ clusters via UV–Vis diffuse reflectance spectroscopy showed that band gap (1.9 eV) is narrower than was expected for the

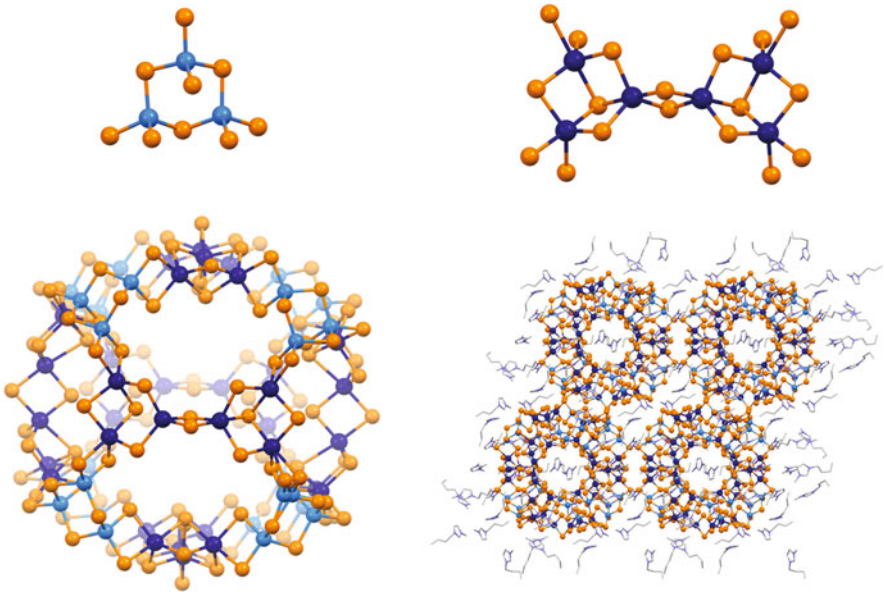

Fig. 32 Building units of discrete cagelike clusters: $\{M_3Se_9\}$ (*top left*) and $\{M_6Se_{18}\}$ (*top right*). The discrete cagelike cluster $[Sn_{36}Ge_{24}Se_{132}]^{24-}$ (*bottom left*), composed of eight $\{Ge_3Se_9\}$ and six $\{Sn_6Se_{18}\}$ units. A fragment of packing of cagelike anions and charge-balancing $[Bmim]^+$ cations (viewed along the *b* direction) (*bottom right*). Ge sites are shown as blue and Sn as *dark blue* [40]

nanodimensional In_2Se_3. This was attributed to a resonance effect due to a ringlike structure.

Discrete, cagelike anionic clusters of group 13 and 14 metal chalogenides are rare, especially those prepared under solvothermal or ionothermal conditions. For instance, the reaction of $[K_4(H_2O)_3][Ge_4Se_{10}]$ and $SnCl_4{\cdot}5H_2O$ in $[Bmmim][BF_4]$ with 2,6-dimethylmorpholine as an additive under ionothermal conditions yielded the discrete cagelike cluster $[Sn_{36}Ge_{24}Se_{132}]^{24-}$ forming ordered superstructure (space group $P2_1/c$) [40]. This cluster anion is comprised of two different types of building blocks: $\{Ge_3Se_9\}$, which represents a trimer of corner-sharing basic tetrahedra $GeSe_4$ (Fig. 32, top left), and $\{Sn_6Se_{18}\}$, which contains a dimer of Sn_3Se_4 semicubes doubly bridged by two Se (Fig. 32, top right). A similar structural motif (i.e. $\{M_3Se_9\}$ unit; see Fig. 32, top left) is also found in a smaller 72-atom supercubooctahedron cluster $[Ga_{15}Ge_9Se_{48}]^{15-}$, prepared by the solid state reaction in a CsCl flux [166]. In 192-atom cluster $[Sn_{36}Ge_{24}Se_{132}]^{24-}$, eight $\{Ge_3Se_9\}$ are located at the vertexes of a cube, while six $\{Sn_6Se_{18}\}$ occupy the vertexes of an octahedron inscribed inside of this cube; the two types of units are linked via the sharing of common Se sites. The resulting cluster is nearly perfectly spherical in shape, with an outer diameter of 2.83 nm (including van der Waals radii of the surface atoms), a cavity with a diameter of 1.16 nm and 12 windows with cross sections of 0.56–0.88 nm (Fig. 32, bottom left). Similar, discrete cagelike clusters with partial metal site disorder $[Bmim]_{24}[Sn_{32.5}Ge_{27.5}Se_{132}]$ was prepared in

[Bmim][BF_4] and crystallized in the space group $P\bar{1}$ (Fig. 32, bottom right). In this superstructure half of the 24 charge-balancing $[Bmim]^+$ cations is arranged at the windows, while the other half is outside of the highly charged cagelike anion. The amine additive is proposed to participate in the formation of Sn-containing units, although the mechanism is not determined yet.

Potentially, such cagelike metal chalcogenide clusters with a large confined space can be used as "molecular flasks" to host species and perform reactions, as the windows of the cluster are not blocked by covalently bonded ligands. Indeed, preliminary results show that $[Sn_{36}Ge_{24}Se_{132}]^{24-}$can trap I_2 molecules and induce heterolytic I–I bond cleavage.

6 Summary and Concluding Remarks

In the present review, some light was shed on the preparation of large, metal chalcogenide clusters and their crystalline superstructures obtained via synthetic routes utilizing reactions in solution under increased temperature and pressure, i.e. solvothermal and ionothermal syntheses. Performing reactions in such conditions shows great potential for both tuning size and composition of a cluster core (e.g. by increased solubility and additional stabilization gained from mutual interactions with carefully chosen stabilizers and/or counterions) and a ligand shell (e.g. by ligand reactions enabled to occur in situ), which assures that materials containing metal chalcogenide clusters can be engineered at several levels.

Both solvothermal and ionothermal routes were shown to be very effective for the synthesis of new clusters with unique structural features and physical properties that are inaccessible using other techniques. An example is the highly ordered distribution of multiple metal components in a cluster, realized as doping a tetrahedral framework with a single metal ion in exact position (such as solvothermal insertion of a single Cu^+ or Mn^{2+} into the host cluster $[Cd_6In_{28}S_{52}(SH)_4]^{12-}$ [41, 42]). The Mn^{2+}-doped cluster shows a prominent red emission at room temperature, which is significantly red shifted in comparison with orange emission observed in traditional Mn^{2+}-doped group 12–16 semiconductors, related by size and composition but without such precisely defined order. An unusual binary superstructure, combining the tetrahedral $[Cu_4In_{16}S_{35}H_4]^{14-}$ and cubic $[Cu_{12}S_8]^{4-}$ clusters with protonated ethylenediamine species, was found to absorb intensely in the near-IR part of the electromagnetic spectrum [122].

Remarkable progress has been achieved with the preparation of progressively larger discrete clusters, with sizes that reach to several nanometers (e.g. tetrahedral clusters $[Cd_{13}In_{22}S_{52}(mim)_4]^{12-}$ and $[Cd_{54}S_{32}(SPh)_{48}(H_2O)_4]^{4-}$ with edge lengths measured between vertex metal sites 1.55 and 1.97 nm, respectively [43, 56]). The dimensions of such cluster cores, having structural similarity with the corresponding bulk crystalline metal chalcogenides, already overlap with those for some colloidal systems. Recently prepared ring- and cagelike clusters (e.g. $[In_{18}Te_{30}(dach)_6]^{6-}$, $[Mn_9In_{33}Se_{60}(dach)_{24}]^{3-}$ or $[Sn_{36}Ge_{24}Se_{132}]^{24-}$ [39, 40,

165]) represent the largest non-tetrahedral frameworks. The presence of ringlike structure is associated with a resonance effect, contributing to the optical properties of such clusters.

The development of new reactants and synthetic procedures is closely connected with the availability of more advanced characterization techniques (such as sophisticated X-ray diffraction instrumentation and processing software, as well as auxiliary analyses), allowing detailed characterization of unusual structural types, e.g. confirming the nature and oxidation state of metals in multinary clusters [49].

Systematic investigation of bonding and structural principles, especially in new structure types, such as tetrahedral/octahedral cluster $[In_{38}S_{65}(H_2O)_6]^{16-}$ [38], will provide useful guidance for the future discovery and development of new cluster-based materials for applications in various fields.

Acknowledgements The authors YH and JFC thank the Natural Sciences and Engineering Research Council (NSERC) of Canada for its continued support of their research programmes. TIL is most grateful to NSERC for a Canada Graduate Scholarship.

References

1. Dance IG (1986) Polyhedron 5:1037–1104. doi:10.1016/S0277-5387(00)84307-7
2. Müller A, Diemann E (1987) Adv Inorg Chem 31:89–122. doi:10.1016/S0898-8838(08)60222-6
3. Ansari M, Ibers J (1990) Coord Chem Rev 100:223–266. doi:10.1016/0010-8545(90)85011-G
4. Krebs B, Henkel G (1991) Angew Chem Int Ed Engl 30:769–788. doi:10.1002/anie.199107691
5. Roof L, Kolis J (1993) Chem Rev 93:1037–1080. doi:10.1021/cr00019a010
6. Dance I, Fisher K (1994) Prog Inorg Chem Vol 41 41:637–803. doi:10.1002/9780470166420.ch9
7. Arnold J (1995) In: Karlin KD (ed) Prog Inorg Chem, vol 43. Wiley, Hoboken, pp 353–417
8. Alivisatos AP (1996) Science 271:933–937. doi:10.1126/science.271.5251.933
9. DeGroot MW, Corrigan JF (2004) In: Fujita M, Creutz PC (eds) Compr Coord Chem II. Elsevier, Amsterdam pp 57–123
10. Corrigan JF, DeGroot MW (2004) In: Rao CNR, Müller A, Cheetham K (eds) The chemistry of nanomaterials: synthesis, properties and applications. Wiley-VCH, Weinheim/Wiley, Chichester, pp 418–451
11. Corrigan JF, Fuhr O, Fenske D (2009) Adv Mater 21:1867–1871. doi:10.1002/adma.200802897
12. Kübel C, Voigt A, Schoenmakers R, Otten M, Su D, Lee T-C, Carlsson A, Bradley J (2005) Microsc Microanal 11:378–400. doi:10.1017/S1431927605050361
13. Friedrich H, Gommes CJ, Overgaag K, Meeldijk JD, Evers WH, de Nijs B, Boneschanscher MP, de Jongh PE, Verkleij AJ, de Jong KP, van Blaaderen A, Vanmaekelbergh D (2009) Nano Lett 9:2719–2724. doi:10.1021/nl901212m
14. Evers WH, Friedrich H, Filion L, Dijkstra M, Vanmaekelbergh D (2009) Angew Chem Int Ed 48:9655–9657. doi:10.1002/anie.200904821
15. Boneschanscher MP, Evers WH, Qi W, Meeldijk JD, Dijkstra M, Vanmaekelbergh D (2013) Nano Lett 13:1312–1316. doi:10.1021/nl400100c
16. Alivisatos AP (1996) J Phys Chem 100:13226–13239. doi:10.1021/jp9535506
17. Nirmal M, Brus L (1999) Acc Chem Res 32:407–414. doi:10.1021/ar9700320

18. Wang Y, Herron N (1990) Phys Rev B 42:7253–7255. doi:10.1103/PhysRevB.42.7253
19. Soloviev VN, Eichhöfer A, Fenske D, Banin U (2000) J Am Chem Soc 122:2673–2674. doi:10.1021/ja9940367
20. Soloviev VN, Eichhöfer A, Fenske D, Banin U (2001) J Am Chem Soc 123:2354–2364. doi:10.1021/ja003598j
21. Collier CP, Vossmeyer T, Heath JR (1998) Annu Rev Phys Chem 49:371–404. doi:10.1146/annurev.physchem.49.1.371
22. Gao Y, Tang Z (2011) Small 7:2133–2146. doi:10.1002/smll.201100474
23. Xie J, Cao S, Good D, Wei M, Ren X (2010) Inorg Chem 49:1319–1321. doi:10.1021/ic9023629
24. Zhang Q, Wu T, Bu X, Tran T, Feng P (2008) Chem Mater 20:4170–4172. doi:10.1021/cm800904d
25. Yang H, Tao W, Le W, PingYun F (2013) Sci China Chem 56:423–427. doi:10.1007/s11426-013-4847-3
26. Talapin DV, Lee J-S, Kovalenko MV, Shevchenko EV (2010) Chem Rev 110:389–458. doi:10.1021/cr900137k
27. Nozik AJ, Beard MC, Luther JM, Law M, Ellingson RJ, Johnson JC (2010) Chem Rev 110:6873–6890. doi:10.1021/cr900289f
28. Konstantatos G, Sargent EH (2010) Nat Nanotechnol 5:391–400. doi:10.1038/nnano.2010.78
29. Wang F, Tan WB, Zhang Y, Fan X, Wang M (2006) Nanotechnology 17:R1–R13. doi:10.1088/0957-4484/17/1/R01
30. Bailey RE, Smith AM, Nie S (2004) Phys E Low Dimens Syst Nanostruct 25:1–12. doi:10.1016/j.physe.2004.07.013
31. Anson CE, Eichhöfer A, Issac I, Fenske D, Fuhr O, Sevillano P, Persau C, Stalke D, Zhang J (2008) Angew Chem Int Ed 47:1326–1331. doi:10.1002/anie.200704249
32. Liu Y, Najafabadi BK, Fard MA, Corrigan JF (2015) Angew Chem Int Ed 54:4832–4835. doi:10.1002/anie.201411944
33. Palchik O, Iyer RG, Liao JH, Kanatzidis MG (2003) Inorg Chem 42:5052–5054. doi:10.1021/ic034600l
34. Palchik O, Iyer RG, Canlas CG, Weliky DP, Kanatzidis MG (2004) Z Anorg Allg Chem 630:2237–2247. doi:10.1002/zaac.200400154
35. Qian YT, Gu YL, Lu J (2004) In: Rao CNR, Müller A, Cheethameds AK (eds) Chemistry of nanomaterials: synthesis, properties and application. Wiley-VCH, Weinheim; Wiley, Chichester, pp 170–207
36. Xu B, Wang X (2012) Dalton Trans 41:4719–4725. doi:10.1039/c2dt11842d
37. Xiong W-W, Zhang G, Zhang Q (2014) Inorg Chem Front 1:292–301. doi:10.1039/c4qi00013g
38. Wu T, Zuo F, Wang L, Bu X, Zheng S-T, Ma R, Feng P (2011) J Am Chem Soc 133:15886–15889. doi:10.1021/ja2066994
39. Wang Y-H, Luo W, Jiang J-B, Bian G-Q, Zhu Q-Y, Dai J (2012) Inorg Chem 51:1219–1221. doi:10.1021/ic202490q
40. Lin Y, Massa W, Dehnen S (2012) J Am Chem Soc 134:4497–4500. doi:10.1021/ja2115635
41. Wu T, Zhang Q, Hou Y, Wang L, Mao C, Zheng S-T, Bu X, Feng P (2013) J Am Chem Soc 135:10250–10253. doi:10.1021/ja404181c
42. Lin J, Zhang Q, Wang L, Liu X, Yan W, Wu T, Bu X, Feng P (2014) J Am Chem Soc 136:4769–4779. doi:10.1021/ja501288x
43. Wu T, Bu X, Liao P, Wang L, Zheng S-T, Ma R, Feng P (2012) J Am Chem Soc 134:3619–3622. doi:10.1021/ja210039u
44. Xiong W-W, Li J-R, Hu B, Tan B, Li R-F, Huang X-Y (2012) Chem Sci 3:1200–1204. doi:10.1039/c2sc00824f
45. Cheetham AK, Ferey G, Loiseau T (1999) Angew Chem Int Ed 38:3268–3292
46. Bu X, Zheng N, Feng P (2004) Chem Eur J 10:3356–3362. doi:10.1002/chem.200306041
47. Feng P, Bu X, Zheng N (2005) Acc Chem Res 38:293–303. doi:10.1021/ar0401754

48. Vaqueiro P (2010) Dalton Trans 39:5965–5972. doi:10.1039/c000130a
49. Wu T, Wang L, Bu X, Chau V, Feng P (2010) J Am Chem Soc 132:10823–10831. doi:10.1021/ja102688p
50. Dehnen S, Eichhöfer A, Fenske D (2002) Eur J Inorg Chem 279–317
51. Dehnen S, Eichhöfer A, Corrigan JF, Fenske D (2004) In: Schmid G (ed) Nanoparticles theory application. Wiley-VCH, Weinheim, pp 107–185
52. Fuhr O, Dehnen S, Fenske D (2013) Chem Soc Rev 42:1871–1906. doi:10.1039/c2cs35252d
53. Moller A, Amann P, Kataev V, Schittner N (2004) Z Anorg Allg Chem 630:890–894. doi:10.1002/zaac.200400034
54. Lin W-Q, Liao X-F, Jia J-H, Leng J-D, Liu J-L, Guo F-S, Tong M-L (2013) Chem Eur J 19:12254–12258. doi:10.1002/chem.201301397
55. Eichhöfer A, Fenske D (2000) J Chem Soc Dalton Trans 941–944. doi:10.1039/a909737f
56. Zheng NF, Bu XH, Lu HW, Zhang QC, Feng PY (2005) J Am Chem Soc 127:11963–11965. doi:10.1021/ja053588o
57. Li HL, Laine A, O'Keeffe M, Yaghi OM (1999) Science 283:1145–1147. doi:10.1126/science.283.5405.1145
58. Zhang Q, Bu X, Han L, Feng P (2006) Inorg Chem 45:6684–6687. doi:10.1021/ic060367q
59. Wu T, Bu X, Zhao X, Khazhakyan R, Feng P (2011) J Am Chem Soc 133:9616–9625. doi:10.1021/ja203143q
60. Wang L, Wu T, Zuo F, Zhao X, Bu X, Wu J, Feng P (2010) J Am Chem Soc 132:3283–3285. doi:10.1021/ja9100672
61. Li H, Kim J, O'Keeffe M, Yaghi OM (2003) Angew Chem-Int Ed 42:1819–1821. doi:10.1002/anie.200250748
62. Han X, Xu J, Wang Z, Liu D, Wang C (2015) Chem Commun 51:3919–3922. doi:10.1039/c5cc00084j
63. Du C-F, Li J-R, Zhang B, Shen N-N, Huang X-Y (2015) Inorg Chem 54:5874–5878. doi:10.1021/acs.inorgchem.5b00652
64. Su WP, Huang XY, Li J, Fu HX (2002) J Am Chem Soc 124:12944–12945. doi:10.1021/ja027830s
65. Wang C, Bu XH, Zheng NF, Feng PY (2002) J Am Chem Soc 124:10268–10269. doi:10.1021/ja020735z
66. Han X, Wang Z, Liu D, Xu J, Liu Y, Wang C (2014) Chem Commun 50:796–798. doi:10.1039/c3cc45439h
67. Lin Q, Bu X, Feng P (2014) Chem Commun 50:4044–4046. doi:10.1039/c4cc00583j
68. Zheng NF, Bu XH, Feng PY (2004) Angew Chem Int Ed 43:4753–4755. doi:10.1002/anie.200460386
69. Beecher AN, Yang X, Palmer JH, LaGrassa AL, Juhas P, Billinge SJL, Owen JS (2014) J Am Chem Soc 136:10645–10653. doi:10.1021/ja503590h
70. Herron N, Calabrese J, Farneth W, Wang Y (1993) Science 259:1426–1428. doi:10.1126/science.259.5100.1426
71. Bendova M, Puchberger M, Schubert U (2010) Eur J Inorg Chem 3299–3306. doi:10.1002/ejic.201000454
72. Feng M-L, Kong D-N, Xie Z-L, Huang X-Y (2008) Angew Chem Int Ed 47:8623–8626. doi:10.1002/anie.200803406
73. Lei Z-X, Zhu Q-Y, Zhang X, Luo W, Mu W-Q, Dai J (2010) Inorg Chem 49:4385–4387. doi:10.1021/ic902572m
74. Zeng X, Yao X, Zhang J, Zhang Q, Wu W, Chai A, Wang J, Zeng Q, Xie J (2015) Inorg Chem Front 2:164–169. doi:10.1039/c4qi00227j
75. Liu Y, Lin Q, Zhang Q, Bu X, Feng P (2014) Chem Eur J 20:8297–8301. doi:10.1002/chem.201402639
76. Xie J, Batten SR, Zou Y, Ren X (2011) Cryst Growth Des 11:16–20. doi:10.1021/cg100926g
77. Vossmeyer T, Reck G, Schulz B, Katsikas L, Weller H (1995) J Am Chem Soc 117:12881–12882. doi:10.1021/ja00156a035

78. Voggu R, Biswas K, Govindaraj A, Rao CNR (2006) J Phys Chem B 110:20752–20755. doi:10.1021/jp0653757
79. Dass A, Guo R, Tracy JB, Balasubramanian R, Douglas AD, Murray RW (2008) Langmuir 24:310–315. doi:10.1021/la702651y
80. Pengo P, Pasquato L (2015) J Fluor Chem 177:2–10. doi:10.1016/j.jfluchem.2015.03.005
81. Zhang Q, Lin Z, Bu X, Wu T, Feng P (2008) Chem Mater 20:3239–3241. doi:10.1021/cm702874s
82. Emge TJ, Romanelli MD, Moore BF, Brennan JG (2010) Inorg Chem 49:7304–7312. doi:10.1021/ic1002989
83. Holligan K, Rogler P, Rehe D, Pamula M, Kornienko AY, Emge TJ, Krogh-Jespersen K, Brennan JG (2015) Inorg Chem 54:8896–8904. doi:10.1021/acs.inorgchem.5b00452
84. Adams RD, Zhang B, Murphy CJ, Yeung LK (1999) Chem Commun 383–384. doi:10.1039/a809443h
85. Løver T, Bowmaker GA, Seakins JM, Cooney RP, Henderson W (1997) J Mater Chem 7:647–651. doi:10.1039/a607065e
86. Hiratani T, Konishi K (2004) Angew Chem Int Ed 43:5943–5946. doi:10.1002/anie.200461190
87. Nguyen KA, Pachter R, Day PN, Su H (2015) J Chem Phys 142:234305. doi:10.1063/1.4922320
88. Lebold TP, Stringle DLB, Workentin MS, Corrigan JF (2003) Chem Commun 1398–1399. doi:10.1039/b302829a
89. Wallbank AI, Borecki A, Taylor NJ, Corrigan JF (2005) Organometallics 24:788–790. doi:10.1021/om049238c
90. Ahmar S, MacDonald DG, Vijayaratnam N, Battista TL, Workentin MS, Corrigan JF (2010) Angew Chem Int Ed 49:4422–4424. doi:10.1002/anie.201000686
91. Tsuboi T, Takaguchi Y, Tsuboi S (2008) Chem Commun 76–78. doi:10.1039/b713680c
92. Fukunaga N, Konishi K (2015) Nanoscale 7:20557–20563. doi:10.1039/c5nr06307h
93. Zhou J, Bian G-Q, Zhang Y, Zhu Q-Y, Li C-Y, Dai J (2007) Inorg Chem 46:6347–6352. doi:10.1021/ic070334q
94. Ewing SJ, Romero ML, Hutchinson J, Powell AV, Vaqueiro P (2012) Z Anorg Allg Chem 638:2526–2531. doi:10.1002/zaac.201200255
95. Ewing SJ, Vaqueiro P (2015) Dalton Trans 44:1592–1600. doi:10.1039/c4dt02819h
96. Wang C, Bu XH, Zheng NF, Feng PY (2002) Angew Chem-Int Ed 41:1959–1961
97. Vaqueiro P (2008) Inorg Chem 47:20–22. doi:10.1021/ic701995p
98. Zheng NF, Bu XG, Wang B, Feng PY (2002) Science 298:2366–2369. doi:10.1126/science.1078663
99. Zheng NF, Bu XH, Feng PY (2003) Nature 426:428–432. doi:10.1038/nature02159
100. Vaqueiro P, Romero ML (2008) J Am Chem Soc 130:9630–9631. doi:10.1021/ja801619e
101. Xu C, Han Y-G, Duan T, Zhang Q-F, Leung W-H (2009) Inorg Chem Commun 12:1053–1056. doi:10.1016/j.inoche.2009.08.018
102. Zhang Q, Bu X, Lin Z, Wu T, Feng P (2008) Inorg Chem 47:9724–9726. doi:10.1021/ic800588q
103. Vaqueiro P, Romero ML, Rowan BC, Richards BS (2010) Chem Eur J 16:4462–4465. doi:10.1002/chem.200903425
104. Wang Y-H, Zhang M-H, Yan Y-M, Bian G-Q, Zhu Q-Y, Dai J (2010) Inorg Chem 49:9731–9733. doi:10.1021/ic100088n
105. Wang Y-H, Jiang J-B, Wang P, Sun X-L, Zhu Q-Y, Dai J (2013) Crystengcomm 15:6040–6045. doi:10.1039/c3ce40270c
106. Vaqueiro P, Romero ML (2009) Inorg Chem 48:810–812. doi:10.1021/ic8020723
107. Zheng N, Bu X, Lauda J, Feng P (2006) Chem Mater 18:4307–4311. doi:10.1021/cm060557z
108. Dance IG, Choy A, Scudder ML (1984) J Am Chem Soc 106:6285–6295. doi:10.1021/ja00333a030

109. Lee GSH, Fisher KJ, Craig DC, Scudder ML, Dance IG (1990) J Am Chem Soc 112:6435–6437. doi:10.1021/ja00173a063
110. Lee GSH, Craig DC, Ma I, Scudder ML, Bailey TD, Dance IG (1988) J Am Chem Soc 110: 4863–4864. doi:10.1021/ja00222a075
111. Vossmeyer T, Reck G, Katsikas L, Haupt E, Schulz B, Weller H (1995) Science 267:1476–1479. doi:10.1126/science.267.5203.1476
112. Gruber F (2012) Z Anorg Allg Chem 638:2467–2469. doi:10.1002/zaac.201200302
113. Yang X-L, Zhang J, Ren S-B, Li Y-Z, Du H-B, You X-Z (2010) Inorg Chem Commun 13:546–549. doi:10.1016/j.inoche.2010.02.001
114. Behrens S, Bettenhausen M, Eichhöfer A, Fenske D (1997) Angew Chem Int Ed 36:2797–2799. doi:10.1002/anie.199727971
115. Behrens S, Fenske D (1997) Berichte Bunsen Ges Phys Chem Chem Phys 101:1588–1592
116. Behrens S, Bettenhausen M, Deveson AC, Eichhöfer A, Fenske D, Lohde A, Woggon U (1996) Angew Chem Int Ed Engl 35:2215–2218. doi:10.1002/anie.199622151
117. Eichhöfer A, Hampe O (2007) J Clust Sci 18:494–504. doi:10.1007/s10876-007-0121-1
118. Lalatonne Y, Richardi J, Pileni MP (2004) Nat Mater 3:121–125. doi:10.1038/nmat1054
119. Min Y, Akbulut M, Kristiansen K, Golan Y, Israelachvili J (2008) Nat Mater 7:527–538. doi:10.1038/nmat2206
120. Bishop KJM, Wilmer CE, Soh S, Grzybowski BA (2009) Small 5:1600–1630. doi:10.1002/smll.200900358
121. Gamez P (2014) Inorg Chem Front 1:35–43. doi:10.1039/c3qi00055a
122. Zhao X-W, Qian L-W, Su H-C, Mo C-J, Que C-J, Zhu Q-Y, Dai J (2015) Cryst Growth Des 15:5749–5753. doi:10.1021/acs.cgd.5b00960
123. Bag S, Trikalitis PN, Chupas PJ, Armatas GS, Kanatzidis MG (2007) Science 317:490–493. doi:10.1126/science.1142535
124. Ferey G (2003) Angew Chem Int Ed 42:2576–2579. doi:10.1002/anie.20021621
125. Bu XH, Zheng NF, Li YQ, Feng PY (2003) J Am Chem Soc 125:6024–6025. doi:10.1021/ja030103s
126. Wu T, Khazhakyan R, Wang L, Bu X, Zheng S-T, Chau V, Feng P (2011) Angew Chem Int Ed 50:2536–2539. doi:10.1002/anie.201006531
127. Zheng NF, Bu XH, Feng PY (2003) J Am Chem Soc 125:1138–1139. doi:10.1021/ja021274k
128. Wu T, Wang X, Bu X, Zhao X, Wang L, Feng P (2009) Angew Chem Int Ed 48:7204–7207. doi:10.1002/anie.200903758
129. Wang L, Wu T, Bu X, Zhao X, Zuo F, Feng P (2013) Inorg Chem 52:2259–2261. doi:10.1021/ic301965w
130. Zhang Q, Zheng S-T, Bu X, Feng P (2012) Z Anorg Allg Chem 638:2470–2472. doi:10.1002/zaac.201200265
131. Xu G, Guo P, Song S, Zhang H, Wang C (2009) Inorg Chem 48:4628–4630. doi:10.1021/ic900376h
132. Brown ID, Altermatt D (1985) Acta Crystallogr Sect B Struct Sci 41:244–247. doi:10.1107/S0108768185002063
133. Brese NE, O'Keeffe M (1991) Acta Crystallogr Sect B Struct Sci 47:192–197. doi:10.1107/S0108768190011041
134. Zhang C, Liu J, Ji M, An Y (2014) Inorg Chem Commun 44:169–172. doi:10.1016/j.inoche.2014.03.028
135. Wang C, Li YQ, Bu XH, Zheng NF, Zivkovic O, Yang CS, Feng PY (2001) J Am Chem Soc 123:11506–11507. doi:10.1021/ja011739r
136. Xie J (2008) Inorg Chem 47:5564–5566. doi:10.1021/ic800721r
137. Zheng NF, Bu XH, Lu HW, Chen L, Feng PY (2005) J Am Chem Soc 127:14990–14991. doi:10.1021/ja055376x
138. Santner S, Dehnen S (2015) Inorg Chem 54:1188–1190. doi:10.1021/ic5026087
139. Freudenmann D, Wolf S, Wolff M, Feldmann C (2011) Angew Chem Int Ed 50:11050–11060. doi:10.1002/anie.201100904

140. Stieler R, Bublitz F, Burrow RA, Manzoni de Oliveira GN, Villetti MA, Pereira MB, Piquini P, Lang ES (2010) J Braz Chem Soc 21:2146–2154. doi:10.1590/S0103-50532010001100017
141. Levchenko TI, Kübel C, Huang Y, Corrigan JF (2011) Chem Eur J 17:14394–14398. doi:10.1002/chem.201102487
142. Levchenko TI, Kübel C, Wang D, Najafabadi BK, Huang Y, Corrigan JF (2015) Chem Mater 27:3666–3682. doi:10.1021/acs.chemmater.5b00586
143. Zhang XJ, Tian YP, Jin F, Wu JY, Xie Y, Tao XT, Jiang MH (2005) Cryst Growth Des 5:565–570. doi:10.1021/cg049695w
144. Jiang J-B, Bian G-Q, Zhang Y-P, Luo W, Zhu Q-Y, Dai J (2011) Dalton Trans 40:9551–9556. doi:10.1039/c1dt10860c
145. Fu M-L, Adams RD, Cristancho D, Leon-Plata P, Seminario JM (2011) Eur J Inorg Chem 660–665. doi:10.1002/ejic.201001062
146. Jiang J-B, Huo P, Wang P, Wu Y-Y, Bian G-Q, Zhu Q-Y, Dai J (2014) J Mater Chem C 2: 2528–2533. doi:10.1039/c3tc32093f
147. Zheng NF, Lu HW, Bu XH, Feng PY (2006) J Am Chem Soc 128:4528–4529. doi:10.1021/ja060006+
148. Li HL, Kim J, Groy TL, O'Keeffe M, Yaghi OM (2001) J Am Chem Soc 123:4867–4868. doi:10.1021/ja010413f
149. Vaqueiro P, Romero ML (2007) Chem Commun 3282–3284. doi:10.1039/b704724j
150. Yue C-Y, Lei X-W, Feng L-J, Wang C, Gong Y-P, Liu X-Y (2015) Dalton Trans 44:2416–2424. doi:10.1039/c4dt02864c
151. Pu Y-Y, Zhang X, You L-S, Bian G-Q, Zhu Q-Y, Dai J (2012) Z Anorg Allg Chem 638: 2498–2502. doi:10.1002/zaac.201200274
152. Melullis M, Clerac R, Dehnen S (2005) Chem Commun 6008–6010. doi:10.1039/b513305j
153. Zheng NF, Bu XH, Feng PY (2002) J Am Chem Soc 124:9688–9689. doi:10.1021/ja020480p
154. Ahamed BN, Arunachalam M, Ghosh P (2010) Inorg Chem 49:4447–4457. doi:10.1021/ic902300c
155. You J-F, Papaefthymiou GC, Holm RH (1992) J Am Chem Soc 114:2697–2710. doi:10.1021/ja00033a050
156. Müller A, Kögerler P, Dress AWM (2001) Coord Chem Rev 222:193–218. doi:10.1016/S0010-8545(01)00391-5
157. Kortz U, Müller A, van Slageren J, Schnack J, Dalal NS, Dressel M (2009) Coord Chem Rev 253:2315–2327. doi:10.1016/j.ccr.2009.01.014
158. Schäffer C, Todea AM, Bögge H, Floquet S, Cadot E, Korenev VS, Fedin VP, Gouzerh P, Müller A (2013) Dalton Trans 42:330–333. doi:10.1039/c2dt32247a
159. Seidlhofer B, Djamil J, Näther C, Bensch W (2011) Cryst Growth Des 11:5554–5560. doi:10.1021/cg201122e
160. Woodward P, Dahl L, Abel E, Crosse B (1965) J Am Chem Soc 87:5251–5253. doi:10.1021/ja00950a049
161. Fenske D, Fischer A (1995) Angew Chem Int Ed Engl 34:307–309. doi:10.1002/anie.199503071
162. Ivanov SA, Kozee MA, Merrill WA, Agarwal S, Dahl LF (2002) J Chem Soc Dalton Trans 4105–4115. doi: 10.1039/b204273h
163. Yamashina Y, Kataoka Y, Ura Y (2014) Inorg Chem 53:3558–3567. doi:10.1021/ic403050c
164. Zhang X, Pu Y-Y, You L-S, Bian G-Q, Zhu Q-Y, Dai J (2013) Polyhedron 52:645–649. doi:10.1016/j.poly.2012.07.092
165. Wang Y-H, Wu J, Zhao X-W, Qian L-W, Zhu Q-Y, Dai J (2015) Chem Commun 51:10668–10671. doi:10.1039/c5cc03404c
166. Huang-Fu S-X, Shen J-N, Lin H, Chen L, Wu L-M (2015) Chem Eur J 21:9809–9815. doi:10.1002/chem.201405719

Struct Bond (2017) 174: 321–374
DOI: 10.1007/430_2016_2

Published online: 21 July 2016

Inorganic Superspheres

Eugenia Peresypkina, Claudia Heindl, Alexander Virovets, and Manfred Scheer

Dedicated to Prof. Dr. Hansgeorg Schnöckel on the occasion of his 75th birthday

Abstract An intriguing inorganic analog of ferrocene, pentaphosphaferrocene [$Cp^R Fe(\eta^5\text{-}P_5)$] (R=Me, Et, CH_2Ph, PhC_4H_9), has the ability to coordinate Cu(I) moieties resulting in giant superspheres of 2.1–4.6 nm in diameter. Smaller hollow supramolecules follow icosahedral C_{80} or C_{140} fullerene topology being constructed of adjacent pentagonal *cyclo*-P_5 moieties and hexagonal Cu_2P_4 or P_2Cu_3Br rings. The same building units can also assemble to spherical and ellipsoid inorganic cores with different fullerene-related topologies. Larger supramolecules based on extended copper halide frameworks possess multilayered structures and form non-fullerene topologies. The size and solubility of the superspheres can be controlled through the variation of the steric demand of the cyclopentadienyl ligands at the pentaphosphaferrocene. The interconversion of supramolecules can be enabled in solution by changing the solvent mixtures. The quasi-spherical voids inside the supramolecules encapsulate various organic, inorganic, and organometallic guest molecules. Furthermore, the metallocene guests are involved in π-stacking with aromatic *cyclo*-P_5 systems of the supramolecular host. The crystals of the obtained supramolecules consist of similar co-crystallized forms, in which different isomerism and porosity can occur. The mutual arrangement of the

E. Peresypkina and A. Virovets
Institut für Anorganische Chemie, Universität Regensburg, Universitätsstr. 31, 93053 Regensburg, Germany

Nikolaev Institute of Inorganic Chemistry SB RAS, Ak. Lavrentiev prosp. 3, Novosibirsk 630090, Russia

C. Heindl and M. Scheer (✉)
Institut für Anorganische Chemie, Universität Regensburg, Universitätsstr. 31, 93053 Regensburg, Germany
e-mail: Manfred.Scheer@ur.de

supramolecules in the crystals is essentially controlled by halogen–Cp* σ–π and Cp*–Cp* π–π stacking interactions. This allows to regard these interactions as the supramolecular synthons. Besides the expected structural motifs typical for close sphere packings, such superspheres form also unusual and low-dense packing motifs.

Keywords Close packing • Copper • Pentaphosphaferrocene • Self-assembly • Supramolecular chemistry • Supramolecular synthons

Contents

1 Introduction

1.1 Clusters Based on Covalent Bonds

In physics, cluster as an intermediate between simple molecules and bulk solids might be simply described as an accumulation of atoms and/or molecules. However, in chemistry, they are mostly referred to polynuclear, often nano-sized compounds in some cases also bearing metal–metal bonds.

Polyoxometallates (POMs) known for almost 200 years are a prominent example in this field [1–4]. POMs are defined by MO_6 octahedra (M=Mo, W, V, Mn, etc.) connected via their vertices, edges, or faces to build up large anionic supramolecules with metals usually in their highest oxidation state. Most of these anions contain the basic structural motif of the Keggin ion, $[(XO_4)(M_{12}O_{36})]^{n-}$,

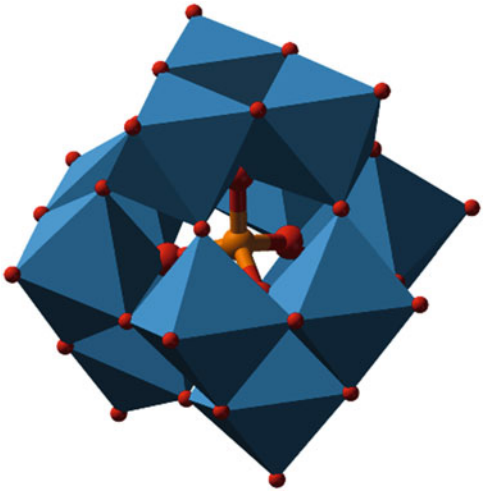

Fig. 1 Silicotungstic acid $H_4[SiW_{12}O_{40}]$ adopting a Keggin structure

X=P, Si, B, etc. (Fig. 1) [5]. Despite their early discovery, the exploration of its variety and applications is still intensively investigated, e.g., by contributions of A. Müller and L. Cronin et al. [1–3]. Among them the largest structurally characterized inorganic cluster is $[H_xMo_{368}O_{1032}(H_2O)_{240}(SO_4)_{48}]^{48-}$ (x~16), entitled "hedgehog," which reaches an outer diameter of ca. 6 nm [6, 7]. Not only POMs, rather metal oxide clusters in general are discussed in [8]. Furthermore, POMs bearing fivefold symmetric subunits are shortly discussed in Sect. 1.3.

Regarding the largest number of metal atoms, $[Ag_{490}S_{188}(StC_5H_{11})_{114}]$, synthesized by Fenske et al., displays the record holder among compounds characterized by single-crystal X-ray diffraction (SC-XRD) [9]. This spherical polynuclear complex and similar transition metal chalcogenide assemblies are assigned to the class of ligand-protected clusters (see [10]) [11, 12]. They are obtained by the reaction of silylated chalcogenide sources with copper and silver salts, respectively, and can be regarded as initial nanoparticles on the way to form binary phases, e.g., α-Ag_2Se [12]. In addition, they are capable of a surface modification to give, e.g., ferrocenyl-decorated nanoclusters [13].

Within the field of ligand-protected clusters, Schnöckel et al. established the class of "metalloid clusters" for compounds, which contain more metal–metal than metal–ligand bonds (see Chap. 6) [14–18]. They succeeded in the formation of $[Al_{50}Cp^*_{12}]$, where the Cp* ligands cover and protect the Al_{50} core [15], and also in $[Ga_{64}(GaR)_{20}]^{4-}$ (R=N(SiMe$_3$)$_2$) the largest structurally characterized Ga cluster so far [18]. This concept is expanded by Schnepf et al. to metalloid clusters of group 14 (see Chap. 6). Another approach to metalloid clusters is to extract discrete Zintl anions (e.g., $[Ge_9]^{4-}$) from the solid state. For example, Fässler and coworkers allow them to react with transition metal complexes to obtain linked compounds and intermetalloid clusters containing interstitial metal atoms or even whole cages [19]. This approach is extended by Dehnen and coworkers to ternary intermetalloid

cluster anions by using binary group 14/15 Zintl anions in combination with main group [20] and transition metal complexes [21], respectively (see [22]).

Concerning gold, a highlight is the X-ray crystal structure of $[Au_{102}(p\text{-}MBA)_{44}]$ (p-MBA=p-mercaptobenzoic acid) nanoparticle, in which the thiol ligands form a monolayer around the gold cluster [23]. Very recently, Dass et al. reported on the structural characterization of the even larger "nanomolecule" $[Au_{133}(SPh\text{-}^tBu)_{52}]$ bearing bulky and rigid ligands that comprise the outer shell and shield the inner gold core [24].

Furthermore, Dahl et al. were able to synthesize large Pd clusters like $[Pd_{145}(CO)_x(PEt_3)_{30}]$ containing an extended Pd core surrounded by phosphine and carbonyl ligands [25, 26]. They are constructed by different layers with interstitial metals to obey in the center the Mackay–Ikosaeder topology. Giant palladium clusters up to $[Pd_{561}L_{60}(OCOCH_3)_{180}]$ were also reported by Zamaraev et al. describing them as a bridge between molecular clusters and particles of colloidal metal [27]. The giant cluster was not structurally characterized and observed using high-resolution transmission electron microscopy.

1.2 Superspheres Based on Coordinative Bonds

All compounds described so far are hold together by covalent bonds and therefore are usually quite stable with the interactions being almost irreversible. In contrast, coordinative bonds are relatively strong, but often weak enough to show dynamic behavior in solution. These interactions are used in metallosupramolecular chemistry, which was established by Constable [28, 29], for example, with the spontaneous formation of dinuclear helicates from bipyridine and copper(I) [30]. This approach utilizes the self-assembly of two types of building blocks: metal salts or complexes bearing free coordination sites and acting as nodes and (mostly organic) Lewis bases with at least two donor atoms for linking the nodes (Fig. 2).

Until now, innumerable metallosupramolecular assemblies have been synthesized, including also discrete spherical clusters [31–38]. Depending on the denticity, rigidity, or flexibility, internal symmetry, and geometry of the building blocks, aggregates of different sizes and shapes can be obtained [39]. Some of these superspheres feature cavities suitable for the encapsulation of small molecules [40–45].

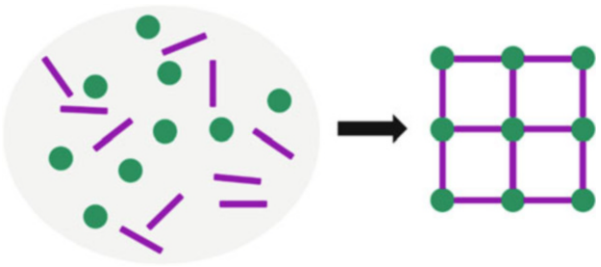

Fig. 2 Schematic representation of the self-assembly approach with nodes (*green*) and linkers (*purple*)

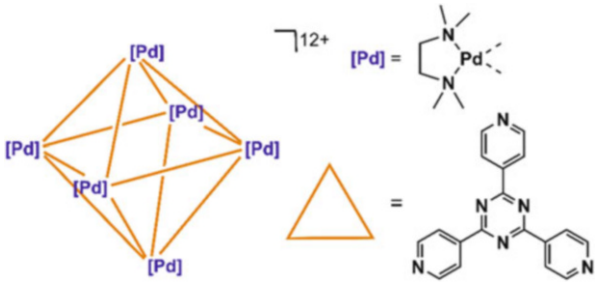

Fig. 3 Schematic representation of an octahedral-shaped cluster obtained by Fujita et al. using a tridentate linker

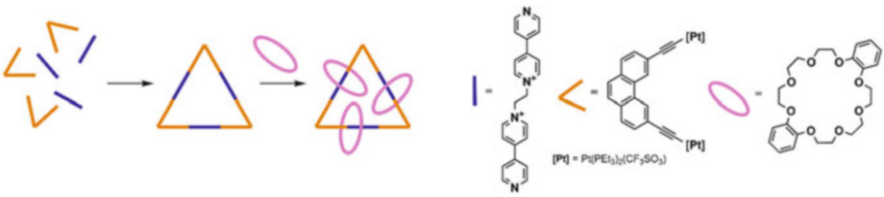

Fig. 4 Molecular necklace obtained by Stang et al.

Thereby, reactive intermediates have been stabilized in such cavities [43, 45, 46], and selected catalytic transformations have been carried out and accelerated inside such metallosupramolecular arrangements [44, 47–50]. Some selected examples are given below.

The group of Fujita obtained structural motifs ranging from tetrahedra, trigonal bipyramids to ball-like spheres and others by using Pd(II) moieties linked by one-, two-, three-, and even four-podale pyridyl ligands (Fig. 3) [51–57]. They are able to incorporate suitable guest molecules and can be applied as an unusual reaction vessel [52, 57], as it has been shown by irradiation of the crystals which initiate photoreactions of the included templates [57].

Recently an unprecedented application attracted special attention: A porous 3D network of cages can be applied as a crystalline sponge by reversible guest uptake of the molecules in the pores or cavities [58]. Another fascinating research area is pursued by Stang et al.: They focus on the formation of catenated systems, such as molecular "necklaces" by using pre-organized building blocks (Fig. 4) [59, 60].

Raymond et al. succeeded in the rational design of coordination clusters with high symmetry, such as M_4L_6 and M_4L_4 tetrahedra and M_8L_6 octahedra (M=tri-or tetravalent metal ion, L=bidentate chelator, Fig. 5) [35, 61–64]. With L being a chiral ligand, these anionic clusters turned out to be enantioselective catalysts for incorporated substrates.

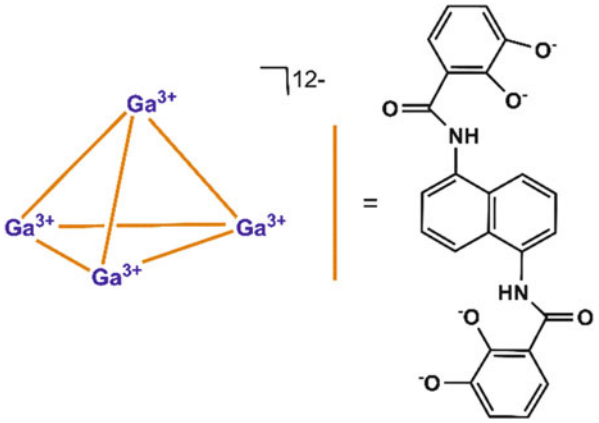

Fig. 5 M_4L_6 tetrahedron containing a tetradentate anionic linker

Fig. 6 C_{60} fullerene

1.3 Fivefold Symmetric Building Blocks

The ligands shown in Figs. 3, 4, and 5 display typical representatives of bi-, tri-, and tetradentate linking units, respectively [33, 34]. Thereby, the geometry of the spacer determines the shape of the supramolecular assembly either appearing as an edge (Figs. 4 and 5) or face (Fig. 3) of the resulting polyhedron. This enables the rational design of clusters [33–35, 39]. As a result, to design a spherical cluster of high symmetry, the use of fivefold symmetric building blocks seems to be one of the most promising approaches. Since an extended structure of pentagons is not possible, a curvature is the natural consequence [65].

The most prominent example for this is the group of fullerenes, the third allotropic modification of carbon [66–68]. They consist of 12 five-membered and (n-20)/2 six-membered carbon rings and form hollow structures and gain remarkable stability, obeying the isolated-pentagon rule. The smallest derivative fulfilling these conditions is the Buckminster fullerene C_{60} simultaneously being the first one discovered (Fig. 6) [69].

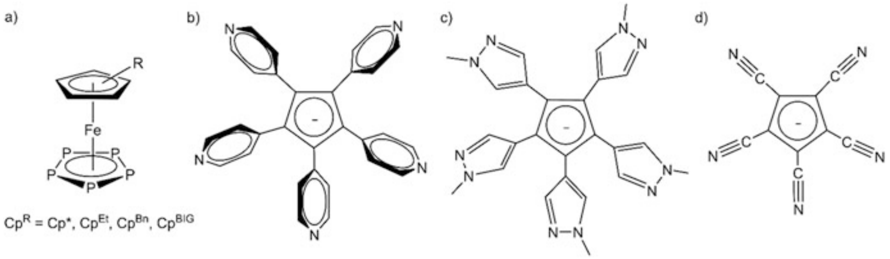

Fig. 7 Pentagonal fivefold symmetric building blocks used in metallosupramolecular chemistry: (**a**) pentaphosphaferrocenes, (**b**) pentakis(4-pyridyl)cyclopentadienyl, (**c**) pentakis-(1-methylpyrazole)cyclopentadienyl, and (**d**) pentacyanocyclopentadienyl

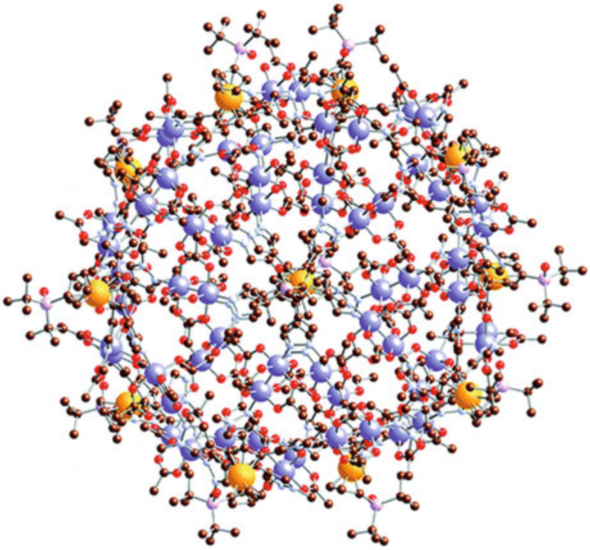

Fig. 8 Modeled structure of $[\{Rh_2(HCO_2)_4\}_{30}\{Fe(C_5(C_3H_2N_2CH_3)_5)(C_5H_4PO(t\text{-}C_4H_9)_2)\}_{12}]$. Reprinted with permission from [71]. Copyright 2015 American Chemical Society

Also in metallosupramolecular chemistry, the potential of pentagons to construct spherical structures has been recognized, even though only a few building blocks are known: The first and most intensively studied ones are the pentaphosphaferrocenes (Fig. 7a). Their capability of forming inorganic superspheres constitutes the main body of this chapter. Other fivefold symmetric ligands which are either based on nitrogen as donating element or on polyoxometalates are shortly described in the following.

Williams and coworkers reported on ferrocene derivatives containing the pentakis(4-pyridyl)cyclopentadienyl [70] (Fig. 7b) and pentakis-(1-methylpyrazole)cyclopentadienyl [71] ligand, respectively (Fig. 7c). Both the former in combination with $[Cu(CH_3CN)_4][PF_6]$ and the latter with a dirhodium(II) tetracarboxylate derivative can form fullerene-like spheres of the type $[(metal)_{30}(ligand)_{12}]$ (Fig. 8). However, these results are mainly based on diffusion

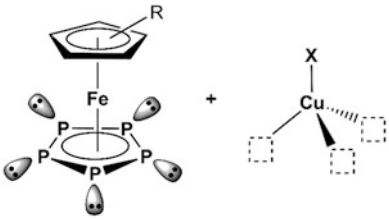

Fig. 9 Pentaphosphaferrocene as a pentadentate ligand in combination with Cu(I) halides as Lewis acids bearing three free coordination sites

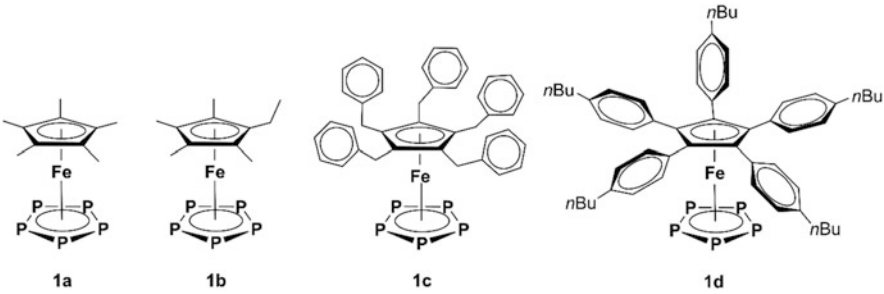

Fig. 10 Pentaphosphaferrocene derivatives **1a–d** used in metallosupramolecular chemistry

studies, light scattering experiments, and molecular modeling, and no single-crystal X-ray structural characterization has been reported.

On the other hand, the group of Wright succeeded in the construction of a salt-like three-dimensional MOF based on fullerene-like units of the pentacyanocyclopentadienyl anion $[C_5(CN)_5]^-$ (Fig. 7d) and sodium cations [72–74]. In this architecture, Na^+ forms pentagonal dodecahedral as well as tetradecahedral cages with the Cp ligands on the pentagonal faces.

Surprisingly, also polyoxometalates may contain units of fivefold symmetry and allow the formation of various Keplerate and fullerene-like structures. In these structures, the linkage of six $\{MoO_6\}$ octahedra with a $\{MoO_7\}$ pentagonal bipyramid creates the pentagonal $\{MoMo_5\}$ fragment [75]. When reacting with metal salts, icosahedral clusters of the general formula $[\{MoMo_5\}_{12}\{linker\}_{30}]$ (linker=e.g., Fe(III), Cr(III)) are obtained [2, 76–78].

Beside this, the linkage of pentaphosphaferrocenes is based on phosphorus as the donating element. Thereby, all linkers bear a *cyclo*-P_5^- ligand, the all-phosphorus analog of the cyclopentadienyl anion. In this, every phosphorus atom bears a lone pair available for coordination, which distinguishes this class of sandwich complex from the carbon derivative ferrocene (Fig. 9). Four derivatives $[Cp^RFe(\eta^5\text{-}P_5)]$ exhibiting an increasing steric demand are used in metallosupramolecular chemistry (Fig. 10): Cp^R=Cp*=η^5-C_5Me_5 (**1a**) [79, 80], Cp^{Et}=η^5-C_5Me_4Et (**1b**) [81], Cp^{Bn}=η^5-$C_5(CH_2Ph)_5$ (**1c**) [82], and Cp^{BIG}=η^5-$C_5(4\text{-}^n BuC_6H_4)_5$ (**1d**) [83].

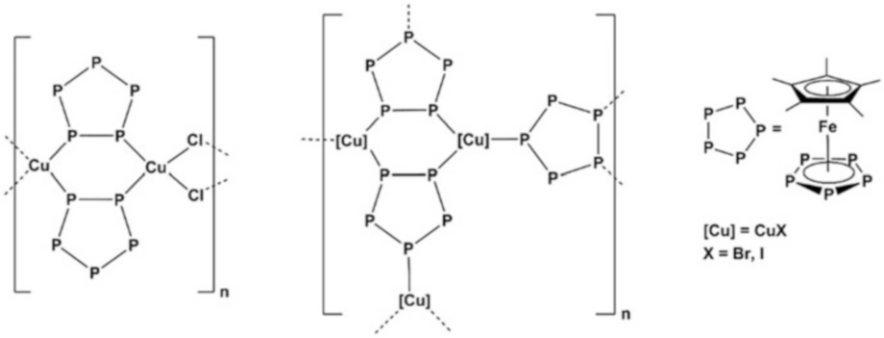

Fig. 11 1D and 2D polymers consisting of **1a** and CuX (X=Cl, Br, I) [87]

As Lewis acid, Cu(I) halides turned out to be an excellent building block, mainly due to two reasons: These salts are known as a versatile family in coordination chemistry as well as crystal engineering, since they are capable of forming diverse aggregates like rings, cubes, ladderlike structures, zigzag chains, large clusters, etc. [84–86]. Furthermore, as Cu(I) prefers a tetrahedral coordination environment, CuX (X=Cl, Br, I) units can be seen as tetrahedral four-connected nodes with three free coordination sites (Fig. 9).

First investigations regarding the coordination behavior of the pentaphosphaferrocene **1a** toward Cu(I) salts gave 1D and 2D polymers with well-known $\{Cu_2X_2\}$ (X=Cl, Br, I) four-membered and $\{Cu_2P_4\}$ six-membered rings (Fig. 11) [88]. In the case of CuCl, a 1,2-coordination of the P_5 ring is present, whereas in the bromide and iodide derivatives, the coordination of a further P atom (1,2,4-coordination) leads to a 2D network. By varying the solvent mixtures and the stoichiometric ratios, a variety of different polymeric products bearing also other coordination modes of the *cyclo*-P_5 ligand, 1,3-coordination, 1,2,3-coordination, and 1,2,3,4-coordination, could be isolated [87]. Also the 1,2,3,4,5-coordination, where every phosphorus atom is used for coordination, is observed: In this case, besides the formation of a 1D tubular polymeric structure [87], the desired curvature is obtained and inorganic closed-shell superspheres form, which are described in the following sections.

1.4 Synthesis of the Pentaphosphaferrocene-Derived Superspheres

In general, all pentaphosphaferrocene-derived clusters discussed in this chapter (Table 1) can be synthesized and crystallized via diffusion reactions within thin Schlenk tubes: Thereby, a dark green solution of the pentaphosphaferrocene (plus the template, if there is one) in dichloromethane, toluene, or *ortho*-dichlorobenzene, respectively, is layered with a colorless solution of the Cu(I) halide in acetonitrile or

Table 1 Structurally characterized pentaphosphaferrocene-based supramolecules

No	Formula	Refcode[a]	Size (nm)	Cavity (nm)	References
2.1.1	Superspheres with I_h-C_{80} topology				
2	$(CH_2Cl_2)@[(Cp^{Bn}FeP_5)_{12}(CuCl)_{20}]\cdot 4.8C_7H_8$	IHAQEP	3.14	0.82	[89]
3	$(CH_2Cl_2)@[(Cp^{Bn}FeP_5)_{12}(CuBr)_{18.44}]\cdot 4.8C_7H_8$	IHAQIT	3.14	0.82	[89]
4	$(CH_2Cl_2)@[(Cp^{Bn}FeP_5)_{12}(CuBr)_{15.59}]\cdot 4.8C_7H_8$	IHAQOZ	3.14	0.82	[89]
5	$(CH_2Cl_2)@[(Cp^{Bn}FeP_5)_{12}(CuBr)_{18.53}]\cdot 4.8C_7H_8$	IHASER	3.14	0.82	[90]
6	$(CH_2Cl_2)@[(Cp^{Bn}FeP_5)_{12}(CuCl)_{15.2}]\cdot 4.8C_7H_8$	IHARUG	3.14	0.82	[89]
7	$(CH_2Cl_2)@[(Cp^{Bn}FeP_5)_{12}(CuCl)_{18.56}]\cdot 4.8C_7H_8$	IHARAM	3.14	0.82	[89]
8	$(CH_2Cl_2)@[(Cp^{Bn}FeP_5)_{12}(CuCl)_{18.8}]\cdot 4.8C_7H_8$	IHAREQ	3.14	0.82	[89]
9	$(CH_2Cl_2)@[(Cp^{Bn}FeP_5)_{12}(CuCl)_{17.6}]\cdot 4.8C_7H_8$	IHARIU	3.14	0.82	[89]
10	$(CH_2Cl_2)@[(Cp^{Bn}FeP_5)_{12}(CuCl)_{19.0}]\cdot 4.8C_7H_8$	IHAROA	3.14	0.82	[89]
11	$Cp_2Fe@[(Cp^{Bn}FeP_5)_{12}(CuCl)_{18.68}]\cdot 4.8C_7H_8$	IHASAN	3.14	0.82	[90]
12	$(o\text{-}C_2B_{10}H_{12})_{0.5}@[(Cp^*FeP_5)_{12}(CuCl)_{20}]$	SURYIO	2.30	0.82	[91]
13	$Cp_2Fe@[(Cp^*FeP_5)_{12}(CuCl)_{20}]$	TATTOZ	2.30	0.77	[89]
14	$CpCrAs_5@[(Cp^*FeP_5)_{12}(CuCl)_{20}]$	TATTUF	2.30	0.78	[89]
15	$(o\text{-}C_2B_{10}H_{12})_{0.5}@[(Cp^*FeP_5)_{12}(CuBr)_{18.8}]\cdot 3.82C_7H_8\cdot 2.23MeCN$	KUCJAV	2.30	0.81	[92]
16	$(o\text{-}C_2B_{10}H_{12})_{0.5}@[(Cp^*FeP_5)_{12}(CuBr)_{18.8}]\cdot 7.33C_7H_8\cdot 0.67MeCN$	KUCJEZ	2.30	0.81	[92]
2.1.2	Superspheres with I-C_{140} topology				
17	$[\{Cp^{BIG}FeP_5\}_{12}Cu_{69.45}Br_{82.70}]\cdot 0.34CH_2Cl_2\cdot 1.3MeCN$	YUZQOB	3.50	0.47	[93]
2.2.1	90-vertex superspheres and their structural modifications				
18	$[Cu(MeCN)_4]^+[\{Cp^*FeP_5\}_{0.5}@(Cp^*FeP_5)_{12}(CuCl)_{25}(MeCN)_{10}]_3\ \{Cp^*FeP_5\}_{0.5}@[(Cp^*FeP_5)_{12}Cu_{24}Cl_{25}(MeCN)_8]^-\cdot 34CH_2Cl_2$	BAPFOO	2.40–2.46	0.61–0.64	[94, 95]
19	$[Cp^*FeP_5]_{0.5}@[(Cp^*FeP_5)_{12}(CuCl)_{25}(MeCN)_{10}]\cdot 6CH_2Cl_2\cdot 1.5MeCN$	GUSKIP	2.36–2.50	0.60–0.65	[94]
20	$[Cp^*FeP_5]_{0.6}@[(Cp^*FeP_5)_{12}(CuCl)_{25}(MeCN)_{10}]\cdot 9.5THF\cdot 2MeCN$	GUSKOV	2.42–2.48	0.64–0.65	[94]
21	$[Cp^*FeP_5]_{0.5}@[(Cp^*FeP_5)_{12}Cu_{25}Cl_{24}(MeCN)_9]$ $[Cp^*FeP_5]0.5@[(Cp^*FeP_5)_{12}Cu_{25}Cl_{26}(MeCN)_9]\cdot 12C_7H_8\cdot 1.5MeCN$	GUSKUB	2.46–2.48	0.61–0.64	[94]
22	$[Cp^{Et}FeP_5]@[(Cp^{Et}FeP_5)_{12}(CuBr)_{25}(MeCN)_{10}]\cdot 2CH_2Cl_2\cdot 1.5MeCN$	TAXDAY	2.42–2.70	0.58–0.66	[94, 96]

23	$[Cp^*FeP_5]@[(Cp^*FeP_5)_{12}(CuBr)_{25}(MeCN)_{10}] \cdot 2.9C_6H_4Cl_2 \cdot 3.9MeCN$	GUSLAI	2.40–2.48	0.58–0.66	[94]
24	$[Cp^*FeP_5]@[(Cp^*FeP_5)_{12}(CuBr)_{25}(MeCN)_{10}] \cdot 2.1C_6H_4Cl_2 \cdot MeCN$	GUSLEM	2.46–2.50	0.59–0.66	[94]
25	$[Cp^*FeP_5]@[(Cp^*FeP_5)_{12}(CuBr)_{25}(MeCN)_{10}] \cdot 10.4C_7H_8 \cdot 0.8MeCN$	GUSLIQ	2.42–2.50	0.60–0.66	[94]
26	$[Cp^*FeP_5]@[(Cp^*FeP_5)_{12}(CuBr)_{25}(MeCN)_{10}] \cdot 5C_7H_8 \cdot 17.7MeCN$	GUSLOW	2.46–2.50	0.60–0.66	[94]
27	$[Cp_2Cr_2(\mu,\eta^5\text{-}As_5)]@[(Cp^*FeP_5)_{12}(CuBr)_{25}(MeCN)_{10}] \cdot 10C_7H_8 \cdot 3MeCN$	TATVAN	2.46–2.50	0.62–0.63	[90]
28	$[Cp^*FeP_5]@[(Cp^*FeP_5)_9\{CuCl\}_{10}] \cdot 2C_7H_8$	OLIWIQ	2.45–3.02	0.80–1.50	[97]
2.2.2	99-vertex supersphere				
29	$C_{60}@[(Cp^*FeP_5)_{13}(CuCl)_{26}(H_2O)_2(CH_3CN)_9] \cdot 6C_6H_4Cl_2 \cdot MeCN$	COVBAR	2.58	1.35	[98]
2.3.1	100-vertex supersphere				
30	$P_4@[(Cp^*FeP_5)_{10}(CuI)_{30.1}(MeCN)_6] \cdot 2MeCN$	DISCUF	2.08–3.33	0.37–1.00	[99]
31	$As_4@[(Cp^*FeP_5)_{10}(CuI)_{29.6}(MeCN)_6] \cdot 4.2MeCN$	DISCOZ	2.09–3.41	0.37–1.00	[99]
2.3.2	162-vertex supersphere				
32	$[(Cp^{Bn}FeP_5)_{12}(CuBr)_{51}(MeCN)_8]$	IHAQUF	3.56	–	[89]
2.3.3	168-vertex supersphere				
33	$(CH_2Cl_2)_{3.4}@[(Cp^{Bn}FeP_5)_{12}\{CuI\}_{54}(MeCN)_{1.46}]$	BORDOD	3.70	0.75	[100]
2.3.4	312-vertex supersphere				
34	$[(Cp^{Bn}FeP_5)_{24}(CuBr)_{96}] \cdot 6.2CH_2Cl_2 \cdot 4.6C_7H_8 \cdot 2.4MeCN$	SURMID	3.70–4.60	1.20–2.50	[101]
2.4	Supramolecule with nonclassical fullerene topology				
35	$[(Cp''Ta(CO)_2(P_4))_6\{CuCl\}_8] \cdot CH_2Cl_2$	TEFNUO	2.19	0.44–0.60	[102]

[a]Reference code in the Cambridge Structural Database (CSD) [103]

mixtures of dichloromethane and acetonitrile. In doing so, the phase boundary turns yellow brownish in the case of X=Cl, Br or orange for X=I. To lower the crystallization rate, an intermediate layer of the pure solvent mixture might be required sometimes. Especially for pentaphosphaferrocenes with a rather small steric demand, such as **1a**, this diffusion method is strictly required, since all clusters obtained are insoluble in common organic solvents or only show a low solubility in CH_2Cl_2/CH_3CN mixtures (**18–27**). In these reactions, big crystals (prisms, rods) of the cluster often start to grow at the interface already after several hours. Unfortunately, the formation of the polymeric coordination products (cf. Sect. 1) cannot be avoided completely. A higher molar ratio of **1a**:CuX than 1:1 (as it is present in the polymers) and diluted conditions are in favor of the inorganic spheres. The yield of isolated crystalline product is usually in the range of 20–50 %.

When the organic shell contains the sterically demanding pentaphosphaferrocenes **1c** and **1d**, the supramolecules show a good solubility mostly in CH_2Cl_2. Hence, they can also be synthesized by stirring the starting materials in pure CH_2Cl_2 or in CH_2Cl_2/CH_3CN solvent mixtures. As the Cp^{Bn} and Cp^{BIG} derivatives do not form polymers in combination with copper halides, the self-assembly of the spherical cluster is mostly quantitative and the products can be isolated in excellent yields of >90 %.

2 Topologies

In the following, the structures of spherical supramolecules derived from pentaphosphaferrocenes are described focusing on the cage topology and its relation to fullerenes. Thereby, classical fullerenes are "cage-like, hollow molecules of pseudospherical symmetry consisting of pentagons and hexagons only, resulting in a convex polyhedron with exactly three edges (bonds) joining every vertex occupied by carbon, idealized as sp^2-hybridized atoms" [104, 105]. Hence, every cluster fulfilling these structural conditions will be assigned to a sphere of fullerene topology in this chapter irrespective of the element it is formed of (Sect. 2.1). If these requirements are only met by the main part of the cluster also exhibiting characteristic deviations from this topology, they will be named "fullerene-like" spheres and discussed in Sect. 2.2. In the case of predominance of non-fullerene structural motifs, where only the *cyclo*-P_5 ligands resemble the fullerene topology, the superspheres are summarized as clusters "beyond the fullerene topology" in Sect. 2.3. In literature, the definition of fullerenes sometimes is broadened with regard to different ring sizes. These spherical derivatives may also contain, for example, heptagons and/or squares and are often regarded as "nonclassical fullerenes" [69, 106, 107]. A cluster, which falls into this category, is described in Sect. 2.4.

2.1 Superspheres with Fullerene Topologies

2.1.1 I_h-C_{80} Topology

In contrast to ferrocene, every phosphorus atom of pentaphosphaferrocenes still bears a lone pair and is therefore capable of a further coordination to a Lewis acid like Cu(I). Due to the fivefold symmetry of the *cyclo*-P_5 ligand and a preferred tetrahedral coordination of the copper atoms, the buildup of fullerene-like spheres is enabled.

In C_{60}, the smallest fullerene obeying the isolated-pentagon rule only one bond between two five-membered rings is present (Fig. 12 left). However, a direct linkage of two pentaphosphaferrocenes via coordinative bonds is not possible, since at least one copper atom as Lewis acid has to be present between them. Therefore, the smallest fullerene-like derivative resembles the C_{80} fullerene, where one additional atom is present between two pentagons (Fig. 12 middle). With different ring combinations, seven C_{80} isomers obeying isolated-pentagon rule are conceivable: D_{5d}, C_{2v}(I), D_2, C_{2v}(II), D_{5h}, D_3, and I_h [66–68]. Interestingly, the calculated energy difference between the first six of them is less than 30 kJ/mol, whereas the I_h-C_{80} isomer (Fig. 12 middle) displays the most unstable one (72 kJ/mol more in energy than the D_{5d} isomer) [108]. Therefore, it is not surprising that the icosahedral I_h-C_{80} cannot be simply extracted from soot as the other derivatives [109, 110], yet it is obtained as endohedral metallofullerene [111, 112], e.g., in $Sc_3N@I_h$-C_{80} [113], $Sc_4O_2@I_h$-C_{80} [114], and $La_2@I_h$-C_{80} [115].

In the case of the superspheres, the combination of the pentaphosphaferrocenes **1a** and **1c** and CuX (X=Cl, Br), respectively, leads to the formation of an icosahedral 80-vertex cluster $[\{Cp^RFe(\eta^5\text{-}P_5)\}_{12}(CuX)_{20}]$ (**2–16**; Cp^R=Cp*, Cp^{Bn}; X=Cl, Br) [89–92]. Thereby, each pentaphosphaferrocene unit shows a 1,2,3,4,5-coordination mode to copper. In turn, the copper ion is bound by three phosphorus atoms and a halide atom as a terminal ligand so that Cu accomplishes its distorted tetrahedral environment. In total, the cluster exhibits 12 **1a/b** units which are linked by 20 CuX moieties. Hence, the 80-vertex framework of 12 five-membered P_5 and 30 six-membered Cu_2P_4 rings displays an entirely carbon-free I_h-C_{80} fullerene

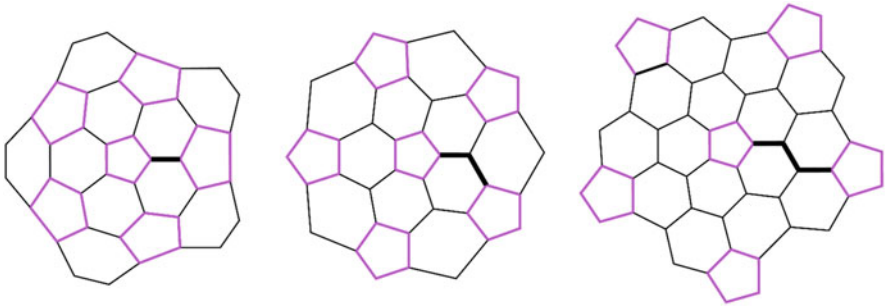

Fig. 12 2D projections of fullerene topologies: C_{60} (*left*), I_h-C_{80} (*middle*) and *I*-C_{140} (*right*)

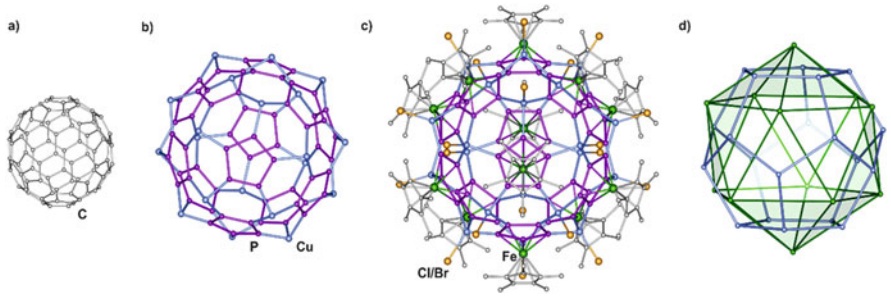

Fig. 13 (**a**) I_h-C_{80}, (**b**) $Cu_{20}P_{60}$ scaffold, and (**c**) complete 80-vertex supersphere containing **1a** and (**d**) polyhedra in $Cu_{20}P_{60}$ scaffold

analog (Fig. 13a–c). Within the supersphere, the Fe atoms which are centered above the *cyclo*-P_5 ligands form an icosahedron, whereas the Cu atoms are located at the vertices of a pentagonal dodecahedron (Fig. 13d).

The inner cavity of the 80-vertex supersphere appears to be spherical in shape with an approximate diameter of 0.8 nm irrespective of the halide used and the substitution pattern of the pentaphosphaferrocene.[1] In contrast, the outer diameter differs widely depending on the size of the Cp^R ligand: It amounts to 2.2–2.3 nm for the derivatives containing **1a** (**12–16**), whereas it is 3.1 nm for those containing the large benzyl ligand **1c** (**2–11**) (Fig. 14). Therefore, the diameter of **1a**-based superspheres is twice and **1c**-based superspheres almost triply as big when compared to the C_{80} with a diameter of 1.1 nm.

In the case of the superspheres **12–16**, applying the pentaphosphaferrocene **1a** and CuX as building blocks, a template-directed approach is crucial for their formation. Therefore, small molecules were added as template to yield the host–guest complexes (template)@[{Cp*Fe(η^5-P_5)}$_{12}${CuX}$_{20}$], X=Cl (**12–14**), Br (**15**, **16**). So far, *o*-carborane (0.79 nm) [91, 92], ferrocene [Cp_2Fe] (0.69 × 0.63 nm) [90], and the sandwich complex [CpCr(η^5-As_5)] (0.69 × 0.75 nm) [90] all with an appropriate size were successfully incorporated in the cavity of the 80-vertex supramolecule (0.8 nm) (Fig. 15). Interestingly, the latter two compounds reveal host–guest π–π stacking interactions of the sandwich complexes (P_5–Cp in **13**; P_5–As_5 in **14**). In the absence of a possible guest molecule, the formation of the

[1] The inner diameters of the cavities were calculated as geometrically opposing atomic distances, minus the van der Waals radii of the respective atoms (e.g., P, 1.80 Å; Cu, 1.40 Å). The term "diameter" is defined here as the diameter of the largest spherical form that is geometrically allowed inside the cavity by the given atoms. The outer diameter is taken as twice the largest distance from the theoretical center of the molecule to the farthest atom, plus twice the van der Waals radius for the respective atom (e.g., H, 1.2 Å).

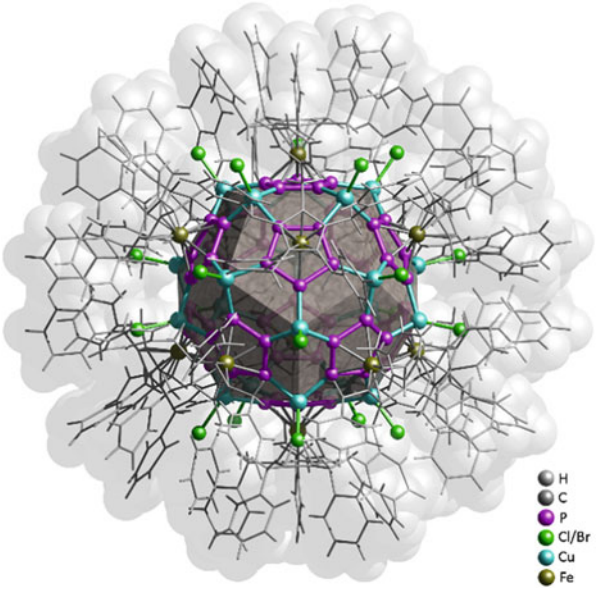

Fig. 14 Molecular structure of **1c**-based supersphere (**2**–**11**)

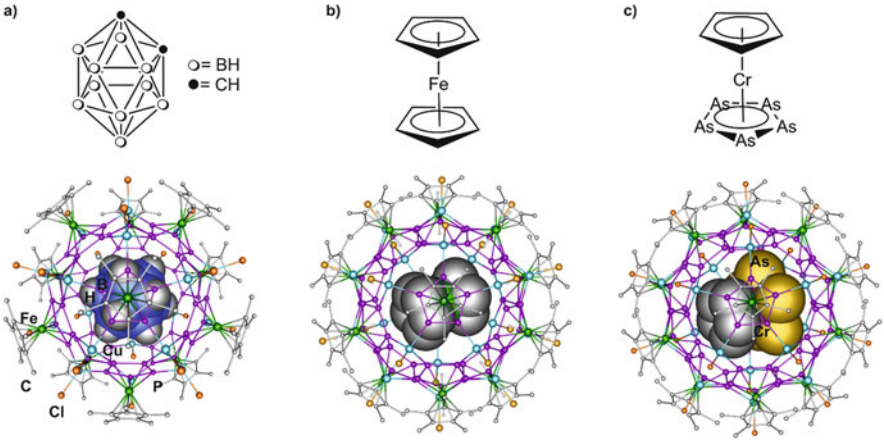

Fig. 15 Templates for the formation of spherical clusters with C_{80} topology **1a**-derived 80-vertex superspheres (**12**–**14**)

polymeric coordination products (Sect. 1.3) is observed. Remarkably, the self-assembly processes of **1c** and CuX (X=Cl, Br) exclusively lead to the formation of inorganic superspheres even in the absence of a template. In the case of **2**–**10**, the inner cavity is filled with one dichloromethane solvent molecule disordered over 32 positions [89].

2.1.2 *I*-C_{140} Topology

The sterically more demanding building block [$Cp^{BIG}Fe(\eta^5\text{-}P_5)$] (**1d**) is also capable of forming clusters with fullerene topology [93]. However, the bulkiness of **1d** leads to a "cluster expansion," and the resulting supersphere **17** shows the same structural topology as the theoretically predicted C_{140} fullerene (Fig. 16). The idealized scaffold of this carbon-free analog consists of 12 *cyclo*-P_5 ligands (60 P), 60 copper and 20 bromine atoms forming 60 six-membered P_2Cu_3Br rings. Therefore, in contrast to the 80-vertex superspheres, some of the halide ligands are now also scaffold constructing and not only terminal. Out of the innumerable isomers possible for the C_{140} fullerene, the icosahedral *I*-C_{140} has been calculated to be the lowest in energy [116, 117]; however it could not be detected so far [118, 119]. In the case of **17**, the inorganic scaffold shows icosahedral symmetry albeit distorted due to the presence of different types of atoms. Note that the polyhedra are idealized because of disorder of the copper and halide ions (see Sect. 3.2 for details).

Another feature of **17** is the multi-shell structure which is unprecedented among the pentaphosphaferrocene-based clusters. The bridging bromides and η-coordinated Cu cations that have not been observed before in structures of supramolecules both support the shell structure. Within the outer shell of the *I*-C_{140} scaffold, a pentagonal dodecahedron of 20 Cu atoms is formed with 30 Br atoms at the edges (Fig. 16b). Additionally as a third shell, a Br_{12} icosahedron displays the central inner core (Fig. 16a). In total, **17** represents an "onion-like" cluster of an icosahedron@dodecahedron@*I*-C_{140}. Due to this structural feature, no empty inner cavity is present capable of a guest encapsulation. The outer diameter including the Cp^{BIG} ligands reaches an impressive value of 3.5 nm (Fig. 16d). The "space-filling" view of **17** exhibits a tight arrangement of the 12 Cp^{BIG} ligands forming a distorted pentagon dodecahedron.

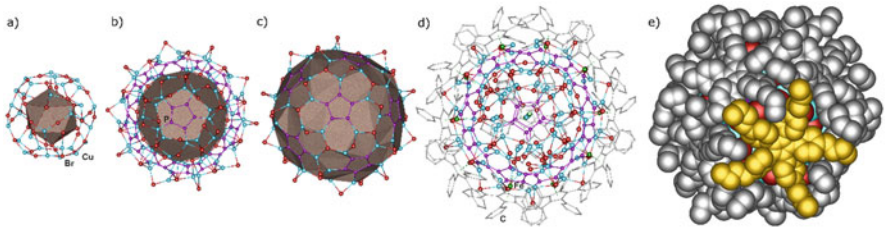

Fig. 16 Multi-shell structure of **17**. One of Cp^{BIG} ligands is highlighted

2.2 *Superspheres with Fullerene-Like Topologies*

2.2.1 90-Vertex Superspheres and Their Structural Modifications

90-vertex superspheres naturally extend the C_{80} fullerene topology represented by 80-vertex spheres. The structural relation between them can be traced back to the largest structural unit they have in common which is a 40-vertex hemisphere $[\{Cp^*Fe(\eta^5\text{-}P_5)\}_6(CuX)_{10}]$ (X=Cl, Br) formed by six five-membered P_5 and ten six-membered Cu_2P_4 rings (Fig. 17a). At the rim the shell has five phosphorus and five copper atoms available for further coordination. Two such fragments would comprise a whole 80-vertex sphere, if fused in that way that every Cu atom connects to a P atom of the other shell. This would require a rotation of the hemispheres by 36° (360°/10) leading to a staggered orientation (Fig. 17c).

If two hemispheres are in eclipsed orientation, the P and Cu atoms face the atoms of the same chemical sort. To avoid this during the self-assembly process, additional X atoms coordinate copper, and $\{Cu(MeCN)_2\}^+$ fragments connect the P atoms. Therefore, ten additional vertices extend the fullerene-like hemispheres, and the 90-vertex supramolecules $[\{Cp^RFe(\eta^5\text{-}P_5)\}_{12}\{CuX\}_{25}(MeCN)_{10}]$ (**18–21**, X=Cl; **22–27**, X=Br; Cp^R=Cp*, Cp^{Et}) are formed (Fig. 17d) [94–96].

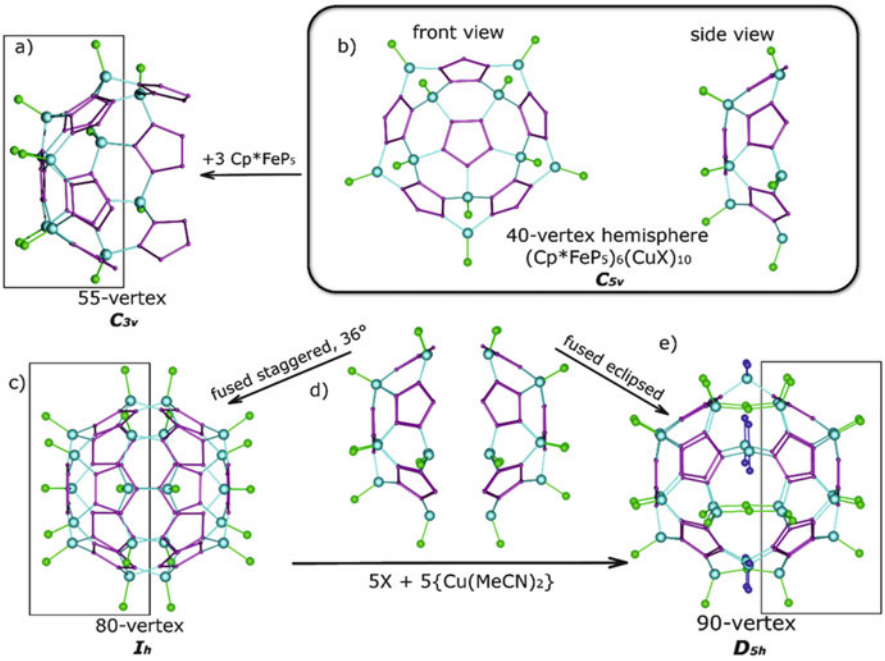

Fig. 17 Structural interrelation between a (**b**) nano-capsule $\{(Cp^*FeP_5)_6(CuX)_{10}\}$ (**28**) and (**c**) 80- and (**d**) 90-vertex superspheres (**18–27**) as a different combination of (**a**) two 40-vertex hemispheres $\{(Cp^*FeP_5)_6(CuX)_{10}\}$

The additional vertices form an *equatorial* part of ten eight-membered Cu_3P_4X rings violating the fullerene topology. The plane of the equator and the direction of the pseudo fivefold axis can naturally be called *equatorial* and *axial*, respectively. The 90-vertex moiety, in which the shells of C_{5v} symmetry are related by a mirror plane, possesses D_{5h} point symmetry. These types of superspheres were only observed with the pentaphosphaferrocenes **1a** and **1b**.

The 40-vertex hemispheres alone have not been observed so far. However, the closest example can be found in the structure of the nano-capsule, $\{Cp^*Fe(\eta^5\text{-}P_5)\}_2@[\{Cp^*Fe(\eta^5\text{-}P_5)\}_9(CuCl)_{10}]_2$ (**28**) [97]. The half-shell of the nano-capsule can also be viewed as a hemisphere with three pentaphosphaferrocenes additionally coordinated on the same hemisphere's side (Fig. 17b). The point symmetry C_{3v} is realized due to a central copper atom coordinating three pentaphosphaferrocene units (Fig. 18a). The host–guest complex **28** consists of two semispherical shells connected by a number of specific intermolecular P–P contacts of 3.61–4.50 Å and possesses 3.0 nm in length (Fig. 18c). The cohesion energy according to DFT and MP2 calculations is about -36 kJ mol^{-1} [97]. The inner cavity amounts to 1.5 nm in the longest of its axes. Interestingly, inside the nano-capsule two pentaphosphaferrocene molecules act as a single template where the Cp* ligands are π–π stacked and form an interplanar distance of 3.67 Å. This is in contrast to the 90-vertex supramolecules, where for steric reasons only one template of a pentaphosphaferrocene can be included into the cavity [94–96]. For the same reason, unique P_5–P_5 interactions were realized in all crystal structures of the 90-vertex supramolecules containing no other guests than pentaphosphaferrocene, which always is in excess in the reaction mixture.

Since the size of the cavity of the 90-vertex superspheres is larger than the pentaphosphaferrocene dimensions, the guest molecule is usually disordered over two or three positions [94]. In contrast to the 80-vertex supramolecules, the interior of the 90-vertex shell is elongated in equatorial direction, and therefore, not all possible orientations of the guest molecules are equivalent. One can subdivide them into two *axial* and ten *equatorial* ones, referring to the direction, to which the axis of the guest molecule is parallel. Both orientations can even occur statistically in the same host molecule (Fig. 19). Among all known complexes, the host and guest

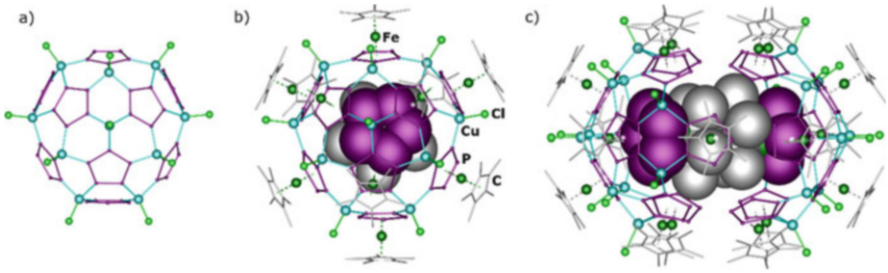

Fig. 18 The nano-capsule $\{(Cp^*FeP_5)_9(CuX)_{10}\}$ (**28**) [97]: (**a**) half-shell (*top view*), (**b**) half-shell and a guest molecule (*space filling*) displaying no π–π stacking interactions with host molecule, and (**c**) nano-capsule embracing two π–π stacked guest molecules

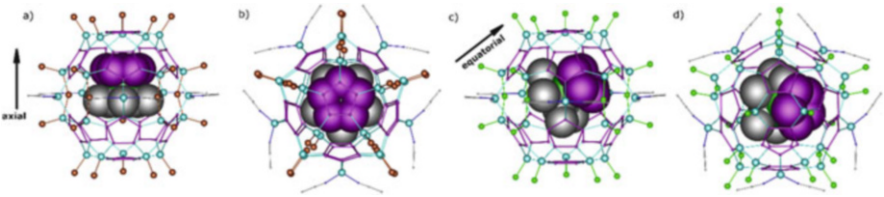

Fig. 19 (**a**, **b**) Axial and (**c**, **d**) equatorial orientations of pentaphosphaferrocene in host–guest complexes of 90-vertex supramolecules

molecules inevitably adopt an eclipsed conformation of stacked P_5–P_5 rings, which are remarkably parallel to one another (the interplanar angle is below 3.5°) [94]. Corresponding dot-to-plane distances (3.77–4.03 Å) justify weak π–π interactions between the *cyclo*-P_5 ligands (Fig. 19). The shortest P–P contacts of 3.53–3.77 Å are close to the doubled van der Waals radius of phosphorus (3.6 Å) [120, 121].

The presence of the equatorial part leads to a deviation of the 90-vertex shell from a spherical shape. The outer dimensions are 2.46–2.70 nm (X=Cl, Br) in axial and 2.36–2.46 nm (X=Cl) or 2.40–2.46 nm (X=Br) in equatorial directions (Table 1) [94]. In the case of the inner cavity, the equatorial diameter is larger than the axial one, irrespectively of the nature of X, and amounts to 1.20–1.28 nm for X=Cl and 1.16–1.20 nm for X=Br [94]. The axial diameter is less affected by the nature of X with values of 1.26–1.30 nm for X=Cl and 1.32 nm for X=Br derivatives. The larger the halogen X (Cl or Br), the longer the five equatorial Cu–X–Cu bridges are the longer the cavity in the axial direction is. This also causes slight relative narrowing of the cavity in the equatorial direction. Therefore chloride-containing hosts possess more isometric cavities and readily allow both axial and equatorial orientations of the [Cp*Fe(η^5-P_5)] guest. In contrast, for bromide-containing hosts, the guest molecules always occupy the axial position. This enables the encapsulation of the triple decker complex [$(CpCr)_2(\mu,\eta^{5:5}$-$As_5)$] (axial size 0.88 nm) (see footnote 1) to give the host–guest complex [$(CpCr)_2(\mu,\eta^{5:5}$-$As_5)$]@[{Cp*Fe(η^5-P_5)}$_{12}$(CuBr)$_{25}$(MeCN)$_{10}$] · 10C_7H_8 · 3MeCN (**27**, Fig. 20) [90], which is not the case for the chloride superspheres. The Cp ligands of the guest molecule are involved in π–π stacking interactions with the *cyclo*-P_5 ligands possessing an interplanar distance of 3.56 Å. Interestingly, the 90-vertex host-guest compounds **26** and **27** are isostructural although exhibiting different guests [94].

Other host–guest complexes based on this topology are rare, showing the robustness of the 90-vertex scaffold. Only a few examples of modifying this topology were observed, namely, 90-vertex superspheres bearing one positive or one negative charge (**18**, **21**) [94]. Multiply charged species have never been observed. All related topologies concern only a modification in the equatorial part. The simplest modification to give an anionic supersphere but retaining the same 90-vertex topology is a substitution of one MeCN ligand by a chloride anion (Fig. 21a, d). The charge of this anion is thereby compensated by a cationic supersphere where one chloride is statistically missing either in the equatorial

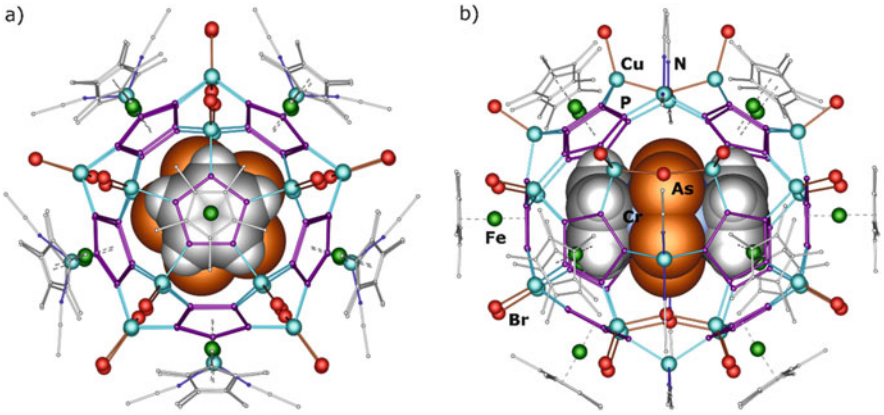

Fig. 20 The host–guest complex **27** [94]

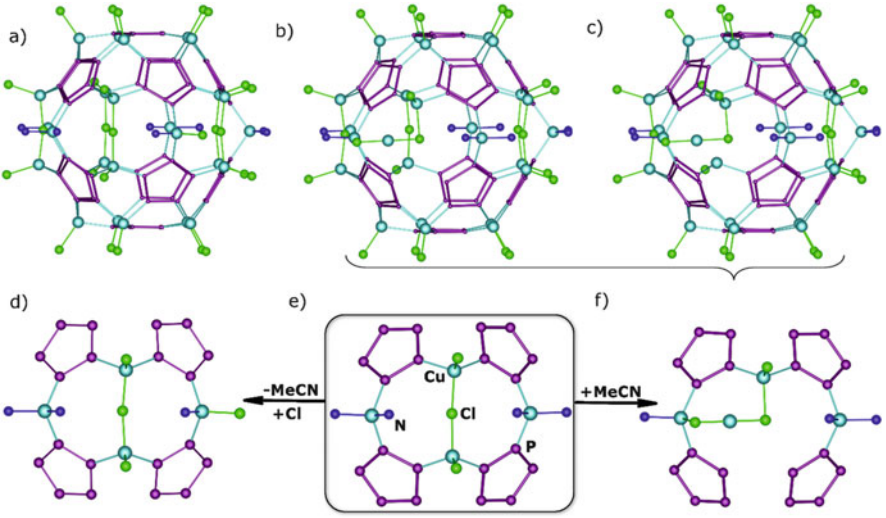

Fig. 21 An anionic 90-vertex supersphere (**a**) $[\{Cp^*Fe(\eta^5\text{-}P_5)\}_{12}Cu_{25}Cl_{26}(MeCN)_9]^-$ and cationic (**b**) 90 and (**c**) (90-1) superspheres $[\{Cp^*Fe(\eta^5\text{-}P_5)\}_{12}Cu_{25}Cl_{24}(MeCN)_9]^+$ in **21** [94]. Structural modifications of (**e**) a fragment of the 90-vertex shell in a fragment (**d**) with Cl-substituted MeCN position and (**f**) with a rearranged CuCl unit. The Cp*, Fe atoms, and carbon atoms of acetonitrile molecules are not shown for clarity

belt or in the adjacent terminal position providing a total positive charge and revealing two moieties with 90 and (90-1) topology (Fig. 21b, c). Furthermore, one of the CuCl fragment migrates from its place between two P atoms and substitutes a MeCN molecule of the neighboring Cu ion (Fig. 21f).

Another anionic supersphere, $[\{Cp^*Fe(\eta^5\text{-}P_5)\}_{12}Cu_{24}Cl_{25}(MeCN)_8]^-$, can be regarded as the result of elimination of a $\{Cu(MeCN)_2\}^+$ unit from the equatorial

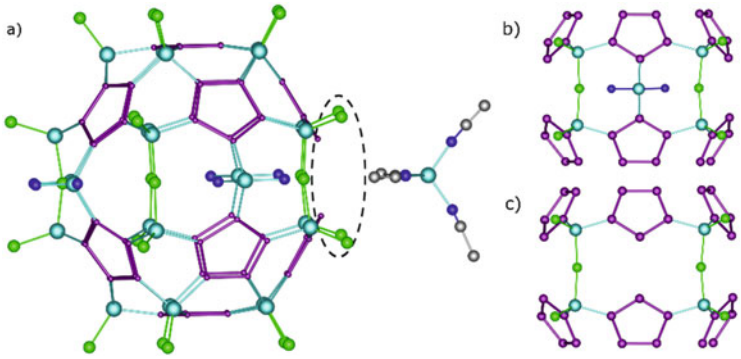

Fig. 22 Anionic (90-1)-vertex supersphere: (**a**) an ionic pair $[Cu(MeCN)_4]^+[(Cp^*Fe(\eta^5\text{-}P_5))_{12}Cu_{24}Cl_{25}(MeCN)_8]^-$ in **18** and the structural modification of (**b**) a fragment of the 90-vetrex shell in (**c**) a fragment vacant in an equatorial Cu^+ position. The Cp*, Fe atoms, and carbon atoms of eight acetonitrile molecules are not shown for clarity

part of the neutral 90-vertex molecule (Fig. 22b, c). In the crystal structure, the anion forms an ionic pair with a $[Cu(MeCN)_4]^+$ cation and co-crystallizes with the neutral 90-vertex molecules according to the formula $[Cu(MeCN)_4]^+[\{Cp^*Fe(\eta^5\text{-}P_5)\}_{0.5}@\{Cp^*Fe(\eta^5\text{-}P_5)\}_{12}\{CuCl\}_{25}(MeCN)_{10}]_3[Cp^*Fe(\eta^5\text{-}P_5)]_{0.5}@[\{Cp^*Fe(\eta^5\text{-}P_5)\}_{12}Cu_{24}Cl_{25}(MeCN)_8]^- \cdot 34CH_2Cl_2$ (**18**).

2.2.2 A 99-Vertex Supersphere

The unprecedented supramolecule $C_{60}@[\{Cp^*Fe(\eta^5\text{-}P_5)\}_{13}(CuCl)_{26}(H_2O)_2(CH_3CN)_9]$ (**29**) formed by the successful encapsulation of the C_{60} fullerene [98]. With 26 Cu atoms connected by 13 units of pentaphosphaferrocene and eight Cl bridges, it comprises a 99-vertex scaffold (Fig. 23).

In the middle of the host molecule in **29**, 12 pentaphosphaferrocenes are bound to 12 {CuCl} units (Fig. 23c). In this barrel-like part, the pentaphosphaferrocenes are arranged in two rows of six molecules. This implies a larger diameter of the host than the 80- and 90-vertex supramolecules that have five of these units in the equatorial part (cf. Fig. 17). This sixfold symmetry of the "barrel" contradicts to the fivefold symmetry of the $\{Cp^*Fe(\eta^5\text{-}P_5)\}$. Consequently, less regular fragments confine such a shell. In the lower part, a threefold arrangement (C_{3v}) of alternating {Cu(MeCN)Cl} and $\{Cu_2(\mu\text{-}Cl)_2(MeCN)_2\}$ units coordinates the P atoms of the "barrel" (Fig. 23). In the upper part, one pentaphosphaferrocene moiety coordinates two {CuCl} and one $\{Cu_3(\mu\text{-}Cl)_2(H_2O)_2Cl\}$ unit (Fig. 23e). In the latter fragment, two sites at two copper atoms are statistically occupied by a chloride and a water molecule. One more position is entirely occupied by a water molecule. All parts are joined together by Cu–P bonds.

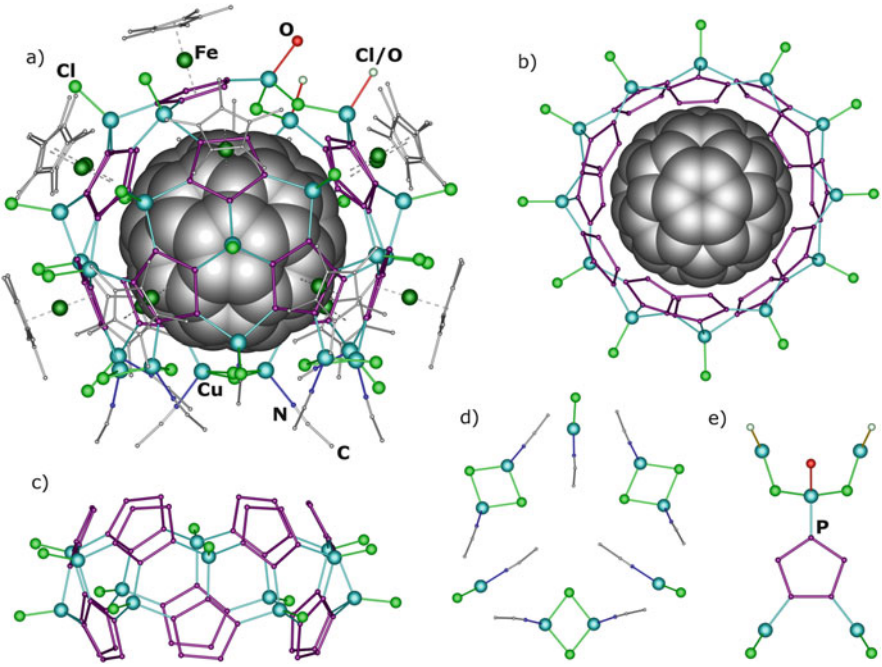

Fig. 23 (**a**) 99-vertex supramolecule encapsulating fullerene C_{60} (**29**) [56]. The central barrel-like part constructed of 12 units of **1a** and 12 {CuCl} units and encapsulating C_{60} molecule, (**b**) *top* and (**c**) *side view*. The (**d**) lower and (**e**) upper caps of the supramolecule

At first sight, the open 36-vertex barrel-like fragment could be closed with a fragment of fullerene topology as observed in the nano-capsule (Fig. 18a). Hence, an 18-vertex $\{CuCl\}\{Cp^*Fe(\eta^5\text{-}P_5)\}_3\{CuCl\}_3$ cone of C_{3v} point symmetry (Fig. 24b) might coordinate to the outer rim composed of exactly six **1a** and six {CuCl} units. Consequently, the question arises why could it not become a capping fragment here and construct a 72-vertex supersphere ($18 \times 2 + 36$)? The reason why this is not the case is that in the nano-capsule, the outer rim is isomeric to that in the 99-vertex supramolecule. The **1a** units coordinate {CuCl} in a 1,3- and 1,2-mode (with respect to the rim), so that the *cyclo*-P_5 ligands are arranged up and down in alternation. Therefore, every non-coordinated phosphorus atom in the second position can coordinate the 18-vertex cone (Fig. 24c). In the 99-vertex supramolecule, the sixfold barrel rim contains only 1,3-coordinating *cyclo*-P_5 ligands and has a larger diameter, 13.0 Å vs. 11.5 Å in **28**. This makes the 18-vertex unit non-complimentary to the barrel (Fig. 24a). Topologically, this fragment could coordinate to a rim with additional six more {CuCl} units following a fullerene-like fashion with six-membered rings. However, such a rim would be too narrow for the 18-vertex cap.

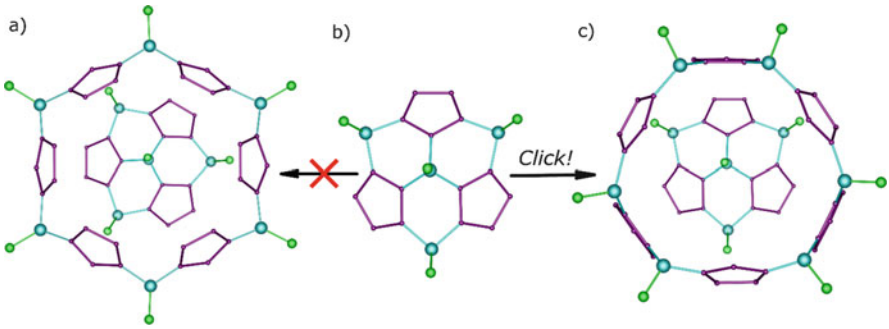

Fig. 24 Impossible and possible self-assembly in **28** and **29**. (**a**) The rim of the barrel-like part of **29** of six **1a** and six {CuCl} units unfit to (**b**) the 18-vertex cap of **28**. (**c**) The rim of **28** assembling with the cap

Based on the widest possible rim constructed of **1a** and single {CuCl} units, the supersphere **29** possesses a larger outer diameter (2.6 nm) than other **1a** derivatives of 80- and 90-vertex spheres. Consequently, the larger size of the barrel is caused by the encapsulated C_{60} guest molecule. The inner cavity proves to be almost spherical and a diameter of 1.35 nm allows the encapsulated guest (0.7 nm) to rotate.

2.3 Superspheres Beyond the Fullerene Topology

The ability of the heavier halogens, Br and I, to agglomerate with metal cations to form expanded structures [84–86] allows the construction of confined inorganic scaffolds of non-fullerene topologies and of nonspherical shape. These supramolecules usually contain less than 12 units of pentaphosphaferrocene which are typical for fullerene topologies. Furthermore, the less predetermined self-assembly often leads to co-crystallization of different forms and/or isomers. This results in intrinsic disorder and statistical occupation of atomic positions in the scaffold. These features are considered in Sect. 3 in more detail, while here only the idealized scaffolds are presented.

2.3.1 An Ellipsoid-Shaped 100-Vertex Supersphere

The smallest representative is a 100-vertex supramolecule found in two formally isostructural compounds, $(E_4)@[\{Cp^*Fe(\eta^5\text{-}P_5)\}_{10}\{CuI\}_x(MeCN)_6]\cdot nMeCN$, E=P, $x = 30.1$, $n = 2$ (**30**), and E=As, $x = 29.6$, $n = 4.6$ (**31**) (Fig. 25a, b) [99]. In the crystal, a solid solution of two or three different species is present (cf. Sect. 3.3). Since the differences between the supramolecules constituting the crystal are slight, the common main component is discussed in the following (for details see Sect. 3.3). It can be described as an ellipsoid-like molecule $[\{Cp^*Fe(\eta^5\text{-}$

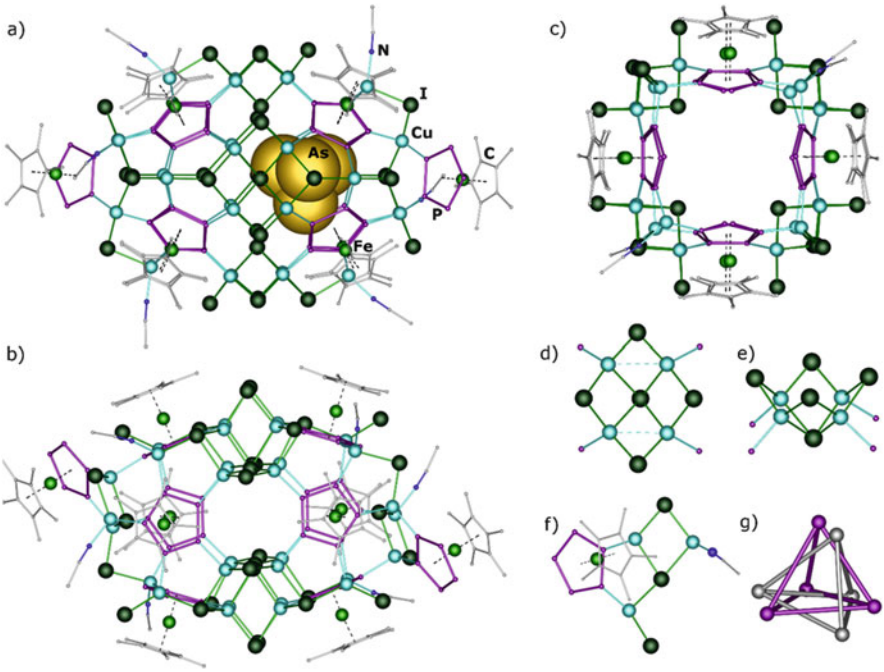

Fig. 25 The isostructural host–guest complexes $(E_4)@[\{Cp^*Fe(\eta^5\text{-}P_5)\}_{10}\{CuI\}_x(MeCN)_6]\cdot n MeCN$, E=P ($x = 30.1$, $n = 2$) (**30**) and (**a**) E=As ($x = 29.6$, $n = 4.6$) (**31**), (**b**) inorganic scaffold constructed from (**c**) the squared equatorial part containing four (**d**, **e**) bowl-like units $\{Cu_4(\mu_4\text{-}I)(\mu_3\text{-}I)(\mu_2\text{-}I)_3\}$ and two (**f**) caps; (**g**) the host P_4 tetrahedral molecule disordered within the cavity of **30**

$P_5)\}_{10}\{CuI\}_{30}(MeCN)_6]$ of D_{2h} symmetry. It contains a total of ten $[Cp^*Fe(\eta^5\text{-}P_5)]$ units, from which only eight construct the scaffold. The equatorial part is formed by four $\{Cu_4(\mu_4\text{-}I)(\mu_3\text{-}I)(\mu_2\text{-}I)_3\}$ units which exhibit a bowl-like geometry (Fig. 25d, e). Two of four Cu···Cu contacts in these units are shortened to 2.86–2.94 Å representing Cu_2 dimers. The other ones are elongated to 3.3–3.5 Å (Fig. 25d). These bowl-like units connect four pentaphosphaferrocene units on each side. The *cyclo*-P_5 ligands are bound with each other in the 3,5-position in alternation by {CuI} and {Cu(MeCN)} units. In this way, a "cube" with two opposite open faces is formed (Fig. 25c). These open faces are capped by $\{Cu_2(\mu_2\text{-}I)_2(MeCN)CuI\}$ fragments that are additionally coordinated by **1a** unit in a 1,2-mode (Fig. 25f).

The supramolecules **30** and **31** are hollow despite the presence of more bulky building Cu_nX_m units compared to the 80- or 90-vertex superspheres. Their cavities being now elongated cannot accommodate larger molecules due to the "bottleneck" of the μ_4-I atoms of four $Cu_4I_5^-$ bowls pointing inside the cavity. Thus, the cavity is divided into two symmetrical parts. Instead, the cavity shape enables the inclusion of an E_4 molecule of white phosphorus and yellow arsenic, respectively. The tetrahedron statistically occupies each part with 50 % probability, where it is orientationally disordered (Fig. 25a, g).

2.3.2 A Tetrahedral-Shaped 162-Vertex Supersphere

The pentabenzyl derivative **1c** is also capable for the formation of inorganic superspheres beyond the fullerene topology. Although the use of up to three equivalents of CuBr leads to the buildup of an 80-vertex scaffold (I_h-C_{80} analog, see Sect. 2.1.1), a large excess of CuBr allows the formation of a supramolecule with a singularly different scaffold for such pentaphosphaferrocene-based spheres: $[\{Cp^{Bn}Fe(\eta^5\text{-}P_5)\}_{12}\{CuBr\}_{51}\{CH_3CN\}_8]$ (**32**).

As in **30** and **31**, different products co-crystallize (see Sect. 3.2). One of them is depicted in Fig. 26a. On the contrary to **30** and **31** with their eight scaffold-constructing and two "terminal" pentaphosphaferrocene moieties, **32** contains 12 **1c** molecules. Yet no fullerene topology is present, since these are linked to each other by polynuclear Cu_nBr_m fragments containing μ_2-, μ_3-, and μ_4-Br atoms rather than single CuBr units as in 80-vertex supramolecule (Fig. 26c). This agglomeration resembles the CuI-cluster motif of **30** and **31** (Sect. 2.3.1).

The constructed ideal skeleton of **32** contains 51 Cu and 60 Br positions. However, due to bromide vacancies (cf. Sect. 3.2), the latter number is reduced from 60 to 51; thus a neutral $[\{Cp^{Bn}Fe(\eta^5\text{-}P_5)\}_{12}\{CuBr\}_{51}\{CH_3CN\}_8]$ cluster is present. Its tetrahedral-shaped scaffold contains 162 non-carbon atoms (60 P, 51 Cu, 51 Br; Fig. 26b), and thus, it is even larger than **30** and **31**. Due to the sterically demanding Cp^{Bn} ligands, **32** reaches an outer diameter of 3.56 nm.

Another interesting feature is obtained in **32**: The internal cavity is occupied by two $\{Cu(CH_3CN)Br\}$ groups, which show a η^2-π-coordination to the *cyclo*-P_5 ligand of **1c** (Fig. 26d). As a consequence, there is no volume accessible for the incorporation of a guest molecule.

The formation of both cluster types deriving from **1c** and CuBr, namely, **35** and **32**, depends on the stoichiometric ratio of CuBr as well as of the amount of CH_3CN present. A systematic variation of these parameters even revealed that these clusters

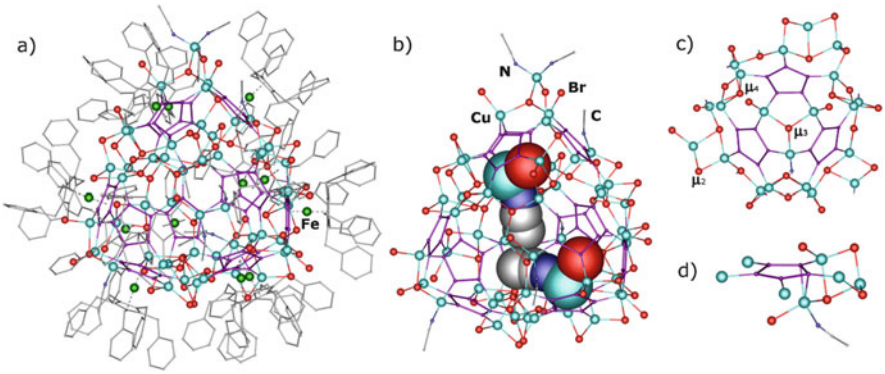

Fig. 26 (**a**) The tetrahedral-shaped cluster **32** derived from **1c** and CuBr, (**b**) the inorganic scaffold with $\{Cu(CH_3CN)Br\}$ units protruding into the cavity, (**c**) the different coordination modes of bridging Br anions and, and (**d**) the η^2-π-coordination to the *cyclo*-P_5 ligand of **1c** unit

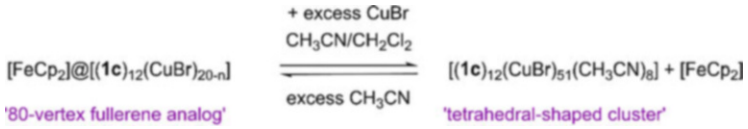

Scheme 1 Reversible capture and release of ferrocene by switching among two different clusters

are able to switch one to another. Thus, first the 80-vertex supersphere is formed in CH_2Cl_2 as solvent, which rearranged to the tetrahedron-shaped supramolecule **32** by adding CuBr. If CH_3CN is added after the formation of **32**, the 80-vertex supramolecule is formed again.

Finally, the combination of the three facts, which are (i) the ability of 80-vertex superspheres to incorporate small molecules, (ii) the absence of a cavity for a guest in **32**, and (iii) the potential of a supramolecular switch, can be used for a reversible encapsulation and release of a guest molecule as it was successfully demonstrated for ferrocene (Scheme 1). The guest molecule interacts with the host by means of specific π-stacking with its aromatic Cp and P_5 rings.

2.3.3 A 168-Vertex Supersphere

Going from bromine to iodine, a similar extended copper halide framework was obtained with **1c** as building block [100]. The 168-vertex supramolecule $(CH_2Cl_2)_{3.4}$@$[(Cp^{Bn}FeP_5)_{12}\{CuI\}_{54}(MeCN)_{1.46}]$ (**33**) contains an almost twice as large {CuI} framework as in **30** and **31** and possesses a diameter of 3.7 nm (Fig. 27). Despite having 12 **1c** units, the supramolecule **33** does not show a fullerene topology, and as it was the case for **30** and **31**, the iodine atoms not only act as a terminal but also as a bridging ligand (Fig. 27c). Thereby, the $\{Cu_4I_2(\mu_4\text{-}I)(\mu\text{-}I)_3\}$ fragment which is σ-coordinated to the *cyclo*-P_5 ring in 1,2-coordination mode (Fig. 27d) resembles the bowl-like $\{Cu_2(\mu_2\text{-}I)_2(MeCN)CuI\}$ units (Fig. 27f) as observed in **30** and **31**.

The idealized copper iodide scaffold (for details see Sect. 3.3) can be constructed from eight tetrahedral $\{CuI_4\}$ units (Fig. 28a) and six similar $\{(Cp^{Bn}FeP_5)_2(CuL)(Cu_2I)_4\}$ blocks, containing different terminal position L. In two blocks, it is occupied by an iodide, and in four by a MeCN molecule (Fig. 28b). These blocks are arranged in the volume forming a giant cube with the eight $\{CuI_4\}$ units in the corners and the six **1c**-containing building blocks as faces (Fig. 28c). The point symmetry of the inorganic scaffold is C_i.

The inner cavity in **33** has a diameter of 0.75 nm and is slightly smaller than that found inside the 80-vertex supramolecules. In the absence of templating molecules, the octahedrally shaped cavity is filled with disordered CH_2Cl_2 molecules.

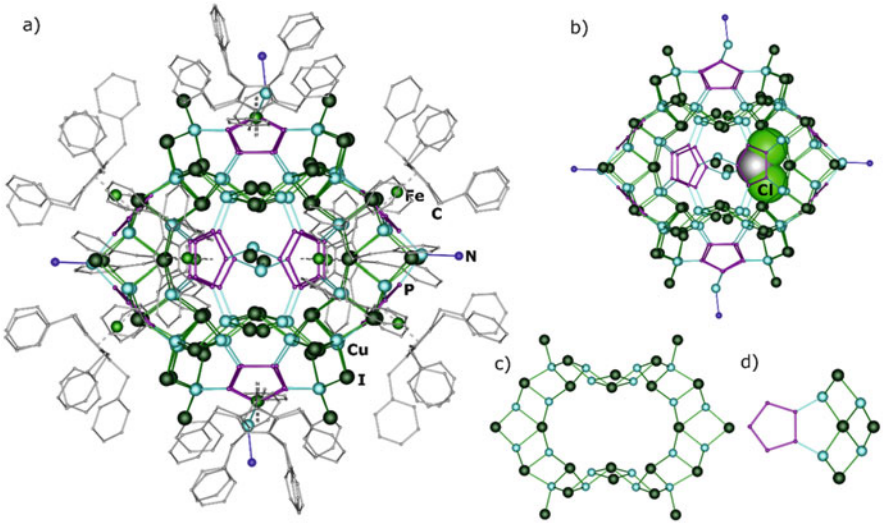

Fig. 27 (**a**) Supramolecule in **33**, (**b**) inorganic core with a guest CH_2Cl_2 molecule, (**c**) fragment of {CuI} framework, and (**d**) $\{Cu_4I_2(\mu_4\text{-}I)(\mu\text{-}I)_3\}$ fragment coordinated to a *cyclo*-P_5 ligand

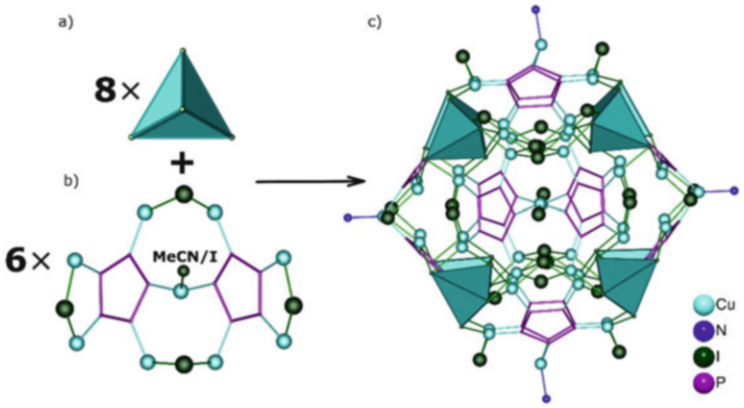

Fig. 28 Step-by-step assembling of the idealized scaffold in **33** from six $\{(Cp^{Bn}FeP_5)_2(CuL)(Cu_2I)_4\}$ and eight $\{CuI_4\}$ units

2.3.4 A Rugby Ball-Shaped 312-Vertex Supersphere

The most striking example of a giant supramolecule with an extended {CuX} scaffold is found in $[\{Cp^{Bn}FeP_5\}_{24}(CuBr)_{96}]$ (**34**) exhibiting 24 units of **1c** connected by 96 {CuBr} units [89]. It was synthesized by the reaction of **1c** with $CuBr_2$, in which Cu(II) is reduced to Cu(I) bromide and **1c** is oxidized as known from the direct oxidation of **1c** [122]. The inorganic scaffold enumerates 312 atoms

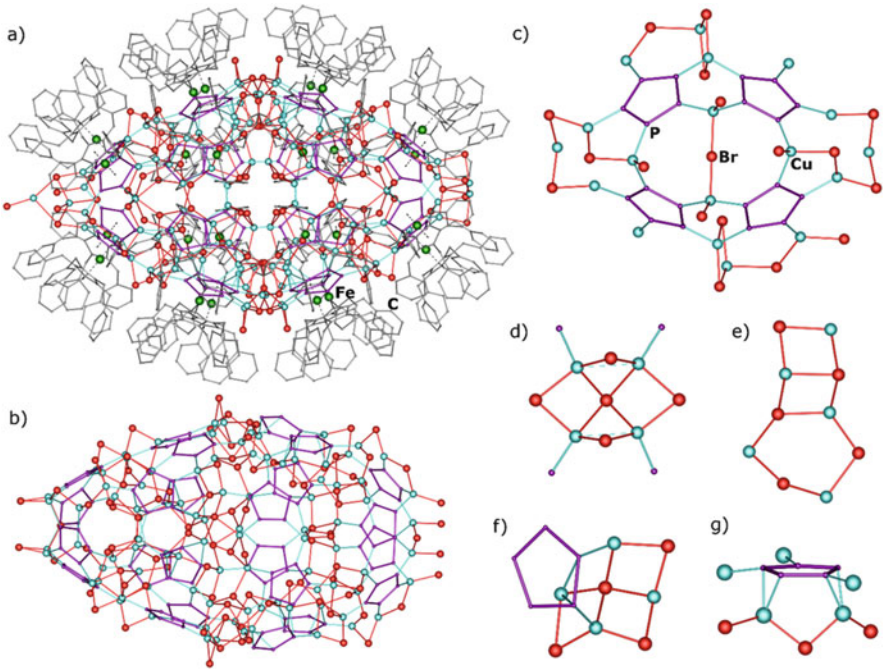

Fig. 29 (**a**) The rugby ball-shaped supramolecule **34**, (**b**) inorganic scaffold containing 312 atoms, top view of the (**c**) ends, and fragments constituting the copper halide framework: (**d**) the bowl-like Cu_4Br_5 unit, (**e**) 4- and 6-membered CuBr rings. η-Coordinated *cyclo*-P_5, which (**f**) forms bowl-like unit and (**g**) demonstrates formation of the inner shell

and opens to a center and closes to the ends (Fig. 29a, b). Four cross sections (or circles) consisting of four, eight, eight, and again four pentaphosphaferrocene molecules predetermine this "rugby ball" shape. The pentaphosphaferrocenes are connected by a complicated copper bromide network. The network appears to be irregular and formed by chance, but in fact it is reproducible from supramolecule to supramolecule almost without disorder. The {CuBr} framework is double layered in the center of the scaffold, where pentaphosphaferrocene **1c** demonstrates σ- and η-coordination of *cyclo*-P_5 ligands (cf. **17**). Some typical fragments of the scaffold are depicted in Fig. 29 (cf. Sect. 3.3). On the contrary, the ends of the rugby ball-shaped molecule are single layered and comprise only σ-coordinated **1c** units connected directly by Cu atoms and by some additional bromide bridges (Fig. 29c). Interestingly, similar capping fragments have also been found in **33**, but contain two instead of four **1c** units (cf. Fig. 28b).

The giant rugby-shaped supramolecule reaches 4.6 nm in length and 3.7 nm in width. These values exceed hitherto all other pentaphosphaferrocene-containing supramolecules. Despite the extended copper halide framework, which forms the double shell, the size of the inner cavity still amounts to 2.5 × 1.2 nm. It is filled with disordered CH_2Cl_2 and CH_3CN molecules.

2.4 *Supramolecule with Nonclassical Fullerene Topology*

Smaller fullerenes ($<C_{60}$) must violate the isolated-pentagon rule; hence the additional steric strain makes them much more labile. However, some of them, the so-called magic number clusters, can also gain remarkable stability. The most prominent example is the D_3-C_{32} molecule, whose stability is ascribed to the spherical aromaticity of this compound leading to a large HOMO–LUMO gap comparable to that in C_{60} [123–125]. Though C_{32} always shows intensive peaks in photoelectron spectra, its synthesis or extraction from soot has not been accomplished yet. More symmetrical isomers bearing a reduced strain energy contain less five-membered and at least few four-membered rings [126–129] and are therefore assigned to the class of "nonclassical" fullerenes [106, 107].

Also this field of fullerene chemistry is visible within the metallosupramolecular approach applying other P_n ligand complexes. Hence, instead of the pentaphosphaferrocenes **1** bearing a P_5 pentagon, now a *cyclo*-P_4 ligand is needed as it is presented in $[Cp''Ta(CO)_2(\eta^4\text{-}P_4)]$ ($Cp''=\eta^5\text{-}C_5H_3{}^tBu_2$; Fig. 30a) [102]. This P_n ligand complex in combination with CuCl is capable for the formation of the carbon-free C_{32} analog $[\{Cp''Ta(CO)_2(\eta^4\text{-}P_4)\}_6(CuCl)_8]$ (**35**, Fig. 30b). Supramolecule **35** consists of six *cyclo*-P_4 complexes bound to eight Cu^I halides in a 1,2,3,4-coordination mode. The inorganic framework comprises 32 non-carbon core atoms (24 P, 8 Cu) and features a Cu_8 cube with a P_4 square above every face (Fig. 30d). Thus, alternating four- and six-membered rings are formed exclusively ("isolated-square rule," Fig. 30c). Furthermore, the tantalum atoms form a Ta_6 octahedron, which includes the cube-shaped inner framework (Fig. 30d). The inner cavity of **35** has a shape of Fedorov's cubooctahedron (truncated octahedron) and a diameter of 0.6 nm, whereas the outer diameter amounts to 2.19 nm (see footnote 1). The cluster topology in **35** also resembles those theoretically proposed for group 13/15 oligomers [130–132] and for boron nitride fullerenes, such as the $B_{16}N_{16}$ isomer with D_{2d} symmetry [133].

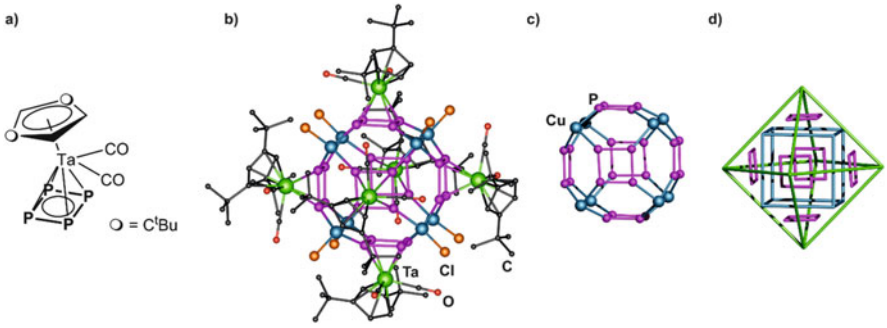

Fig. 30 (**a**) The *cyclo*-P_4 complex $[Cp''Ta(CO)_2(\eta^4\text{-}P_4)]$, (**b**) molecular structure of **35**, (**c**) inorganic scaffold of **35**, and (**d**) polyhedra in **35**

3 Look Closer: Individual Compound vs. Solid Solution of Supramolecules

The formation of rather weak coordinative bonds offers more than one possibility of bonding between the structural fragments where each "choice" is energetically equally favored. Such "vicissitudes" of the self-assembly can lead to numerous errors in repeating of the same supramolecule. This process can be compared with errors during a DNA replication that can cause mutations; the number of mutations depends on the complexity of a molecule and on the changing environment, which either favors the replication or not.

These errors in self-assembly of supramolecules or their structural variation can be classified in view of the most frequently repeated molecular structure as a reference point for the deviating examples. The individual structure of every supramolecule cannot be explored with SC-XRD, i.e., only the average structure within the crystalline material can be determined. The crystals of supramolecules with and without "errors" co-crystallize and form solid solutions. As a result, various forms of static disorder coexist in the crystal structure. In this context, the molecular structure can demonstrate a number of structural variations: *vacancies*, *isomers*, and the presence of *additional* or *different* fragments. The number and structure of forms/isomers in which the supramolecules co-crystallize as well as the composition of a solid solution in most complicated cases cannot be estimated. These factors are described in more detail in this section.

3.1 Single {CuX} Vacancies in the Inorganic Scaffold

The extensive frameworks, polymers, or spherical agglomerates, containing a large number of atoms, retain their structure even if some of the constituents are missing. The simplest case of this phenomenon has already been discussed with an example of (90-1)-vertex superspheres (Sect. 2.2.1). In that case, the supramolecules still can be regarded as an individual compound, especially taking into account the examples of charged species, where the vacancies are enforced by the requirements of electroneutrality. The superspheres with partly vacant ideal scaffolds are called in the following as porous.

In most cases, the notion of an individual compound cannot be used anymore. This can be illustrated with the structure of a porous supramolecule based on 80-vertex fullerene topology, namely, the host–guest complex $(o\text{-}C_2B_{10}H_{12})_{0.5}$@ $[\{Cp^*Fe(\eta^5\text{-}P_5)\}_{12}\{CuBr\}_{20\text{-}n}]$ (**16**), where the average number n of vacant positions per supramolecule (porosity) is 1.2 [92]. The inorganic core statistically lacks 1.2 units in two {CuBr} positions. In the triclinic crystal structure, the vacancies are partly ordered, most probably due to specific orientation of the toluene solvent molecules. They point toward the vacancy in the scaffold, where the {CuBr} unit is missing and may play a role of an "anchor" fixing the orientation of the

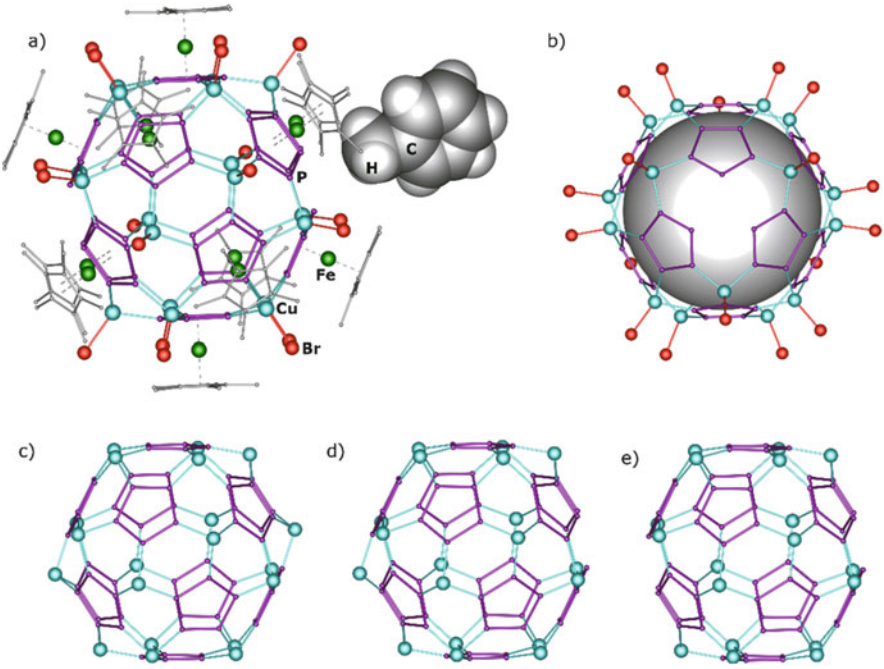

Fig. 31 Vacancies in the (80-*n*)-vertex supramolecules. (**a**) (80-2)-vacant supramolecule with a toluene molecule blocking one of the vacancies in **16**; (**b**) the {CuBr} vacancy; and (**c**) complete 80-, (**d**) and vacant (80-1)-, and (**e**) (80-2)-vertex supramolecules coexisting in crystal

supramolecule (Fig. 31a). In this case, complete 80- and vacant (80-1)- and (80-2)-vertex supramolecules coexist in the crystal (Fig. 31c–e), containing 20, 19, and 18 {CuBr} units in their scaffold, respectively. Moreover, for the (80-2)-vertex supersphere, only one centrosymmetric isomer is possible, in which the missing {CuBr} units are opposed due to the symmetry (Fig. 31e).

The ratio of different supramolecules in the resulting solid solution depends on the location and occupation factors of the disordered atoms, which drastically reduce the number of possible combinations [92]. All possible compositions can be derived from a system of equations and inequations taking into account all these factors. The simplest one for **16** giving $20\text{-}n = 18.8$ is 20 % of (80-2)-vertex and 80 % of (80-1)-vertex porous supramolecules.

A different interpretation is required when the same (80-*n*)-vertex supramolecules crystallize in a high-symmetrical cubic phase. A series of (guest)@$[\{Cp^{Bn}Fe(\eta^5\text{-}P_5)\}_{12}\{CuX\}_{20\text{-}n}]$, X=Cl, Br and guest=$CH_2Cl_2$ or $[Cp_2Fe]$ demonstrate a variable average porosity, $n = 0$–4.6 [89]. In the crystal, there are two crystallographically unique {CuX} units constituting a supramolecule with crystallographic T_h symmetry. One {CuX} position is always fully occupied; the other is often partly vacant. These fully occupied {CuX} units and the 12 pentaphosphaferrocenes **1c** confine the minimal 68-vertex cuboidal scaffold with

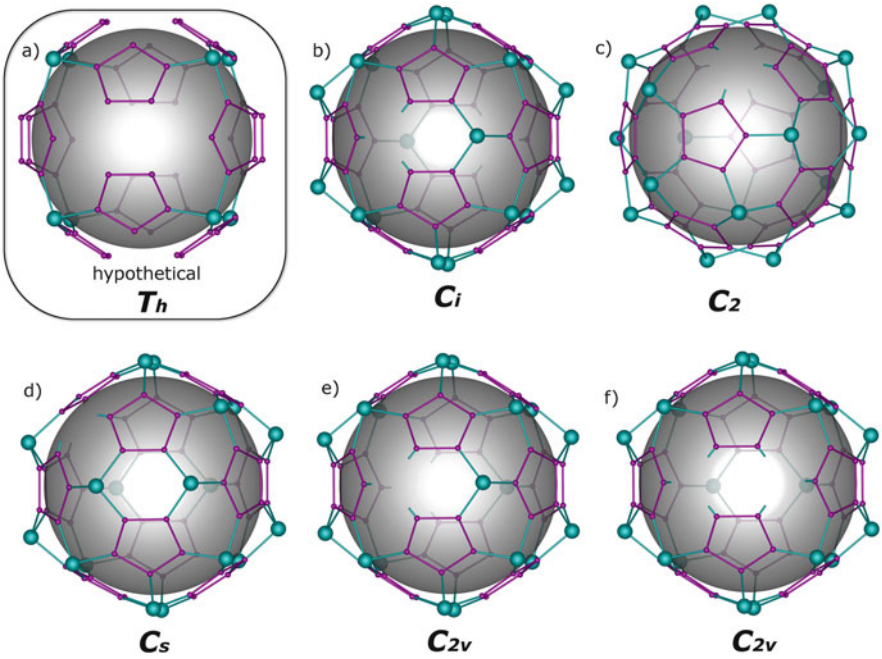

Fig. 32 *n*-Vacant 80-vertex supramolecules. (**a**) A hypothetic minimal 68-vertex (80-12) scaffold containing all possible vacancies; (**b–f**) all isomers for (80-2) supramolecules that differ in point symmetry

12 vacancies that has not been observed yet (Fig. 32a). It is always supported by a variable number of (12-*n*) additional {CuBr} units. In this case, different *n*-vacant molecules as well as isomeric molecules with the same *n* can coexist, in contrast to **16**. For example, for the (80-2)-vertex supersphere, five isomers are possible (Fig. 32b–f).

Thus, the supramolecules with the idealized C_{80} fullerene topology always form solid solutions, in which porous or complete supramolecules co-crystallize in the particular ratios. Even if *n* is an integer number, the co-crystallization of different forms is possible. For example, solely (80-1)-vertex supramolecules in **10** have the same chemical composition as the complete and the (80-2)-vertex supramolecules co-crystallizing in a 1:1 ratio ($80 \times 0.5 + 78 \times 0.5 = 79$). Such a phenomenon is eventually a function of the steric demand of the Cp derivatives. Once the vacancies in the individual supramolecule are shielded, the supramolecules have the same shape and naturally co-crystallize regardless of the CuX content. As a consequence, the unit cell parameters in isostructural series correlate neither with the nature of the halide nor with the index *n*. Needless to say that the shielding by Cp* is less effective than that of the much bulkier Cp^{Bn} ligands. Therefore, the **1c** derivatives usually exhibit more vacancies than the (80-*n*)-vertex Cp* derivatives. This ability of the 80-vertex scaffold to bear vacancies causes the high stability of **3–11** in a wide range of the CuX (X=Cl, Br) concentrations.

3.2 *Single-Atom Vacancies in the Extended {CuX} Framework*

The vacancies at the copper positions are intrinsic for supramolecules based on the extended CuX scaffolds, such as **17** and **32**–**34**. This is caused by coordination requirements of the metal atom, which needs to complete its coordination sphere with four or three X or phosphorus atoms forming a tetrahedron or, rarely, a triangle. The X atoms can only be bridging or terminal that implies a less strict demand of only one or two metal atoms in the coordination sphere of X. When one copper atom is missing, a bridging X atom becomes terminal (Fig. 33). As for the *cyclo*-P_5 ligand, two coordinative bonds with two Cu atoms are also sufficient to keep the connectivity of a sphere (see, e.g., Fig. 32a). In low-dimensional polymers, such vacancies would often result in a breakdown of the pattern, but confined shells are capable for a loss of many vertices without falling apart. On the other hand, every missing copper monocation requires a compensation of the negative charge, which is in contrast to previously described vacancies of neutral {CuX} units. In the scaffold, the negative charge can be compensated in two ways. The replacement of X by a neutral ligand (acetonitrile) offers one opportunity (Fig. 28b, Sect. 2.3.3). The elimination of X accompanied by a reduction of the coordination number of the copper cation from four to three is another possibility. The latter is realized in the CuBr scaffold of the tetrahedral-shaped supramolecule **32**.

At self-assembly of the CuX frameworks, the "error" in X positions can be easily restored by missing copper or statistical occupancy of X itself. For this reason, in CuX frameworks the number of halogen positions in the idealized scaffold usually is more than that of copper. The only exception is the framework of **33**.

This structural feature of a {CuX} framework also implies an amazing flexibility, because every Cu position can be voluntarily vacant. Consequently, the probability of the "replication errors" dramatically increases. For this reason, the idealized structure of **17** described in Sect. 2.1.2 proved to be so vacant that all Cu positions are partly occupied. Interestingly, the population of the available cationic positions in the scaffold of **17** decreases on going from the outer to the

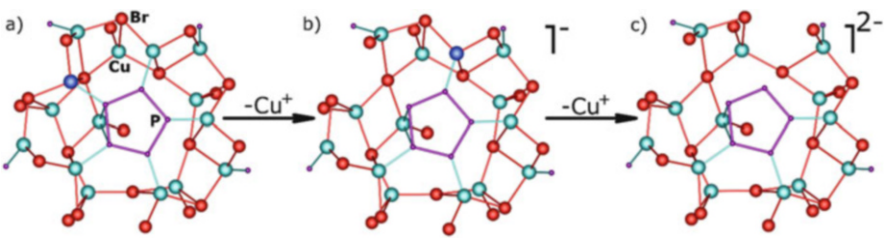

Fig. 33 (**a**) Section of CuX framework surrounding a *cyclo*-P_5 ligand in **17**. Step-by-step removing of one Cu^+ (**b**, **c**) that results neither in breaking coordination requirements of X or *cyclo*-P_5 nor in disintegration of the expended framework. The blue-highlighted Cu^+ in (**a**) is removed in the consecutive (**b**) figure and so on

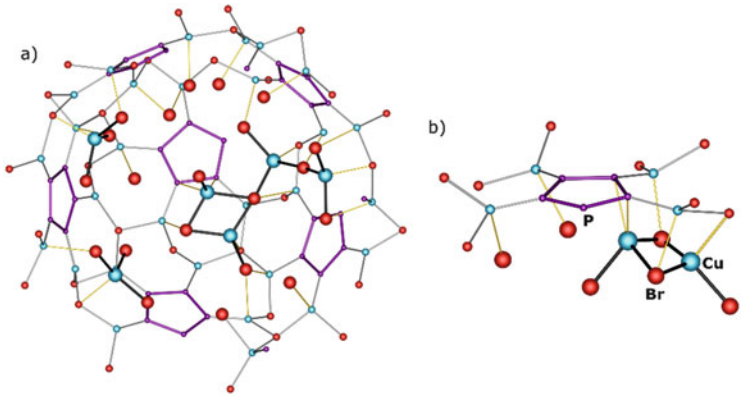

Fig. 34 (**a**) A fragment of 140-vertex supramolecule shell (**17**), (**a**) *inside view* and (**b**) *side view*. The atoms of the inside shells are shown in big balls and black bonds. The atoms of the outer shell are shown in smaller radius and gray bonds. The yellow bonds connect the shells

inner shells (Fig. 34). Such an enormous disorder suppresses any estimation of the number and composition of the coexisting isomers. Despite this fact, the superspheres of this type are a well-reproducible product.

3.3 Additional or Missing Polyatomic Groups in the Scaffold

An even more structurally complicated situation is a co-crystallization of supramolecules with variable scaffolds, which cannot be related as complete and vacant ones. If structural variations involve larger fragments than single Cu cations or neutral {CuX} units, they still can be described as vacancies. This is the case if polyatomic fragments additionally coordinate the parent scaffold or are statistically absent, e.g., in the 100-vertex supramolecules described in Sect. 2.3.1, (E_4)@[{Cp*Fe$(\eta^5$-$P_5)\}_{10}\{CuI\}_x(MeCN)_6]\cdot n$MeCN, E=P ($x=30.1$, $n=2$) (**30**) and E=As ($x=29.6$, $n=4.6$) (**31**) (Fig. 25a, b) [99]. The structural variations always concern the caps of the supramolecule that might indicate that the capping parts have been assembled last. The most representative structure [{Cp*Fe$(\eta^5$-$P_5)\}_{10}\{CuI\}_x(MeCN)_6$] contains 30 CuI units ($x=30$). Compared to it, in **31** a vacancy appears for that Cu (NCMe) unit, which is always present in **30** (Fig. 35a, b). Therefore, compound **31** can be a result of co-crystallization of the supramolecules with either $x=29$ (40 %) and 30 (60 %) or with $x=28$ (20 %) and 30 (80 %).

In contrast, the missing Cu(NCMe) unit in **31** is always present in **30**. But **30** has another structural modification that are two additional terminal {CuI} groups coordinated to one or two P_5 rings (Fig. 35b). In addition to the most representative [{Cp*Fe$(\eta^5$-$P_5)\}_{10}\{CuI\}_x(MeCN)_6$], where $x=30$, the supramolecules with $x=31$ and 32 also coexist, though as a small portion. The [{Cp*Fe$(\eta^5$-$P_5)\}_{10}\{CuI\}_{32}(MeCN)_6$] is

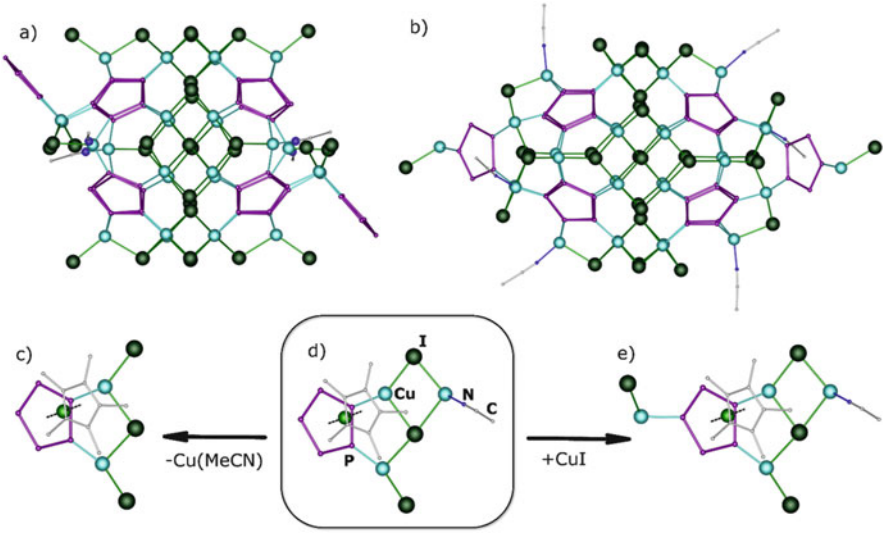

Fig. 35 Slight variations in the scaffold of supramolecules (**a**) **31** and (**b**) **30**. (**c**) The missing Cu (MeCN) units in **31** and (**e**) additional CuI units in **30** compared to (**d**) the cap of the majority of supramolecules (cf. Fig. 25)

depicted in Fig. 35b. It contains two more terminal {CuI} groups coordinated to one or two P_5 rings. The ratio between $x = 30$ and 31 or 30 and 32 in the crystal can be 90 %:10 % or 95 %:5 %, respectively. However, diffraction data do not allow distinguishing between these two possibilities.

In the scaffold of **33**, the structural variations are intrinsic compared to **31** and **30**, where no requirements of electroneutrality exist. On the contrary, the idealized scaffold presented in Sect. 2.3.3 has a composition of $[(Cp^{Bn}FeP_5)_{12}Cu_{62}I_{58}(MeCN)_4]$ and should bear a positive charge of +4. To compensate this, some of the Cu and I as well as some terminal MeCN ligands occupy their positions partly (Fig. 36), giving an average composition of all coexisting forms of supramolecules of $[(Cp^{Bn}FeP_5)_{12}\{CuI\}_{54}(MeCN)_{1.46}]$.

An even more complicated situation is observed in the capping fragments of the rugby ball-shaped supramolecule (**34**) described in Sect. 2.3.4 [101]. Its idealized scaffold has D_2 point symmetry, which is higher that the symmetry of any form of the supramolecule. The Cu_2Br_3 units in the center of the capping fragment are not involved in the {CuBr} network (Fig. 37, middle). This is most likely the reason for a severe disorder in this part of the inorganic scaffold as the Cu_2Br_3 units are the simplest and predominant cap. The entire framework has formed separately, and the {CuBr} fragments in-between four bulky **1c** units can aggregate independently and randomly. As an example, two different noncontradictory possibilities are shown as the right and left part in Fig. 29a. A more complete overview of imaginable structural variations of the framework is presented in Fig. 37. The possible forms

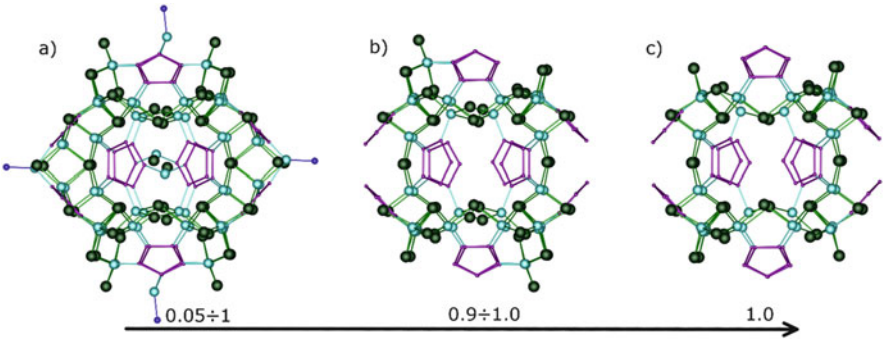

Fig. 36 Some structural variations of the framework in **33**. The atoms of the scaffold with occupancies (**a**) 0.05–1, (**b**) more than 0.9, and (**c**) only full occupancies are shown

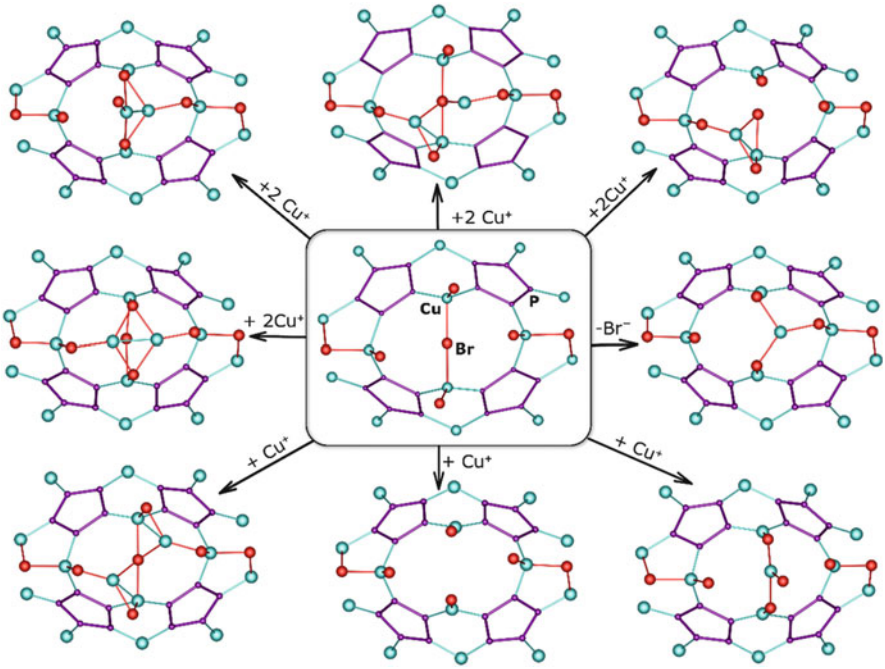

Fig. 37 Structural variations of the capping framework in **34**

are caused by different positions of copper cations that shows again the variability of the copper halide aggregation.

In this case the structural variations involve larger fragments and cannot be considered as vacancies or additions. These groups overlap in the crystal structure and must be described as a solid solution of the molecules with variable scaffold

and porosity. In this case, even the estimation of the number of the constituting units is an ambiguity, nothing to say of the composition of the corresponding mixture.

Thus, the supramolecules preferably form solid solutions of similar co-crystallized forms. Moreover, the unit cell parameters of a structural series of the same type supramolecules can be very similar, despite sometimes significant structural variations, e.g., porosity of the scaffold, the presence of quite large additional fragments, or different distribution of solvent molecules. It seems that the mutual arrangement of large supramolecules in the crystal is steady to their different compositions and reorientations as well as to the variation in the solvent portion. In many cases it is proved that not only products of different syntheses and crystallization procedures, but even every single crystal has a variable crystal structure and composition of the same parent type. The study of packing of the supramolecules regardless of solvent molecules is therefore justified.

4 Intermolecular Interactions Between the Supramolecules

In supramolecular chemistry the notion of a synthon as a repeating structural pattern based on intermolecular interactions (primarily, H bonds) was formulated by G. Desiraju in 1995 [134, 135]. The arrangement of supramolecules can be regarded as the synthon if it provides a robust geometry and can predictably be formed in crystal engineering owing to specific interactions.

What are the intermolecular interactions the superspheres are capable of? The outer surface in the supramolecules is confined by the organic cyclopentadienyl ligands capable of π–π interactions, if an aromatic system is not sterically hindered by a bulky substituent R. Consequently these interactions are only possible for Cp* and Cp^{Et} derivatives. The Cp^{R} ligands of high steric demand, Cp^{Bn} and Cp^{BIG}, do not participate in intermolecular π–π interactions. Instead, Cp^{Bn} forms intramolecular bonds of H···π type between benzyl rings [82]. These bulkier Cp^{Bn} and Cp^{BIG} ligands promote formation of larger supramolecules as from a solubility point of view, as well as from the favored copper halide agglomeration, as it was discussed in Sect. 2.1. Another opportunity for intermolecular interactions is the X anions capable for σ–π interactions with aromatic systems and halogen bonding [136, 137]. Despite the extended copper halide frameworks, halides are often hidden by cyclopentadienyl ligands. Additionally, bridging X anions provide fewer opportunities for specific interactions as terminal ones. For this reason, only Cp* and Cp^{Et} derivatives with terminal X anions are considered in this section. Furthermore, a halogen bonding between the superspheres is not observed.

4.1 Supramolecular Synthons

In the crystals of the supramolecules, two types of directed intermolecular bonding are observed in addition to van der Waals interactions that are π–π interactions between Cp* or Cp^{Et} ligands and σ–π interactions between terminal halides and Cp^{R} ligands. These interactions are found for many supramolecules of different types. Furthermore, their geometry is reproducible from structure to structure. All this supports a synthon approach to intermolecular interactions of superspheres [138].

The most frequent synthon is based on *halogen–π interactions* (σ–π synthon) [139–142]. The synthon is typical for a terminal X atom (X=Cl, Br) and is therefore found in superspheres of suitable scaffolds, namely, in the 80-, 90-, and 99-vertex superspheres and the nano-capsule (Fig. 38). The geometry of X–π interactions requires that the X atom faces the π-system at a distance shorter than the sum of the van der Waals radii of an sp^2-hybridized carbon atom and the respective halide atom. In addition, the Cu–X bond should be perpendicular to the π-system, with the X atom pointing to its center. Therefore, the Cl-π and Br-π distances amount to 3.20–3.61 and 3.29–3.60 Å, respectively [94, 98]. Values beyond 3.45 and 3.53 Å exceed the sum of the van der Waals radii [120, 121]. Only once the synthon is

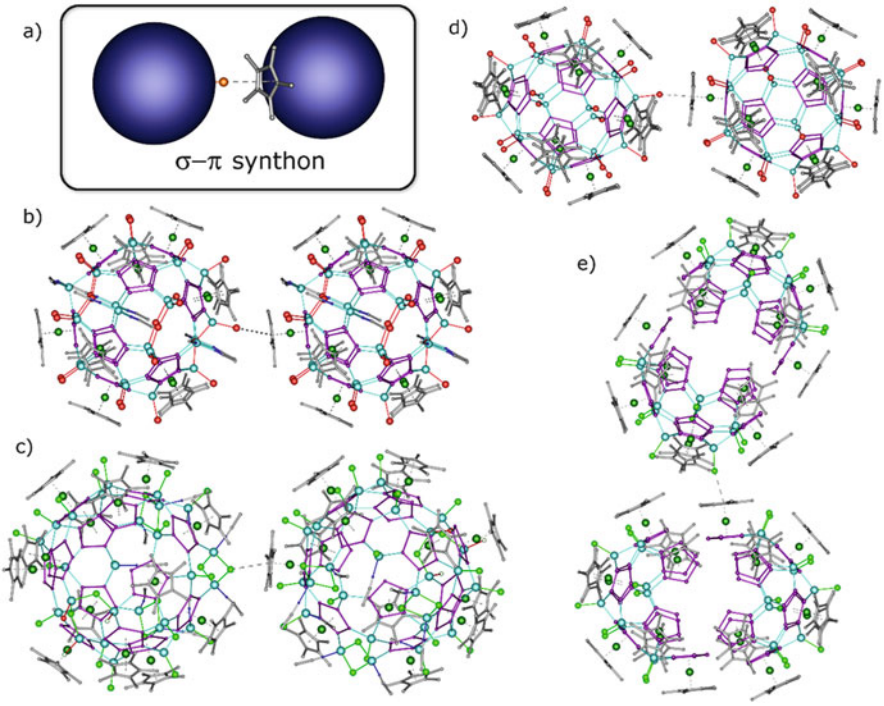

Fig. 38 The (**b**) 90-, (**c**) 99-, and (**d**) 80-vertex superspheres and (**e**) nano-capsule forming (**a**) a σ–π supramolecular synthon via X–Cp* interactions

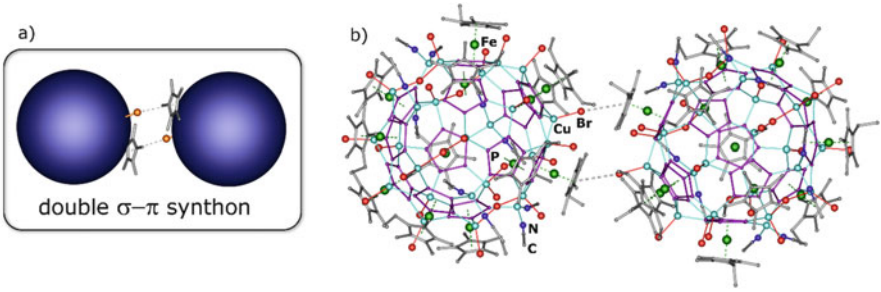

Fig. 39 (**a**) Double σ–π supramolecular synthon found in the (**b**) 90-vertex Cp^{Et}-based supersphere **22**

formed, which is based on a μ-Cl anion in the 99-vertex supramolecule (Fig. 38c). Expectedly, the μ-Cl–π distance is 3.63 Å that is longer than the minimal distance involving terminal Cl. The bridging X atoms of the equatorial part of the 90-vertex superspheres are unable to form the synthon, because they are shielded by the $[Cu(MeCN)_2]^+$ units. A unique example of a double σ–π synthon is found in **22** (Fig. 39). In this case, the synthon geometry is distorted; the angle between the Cu–Br bond and the center of the aromatic planar fragment is 171.6°, while the Cu–Br–π angle is 127°. The corresponding dot-to-plane distance that is 3.32 Å agrees with the literature data range from ca. 3.13 to 3.70 Å for X–π contacts [139–142].

The other opportunity of agglomeration is *π-stacking interaction* or, in other words, formation of a π–π synthon. Two types of them were observed: classical face to face and slipped (or offset) [143]. Both are characteristic of various supramolecules, the 80- and 90-vertex spheres and the nano-capsule (Fig. 40). The latter example displays that the formation of the π–π synthon is not shape dependent. Typical interplanar Cp*–Cp* distances of 3.34–3.52 Å are common for π stacking [94, 97, 143].

Peculiar indirect interaction between 90-vertex superspheres is observed in **23** and **24**. 1,2-Dichlorobenzene molecules mediate the π stacking of the large molecules (Fig. 40d). Solvent molecules possessing a π system like toluene, 1,2-dichlorobenzene, or acetonitrile can also mediate π–π interactions of the superspheres. On the other hand, the excess of these molecules can suppress the intermolecular Cp*–Cp* interactions between the supramolecules. As a typical example, the (80-*n*)-vertex molecules in **16** are surrounded by numerous toluene molecules, which block Cp* ligands. For this reason, only σ–π synthons are found in **16**. Being irreproducible, the interaction with a solvent cannot be regarded as a synthon. Another typical solvent, dichloromethane, can also interact with the Cp* ligand in a σ–π mode. This factor also diminishes the occurrence of the π–π synthon.

Hence it is not surprising that no structure is based solely on π–π synthons, and if they are observed, they are always accompanied by the σ–π synthons. Moreover, the σ–π synthons usually predominate in every structure (cf. Fig. 43). The only contrary example is **20**, which is depicted in Fig. 42h, where the π–π synthon leads to a trigonal layer of 90-vertex supramolecules. No synthons are realized in **12** and the isostructural clusters **30** and **31**. In **12**, the Cp* ligands could interact with

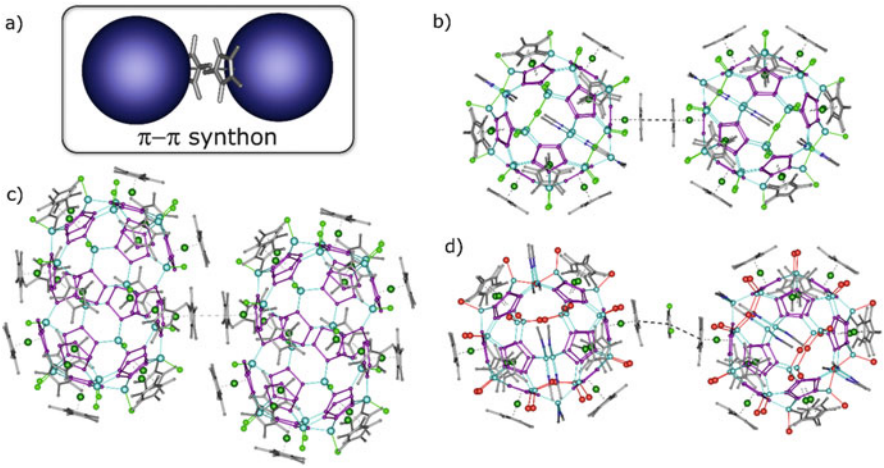

Fig. 40 The (**b**) 90-vertex superspheres in **20** and (**c**) nano-capsule **28** forming (**a**) π–π supramolecular synthon via Cp*–Cp* interactions. (**d**) A solvent-mediated π–π interactions between 90-vertex superspheres in **23**

toluene molecules, which could not be localized due to the high cubic symmetry. In **30** and **31**, the supramolecules are based on an extended CuI framework with only bridging iodides (Fig. 25), and no specific interactions between the supramolecules are found, except for elongated (4.42–4.43 Å) van der Waals I–I contacts. Iodine-based synthons are therefore not found for supramolecules yet [138].

The number of terminal X anions per supramolecule normally predominates or is nearly equal to the number of Cp* ligands. For the 80- and 90-vertex superspheres, CuX_{term}:**1a/1b** is 20:12, for the nano-capsule 18:20, and for the 99-vertex 17:13. Along with the already mentioned steric reasons and the competition with the solvent molecules, the σ–π synthon can be regarded as the most important factor in the aggregation of Cp*- and Cp^{Et}-containing supramolecules.

4.2 Supramolecular Architectures Based on the Synthons

Despite their huge size, the supramolecules do aggregate in the crystal via specific patterns of intermolecular interactions introduced in Sect. 4.1 as synthons. The supramolecular architectures are mainly based on the most frequent σ–π supramolecular synthon; it also induces the wider variety of aggregated 1D, 2D, and 3D patterns. In some cases the mutual arrangement of the superspheres is provided by this synthon only. The resulting agglomerates can be 2D with Kagome (**kgm**[2] in **15**, **16**)

[2] Hereinafter bold-typed symbols correspond to the notation used in RCSR database, http://rcsr.net [144, 145]

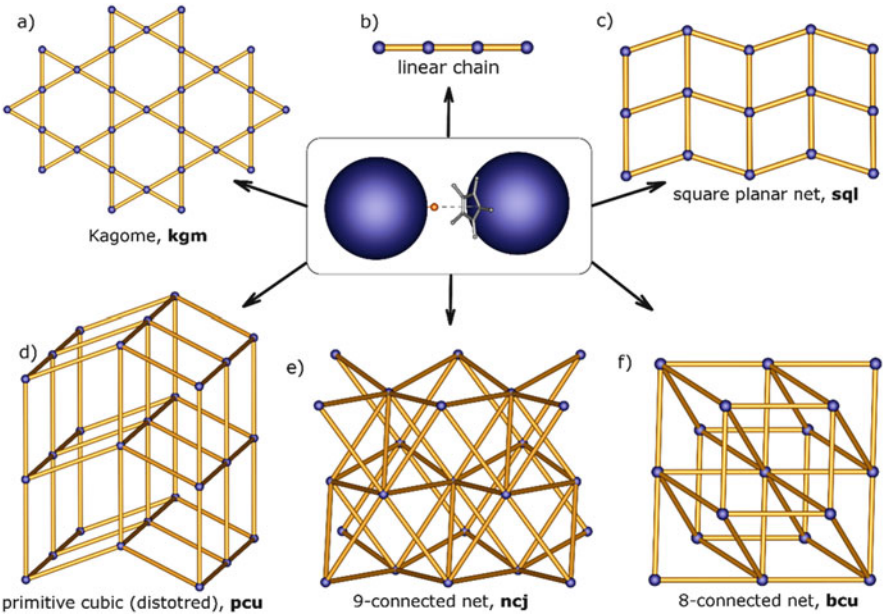

Fig. 41 The supramolecular architectures (**a**–**f**) in the structures of superspheres based on the σ–π supramolecular synthon

or square (**sql**) pattern (**29**), as well as 3D with primitive cubic (**pcu**) and 9-connected **ncj** net (Fig. 41). The **sql** and **pcu** nets are geometrically distorted because the Cp* ligands and CuX units in all the fullerene-like superspheres are naturally inclined by ~72°. Both arrangements require 90° between the synthons for the most symmetrical case. In the same time, the smallest possible angle of ~57° enables the almost undistorted triangular Kagome pattern (Fig. 42a). The superspheres of the same type are capable of different patterns via specific combinations of the synthons [138].

As discussed before, the π–π synthon is rarer. It provides only low-dimensional patterns, namely, a zigzag chain in **19** and **23**, and hexagonal and square layers (**20**, **28**). Moreover, the π–π synthon always appears together with the σ–π one; the latter always increases the dimensionality of the π–π-based assembly to 3D (Fig. 43). For example, σ–π-based puckered square nets in **19** in combination with the zigzag chain (Fig. 42c, d) form a peculiar 6,7-connected framework (Fig. 43b). The π–π-based hexagonal layers in **20** (Fig. 42h) are joined to each other via σ–π synthons resulting in a primitive hexagonal (**hex**) framework (Fig. 43a). Similarly, both **pcu** and **fcu** architectures involve π–π-based square layers when combined either with σ–π-based square layers or with **bcu** motifs, respectively (Fig. 43c, e).

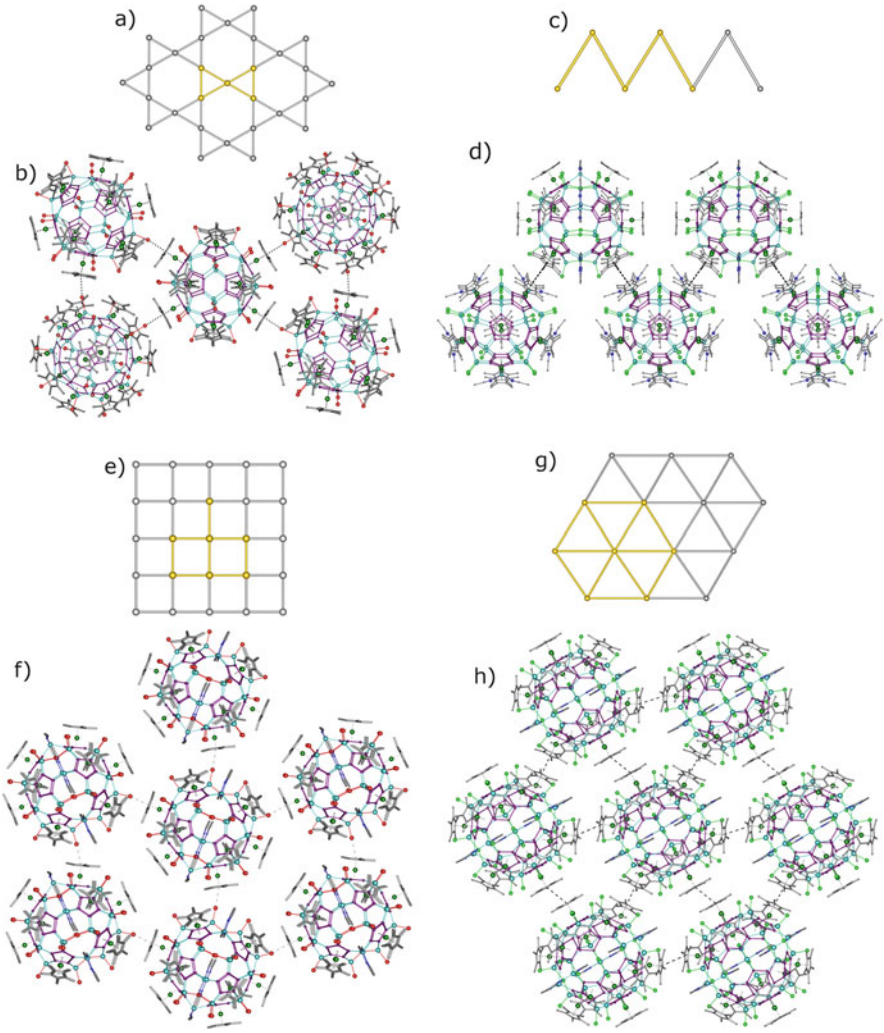

Fig. 42 An example of supramolecular assemblies based on the σ–π or π–π supramolecular synthons: (**a**) Kagome pattern in (**b**) **16**, (**c**) zigzag chain in (**d**) **19**, (**e**) **sql** in (**f**) **24**, and (**g**) trigonal layer in (**h**) **20**. The yellow highlight corresponds to the depicted patterns of the superspheres

The predetermined arrangement of CuX and FeCp* functional groups in the supramolecule impedes the synthon geometry requirements. Together with steric factors, this eventually limits the ability of the supramolecule to form the synthons. Therefore, some supramolecules are only involved in nondirectional van der Waals interactions. Thus, these supramolecular architectures span the molecular packings that will be discussed in the following section.

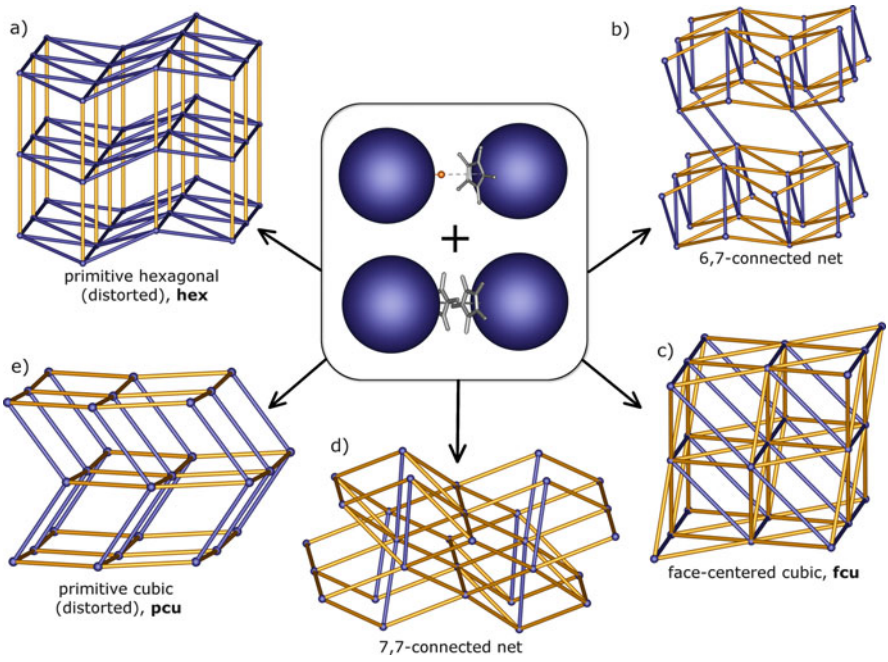

Fig. 43 The 3D supramolecular architectures built on σ–π and π–π supramolecular synthons. *Yellow and blue edges* correspond to the σ–π and the π–π synthons, respectively

5 Do the Superspheres Form Close Sphere Packing?

The peculiarity of pentaphosphoferrocene-based supramolecules is their nearly spherical shape. It makes them an unusual bridge between traditional crystal chemistry with its major concept of the closest packing of spheres and supramolecular chemistry [146]. In this section the packing motifs observed in the crystal structures of the superspheres are discussed in comparison with the packing of equisized spheres. To denote a packing, well-known traditional notations[3] are used alongside with symbols of 3D nets [144, 145].

The supramolecules expectedly demonstrate one of three packing motifs known for equal spheres: three-layered cubic close (f.c.c.), two-layered hexagonal close (h.c.p.), and body-centered cubic (b.c.c.) (Fig. 44). The packing motif does not depend on the crystallographic symmetry that varies from triclinic to cubic space groups (Table 2). In the cubic structures, the corresponding packing motif is geometrically ideal and is distorted in the less symmetrical structures.

[3] In these notations, common packings as face-centered cubic (f.c.c.) are also known as **fcu** net, hexagonal close packing (h.c.p.) as **hcp**, and body-centered cubic as **bcu-x** type.

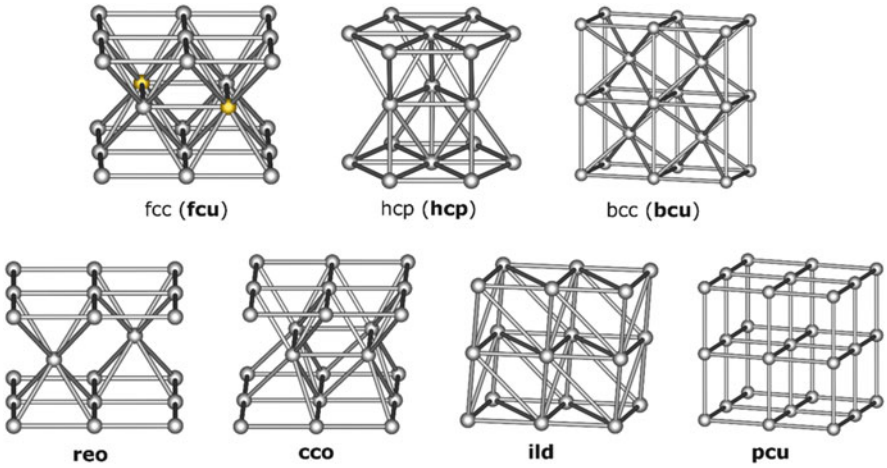

Fig. 44 Idealized nets corresponding to the packing motifs observed in the structures of supramolecules (cf. Table 2). When yellow balls are removed from f.c.c., **reo** is realized

The f.c.c. packing motif is realized in the structures of nearly all supramolecules with non-fullerene topology except for **32**. The crystal packing in compound **28** also can be described as f.c.c. packing of $[\{Cp^*FeP_5\}_9\{CuCl\}_{10}]_2$ dimers.

The hexagonal close packing motif is observed in four crystal structures of the 90-vertex superspheres **18**, **23**, **24**, and **20**. The body-centered cubic motif was found in the structures of the 80-vertex supramolecules based on **1c** (**2**–**11**), in one of the 90-vertex supersphere, **22**, and in the structure of giant tetrahedral-shaped supramolecule **32**. In the structures of **25** and **27**, the b.c.c. packing is seriously distorted to form a 10-connected **cco** net as four of the 14 neighboring supramolecules are by ca. ~20 % more distant than the ten nearest ones. Taking into account both ten close and four farther neighbors, the resulting packing corresponds to b.c.c.[4]

Surprisingly, the packing of supramolecules not always falls into these common types. In the crystal, the supramolecules **35** occupy special positions (0 0 ½) on the inversion point of the C_{3i} axis of the space group $R\bar{3}$ (Table 2). At a first sight, a combination of the special position and the rhombohedral translations should result in the three-layered f.c.c. packing motif. In fact, another packing motif, **ild**, is realized. Every supramolecule in **35** is surrounded by 12 and 44 neighbors in the first and the second coordination spheres as in f.c.c. The difference appears only in the third coordination sphere of the supramolecule, which comprises 98 molecules instead of 96 in f.c.c. In addition, the **ild** sphere packing has a packing coefficient of 53.7 %,[5] which is less than that of 74 % known for f.c.c. packing. The nearest

[4] With additional four edges taken into account, the **cco** net transforms to **bcu-x** (b.c.c.).

[5] Calculated from the crystallographic data for an idealized net stored in RCSR database, http://rcsr.net/nets/ild

Table 2 Crystal packing motifs in the structures of pentaphosphaferrocene-based supramolecules

No	Formula	Refcode[a]	Sp. gr.	Site symm[b]	CN[c]	Motif[d]
17	$[\{Cp^{BIG}FeP_5\}_{12}Cu_{69.45}Br_{82.70}] \cdot 0.34CH_2Cl_2 \cdot 1.3MeCN$	YUZQOB	*C*2/*c*	C_2	12	**fcu**
26	$[Cp^*FeP_5]@[(Cp^*FeP_5)_{12}(CuBr)_{25}(MeCN)_{10}] \cdot 5C_7H_8 \cdot 17.7MeCN$	GUSLOW	*Cmc*2_1	C_s	12	**fcu**
29	$C_{60}@[\{Cp^*FeP_5\}_{13}(CuCl)_{26}(H_2O)_2(CH_3CN)_9] \cdot 6C_6H_4Cl_2 \cdot MeCN$	COVBAR	*Pnma*	C_s	12	**fcu**
31	$As_4@[\{Cp^*FeP_5\}_{10}(CuI)_{29.6}(MeCN)_6] \cdot 4.2MeCN$	DISCOZ	*P*2_1/*n*	C_i	12	**fcu**
33	$(CH_2Cl_2)_{3.4}@[(Cp^{Bn}FeP_5)_{12}\{CuI\}_{54}(MeCN)_{1.46}]$	BORDOD	$P\bar{1}$	C_i	12	**fcu**
34	$[\{Cp^{Bn}FeP_5\}_{24}(CuBr)_{96}] \cdot 6.2(CH_2Cl_2) \cdot 4.6(C_7H_8) \cdot 2.4(MeCN)$	SURMID	*I*222	D_2	12	**fcu**
28	$[Cp^*FeP_5]@[\{Cp^*FeP_5\}_9\{CuCl\}_{10}] \cdot 2(C_7H_8)$	OLIWIQ	*P*2_1/*n*	C_i	12	**fcu**
18	$[Cu(MeCN)_4]^+[\{Cp^*FeP_5\}_{0.5}@(Cp^*FeP_5)_{12}(CuCl)_{25}(MeCN)_{10}]_3\ \{Cp^*FeP_5\}_{0.5}@[(Cp^*FeP_5)_{12}Cu_{24}Cl_{25}(MeCN)_8]^- \cdot 34CH_2Cl_2$	BAPFOO	$P\bar{1}$	C_i	12	**hcp**
20	$[Cp^*FeP_5]_{0.6}@[(Cp^*FeP_5)_{12}(CuCl)_{25}(MeCN)_{10}] \cdot 9.5THF \cdot 2MeCN$	GUSKOV	$P\bar{1}$	C_i	12	**hcp**
23	$[Cp^*FeP_5]@[(Cp^*FeP_5)_{12}(CuBr)_{25}(MeCN)_{10}] \cdot 2.9C_6H_4Cl_2 \cdot 3.9MeCN$	GUSLAI	*Pbca*	C_1	12	**hcp**
24	$[Cp^*FeP_5]@[(Cp^*FeP_5)_{12}(CuBr)_{25}(MeCN)_{10}] \cdot 2.1C_6H_4Cl_2 \cdot MeCN$	GUSLEM	*Pbcm*	C_s	12	**hcp**
2	$(CH_2Cl_2)@[(Cp^{Bn}FeP_5)_{12}(CuCl)_{20}] \cdot 4.8C_7H_8$	IHAQEP	*Pm*$\bar{3}$*n*	T_h	14	**bcu-x**
22	$[Cp^{Et}FeP_5]@[(Cp^{Et}FeP_5)_{12}(CuBr)_{25}(MeCN)_{10}] \cdot 2CH_2Cl_2 \cdot 1.5MeCN$	TAXDAY	*Cm*	C_s	14	**bcu-x**
32	$[\{Cp^{Bn}FeP_5\}_{12}(CuBr)_{51}(MeCN)_8]$	IHAQUF	*Fddd*	C_2	14	**bcu-x**
25	$[Cp^*FeP_5]@[(Cp^*FeP_5)_{12}(CuBr)_{25}(MeCN)_{10}] \cdot 10.4C_7H_8 \cdot 0.8MeCN$	GUSLIQ	*Cmc*2_1	C_s	10	**cco**
27	$[Cp_2Cr_2(\mu,\eta^5\text{-}As_5)]@[(Cp^*FeP_5)_{12}(CuBr)_{25}(MeCN)_{10}] \cdot 10C_7H_8 \cdot 3MeCN$	TATVAN	*Cmc*2_1	C_s	10	**cco**
12	$(C_2B_{10}H_{12})_{0.5}@[(Cp^*FeP_5)_{12}(CuCl)_{20}]$	SURYIO	*Fm*$\bar{3}$*c*	T_h	6	**pcu**
16	$(o\text{-}C_2B_{10}H_{12})_{0.5}@[(Cp^*FeP_5)_{12}(CuBr)_{18.8}] \cdot 7.33C_7H_8 \cdot 0.67MeCN$	KUCJEZ	$P\bar{1}$	C_i	8	**reo**
19	$[Cp^*FeP_5]_{0.5}@[(Cp^*FeP_5)_{12}(CuCl)_{25}(MeCN)_{10}] \cdot 6CH_2Cl_2 \cdot 1.5MeCN$	GUSKIP	*Pbam*	C_s	12,13	**12,13T2**
21	$[Cp^*FeP_5]_{0.5}@[(Cp^*FeP_5)_{12}Cu_{25}Cl_{24}(MeCN)_9]$ $[Cp^*FeP_5]0.5@[(Cp^*FeP_5)_{12}Cu_{25}Cl_{26}(MeCN)_9] \cdot 12C_7H_8 \cdot 1.5MeCN$	GUSKUB	$P\bar{1}$	C_1	11, 12	*new*[e]
35	$[\{Cp''Ta(CO)_2(P_4)\}_6\{CuCl\}_8] \cdot CH_2Cl_2$	TEFNUO	$R\bar{3}$	C_{3i}	12	**ild**

[a]Reference code in the Cambridge Structural Database (CSD) [103]
[b]Crystallographic site symmetry of the supramolecule
[c]The number of neighboring supramolecules
[d]Symbol of the corresponding topological type according to symbols used in RCSR and ToposPro databases [144, 145]. Each net can be accessed via http://rcsr.net/nets/<net symbol>
[e]Topological type is not listed in RCSR and ToposPro databases

environment of the node in the *idealized* **ild** and **fcu** nets is also quite different, but the distortion in the crystal structure of the supramolecules can make the visual determination of the exact packing motif ambiguous.

In the ionic compound **21**, the cation $[(Cp^*FeP_5)_{12}Cu_{25}Cl_{24}(MeCN)_9]^+$ and the anion $[(Cp^*FeP_5)_{12}Cu_{25}Cl_{26}(MeCN)_9]^-$ have different environments. Every cation is surrounded by five cations and seven anions, while every anion has only 11 neighbors (seven cations and four anions). Corresponding 11,12-connected net belongs to a yet unlisted packing type, but most probably it is related to 12-connected f.c.c. or h.c.p. and might be treated as their distortion. Analogously, two crystallographically unique supramolecules in **19** have a different environment. The resulting crystal packing belongs to a rare **12,13T2** type (Table 2).

The crystal structures of the giant supramolecules possess huge intermolecular voids. Even an optimal close sphere packing of the supramolecules leaves enough space for numerous solvent molecules. In **18** the number of only localized CH_2Cl_2 molecules amounts to 34. The theoretical radius of the, e.g., octahedral void in the f.c.c. packing is equal to 41 % of the radius of a sphere. Therefore, for supramolecules with diameters of 3–4 nm, the expected diameter of the void is 1.2–1.6 nm. Indeed, the huge supramolecules **17** and **33** demonstrate f.c.c. packing motifs, and the volume of the intermolecular voids reaches 537 and 1,810 $Å^3$ per supramolecule, respectively [93, 100]. Because of the lack of strong intermolecular interactions, the solvent molecules are mostly disordered, and in many cases their localization by SC-XRD becomes impossible even at low temperature.

The f.c.c. and h.c.p. structural motifs are optimal sphere packings, and for superspheres they have minimal possible though still huge voids. Therefore, the appearance of much less dense packing motifs is hardly expected in view of crystal stability. Nevertheless, the **1a**-derived 80-vertex supramolecules form low-dense **reo**[6] and primitive cubic packing motifs (Table 2, Figs. 45 and 46) [90–92, 94–96].

The **reo** motif can be interpreted as face-centered cubic packing, where one of every four spheres is removed in a regular way (Fig. 44). The packing coefficient is thus equal to ¾ of those of f.c.c., namely, 74 % × 3/4 = 55.5 %. As a result, every supramolecule is surrounded by eight neighboring ones instead of 12 in f.c.c. The triclinic unit cell in both isostructural compounds **15** and **16** is metrically *pseudo*-cubic. In addition to the pseudo-merohedral twinning, it makes crystal packing to be almost undistorted from an ideal **reo** (Fig. 46a) [92]. A huge cavity between the supramolecules corresponds to a "missing sphere" in f.c.c. In the structure, it is filled with partly disordered solvent molecules (Fig. 46c).

The ideal primitive cubic packing is surprisingly realized in a series of isostructural compounds **12–14**. They crystallize in the cubic space group $Fm\bar{3}c$, where 80-vertex supramolecules occupy edge-, face-, and body-centered positions of the face-centered cubic cell. The distance between the centers of the supramolecules is equal to $a/2$ (Fig. 45). This packing is even less dense than the **reo** type found for **15** and **16**. Indeed, the packing coefficient of the ideal **reo**

[6] Arrangement of oxygen atoms in the ReO_3 or cubic perovskite structures

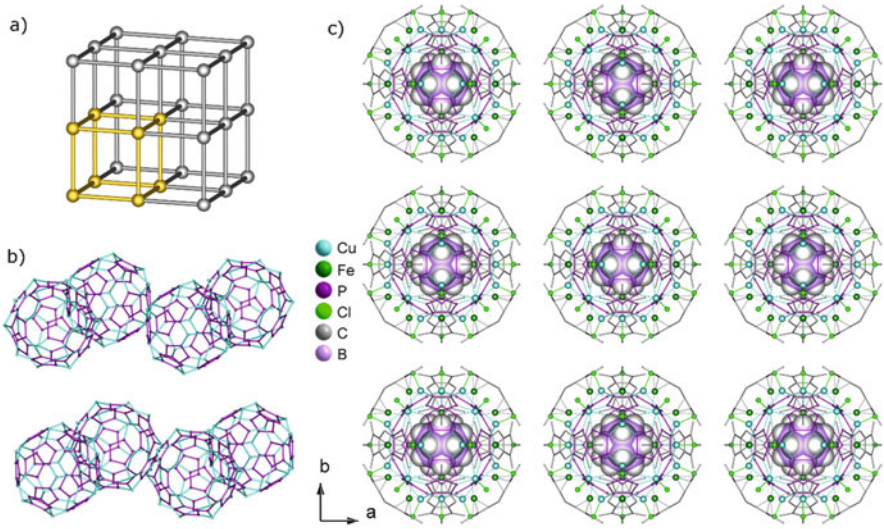

Fig. 45 (**a**) An ideal **pcu** motif; (**b**) the same motif (highlighted in *yellow* in (**a**)) formed by superspheres in **12**; only copper (*blue*) and phosphorus (*purple*) atoms are shown for clarity; (**c**) a primitive cubic crystal packing

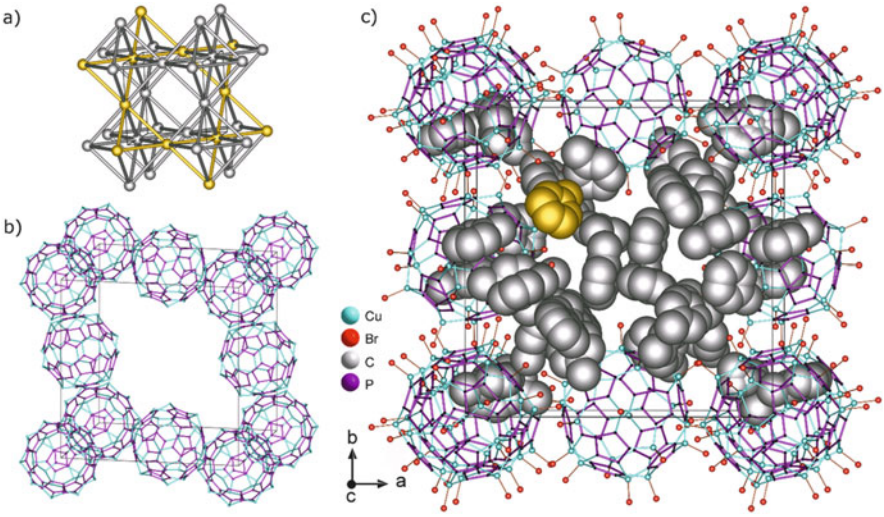

Fig. 46 (**a**) An ideal **reo** topological motif (Kagome layer is highlighted in *yellow*); (**b**) a large cavity provided by this motif (only 90-vertex shells are shown); (**c**) the same motif in a crystal packing in **16**. Fe and H atoms, Cp* ligands, and $C_2B_{10}H_{12}$ guest molecules are omitted for clarity; toluene solvent molecules are presented in space-filling mode; one of them is shown in yellow

packing is only 52.4 % (cf. with 74 % for f.c.c.). As a result, the crystals, which are quite stable in the mother solution, very quickly lose solvent and crystallinity out of it [91].

The reason why the 80-vertex supramolecules based on **1a** form so low-dense packings as **reo** and primitive cubic is not yet clear. The **reo** packing might occur due to **kgm** supramolecular synthon-based assenblies. One should bear in mind that huge cavities in the crystal packing are compatible by size with the supramolecules themselves. These cavities should be stuffed with solvent molecules to stabilize low-dense crystal packings. Unfortunately, the localization of the solvent molecules faces many objective obstacles. In **15** and **16**, especially in the latter, we succeeded in the localization of some disordered solvent molecules toluene and MeCN lying in the cavity between the supramolecules (Fig. 46c). Calculations of an empty space in **16** still reveal total potential volume of 1,692 $Å^3$ per supramolecule accessible for solvent [147]. In the case of cubic **12–14**, it appears to be impossible to localize solvent molecules. In this case calculations show even larger potential volume of 4,036 $Å^3$ per supramolecule containing 1,432 e^- that would correspond to 28 toluene or 65 MeCN molecules.

Thus in most cases, the crystal packing of pentaphosphaferrocene-based supramolecules can be described as sphere packing according to three common motifs: face-centered cubic, hexagonal close, and body-centered cubic. In some cases the distortion of the packing leads to less common motifs like **cco** and **ild**. The cavities between supramolecules are filled with disordered solvent molecules that in most cases could not be localized completely. The most interesting and unexpected packing motifs, **reo** and ideal primitive cubic, are observed for 80-vertex supramolecules based on **1a**. The latter, being the least dense, is responsible for easy amorphization of the crystals in air.

6 Summary and Concluding Remarks

Among complexes containing cyclic and cage-like E_n ligands (E=pnictogen or chalcogen), the pentaphosphaferrocenes possess a unique ability to give rise to an abundance of compounds. The presence of a rigid and chemically stable pentagonal P_5 ring makes the pentaphosphaferrocenes a versatile building block in supramolecular chemistry. The coordination of Cu^+ units to the *cyclo*-P_5 ligand results in numerous novel products. The self-assembled spherical supermolecules can be isolated in high yields and contain up to hundreds of non-carbon atoms. A tetrahedral coordination of copper together with the predetermined fivefold symmetry of the *cyclo*-P_5 ligand favors the formation of giant hollow cages. Among them, the one-shell superspheres, in which five-membered *cyclo*-P_5 units alternate with Cu_2P_4 six-membered rings, possess icosahedral I_h-C_{80} fullerene topology. A multi-shell supramolecule built up from 12 *cyclo*-P_5 units and 60 six-membered P_2Cu_3Br rings represents an inorganic analog of the theoretically predicted icosahedral *I*-C_{140} fullerene. A series of supramolecules consist of fullerene-like

fragments, where the spherical 90- and 99-vertex inorganic scaffolds as well as ellipsoidal nano-capsules can be obtained quantitatively.

The ability of copper halides for aggregation opens the gate to more sophisticated supramolecules beyond the fullerene topology. They do not exclusively consist of 12 *cyclo*-P_5 units but also of eight and even 24 pentaphosphaferrocene building blocks and contain 100, 162, and 168 vertices in the inorganic core. In addition the largest supramolecule with unprecedented 312 core atoms achieves nanoscale dimensions of 3.7×4.6 nm and is 62 times larger than one molecule of the C_{60} fullerene. The way to these larger supramolecules lies in variation of the steric demand of the substituents at the cyclopentadienyl ring of the pentaphosphaferrocene. In this manner the size and solubility of the products can be controlled. By changing the mixtures of solvents, one can switch between the supramolecules with fullerene and non-fullerene topologies.

These amazing self-assemblies can also encapsulate various guests, starting from small, air-sensitive P_4, and light-sensitive As_4 molecules and ending with the fullerene C_{60}. Thereby the ferrocene and pentaphosphaferrocene molecules interact with the host molecule by means of specific π-stacking with its aromatic P_5 rings.

Since the self-assembly process of such a complicated supramolecular structures is not entirely specific, the structural variations in replication of the supramolecules occur. Therefore, in the crystal the supramolecules with and without structural divergence co-crystallize and form solid solutions. For this reason, the molecular structure of a supersphere can demonstrate isomerism and be complete or porous through the presence or absence not only of single atoms but also of polyatomic fragments.

The supramolecules are capable for halogen–π and π–π intermolecular interactions. Unexpectedly, the reproducible patterns – the supramolecular synthons – allow additional agglomeration of superspheres in the crystal. The resulting supramolecular assemblies enumerate a variety of 1D to 3D connectivities. These assemblies span molecular packings, which in turn demonstrate structural motifs from classical close packings of rigid identical spheres to unexpected low-dense packings.

Acknowledgments The European Research Council (ERC) is acknowledged for the support in the SELFPHOS AdG339072 project. C.H. is grateful for a Ph.D. fellowship of the Fonds der Chemischen Industrie.

References

1. Kopilevich S, Gil A, Garcia-Rates M, Bonet-Avalos J, Bo C, Müller A, Weinstock IA (2012) J Am Chem Soc 134:13082–13088
2. Schaeffer C, Todea AM, Boegge H, Cadot E, Gouzerh P, Kopilevich S, Weinstock IA, Mueller A (2011) Angew Chem Int Ed 50:12326–12329
3. Long DL, Tsunashima R, Cronin L (2010) Angew Chem Int Ed 49:1736–1758

4. Berzelius JJ (1826) Poggendorffs Ann Phys Chem 6:369–392
5. Pope MT, Mueller A (1991) Angew Chem 103:56–70
6. Mueller A, Botar B, Das SK, Boegge H, Schmidtmann M, Merca A (2004) Polyhedron 23:2381–2385
7. Müller A, Beckmann E, Bögge H, Schmidtmann M, Dress A (2002) Angew Chem Int Ed 41:1162–1167
8. Mehring M (2016) Large metal oxide clusters. Struct Bond. doi:10.1007/430_2016_4
9. Anson C, Eichhöfer A, Issac I, Fenske D, Fuhr O, Sevillano P, Persau C, Stalke D, Zhang J (2008) Angew Chem Int Ed 47:1326–1331
10. Corrigan JF (2016) Large metal chalcogenide clusters. Struct Bond. doi:10.1007/430_2016_5
11. Fuhr O, Dehnen S, Fenske D (2013) Chem Soc Rev 42:1871–1906
12. Corrigan JF, Fuhr O, Fenske D (2009) Adv Mater 21:1867–1871
13. Liu Y, Khalili-Najafabadi B, Azizpoor-Fard M, Corrigan JF (2015) Angew Chem 127:4914–4917
14. Schnöckel H, Schnepf A, Whetten RL, Schenk C, Henke P (2011) Z Anorg Allg Chem 637:15–23
15. Schnöckel H, Schnepf A (2011) Aluminium and Gallium Clusters. Wiley, Hoboken, p 402
16. Vollet J, Hartig JR, Schnöckel H (2004) Angew Chem Int Ed 43:3186–3189
17. Schnepf A, Jee B, Schnöckel H, Weckert E, Meents A, Luebbert D, Herrling E, Pilawa B (2003) Inorg Chem 42:7731–7733
18. Schnepf A, Schnöckel H (2001) Angew Chem Int Ed 40:712–715
19. Fässler TF (2011) Struct Bond 140:91–131
20. Lin Y, Massa W, Dehnen S (2012) J Am Chem Soc 134:4497–4500
21. Lips F, Dehnen S (2009) Angew Chem Int Ed 48:6435–6438
22. Dehnen S (2015) Binary and ternary intermetalloid clusters. Struct Bond. doi:10.1007/430_2015_5002
23. Jadzinsky PD, Calero G, Ackerson CJ, Bushnell DA, Kornberg RD (2007) Science 318:430–433
24. Dass A, Theivendran S, Nimmala PR, Kumara C, Jupally VR, Fortunelli A, Sementa L, Barcaro G, Zuo X, Noll BC (2015) J Am Chem Soc 137:4610–4613
25. Mednikov EG, Jewell MC, Dahl LF (2007) J Am Chem Soc 129:11619–11630
26. Tran NT, Powell DR, Dahl LF (2000) Angew Chem 112:4287–4291
27. Vargaftik MN, Moiseev II, Kochubey DI, Zamaraev KI (1991) Faraday Discuss 92:13–29
28. Constable EC (1994) Chem Ind 2:56–59
29. Lehn JM (1995) Supramolecular Chemistry. Wiley-VCH, Weinheim
30. Lehn JM, Rigault A, Siegel J, Harrowfield J, Chevrier B, Moras D (1987) Proc Natl Acad Sci USA 84:2565–2569
31. Zarra S, Wood DM, Roberts DA, Nitschke JR (2015) Chem Soc Rev 44:419–432
32. Meng W, League AB, Ronson TK, Clegg JK, Isley WC, Semrouni D, Gagliardi L, Cramer CJ, Nitschke JR (2014) J Am Chem Soc 136:3972–3980
33. Young NJ, Hay BP (2013) Chem Commun 49:1354–1379
34. Cook TR, Zheng YR, Stang PJ (2013) Chem Rev 113:734–777
35. Mugridge JS, Bergman RG, Raymond KN (2012) J Am Chem Soc 134:2057–2066
36. Saalfrank RW, Scheurer A (2012) Top Curr Chem 319:125–170
37. Laughrey Z, Gibb BC, Laughrey Z, Gibb BC (2011) Chem Soc Rev 40:363–386
38. Dalgarno SJ, Power NP, Atwood JL (2008) Coord Chem Rev 252:825–841
39. Chen L, Chen Q, Wu M, Jiang F, Hong M (2015) Acc Chem Res 48:201–210
40. Cullen W, Turega S, Hunter CA, Ward MD (2015) Chem Sci 6:625–631
41. Ajami D, Rebek J (2013) Acc Chem Res 46:990–999
42. Jin P, Dalgarno SJ, Atwood JL (2010) Coord Chem Rev 254:1760–1768
43. Mal P, Breiner B, Rissanen K, Nitschke JR (2009) Science 324:1697–1701
44. Pluth MD, Bergman RG, Raymond KN (2007) Science 316:85–88
45. Sato S, Iida J, Suzuki K, Kawano M, Ozeki T, Fujita M (2006) Science 313:1273–1276

46. Steinfeld G, Lozan V, Krüger HJ, Kersting B (2009) Angew Chem Int Ed 48:1954–1957
47. Brown CJ, Toste FD, Bergman RG, Raymond KN (2015) Chem Rev 115:3012–3035
48. Hastings CJ, Pluth MD, Bergman RG, Raymond KN (2010) J Am Chem Soc 132:6938–6945
49. Pluth MD, Bergman RG, Raymond KN (2007) Angew Chem Int Ed 46:8587–8589
50. Yoshizawa M, Tamura M, Fujita M (2006) Science 312:251–254
51. Fujita M, Tominaga M, Hori A, Therrien B (2005) Acc Chem Res 38:369–378
52. Inokuma Y, Kawano M, Fujita M (2011) Nat Chem 3:349–358
53. Klosterman JK, Iwamura M, Tahara T, Fujita M (2009) J Am Chem Soc 131:9478–9479
54. Sato S, Ishido Y, Fujita M (2009) J Am Chem Soc 131:6064–6065
55. Sun QF, Iwasa J, Ogawa D, Ishido Y, Sato S, Ozeki T, Sei Y, Yamaguchi K, Fujita M (2010) Science 328:1144–1147
56. Sun WY, Yoshizawa M, Kusukawa T, Fujita M (2002) Curr Opin Chem Biol 6:757–764
57. Yoshizawa M, Klosterman JK, Fujita M (2009) Angew Chem Int Ed 48:3418–3438
58. Inokuma Y, Yoshioka S, Ariyoshi J, Arai T, Hitora Y, Takada K, Matsunaga S, Rissanen K, Fujita M (2013) Nature 495:461–466
59. Li S, Huang J, Zhou F, Cook TR, Yan X, Ye Y, Zhu B, Zheng B, Stang PJ (2014) J Am Chem Soc 136:5908–5911
60. Vajpayee V, Song YH, Cook TR, Kim H, Lee Y, Stang PJ, Chi KW (2011) J Am Chem Soc 133:19646–19649
61. Kaphan DM, Lewin MD, Bergman RG, Raymond KN, Toste FD (2015) Science 350:1235–1238
62. Zhao CF, Sun QF, Hart-Cooper WM, Di Pasquale AG, Toste FD, Bergman RG, Raymond KN (2013) J Am Chem Soc 135:18802–18805
63. Wang ZJ, Clary KN, Bergman RG, Raymond KN, Toste FD (2013) Nat Chem 5:100–103
64. Pluth MD, Raymond KN (2007) Chem Soc Rev 36:161–171
65. Williams AF (2011) Coord Chem Rev 255:2104–2110
66. Nakanishi T (2010) Chem Commun 46:3425–3436
67. Dresselhaus MS, Dresselhaus G, Eklund PC (1996) Science of fullerenes and carbon nanotubes. Academic, Cambridge
68. Fowler PW, Manolopoulos DE (1995) An atlas of fullerenes. Clarendon, Oxford
69. Kroto HW, Heath JR, O'Brien SC, Curl RF, Smalley RE (1985) Nature 318:162–163
70. Oms O, Jarrosson T, Tong LH, Vaccaro A, Bernardinelli G, Williams AF (2009) Chem Eur J 15:5012–5022
71. Tong LH, Guenee L, Williams AF (2011) Inorg Chem 50:2450–2452
72. Less RJ, Wilson TC, Guan B, McPartlin M, Steiner A, Wood PT, Wright DS (2013) Eur J Inorg Chem:1161–1169
73. Bacsa J, Less RJ, Skelton HE, Soracevic Z, Steiner A, Wilson TC, Wood PT, Wright DS (2011) Angew Chem Int Ed 50:8279–8282
74. Webster OW (1966) J Am Chem Soc 88:4055–4060
75. Müller A, Krickemeyer E, Bögge H, Schmidtmann M, Peters F (1998) Angew Chem Int Ed 37:3359–3363
76. Schaffer C, Todea AM, Gouzerh P, Muller A (2012) Chem Commun 48:350–352
77. Todea AM, Merca A, Bögge H, van Slageren J, Dressel M, Engelhardt L, Luban M, Glaser T, Henry M, Müller A (2007) Angew Chem Int Ed 46:6106–6110
78. Muller A, Todea AM, Bogge H, van Slageren J, Dressel M, Stammler A, Rusu M (2006) Chem Commun 3066–3068
79. Detzel M, Mohr T, Scherer OJ, Wolmershäuser G (1994) Angew Chem 106:1142–1144
80. Scherer OJ, Brück T (1987) Angew Chem 99:59
81. Scherer OJ, Brück T, Wolmershäuser G (1988) Chem Ber 121:935–938
82. Dielmann F, Merkle R, Heinl S, Scheer M (2009) Z Naturforsh B 64:3–10
83. Heinl S, Balazs G, Scheer M (2014) Phosphorus Sulfur Silicon Relat Elem 189:924–932
84. Peng R, Li M, Li D (2010) Coord Chem Rev 254:1–18
85. Arnby CH, Jagner S, Dance I (2004) CrystEngComm 6:257–275

86. Hartl H, Fuchs J (1986) Angew Chem Int Ed 25:569–570
87. Dielmann F, Schindler A, Scheuermayer S, Bai J, Merkle R, Zabel M, Virovets AV, Peresypkina EV, Brunklaus G, Eckert H, Scheer M (2012) Chem Eur J 18:1168–1179
88. Bai J, Virovets AV, Scheer M (2002) Angew Chem Int Ed 41:1737–1740
89. Dielmann F, Fleischmann M, Heindl C, Peresypkina EV, Virovets AV, Gschwind RM, Scheer M (2015) Chem Eur J 21:6208–6214
90. Schindler A, Heindl C, Balazs G, Groeger C, Virovets AV, Peresypkina EV, Scheer M (2012) Chem Eur J 18:829–835
91. Scheer M, Schindler A, Gröger C, Virovets AV, Peresypkina EV (2009) Angew Chem Int Ed 48:5046–5049
92. Peresypkina EV, Heindl C, Schindler A, Bodensteiner M, Virovets AV, Scheer M (2014) Z Kristallogr – Cryst Mater 229:735–740
93. Heinl S, Peresypkina E, Sutter J, Scheer M (2015) Angew Chem Int Ed 54:13431–13435
94. Scheer M, Schindler A, Bai J, Johnson BP, Merkle R, Winter R, Virovets AV, Peresypkina EV, Blatov VA, Sierka M, Eckert H (2010) Chem Eur J 16:2092–2107
95. Bai J, Virovets AV, Scheer M (2003) Science 300:781–783
96. Scheer M, Bai J, Johnson BP, Merkle R, Virovets AV, Anson CE (2005) Eur J Inorg Chem 2005:4023–4026
97. Welsch S, Groeger C, Sierka M, Scheer M (2011) Angew Chem Int Ed 50:1435–1438
98. Scheer M, Schindler A, Merkle R, Johnson BP, Linseis M, Winter R, Anson CE, Virovets AV (2007) J Am Chem Soc 129:13386–13387
99. Schwarzmaier C, Schindler A, Heindl C, Scheuermayer S, Peresypkina EV, Virovets AV, Neumeier M, Gschwind R, Scheer M (2013) Angew Chem Int Ed 52:10896–10899
100. Dielmann F, Heindl C, Hastreiter F, Peresypkina EV, Virovets AV, Gschwind RM, Scheer M (2014) Angew Chem Int Ed 53:13605–13608
101. Heindl C, Peresypkina EV, Virovets AV, Kremer W, Scheer M (2015) J Am Chem Soc 137:10938–10941
102. Johnson BP, Dielmann F, Balázs G, Sierka M, Scheer M (2006) Angew Chem Int Ed 45:2473–2475
103. Allen FH (2002) Acta Crystallogr B58:380–388
104. Schwerdtfeger P, Wirz LN, Avery J (2015) Wiley Interdiscip Rev Comput Mol Sci 5:96–145
105. Schultz HP (1965) J Org Chem 30:1361–1364
106. Bhola BR, Bally T, Valente A, Cyranski MK, Dobrzycki L, Spain SM, Rempala P, Chin MR, King BT (2010) Angew Chem Int Ed 49:399–402
107. Qian W, Chuang SC, Amador RB, Jarrosson T, Sander M, Pieniazek S, Khan SI, Rubin Y (2003) J Am Chem Soc 125:2066–2067
108. Furche F, Ahlrichs R (2001) J Chem Phys 114:10362–10367
109. Wang CR, Sugai T, Kai T, Tomiyama T, Shinohara H (2000) Chem Commun 557–558
110. Hennrich FH, Michel RH, Fischer A, Richard-Schneider S, Gilb S, Kappes MM, Fuchs D, Bürk M, Kobayashi K, Nagase S (1996) Angew Chem Int Ed 35:1732–1734
111. Popov AA, Yang S, Dunsch L (2013) Chem Rev 113:5989–6113
112. Rodriguez-Fortea A, Balch AL, Poblet JM (2011) Chem Soc Rev 40:3551–3563
113. Stevenson S, Rice G, Glass T, Harich K, Cromer F, Jordan MR, Craft J, Hadju E, Bible R, Olmstead MM, Maitra K, Fisher AJ, Balch AL, Dorn HC (1999) Nature 401:55–57
114. Stevenson S, Mackey MA, Stuart MA, Phillips JP, Easterling ML, Chancellor CJ, Olmstead MM, Balch AL (2008) J Am Chem Soc 130:11844–11845
115. Yamada M, Someya C, Wakahara T, Tsuchiya T, Maeda Y, Akasaka T, Yoza K, Horn E, Liu MTH, Mizorogi ON, Nagase S (2008) J Am Chem Soc 130:1171–1176
116. Xu L, Cai W, Shao X (2006) J Phys Chem A 110:9247–9253
117. Cai W, Xu L, Shao N, Shao X, Guo Q (2005) J Chem Phys 122:184318/184311–184318/184319
118. Manna AK, Pati SK (2013) Chem Phys 426:23–30
119. Adams GB, Sankey OF, Page JB, O'Keeffe M, Drabold DA (1992) Science 256:1792–1795

120. Mantina M, Chamberlin AC, Valero R, Cramer CJ, Truhlar DG (2009) J Phys Chem A 113:5806–5812
121. Bondi A (1964) J Phys Chem 68:441–451
122. Butovskii MV, Balázs G, Bodensteiner M, Peresypkina E, Sutter J, Virovets A, Scheer M (2013) Angew Chem Int Ed 52:2972–2976
123. Lu X, Chen Z (2005) Chem Rev 105:3643–3696
124. Kietzmann H, Rochow R, Gantefor G, Eberhardt W, Vietze K, Seifert G, Fowler PW (1998) Phys Rev Lett 81:5378–5381
125. Kroto HW (1987) Nature 329:529–531
126. Wang WW, Dang JS, Zhao X (2012) Chem Phys Lett 536:77–81
127. Wang W, Dang J, Zhao X (2011) Phys Chem Chem Phys 13:14629–14635
128. Zhao X, Slanina Z, Ozawa M, Osawa E, Deota P, Tanabe K (2000) Fullerene Sci Technol 8:595–613
129. Gao YD, Herndon WC (1993) J Am Chem Soc 115:8459–8460
130. Timoshkin AY, Schaefer HF III (2005) Inorg Chem 44:843–845
131. Timoshkin AY, Schaefer HF III (2004) J Am Chem Soc 126:12141–12154
132. Timoshkin AY (2002) Inorg Chem Commun 5:274–277
133. Strout DL (2004) Chem Phys Lett 383:95–98
134. Desiraju G (1995) Angew Chem Int Ed 34:2311–2327
135. Corey EJ (1967) Pure Appl Chem 14:19–37
136. Metrangolo P, Neukirch H, Pilati T, Resnati G (2005) Acc Chem Res 38:386–395
137. Metrangolo P, Meyer F, Pilati T, Resnati G, Terraneo G (2008) Angew Chem Int Ed 47:6114–6127
138. Peresypkina E, Virovets A, Scheer M (2016) Cryst Growth Des 16:2335–2341
139. Wheeler SE, Bloom JWG (2014) J Phys Chem A 118:6133–6147
140. Adams H, Cockroft SL, Guardigli C, Hunter CA, Lawson KR, Perkins J, Spey SE, Urch CJ, Ford R (2004) ChemBioChem 5:657–665
141. de Hoog P, Gamez P, Mutikainen I, Turpeinen U, Reedijk J (2004) Angew Chem Int Ed 43:5815–5817
142. Noman A, Rahman MM, Bishop R, Craig DC, Scudder ML (2004) Org Biomol Chem 2:175–182
143. Janiak C (2000) Dalton Trans:3885–3896
144. O'Keeffe M, Peskov MA, Ramsden SJ, Yaghi OM (2008) Acc Chem Res 41:1782–1789, http://rcsr.net
145. Blatov VA, Shevchenko AP, Proserpio DM (2014) Cryst Growth Des 14:3576–3586, http://topospro.com
146. Wells AF (1984) Structural inorganic chemistry, 5th edn. Clarendon, Oxford
147. Spek AL (2009) Acta Cryst D65:148–155

Struct Bond (2017) 174: 375–376
DOI: 10.1007/430_2016_14

Published online: 10 February 2017

Erratum to: Cooperative Effects in Clusters and Oligonuclear Complexes of Transition Metals in Isolation

Gereon Niedner-Schatteburg

Erratum to: Struct Bond
DOI: 10.1007/430_2016_11

Inadvertently the position of Figure 4 and Figure 5 is interchanged. The current image of Fig. 5 should be the image of Fig. 4 and vice-versa. However the figure captions of both these figures are correct. The correct figures are given below.

The updated online version of the original chapter can be found under DOI 10.1007/430_2016_11

G. Niedner-Schatteburg (✉)
Fachbereich Chemie and State Research Center OPTIMAS, TU Kaiserslautern, 67663 Kaiserslautern, Germany
e-mail: gns@chemie.uni-kl.de

Figure 4 should be displayed as follows:

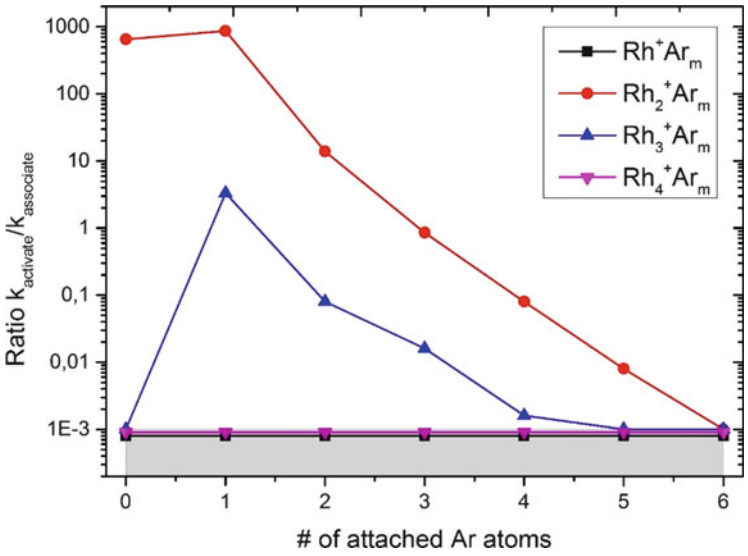

Fig. 4 Ratio of room temperature methane activation $k_{activate}$ and association $k_{associate}$ by Rh^+Ar_m clusters as a function of m. Depicted ratios of the cases Rh^+Ar_m and $Rh_4^+Ar_m$ are upper limits. Other data stem from [319] and [320] with some estimates included

Figure 5 should be displayed as follows:

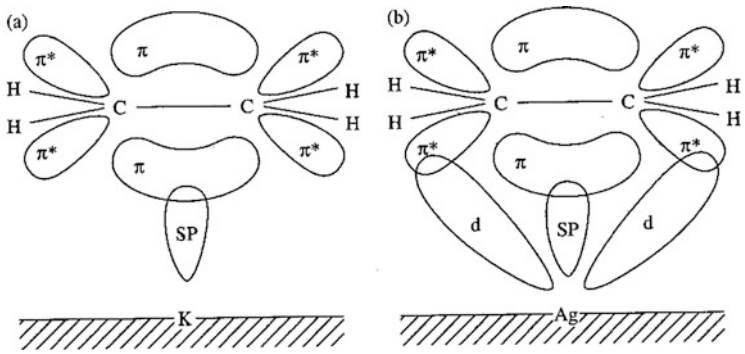

Fig. 5 Sketch of orbitals involved in olefine bonding with: (**a**) main group and (**b**) transition metal cations (reproduced with permission from [325]). Sizes are not to scale, symmetries hold. Filled d-orbitals of TMs may donate into empty π* orbitals at the olefin and enable C–C or C–H activation. Main group metals largely fail to do so. Empty or partially filled d-orbitals of early TMs may accept electron density from occupied π orbitals, likewise assisting in C–C activation

Index